materials

Special Issue Reprint

Heat Treatments and Performance of Alloy and Metal

Edited by
Xianfei Ding

mdpi.com/journal/materials

MDPI

Heat Treatments and Performance of Alloy and Metal

Heat Treatments and Performance of Alloy and Metal

Editor

Xianfei Ding

MDPI

Basel • Beijing • Wuhan • Barcelona • Belgrade • Novi Sad • Cluj • Manchester

Editor
Xianfei Ding
Cast Titanium Alloys R&D
Center
AECC Beijing Institute of
Aeronautical Materials
Beijing
China

Editorial Office
MDPI
St. Alban-Anlage 66
4052 Basel, Switzerland

This is a reprint of articles from the Special Issue published online in the open access journal *Materials* (ISSN 1996-1944) (available at: www.mdpi.com/journal/materials/special_issues/19209H23C2).

For citation purposes, cite each article independently as indicated on the article page online and as indicated below:

Lastname, A.A.; Lastname, B.B. Article Title. *Journal Name* **Year**, *Volume Number*, Page Range.

ISBN 978-3-7258-1204-2 (Hbk)
ISBN 978-3-7258-1203-5 (PDF)
doi.org/10.3390/books978-3-7258-1203-5

Contents

About the Editor

Xianfei Ding

Xianfei Ding, Ph.D., Senior Engineer, Graduate Supervisor, is currently serving as a research director at the Beijing Institute of Aeronautical Materials (BIAM). His research interests mainly focus on the design and solidification process control of high-temperature structural materials, the design, preparation, and precision casting of high-temperature titanium and titanium aluminum intermetallic compound materials, and precision forming technology such as powder metallurgy. He has received the first prize in non-ferrous metal industry technology and has presided over and undertaken more than 30 scientific research projects, including the National Science and Technology Major Project, the National 863 Project, the National Natural Science Foundation of China, and the Beijing Natural Science Foundation. Currently, he has published more than 120 papers in international journals such as A*cta Mater* and *Scripta Mater.* Moreover, he has applied for more than 30 patents, including 27 national invention patents.

Preface

This Special Issue provides readers with up-to-date information on the recent progress in the heat treatment, processing, characterization, and applications of alloys or metals, such as titanium alloys, intermetallics, superalloys, high-entropy alloys, etc. The papers published in this Special Issue are mainly in line with the following aspects: processes, properties, and performance.

Xianfei Ding
Editor

materials

MDPI

Review

Review on Progress of Lamellar Orientation Control in Directionally Solidified TiAl Alloys

Han Liu [1,2,3], Xianfei Ding [1,2,3,*], Xiao Zong [1,2,3], Hong Huang [1,2,3], Hai Nan [1,2,3], Yongfeng Liang [4] and Junpin Lin [4,*]

[1] Cast Titanium Alloy R&D Center, Beijing Institute of Aeronautical Materials, Beijing 100095, China
[2] Beijing Engineering Research Center of Advanced Titanium Alloy Precision Forming Technology, Beijing 100095, China
[3] Beijing Institute of Aeronautical Materials Co., Ltd., Beijing 100094, China
[4] State Key Laboratory for Advanced Metals and Materials, University of Science and Technology Beijing, Beijing 100083, China
* Correspondence: xianfeimail@gmail.com (X.D.); linjunpin@ustb.edu.cn (J.L.)

Abstract: TiAl alloys have excellent high-temperature performance and are potentially used in the aerospace industry. By controlling the lamellar orientation through directional solidification (DS) technology, the plasticity and strength of TiAl alloy at room temperature and high temperatures can be effectively improved. However, various difficulties lie in ensuring the lamellar orientation is parallel to the growth direction. This paper reviews two fundamental thoughts for lamellar orientation control: using seed crystals and controlling the solidification path. Multiple specific methods and their progress are introduced, including α seed crystal method, the self-seeding method, the double DS self-seeding method, the quasi-seeding method, the pure metal seeding method, and controlling solidification parameters. The advantages and disadvantages of different methods are analyzed. This paper also introduces novel ways of controlling the lamellar orientation and discusses future development.

Keywords: TiAl alloys; directional solidification; lamellar orientation; seed crystal; solidification parameters

Citation: Liu, H.; Ding, X.; Zong, X.; Huang, H.; Nan, H.; Liang, Y.; Lin, J. Review on Progress of Lamellar Orientation Control in Directionally Solidified TiAl Alloys. *Materials* **2023**, *16*, 4829. https://doi.org/10.3390/ma16134829

Academic Editor: Francesco Iacoviello

Received: 6 June 2023
Revised: 28 June 2023
Accepted: 28 June 2023
Published: 5 July 2023

1. Introduction

The development of the aviation and aerospace industries raises higher requirements for high-temperature structural materials. Due to their low density, high specific strength, and notable high-temperature performance, TiAl alloys are gradually becoming a new generation of high-temperature structural materials, possibly replacing some Ni-based superalloys in the near future [1–3]. However, traditional TiAl alloys possess low plasticity and poor creep properties at room temperature or high temperatures, which limits their further application [4–6].

Directional solidification (DS) technology is beneficial to control the consistency of lamellar orientation and enhancing the high-temperature plasticity and creep properties of TiAl alloys [7]. Previous research has shown that directionally solidified TiAl alloys with aligned lamellae have diverse mechanical properties in different directions [8,9]. When the lamellar orientation is perpendicular to the load direction, the plasticity is relatively poor. When the lamellar orientation is parallel to the load direction, the tensile strength and elongation at room temperature are balanced and relatively high [10]. For example, Chen et al. reported that Ti-45Al-8Nb PST single crystal alloy with aligned parallel lamellae had a yield strength of 708 MPa and an average tensile ductility of 6.9% at room temperature. Moreover, at high temperatures, it still maintained the anisotropy of mechanical properties [11]. For aero-engines, the stress borne by their turbine blades is mainly unidirectional. The application of directionally solidified TiAl alloys can effectively reduce the structural weight and improve the thrust-to-weight ratio of the engine.

In previous studies, researchers have proposed two fundamental theories for controlling lamellar orientation. One is using a certain seed alloy, of which the primary phase is α or β and the solidification phase is α. It has a stable or nearly stable lamellar structure [12]. The seed crystal is placed with lamellae parallel to the growth direction to align the lamellar orientation of the master alloy. The other theory is controlling the solidification path, ensuring the leading phase is β. According to Burgers' relationship $\{110\}_\beta // (0001)_\alpha$ and $<111>_\beta \| <11\bar{2}0>_\alpha$ and Blackburn's relationship $(0001)_\alpha \| \{111\}_\gamma$ and $<11\bar{2}0>_\alpha \| <110>_\gamma$, since the preferred orientation of β phase is <100>, the final lamellar orientation is 0° or 45° to the growth direction [13].

Based on these two fundamental theories, the methods of controlling lamellar orientation can be developed from the perspectives of deciding seed alloy composition and adjusting solidification parameters. The purpose of this paper is to summarize the theories of lamellar orientation control, describe the application scope and mechanism of various methods, and look forward to novel methods for lamellar orientation control.

2. Difficulties and Critical Problems in Lamellar Orientation Control

At present, the methods of lamellar orientation control are mostly applied in the laboratory; there are few reports on the industrialized production of directionally solidified TiAl alloy bars or components. The solidification modes of multi-component TiAl alloys are not clear yet, bringing difficulties in obtaining single crystal or columnar crystals with consistent lamellar orientation. Furthermore, the application range of traditional α phase seeds remains relatively limited; the quasi-seed method [14,15] and the self-seeding method [16–18] require specific master alloy compositions.

A direct relationship exists between lamellar orientation and the growth direction of the primary phase, as shown in Figure 1 [19]. Nevertheless, factors affecting solidification paths are complicated and diverse. On the one hand, alloy composition directly affects the solidification process. Ding et al. [20] proposed that under the same solidification parameters, as the composition varies, there are four different solidification modes for different Nb-TiAl alloys, namely, single β, hypo-peritectic, hyper-peritectic, and single α. On the flip side, the solidification parameters play a critical role in determining the solidification path of a certain TiAl alloy. Growth rate and temperature gradient show great influence on the solidification paths. In most cases, certain solidification modes need to be determined by experiments.

Yamaguchi et al. [21–27] have developed a series of seed alloys suitable for DS by the optical floating zone method, such as Ti-43Al-3Si, Ti-46Al-1.5Mo-(1.0,1.2,1.5) Si, Ti-46Al-1.5Mo-0.2C, etc. Kim et al. have developed Ti-46Al-3Nb-0.6Si-0.2C [28]. Although Ti-43Al-3Si has been applied to some extent, the composition is generally different from master alloys, resulting in an uneven composition and a relatively long transition zone [12] after DS, which reduces the mechanical properties of the materials. In previous studies, the samples obtained by DS through the floating zone method had better structure and mechanical performance, but their size remained far from practical application. In order to realize the industrial application of directionally solidified alloys, a sample should possess a columnar or single crystal structure, and the lamellar orientation should be parallel to the growth direction. However, due to heat flow deflection, mold deformation, and the limitation of the continuity of grain growth, it is difficult to obtain lamellar orientation consistency in large specimens.

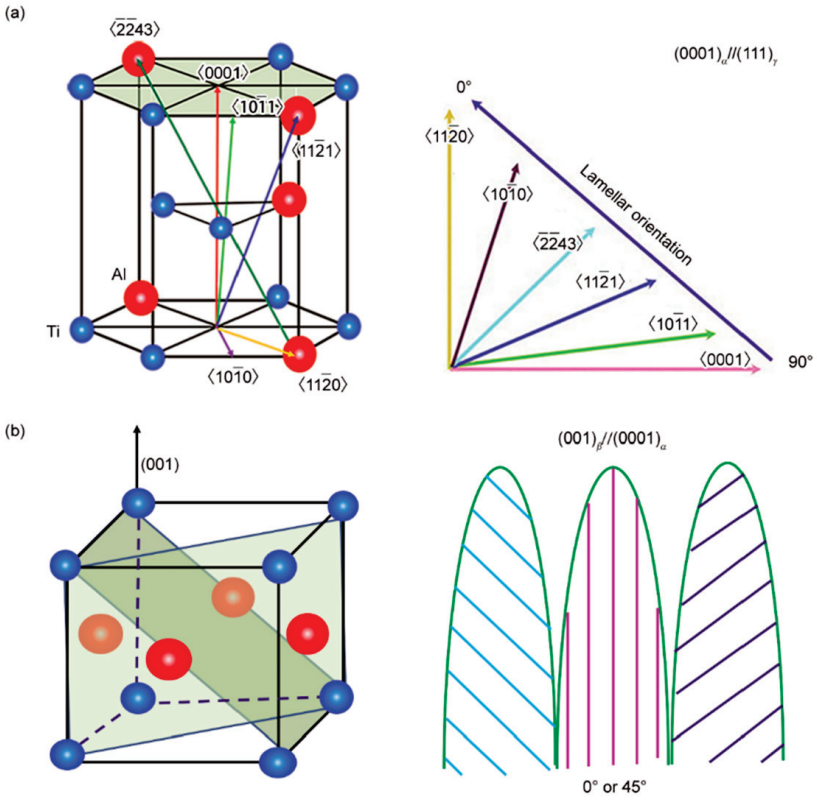

Figure 1. Schematics of the relationship between the lamellar orientation and the growth direction of the primary phases: (**a**) crystal orientation and lamellar orientation of α phase; and (**b**) crystal orientation and lamellar orientation of β phase [19].

3. Seed Crystal Method and Principles

The seed crystal methods are efficient and mature in preparing Ni-based superalloy single crystal turbine blades. For TiAl alloys, studies found that the fundamental principle of lamellar orientation control was that the properly aligned lamellar structure was generated by $\alpha \rightarrow \alpha/\gamma \rightarrow \alpha_2/\gamma$ or $\alpha \rightarrow \alpha_2 \rightarrow \alpha_2/\gamma$ phase transition. The seed technique uses TiAl alloy with parallel lamellae as seed crystal for directional solidification; the leading α phase grows along its non-preferred <11$\bar{2}$0> orientation. Consequently, a TiAl alloy with a full lamellar structure completely parallel to the growth direction is prepared. Moreover, the leading α phase can be obtained by peritectic solidification or generated under certain conditions, which gives rise to other seed methods besides the traditional α seed crystal method, including the self-seeding method, double DS self-seeding method, quasi-seeding method, and pure metal seeding method.

3.1. α Seed Crystal Method

Yamaguchi et al. [24] proposed that during the DS process, there is a definite positional relationship between the γ phase and α phase, so the orientation of the high-temperature α phase must be controlled. They raised four conditions for qualified α seed crystals: (i) the primary phase is α phase; (ii) when heating to $\alpha \rightarrow \alpha_2/\gamma$ transition point, the lamellar structure is stable and α phase simply transforms to α_2 phase; (iii) during heating, α phase is thermodynamically stable and the volume fraction of α phase increases by thickening of α lamellae rather than new nucleation; (iv) the mentioned process is reversible and the original orientation of lamellar structure can be retained during cooling. Among the alloys that meet the four conditions, Ti-43Al-3Si has been confirmed as a widely applicable seed crystal. Generally, after cutting the Ti-43Al-3Si seed ingot, its lamellar structure is perpendicular to the axial direction and needs to be rotated 90° and bonded to the bottom of the master alloy. Kim et al. [29] improved the efficiency of this method by pouring the

melt into a metal mold. Due to the chill effect, α grains grow along the direction <0001>, perpendicular to the inner wall of the mold and parallel to the axial direction. According to the Blackburn relationship, after the seeding process, the lamellae will be parallel to the axial direction.

In recent years, novel research on traditional α seeds has included Du et al. [30–32] using Ti-43Al-3Si seed to prepare large-size Ti-47Al samples. They fixed the master alloy rod on the feeding mechanism and the seed rod with the same diameter on the pulling mechanism melted the upper part of the seed crystal and the lower part of the master alloy by electromagnetic induction heating, and then the metal formed a 10~20 mm long melting zone under the electromagnetic restraint. In the initial stage of seeding, a large number of initial α grains were nucleated on the seed and grew along the non-preferred direction <11$\bar{2}$0>. After the competitive growth of α grains in the transition zone, the main part of the rod was only composed of one grain. The maximum width is 16 mm, and the lamellar structure is parallel to the axial direction.

Ti-43Al-3Si is able to seed certain high-Nb-TiAl alloys. According to Yue et al. [4], the seed crystal with the same diameter as the parent alloy was cut and placed beneath the parent alloy Ti–46Al–5Nb-0.18C-0.3Si. After DS, it could be found that the lamellar structure of the seed crystal was coarsened during long-term annealing, but the lamellar orientation was still parallel to the crystal's growth direction. Although a large number of fine-grained Ti_5Si_3 phases were distributed in the seed region, they did not affect the lamellar orientation. During the heating and remelting processes, the lamellar structure became extraordinarily stable due to the presence of a large number of Ti_5Si_3. In the transition zone, coarse α dendrites grew along the non-preferred orientation, and Ti_5Si_3 almost disappeared in this zone, then completely disappeared in the DS region. This proved that Ti-43Al-3Si may have limited influence on the mechanical properties of the main part of the sample.

The disadvantages of the traditional α seed crystal method mainly lie in the demanding kinetic conditions and long transition zone. Other novel seed methods aim to solve both problems.

3.2. Self-Seeding Method

To reduce the negative influence of an overlong transition zone, Fan et al. [17] developed a kind of in-situ self-seeding method. Essentially, it can be seen as an α seed crystal method, but the seed crystal has the same composition as the master alloy. The sample can be directly cut from the parent alloy ingot for conducting DS without the preparation of seeds. The lamellar orientation of the unmelted zone is parallel to the growth direction, while the alloy solidifies in the α phase and can grow in non-preferred orientations under appropriate solidification parameters.

For a specific composition Ti-46Al-0.5W-0.5Si, a cut sample was directly used for DS, and the bottom of the sample acted as a seed; the schematic is shown in Figure 2 [33]. The growth principle of the seed crystal part is similar to that proposed by Kim et al. [34]. Since the seed and the master alloy had the same composition, the length of the transition zone decreased significantly. Although the lamellar orientation in the area of the seed crystal was parallel to the growth direction, with the change of solidification parameters, the angle between the lamellar orientation and the growth direction in the DS region may change in the range of 0°~45°, considering that the growth of grains was affected by both heat flow and interfacial tension, causing the growth direction of α phase to be between the heat flow direction and the preferred growth direction.

Fan et al. [16] also studied the preparation of directionally solidified Ti-49Al alloy by self-seeding. Other alloys that can adopt self-seeding include Ti-50Al-4Nb [18] since the Al-equivalent of composition is similar to Ti-49Al. During the seeding process, it was found that the primary dendrite growth direction of non-preferred grains always deviated from the axial direction at the solid-liquid interface. This may be due to the comprehensive effects of interface energy anisotropy and heat flow direction. In the subsequent growth

process, grains with different orientations competed for growth. At low growth rates, utilizing the growth advantages of non-preferred crystals could obtain nearly parallel layered structures. However, at high growth rates, some grains nucleated at the inner wall of the mold and grew poorly oriented grains, which hindered the growth of grains with parallel orientation.

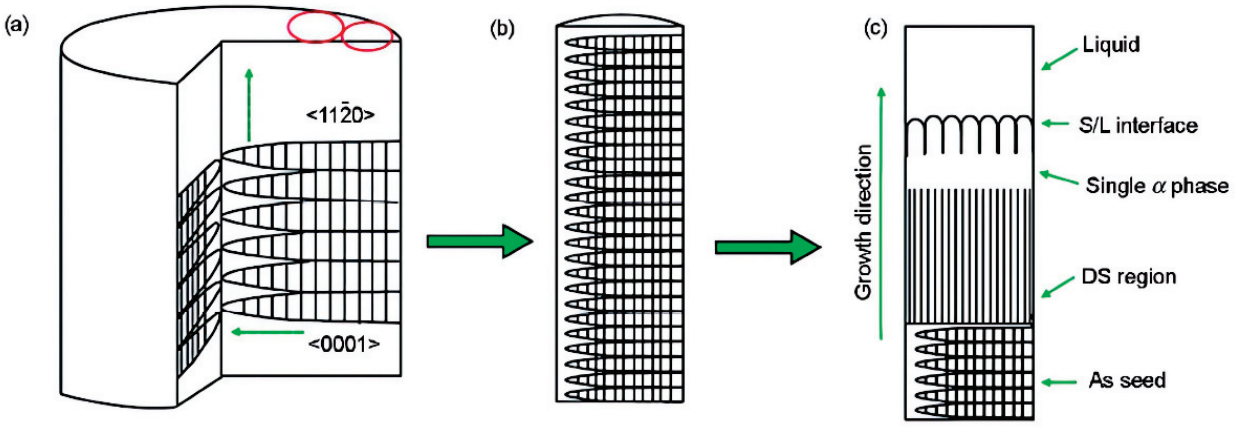

Figure 2. Schematic diagram of preparing specimens for lamellar orientation control by self-seeding method (SST) [33]. (**a**) structures of master ingot, (**b**) structures of seeding specimen, (**c**) solidification processing of SST.

3.3. Double DS Self-Seeding Method

The composition of the novel high-Nb-TiAl alloy is very different from that of traditional α seeds, resulting in an excessively long zone and non-negligible performance degradation. Ding et al. [35] demonstrated the double DS self-seeding method, which includes two DS processes. First, determine the solidification parameters and conduct the first DS process of a sample rod so that the primary phase is β, the solidification undergoes a peritectic process. Subsequently, the sample is rotated 180° along the axial direction to conduct the second DS process with exactly the same solidification parameters.

The method was used to prepare a directionally solidified Ti-46Al-5Nb alloy [36]. It was found that the lamellar orientation of some dendrites in the initial growth zone of secondary DS alloy was the same as that in the annealing zone at the withdrawing rate of 30 μm/s, and the angle between lamellar orientation and growth direction was 30°, but in the DS region, the lamellar orientation and growth direction were parallel. The lamellar orientation can be controlled parallel to the axial direction by the complete peritectic transformation L + β → α in dendrites, ensuring the consistency of the high-temperature α phase. The transition was carried out in the dendrite and interdendritic regions as the interdendritic liquid entered the nuclei of β dendrites. The interdendritic spacing is an important parameter in controlling peritectic phase transformation, and the schematic is shown in Figure 3 [36]. If the interdendritic spacing is narrow, the peritectic transformation in the β-dendrite region is incomplete after depletion of the liquid phase. Conversely, if the interdendritic spacing is wide, some α phase may precipitate directly from the liquid phase, resulting in a lamellar structure parallel to the radial direction. Another situation is when single β solidification happens, causing 12 variants, making it difficult to acquire consistent lamellar orientation.

Peritectic reactions can be carried out at relatively low G/v values; hence, the double DS method can be applied to a large range of withdrawing rates, which actually reduces the requirements for DS equipment [37].

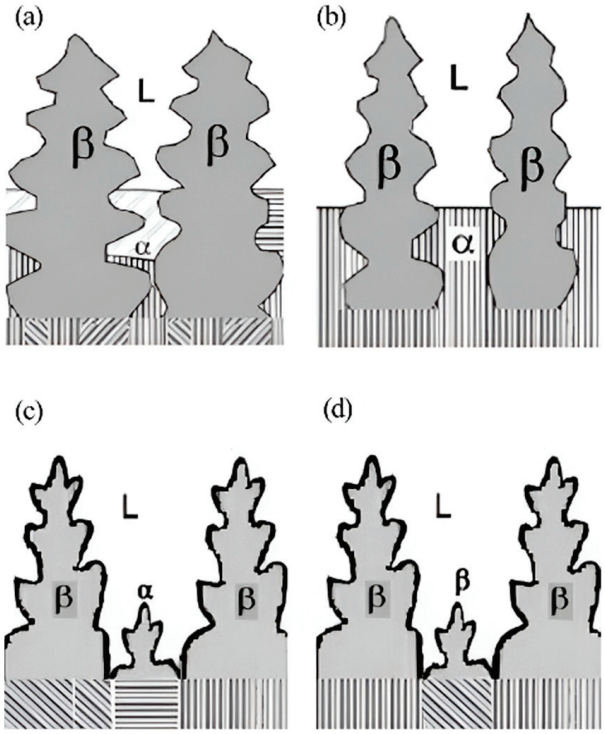

Figure 3. Schematic growth morphologies of TiAl alloys during the second DS, showing the growth morphologies with narrow (**a**), appropriate (**b**), and wide (**c**) interdendritic spacing, and the one (**d**) in the double DS under the different DS conditions. Reprinted with permission from Ref. [36]. 2011, ELSEVIER.

3.4. Quasi-Seeding Method

In order to solve the limitation of traditional α seed crystals, Du et al. [15] proposed to develop a class of quasi-seed crystals that are different from traditional α seed crystals in that they cannot thermodynamically meet the requirements of α seed crystals but can meet the seeding requirements by controlling kinetic conditions. The primary phase of a quasi-seed crystal is β, and under certain conditions, the quasi-seed solidifies in the form of a peritectic α phase, and then the lamellar structure becomes parallel to the axial direction of the ingot. This requires special heating procedures that ensure the lamellar structure of the quasi-seed crystals remains stable during heating and remelting.

The solidification characteristics of Ti-48Al-2Nb-2Cr and Ti-48Al-6Nb-1Cr alloys are very similar to those of commonly applied Ti-47Al alloys and are suitable as quasi-seed crystals. The characteristics of these two alloys include that the primary phase is β, the solidification mode is hyper-peritectic, and peritectic α solidification is easy to achieve. In addition, the alloys are sensitive to the heat treatment, after which the lamellar orientation is changeable so as to actualize different seeding processes.

The preparation method of the Ti-48Al-2Nb-2Cr quasi-seed crystal was the same as that of the Ti-43Al-3Si seed crystal, mentioned in Section 3.2. The melt was poured into the mold at room temperature, forming a peritectic α phase that nucleated at the inner wall of the mold and grew along the temperature gradient. After natural cooling, the quasi-seeded lamellar structure was parallel to the axial direction. According to the phase selection diagram and the numerical simulation of the solidification process of the seed ingot, it could be found that the range of G/v value is located in the α cell/dendrite solidification area, which proved that the primary phase was α. During heating and remelting, when the heating rate of the stage from 900 °C to 1450 °C was above 61 °C/min, a small amount of precipitation may lead to the generation of γ grains but does not affect the overall stability of lamellar orientation. Subsequently, at a high cooling rate, the lamellae were well preserved.

Figure 4 [14] describes the microstructure of the alloy at different locations after DS at a withdrawing rate of 10 μm/s, using Ti-48Al-2Nb-2Cr alloy as the seed crystal. The annealing area exhibited a typical duplex microstructure, where high-temperature α grains were transformed from α/γ lamellae during rapid heating well-aligned columnar grains with ideal lamellar microstructure were obtained under the seeding of these α grains. Competitive growth was observed between adjacent columnar grains, eventually forming the stable lamellar structure shown in Figure 4c. The nucleation and growth of γ grains are the most critical factors affecting the stability of the lamellar microstructure during heat treatment. If the nucleation and growth of the γ phase are restricted, high-temperature α grains with poor orientation originating from the γ phase will not be generated in the DS region, and the lamellar microstructure may remain unchanged.

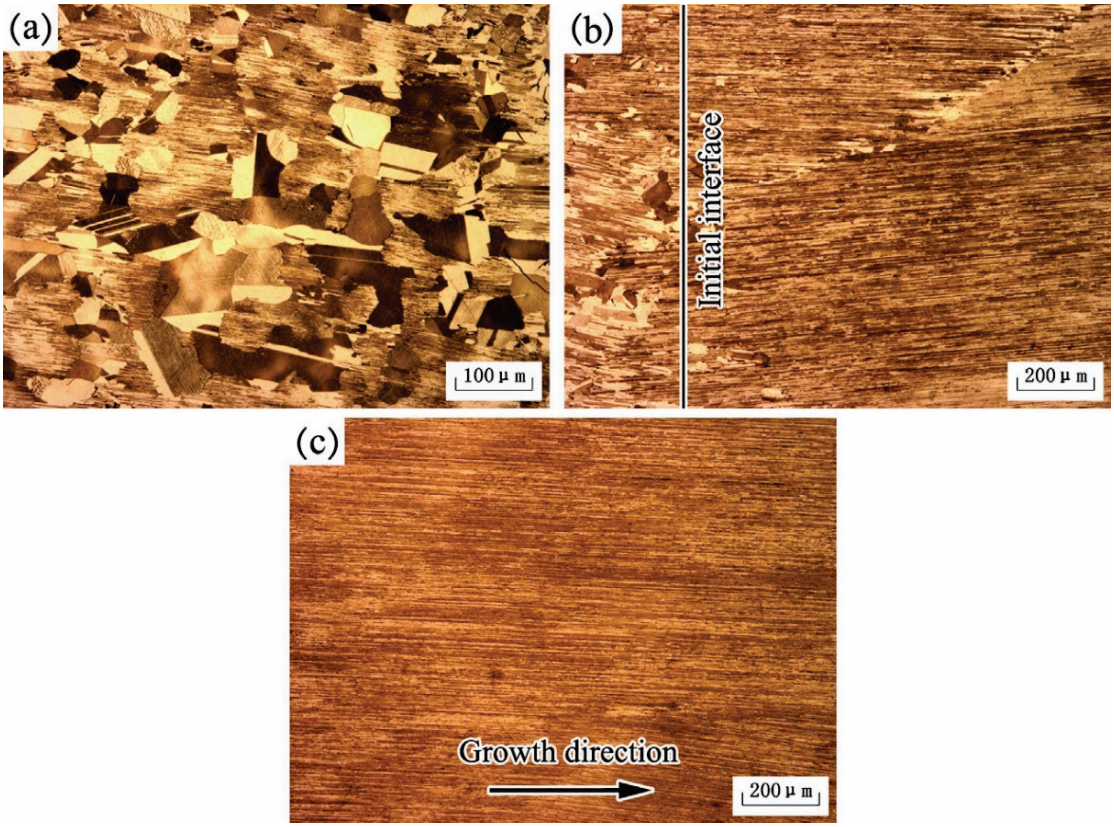

Figure 4. Microstructures of annealing region (**a**), initial interface (**b**), and DS region (**c**) of the electromagnetic confinement directional solidification (EMCDS) sample at the growth velocity of 10 μm/s. Reprinted with permission from Ref. [14]. 2015, ELSEVIER.

For another example, the lamellar structure of Ti-48Al-6Nb-1Cr remained stable during rapid heating and remelting; in this process, the γ phase did not grow up, despite the fact that a large number of fine equiaxial γ grains appeared at the initial solidification interface. Unsurprisingly, these grains did not affect the seeding process, and the lamellar structure in the final DS region grew continuously and had a fine orientation.

3.5. Pure Metal Seeding Method

The principle of using pure metal seeding is that the pure metal can act as a component in the master alloy and form the seed crystal region through the solute exchange; therefore, the seeding progress effectively reduces the length of the transition zone and the influence of the mushy zone. Liu et al. [9,38] systematically elaborated on this method and reported pure Ti or Nb as seed crystals.

Pure Ti was used as a kind of seed crystal in the Ti-47Al-0.5W-0.5Si alloy and the Ti-47Al binary alloy. By connecting the pure Ti seed below the master alloy and ensuring that

the bonding interface is lower than the initial DS interface, the sample can be completely melted during the process of heating and thermal treatment. Solute exchange and diffusion occur between the seed and the master alloy. At the beginning of the DS process, the leading β phase grew in preferred orientation <001>. As the Al content rose, leading β dendrites transformed into the α phase through peritectic transformation, and the leading α phase was nucleated on the basis of the α phase that underwent the peritectic transformation and inherited its lamellar orientation, as shown in Figure 5. There were angles of 10–20° between the lamellar and the growth direction, which was due to the certain deviation between the leading phase's preferred direction and the growth direction.

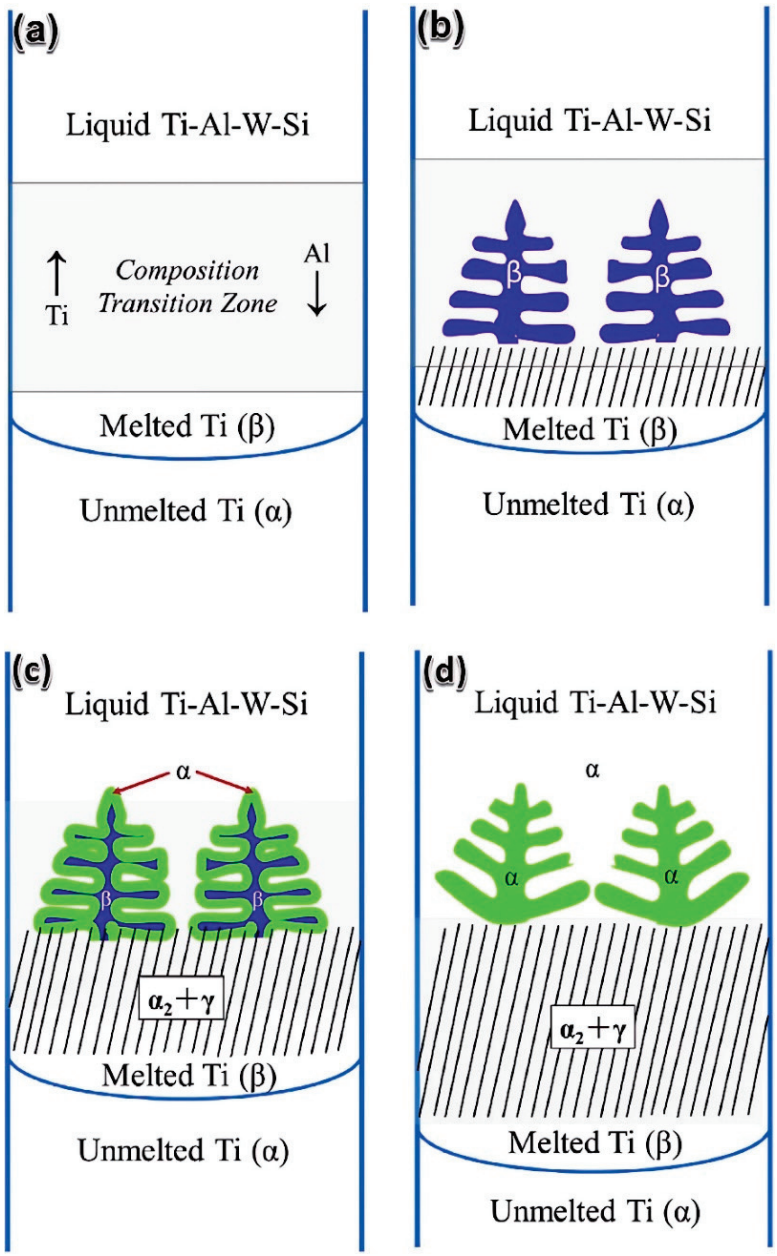

Figure 5. Schematic illustration of the β seeding technique in directionally solidified Ti-47Al-0.5W-0.5Si: (**a**) the form of the composition transition zone; (**b**) the initial directional solidification stage in the composition transition zone; (**c**) the primary β dendrite is transformed into α grain; and (**d**) the growth of α phase in steady-state growth region. Reprinted with permission from Ref. [38]. 2016, ELSEVIER.

Since Nb and β-Ti both belong to body-centered cubic structure, the low mismatch degree between Nb and β-Ti causes a completely coherent interface; therefore, β-Ti has a very strong ability for heterogeneous nucleation on the Nb-based interface. This makes it possible for pure Nb to serve as a seed crystal for Ti-47Al-1.0W-0.5Si and similar alloys. Massive Nb addition improved $\beta \rightarrow \alpha$ transformation temperature, making the β phase difficult to transform to α phase during the cooling process. A large number of B2 phases were generated at a position close to the crystallization interface. With the further increase in distance, the B2 phase disappeared and a lamellar structure ($\alpha_2 + \gamma$) appeared, in which only Ti_5Si_3 existed. Several grains were formed in front of the crystal interface; the angles between the lamellar orientation and the growth direction of each grain were within 45°.

4. Controlling Solidification Parameters

As mentioned previously, the lamellar structure is obtained from the α parent phase, which is affected by the solidification process and solid-state phase transition. Controlling solidification parameters involves determining the temperature gradient and the growth rate of the sample to achieve a specific solidification mode, resulting in lamellae approximately parallel to the growth direction. The determination of these parameters is based on the TiAl alloy phase selection diagram and experiments.

During directional solidification, the nucleation process can be explained by the constitutional supercooling theory. As a result of the generally fixed temperature gradient, the undercooling degree of components can be controlled by simply controlling growth rates or withdrawing rates in practical operation. It is crucial to ensure that the undercooling degree of the solidification interface is lower than the nucleation undercooling degree of the primary β phase. Otherwise, new grains will form in front of the solidification interface, and the growth direction will not be influenced by the aligned lamellae.

Chen et al. [11] proposed that the nucleation barrier in the 45° direction is higher than that in the 0° direction; that is, at the same degree of undercooling, there exists a critical velocity named v_c. When the pulling velocity is higher than v_c, the angle between the lamellar and growth directions is 45°, or the angle is 0°. This phenomenon can be described by the change in the free energy of the entire system.

Further, Zheng et al. [39] described the change of Gibbs free energy (ΔG) when α phase nucleates in β matrix:

$$\Delta G = -V\Delta G_v + A\gamma + V\Delta G_s$$

These results indicate that the Gibbs free energy changes consist of the decrease in volume free energy ($-V\Delta G_v$), the increase of β/α interfacial free energy ($A\gamma$), and the increase of misfit free energy ($V\Delta G_s$). The decrease in volume-free energy is the main driving force of nucleation, but the change in volume-free energy and mismatch-free energy is independent of the crystallographic orientation of α and β. The directional phase transition is considered to be carried out on a two-dimensional plane, where the driving force of the phase transition is parallel to the axial direction, and the different unit area interfacial energy γ perpendicular to the driving force direction caused by different β/α interfaces has an important effect on the lamellar direction. Since the interfacial energy of $(00\bar{1})_\beta//(11\bar{2}0)_\alpha$ is lower than that of $(00\bar{1})_\beta//(10\bar{1}2)_\alpha$, the 0° lamellar structure is easier to form than the 45° lamellar structure under general circumstances, but the 45° lamellar structure forms easier when the undercooling degree is sufficient. The schematic is illustrated in Figure 6.

Similar conclusions were obtained by Fan et al. [40–43] on the solidification parameters of Ti-49Al. The degree of undercooling must be lower than the degree of nucleation undercooling in the primary β phase. When the growth rate was taken as a variable, the degree of interfacial undercooling decreased first and then increased. The growth rate below the undercooling degree of the β phase ranged from v_1 to v_2, which could ensure the subsequent continuous growth of the α phase. As the temperature gradient increased, the range of growth rates expanded. When the temperature gradient was taken as a variable, the trend was similar. A temperature gradient ranging from G_1 to G_2 allowed continuous growth of the α phase, and the value of G_1 ascends with an increasing growth rate. A

higher G ensured continuous growth at a higher v. When G was 12.1 K/mm and v was 20 μm/s, the α phase grew along $<11\bar{2}0>_\alpha$ direction, leading the lamellae orientation close to 0°.

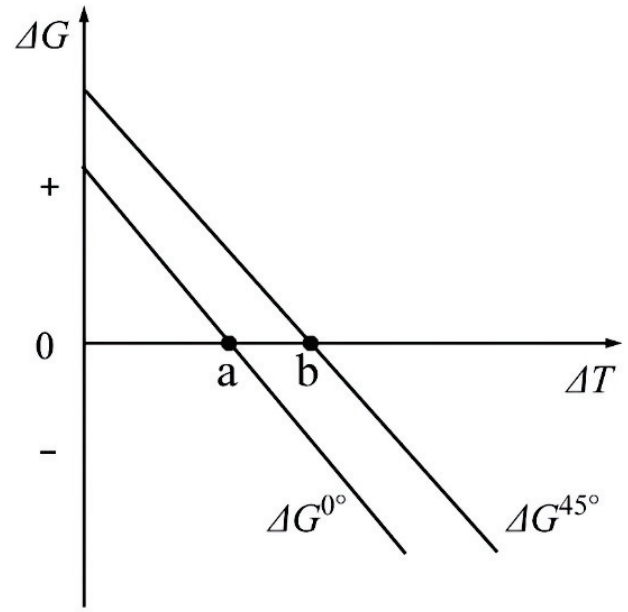

Figure 6. Variation of the free energy change with nucleation undercooling for 0° or 45° oriented growing α phase. Reprinted with permission from Ref. [39]. 2022, MDPI AG.

Liu et al. [44] believed that the growth rate of Ti-47Al could be directly controlled without using seed crystals. When the growth rate was 10 μm/s, the angle between lamellar orientation and growth direction was 45°, while the angle was 0° at a growth rate of 3 or 20 μm/s. For all three growth rates, the primary phase was α and remained unchanged, inferring that the initial DS interface affected the lamellar orientation.

When the growth rate varies greatly, it is easy to undergo a change in solidification mode on most occasions. Jiang et al. [45] found that for Ti-44Al-9Nb-1Cr-0.2W-0.2Y alloy, within the range of growth rate of 10~20 μm/s, as the growth rate increased, the angles between the columnar grain orientation and the ingot axial direction gradually decreased, and the preferred grain orientation gradually changed from the heat flow direction to the pulling direction. Moreover, the difference in growth rate caused changes in the primary solidification phase. Initially, it solidified as a single β phase, but when the growth rate reached 20 μm/s, the lamellar orientation included cases where it formed hypo-peritectic solidification with angles of 45° or 90° to the growth direction, indicating that single-α solidification occurred. Wang et al. [46] found that for Ti-47Al-6Nb-0.1C alloy, at growth rates of 5 μm/s or 8.33 μm/s, the lamellae with small angles to the growth direction accounted for the major proportion because of primary β solidification. The angles increased with the increase in growth rates. When the growth rate increased to 16.67 μm/s, lamellae with a near 90° angle accounted for the major proportion, which is related to primary α solidification.

The research by Luo et al. [47] on the Ti-45Al-5Nb alloy revealed similar patterns. Within a growth rate range of 5~20 μm/s and a temperature gradient range of 15~20 K/mm, the primary solidification phase was β, and the alloy underwent the following $\beta \rightarrow \alpha$ and $\alpha \rightarrow \alpha_2 + \gamma$ transformations, resulting in lamellae at angles of 0° or 45° to the growth direction. At a temperature gradient of 20 K/mm and a growth rate higher than 20 μm/s, the primary solidification phase changed from β to α, and the alloy underwent single-phase α solidification, resulting in lamellae at an angle of 90° to the growth direction. The determination of the primary phase can generally be based on the theory of the interface temperature response function, as shown in Figure 7.

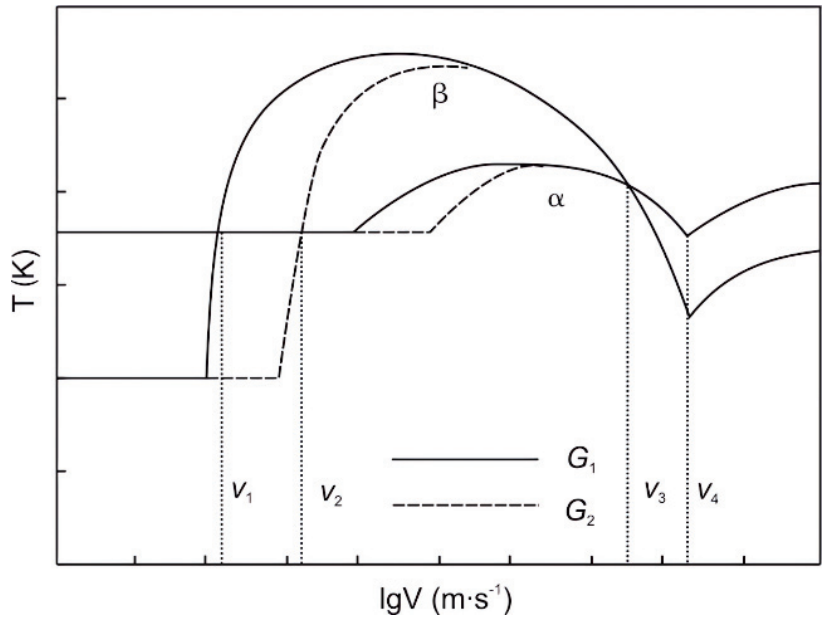

Figure 7. Schematic of interfacial temperature response function with growth rate and temperature gradient. Reprinted with permission from Ref. [47]. 2016, Springer Nature.

Since it is difficult for most alloy compositions to obtain proper lamellar direction only by controlling solidification parameters. In most cases, seed crystals are used jointly.

5. Novel Ways for Controlling Lamellar Orientation

Thermal stabilization (TS) or heat treatment (HT) is also used to optimize lamellar orientation. Generally, the heat preservation before DS is called TS, and the heating operation on the sample after DS is called HT. TS ensures a higher temperature gradient and promotes the stable formation of the transition zone, while HT effectively optimizes the orientation and uniformity of the lamellae.

Ding et al. [48] first studied the post-solidification HT of Ti-45Al-8.5Nb. Two HT procedures, HT1 (1250 °C for 24 h + 900 °C for 30 min + air cooling), and HT2 (1400 °C for 12 h + 900 °C for 30 min + air cooling), were selected. After HT1, lamellar orientation did not change significantly, but after HT2, lamellar orientation became parallel to the growth direction. This is due to the fact that the maximum temperature of HT1 was too low to reach the α transition point, so the lamellae are not decomposed. The HT2 temperature promoted the fusion of the high-temperature α phase, and then the macrostructure was close to a single crystal.

Zhang et al. [49] performed thermal stabilization on Ti-46Al-5Nb alloy before DS and proved that proper TS is necessary to generate L + β + α three-phase zone in the mushy zone, which benefits the control of the microstructure in the DS zone of peritectic TiAl alloy. When the TS time was 30 min, a three-phase zone appeared in the mushy zone. As the TS time increased to 60 min, the liquid in the mushy region disappeared, and columnar β and α grains could be observed in the mushy zone, indicating that the near-steady state had been reached during the TS period. After remelting, the crystal grew during DS, relying on the high-temperature interface in the mushy region, which inherited the crystal orientation formed during TS. Specifically, the α phase recovers on the basis of the β phase orientation through L + β → α peritectic transformation, and a parent α grain usually forms only one lamellar colony during cooling. At the same time, the TS treatment can make the β dendrites grow evenly and make the same peritectic transformation occur in different β dendrites, so as to obtain the lamellar parallel to the axial columnar crystals.

Directional heat treatment (DHT) requires the sample to be pulled into the cooling medium at a certain rate during the HT process. After DS, Chen et al. [50] conducted DHT for Ti-44Al-6Nb-1Cr alloy at a temperature of 1750 K and a pulling rate of 4.17 μm/s. The

temperature was chosen based on the findings of Liu et al. [51], who demonstrated that for TiAl alloys with original β solidification characteristics, the heat treatment temperature should lie within the β phase region. After a single DHT, a complete single β transition occurred in the effectively heat-treated grains, followed by $\alpha \rightarrow \alpha_2 + \gamma$ processes. Therefore, the angle between the orientation of most lamellar structures and the growth direction of columnar grains was observed to be 0° or 45°. With the increase in the number of DHT cycles, the lamellar colonies grew, and the columnar grain size obviously increased, as shown in Figure 8. Simultaneously, the improvement in the orientation of the lamellar clusters was significant. After four DHT cycles, they observed that all the lamellar clusters derived from a single columnar grain exhibited the same orientation.

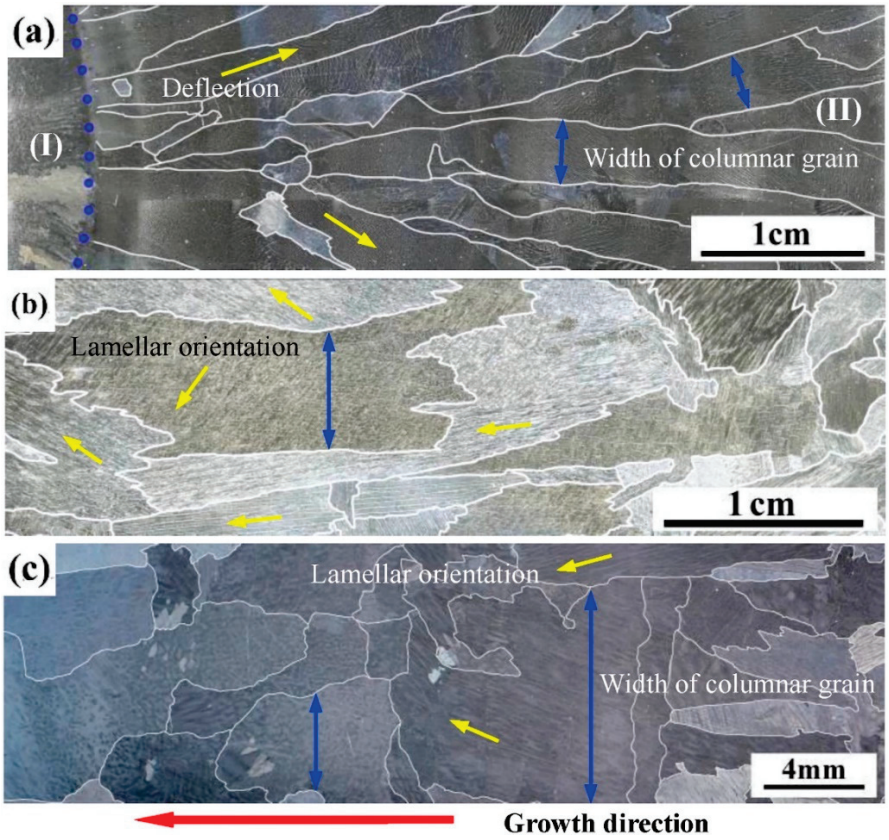

Figure 8. Macrostructure of Ti-44Al-6Nb-1Cr alloys. (**a**) Directionally solidified alloy; (**b**) DHT-1 alloy; and (**c**) DHT-4 alloy. Reprinted with permission from Ref. [50]. 2021, ELSEVIER.

Chen et al. [6] also conducted DHT on Ti-44Al-6Nb-1Cr-2V samples at a temperature of 1730 K and a growth rate of 4.17 μm/s. Before heat treatment, it was found that the samples had obtained α_2/γ full lamellar structure through a typical peritectic transformation. After a single DHT, the average angle between the alloy grains and the axial direction became significantly smaller, while the grains near the surface showed a slighter deflection. Considering that the angle between the arrangement direction of lamellar phases and the axial direction of columnar grains did not change, apparently from a macroscopic point of view, DHT slightly optimized the lamellar orientation of the alloy.

Li et al. [52] investigated lamellar orientation control of β-solidified Ti-43.5Al-4Nb-1Mo-0.1B alloy using a high withdrawing rate combined with thermal stabilization. The thermal stabilization process involved holding the sample at 1973 K for an hour to establish a stable liquid-solid phase and β/α phase interface, as well as creating a relatively high temperature gradient. Additionally, the $(111)_\beta$ plane facing the melt exhibited the lowest loss rate of interface atoms during the melting process, while other β grains on different crystal planes were more prone to lose. The thermal stabilization resulted in the expansion

and fusion of β grains, and accordingly, β grains with suitable orientation contributed to the subsequent generation of single crystals. A high withdrawing rate of 100 μm/s could also ensure the grain selection of the α phase and lead to complete peritectic transformation. In the competition growth process of grains, α grains with lamellae parallel to the axial direction would dominate and ultimately form a near PST crystal.

6. Conclusions and Prospects of Lamellar Orientation Control

(1) There are variations in the application scenarios for seed techniques and methods for controlling solidification parameters. The traditional α seed crystal method and the pure metal seeding method have certain requirements for the composition of the master alloy and the planar growth of α phase interface. The double DS self-seeding method and the quasi-seed method require the occurrence of peritectic transformation during the solidification process, thus obtaining a lamellar an orientation close to 0°. Controlling solidification parameters demands the growth of the entire β phase during the solidification process, and by precisely adjusting the withdrawing rate, the occurrence of complete peritectic transformation is controlled, and lamellar structure parallel to the growth direction can be obtained.

(2) Further research on controlling lamellar orientation should focus on simplifying the preparation of seed crystals, determining solidification parameters, and improving the heat treatment process. The double DS self-seeding method allows for obtaining the seed crystal directly by cutting a sample after single DS, eliminating the need for casting a seed crystal ingot. Precise control of the growth rate can effectively promote the growth of directional columnar crystals or single crystals, and the temperature gradient can be adjusted by controlling the output power of the equipment using a combination of machine learning algorithms. Before the withdrawal process, the sample should undergo thermal stabilization treatment, followed by heat treatment after DS. To optimize the lamellar orientation, the heat treatment temperature should be above the α transition point. The combination of the seed crystal method and controlling solidification parameters is particularly practical for controlling the lamellar orientation of large samples.

Funding: This research was funded by the Beijing Natural Science Foundation (No. 2222092) and the National Science and Technology Major Project (No. J2019-VI-0003-0116).

Institutional Review Board Statement: The study did not require ethical approval. Studies are not involving humans or animals.

Informed Consent Statement: Not applicable.

Data Availability Statement: No new data were created.

Acknowledgments: This research was financially supported by the Beijing Natural Science Foundation (No. 2222092) and the National Science and Technology Major Project (No. J2019-VI-0003-0116).

Conflicts of Interest: The authors declare no conflict of interest.

References

1. Kwak, S.; Kim, J.; Ding, H.; Xu, X.; Chen, R.; Guo, J.; Fu, H. Machine learning prediction of the mechanical properties of γ-TiAl alloys produced using random forest regression model. *J. Mater. Res. Technol.* **2022**, *18*, 520–530. [CrossRef]
2. Huang, H.; Ding, H.; Xu, X.; Chen, R.; Guo, J.; Fu, H. Microstructure transition of γ-TiAl alloys with abrupt cross-sections in yttria ceramic moulds during directional solidification by electromagnetic cold crucible. *J. Mater. Res. Technol.* **2022**, *19*, 368–381. [CrossRef]
3. Duan, B.; Mao, L.; Yang, Y.; Feng, Q.; Zhang, X.; Li, H.; Jiao, L.; Zhang, R.; Lu, X.; Chen, G.; et al. Preparation of Ti-46Al-8Nb Alloy Ingots beyond Laboratory Scale Based on BaZrO3 Refractory Crucible. *Metals* **2022**, *12*, 524. [CrossRef]
4. Yue, X.A.; Shen, J.; Xiong, Y.; Li, Q.; Zheng, S. Microstructure, fracture toughness and high-temperature tensile property of large size Ti–46Al–5Nb-0.18C-0.3Si alloy with oriented lamella by electromagnetic confinement directional solidification. *Mater. Sci. Eng. A* **2021**, *812*, 141139. [CrossRef]
5. Wang, H.; Wang, Q.; Zeng, L.; Zhang, H.; Ding, H. Microstructure, mechanical and tribological performances of a directionally solidified γ-TiAl alloy. *Mater. Charact.* **2021**, *179*, 111393. [CrossRef]

6. Chen, R.; Liu, Y.; Xue, X.; Fang, H.; Tan, Y.; Cui, H. Optimizing microstructure and mechanical properties of directionally solidified Ti44Al6Nb1Cr2V alloy by directional heat treatment. *Mater. Charact.* **2021**, *179*, 111354. [CrossRef]
7. Wang, Q.; Zeng, L.; Ding, H.; Chen, R.; Guo, J.; Fu, H. On the high temperature deformation of a directionally solidified γ-TiAl alloy. *Mater. Sci. Eng. A* **2019**, *758*, 19–27. [CrossRef]
8. Wang, Q.; Ding, H.; Zhang, H.; Chen, R.; Guo, J.; Fu, H. Influence of Mn addition on the microstructure and mechanical properties of a directionally solidified γ-TiAl alloy. *Mater. Charact.* **2018**, *137*, 133–141. [CrossRef]
9. Liu, T.; Luo, L.S.; Zhang, D.H.; Wang, L.; Li, X.Z.; Chen, R.R.; Su, Y.Q.; Guo, J.J.; Fu, H.Z. Comparison of microstructures and mechanical properties of as-cast and directionally solidified Ti-47Al-1W-0.5Si alloy. *J. Alloys Compd.* **2016**, *682*, 663–671. [CrossRef]
10. Liu, G.; Wang, Z.; Li, X.; Su, Y.; Guo, J.; Fu, H.; Wang, G. Continued growth controlling of the non-preferred primary phase for the parallel lamellar structure in directionally solidified Ti–50Al–4Nb alloy. *J. Alloys Compd.* **2015**, *632*, 152–160. [CrossRef]
11. Chen, G.; Peng, Y.; Zheng, G.; Qi, Z.; Wang, M.; Yu, H.; Dong, C.; Liu, C.T. Polysynthetic twinned TiAl single crystals for high-temperature applications. *Nat. Mater.* **2016**, *15*, 876–881. [CrossRef] [PubMed]
12. Johnson, D.R.; Inui, H.; Muto, S.; Omiya, Y.; Yamanaka, T. Microstructural development during directional solidification of α-seeded TiAl alloys. *Acta Mater.* **2006**, *54*, 1077–1085. [CrossRef]
13. Saari, H.; Beddoes, J.; Seo, D.Y.; Zhao, L. Development of directionally solidified γ-TiAl structures. *Intermetallics* **2005**, *13*, 937–943. [CrossRef]
14. Du, Y.; Shen, J.; Xiong, Y.; Shang, Z.; Fu, H. Stability of lamellar microstructures in a Ti–48Al–2Nb–2Cr alloy during heat treatment and its application to lamellae alignment as a quasi-seed. *Intermetallics* **2015**, *61*, 80–84. [CrossRef]
15. Du, Y.; Shen, J.; Xiong, Y.; Li, Q.; Fu, H. Quasi-Seeding Mechanism in Lamellae Alignment of TiAl Alloys During Directional Solidification. *Metall. Mater. Trans. A* **2019**, *50*, 4166–4177. [CrossRef]
16. Fan, J.; Wei, Z.; Li, Y.; Wang, Y.; Wu, S.; Zhou, X.; Liu, J.; Guo, J. Lamellae Orientation Control and Mechanical Properties of Directionally Solidified Binary Ti-49Al Alloy in Oxide Ceramics Crucible. *Int. J. Met.* **2021**, *16*, 622–633. [CrossRef]
17. Fan, J.; Liang, L.; Li, Y.; Wu, S.; Wang, X.; Li, Y.; Liu, J.; Guo, J. Effect of lamellae orientation on tensile properties of directionally solidified Ti–46Al–0.5W–0.5Si alloy. *Mater. Sci. Technol.* **2021**, *37*, 772–784. [CrossRef]
18. Liu, G.; Li, T.; Fu, T.; Liu, H.; Deng, X.; Li, J.; Wang, Z.; Wang, G. Morphology and competitive growth during the development of the parallel lamellar structure by self-seeding in directionally solidified Ti-50Al-4Nb alloy. *J. Alloys Compd.* **2016**, *682*, 601–609. [CrossRef]
19. Chen, Z.; Ding, H.; Chen, R.; Guo, J.; Fu, H. Microstructural Evolution and Mechanism of Solidified TiAl Alloy Applied Electric Current Pulse. *Acta Met. Sin.* **2019**, *55*, 611–618.
20. Ding, X.F.; Liu, H.; Zhang, F.Q.; Zhang, L.W.; Huang, H.; Nan, H.; Su, Y.Q.; Lin, J.P. Microstructure characteristics of the directionally solidified TiAl-Nb alloys with different solidification modes. *Mater. Today Commun.* **2022**, *32*, 103770. [CrossRef]
21. Johnson, D.R.; Inui, H.; Yamaguchi, M. Directional solidification and microstructural control of the TiAl/Ti3Al lamellar microstructure in TiAl-Si alloys. *Acta Mater.* **1996**, *44*, 2523–2535. [CrossRef]
22. Johnson, D.R.; Masuda, Y.; Inui, H.; Yamaguchi, M. Alignment of the TiAl/Ti3Al lamellar microstructure in TiAl alloys by growth from a seed material. *Acta Mater.* **1997**, *45*, 2523–2533. [CrossRef]
23. Johnson, D.R.; Chihara, K.; Inui, H.; Yamaguchi, M. Microstructural control of TiAl-Mo-B alloys by directional solidification. *Acta Mater.* **1998**, *46*, 6529–6540. [CrossRef]
24. Yamaguchi, M.; Johnson, D.R.; Lee, H.N.; Inui, H. Directional solidification of TiAl-base alloys. *Intermetallics* **2000**, *8*, 511–517. [CrossRef]
25. Lee, H.N.; Johnson, D.R.; Inui, H.; Oh, M.H.; Wee, D.M.; Yamaguchi, M. Microstructural control through seeding and directional solidification of TiAl alloys containing Mo and C. *Acta Mater.* **2000**, *48*, 3221–3233. [CrossRef]
26. Muto, S.; Yamanaka, T.; Lee, H.N.; Johnson, D.R.; Inui, H.; Yamaguchi, M. Directional solidification of TiAl-based alloys and properties of directionally solidified ingots. *Adv. Eng. Mater.* **2001**, *3*, 391–394. [CrossRef]
27. Lee, H.N.; Johnson, D.R.; Inui, H.; Oh, M.H.; Wee, D.M.; Yamaguchi, M. A composition window in the TiAl-Mo-Si system suitable for lamellar structure control through seeding and directional solidification. *Mater. Sci. Eng. a-Struct. Mater. Prop. Microstruct. Process.* **2002**, *329*, 19–24. [CrossRef]
28. Kim, J.H.; Kim, S.W.; Lee, H.N.; Oh, M.H.; Inui, H.; Wee, D.M. Effects of Si and C additions on the thermal stability of directionally solidified TiAl–Nb alloys. *Intermetallics* **2005**, *13*, 1038–1047. [CrossRef]
29. Kim, S.E.; Lee, Y.T.; Oh, M.H.; Inui, H.; Yamaguchi, M. Directional solidification of TiAl-Si alloys using a polycrystalline seed. *Intermetallics* **2000**, *8*, 399–405. [CrossRef]
30. Du, Y.; Shen, J.; Xiong, Y.; Shang, Z.; Wang, L.; Fu, H. Lamellar microstructure alignment and fracture toughness in Ti–47Al alloy by electromagnetic confinement and directional solidification. *Mater. Sci. Eng. A* **2015**, *621*, 94–99. [CrossRef]
31. Du, Y.; Shen, J.; Xiong, Y.; Shang, Z.; Qin, L.; Fu, H. Microstructural development and room temperature tensile property of directionally solidified Ti–47Al alloys by electromagnetic confinement and directional solidification. *J. Mater. Res.* **2018**, *33*, 958–966. [CrossRef]
32. Du, Y.; Shen, J.; Xiong, Y.; Ren, C.; Fu, H. Lamellar Microstructure Alignment in Ti-47Al Alloy by Electromagnetic Confinement and Directional Solidification Using a Seed. *JOM* **2015**, *67*, 1258–1264. [CrossRef]
33. Fan, J.; Guo, J.; Long, W.; Su, Y.; Li, X.; Li, F.; Fu, H. Lamellar orientation control of directionally solidified Ti–46Al–0·5W–0·5Si alloy by self-seeding technology. *Mater. Sci. Technol.* **2013**, *30*, 183–188. [CrossRef]

34. Kim, S.E.; Lee, Y.T.; Oh, M.H.; Inui, H.; Yamaguchi, M. Directional solidification of TiAl base alloys using a polycrystalline seed. *Mater. Sci. Eng. A-Struct. Mater. Prop. Microstruct. Process.* **2002**, *329*, 25–30. [CrossRef]
35. Ding, X.F.; Lin, J.P.; Zhang, L.Q.; Su, Y.Q.; Chen, G.L. Microstructural control of TiAl–Nb alloys by directional solidification. *Acta Mater.* **2012**, *60*, 498–506. [CrossRef]
36. Ding, X.F.; Lin, J.P.; Zhang, L.Q.; Su, Y.Q.; Wang, H.L.; Chen, G.L. Lamellar orientation control in a Ti–46Al–5Nb alloy by directional solidification. *Scr. Mater.* **2011**, *65*, 61–64. [CrossRef]
37. Ding, X.F.; Lin, J.P.; Qi, H.; Zhang, L.Q.; Song, X.P.; Chen, G.L. Microstructure evolution of directionally solidified Ti–45Al–8.5Nb–(W, B, Y) alloys. *J. Alloys Compd.* **2011**, *509*, 4041–4046. [CrossRef]
38. Liu, T.; Luo, L.; Su, Y.; Guo, J.; Fu, H. Lamellar orientation control of Ti–47Al–0.5W–0.5Si by directional solidification using β seeding technique. *Intermetallics* **2016**, *73*, 1–4. [CrossRef]
39. Zheng, G.; Peng, H.; Gu, X.; Jin, Z.; Chen, Y.; Qi, Z.; Xu, H.; Chen, F.; Cao, Y.; Feng, C.; et al. Crystallographic Origin of Phase Transformation and Lamellar Orientation Control for TiAl-Based Alloys. *Crystals* **2022**, *12*, 634. [CrossRef]
40. Fan, J.; Zhang, C.; Wu, S.; Gao, H.; Wang, X.; Guo, J.; Fu, H. Effects of solidification parameters on the growth direction of α phase in directionally solidified Ti-49Al alloy. *Intermetallics* **2017**, *90*, 113–118. [CrossRef]
41. Fan, J.; Li, X.; Su, Y.; Guo, J.; Fu, H. Effect of growth rate on microstructure parameters and microhardness in directionally solidified Ti–49Al alloy. *Mater. Des.* **2012**, *34*, 552–558. [CrossRef]
42. Fan, J.; Li, X.; Su, Y.; Chen, R.; Guo, J.; Fu, H. Dependency of microstructure parameters and microhardness on the temperature gradient for directionally solidified Ti–49Al alloy. *Mater. Chem. Phys.* **2011**, *130*, 1232–1238. [CrossRef]
43. Fan, J.; Li, X.; Su, Y.; Chen, R.; Guo, J.; Fu, H. Directional solidification of Ti–49 at.%Al alloy. *Appl. Phys. A* **2011**, *105*, 239–248. [CrossRef]
44. Liu, T.; Tao, J.; Cai, X.; Chen, D.; Li, J.; Luo, L.; Cheng, Z.; Su, Y. Effect of growth rate on microstructure evolution in directionally solidified Ti-47Al alloy. *Heliyon* **2022**, *8*, e08704. [CrossRef]
45. Jiang, Z.-H.; Li, N.; Zhang, H.-X.; Zhao, C.-Z. The Effect of Growth Rate on the Microstructure and Tensile Behaviour of Directionally Solidified Ti-44Al-9Nb-1Cr-0.2W-0.2Y Alloys. *Metals* **2018**, *8*, 535. [CrossRef]
46. Wang, Q.; Chen, R.; Gong, X.; Guo, J.; Su, Y.; Ding, H.; Fu, H. Microstructure control and creep behavior of Ti-47Al-6Nb-0.1C alloy by directional solidification. *Intermetallics* **2018**, *94*, 152–159. [CrossRef]
47. Luo, L.S.; Liu, T.; Li, K.; Su, Y.Q.; Guo, J.J.; Fu, H.Z. Microstructures, micro-segregation and solidification path of directionally solidified Ti-45Al-5Nb alloy. *China Foundry* **2016**, *13*, 107–113. [CrossRef]
48. Ding, X.-F.; Lin, J.-P.; Zhang, L.-Q.; Chen, G.-L. Effects of heat treatment on microstructure of directionally solidified Ti-45Al-8Nb-(W, B, Y) alloy. *Trans. Nonferrous Met. Soc. China* **2011**, *21*, 26–31. [CrossRef]
49. Zhang, L.; Lin, J.; He, J.; Yin, J.; Ding, X. Influence of thermal stabilization treatment on the subsequent microstructure development during directional solidification of a Ti–46Al–5Nb alloy. *Intermetallics* **2015**, *63*, 67–72. [CrossRef]
50. Chen, R.; Liu, Y.; Xue, X.; Fang, H.; Tan, Y.; Cui, H. Study on improving microstructure and mechanical properties of directionally solidified Ti44Al6Nb1Cr alloy by cyclic DHT. *Mater. Sci. Eng. A* **2021**, *809*, 140912. [CrossRef]
51. Liu, Y.L.; Xue, X.; Tan, Y.M.; Fang, H.Z.; Cui, H.Z.; Chen, R.R. Microstructure formation and elevated temperature mechanical properties of directionally solidified Ti44Al6Nb1Cr alloy. *Mater. Sci. Eng. A-Struct. Mater. Prop. Microstruct. Process.* **2020**, *797*, 140038. [CrossRef]
52. Li, Z.; Luo, L.; Su, Y.; Wang, B.; Wang, L.; Liu, T.; Yao, M.; Liu, C.; Guo, J.; Fu, H. A high-withdrawing-rate method to control the orientation of (γ + α2) lamellar structure in a β-solidifying γ-TiAl-based alloy. *Mater. Sci. Eng. A* **2022**, *857*, 144078. [CrossRef]

materials

MDPI

Article

Effects of Thermal Exposure on the Microstructure and Mechanical Properties of a Ti–48Al–3Nb–1.5Ta Alloy via Powder Hot Isostatic Pressing

Zhenbo Zuo [1,2], Rui Hu [1,*], Qingxiang Wang [2], Zitong Gao [1], Xian Luo [1], Yunjin Lai [2], Sa Xue [2], Min Xiang [2], Xiaohao Zhao [2] and Shaoqiang Li [2]

[1] State Key Laboratory of Solidification Processing, Northwestern Polytechnical University, Xi'an 710072, China; zuozhenbo@mail.nwpu.edu.cn (Z.Z.)
[2] Sino-Euro Materials Technologies of Xi'an Co., Ltd., Xi'an 710018, China
* Correspondence: rhu@nwpu.edu.cn; Tel.: +86-29-88492172

Abstract: Research on how thermal exposure affects the microstructure and mechanical properties of the Ti–48Al–3Nb–1.5Ta (at. %) alloy, which is prepared via powder hot isostatic pressing (P–HIP), is essential since this low-density alloy shows promise for use in high-temperature applications, particularly for aero-engines, which require long-term stable service. In this study, a P–HIP Ti–48Al–3Nb–1.5Ta (at. %) alloy was exposed to high temperatures for long durations. The phase, microstructure and mechanical properties of the P–HIP Ti–48Al–3Nb–1.5Ta alloy after thermal exposure under different conditions were analyzed using XRD, SEM, EBSD, EPMA, TEM, nanomechanical testing and tensile testing. The surface scale is composed of oxides and nitrides, primarily Al_2O_3, TiO_2, and TiN, among which Al_2O_3 is preferentially generated and then covered by rapidly growing TiO_2 as the thermal exposure duration increases. The nitrides appear later than the oxides and exist between the oxides and the substrate. With increasing exposure temperature and duration, the surface scale becomes more continuous, TiO_2 particles grow larger, and the oxide layer thickens or even falls off. The addition of Ta and Nb can improve the oxidation resistance because Ta^{5+} and Nb^{5+} replace Ti^{4+} in the rutile lattice and weaken O diffusion. Compared with the P–HIP Ti–48Al–3Nb–1.5Ta alloy, after thermal exposure, the grain size does not increase significantly, and the γ phase increases slightly (by less than 3%) with the decomposition of the α_2 phase. With increasing thermal exposure duration, the γ phase exhibits discontinuous coarsening (DC). Compared with the P–HIP Ti–48Al–3Nb–1.5Ta alloy, the hardness increases by about 2 GPa, the tensile strength increases by more than 50 MPa, and the fracture strain decreases by about 0.1% after thermal exposure. When the depth extends from the edge of the thermally exposed specimens, the hardness decreases overall.

Keywords: Ti–48Al–3Nb–1.5Ta; thermal exposure; oxidation; stability

Citation: Zuo, Z.; Hu, R.; Wang, Q.; Gao, Z.; Luo, X.; Lai, Y.; Xue, S.; Xiang, M.; Zhao, X.; Li, S. Effects of Thermal Exposure on the Microstructure and Mechanical Properties of a Ti–48Al–3Nb–1.5Ta Alloy via Powder Hot Isostatic Pressing. *Materials* **2024**, *17*, 794. https://doi.org/10.3390/ma17040794

Academic Editor: Tomasz Czujko

Received: 21 December 2023
Revised: 1 February 2024
Accepted: 1 February 2024
Published: 7 February 2024

1. Introduction

The TiAl alloy is a promising high-temperature material for aerospace applications because of its low density, exceptional creep and high-temperature oxidation resistance [1–6]. A stable structure and mechanical performance at high temperatures for a long service life are essential for TiAl alloys to be used as high-temperature structural materials in equipment that requires high safety and stability [7]. It has been demonstrated that under prolonged thermal exposure at high temperatures, the microstructure and phase composition of the TiAl alloy undergo changes, including continuous coarsening, discontinuous coarsening (DC) of the lamella, and the production of equiaxed grains [8]. The related phase transformations are α_2 lamella decomposition (vertical and parallel decomposition) [9,10] and B2 phase transformation (B2 → ω and B2 → γ) [11]. The microstructural evolution of the TiAl alloy at high temperatures is affected by the composition, structure, temperature, duration and other factors, and long-term thermal exposure promotes microstructural

evolution [12]. Essentially, thermodynamics determine whether the microstructure is stable at high temperatures, whereas dynamics control the rate and degree of evolution [3]. The evolution of the microstructure directly affects the mechanical properties of TiAl alloys. For instance, the hardness of 47Al–2Nb–2Mn–0.8%TiB_2 (volume fraction) and Ti–45Al alloys decreases when the lamella spacing coarsens [13].

The oxidation resistance of the TiAl alloy is intimately tied to the Al_2O_3 protective layer, which cannot fully develop although the TiAl alloy has a high Al content. Meanwhile, TiO_2 grows rapidly but cannot offer long-term antioxidative protection [14]. Therefore, the oxidation resistance of traditional TiAl alloys is insufficient above 800 °C [15,16].

Previous research [17–27] reveals that the addition of alloying elements, such as W, Mo, Ta and Nb, can prevent the lamella from coarsening and significantly improve the high-temperature oxidation resistance of the TiAl alloy; among these, the effects of Ta and Nb are particularly notable. Nb can efficiently improve the outward diffusion rate of Al while reducing the growth rate of TiO_2 particles and the diffusion rate of O [24,28,29]. With increasing Nb concentration, the TiAl alloy's high-temperature oxidation resistance increases linearly [30]. The addition of Ta limits the solubility of O in the TiAl alloy and prevents TiO_2 from growing at high temperatures because of its low diffusion coefficient [31].

According to previous studies [32–34], the addition of Ta to TiAl alloys can improve their mechanical properties, including their tensile strength, compressive strength and hardness, due to solution strengthening and refinement of the massive γ phase by controlling metastable microstructural evolution [35–37]. Ta and Nb elements can extend the cooling rate requirement for the $\alpha \rightarrow \gamma_m$ massive transformation to avoid the quenching of cracks caused by an excessive cooling rate [38]. The solution effect of Ta addition is stronger than that of Nb, which can effectively increase creep resistance without changing the phase transformation path [39], and Ta can improve the plasticity of the TiAl alloy more obviously than Nb [40]. In addition, Ta and Nb, which promote massive transformation and inhibit lamella transformation at low temperatures, have low diffusion coefficients in the α and γ phases. Segregation occurs with the addition of Ta and Nb elements [41,42], although they improve the high-temperature performance and oxidation resistance of the TiAl alloy. However, powder metallurgy is an ideal preparation method because it achieves chemical homogeneity and fine grains while avoiding segregation [43].

The present work is focused on the investigation of the thermal exposure characteristics of a new powder metallurgical TiAl alloy containing Nb and Ta prepared by powder hot isostatic pressing (P–HIP). Ti–48Al–3Nb–1.5Ta (at. %) alloy, as a hyperperitectic TiAl with almost no B2 phase, can prevent microstructure instability and performance reduction from B2 decomposition at high temperatures. Proper addition of Ta and Nb can improve the oxidation resistance and mechanical performance at high temperatures. The improved segregation of Nb and Ta and the promotion of microstructure homogeneity through the P–HIP process are expected to further elevate the service temperature of TiAl alloys. The application of the material at high temperatures is directly impacted by alterations in the microstructure and mechanical properties with long-term thermal exposure. However, the thermal exposure characteristics of P–HIP Ti–48Al–3Nb–1.5Ta alloy are currently unclear. For application guidance, such as for aero-engines used in harsh environments requiring long-term stable service, it is vital to study the effects of thermal exposure on the microstructure and mechanical properties of the P–HIP Ti–48Al–3Nb–1.5Ta alloy. In this study, the surface morphology, microstructural evolution and mechanical performance of the P–HIP Ti–48Al–3Nb–1.5Ta (at. %) alloy during thermal exposure were investigated and clarified.

2. Materials and Methods

Ti–48Al–3Nb–1.5Ta (at. %) prealloyed powders were prepared using SS-PREP® from Sino-Euro Materials Technologies of Xi'an Co., Ltd. (Sino-Euro, Xi'an, China) and then sieved into 45–250 μm sized powders. The powders were mostly perfect spherical in shape, as shown in Figure 1. The specific prealloyed powders were poured into steel capsules and degassed at 400 °C for 4 h to remove air. The stem at the top of the capsule was welded

when the vacuum of the capsule reached 1×10^{-4} Pa. The sealed capsules were placed in the HIP furnace and heated to 1200 °C with a heating rate of 4 °C/min and pressurized up to 150 MPa for 4 h, followed by cooling at 5 °C/min to room temperature.

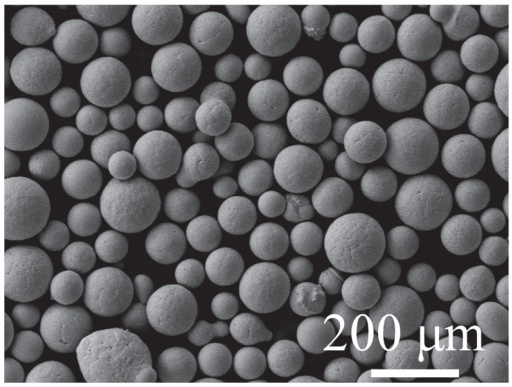

Figure 1. The typical morphology of SS-PREP® Ti−48Al−3Nb−1.5Ta powders in the range of 45–250 μm.

The 10 × 10 × 10 mm specimens were cut from the P–HIP Ti–48Al–3Nb–1.5Ta alloy billet after the capsules were removed. Some specimens were put into quartz tubes and sealed before exposure (sealed specimens), while the others were exposed directly (unsealed specimens). The unsealed specimens were used to analyze the surface morphology and scale constitution, and the sealed specimens were used to analyze the microstructural evolution and mechanical properties. The sealed specimens with the size of φ8 × 67 mm after thermal exposure were machined into specimens with a diameter of 3 mm and a gauge length of 15 mm for tension testing at room temperature. The exposure temperatures were 800 °C, 850 °C and 900 °C and the duration was 100 h, 300 h, 500 h, 800 h or 1000 h.

The phase constituents were analyzed using X-ray diffraction (XRD, Bruker D8 DISCOVER A25, Bruker, Billerica, MA, USA) with Co Kα radiation at a rate of 2.5°/min from 20° to 90° at room temperature. The surface morphology, microstructure and element distribution were analyzed using scanning electron microscopy (SEM, ZEISS Sigma 300, Oberkochen, Germany) equipped with an energy-dispersive X-ray spectrometer (EDX, ZEISS Sigma 300, Oberkochen, Germany), an electron probe microanalyzer (EPMA, SHIMADZU EPMA-1720, Kyoto, Japan) and a transmission electron microscope (TEM, FEI Talos F200X TEM, Hillsboro, OR, USA). The crystallographic features were further analyzed using electron backscattered diffraction (EBSD, ZEISS Sigma 300, Oberkochen, Germany). The hardness was analyzed using a nanomechanical testing system (Hysitron TI-950, Bruker, Billerica, MA, USA) with a 10 mN force. The tensile performance was determined using a microcomputer-controlled electron universal testing machine (CMT5105, Sansi Yongheng, Ningbo, China) according to GB/T 228.1-2021 (Chinese Standard) [44].

The 10 × 10 × 10 mm sealed specimens were cut in half and mechanically mounted in epoxy resin, polished with SiC abrasive papers and a polishing cloth and, finally, polished by a vibratory polisher; these were then used for SEM and EBSD analyses on internal cross-sections. The specimens for TEM were first cut into a 400 μm thick slice from the middle of the 10 × 10 × 10 mm sample, then manually ground to a 50 μm thickness with SiC abrasive papers and, finally, subjected to ion milling. The hardness inside the specimens was obtained as arithmetic mean values from ten testpoint measurements approximately evenly distributed along a straight line of one 10 × 10 × 10 mm sample with the same preparation method as for EBSD. Near-surface hardness testing was conducted on unsealed specimens along the cross-section from the edge with an interval of 3.5 μm for a total 10 testpoints.

3. Results and Discussions

3.1. Microstructures of the P–HIP Ti–48Al–3Nb–1.5Ta Alloy

The P–HIP Ti–48Al–3Nb–1.5Ta alloy consists of 95.05% γ and 4.95% α_2 phases, as represented in the EBSD phase map (Figure 2a,b), because the metastable α_2 phase in the prealloyed powders almost completely transforms into the γ phase during the P–HIP process at 1200 °C, which occurs at the top of the single γ-phase area. The microstructures of the P–HIP Ti–48Al–3Nb–1.5Ta alloy were characterized mainly as near-gamma and locally duplex, as indicated in Figure 2c, consisting of γ (dark) and α_2 (gray) phases with an average grain size of 5.9 μm, which is much more refined than those of the conventionally cast alloy as powder metallurgy is an effective method for refining grains. The EDS mapping (Figure 2d) of the magnified area of Figure 2c shows the α_2 (Al-lean)/γ (Al-rich) lamella structure in the P–HIP Ti–48Al–3Nb–1.5Ta alloy. The TEM bright-field (BF) image (Figure 2e) and selected-area electron diffraction (SAED) patterns with different axes (Figure 2f–h) of the marked area in Figure 2e show the irregular α_2 phase.

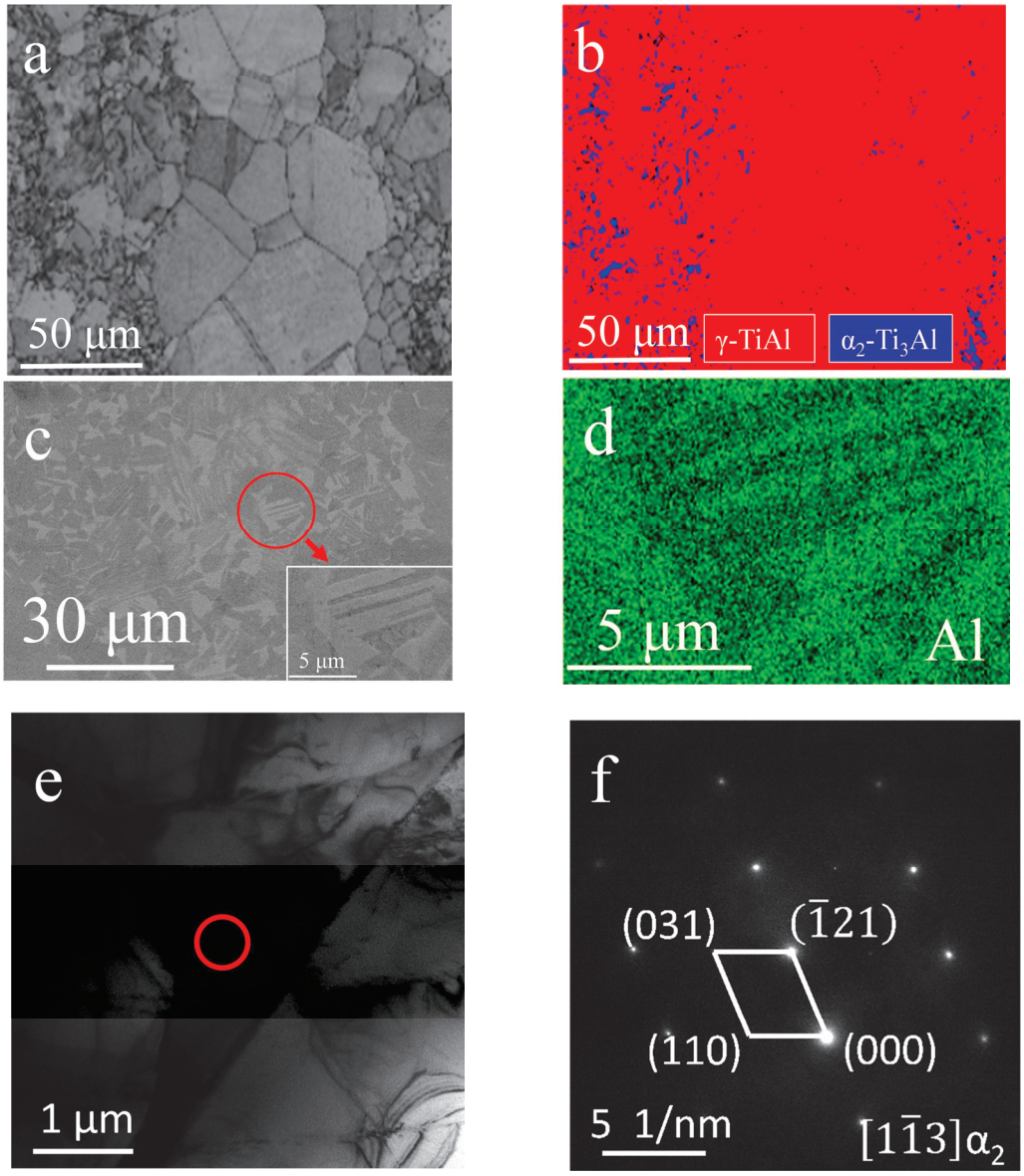

Figure 2. *Cont.*

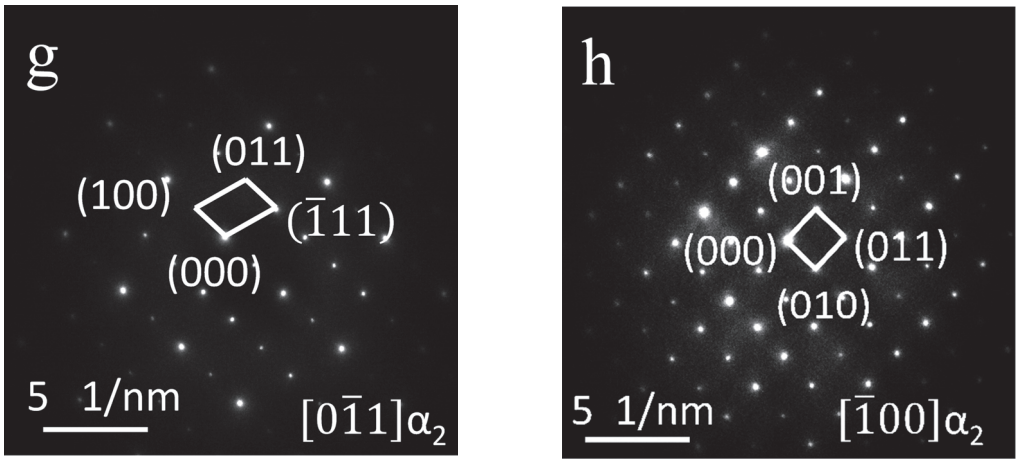

Figure 2. Microscopic analysis of the P–HIP Ti–48Al–3Nb–1.5Ta alloy: (**a**,**c**) Microstructures; (**b**) EBSD phase map of Figure 2a; (**d**) EDS mapping of Figure 2c; (**e**) TEM BF image; (**f**–**h**) SAED of the marked area of Figure 2e with different axes.

3.2. Characterization of the Surface Scale

Because the type of surface scale after exposure determines the oxidation resistance, XRD analysis of the unsealed specimens' surfaces was conducted to analyze the phase constitution, as shown in Figure 3. The XRD patterns and phase constitution were almost the same under different thermal-exposure conditions. α–Al_2O_3 and rutile–TiO_2 were the primary components, and TiN and Ti_2AlN were also detected. In addition, the patterns include γ and α_2 phases, without a B2 phase detected as a peritectic TiAl [32], which are consistent with the P–HIP Ti–48Al–3Nb–1.5Ta alloy. The intensity of the γ and α_2 phases decreases with increasing exposure temperature and duration. The peak of TiO_2 becomes more prominent as the exposure duration increases at 800 °C, while notable peaks of TiO_2 are discernible following thermal exposure at 850 °C and 900 °C for 100 h. A strong peak of TiN appears after exposure at 900 °C for 100h. However, as time passes, the TiN peak significantly weakens, indicating that TiN is generated rapidly at 900 °C and is subsequently covered by the continuously growing oxides of Ti and Al. No significant changes were observed in the α–Al_2O_3 peaks with variations in temperature and duration, indicating that α–Al_2O_3 is preferentially formable and relatively stable. Moreover, weak peaks of Ti_2AlN were observed under different exposure conditions.

To investigate the scale characteristics, the surface morphologies of P–HIP Ti–48Al–3Nb–1.5Ta alloy after thermal exposure to different conditions were analyzed, as shown in Figure 4. The surface scale is mainly composed of irregularly shaped clusters and prismatic particles. EDS analysis was conducted on different surface areas of the specimen exposed at 800 °C for 1000 h, as shown in Figure 5 and Table 1. The results indicate that the surface scale is mainly composed of Ti, Al and O elements. There exists a higher content of Ti in prismatic particles (Locations 1, 2, 3, 4 and 6), while there exists a higher content of Al in irregularly shaped particles (Locations 7 and 8). Moreover, particles containing all Ti, Al, Nb and Ta elements are also observed (Location 5). According to the EDS and XRD results, the prismatic particles are TiO_2, and the irregularly shaped particles are Al_2O_3. The surface morphologies change significantly with increasing exposure temperature and duration. Similarly fine and uneven scales were observed on the surface of the P–HIP Ti–48Al–3Nb–1.5Ta alloy exposed at 800 °C and 850 °C for 100 h, as shown in Figure 4a,f, and locally accumulated regions form at 850 °C. As the exposure duration increases, the surface scale becomes more continuous and accumulates, and TiO_2 particles increase and grow. The surface of the Ti–48Al–3Nb–1.5Ta alloy exposed at 900 °C for 100 h displays an almost completely filled scale, as shown in Figure 4k, and TiO_2 particles increase and grow significantly with increasing exposure duration, as shown in Figure 4o. The average size of the TiO_2 particles increased from 1.74 μm to 4.02 μm while the maximum size increased

from 4.96 μm to 12.70 μm, with the shape changing from equiaxed particles to elongated particles as the exposure duration extended from 100 h to 1000 h. A similar phenomenon has been reported in S. Taniguchi's previous research [30]. As the TiO_2 particles grow larger, fine TiO_2 particles are generated between the large particles with gaps appearing, indicating that the oxidation resistance of the TiO_2 layer is poor at high temperatures.

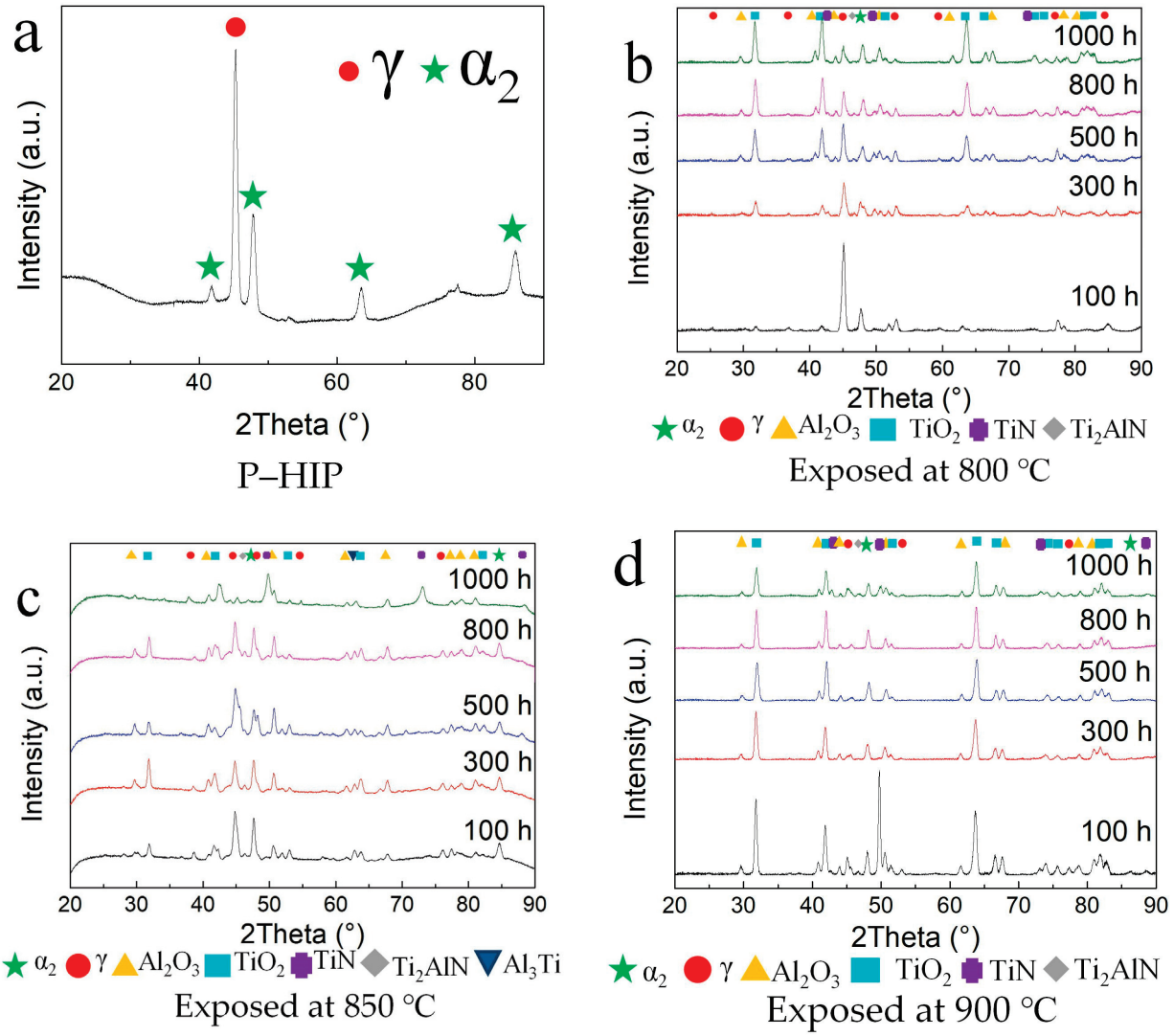

Figure 3. XRD patterns of the Ti–48Al–3Nb–1.5Ta (at. %) alloy: (**a**) P–HIP; (**b**) Exposed at 800 °C; (**c**) Exposed at 850 °C; (**d**) Exposed at 900 °C.

Table 1. EDS analysis results of the P–HIP Ti–48Al–3Nb–1.5Ta alloy (at. %) exposed at 800 °C for 1000 h shown in Figure 5.

Position	Ti	Al	O	Nb	Ta	C
1	27.57	-	68.71	-	-	3.72
2	39.58	0.43	56.89	-	-	3.11
3	27.61	-	68.21	-	-	4.18
4	33.13	5.86	61.01	-	-	-
5	17.43	7.35	48.23	0.99	0.43	25.58
6	26.34	0.72	69.68	-	-	3.25
7	6.50	26.73	66.78	-	-	-
8	2.67	25.89	58.14	-	-	13.30

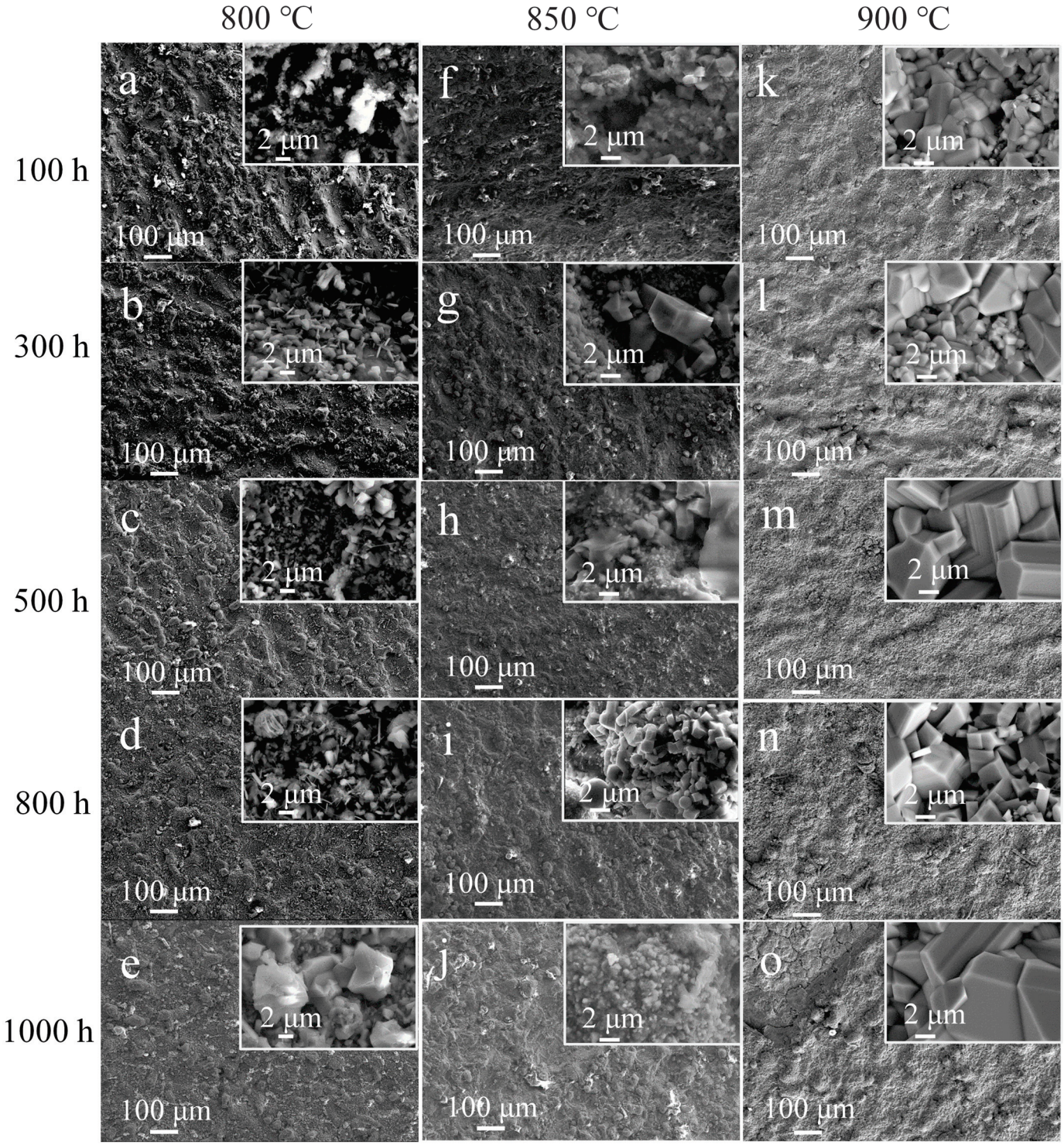

Figure 4. Surface morphology of the P–HIP Ti–48Al–3Nb–1.5Ta (at. %) alloy after thermal exposure to different conditions: (**a**) 800 °C, 100 h; (**b**) 800 °C, 300 h; (**c**) 800 °C, 500 h; (**d**) 800 °C, 800 h; (**e**) 800 °C, 1000 h; (**f**) 850 °C, 100 h; (**g**) 850 °C, 300 h; (**h**) 850 °C, 500 h; (**i**) 850 °C, 800 h; (**j**) 850 °C, 1000 h; (**k**) 900 °C, 100 h; (**l**) 900 °C, 300 h; (**m**) 900 °C, 500 h; (**n**) 900 °C, 800 h; (**o**) 900 °C, 1000 h.

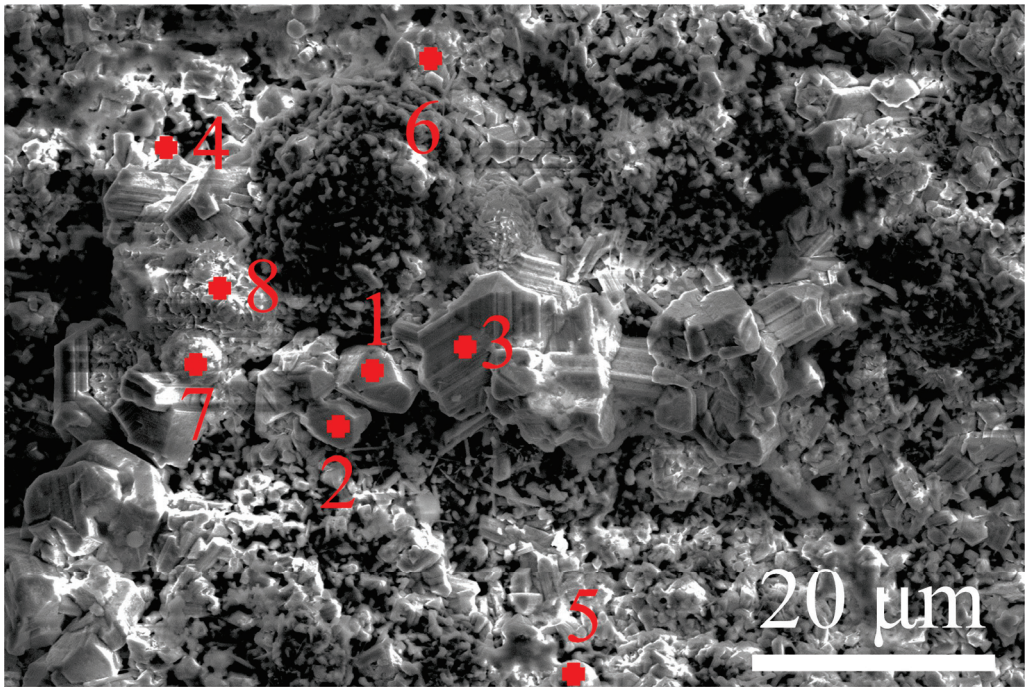

Figure 5. The surface morphology of the P–HIP Ti–48Al–3Nb–1.5Ta alloy exposed at 800 °C for 1000 h, with marks 1–8 indicating the EDS positions.

In order to further analyze the distribution of different components of the surface scale after thermal exposure, EPMA mapping was performed on the near-surface of the specimens after thermal exposure at 800 °C, 850 °C and 900 °C for 100 h and 1000 h, respectively, as shown in Figure 6. The nitride layer is above the substrate and below the oxide layer. The oxidation of the TiAl alloy in air, broadly speaking, includes both oxidation and nitridation, and oxidation is usually superior to nitridation at a sufficiently high partial pressure of oxygen, which ensures the formation of a scale composed of TiO_2 and Al_2O_3. When the oxide layer covers the entire surface of the substrate, further reactions are controlled by the inward diffusion of oxygen and nitrogen [45]. The oxidation layer exhibits a certain hindrance to the diffusion of these elements. Therefore, the activity of oxygen and nitrogen gradually decreases as the diffusion depth increases. Oxygen activity decreases faster because it is consumed preferentially. When the oxygen activity is lower than a certain critical value—that is, when the oxidation affected zone reaches a certain depth—it is conducive to the appearance of nitridation on the substrate. TiN is an excellent diffusion barrier that can prevent the diffusion of oxygen toward the substrate [46]. As a consequence, the typical structure of the scale on the exposed surface of P–HIP Ti–48Al–3Nb–1.5Ta alloy consists of external oxides and internal nitrides. The formation of the nitride sublayer below the oxide is significantly influenced by alloying elements such as Nb and Ta, which impede the diffusion of nitrogen toward the substrate [47].

The formation sequence and growth mode of oxides in the oxide layer are related to the free energy of formation and the activation energy of growth. The free energy of formation of the two oxides is highly negative at 800–900 °C; that is, they have a very low equilibrium decomposition pressure [48]. Therefore, TiAl alloys are prone to oxidation and form stable oxides in this temperature range [49]. According to the oxidation behavior of the TiAl alloy [12,50], Al_2O_3 is formed on the surface of the substrate during the initial stage of oxidation. With the formation of the Al_2O_3 layer, the Al on the surface of the TiAl substrate is gradually consumed, while Al diffuses slowly in the TiAl substrate. It is difficult to diffuse to the surface in a short time to replenish the consumed Al; thus, an Al-lean layer is formed below the thin layer of Al_2O_3, and the concentration of Ti in this layer gradually increases. When the Ti content reaches the critical value, it reacts with the inwardly diffused oxygen to form Ti oxides [51]. Common Ti oxides include TiO, Ti_2O_3

and TiO_2, among which TiO_2 has the best high-temperature stability [30]. The content of Al_2O_3 on the surface scale was higher than that of TiO_2 after exposure at 850 °C for 100 h, as shown in Figure 4, and the thickness of the Al_2O_3 layer was greater than that of the TiO_2 layer, as shown in Figure 6. However, the growth-activation energy of Al_2O_3 (502.4 kJ/mol) is higher than that of TiO_2 (59.5 kJ/mol) [52], so the growth rate of TiO_2 is much higher than that of Al_2O_3. With an increase in the exposure duration, TiO_2 particles gradually cover the Al_2O_3 particles, resulting in a TiO_2 layer formed on the Al_2O_3 layer [30], similar to the variation in surface morphologies shown in Figure 4.

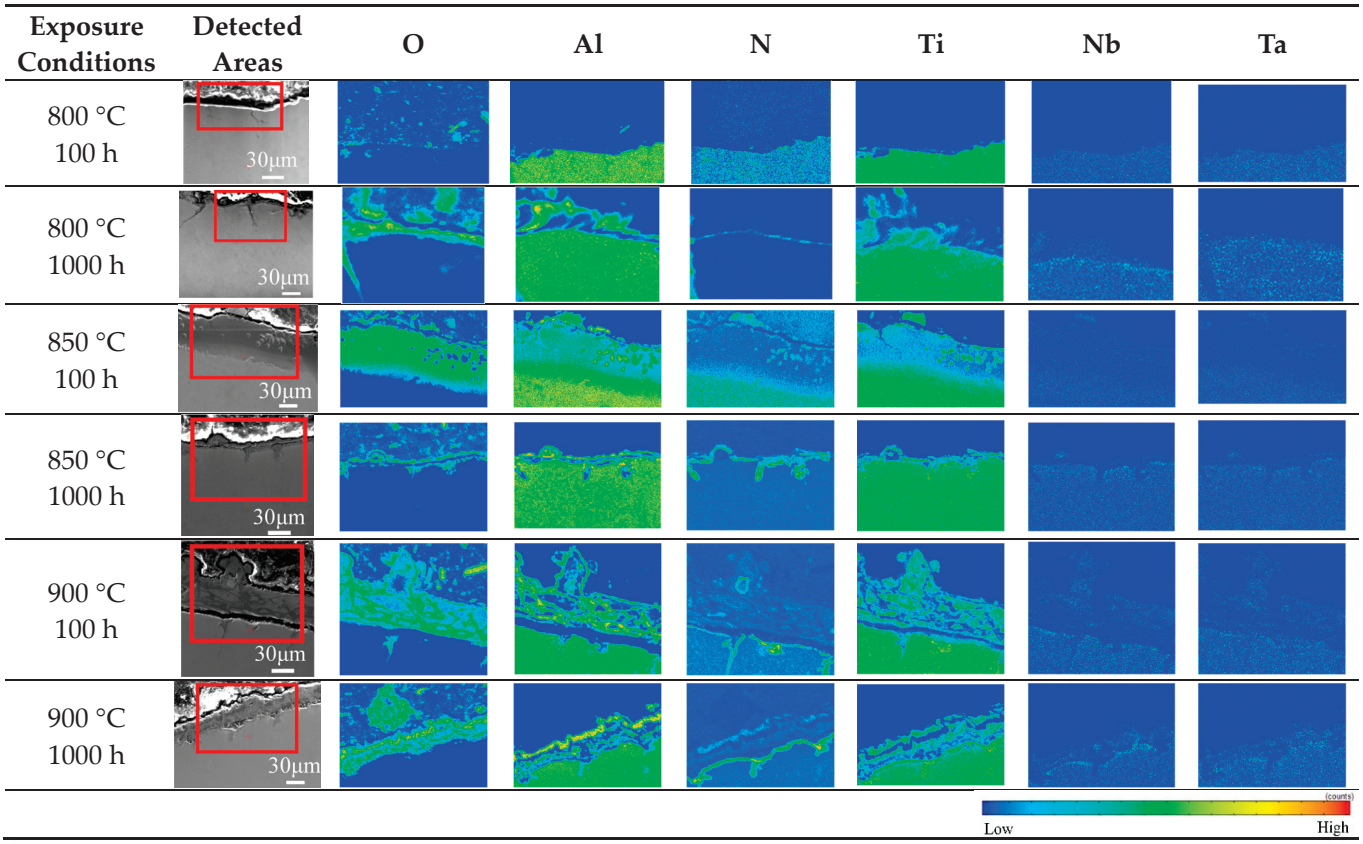

Figure 6. EPMA mapping on the near-surface of the P–HIP Ti–48Al–3Nb–1.5Ta alloy after exposure to different conditions, and the red squares in the column two show the detected areas.

Rutile TiO_2 is a non-stoichiometric compound. Because of the large number of vacancy defects, this TiO_2 layer allows for a fast diffusion rate of oxygen atoms, which represents a good path for oxygen penetration into the substrate [53]. Al_2O_3 is an ionically bonded compound with a dense structure, in which the diffusion rate of oxygen atoms is four orders of magnitude lower than that in the TiO_2 layer. Therefore, once a continuous dense Al_2O_3 layer is formed, the diffusion of oxygen atoms almost terminates. Although the TiO_2 layer cannot effectively prevent the oxidation of the substrate, it also reduces the oxygen concentration to a certain extent. Coupled with the obstructing effect of the Al_2O_3 layer, the oxygen concentration is further reduced, and the diffusion path of oxygen atoms becomes narrower and narrower, so the oxidation mass gain becomes slower and slower [30].

The addition of alloying elements can decrease the vacancy-formation energy of Al and increase that of Ti. As the Al vacancy concentration increases, it is easier for Al to diffuse to the surface and react with oxygen atoms, improving the oxidation resistance at high temperatures with a good Al_2O_3 protective film formed on the surface of the TiAl alloy [54]. Nb and Ti have the same valence electron structure and ionic radius, and they can be miscible in any proportion. Nb can occupy the normal Ti site. The replacement of Ti^{4+} with Nb^{5+} reduces the defect concentration of TiO_2 as well as the diffusion rate

of oxygen and metal ions in the oxide layer, inhibiting the formation and growth of TiO_2 and facilitating the formation of a continuous dense Al_2O_3 layer on the surface of the TiAl alloy [24]. As the neighbor in the periodic table, Ta is similar to Nb, which can also reduce the oxygen solubility in the TiAl alloy and inhibit TiO_2 growth [55]. Ta^{5+} replaces Ti^{4+} in the TiO_2 lattice, resulting in an excess positive charge. The concentration of O^{2-} vacancies, which are responsible for O diffusion, decreases to offset this increase. Nb and Ta are both effective alloying elements that improve the oxidation resistance of TiAl alloys, and the oxidation rate at high temperatures of TiAl alloys containing Nb and Ta is significantly lower than that of simple binary TiAl alloys with the same Al content [47]. There are very small amounts of Nb and Ta in the oxide layer above the nitride layer, as we can see from the 900 °C EPMA mapping results in Figure 6, whereas there is no such phenomenon at 800 °C and 850 °C, because the ability of Nb and Ta to diffuse toward the substrate surface increases with increasing temperature. Because there is no diffraction peak for oxides of Ta or Nb in the XRD patterns, it is assumed that they replace Ti in the rutile lattice [31], thus impeding the oxidation process at higher temperatures.

The variation in the oxide-layer thickness after thermal exposure was further analyzed using EDS line scanning, as shown in Figure 7. With increasing thermal exposure temperature and duration, the oxide-layer thickness gradually increases at a slow rate. The thicknesses of the oxide layer are about 12.7 μm and 23.7 μm after thermal exposure for 1000 h at 800 °C and 850 °C, respectively, which is smaller than 24.5 μm, the thickness of a Ti–47.5Al–2.5V–1.0Cr–0.2Zr (at %) oxide layer after exposure at 750 °C for 300 h [56], indicating superior oxidation resistance. The thickness of the oxide layer is about 25.2 μm after thermal exposure at 900 °C for 800 h, and the decrease in the oxide-layer thickness after 1000 h may be related to the spalling of the oxide layer.

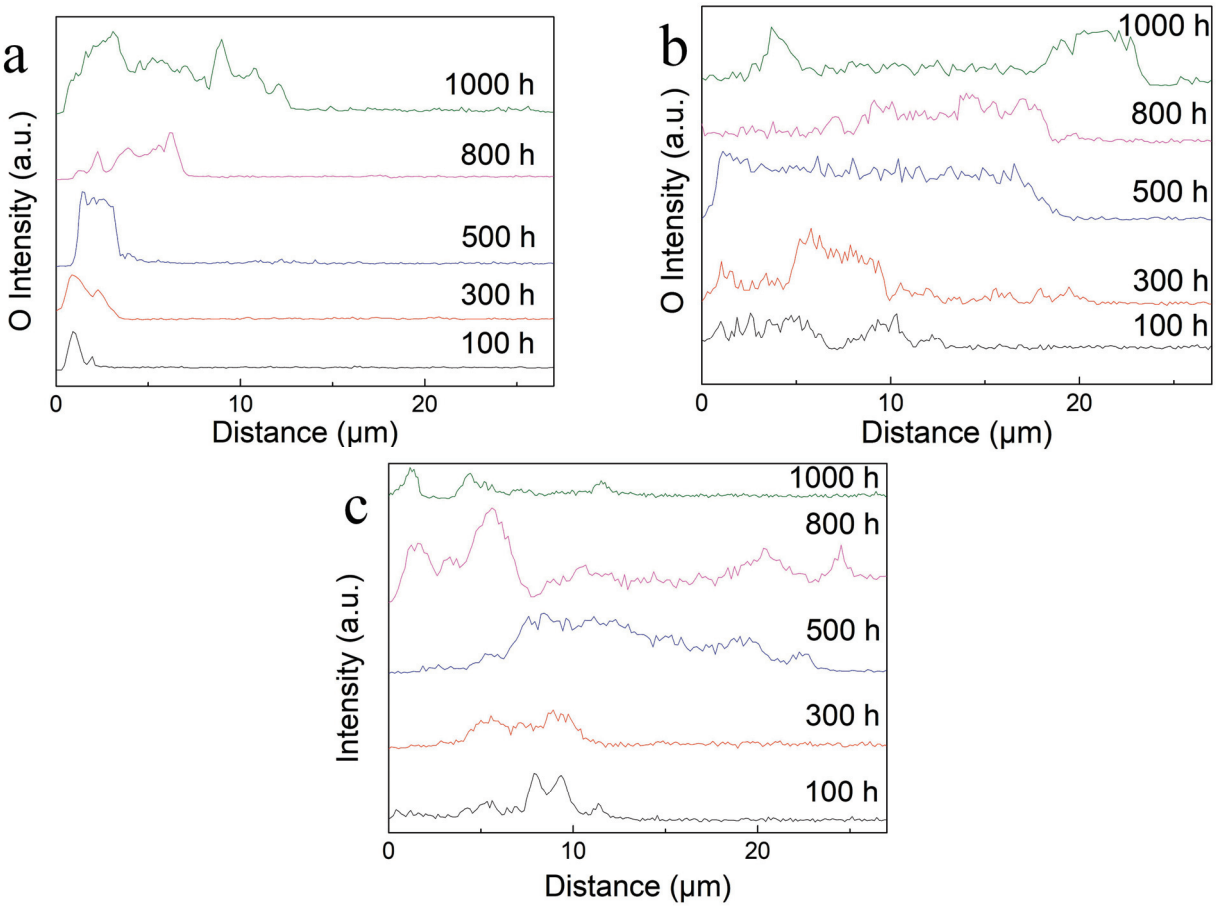

Figure 7. Oxygen contents vary with the depth of different sample surfaces after exposure: (**a**) At 800 °C; (**b**) At 850 °C; (**c**) At 900 °C.

In general, the oxide layer becomes significantly continuous with increasing exposure temperature, especially for short exposure durations. However, after exposure for 1000 h, the surface morphologies all show a continuous and fully filled scale, similar to that in a previous study [57].

3.3. Microstructure Stability

In order to analyze the microstructural evolution of the P–HIP Ti–48Al–3Nb–1.5Ta alloy during thermal exposure, BSE-SEM microstructure morphology analysis and EBSD phase-composition analysis were performed on the internal cross-sections of the sealed specimens after exposure to different conditions, as shown in Figures 8 and 9. The dark region is the γ phase, whereas the white region is the α_2 phase in Figure 8. The phase composition and grain-size distribution analyzed using EBSD are shown in Table 2 and Figure 10. The results reveal that the grain size does not grow significantly after thermal exposure to different conditions, and the γ phase increases slightly, less than 3.5%, compared with P–HIP, as depicted in Section 3.1. The increase in the γ-phase volume fraction is caused by the α_2-phase dissolution at 800–900 °C, and longitudinal and transverse dissolution leads to thinning and fracture of the α_2 lamella [58,59]. At the same time, with the extension of the thermal exposure duration, the DC of the γ phase is observed near the grain boundaries due to the reduction of lamella near the grain boundaries, which expands the γ phase region, as marked in the microstructure after exposure at 850 °C for 1000 h in Figure 8.

Table 2. EBSD phase constitution of the Ti–48Al–3Nb–1.5Ta alloy after thermal exposure to different conditions.

Temperature (°C)	Duration (h)	γ Phase (%)	α_2 Phase (%)
800	100	$96.9^{+0.33}_{-0.15}$	$3.1^{+0.58}_{-0.17}$
	1000	$95.5^{+0.26}_{-0.09}$	$4.5^{+0.39}_{-0.21}$
850	100	$97.5^{+0.25}_{-0.36}$	$2.5^{+0.77}_{-0.61}$
	1000	$98.5^{+0.31}_{-0.11}$	$1.5^{+0.42}_{-0.46}$
900	100	$97.5^{+0.15}_{-0.29}$	$2.5^{+0.61}_{-0.42}$
	1000	$97.5^{+0.11}_{-0.30}$	$2.5^{+0.43}_{-0.55}$

Although the γ lamella and the α_2 lamella have an interphase distribution, the adjacent interfaces are not parallel to each other, and the shape of the γ lamella and α_2 is probably irregular or even curved. The thicknesses of different γ lamellae vary greatly, and the γ lamella is not regular but is like a wedge embedded within α_2 lamellae. In addition, there is a great difference in the thicknesses of different α_2 lamellae. The widest reaches 2.4 μm, while the narrowest is only 120 nm in the P–HIP Ti–48Al–3Nb–1.5Ta alloy, as shown in Figure 2c. This difference leads to a high content of α_2 lamella in local areas, resulting in a state of agglomeration and decomposition during thermal exposure. The α_2 lamella is metastable, leading to a tendency to transform into the most stable form during long-term exposure at high temperatures. Therefore, the metastable α_2 lamella decomposes into a fine α_2 + γ lamella [60], and the newly generated γ/α_2 interface is parallel to the original α_2 lamella, which is called "parallel decomposition" [9].

To reduce the total free energy of the system under long-term high temperatures, three types of microstructural evolutions may be generated for the lamella structure of the TiAl alloy: (1) phase transformations, (2) continuous coarsening, and (3) discontinuous coarsening. The phase transformation is manifested as the dissolution of the α_2 lamella, causing the volume fraction and composition of the γ and α_2 phases to change toward the equilibrium volume fraction and phase composition determined by the Ti-Al binary-phase diagram at this temperature [61], reducing the chemical free energy of the system [62]. Since α_2/γ is a low-energy semi-coherent flat interface in the lamella structure of the TiAl alloy and satisfies the Blackburn orientation relation, i.e., $\{111\}_\gamma \parallel \{0001\}_{\alpha_2}$ and

$< 11\bar{2}0 >_{\alpha_2} \parallel < 110 >_{\gamma}$, there is no obvious interfacial curvature. Therefore, continuous coarsening within the lamella is relatively difficult. However, the lamella structure has poor thermal stability and is prone to DC with grain boundary migration because of the existence of steps between α_2 and γ lamellae at the grain boundaries [63].

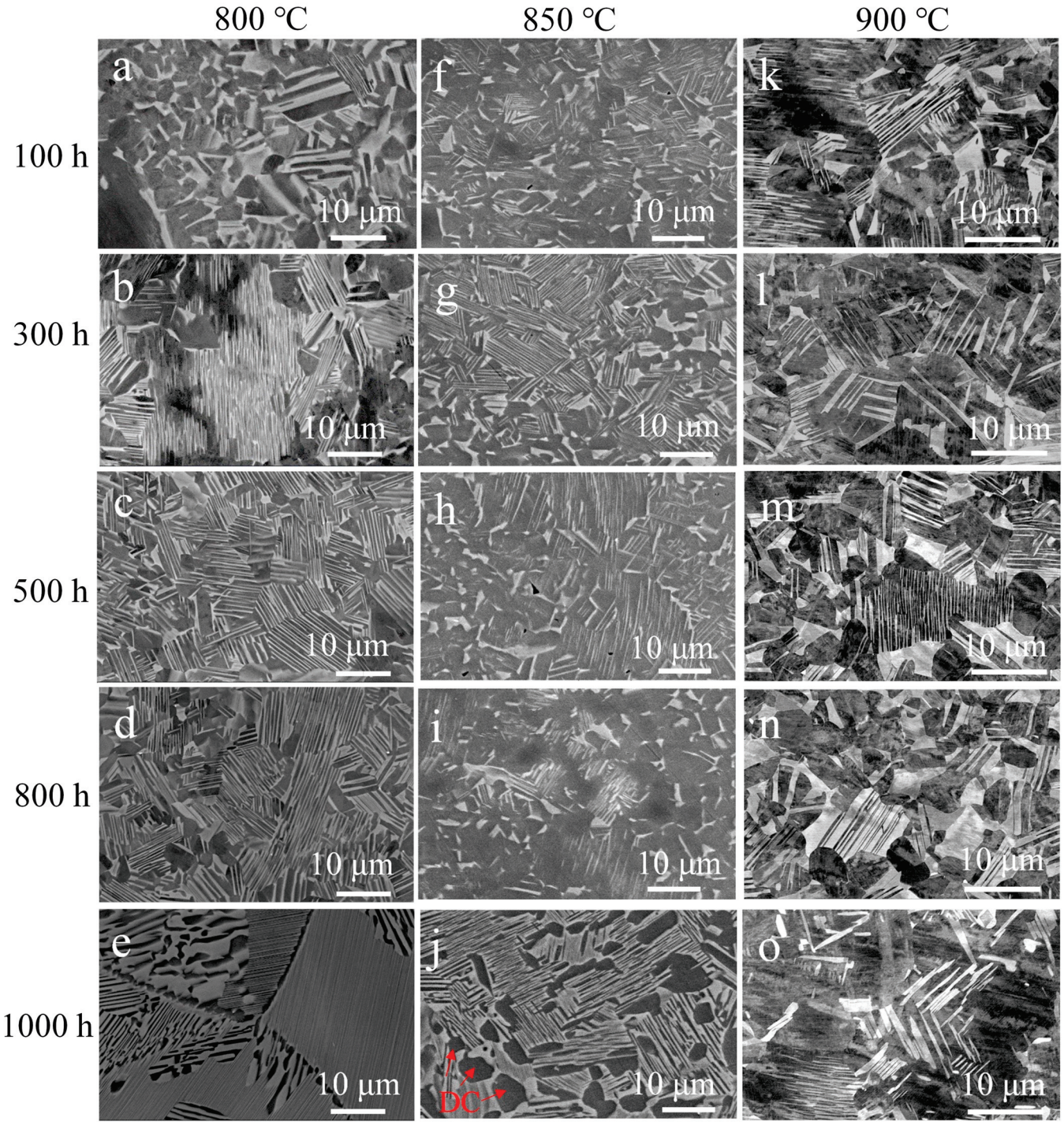

Figure 8. Microstructures of the Ti–48Al–3Nb–1.5Ta alloy after exposure to different conditions: (**a**) 800 °C, 100 h; (**b**) 800 °C, 300 h; (**c**) 800 °C, 500 h; (**d**) 800 °C, 800 h; (**e**) 800 °C, 1000 h; (**f**) 850 °C, 100 h; (**g**) 850 °C, 300 h; (**h**) 850 °C, 500 h; (**i**) 850 °C, 800 h; (**j**) 850 °C, 1000 h; (**k**) 900 °C, 100 h; (**l**) 900 °C, 300 h; (**m**) 900 °C, 500 h; (**n**) 900 °C, 800 h; (**o**) 900 °C, 1000 h.

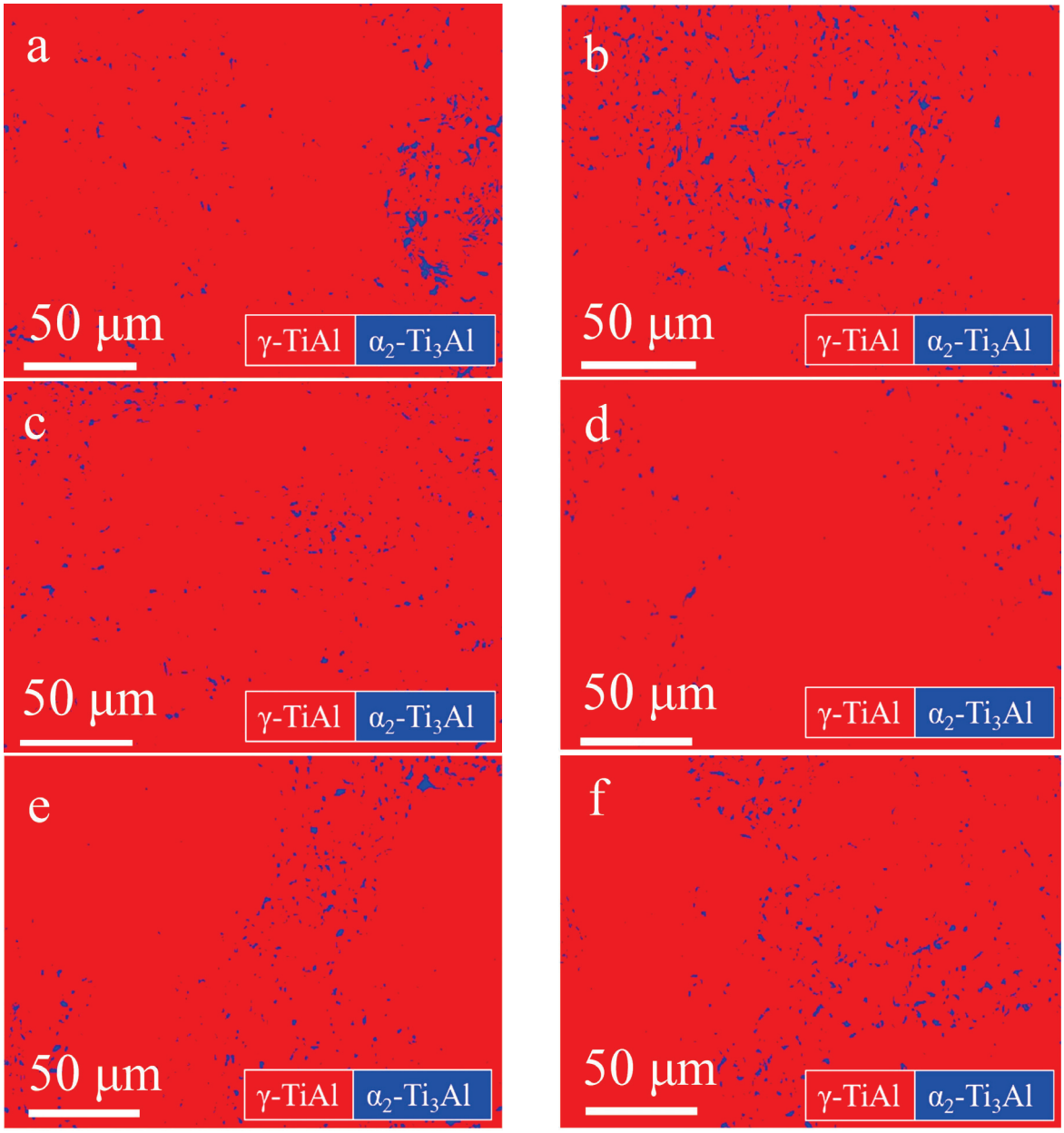

Figure 9. EBSD phase constitutions of the Ti–48Al–3Nb–1.5Ta alloy after exposure to different conditions: (**a**) 800 °C, 100 h; (**b**) 800 °C, 1000 h; (**c**) 850 °C, 100 h; (**d**) 850 °C, 1000 h; (**e**) 900 °C, 100 h; (**f**) 900 °C, 1000 h.

The specimens exposed at 800 °C for 1000 h were analyzed using TEM, and the BF images, SAED and EDS are shown in Figure 11 and Table 3. It can be seen that the matrix consists of a γ phase, the massive precipitate near the grain boundaries has an α_2 phase, and there are γ-phase twins. In addition, the nanotwins can be seen from the BF images and SAED in Figure 11f,g. The 6 nm average width of these nanotwins is the result of plastic deformation during the P–HIP process at 150 MPa pressure, and it remained so after thermal exposure because the annealing twins' width is in the micro dimension [64].

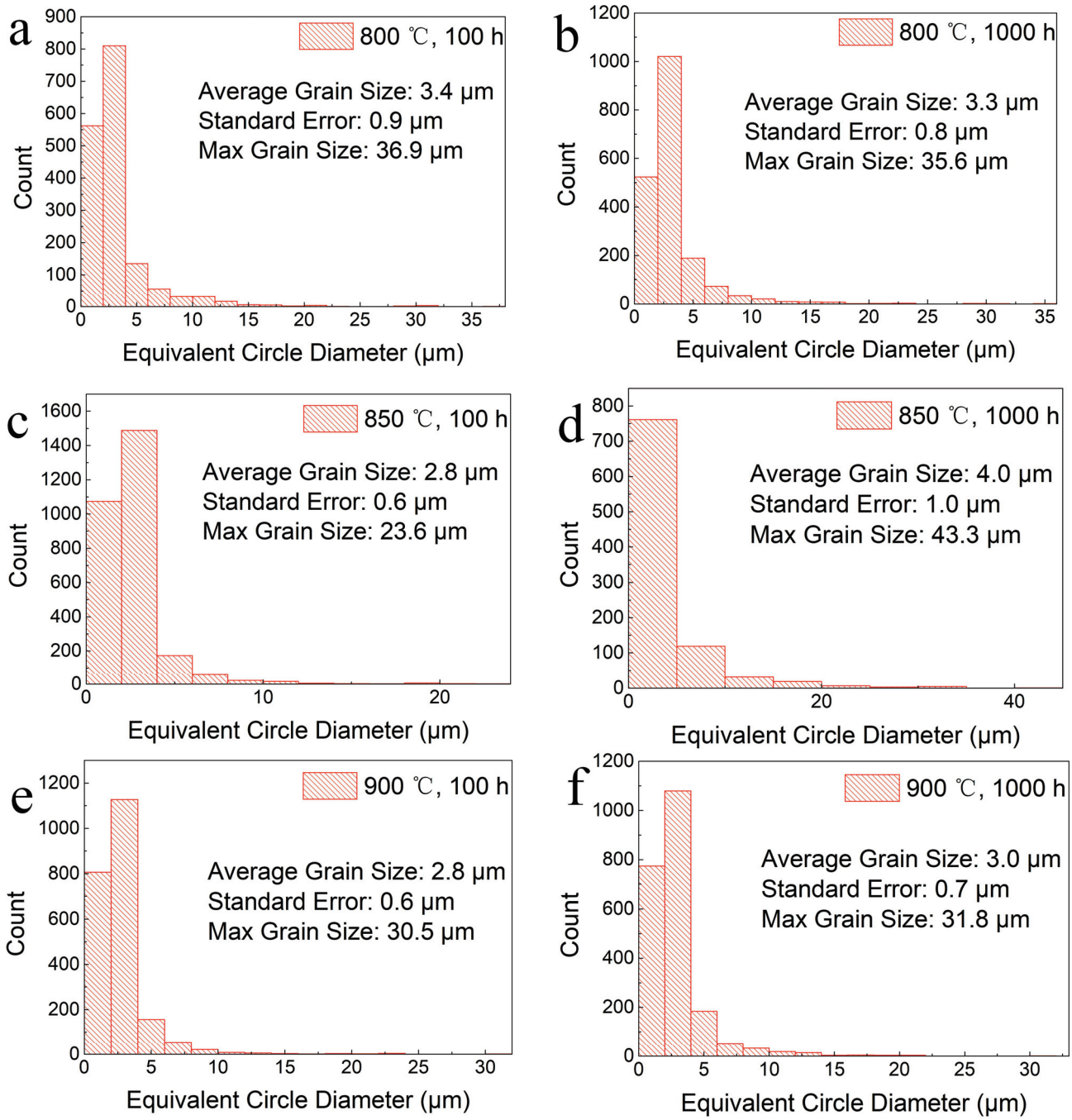

Figure 10. Grain size distributions of the Ti–48Al–3Nb–1.5Ta alloy after exposure to different conditions: (**a**) 800 °C, 100 h; (**b**) 800 °C, 1000 h; (**c**) 850 °C, 100 h; (**d**) 850 °C, 1000 h; (**e**) 900 °C, 100 h; (**f**) 900 °C, 1000 h.

Table 3. EDS results of site 1 and site 2 in Figure 11a (at. %).

Element	Al	Ti	Nb	Ta
1	31.62	65.32	1.53	1.50
2	49.88	45.61	2.94	1.55

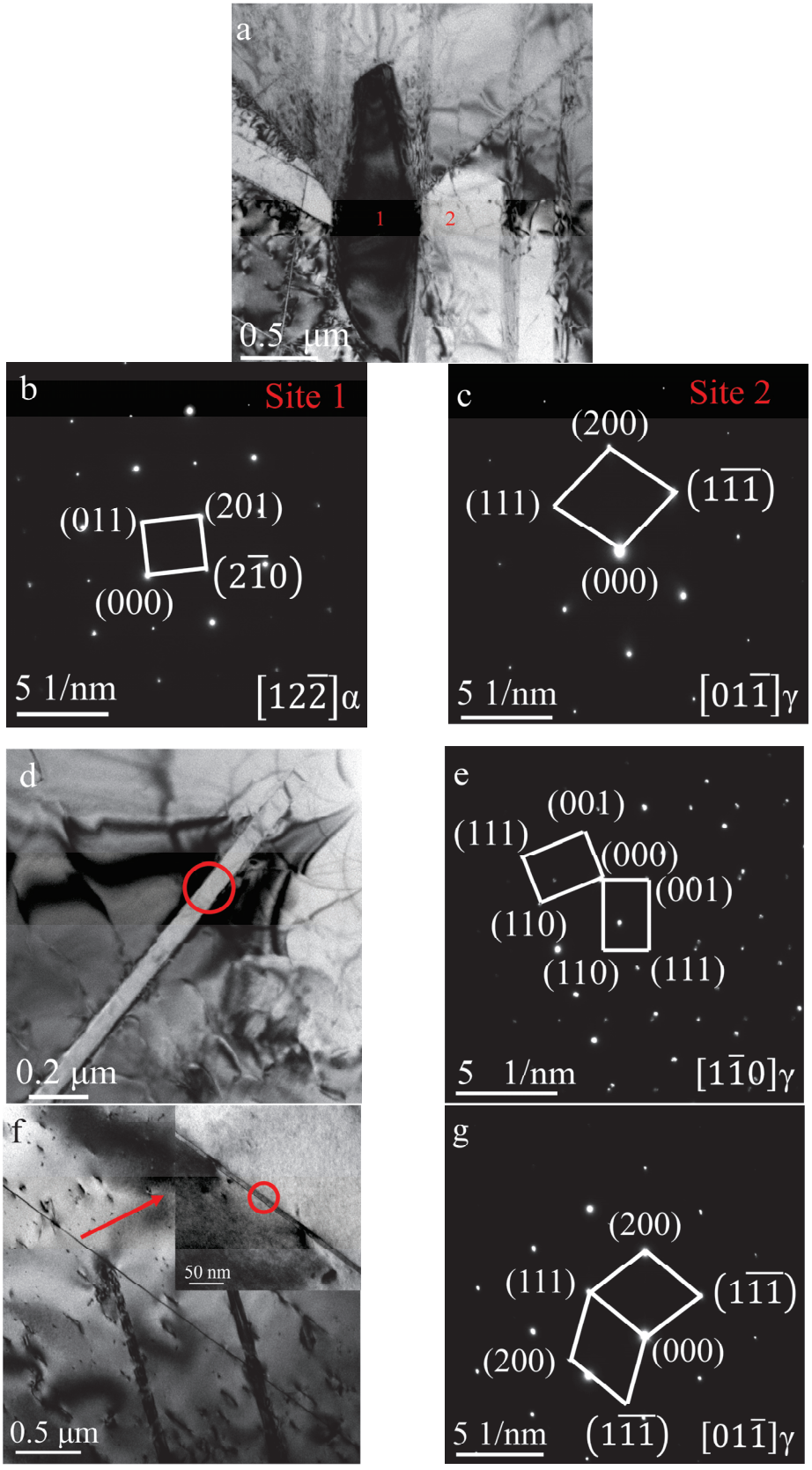

Figure 11. TEM images of the P–HIP Ti–48Al–3Nb–1.5Ta alloy exposed at 800 °C for 1000 h: (**a**) BF image showing two phases; (**b**) SAED of site 1 in Figure 11a; (**c**) SAED of site 2 in Figure 11a; (**d**) BF image of γ-phase twins; (**e**) SAED of circled area in Figure 11d; (**f**) BF image of nanotwins; (**g**) SAED of circled area in Figure 11f.

3.4. Mechanical Performance

To investigate the effects of thermal exposure on the mechanical performance of the P–HIP Ti–48Al–3Nb–1.5Ta alloy, nanoindentation analysis was performed on specimens after thermal exposure to different conditions, as shown in Figure 12. The hardness after thermal exposure at 850 and 900 °C increases by about 2 GPa compared with the hardness of the P–HIP state, which is 4.6 GPa. This is mainly due to the O solution during thermal exposure, which causes lattice distortion of the matrix and the formation of new phases, resulting in surface hardening of the alloy [65]. The hardness after thermal exposure at 850 °C and 900 °C is higher than that at 800 °C, indicating that oxidation is more serious at higher temperatures. With the extension of thermal exposure duration, the hardness fluctuates in a narrow range and tends to decrease to different degrees, which is related to the equiaxed γ grains increasing and growing continuously, the α_2 phase decreasing and the lamella coarsening [14]. The strength of the TiAl alloy is inversely proportional to the grain size following the Hall–Petch formula. Therefore, the $\alpha_2 + \gamma$ lamella coarsening and equiaxed γ growth during thermal exposure reduce the hardness and tensile properties of the alloy. The lamella spacing is negatively correlated with the hardness of the nanoindentation; that is, the larger the lamella spacing, the smaller the hardness of the nanoindentation. When the indenter is pressed into the matrix, plastic deformation occurs near the indenter, and elastic deformation occurs in the area away from the indenter. The main mechanism of plastic deformation is dislocation slip. When the γ/α_2 lamella spacing is small, the dislocation slip encounters more γ/α_2 boundaries, resulting in higher hardness values. During thermal exposure at 800–900 °C, a phase transformation from α_2 to γ will occur, and the hardness of the γ phase is less than that of the α_2 phase, so there will be a trend of hardness decline with the extension of thermal exposure duration.

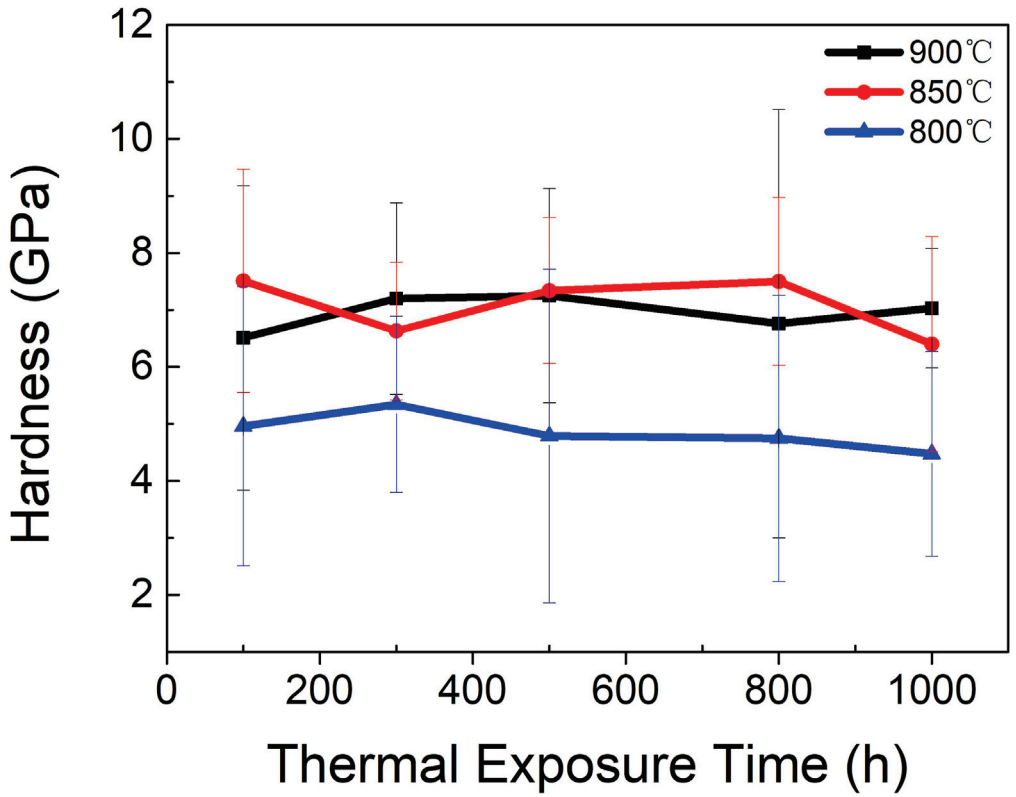

Figure 12. Hardness of the Ti–48Al–3Nb–1.5Ta alloy after exposure to different conditions.

To clarify the variation rule of hardness in the near-surface region of the P–HIP Ti–48Al–3Nb–1.5Ta alloy along the depth direction after thermal exposure at 800 °C for different durations, nanoindentation tests were conducted along the depth direction from the edge

of the unsealed specimens. The hardness results are shown in Figure 13. From the results of thermal exposure for 100 h, 300 h and 500 h, it can be seen that the hardness decreases with increasing depth from the specimen surface, since an O solution on the surface of the alloy leads to surface hardening. For titanium alloys, the relationship between hardness and surface O concentration can be expressed as follows [66]:

$$\mathrm{H} = H_0 + \mathrm{b}(x_O)^{\frac{1}{2}} \quad (1)$$

where H represents the hardness at the specified position, H_0 represents the hardness of the matrix, b is a constant, and x_O represents the O infiltration concentration at the specified position. As the O concentration gradually decreases from the surface along the depth direction, the hardness gradually decreases accordingly. In addition, an "influence zone" with an increased α_2 volume fraction is formed below the oxide layer in the TiAl alloy, the hardness of which is higher than that of the matrix, and the hardness gradually decreases from the edge to the matrix [66]. After thermal exposure for 800 h, the hardness values fluctuated greatly, which may be due to lamella coarsening and grain growth, and the test indenter easily fell into different phases with large differences in hardness. According to the nanoindentation hardness of the PST–TiAl alloy [67], the hardness of γ phase nanoindentation is 5.2 ± 0.1 GPa, and that of α_2 phase nanoindentation is 7.4 ± 0.5 GPa. It should be noted that the low hardness values after exposure for 1000 h may be related to the local spallation of the oxide layer.

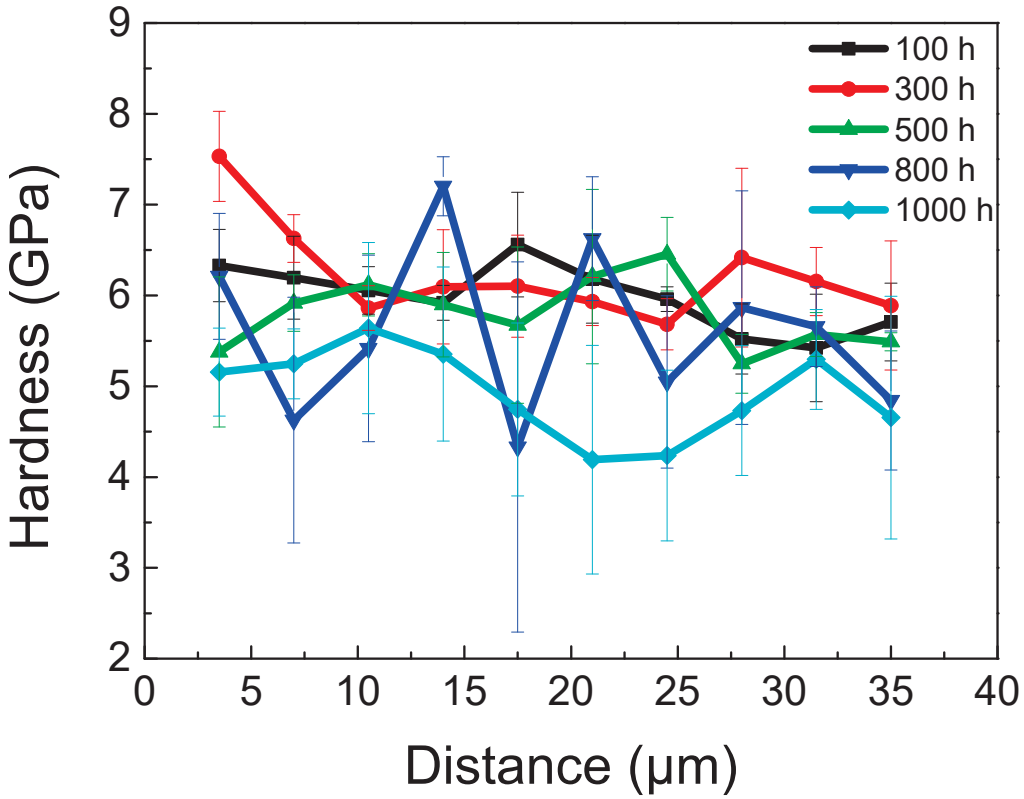

Figure 13. Hardness variation along the depth direction from the edge of the specimens after exposure at 800 °C for different durations.

Tensile tests at room temperature were performed on specimens exposed at 800 °C for 100 and 1000 h, respectively. The stress–strain curves together with the result of the P–HIP Ti–48Al–3Nb–1.5Ta alloy are shown in Figure 14. After thermal exposure at 800 °C for 100 and 1000 h, the tensile strengths were 491 MPa and 409 MPa, respectively, and the fracture strain was 0.23%. The fracture morphology of the tensile specimen exposed at 800 °C for

1000 h is shown in Figure 15, which indicates a typical brittle cleavage section, as expected. Nanotwins, as shown in Figure 11, are a special type of plane defect that can greatly hinder the dislocation movement and enhance the strength of alloys, particularly when the slip plane and Burgers vectors are not aligned with the twin boundaries [68]. Compared with the P–HIP Ti–48Al–3Nb–1.5Ta alloy, whose tensile strength is 357.09 MPa and whose fracture strain is 0.32%, the strength increases by more than 50 MPa and the fracture strain decreases by about 0.1% after the thermal exposure. Although the fracture strain of this TiAl alloy is marginally less than that reported in conventional TiAl alloys, preliminary results have shown that the microstructure and properties of the alloy can be optimized through heat treatments to increase its plasticity and to meet application requirements. The excellent oxidation resistance of this alloy is the primary topic of this study; subsequent studies will focus on the modification of the microstructure and characteristics by heat treatment.

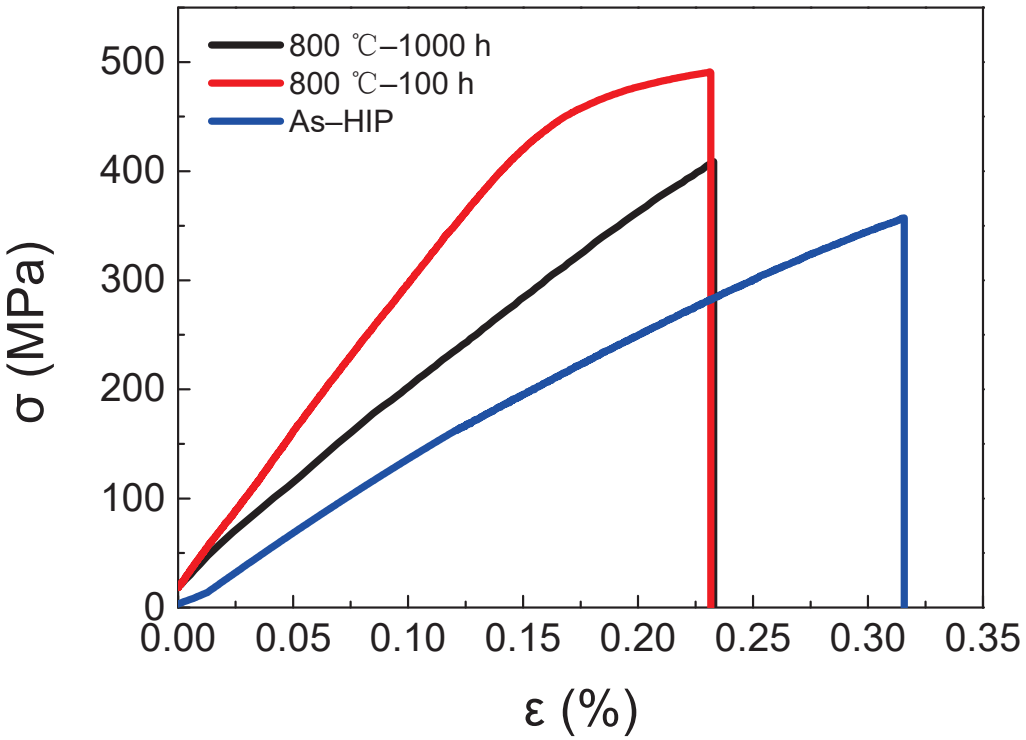

Figure 14. Tensile stress–strain curve of P–HIP after exposure at 800 °C for 100 and 1000 h.

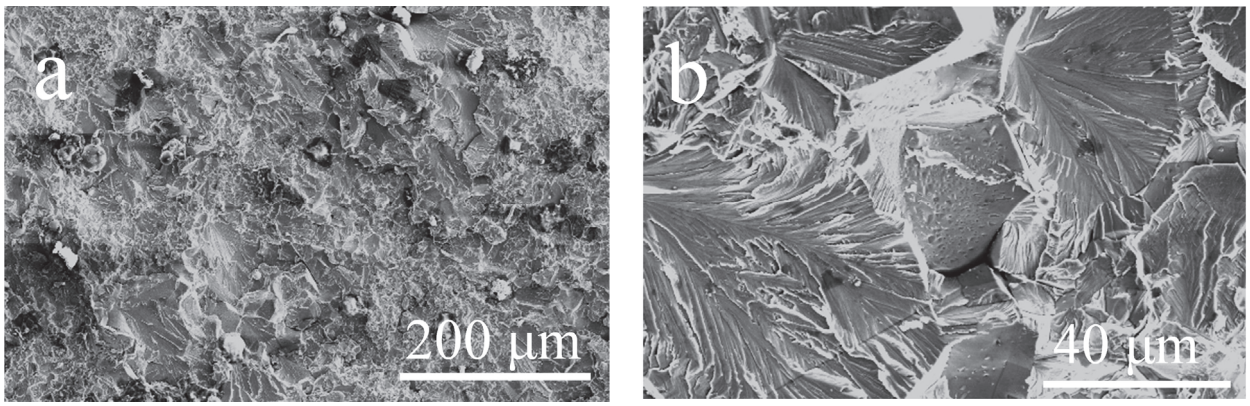

Figure 15. SEM images of the fracture surfaces after exposure at 800 °C for 1000 h: (**a**) Low magnification; (**b**) High magnification.

The increase in strength after thermal exposure may be due to the increased oxygen content of the alloy [69]. In addition, during thermal exposure at 800 °C, $\alpha_2 \rightarrow \gamma$ phase transformation occurs, γ grains precipitate in the $\alpha_2 + \gamma$ lamellae, and this parallel decomposition in the lamella makes the lamella refined to a certain extent. The thin lamella provides more obstacles to dislocations and twins, and it reduces internal stress by reducing the length of dislocation accumulation at the interface, thereby increasing resistance to cross-lamella deformation, resulting in higher tensile strength after thermal exposure at 800 °C for 100 h and 1000 h compared with the P–HIP state [9]. The tensile strength after thermal exposure for 1000 h was lower than that after thermal exposure for 100 h, mainly because of the influence of grain-size growth, according to the Hall–Patch formula. The appearance and stepwise growth of the Al-lean layer during thermal exposure will lead to the formation of a brittle layer on the surface, resulting in a decrease in the tensile fracture strain at room temperature [70]. In addition, the decrease in tensile fracture strain at room temperature after thermal exposure may also be related to the residual stress on the surface [8]. Moreover, it has been shown that the instability of the lamella colony also causes the ductility of the alloy to deteriorate, and during long-term exposure, the fracture strain decreases because of the decomposition of α_2 lamellae and the merger of adjacent γ lamellae [9].

4. Conclusions

The Ti–48Al–3Nb–1.5Ta alloy was prepared by powder hot isostatic pressing (P–HIP) at 1200 °C with 150 MPa for 4 h and exposed at 800 °C, 850 °C and 900 °C for 100 h, 300 h, 500 h, 800 h and 1000 h. The surface-scale characterization, microstructure stability and mechanical performance of the P–HIP Ti–48Al–3Nb–1.5Ta alloy after thermal exposure were investigated and clarified. The main conclusions are as follows:

1. The surface scale is composed of oxides and nitrides, mainly Al_2O_3, TiO_2, TiN and Ti_2AlN; among these, Al_2O_3 is preferentially generated and then covered by rapidly growing TiO_2 as the thermal exposure duration increases. The nitrides appear later than the oxides and exist between the oxide layer and the substrate. With increasing thermal exposure temperature and duration, the surface scale becomes more continuous, the prismatic TiO_2 particles grow larger, and the oxide layer thickens. The average size of the TiO_2 particles increased from 1.74 μm to 4.02 μm while the maximum size increased from 4.96 μm to 12.70 μm, with the shape changing from equiaxed particles to elongated particles, as the exposure duration extended from 100 h to 1000 h at the exposure temperature of 900 °C;
2. The addition of Ta and Nb can improve the oxidation resistance of TiAl alloys, and the oxidation resistance of Ti–48Al–3Nb–1.5Ta alloy is superior to that of the Ti–47.5Al–2.5V–1.0Cr–0.2Zr alloy, because Ta^{5+} and Nb^{5+} replace Ti^{4+} in the rutile lattice and weaken O diffusion, thus impeding the oxidation process;
3. Compared with the P–HIP Ti–48Al–3Nb–1.5Ta alloy, the grain size does not increase significantly, and the γ phase increases slightly (less than 3%) with the decomposition of the α_2 phase after thermal exposure. With increasing thermal exposure duration, the γ phase initiates discontinuous coarsening (DC) due to the reduction in lamellae near the grain boundaries, which expands the γ-phase region;
4. Compared with the P–HIP Ti–48Al–3Nb–1.5Ta alloy, the hardness increases by about 2 GPa, the tensile strength increases by more than 50 MPa and the fracture strain decreases by about 0.1% after thermal exposure. With the extension of the thermal exposure duration, the hardness tends to decrease, because of the equiaxed γ grains increasing and growing continuously, the α_2 phase decreasing and the lamellae coarsening. As the depth increases from the surface of the P–HIP Ti–48Al–3Nb–1.5Ta alloy after thermal exposure, the hardness decreases overall.

The P–HIP Ti–48Al–3Nb–1.5Ta alloy, a potential low-density alloy, exhibits attractive microstructure stability and does not significantly lose mechanical properties after thermal exposure at 800–900 °C for up to 1000 h. This study will provide beneficial guidance for

high temperature applications involving weight reduction. Future research will focus on how heat treatments can improve the alloy's microstructure and plasticity.

Author Contributions: Conceptualization, Z.Z., R.H. and Q.W.; methodology, Z.Z., Z.G. and Y.L.; formal analysis, Z.Z. and S.L.; investigation, S.X. and X.Z.; resources, M.X. and X.Z. data curation, Z.Z., S.X. and M.X.; writing—original draft preparation, Z.Z.; writing—review and editing, R.H., Z.G., X.L. and Q.W.; supervision, R.H., Y.L. and S.L. All authors have read and agreed to the published version of the manuscript.

Funding: This research was funded by the Key R&D Program of Shaanxi (grant number 2022GY-388) and the Xi'an Science and Technology Project (grant number 21XJZZ0077).

Institutional Review Board Statement: Not applicable.

Informed Consent Statement: Not applicable.

Data Availability Statement: All the data generated during this study are included in this article.

Acknowledgments: We would like to thank everyone who supplied help.

Conflicts of Interest: Authors Zhenbo Zuo, Qingxiang Wang, Yunjin Lai, Sa Xue, Min Xiang, Xiaohao Zhao and Shaoqiang Li were employed by Sino-Euro Materials Technologies of Xi'an Co., Ltd. The remaining authors declare that the research was conducted in the absence of any commercial or financial relationships that could be construed as a potential conflict of interest.

References

1. Appel, H.F.; Paul, J.; Oehring, M. *Gamma Titanium Aluminide Alloys Science and Technology*; Wiley-VCH: Weinheim, Germany, 2011; p. 469. [CrossRef]
2. Kim, Y.; Kim, S. Advances in Gammalloy Materials–Processes–Application Technology: Successes, Dilemmas, and Future. *Jom* **2018**, *70*, 553–560. [CrossRef]
3. Kothari, K.; Radhakrishnan, R.; Wereley, N.M. Advances in gamma titanium aluminides and their manufacturing techniques. *Prog. Aerosp. Sci.* **2012**, *55*, 1–16. [CrossRef]
4. Chandran, A.; Ganesan, H.; Cyron, C.J. Studying the effects of Nb on high-temperature deformation in TiAl alloys using atomistic simulations. *Mater. Des.* **2024**, *237*, 112596. [CrossRef]
5. Guo, R.; Xiong, G.; Liu, J.; Wang, Y.; Davoodi, D.; Miri, R.; Tayebi, M. Tribological behavior of Ti-Al-Nb alloy with different Ta additions for high temperature applications. *Mater. Lett.* **2023**, *330*, 133324. [CrossRef]
6. Chen, X.; Tang, B.; Wei, B.; Zhang, X.; Li, J. Investigation on recrystallization behavior of Ti-47Al-1.5Re-X (Cr, Mn, V, Nb) alloy during hot deformation. *Mater. Lett.* **2023**, *331*, 133484. [CrossRef]
7. Hu, R.; Wang, X.; Yang, J.; Fu, H. Microstructures Thermal Stability and Evolution Mechanism of TiAl-Base Alloys and Their Effects on Mechanical Properties. *Aerosp. Sci. Technol.* **2017**, *23*, 30–39. [CrossRef]
8. Pather, R.; Mitten, W.A.; Holdway, P.; Ubhi, H.; Wisbey, A.; Brooks, J. The effect of high temperature exposure on the tensile properties of γ TiAl alloys. *Intermetallics* **2003**, *11*, 1015–1027. [CrossRef]
9. Huang, Z.W.; Cong, T. Microstructural instability and embrittlement behaviour of an Al-lean, high-Nb γ-TiAl-based alloy subjected to a long-term thermal exposure in air. *Intermetallics* **2010**, *18*, 161–172. [CrossRef]
10. Huang, Z.W.; Voice, W.; Bowen, P. The effects of long-term air exposure on the stability of lamellar TiAl alloys. *Intermetallics* **2000**, *8*, 417–426. [CrossRef]
11. Huang, Z.W. Thermal stability of Ti–44Al–4Nb–4Zr–0.2Si–1B alloy. *Intermetallics* **2013**, *42*, 170–179. [CrossRef]
12. Zhou, L.Z.; Lupinc, V.; Guo, J.T. Microstructural stability of the intermetallic Ti–45Al–2W–0.5Si–0.5B in the 800–980 °C temperature range. *Mater. Sci. Eng. A* **2003**, *354*, 97–105. [CrossRef]
13. Seo, D.Y.; Zhao, L.; Beddoes, J. Microstructural evolution during heat treatments in Ti-45 and 47Al–2Nb–2Mn + 0.8vol.%TiB2 XDTM alloys. *Mater. Sci. Eng. A* **2002**, *329*, 130–140. [CrossRef]
14. Leyens, C.; Braun, R.; Frohlich, M.; Hovsepian, P. Recent progress in the coating protection of gamma titanium-aluminides. *Jom* **2006**, *58*, 17–21. [CrossRef]
15. Pan, Y.; Han, D.; Huang, S.; Niu, Y.; Liang, B.; Zheng, X. Thermal insulation performance and thermal shock resistance of plasma-sprayed TiAlCrY/$Gd_2Zr_2O_7$ thermal barrier coating on γ-TiAl alloy. *Surf. Coat. Technol.* **2023**, *468*, 129715. [CrossRef]
16. Zhang, K.; Xin, L.; Ma, T.; Chang, H.; Lu, Y.; Feng, C.; Zhu, S.; Wang, F. Investigation of the role of silicon in TiAlSiN coating deposited on TiAl alloys during long-term oxidation. *Corros. Sci.* **2022**, *204*, 110394. [CrossRef]
17. Haanappel, V.A.C.; Clemens, H.; Stroosnijder, M.F. The high temperature oxidation behaviour of high and low alloyed TiAl-based intermetallics. *Intermetallics* **2002**, *10*, 293–305. [CrossRef]
18. Xiang, L.L.; Zhao, L.L.; Wang, Y.L.; Zhang, L.; Lin, J. Synergistic effect of Y and Nb on the high temperature oxidation resistance of high Nb containing TiAl alloys. *Intermetallics* **2012**, *27*, 6–13. [CrossRef]

19. Hadi, M.; Bayat, O.; Meratian, M.; Shafyer, A.; Ebrahimzadeh, I. Oxidation Properties of a Beta-Stabilized TiAl Alloy Modified by Rare Earth Elements. *Oxid. Met.* **2018**, *90*, 421–434. [CrossRef]
20. Du, H.L.; Aljarany, A.; Datta, P.K.; Burnell, J. Oxidation behaviour of Ti–46.7Al–1.9W–0.5Si in air and Ar–20%O_2 between 750 and 950 °C. *Corros. Sci.* **2005**, *47*, 1706–1723. [CrossRef]
21. Pilone, D.; Felli, F. Isothermal oxidation behaviour of TiAl–Cr–Nb–B alloys produced by induction melting. *Intermetallics* **2012**, *26*, 36–39. [CrossRef]
22. Wendler, B.G.; Kaczmarek, Ł. Oxidation resistance of nanocrystalline microalloyed γ-TiAl coatings under isothermal conditions and thermal fatigue. *J. Mater. Process. Technol.* **2005**, *164*, 947–953. [CrossRef]
23. Haanappel, V.A.C.; Clemens, H.; Stroosnijder, M.F. The effect of microstructure on the oxidation behaviour of Ti-46.5Al-4(Cr,Nb,Ta,B) and Ti-47 Al-4(Cr,Nb,Mo,B). *Mater. High Temp.* **2002**, *19*, 19–24. [CrossRef]
24. Przybylski, K.; Prazuch, J.; Brylewski, T.; Durda, E. High Temperature Oxidation Behaviour of Tial8Nb Alloy. *Arch. Metall. Mater.* **2013**, *58*, 477–480. [CrossRef]
25. Mengis, L.; Ulrich, A.S.; Watermeyer, P.; Liebscher, C.; Galetz, M. Oxidation behaviour and related microstructural changes of two β0–phase containing TiAl alloys between 600 °C and 900 °C. *Corros. Sci.* **2021**, *178*, 109085. [CrossRef]
26. Banumathy, S.; Sruti Neelam, N.; Chandravanshi, V.; Bhattacharjee, A.; Ravi, K. The Effect of Nb addition on microstructure, oxidation behavior and strength of some γ-TiAl alloys. *Mater. Today Proc.* **2018**, *5*, 5514–5520. [CrossRef]
27. Małecka, J. Resistance to High-Temperature Oxidation of Ti-Al-Nb Alloys. *Materials* **2022**, *15*, 2137. [CrossRef]
28. Mitoraj, M.; Godlewska, E.; Heintz, O.; Geoffroy, N.; Fontana, S.; Chevalier, S. Scale composition and oxidation mechanism of the Ti–46Al–8Nb alloy in air at 700 and 800 °C. *Intermetallics* **2011**, *19*, 39–47. [CrossRef]
29. Fergus, J.W. Review of the effect of alloy composition on the growth rates of scales formed during oxidation of gamma titanium aluminide alloys. *Mater. Sci. Eng. A* **2002**, *338*, 108–125. [CrossRef]
30. Li, X. Research on Microstructure and Mechanical Properties of Ti-45Al-10Nb Alloy Prepared by Powder Metallurgy. Ph.D. Thesis, Harbin Institute of Technology, Harbin, China, 2014.
31. Pfeiler, M.; Scheu, C.; Hutter, H.; Schnöller, J.; Michotte, C.; Mitterer, C.; Kathrein, M. On the effect of Ta on improved oxidation resistance of Ti–Al–Ta–N coatings. *J. Vac. Sci. Technol. A* **2009**, *27*, 554–560. [CrossRef]
32. Pan, H.; Zhang, K.; Chen, J.; Zhang, X.; Zhao, H.; Hu, R. Variant selection of massive γ subgrains and corresponding mechanical properties in Ta containing γ-TiAl-based alloys. *Mater. Lett.* **2023**, *333*, 133689. [CrossRef]
33. Chen, S.; Tan, Y.; Wang, X.; Cao, F.; Wang, L.; Su, Y.; Guo, J. Individual and synergistic effects of Ta and Mn on optimizing the microstructures and mechanical properties of TiB reinforced high Nb–TiAl composites. *J. Mater. Res. Technol.* **2023**, *23*, 209–220. [CrossRef]
34. Liu, Z.; Wang, C.; Wang, W.; Xu, G.; Liu, X. Effects of Tantalum on the microstructure and properties of Ti-48Al-2Cr-2Nb alloy fabricated via laser additive manufacturing. *Mater. Charact.* **2021**, *179*, 111317. [CrossRef]
35. Gao, Z.; Hu, R.; Huang, Z.; Wu, Y.; Li, J.; Zhou, M. Metastable transformation behavior in a Ta-containing TiAl-Nb alloy during continuous cooling. *J. Alloy Compd.* **2022**, *904*, 164088. [CrossRef]
36. Zhang, K.; Hu, R.; Lei, T.; Yang, J. Refinement of massive γ phase with enhanced properties in a Ta containing γ-TiAl-based alloys. *Scr. Mater.* **2019**, *172*, 113–118. [CrossRef]
37. Zhang, K.; Hu, R.; Li, J.; Yang, J.; Gao, Z. Grain refinement of 1 at.% Ta-containing cast TiAl-based alloy by cyclic air-cooling heat treatment. *Mater. Lett.* **2020**, *274*, 127940. [CrossRef]
38. Hu, D.; Huang, A.J.; Wu, X. On the massive phase transformation regime in TiAl alloys: The alloying effect on massive/lamellar competition. *Intermetallics* **2007**, *15*, 327–332. [CrossRef]
39. Lapin, J.; Pelachová, T.; Dománková, M. Long-term creep behaviour of cast TiAl-Ta alloy. *Intermetallics* **2018**, *95*, 24–32. [CrossRef]
40. Saage, H.; Huang, A.J.; Hu, D.; Loretto, M.H.; Wu, X. Microstructures and tensile properties of massively transformed and aged $Ti_{46}Al_8Nb$ and $Ti_{46}Al_8Ta$ alloys. *Intermetallics* **2009**, *17*, 32–38. [CrossRef]
41. Loretto, M.H.; Wu, Z.; Chu, M.Q.; Saage, H.; Hu, D.; Attallah, M.M. Deformation of microstructurally refined cast $Ti_{46}Al_8Nb$ and $Ti_{46}Al_8Ta$. *Intermetallics* **2012**, *23*, 1–11. [CrossRef]
42. Lapin, J.; Gabalcová, Z. Solidification behaviour of TiAl-based alloys studied by directional solidification technique. *Intermetallics* **2011**, *19*, 797–804. [CrossRef]
43. Yan, M.; Yang, F.; Lu, B.; Chen, C.; Sui, Y.; Guo, Z. Microstructure and Mechanical Properties of High Relative Density γ-TiAl Alloy Using Irregular Pre-Alloyed Powder. *Metals* **2021**, *11*, 635. [CrossRef]
44. *GB/T 228.1*; Metallic materials—Tensile testing—Part 1: Method of test at room temperature. Standardization Administration of China: Beijing, China, 2021.
45. Bik, M.; Galetz, M.; Mengis, L.; White, E.; Wieczorek, W.; Łyszczarz, K.; Mroczka, K.; Marchewka, J.; Sitarz, M. Oxidation behaviour of uncoated and PDC-SiAlOC glass-coated TiAl at 750 °C in dry and humid air. *Appl. Surf. Sci.* **2023**, *632*, 157601. [CrossRef]
46. Pérez, P. Influence of nitriding on the oxidation behaviour of titanium alloys at 700 °C. *Surf. Coat. Technol.* **2005**, *191*, 293–302. [CrossRef]
47. Vojtěch, D.; Popela, T.; Kubásek, J.; Maixner, J.; Novák, P. Comparison of Nb- and Ta-effectiveness for improvement of the cyclic oxidation resistance of TiAl-based intermetallics. *Intermetallics* **2011**, *19*, 493–501. [CrossRef]

48. Kovács, K.; Perczel, I.V.; Josepovits, V.K.; Kiss, G.; Réti, F.; Deák, P. In situ surface analytical investigation of the thermal oxidation of Ti–Al intermetallics up to 1000 °C. *Appl. Surf. Sci.* **2002**, *200*, 185–195. [CrossRef]
49. Gale, W.F.; Totemeier, T.C. 8—Thermochemical data. In *Smithells Metals Reference Book*, 8th ed.; Gale, W.F., Totemeier, T.C., Eds.; Butterworth-Heinemann: Oxford, UK, 2004; pp. 1–8. ISBN 978-0-7506-7509-3.
50. Dudziak, T.; Rząd, E.; Morgiel, J.; Wytrwal-Sarna, M.; Kirchner, A.; Pomorska, M.; Boron, L.; Polczyk, T.; Moskal, G.; Toboła, D.; et al. Scale mass gain, morphology and phase composition of air and steam oxidized electron beam melted and cast Ti–48Al–2Nb–0.7Cr–0.3Si alloys. *Intermetallics* **2022**, *145*, 107553. [CrossRef]
51. Pan, Y.; Yang, Y.; Zhou, Q.; Qu, X.; Cao, P.; Lu, X. Achieving synergy of strength and ductility in powder metallurgy commercially pure titanium by a unique oxygen scavenger. *Acta Mater.* **2024**, *263*, 119485. [CrossRef]
52. Taylor, T.N.; Paffett, M.T. Oxide properties of a γ-TiAl: A surface science study. In *High Temperature Aluminides and Intermetallics*; Whang, S.H., Pope, D.P., Liu, C.T., Eds.; Elsevier: Oxford, UK, 1992; pp. 584–590. ISBN 978-1-85166-822-9.
53. Huang, H.; Yan, H.; Duan, M.; Ji, J.; Liu, X.; Jiang, H.; Liu, B.; Sajid, S.; Cui, P.; Li, Y.; et al. TiO_2 surface oxygen vacancy passivation towards mitigated interfacial lattice distortion and efficient perovskite solar cell. *Appl. Surf. Sci.* **2021**, *544*, 148583. [CrossRef]
54. Ping, F.; Hu, Q.; Bakulin, A.V.; Kulkova, S.E.; Yang, R. Alloying effects on properties of Al_2O_3 and TiO_2 in connection with oxidation resistance of TiAl. *Intermetallics* **2016**, *68*, 57–62. [CrossRef]
55. Vojtech, D.; Cizkovsky, J.; Novak, P.; Serak, J.; Fabian, T. Effect of niobium on the structure and high-temperature oxidation of TiAl–Ti_5Si_3 eutectic alloy. *Intermetallics* **2008**, *16*, 896–903. [CrossRef]
56. Wang, H.; Zhu, C.; Zhang, J.; Cao, R. Influence of Thermal Exposure at Different Temperatures on Room Temperature Tensile Ductility of Cast TiAl Alloy. *J. Mater. Eng.* **2018**, *46*, 151–156. [CrossRef]
57. Narayana, P.L.; Kim, J.H.; Yun, D.W.; Kim, S.; Reddy, N.S.; Yeom, J.; Seo, D.; Hong, J. High temperature isothermal oxidation behavior of electron beam melted multi-phase γ-TiAl alloy. *Intermetallics* **2022**, *141*, 107424. [CrossRef]
58. Panin, P.V.; Zavodov, A.V.; Lukina, E.A. Effect of thermal exposure on microstructure evolution and mechanical properties of cast beta-solidifying TiAl-based alloy doped with Gd. *Intermetallics* **2022**, *145*, 107534. [CrossRef]
59. Li, D.; Zhang, G.; Lu, G.; Liu, Y.; Wang, J.; Liu, C. Precipitation of Ti_2Al phases at lamellar interfaces in a high-Nb-containing TiAl alloy during thermal exposure. *J. Mater. Sci. Technol.* **2022**, *126*, 132–140. [CrossRef]
60. Wang, Y.; Xue, X.; Kou, H.; Qiang, F.; Yu, Y.; Yin, Z.; Li, J. Microstructure Characterization and Thermal Stability of TNM Alloy Fabricated by Powder Hot Isostatic Pressing. *Metals* **2021**, *11*, 1720. [CrossRef]
61. Zheng, G.; Tang, B.; Zhao, S.; Wang, W.Y.; Ding, Y.; Zhao, Z.; Zhu, L.; Li, J. Revealing cellular reaction mechanisms and high-temperature structure stability in β-stabilized TiAl alloy. *Mater. Charact.* **2023**, *203*, 113110. [CrossRef]
62. Karadge, M.; Gouma, P.I. A structural aspect of α(α2) → lamellar α2 + γ transformation in γ-TiAl. *Phil. Mag. Lett.* **2004**, *84*, 451–459. [CrossRef]
63. Boehlert, C.J.; Dimiduk, D.M.; Hemker, K.J. The phase evolution, mechanical behavior, and microstructural instability of a fully-lamellar Ti–46Al(at.%) alloy. *Scr. Mater.* **2002**, *46*, 259–267. [CrossRef]
64. Haase, C.; Barrales-Mora, L.A. Influence of deformation and annealing twinning on the microstructure and texture evolution of face-centered cubic high-entropy alloys. *Acta Mater.* **2018**, *150*, 88–103. [CrossRef]
65. Brice, D.A.; Rahimi, R.M.; Bahr, D.F. Hardening Particulate Ti Media Through Controlled Oxidation. *Metall. Mater. Trans. A* **2019**, *50*, 3980–3984. [CrossRef]
66. Gardner, H.M.; Gopon, P.; Magazzeni, C.M.; Radecka, A.; Fox, K.; Rugg, D.; Wade, J.; Armstrong, D.E.J.; Moody, M.P.; Bagot, P.A.J. Quantifying the effect of oxygen on micro-mechanical properties of a near-alpha titanium alloy. *J. Mater. Res.* **2021**, *36*, 2529–2544. [CrossRef]
67. Göken, M.; Kempf, M.; Nix, W.D. Hardness and modulus of the lamellar microstructure in PST-TiAl studied by nanoindentations and AFM. *Acta Mater.* **2001**, *49*, 903–911. [CrossRef]
68. Kienl, C.; León-Cázares, F.D.; Rae, C.M.F. Deformation twinning during high temperature compression tests of the Ni-base superalloy ATI 718Plus®. *Acta Mater.* **2022**, *225*, 115743. [CrossRef]
69. Amann, F.; Poulain, R.; Delannoy, S.; Couzinié, J.P.; Clouet, E.; Guillot, I.; Prima, F. An improved combination of tensile strength and ductility in titanium alloys via oxygen ordering. *Mater. Sci. Eng. A.* **2023**, *867*, 144720. [CrossRef]
70. Zhu, C.L.; Li, S.; Li, H.Z.; Zhang, J. Effect of Thermal Exposure at 750 °C on Room Temperature Tensile Ductility of Cast Tial Alloy with Directional Lamellar Microstructure. *Acta Metall. Sin.* **2014**, *50*, 1478–1484. [CrossRef]

materials

MDPI

Article

Microstructure and Mechanical Properties of a New TWIP Steel under Different Heat Treatments

Jiaruiming Zhang [1], Yu Bai [1,2,*], Wenxue Fan [2], Guanghe Zhang [3], Wenhui Zhang [3], Yang Yang [4] and Hai Hao [1,2,*]

[1] Key Laboratory of Solidification Control and Digital Preparation Technology (Liaoning Province), School of Materials Science and Engineering, Dalian University of Technology, Dalian 116024, China; zhangyuanxiang@mail.dlut.edu.cn
[2] Ningbo Research Institute of Dalian University of Technology, Ningbo 315016, China; fanwenxuedl@163.com
[3] Zhejiang Ruitai Suspension System Technology Co., Ltd., Ningbo 315500, China; hyl171129@163.com (G.Z.); yyc_30@163.com (W.Z.)
[4] Ningbo Branch of China Academy of Ordnance Science, Ningbo 315103, China; yynbbky@126.com
* Correspondence: ybai@dlut.edu.cn (Y.B.); haohai@dlut.edu.cn (H.H.); Tel.: +86-411-84709458 (Y.B.); +86-411-84709458 (H.H.)

Abstract: The effects of solution treatment and annealing temperature on the microstructure and mechanical properties of a new TWIP steel that was alloyed from aluminum (Al), silicon (Si), vanadium (V), and molybdenum (Mo) elements were investigated by a variety of techniques such as microstructural characterization and room tensile testing. The austenite grain size grew slowly with the increase in annealing temperature. The relatively weak effect of the solution treatment and annealing temperature on the austenite grain size was attributed to the precipitation of MC and M_2C, which hindered the growth of the austenite grain. The plasticity of the TWIP steel in cold rolling and annealing after solution treatment was obviously higher than that in cold rolling and annealing without solution treatment. This was because the large-size precipitates redissolved in the matrix after solution treatment, which were not retained in the subsequently annealed structure. Through cold rolling and annealing at 800 °C after solution treatment, the prepared steel exhibited excellent strength and plasticity simultaneously, with a yield strength of 877 MPa, a tensile strength of 1457 MPa, and an elongation of 46.1%. The strength improvement of the designed TWIP steel was mainly attributed to the grain refinement and precipitation strengthening.

Keywords: alloying; heat treatment; grain size; nano-precipitation; mechanical properties

Citation: Zhang, J.; Bai, Y.; Fan, W.; Zhang, G.; Zhang, W.; Yang, Y.; Hao, H. Microstructure and Mechanical Properties of a New TWIP Steel under Different Heat Treatments. *Materials* **2024**, *17*, 2080. https://doi.org/10.3390/ma17092080

Academic Editor: Gábor Harsányi

Received: 10 March 2024
Revised: 16 April 2024
Accepted: 22 April 2024
Published: 28 April 2024

1. Introduction

At present, lightweight, energy-saving, and emissions-reducing vehicles with high safety performance have become the inevitable trend in the development of new energy vehicles [1,2]. Since twinning-induced plasticity (TWIP) steel has both a high tensile strength and high plasticity, it exhibits significant application prospects in lightweight automotives [3,4]. The outstanding comprehensive mechanical properties result from several different deformation mechanisms, which are dislocation slip and deformation twinning. Deformation twinning is closely related to the low stacking fault energy values of TWIP steels. However, the characteristic austenitic microstructure of TWIP steels induces a lower yield strength in the range of 200–400 MPa, which is a technical bottleneck in the large-scale application of TWIP steels [5]. Therefore, it is an urgent problem to improve the yield strength of TWIP in order to ensure high plasticity. The widely recognized methods for improving the strength of TWIP steels include alloying and heat treatment [6,7]. Alloying is the addition of alloying elements to TWIP steels to improve the strength through solid solution strengthening and precipitation strengthening. Heat treatment is a way to improve the strength of TWIP steel by fine-grain strengthening via cold rolling and annealing [8–12].

Up to now, the researchers have developed several series of TWIP steels, which are classified into three generations [13]. The first generation of TWIP steels is Fe-Mn-Si-Al

TWIP steel with a single austenite phase, which is attributed to the high Mn, Si, and Al contents. This type of high manganese steel exhibits higher plasticity, but the yield strength is relatively low, and its tensile strength is moderate. Because of the high content of Al and Si elements, the flow properties are poor, and there are certain problems in the casting and plating process. In order to solve the above problems, the researchers have developed second-generation TWIP steels with a composition of Fe-Mn-C. The strength is significantly improved due to its high content of C. However, there are also problems such as lower yield strength and hydrogen-induced delayed cracking. Therefore, the third-generation TWIP steel, which was alloyed with Al, Nb, V, Ti, Mo, and other elements on the basis of Fe-Mn-C is proposed. Some studies have shown that TWIP steel can achieve a good combination of strength and plasticity through the alloying of the above elements.

Lee et al. [14] added Si to Fe-18Mn-0.6C TWIP steel. When 1.5 wt.% Si was added, the yield strength was increased to higher than 500 MPa, and the tensile strength was increased to higher than 1200 MPa after annealing, but the plasticity was significantly reduced. By adding Al to Fe-Mn-C TWIP steel, it was found that the grain was refined, and the yield strength was increased, but the tensile strength was decreased [15]. When micro-alloying elements such as Nb, V, and Mo were added to TWIP steel, the micro-alloying elements were precipitated in the form of nanoscale carbide. The dispersed precipitates improved the strength of the material by hindering the movement of dislocation [16]. Moon et al. [17] added Mo to Fe-Mn-C-Al steel and found that the age-hardening behavior was changed due to the formation of κ-carbide precipitation, which increased the strength of steel but also reduced the plasticity. Razavi [18] and Nasajpour et al. [19] added about 1 wt.% Mo to TWIP steel to increase the yield strength from 200 MPa to higher than 400 MPa after cold rolling and annealing. V and Mo were simultaneously added to Fe-Mn-C-Al steel. Although the yield strength was increased to 785 MPa, the elongation was only about 20% [20]. Scott et al. [21] found that the strength of annealed and cold-rolled steel was not significantly improved (about 30 MPa) when 0.25 wt.% Nb was added to Fe-22Mn-0.6C. Compared with the addition of Nb, when adding 0.2 wt.% V to Fe-22Mn-0.6C, V carbides (VCs) mainly precipitated in the annealing process, and the size of the precipitates was smaller than Nb carbides. The yield strength and tensile strength were increased by 150 MPa and 100 MPa after annealing, respectively. The increase in strength was greater than that of Nb; meanwhile, the adverse effect on plasticity was less than that of Nb due to the small precipitate size. According to the above research, it can be seen that only adding one alloying element to TWIP steel makes it challenging to improve the strength and maintain high plasticity at the same time. Therefore, this paper intends to add multiple reinforcement elements such as Al, Si, V, and Mo to Fe-22Mn-0.6C TWIP.

In addition, heat treatment is an effective method for tailoring the balance of strength and elongation. Escobar et al. [22] studied the microstructure and mechanical properties of Fe-22Mn-0.45C TWIP steel at different annealing temperatures. It was found that the hardness of the TWIP steel increased with the rising cold deformation and decreasing annealing temperature. Therefore, the strength of TWIP steel can be improved by controlling annealing temperature and cold rolling deformation. In order to improve the plasticity of the TWIP steel, solid solution treatment was conducted [23]. When the solution temperature increased from 900 °C to 1150 °C, the yield strength of Fe-24Mn-0.5C-3.4Cr-0.3Mo-0.2Si after solid solution treatment decreased from 334 MPa to 317 MPa, but the elongation increased to 78%. When the temperature of the solution treatment is too high, the grain size becomes coarse. Although the plasticity is improved, the yield strength is reduced. The improvement of plasticity is not obvious when the solution temperature is too low. Therefore, the temperature of the solution treatment needs to be accurately controlled through a phase diagram. This paper attempted to improve the yield strength, tensile strength and elongation of Fe-Mn-C steel by alloying and adjusting the heat treatment process.

2. Materials and Methods

2.1. Experimental Materials

A typical high-strength TWIP steel Fe-22Mn-0.6C was selected as a basic material, and then JMatPro software (version 13.0) was utilized to optimize the chemical composition of TWIP steel. In the simulation, the general steel database and the quench properties tool in the phase temperature module were selected. The microstructure of the sample after quenching can be simulated by analyzing the phase diagram of adding different alloy components. Since the phase content in the microstructure is different with different added contents of various alloying elements, combined with the properties of each phase drawn from separate material databases, the mechanical properties of the materials can be predicted according to the phase composition. Therefore, it was used to calculate the influence of Al, Si, Mo, and V elements on the tensile strength, yield strength, and elongation of TWIP steel. The optimized composition of the new TWIP steel was obtained, and the specific alloy composition is shown in Table 1.

Table 1. Chemical composition of the newly designed TWIP steel. (wt.%).

Fe	Mn	Al	Si	Mo	C	V	S	P
Bal.	22	1.48	1.52	1	0.62	0.2	0.0161	0.0079

2.2. Experimental Procedures and Methods

The designed alloy was melted by a ZG-50 melting furnace and casted into a round bar with a diameter of 80 mm and a length of 200 mm. The ingot was heated at 1200 °C and held for 2 h, then hot forging and hot rolling were carried out to obtain a plate with dimensions of 280 mm × 112 mm × 30 mm. The hot rolling process with the total reduction of 40% was conducted with an initial rolling temperature of 1200 °C and a final rolling temperature of 950 °C. Then, different solution treatments were carried out: one was cold-rolled directly after hot rolling, and the other one was cold-rolled after holding at 1100 °C for 2 h followed by water cooling. The specimens are hereafter referred to as non-solid-solution-treated and solid-solution-treated, respectively. A ZK-NS9B rolling mill was used for multiple-pass cold rolling, with a rolling reduction of 70%. The cold-rolled samples were annealed at 750 °C, 800 °C, and 850 °C for 10 min, respectively, in a DZ47-60 heat treatment furnace, followed by water quenching. The experimental flow is shown in Figure 1.

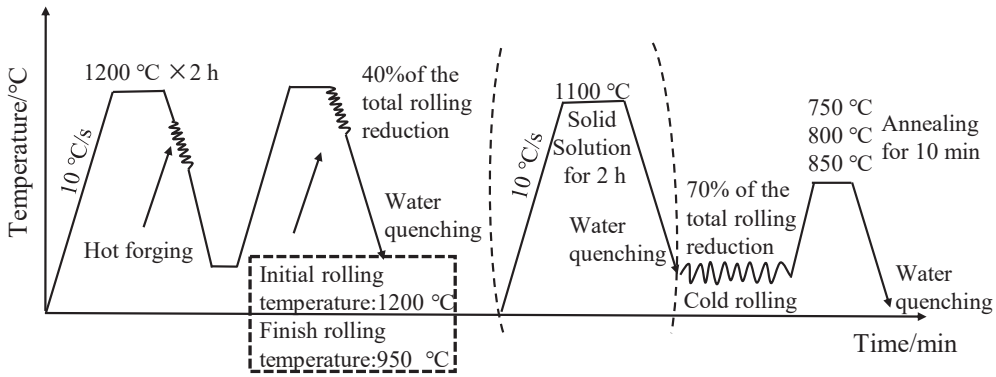

Figure 1. Flow chart of preparation experiment.

The samples were electrolytically polished for 20 s in a mixed solution of 10% (volume fraction) $HClO_4$ + 90% ethanol under an electrical voltage of 30 V. A SU5000 scanning electron microscope (SEM) was used to observe the microstructures. Two sizes of precipitates were observed in the microstructure. One is a large precipitate with a size of several hundred nanometers, which can be observed in SEM, and the precipitated phase is named as the large-size precipitate. The other is a precipitate of about ten nanometers observed in

the transmission electron microscopy (TEM), which was named the small-size precipitate. The scale tool of the SEM software (version 13.0) was used to measure the large-size precipitates. A JEOL JEM-2100F (TEM) was used to analyze the small-size precipitates, which were extracted by the carbon extraction replication technique. For the crystallographic analysis, the microstructures were observed by IT800-SHL SEM equipped with electron back scatter diffraction (EBSD). The phases after annealing at different temperatures were analyzed using a D8 Advance Bruker X-ray diffractometer with a Cu target and a scanning range of 20–90°.

The tensile test samples were cut out from the cold-rolled plate along the rolling direction, and the size was referred to GB/T 228-2002 [24]. The tensile test specimen size is shown in Figure 2. After annealing at different temperatures, the tensile test samples were tested at room temperature by a CMT4304-DZ tensile testing machine with a cross-head speed of 0.5 mm/min.

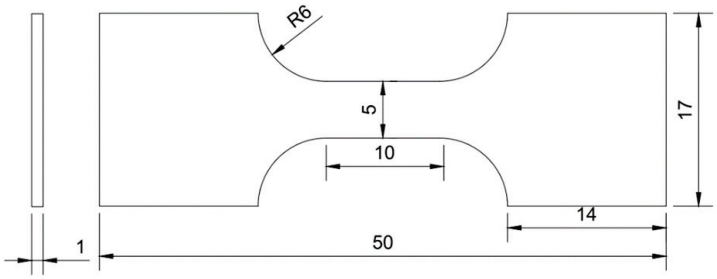

Figure 2. Illustration of tensile test specimen.

3. Results and Discussion

3.1. Determination of Alloy Composition Bases in Prediction of Mechanical Properties

Since the composition design of ultra-high-strength steel has a long research and development period, material design relying on calculation tools can reduce the number of tests and improve the efficiency of material research and development [25]. Therefore, in this paper, Java-based Materials Properties (JMatPro) software (version 13.0) was used to calculate the mechanical properties and phase diagram of the newly designed TWIP steels by adding Al, Si, Mo, and V elements. The brittle fracture occurs in TWIP steels with Si addition greater than 3 wt.%. It also affects the galvanizing quality of hot-rolled sheets [14,26]. Therefore, the addition amount of Si should usually be controlled within 3 wt.%. Figure 3a Fe-22Mn-0.6C-xSi shows the change in strength and plasticity with the increase in Si content. It can be observed that the increase in Si content in Fe-22Mn-0.6C TWIP steel improves the yield strength and tensile strength. The most significant increase in strength is observed when the Si addition is 1.5 wt.%. Meanwhile, the elongation is basically unchanged within 3 wt.% of Si content. Therefore, the addition of the Si element is determined as 1.5 wt.%.

Frommeyer et al. [27] found that when the content of Al in Fe-Mn-C steel exceeds 3 wt.%, it is easy to form an AlN inclusion and generate oxidation during casting [28]. Therefore, the amount of Al addition should be within 3 wt.%. On the other hand, it also prevents the delayed fracture and notch sensitivity of TWIP steel. The calculated results of the influence of Al content on the strength of the alloy are shown in Figure 3b. It can be seen that the yield strength and tensile strength are increased by about 30 MPa for every 1% content of Al. When the amount of Al is higher than 1.5 wt.%, the plasticity decreases significantly. Therefore, it is determined that the amount of aluminum is 1.5 wt.%, which can improve the strength and maintain the plasticity.

It has been reported that the addition of Mo with a mass fraction of 0.5% to 2% in high-manganese steel can effectively improve the strength of the casting [29]. The effect of Mo content on the strength and plasticity of the Fe-22Mn-0.6C steel is shown in Figure 3c. It can be seen that the strength of the alloy increases with the increase in Mo content. When

the content of Mo is greater than 1.5 wt.%, the plasticity obviously decreases. Since the general amount of Mo added in the literature is about 1 wt.%, the added content of Mo is determined to be 1 wt.%. In the Fe-C phase diagram, when the V content exceeds 0.2%, the A_3 point increases and austenitic stability decreases [30], so the added amount of V alloying is determined to be 0.2 wt.%.

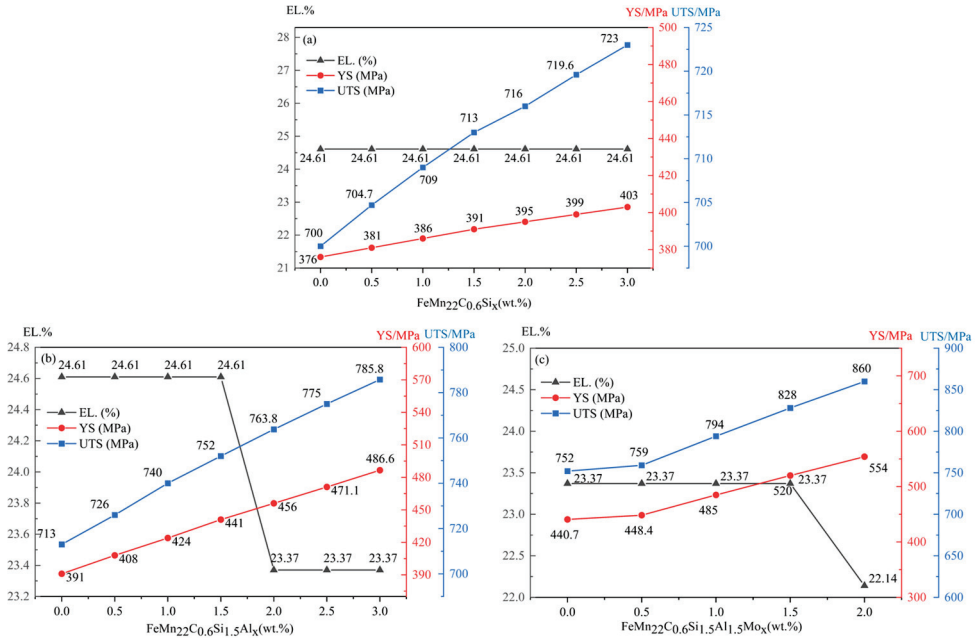

Figure 3. Variation in alloy strength and elongation with different element contents. (**a**) Fe-22Mn-0.6C-xSi; (**b**) Fe-22Mn-0.6C-1.5Si-xAl; (**c**) Fe-22Mn-0.6C-1.5Si-1.5Al-xMo.

According to the calculation results, the designed alloy composition Fe-22Mn-0.6C-1.5Si-1.5Al-1Mo-0.2V (wt.%) shows relatively good comprehensive mechanical properties. Hence, the newly studied TWIP steel with the above chemical composition is presented in this paper. The yield strength of the alloy steel is increased by 143 MPa, and the tensile strength is increased by 128 MPa compared with the Fe-22Mn-0.6C matrix.

3.2. Phase Diagram and Phase Content Calculation

As shown in Figure 4a, the equilibrium phase diagram of the Fe-22Mn-0.6C-1.5Si-1.5Al-1Mo-0.2V steel was calculated by using JMatPro software (version 13.0). According to the phase diagram, the alloy begins to enter the solid phase zone at 1250 °C, and the matrix is all austenite at 1008–1250 °C. In addition, to ensure that carbides are stable at high temperatures and maintain a fine grain size, the temperature of the solid solution should not be too high. Therefore, 1100 °C was selected as the solution treatment temperature in this paper. In order to prevent excessive types and quantities of precipitated phases from reducing plasticity, 750 °C, 800 °C, and 850 °C were selected as the annealing temperatures in this paper, so that the microstructure could be a fine austenitic matrix with two kinds of precipitates. One precipitate is M(C,N) phase, which starts to precipitate at 1008 °C. The other precipitates is the M_2(C,N) phase, which starts to precipitate at 907 °C. Figure 4b–d shows the distribution of elements in the phases M(C,N), M_2(C,N), and M_7C_3, where M represents elements such as Fe, Mn, Mo, and V. M(C,N) represents carbides of V and Mo. M_2(C,N) is a carbide of Mo, Mn, and V. M_7C_3 is a carbide of Mn, Fe, and Mo.

Figure 4e,f shows the distribution of Al and Si in different phases. It can be seen that 1.5 wt.% Al and 1.5 wt.% Si are almost solidly dissolved in the austenitic matrix. The Al and Si atoms enter the matrix crystal lattice, which distorts the crystal lattice and forms an elastic stress field. The stress field has a strong effect on the stress field around the

dislocation, which causes the strengthening and enhancement of the yield strength of the material, as predicted in Figure 3.

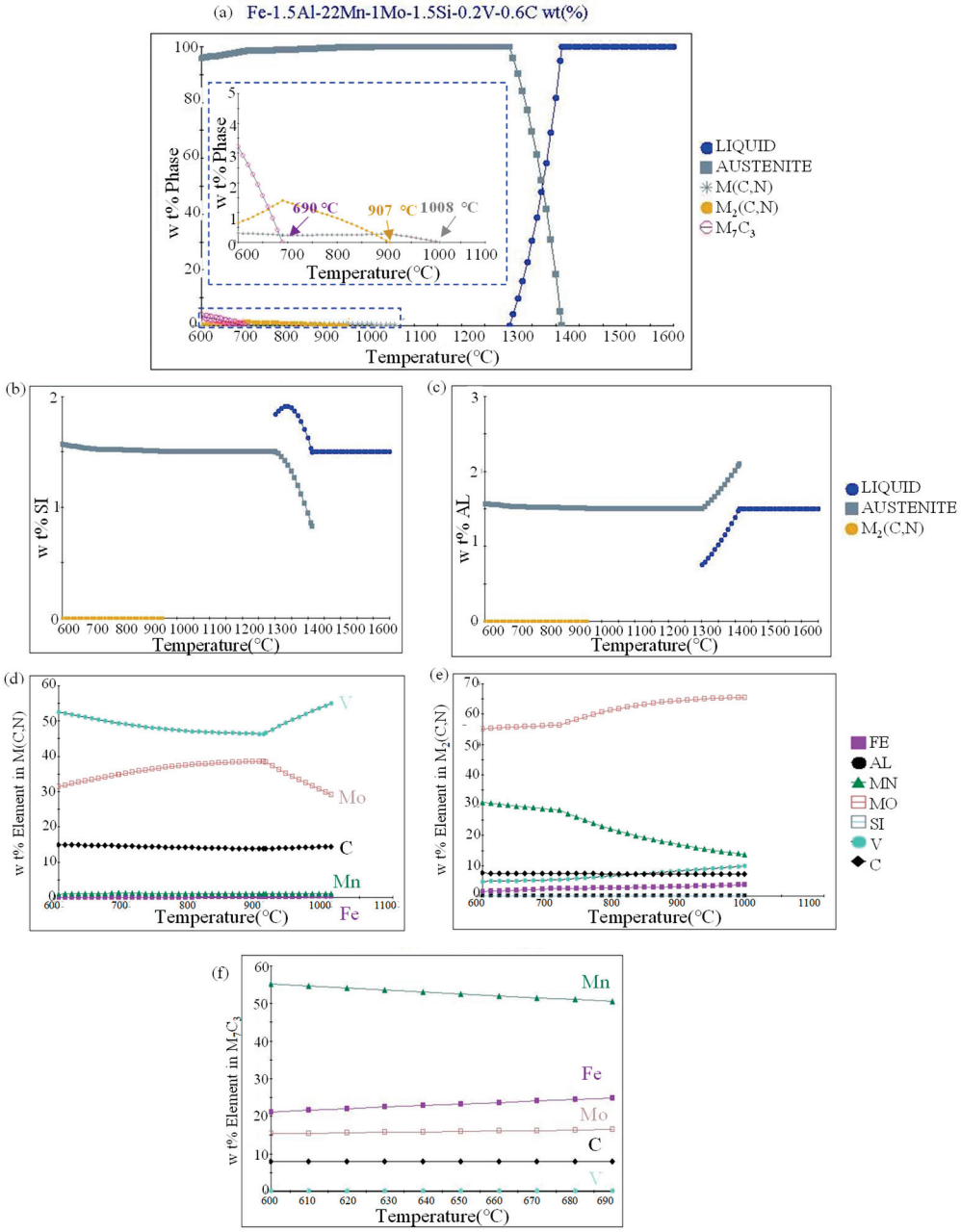

Figure 4. (**a**) Equilibrium phase diagram of Fe-22Mn-0.6C-1.5Si-1.5Al-1Mo-0.2V steel; (**b**,**c**) distribution of aluminum and silicon in different phases; (**d**–**f**) composition of three kinds of precipitated phases.

3.3. Microstructure Evolution

In order to explore the effect of solid solution treatment and different annealing temperatures on the microstructure of the new TWIP steel after cold rolling and annealing, XRD phase analysis was conducted. Figure 5 shows the X-ray diffraction pattern of the new TWIP steel after cold rolling and annealing under the conditions of non-solid solution and solution treatment. It can be observed that only one austenite phase (γ) peak is found in both samples, whether it is solution-treated or not. The absence of martensitic peaks in the XRD patterns indicates that a martensitic phase transformation has not occurred. Presumably due to the small content of the precipitated phase, a corresponding obvious

diffraction peak was not found in the X-ray diffraction profiles. Therefore, the identification of the precipitated phase also required further characterization by SEM and TEM.

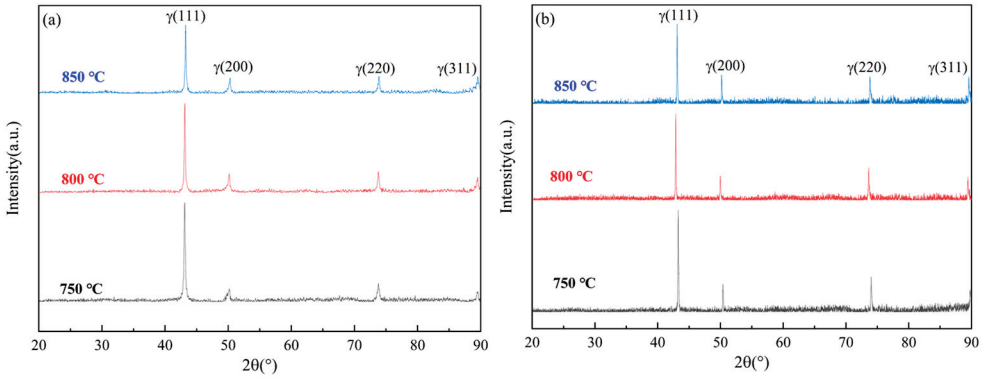

Figure 5. X-ray diffraction pattern of the new TWIP steel after cold rolling and annealing. (**a**) non-solid solution; (**b**) with solid solution treatment.

Figure 6a–c shows the microstructures of samples annealed at 750 °C, 800 °C, and 850 °C for 10 min, respectively, without solid solution treatment before the cold rolling process. It can be seen that there are also a small number of deformed structures after annealing at 750 °C. This indicates that the sample was not fully recrystallized at 750 °C. Grains were completely recrystallized at 800 °C and 850 °C. At the 800 °C annealing temperature, there were a large number of annealing twins and some elliptical bright precipitate phases were distributed inside the grains and at the grain boundaries. In addition, it can be observed that the precipitates reflected a growing tendency when the annealing temperature increased to 850 °C; the growth of the grain size and precipitates was not obvious. The austenite grain size and precipitated phase size of the experimental steels were measured by the linear intercept method (and by counting the grain and twin boundaries), and the result is shown in Figure 7. The grain size rose from 1.26 μm to 1.88 μm and the large size of the precipitates grew by 90.1 nm when the annealing temperature increased from 750 to 850 °C. The large-size precipitates grew significantly, but the grain size obviously did not grow with the increase in annealing temperature.

Figure 6d–f shows the microstructures of the cold-rolled and annealed samples after 2 h of solid solution treatment at 1100 °C. It can be observed that the grain size tended to grow with the increase in annealing temperature, and the grain size increased from 1.42 μm and 1.67 μm to 2 μm. The size of the precipitates after solution treatment was obviously smaller than that in the non-solid solution (as can be seen in Figure 6). With an increase in annealing temperature from 750 °C to 850 °C, the increase in grain size between adjacent temperatures was small, approximately ~0.3 μm on average (see Figure 7), and the increase in the precipitated phase size between adjacent temperatures was approximately ~90 nm.

In general, the austenite grain size of Fe-Mn-C steels obviously increased with an increase in annealing temperature [31–33]. However, the grain growth of austenite was so large that even the annealing temperature interval was 50 °C. This should be attributed to the presence of nano-sized precipitates. In the annealing temperature range of 750–850 °C, there were nano-sized particles inside the grains as well as on the grain boundaries (Figure 6). These particles can effectively hinder grain boundary migration and reduce the grain growth rate during the annealing process, resulting in a smaller grain size and coarsening with the elevated temperature. Therefore, the grain size growth was not obvious with the increase in annealing temperature. After solid solution treatment at 1100 °C, the size of the precipitates was smaller than that in the non-solid-solution-treated sample (see Figure 7). The decrease in the size of the precipitates after solid solution treatment is due to the large-size precipitate phase being dissolved into the matrix during solid solution treatment, and then precipitates with smaller sizes forming again during annealing at lower temperatures and short annealing times.

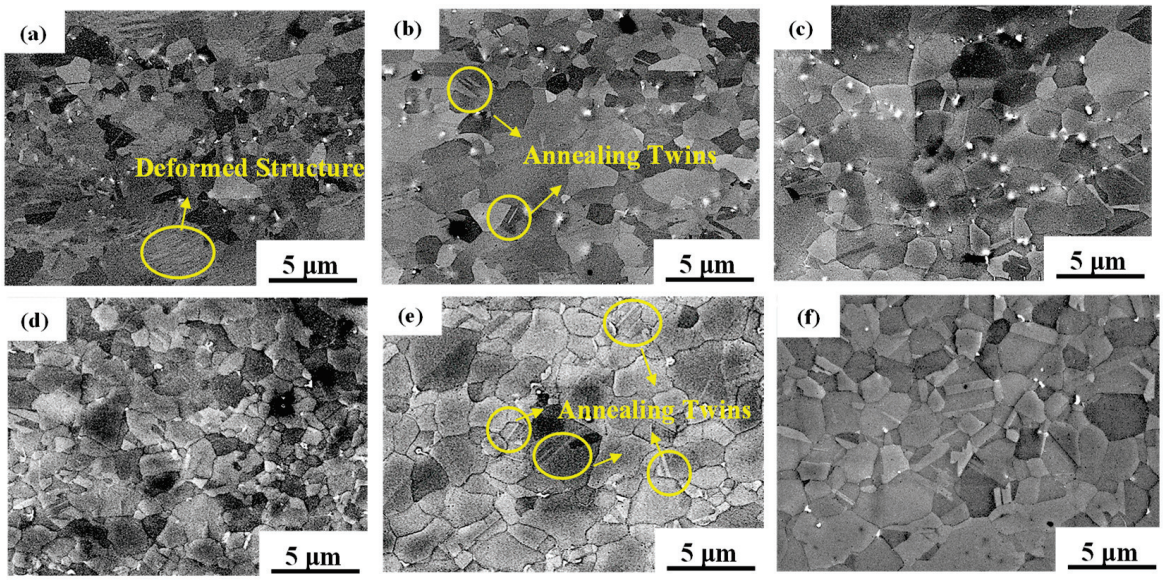

Figure 6. SEM images of the samples with different heat treatments. (**a**–**c**) Cold-rolled and annealed at 750 °C, 800 °C, and 850 °C for 10 min with non-solid solution treatment; (**d**–**f**) cold-rolled and annealed at 750 °C, 800 °C, and 850 °C for 10 min after solid solution treatment at 1100 °C for 2 h.

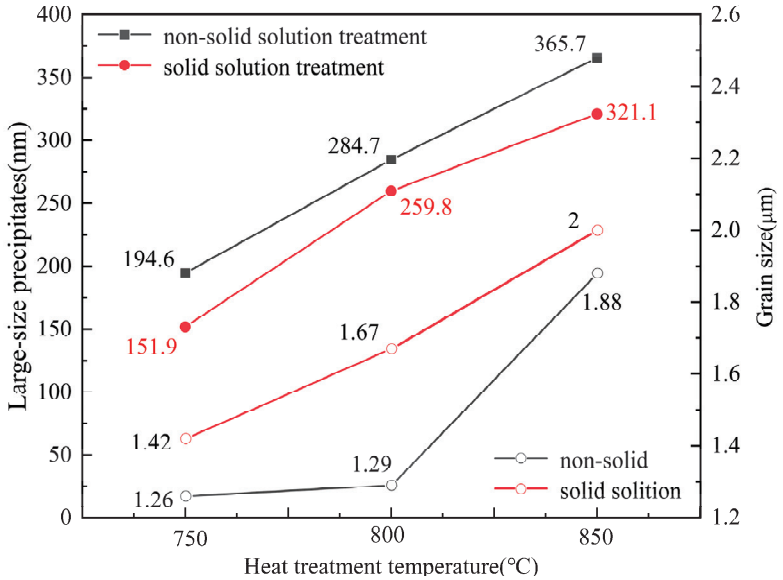

Figure 7. Size changes under different heat treatment processes.

As shown in Figure 6, small-size nanoscale precipitates can be faintly seen in the grain. The characterization of small-size precipitates under SEM is not clear, so TEM is used to observe the distribution of the small-size precipitate phase, morphology, and size.

Figure 8 shows the EBSD grain boundary maps of the TWIP steel under different heat treatment conditions, where small-angle grain boundaries, large-angle grain boundaries, and twin boundaries are represented by green, black, and red, respectively. The twin boundary density data obtained by SEM showed that the fraction of annealing the twin boundary increased from 14% to 29% when the annealing temperature increased from 750 °C to 800 °C and decreased from 29% to 26% when the annealing temperature increased to 850 °C with solution treatment. In the condition of non-solid solution treatment, the twin density increased from 15% to 21% when the annealing temperature increased from 750 °C to 800 °C. When the annealing temperature increased to 850 °C, the twin boundary density decreased from 21% to 20%. The twin boundary density increased first and then

decreased with the increase in annealing temperature. It reached the highest at 800 °C, regardless of the solution type. In addition, the density of the twin boundary after solution treatment was higher than that in the non-solid solution. A higher density of the annealing twin means a higher strength can be obtained.

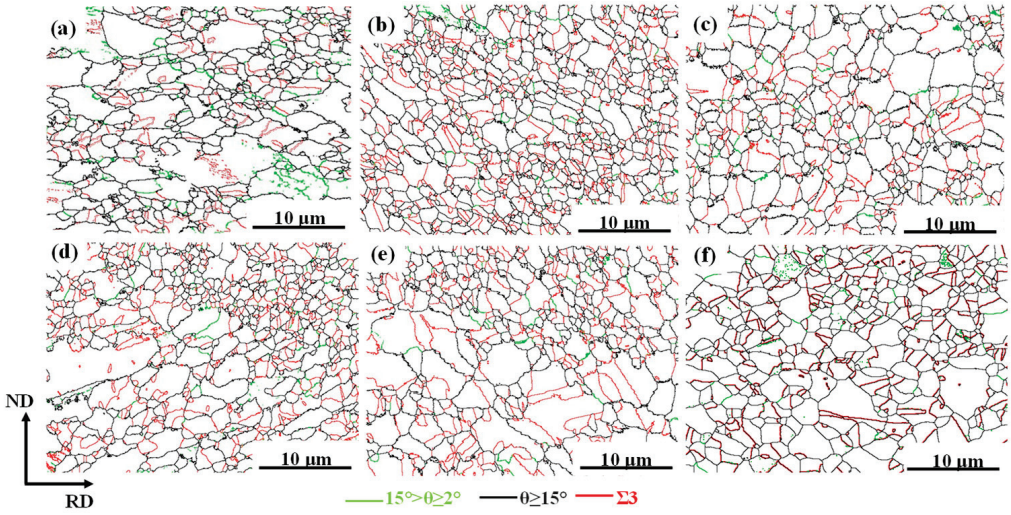

Figure 8. EBSD diagrams of grain boundary with different heat treatment processes. (**a**–**c**) Annealing at 750 °C, 800 °C, and 850 °C without solution treatment; (**d**–**f**) annealing at 750 °C, 800 °C, and 850 °C, respectively, under solution treatment at 1100 °C.

In order to further study the small-size precipitates, the microstructures of the TWIP steel were observed by TEM through extraction phase analysis. Figure 9 shows the morphology, size, and distribution of the small-size precipitates in the matrix. It can be observed that the precipitates mainly existed in circle and oval shapes. As shown in Figure 9a, the precipitates were concentrated and agglomerated together in the specimen annealed at 800 °C without the solid solution. The average grain size of the precipitated phase is 18 nm in Figure 9a. Compared with the specimen without solid solution treatment, the size of the precipitated phase is obviously reduced and the distribution in the matrix is more uniform in the 800 °C annealed specimen with solid solution treatment. The average grain size of the precipitated phase is 7.2 nm in Figure 9b. Figure 9b–d shows the relationship between the size and distribution of the small-size precipitates as the annealing temperature increases. Compared with the concentrated distribution without the solid solution, the precipitated phase was distributed in a band under the conditions of the solid solution. Meanwhile, the size of the small-size precipitates decreased first and then increased as the annealing temperature increased. The size of the small-size precipitates was the smallest at 800 °C with the solid solution.

Figure 10 shows the morphology and energy spectrum of the precipitates under TEM observation. It can be seen that the diffraction peak profiles of point A (the precipitated phase with a larger size) and point B (the precipitated phase with a smaller size) are different. The specific composition is shown in Table 2. Based on the elemental species of the precipitated phase calculated by the JMatPro software (version 13.0), it was determined that point A is the $M_2(C,N)$ phase, in which M mainly represents V, Mo and Mn elements. Point B is the M(C,N) phase, in which M mainly represents V and Mo elements. Since no nitrogen element was found in the scanning region, A is the M_2C phase and point B is the MC phase.

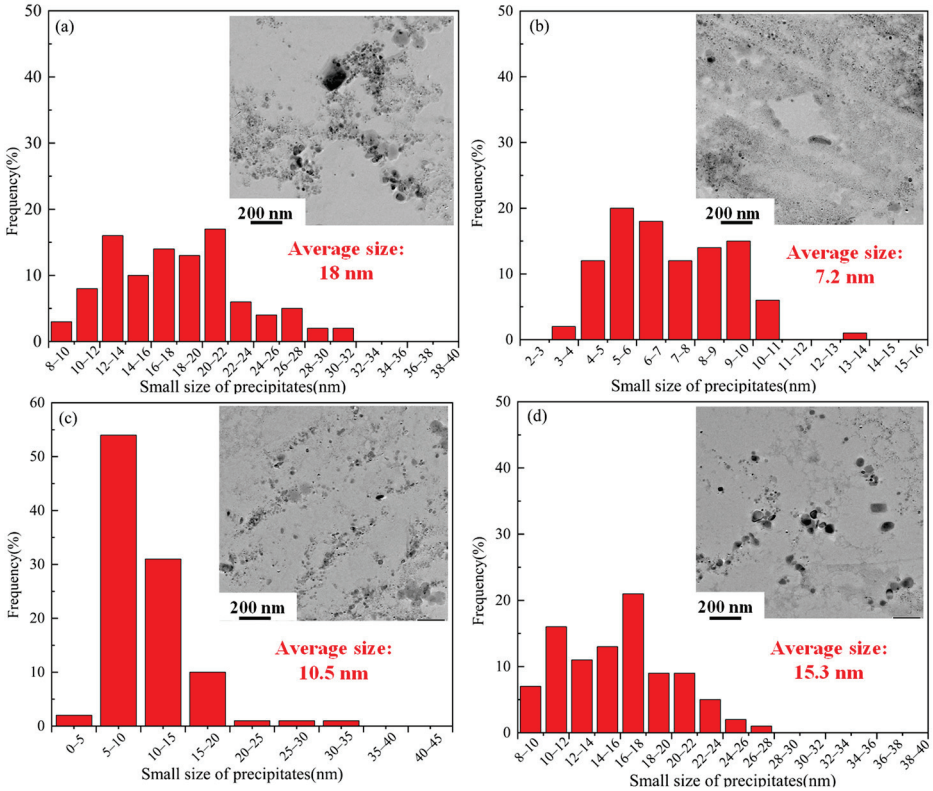

Figure 9. TEM images of the precipitated phase. (**a**) Non-solid solution and annealing at 800 °C; (**b**) solid solution and annealing at 800 °C; (**c**) solid solution and annealing at 750 °C; (**d**) solid solution and annealing at 850 °C.

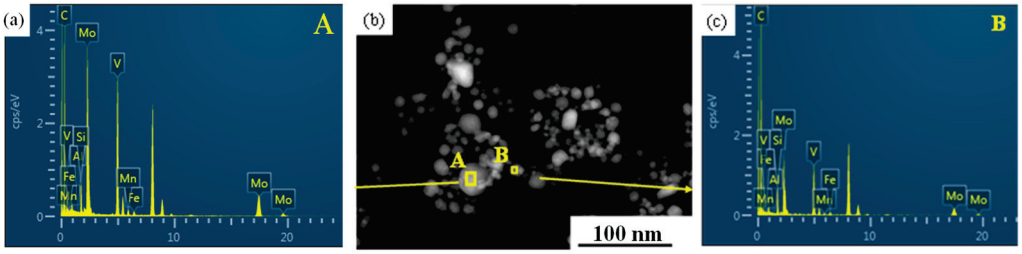

Figure 10. TEM images of morphology and energy spectrum. (**a**,**c**) energy spectrum of precipitates of point A and B, respectively, in (**b**); (**b**) TEM morphology of precipitates cold-rolled and annealed at 850 °C after solid solution treatment at 1100 °C.

Table 2. TEM-EDS results (at.%) for the different phases in point A and B in Figure 10.

	C	V	Mo	Si	Mn	Fe	Al
A	75.3	12.4	8.5	2.8	0.6	0.4	0.1
B	89.5	4.7	3.0	2.5	0.1	0.2	-

As shown in Figures 6 and 10, the precipitation phase in the cold-rolled and annealed new TWIP steel can be roughly divided into two categories: the first category is the large particles with sizes larger than 100 nm under the scanning electron microscope observation; the second category is the other composite precipitation of MC and M_2C.

3.4. Effect of Solid Solution Treatment and Annealing Temperature on Mechanical Properties

Figure 11 shows the engineering stress–strain curves of the new TWIP steel after cold rolling and annealing. The new TWIP steel shows a continuous yield without an obvious

yield plateau during the tensile process. In Figure 11a, in the non-solid-solution-treated specimens, the yield strength decreases, and the tensile strength decreases first and then increases slightly with the increase in annealing temperature, but the tensile strength does not change significantly. The reason why the strength does not change significantly is that the grain size does not increase significantly with the increase in annealing temperature. In Figure 11b, in the specimens with solid solution treatment, the yield strength and tensile strength increases first and then decreases as the annealing temperature rises. The elongation of the specimens with solid solution treatment is significantly higher than that without solution treatment. The specific mechanical properties are shown in Table 3. A good balance between high strength and high plasticity is achieved when cold rolling and annealing at 800 °C for 10 min after solid solution treatment. The yield strength is higher than that of Fe-22Mn-0.6C TWIP, whose grain size is about 1 μm in the literature. Furthermore, its plasticity is not greatly affected [34]. This indicates that the modification of the chemical composition and preparation process enhanced the mechanical properties.

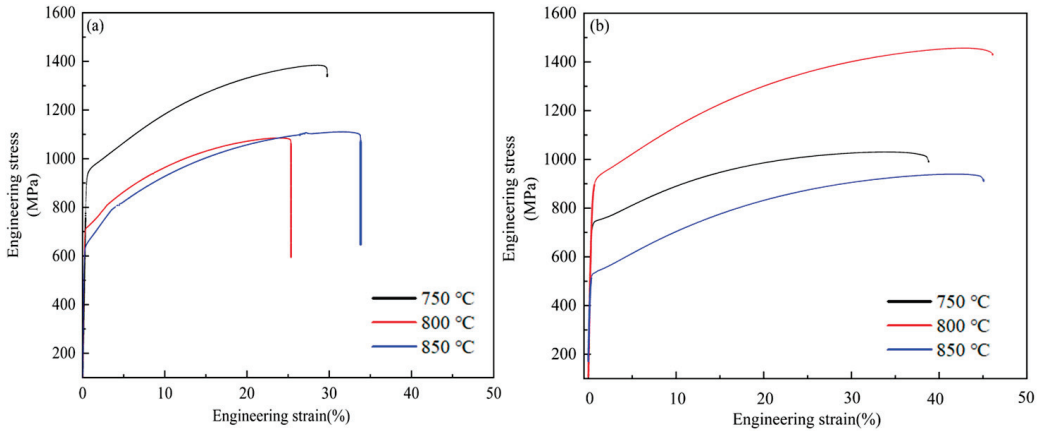

Figure 11. Engineering stress–strain curves of test steel under different heat treatment processes. (**a**) Engineering stress–strain curves of annealing at 750 °C, 800 °C and 850 °C for 10 min under non-solid solution condition; (**b**) Stress–strain curve of cold rolling and annealing with solid solution.

Table 3. Mechanical properties data under different heat treatment conditions.

	Annealing Conditions	Yield Strength (MPa)	Tensile Strength (MPa)	Total Elongation (%)	Grain Size (μm)
Non-solid solution	750 °C 10 min	781	1154	29	1.26
	800 °C 10 min	739	1086	25.3	1.29
	850 °C 10 min	636	1110	33.8	1.88
Solid solution at 1100 °C	750 °C 10 min	729	1030	38.8	1.42
	800 °C 10 min	877	1457	46.1	1.67
	850 °C 10 min	523	939	45.1	2

Generally, yield strength and tensile strength decrease monotonically, and elongation increases monotonically with increasing annealing temperature [35]. The fluctuation in the mechanical properties of the new TWIP steel in this experiment does not conform to the conventional law. It is known that the increase in flow stress of metallic materials is related to the following aspects: solid solution strengthening, dislocation strengthening, precipitation strengthening, and grain refinement. It is generally known that the increase in flow stress is the sum of the above strengthening mechanisms. In the present study, the chemical compositions were the same for all specimens, and the microstructures of the cold-rolled and annealed specimens were fully recrystallized so that the initial dislocation density was supposed to be the same. Thus, the solid solution strengthening and dislocation

strengthening effect on yield strength enhancement did not make a difference for the specimens, whether solution-treated or not. The grain size and the amount of precipitated phase were changed by changing the annealing temperature and solid solution conditions. Therefore, the contribution of fine grain strengthening and precipitation strengthening to the flow strength was changed in the different specimens. Due to the grain size being refined to about 1.5 μm on average after cold rolling and annealing, the strength was greatly improved. However, the change in grain size was not obvious, whether the specimens were solid-solution-treated or not, and was followed by the same annealing condition. Therefore, the strength enhancement of the solid-solution-treated specimens was not related to the grain size, but probably related to the nanoscale precipitates.

According to the inference of Gladma [36], the increase in strength generated by the second phase particle is shown in Equation (1):

$$\Delta YS_p = 0.538\mathrm{Gb}\left(\frac{f^{-\frac{1}{2}}}{X}\right)\ln\left(\frac{\mathrm{X}}{2b}\right) \quad (1)$$

where G is the shear modulus in MPa, f is the volume fraction of the MC and M_2C precipitates, and X is the mean particle diameter expressed in μm. From Formula (1), it can be found that increasing the volume fraction of precipitates and decreasing the average diameter of precipitates were conducive to increasing the contribution of precipitation strengthening in steel. In Figure 6, the size of the precipitates observed under SEM is larger than 100 nm. It not only can not improve the strength, but also cause a reduction in plasticity. The plasticity also decreases due to the increase in the number of large-size precipitates [37]. The size of the large-size precipitates under the condition of non-solid solution treatment was larger than that in the solid solution treatment; therefore, the plasticity with solid solution treatment was greater than that without solid solution treatment. The precipitates below 10 nm that were observed under TEM were fully involved in precipitation strengthening and ensured the strength and plasticity of the material, according to the Formula (1). In Figure 9b, when the annealing temperature is 800 °C, the size of precipitated phase is the smallest and the content of precipitates is the highest. The precipitates can effectively hinder the dislocation movement and strengthening of the matrix. They can also hinder grain boundary movement and increase the strength [38]. Furthermore, the higher annealing twin boundary density in the specimen annealed at 800 °C reduced the dislocation-free path as well as prevented dislocation movement, which also contributed to the enhancement of strengthening. Therefore, the strength was highest when annealing at 800 °C after solid solution treatment. The increase in the content of the M_2C and MC phases was the main reason for the increase in the flow stress.

4. Conclusions

The effects of annealing temperature and solution treatment on the microstructure and mechanical properties of a new TWIP steel were studied. A heat treatment method was explored to improve the strength and ductility. After solid solution treatment at 1100 °C for 2 h, cold rolling, and annealing at 800 °C for 10 min, the new TWIP steel (Fe-22Mn-0.6C-1.5Si-1.5Al-1Mo-0.2V) showed the best comprehensive mechanical properties; the yield strength increased to 877 MPa. At the same time, the tensile strength increased to 1457 MPa, and the elongation reached 46.1%. Compared with Fe-22Mn-0.6C TWIP steel having a grain size of 2um, the yield strength of the TWIP steel after alloying and heat treatment in this paper increased by 447 MPa, and the tensile strength increased by 321 MPa, although the elongation somehow decreased [39]. The improvement of strength was mainly due to fine grain strengthening and precipitation strengthening. The grain size after annealing at 800 °C reached 1.67 μm; meanwhile, a large number of dispersed MC and M_2C phases with sizes of about 10 nm that precipitated from the matrix hindered the dislocation movement and improved the strength.

Author Contributions: J.Z.: conceptualization, software, methodology, and writing—original draft. W.F.: methodology and writing—review and editing. Y.B.: supervision, writing—review and editing and funding acquisition. H.H.: supervision, funding acquisition, writing—review and editing, and supervision. G.Z., W.Z. and Y.Y.: supervision and guidance, project administration, resources. All authors have read and agreed to the published version of the manuscript.

Funding: The work was supported by the National Natural Science Foundation of China [52201110], the Major Projects of Science and Technology Innovation 2025 Ningbo [2022Z048], and the Fundamental Research Funds for the Central Universities, Dalian University of Technology.

Institutional Review Board Statement: Not applicable.

Informed Consent Statement: Not applicable.

Data Availability Statement: Data are contained within the article.

Conflicts of Interest: Authors Guanghe Zhang and Wenhui Zhang were employed by the company Zhejiang Ruitai Suspension System Technology Co., Ltd. The remaining authors declare that the research was conducted in the absence of any commercial or financial relationships that could be construed as a potential conflict of interest.

References

1. Horvath, C.D. Advanced Steels for Lightweight Automotive Structures. In *Materials, Design and Manufacturing for Lightweight Vehicles*; Woodhead Publishing: Sawston, UK, 2021; pp. 39–95. [CrossRef]
2. Bleck, W.; Brühl, F.; Ma, Y.; Sasse, C. Materials and Processes for the Third-Generation Advanced High-Strength Steels. *BHM Berg-Hüttenmännische Monatshefte* **2019**, *164*, 466–474. [CrossRef]
3. De Cooman, B.C.; Estrin, Y.; Kim, S.K. Twinning-Induced Plasticity (Twip) Steels. *Acta Mater.* **2018**, *142*, 283–362. [CrossRef]
4. Zhang, Y.; Lai, X.; Zhu, P.; Wang, W. Lightweight Design of Automobile Component Using High Strength Steel Based On Dent Resistance. *Mater. Des.* **2006**, *27*, 64–68. [CrossRef]
5. Fu, L.; Fan, L.; Li, Z.; Sun, N.; Wang, H.; Wang, W.; Shan, A. Yield Behaviour Associated with Stacking Faults in a High-Temperature Annealed Ultra-Low Carbon High Manganese Steel. *Mater. Sci. Eng. A* **2013**, *582*, 126–133. [CrossRef]
6. Bhat, M.S.; Garrison, W.M., Jr.; Zackay, V.F. Relations Between Microstructure and Mechanical Properties in Secondary Hardening Steels. *Mater. Sci. Eng.* **1979**, *41*, 1–15. [CrossRef]
7. Tomita, Y. Development of Fracture Toughness of Ultrahigh Strength, Medium Carbon, Low Alloy Steels for Aerospace Applications. *Int. Mater. Rev.* **2000**, *45*, 27–37. [CrossRef]
8. An, X.H.; Wu, S.D.; Zhang, Z.F.; Figueiredo, R.B.; Gao, N.; Langdon, T.G. Enhanced Strength–Ductility Synergy in Nanostructured Cu and Cu–Al Alloys Processed by High-Pressure Torsion and Subsequent Annealing. *Scr. Mater.* **2012**, *66*, 227–230. [CrossRef]
9. Valiev, R.Z.; Islamgaliev, R.K.; Alexandrov, I.V. Bulk Nanostructured Materials From Severe Plastic Deformation. *Prog. Mater. Sci.* **2000**, *45*, 103–189. [CrossRef]
10. Tsuji, N.; Ito, Y.; Saito, Y.; Minamino, Y. Strength and Ductility of Ultrafine Grained Aluminum and Iron Produced by Arb and Annealing. *Scr. Mater.* **2002**, *47*, 893–899. [CrossRef]
11. Yan, F.K.; Liu, G.Z.; Tao, N.R.; Lu, K. Strength and Ductility of 316L Austenitic Stainless Steel Strengthened by Nano-Scale Twin Bundles. *Acta Mater.* **2012**, *60*, 1059–1071. [CrossRef]
12. Zhao, Y.; Topping, T.; Bingert, J.F.; Thornton, J.J.; Dangelewicz, A.M.; Li, Y.; Liu, W.; Zhu, Y.; Zhou, Y.; Lavernia, E.J. High Tensile Ductility and Strength in Bulk Nanostructured Nickel. *Adv. Mater.* **2008**, *20*, 3028–3033. [CrossRef]
13. Mijangos, D.; Mejia, I.; Cabrera, J.M. Influence of Microalloying Additions (Nb, Ti, Ti/B, V and Mo) on the Microstructure of TWIP Steels. *Metallogr. Microstruct. Anal.* **2022**, *11*, 524–536. [CrossRef]
14. Lee, S.; Park, I.; Jung, J.; Lee, Y. The Effect of Si On Hydrogen Embrittlement of Fe-18Mn-0.6C-Xsi Twinning-Induced Plasticity Steels. *Acta Mater.* **2016**, *103*, 264–272. [CrossRef]
15. Zhang, C.; Zhi, H.; Antonov, S.; Chen, L.; Su, Y. Hydrogen-Enhanced Densified Twinning (Hedt) in a Twinning-Induced Plasticity (Twip) Steel. *Scr. Mater.* **2021**, *190*, 108–112. [CrossRef]
16. Yen, H.; Huang, M.; Scott, C.P.; Yang, J. Interactions between Deformation-Induced Defects and Carbides in a Vanadium-Containing Twip Steel. *Scr. Mater.* **2012**, *66*, 1018–1023. [CrossRef]
17. Moon, J.; Park, S.; Jang, J.H.; Lee, T.; Lee, C.; Hong, H.; Suh, D.; Kim, S.H.; Han, H.N.; Lee, B.H. Atomistic Investigations of K-Carbide Precipitation in Austenitic Fe-Mn-Al-C Lightweight Steels and the Effect of Mo Addition. *Scr. Mater.* **2017**, *127*, 97–101. [CrossRef]
18. Razavi, G.R.; Rizi, M.S.; Zadeh, H.M. Effect of a Mo Addition On the Properties of High-Mn Steel. *Mater. Technol.* **2013**, *47*, 611.
19. Nasajpour, A.; Kokabi, A.; Davami, P.; Nikzad, S. Effect of Molybdenum on Mechanical and Abrasive Wear Properties of Coating of as Weld Hadfield Steel with Flux-Cored Gas Tungsten Arc Welding. *J. Alloys Compd.* **2016**, *659*, 262–269. [CrossRef]
20. Guan, J.; Yuan, Q.; Zhang, Q.; Qiao, W.; Xu, G. Simultaneous Enhancement of Strength and Toughness in a Medium-Carbon Martensitic Steel by Ti-Mo Addition. *J. Mater. Eng. Perform.* **2022**, *31*, 4273–4281. [CrossRef]

21. Scott, C.; Remy, B.; Collet, J.; Cael, A.; Bao, C.; Danoix, F.; Malard, B.; Curfs, C. Precipitation Strengthening in High Manganese Austenitic Twip Steels. *Int. J. Mater. Res.* **2011**, *102*, 538–549. [CrossRef]
22. Escobar, J.; Jiménez, J.L.; Artigas, A.; Perez-Ipiña, J.; Monsalve, A. Influence of Cold Deformation On Carbide Precipitation Kinetics in a Fe-22Mn-0.45C Twip Steel. *Materials* **2022**, *15*, 3748. [CrossRef]
23. Wang, X.; Sun, X.; Song, C.; Chen, H.; Tong, S.; Han, W.; Pan, F. Evolution of Microstructures and Mechanical Properties During Solution Treatment of a Ti–V–Mo-Containing High-Manganese Cryogenic Steel. *Mater. Charact.* **2018**, *135*, 287–294. [CrossRef]
24. *GB/T 228-2002*; Metal Materials Tensile Test Method at Room Temperature. General Administration of Quality Supervision, Inspection and Quarantine of the People's Republic of China: Beijing, China, 2002.
25. Guo, Z.; Saunders, N.; Schillé, J.P.; Miodownik, A.P. Material Properties for Process Simulation. *Mater. Sci. Eng. A* **2009**, *499*, 7–13. [CrossRef]
26. Zhuang, C.; Liu, J.; Li, C.; Tang, D. Study On High Temperature Solidification Behavior and Crack Sensitivity of Fe-Mn-C-Al Twip Steel. *Sci. Rep.* **2019**, *9*, 15962. [CrossRef]
27. Frommeyer, G.; Brüx, U. Microstructures and Mechanical Properties of High-Strength Fe-Mn-Al-C Light-Weight Triplex Steels. *Steel Res. Int.* **2006**, *9–10*, 627–633. [CrossRef]
28. Chin, K.; Kang, C.; Shin, S.Y.; Hong, S.; Lee, S.; Kim, H.S.; Kim, K.; Kim, N.J. Effects of Al Addition On Deformation and Fracture Mechanisms in Two High Manganese Twip Steels. *Mater. Sci. Eng. A* **2011**, *528*, 2922–2928. [CrossRef]
29. Howell, R.; Weerasooriya, T.; Van Aken, D. Tensile, High Strain Rate Compression and Microstructural Evaluation of Lightweight Age Hardenable Cast Fe-30Mn-9Al-XSi-0.9C-0.5Mo Steel. *Int. J. Met.* **2010**, *4*, 7–18. [CrossRef]
30. Johnson, R.A. Phase Stability of Fcc Alloys with the Embedded-Atom Method. *Phys. Rev. B Condens. Matter* **1990**, *41*, 9717–9720. [CrossRef]
31. Lan, H.F.; Du, L.X.; Li, Q.; Qiu, C.L.; Li, J.P.; Misra, R.D.K. Improvement of Strength-Toughness Combination in Austempered Low Carbon Bainitic Steel: The Key Role of Refining Prior Austenite Grain Size. *J. Alloys Compd.* **2017**, *710*, 702–710. [CrossRef]
32. Lee, S.; Lee, Y. Prediction of Austenite Grain Growth During Austenitization of Low Alloy Steels. *Mater. Des.* **2008**, *29*, 1840–1844. [CrossRef]
33. Santos, D.B.; Saleh, A.A.; Gazder, A.A.; Carman, A.; Duarte, D.M.; Ribeiro, É.A.S.; Gonzalez, B.M.; Pereloma, E.V. Effect of Annealing On the Microstructure and Mechanical Properties of Cold Rolled Fe–24Mn–3Al–2Si–1Ni–0.06C Twip Steel. *Mater. Sci. Eng. A* **2011**, *528*, 3545–3555. [CrossRef]
34. Bouaziz, O.; Allain, S.; Scott, C.P.; Cugy, P.; Barbier, D. High Manganese Austenitic Twinning Induced Plasticity Steels: A Review of the Microstructure Properties Relationships. *Curr. Opin. Solid State Mater. Sci.* **2011**, *15*, 141–168. [CrossRef]
35. Frommeyer, G.; Brüx, U.; Neumann, P. Supra-Ductile and High-Strength Manganese-Trip/Twip Steels for High Energy Absorption Purposes. *Isij Int.* **2003**, *43*, 438–446. [CrossRef]
36. Gladman, T. Precipitation hardening in metals. *Mater. Sci. Technol.* **1999**, *15*, 30–36. [CrossRef]
37. Kang, S.; Jung, Y.; Jun, J.; Lee, Y. Effects of Recrystallization Annealing Temperature on Carbide Precipitation, Microstructure, and Mechanical Properties in Fe–18Mn–0.6C–1.5Al Twip Steel. *Mater. Sci. Eng. A* **2010**, *527*, 745–751. [CrossRef]
38. Grässel, O.; Krüger, L.; Frommeyer, G.; Meyer, L.W. High Strength Fe–Mn–(Al, Si) Trip/Twip Steels Development-Properties-Application. *Int. J. Plast.* **2000**, *10–11*, 1391–1409. [CrossRef]
39. Hwang, S.; Park, M.; Bai, Y.; Shibata, A.; Mao, W.; Adachi, H.; Sato, M.; Tsuji, N. Mesoscopic Nature of Serration Behavior in High-Mn Austenitic Steel. *Acta Mater.* **2021**, *205*, 116543. [CrossRef]

materials

MDPI

Article

The Variation Patterns of the Martensitic Hierarchical Microstructure and Mechanical Properties of 35Si2MnCr2Ni3MoV Steel at Different Austenitizing Temperatures

Zhipeng Wu [1], Chao Yang [1], Guangyao Chen [1], Yang Li [1], Xin Cao [2], Pengmin Cao [3], Han Dong [1,2] and Chundong Hu [1,2,*]

[1] School of Materials Science and Engineering, Shanghai University, Shanghai 200444, China; reay777@126.com (Z.W.); alphayangchao@shu.edu.cn (C.Y.); cgybless1@shu.edu.cn (G.C.); gody1106040057@163.com (Y.L.); donghan@shu.edu.cn (H.D.)
[2] Zhejiang Institute of Advanced Materials, Shanghai University, Jiaxing 314100, China; caoxin961113@163.com
[3] Zhongyuan Special Steel Co., Ltd., Jiyuan 459000, China; 15713905226@163.com
* Correspondence: huchundong99@163.com

Abstract: This study investigates the influence of varying austenitizing temperatures on the microstructure and mechanical properties of 35Si2MnCr2Ni3MoV steel, utilizing Charpy impact testing and microscopic analysis techniques such as scanning electron microscopy (SEM) and electron backscatter diffraction (EBSD). The findings reveal that optimal combination of strength and toughness is achieved at an austenitizing temperature of 980 °C, resulting in an impact toughness of 67.2 J and a tensile strength of 2032 MPa. The prior austenite grain size initially decreases slightly with increasing temperature, then enlarges significantly beyond 1100 °C. The martensite blocks' and packets' structures exhibit a similar trend. The proportion of high–angle grain boundaries, determined by the density of the packets, peaks at 980 °C, providing maximal resistance to crack propagation. The amount of retained austenite increases noticeably after 980 °C; beyond 1200 °C, the coarsening of packets and a decrease in density reduce the likelihood of trapping retained austenite. Across different austenitizing temperatures, the steel demonstrates superior crack initiation resistance compared to crack propagation resistance, with the fracture mode transitioning from ductile dimple fracture to quasi–cleavage fracture as the austenitizing temperature increases.

Keywords: ultra–high strength steel; mechanical properties; microstructure

Citation: Wu, Z.; Yang, C.; Chen, G.; Li, Y.; Cao, X.; Cao, P.; Dong, H.; Hu, C. The Variation Patterns of the Martensitic Hierarchical Microstructure and Mechanical Properties of 35Si2MnCr2Ni3MoV Steel at Different Austenitizing Temperatures. *Materials* **2024**, *17*, 1099. https://doi.org/10.3390/ma17051099

Academic Editor: Francesco Iacoviello

Received: 18 January 2024
Revised: 21 February 2024
Accepted: 25 February 2024
Published: 28 February 2024

1. Introduction

Ultra–high–strength steels are crucial in aerospace applications and are extensively used in the manufacturing of armor–piercing shell bodies. With advancing technological demands for penetration depth and initial shell velocity, these shell bodies require heightened strength to withstand the load. However, as the strength of steel reaches a certain threshold, its toughness is significantly compromised. This contradictory tendency escalates with increased strength, adversely affecting service safety and limiting the application of ultra–high–strength steels in armor–piercing shells. To achieve a balanced match between strength and toughness in ultra–high–strength steels, traditional high–alloy versions largely depend on the inclusion of precious metal elements like cobalt and nickel to enhance toughness, resulting in high production costs. Therefore, from an economic perspective, they are no longer suitable for large–scale industrial production. On the contrary, low–alloy ultra–high–strength steels represent an important development direction due to their relatively low cost. The AISI 4130, AISI 4140, and AISI 4340 alloy steel series in the United States are typical representatives of early low–alloy ultra–high–strength and

–toughness steels [1,2]. Among them, AISI 4130 was the earliest developed ultra–high–strength alloy steel. To achieve the best combination of strength and toughness, this steel is often subjected to tempering treatment. However, its yield strength and tensile strength are 880 and 980 MPa, respectively, which do not meet the requirements of ultra–high–strength alloy steels. Therefore, on the basis of 4130 steel, the carbon content is increased to 0.4%, and small amounts of Ni and Mo elements are added to form 4340 steel. Most of the subsequently developed low–alloy ultra–high–strength steels have been continuously improved based on the AISI 4130 and AISI 4340 alloy steel series. Due to the higher carbon content in low–alloy carbon steels, their strength is high after quenching, but their ductility is poor. Therefore, Krauss [3] conducted low–temperature tempering treatment (150–200 °C) on martensitic carbon steel and low–alloy carbon steel. Their results showed that the strength of low–temperature tempered martensite is related to the dynamic work hardening of dislocations and transition carbides in martensite crystals, which is determined by the carbon content. In steel with 0.5% C, when second–phase particles are dispersed in the tempered martensite matrix, toughness notches form on them and lead to plastic fracture. In low–temperature tempered martensitic steels with more than 0.5% C, brittle intergranular fractures easily occur along the original austenite grain boundaries. Therefore, the carbon content in low–alloy ultra–high–strength steels generally should not exceed 0.5%, and appropriate low–temperature tempering treatment is usually required to improve their toughness. In order to further enhance the toughness of low–alloy ultra–high–strength steels, Chang and Smith [4] studied the effect of Si element on the tempering hardness and microstructure of martensite and discovered the beneficial role of Si in low–alloy ultra–high–strength steels, laying the foundation for the development of 300 M steel. In 1952, the International Nickel Company in the United States developed and designed 300 M steel, which was developed based on AISI 4340 steel by adding 1.52.0% Si element and slightly adjusting the V content. With proper element control and heat treatment processes, the development of low–alloy ultra–high–strength steels has become increasingly mature and is now rapidly progressing towards higher strength, toughness, and lower cost. For example, Fe–0.25C–1.6Si–1.5Mn–0.5Cr–0.3Mo steel developed by the Russian researcher Tkachev [5] achieved a tensile strength of 1840 MPa and an impact energy of 87 J after quenching at 950 °C and tempering at 280 °C. These properties are comparable to those of high–alloy ultra–high–strength steels such as AerMet 100 (AerMet is a registered trade mark of CRS Holdings, Inc., Philadelphia, PA, USA), but at a significantly reduced cost.

Building on previous research, our team has developed a novel low–alloy ultra–high strength 35Si2MnCr2Ni3MoV steel, costing only one–eighth of the price of AerMet 100 steel. However, achieving optimal properties necessitates precise thermal processing. Both excessively high and low austenitizing temperatures can directly affect the distribution of alloy elements and subsequent phase transformations during quenching, particularly martensitic transformations, thus significantly influencing the material's properties. Recent studies on common low–alloy ultra–high strength steels indicate that austenitizing temperature affects the prior austenite grain size, indirectly impacting final toughness [6]. The solid solution and martensitic transformation strengthening effects in ultra–high strength steels are also related to austenitizing temperature [7]. Austenitizing can enhance microstructural uniformity and reduce segregation [8–10]. Therefore, the temperature plays a significant role in affecting the outcomes of austenitizing treatment, including microstructural uniformity, solid solution strengthening, and martensitic transformation strengthening.

Based on this, the influence of different austenitizing temperatures on the microstructure and mechanical properties of 35Si2MnCr2Ni3MoV steel is analyzed in this paper. The variation patterns of the size of the martensitic multilevel structure units after different austenitizing temperatures and the transition of fracture mechanisms at different austenitizing temperatures are investigated. The aim of this analysis is to provide a theoretical basis for the rational design of heat treatment processes for 35Si2MnCr2Ni3MoV steel in industrial production.

2. Materials and Methods

The chemical composition of the 35Si2MnCr2Ni3MoV steel used in the experiments is presented in Table 1.

Table 1. Chemical composition of the studied steel (in wt.%).

Fe	C	Si	Mn	Cr	Ni	Mo	V
Balance	0.35	1.62	0.86	1.62	3.02	0.45	0.22

The steel was produced using a vacuum induction plus vacuum self–consumption remelting process. The ingot underwent forging heating, triple drawing, billet precision forging, and post–forging annealing, then was processed into a rod with the dimensions of φ170 mm × 80 mm.

The phase transformation points of 35Si2MnCr2Ni3MoV steel were determined using a dilatometer (DIL805A, TA, Milford, MA, USA), which guided the establishment of appropriate austenitizing and tempering temperatures.

The dilatometry samples, in a post–forging annealed state, were sized at φ4 × 10 mm. The heating rate for the measurement was set at 0.1 °C/s, and the cooling rate was set at 20 °C/s. Based on the determined transformation points of Ac1 = 760 °C, Ac3 = 816 °C, and Ms = 270 °C, the heat treatment process is depicted in Figure 1b.

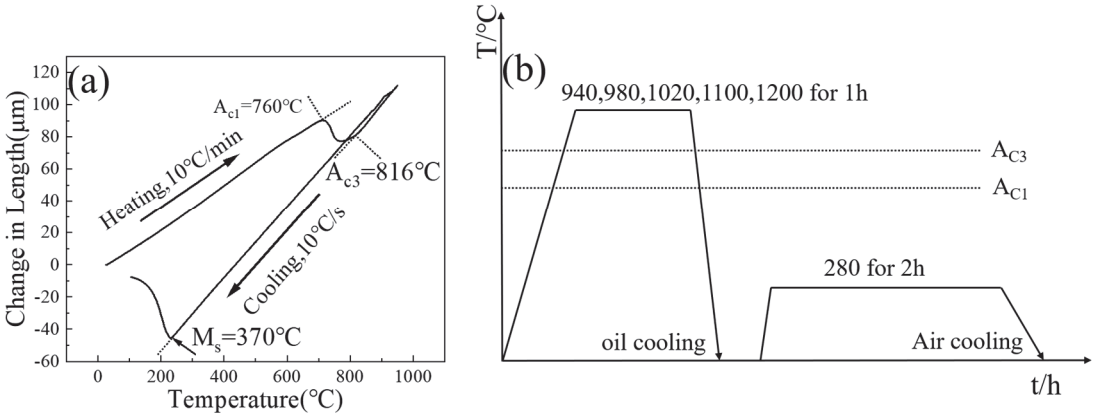

Figure 1. (**a**) Thermal expansion curve; (**b**) heat treatment process system.

The impact specimens, measuring 10 × 10 × 55 mm and featuring a 2 mm deep U–shaped notch, were utilized for room temperature impact testing using a testing machine (Instron 750MPX, Boston, MA, USA) with three samples tested at each temperature (test with reference to standard ASTM E23-2018 [11]). Metallographic samples, measuring 10 × 10 × 5 mm, were prepared and subjected to etching using a 4% nitric acid alcohol solution.

The macroscopic and microscopic morphology of impact fracture surfaces was examined using a stereomicroscope (ZEISS Stemi 508, Carl Zeiss, Jena, Germany) and a field emission scanning electron microscope (FEI Apreo 2S HiVac, Thermo Fisher Scientific Waltham, MA, USA). The martensitic substructure in the microstructure was observed and analyzed via EBSD (Bruker QUANTAX EBSD 400i e–Flash^{FS}, Bruker, Billerica, MA, USA), in combination with software such as AZtecCrystal v2.1, MATLAB(R2022a), and MTEX toolbox v5.9.1.

3. Results and Discussion

Figure 2 presents the morphology of the prior austenite grain sizes at different austenitizing temperatures, reconstructed using AZtecCrystal software. By means of the intersecting line method (refer to standard ASTM E112–13 [12]), the average grain size after reconstruction was estimated. (We understand that Figure 2 represents a cross–section of

mostly uniform grains. Some display the whole diameter, while others are just a small part of the sphere cross–section, thus appearing as small grains. This was taken into account in the estimation of the average grain size). As observed from Figure 2a–e, at austenitizing temperatures of 940, 980 and 1020 °C, the average grain size does not change significantly. Twins [5] are observable within the grains at 980 °C and 1020 °C. As the temperature further increases to 1100 °C, there is a noticeable increase in grain size, and at 1200 °C, the grains undergo severe coarsening, with only the prior austenite grain boundaries being observable. With the austenitizing temperature rising from 940 °C to 1200 °C, the grain size in the steel first decreases from 31.3 μm to 27.6 μm and then increases to 85.6 μm, as specifically fitted and shown in Figure 2f. The significant increase in grain size is attributed to the enhanced movement and diffusion ability of boundary atoms with increasing temperature, accelerating the rate of grain boundary engulfment. According to the Hall–Petch formula, strength is inversely related to the prior austenite grain size [13]. Given a constant total plastic deformation, the growth of grains results in dislocation motion occurring in fewer grains, leading to uneven plastic deformation and a propensity for stress concentration. This uneven distribution of deformation can reduce plastic toughness.

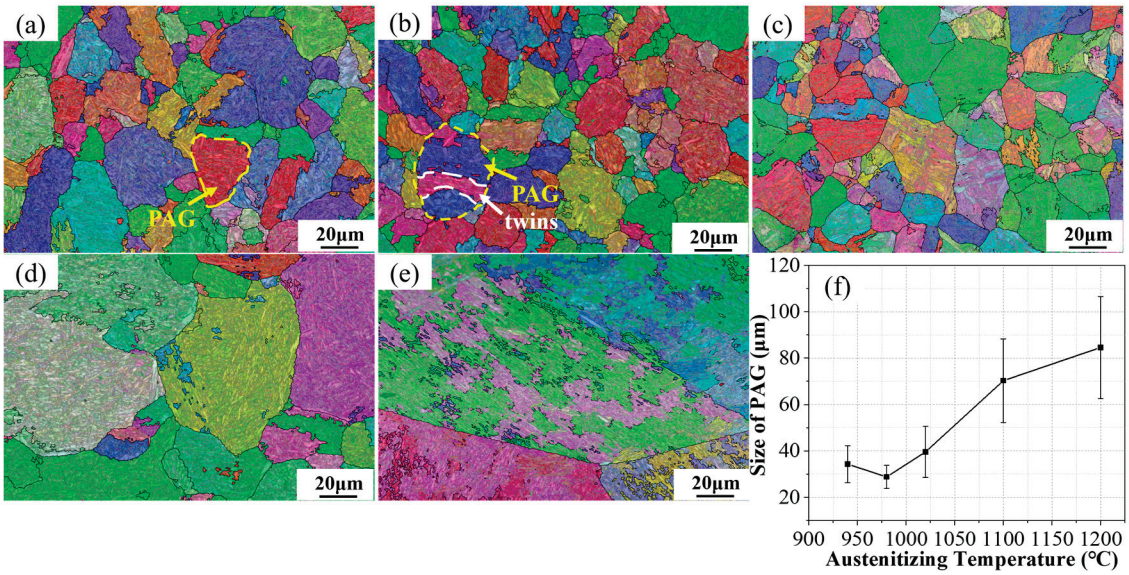

Figure 2. IPF map of reconstructed parent austenite grains with the parent grain boundaries in yellow and parent austenite twin boundaries in white after austenitizing at 940 °C (**a**), 980 °C (**b**), 1020 °C (**c**), 1100 °C (**d**), and 1200 °C (**e**) and the average grain size statistics (**f**).

In addition to the changes in the prior austenite grain size affecting both the strength and toughness of the alloy, research by Luo [14] suggests that the refinement of the martensitic microstructure may also play a similar role. Therefore, it is necessary to further explore the width variation of martensite blocks and packets at different austenitizing temperatures. The morphology of martensite packets was reconstructed using MATLAB and the MTEX toolbox [15]. The authors point out that typically, a complete martensitic package contains variants of four colors, which allows us to distinguish some martensitic slat packages quite well. The results are depicted in Figure 3. From Figure 3a–c, it can be observed that the size of the packet changes minimally in the 940 to 1020 °C range. However, as the austenitizing temperature increases to 1100 °C, the size of the packet notably enlarges, and further increases when the temperature reaches 1200 °C. The sizes of martensite packets at five different temperatures were statistically analyzed with 30 measurements each, and the fitted sizes are shown in Figure 3f. At austenitizing temperatures of 940, 980, 1020, 1100, and 1200 °C, the average size of the martensite packets is 18.8, 16.5, 19.9, 26.6, and 41.9 μm, respectively. As the austenitizing temperature increases from 940 °C to 1200 °C,

the size of the packets first decreases and then increases, following the same trend as the prior austenite grain size.

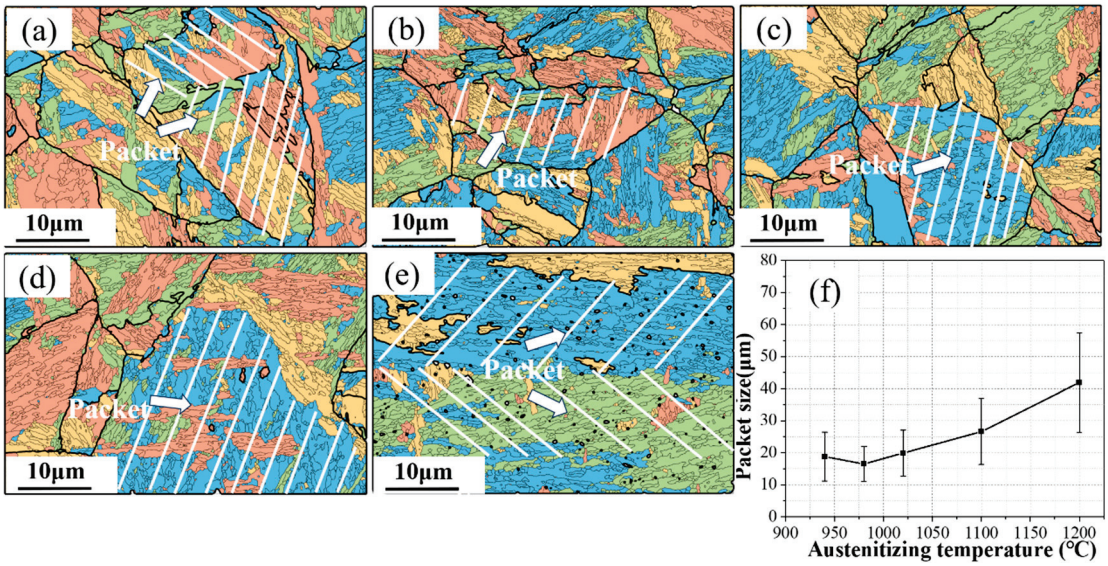

Figure 3. EBSD map showing the four different type of martensite packets and grain boundaries of the reconstructed austenite grains at 940 °C (**a**), 980 °C (**b**), 1020 °C (**c**), 1100 °C (**d**), and 1200 °C (**e**) and the average packet statistics (**f**).

To accurately quantify the size of martensite packets, this study referenced the relationship between the various hierarchical structures of martensite as proposed by E.I. Galindo–Nava [16].

$$D_{Packet} = \sqrt{\frac{3\sqrt{3}}{8N_p}} D_{PAG} \tag{1}$$

$$d_{block} = \frac{1}{N_b} D_{Packet} \tag{2}$$

This formula considers N_b as the number of packets in each block, with the number of packets in each block depending on the block's size. Typically, this ranges from two packets in blocks of about 2 μm in size to six packets in blocks exceeding 10 μm. Research by Tkachev [5] and others indicates that the average N_b value in the experiments is five.

Based on this formula, the sizes of 300 packets at five different austenitizing temperatures were statistically analyzed, with the results shown in Figure 4. At these varying austenitizing temperatures, the average widths of the martensite blocks were 0.954, 0.795, 0.958, 1.081, and 1.375 μm, respectively. Although these changes in packet size were smaller compared to those in blocks, the results still confirm that the sizes of martensite blocks and packets are influenced by the size of the prior austenite grains.

High–angle grain boundaries (HAGBs) in martensite greatly inhibit crack propagation [17]—as the crystal orientation angle increases, cracks consume more shear energy when crossing these boundaries, leading to significant deviation in the crack propagation direction at HAGBs [18–20]. Therefore, the proportion of high–angle grain boundaries to some extent reflects the toughness differences of steel at various austenitizing temperatures. As shown in Figure 5a–e, the proportions of HAGBs at different austenitizing temperatures were quantified, with values of 63.3%, 67.3%, 59.4%, 58.8%, and 48.2%, respectively. In these figures, red and green lines represent low–angle and high–angle grain boundaries, respectively. With increasing austenitizing temperature, the proportion of HAGBs first increases and then decreases, reaching its peak at 980 °C. This indicates that at an austenitizing temperature of 980 °C, the block size is the smallest and the interface is the most numerous, which corresponds with the previously observed trends in block size variation.

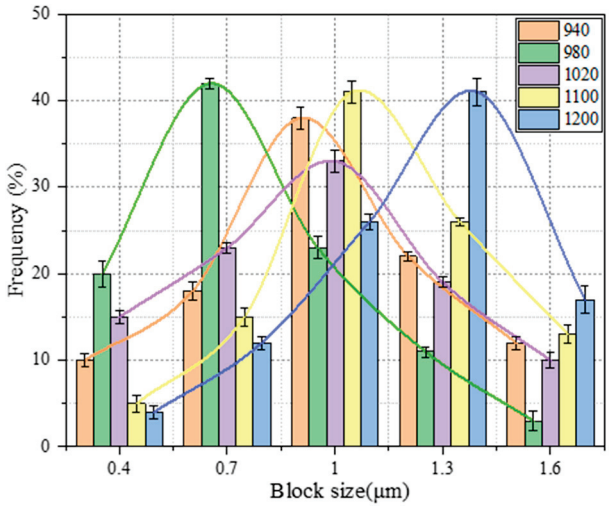

Figure 4. The distributions of martensite block sizes at five austenitizing temperatures. The connected lines are shown to exhibit a Gaussian distribution.

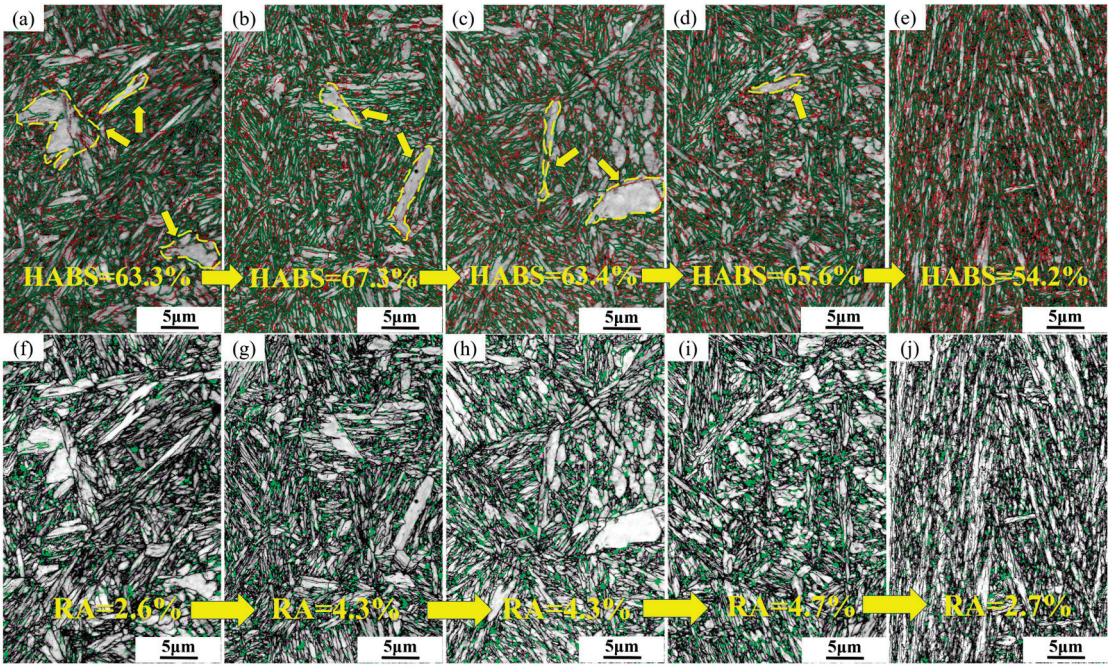

Figure 5. The amount of high–angle grain boundaries and retained austenite at five austenitizing temperatures. The yellow arrows and numbers represent the specific values after the change with temperature. (**a**,**f**) 940 °C; (**b**,**g**) 980 °C; (**c**,**h**) 1020 °C; (**d**,**i**) 1100 °C; (**e**,**j**) 1200 °C.

Retained austenite also impedes crack propagation in steel, and its amount can be influenced by changing the austenitizing temperature of the steel. Figure 5i, j show the amounts of retained austenite at different austenitizing temperatures. For austenitizing temperatures of 940, 980, 1020, 1100, and 1200 °C, the retained austenite contents are 2.6%, 4.3%, 4.3%, 4.7%, and 2.7%, respectively. Observations reveal that in Figure 5f–h, where massive and striated martensitic substructures are present (indicated by arrows), the distribution of retained austenite is low. As the austenitizing temperature increases, these massive and striated substructures diminish or disappear. Retained austenite is primarily distributed along high–angle and low–angle grain boundaries. With increasing austenitizing temperature, the amount of retained austenite in the steel significantly rises, related to the solubility of stable austenite–forming elements in the steel. However, at 1200 °C, the amount of retained austenite notably decreases due to severe grain coarsening

at this temperature, which consequently reduces the density of the block substructure and lowers the probability of the presence of retained austenite at the block boundaries.

A rough assessment of material toughness can be performed by evaluating the proportions of the crack initiation zones (1), fast crack propagation zones (2), and shear lip (3) in the macroscopic fracture surface of steel. It is generally believed that larger proportions of the crack initiation zones and shear lip indicate better ductility and toughness of the material [21]. Figure 6 shows the impact fracture morphologies of the alloy steel at different austenitizing temperatures. The proportions of the shear lip and crack initiation zones in the impact fractures after different austenitizing temperatures were calculated using Image–Pro Plus 6.0 software, resulting in 26.5%, 26%, 22.3%, 21.4%, and 17.6%, respectively. It was found that the ductility and toughness of the material are relatively better at austenitizing temperatures of 940 °C and 980 °C.

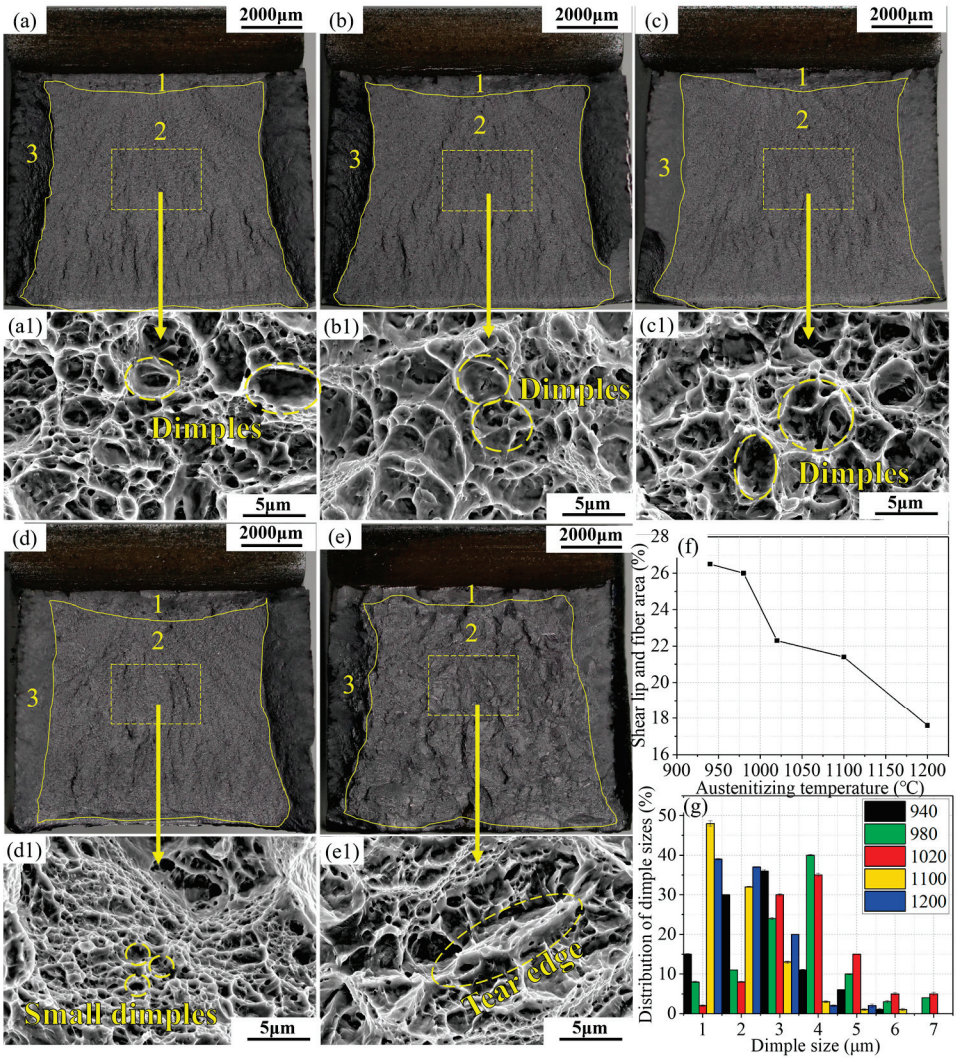

Figure 6. Macroscopic fracture surfaces of the Charpy U–notch specimens of the 940 °C (**a**), 980 °C (**b**), 1020 °C (**c**), 1100 °C (**d**), and 940 °C (**e**) steel. (**a1**–**e1**) correspond to the SEM images of stable crack propagation zones. The proportion of area of shear lip fiber area in five specimens is shown in (**f**) and the distributions of dimple sizes are shown in (**g**). The numbers 1, 2 and 3 correspond to the crack initiation, fast crack propagation zones and shear lip.

Figure 6a1–e1 show the microscopic morphology in the rapid propagation region. Observations from Figure 6a1–c1 reveal that at austenitizing temperatures of 940 to 1020 °C, the fracture is mainly composed of dense dimples with relatively large sizes. As the temperature increases to 1100 °C (Figure 6d1), the size of the dimples significantly reduces,

and at 1200 °C, clear tear ridges appear in the fracture, indicating a transition in the fracture mode of the test steel from ductile dimple fracture to quasi–cleavage fracture. The sizes of approximately 1000 dimples were measured using the linear intercept method, with the results shown in Figure 6f. At austenitizing temperatures of 940, 980, 1020, 1100, and 1200 °C, the average dimple sizes are 3.25, 3.64, 3.46, 2.24, and 2.37 μm, respectively. With increasing austenitizing temperature, the average diameter of the dimples first increases and then decreases, reaching its maximum at 980 °C. According to Hilders' research [22], impact toughness is inversely related to the square root of the average dimple size, indicating that at an austenitizing temperature of 980 °C, the toughness is relatively improved.

Figure 7 presents the load–deflection and energy–deflection curves obtained from oscillatory shock testing at five different austenitizing temperatures. The results show that as the austenitizing temperature increases, the impact energy absorption first rises and then falls, reaching a maximum of 67.2 J at 980 °C and decreasing by about 50% at 1200 °C. At different quenching temperatures, the proportion of E_i (energy to initiate crack) is higher than E_p (energy to propagate crack), indicating that the specimens have better crack initiation resistance, with E_i dominating the energy absorption during the entire impact process. In many studies [23–25], it was noted that the ratio of crack propagation energy to initiation energy reflects the ductile–brittle fracture state of the material. At different austenitizing temperatures, the E_p/E_i ratio is <1, suggesting that the material tends to brittle fracture. When the quenching temperature reaches 1200 °C, E_i and E_p are 17.9 J and 13.1 J, respectively, with E_i decreasing by 62% from its highest value and E_p decreasing by 38%. This indicates that at 1200 °C, the crack in the impact specimen is in the most susceptible state for initiation and propagation, and its resistance to crack initiation and propagation significantly diminishes. The proportions of E_i and E_p are 57.7% and 42.3%, respectively, with the proportion of E_i decreasing by about 20% and that of E_p increasing by 20%, indicating a decrease in the dominant role of E_i in the entire impact fracture process. The maximum load Pm shows a decreasing trend with increasing austenitizing temperature, dropping from 44 KN at 940 °C to 33.7 KN at 1200 °C. Dynamic yield strength reflects the level of impact toughness; the higher the dynamic yield strength, the greater the impact toughness.

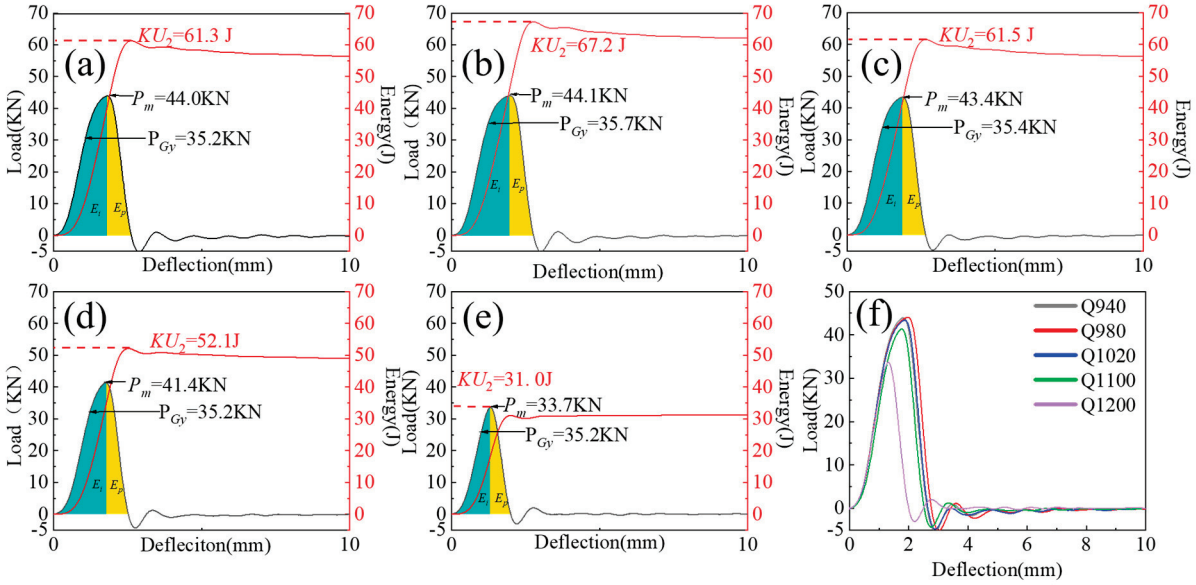

Figure 7. The effect of austenitizing temperature on the load–deflection curve and energy–deflection curve: (**a**) 940 °C; (**b**) 980 °C; (**c**) 1020 °C; (**d**) 1100 °C; (**e**) 1200 °C; (**f**) general overview. E_i and E_p represent energy to initiate crack and energy to propagate crack.

The dynamic yield strength σ_{GYd} can be calculated using the following formula [26]:

$$\sigma_{GYd} = \frac{3.732 P_{GY} W}{C_{GY}(W-a)^2 B} \quad (3)$$

where W represents the width of the specimen (10 mm); B is the thickness of the specimen (10 mm); a is the notch depth (2 mm); and C_{GY} depends on the shape of the indenter and the radius at the root of the notch, and is taken as 1.336 in this study [26]. The dynamic ultimate tensile strength σ_{UYd} can be obtained using a similar relationship, with the formula being as follows [26]:

$$\sigma_{UTSd} = \frac{\eta_{Pm} P_m W}{(W-a)^2 B} \quad (4)$$

where η_{pm} is an empirical factor depending on the ratio between shear stress and tensile stress, as well as the constraint factor at maximum load. In this study, η_{pm} is taken as 2.929, a value referenced from calculations for AISI 4340 steel and AISI 4340M steel after quenching and low–temperature tempering [26,27], due to their similar alloy compositions and mechanical properties.

The calculated results are shown in Figure 8. From the figure, it can be observed that the dynamic ultimate tensile strength of the alloy steel is positively correlated with the maximum load. Between 940 °C and 1020 °C, the strength of the steel studied is approximately 2000 MPa, peaking at 2032 MPa at 980 °C. When the quenching temperature is increased to 1100 °C, the strength drops to 1895 MPa, and at a quenching temperature of 1200 °C, it rapidly decreases to 1542 MPa, a reduction of about 500 MPa compared to the peak at 980 °C.

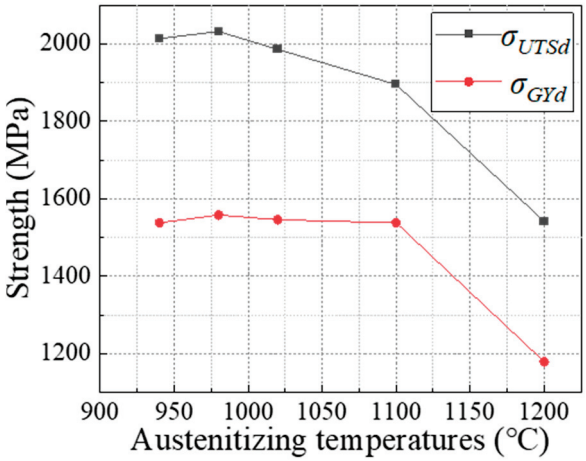

Figure 8. Dynamic yield strength and tensile strength at different austenitizing temperatures.

4. Conclusions

1. At an austenitizing temperature of 980 °C, 35Si2MnCr2Ni3MoV steel achieves the optimal combination of strength and toughness. At this temperature, the steel's impact energy is 67.2 J, and the dynamic tensile strength determined by instrumented impact test is 2032 MPa.
2. The studied steels show a slight decrease and then an increase in grain size with increasing temperature, with a pronounced coarsening after 1100 °C. Martensitic lath blocks and packets exhibit the same trend.
3. The proportion of high–angle grain boundaries is determined by the density of lath packets. The highest proportion occurs at 980 °C, providing the strongest resistance to crack propagation. As the solubility of stable austenite–forming elements increases with temperature, the amount of retained austenite significantly increases after 980 °C,

reaching a peak of 4.7% at 1100 °C. After 1200 °C, as the lath packets coarsen and their density decreases, the probability of trapping retained austenite reduces.

4. 35Si2MnCr2Ni3MoV steel demonstrates superior crack initiation resistance compared to crack propagation resistance. As the austenitizing temperature increases, the fracture mode of 35Si2MnCr2Ni3MoV steel transitions from ductile dimple fracture to quasi–cleavage fracture.

Author Contributions: Conceptualization, C.H. and H.D.; methodology, H.D.; software, Z.W.; validation, Z.W., C.H. and C.Y.; formal analysis, Z.W., Y.L. and C.Y.; investigation, X.C.; resources, P.C.; data curation, P.C.; writing—original draft preparation, Z.W.; writing—review and editing, G.C.; visualization, G.C.; supervision, C.H.; project administration, C.H.; funding acquisition, G.C. and C.H. All authors have read and agreed to the published version of the manuscript.

Funding: This research received no external funding.

Institutional Review Board Statement: Not applicable.

Informed Consent Statement: Not applicable.

Data Availability Statement: Data are contained within the article.

Acknowledgments: The authors would like to thank Tkachev from Russia for his help with the MTEX software.

Conflicts of Interest: Author Pengmin Cao was employed by the company Zhongyuan Special Steel Co., Ltd.. The remaining authors declare that the research was conducted in the absence of any commercial or financial relationships that could be construed as a potential conflict of interest.

References

1. Nunes, M.M.; Silva, E.M.D.; Renzetti, R.A.; de Brito, T.G. Analysis of quenching parameters in AISI 4340 steel by using design of experiments. *Mater. Res.* **2018**, *22*. [CrossRef]
2. Saeidi, N.; Ekrami, A. Microstructure–Toughness Relationship in AISI 4340 Steel. *Defect Diffus. Forum* **2011**, *312–315*, 110–115. [CrossRef]
3. Krauss, G. Deformation and fracture in martensitic carbon steels tempered at low temperatures. *Metall. Mater. Trans. B* **2011**, *32*, 205–221. [CrossRef]
4. Chang, L.; Smith, G.D.W. The silicon effect in the tempering of martensite in steels. *Le J. Phys. Colloq.* **1984**, *45*, C9-397–C9-401. [CrossRef]
5. Tkachev, E.; Borisov, S.; Belyakov, A.; Kniaziuk, T.; Vagina, O.; Gaidar, S.; Kaibyshev, R. Effect of quenching and tempering on structure and mechanical properties of a low–alloy 0.25 C steel. *Mater. Sci. Eng. A* **2023**, *868*, 144757. [CrossRef]
6. Babu, N.K.; Suresh, M.R.; Sinha, P.P.; Sarma, D.S. Effect of austenitizing temperature and cooling rate on the structure and properties of a ultrahigh strength low alloy steel. *J. Mater. Sci.* **2006**, *41*, 2971–2980. [CrossRef]
7. Hidalgo, J.; Santofimia, M.J. Effect of prior austenite grain size refinement by thermal cycling on the microstructural features of as–quenched lath martensite. *Metall. Mater. Trans. A* **2016**, *47*, 5288–5301. [CrossRef]
8. Caballero, F.G.; Capdevila, C.; de Andrés, C.G. Evaluation and review of simultaneous transformation model in high strength low alloy steels. *Mater. Sci. Technol.* **2002**, *18*, 534–540. [CrossRef]
9. Carlson, M.F.; Narasimha Rao, B.V.; Thomas, G. The effect of austenitizing temperature upon the microstructure and mechanical properties of experimental Fe/Cr/C steels. *Metall. Trans. A* **1979**, *10*, 1273–1284. [CrossRef]
10. Kim, H.D.; Kim, I.S. Effect of austenitizing temperature on microstructure and mechanical properties of 12% Cr steel. *ISIJ Int.* **1994**, *34*, 198–204. [CrossRef]
11. *ASTM E23–2023*; ASTM 2023 Standard Specification for Standard Test Methods for Notched Bar Impact Testing of Metallic Materials. ASTM: West Conshohocken, PA, USA, 2023.
12. *ASTM E112–13*; ASTM 2021 Standard Specification for Standard Test Methods for Determining Average Grain Size. ASTM: West Conshohocken, PA, USA, 2021.
13. Saada, G. Hall–Petch revisited. *Mater. Sci. Eng. A* **2005**, *400*, 146–149. [CrossRef]
14. Luo, H.; Wang, X.; Liu, Z.; Yang, Z. Influence of refined hierarchical martensitic microstructures on yield strength and impact toughness of ultra–high strength stainless steel. *J. Mater. Sci. Technol.* **2020**, *51*, 130–136. [CrossRef]
15. Niessen, F.; Nyyssönen, T.; Gazder, A.A.; Hielscher, R. Parent grain reconstruction from partially or fully transformed microstructures in MTEX. *J. Appl. Crystallogr.* **2022**, *55*, 180–194. [CrossRef]
16. Galindo–Nava, E.I.; Rivera–Díaz–del–Castillo, P.E.J. A model for the microstructure behaviour and strength evolution in martensite. *Acta Mater.* **2015**, *98*, 81–93. [CrossRef]
17. Winning, M.; Rollett, A.D. Transition between low and high angle grain boundaries. *Acta Mater.* **2005**, *53*, 2901–2907. [CrossRef]

18. Brandon, D.G. The structure of high–angle grain boundaries. *Acta Metall.* **1966**, *14*, 1479–1484. [CrossRef]
19. Fischmeister, H.F. Structure and properties of high angle grain boundaries. *Le J. Phys. Colloq.* **1985**, *46*, 3–23. [CrossRef]
20. Saeidi, N.; Ekrami, A. Comparison of mechanical properties of martensite/ferrite and bainite/ferrite dual phase 4340 steels. *Mater. Sci. Eng. A* **2009**, *523*, 125–129. [CrossRef]
21. Caballero, F.G.; Santofimia, M.J.; García–Mateo, C.; Chao, J.; De Andres, C.G. Theoretical design and advanced microstructure in super high strength steels. *Mater. Des.* **2009**, *30*, 2077–2083. [CrossRef]
22. Hilders, O.A.; Santana, M.G. Toughness and fractography of austenitic type 304 stainless steel with sensitization treatments at 973 K. *Metallography* **1988**, *21*, 151–164. [CrossRef]
23. Park, M.; Park, G.W.; Kim, S.H.; Choi, Y.W.; Kim, H.C.; Kwon, S.H.; Noh, S.; Jeon, J.B.; Kim, B.J. Tensile and Charpy impact properties of heat–treated high manganese steel at cryogenic temperatures. *J. Nucl. Mater.* **2022**, *570*, 153982. [CrossRef]
24. Sohn, S.S.; Hong, S.; Lee, J.; Suh, B.C.; Kim, S.K.; Lee, B.J.; Kim, N.J.; Lee, S. Effects of Mn and Al contents on cryogenic–temperature tensile and Charpy impact properties in four austenitic high–Mn steels. *Acta Mater.* **2015**, *100*, 39–52. [CrossRef]
25. Fereiduni, E.; Banadkouki, S.G. Improvement of mechanical properties in a dual–phase ferrite–martensite AISI4140 steel under tough–strong ferrite formation. *Mater. Des.* **2014**, *56*, 232–240. [CrossRef]
26. Lucon, E. Estimating dynamic ultimate tensile strength from instrumented Charpy data. *Mater. Des.* **2016**, *97*, 437–443. [CrossRef]
27. Server, W.L. General Yielding of Charpy V–Notch and Precracked Charpy Specimens. *J. Eng. Mater. Technol.* **1978**, *100*, 183. [CrossRef]

materials

MDPI

Article

Regulation Law of Tempering Cooling Rate on Toughness of Medium-Carbon Medium-Alloy Steel

Chao Yang [1], Tingting Xu [2], Hongshan Zhao [1,3], Chundong Hu [1,3,*] and Han Dong [1,3]

[1] School of Materials Science and Engineering, Shanghai University, Shanghai 200444, China; alphayangchao@shu.edu.cn (C.Y.); boyushankf@126.com (H.Z.); donghan@shu.edu.cn (H.D.)
[2] Zhongyuan Special Steel Co., Ltd., Jiyuan 459000, China; xuting_1@163.com
[3] Zhejiang Institute of Advanced Materials, Shanghai University, Jiaxing 314100, China
* Correspondence: huchundong99@163.com

Abstract: Temper embrittlement is a major challenge encountered during the heat treatment of high-performance steels for large forgings. This study investigates the microstructural evolution and mechanical properties of Cr-Ni-Mo-V thick-walled steel, designed for large forgings with a tensile strength of 1500 MPa, under different tempering cooling rates. Optical microscopy (OM), scanning electron microscopy (SEM), and electron backscatter diffraction (EBSD) were employed to analyze the microstructural features. The results demonstrate that the embrittlement occurring during air cooling after tempering is attributed to the concentration of impurities near Fe_3C at the grain boundaries. The low-temperature impact toughness at −40 °C after water quenching reaches 29 J due to the accelerated cooling rate during tempering, which slows down the diffusion of impurity elements towards the grain boundaries, resulting in a reduced concentration and dislocation density and an increased stability of the grain boundaries, thereby enhancing toughness. The bainite content decreases and the interface between martensite and bainite undergoes changes after water quenching during tempering. These alterations influence the crack propagation direction within the two-phase microstructure, further modifying the toughness. These findings contribute to the understanding of temper embrittlement and provide valuable guidance for optimizing heat treatment processes to enhance the performance of high-performance steels in large forgings.

Keywords: temper embrittlement; medium-carbon medium-alloy steel; martensite; bainite; toughness

Citation: Yang, C.; Xu, T.; Zhao, H.; Hu, C.; Dong, H. Regulation Law of Tempering Cooling Rate on Toughness of Medium-Carbon Medium-Alloy Steel. *Materials* **2024**, *17*, 205. https://doi.org/10.3390/ma17010205

Academic Editor: Pavel Novák

Received: 16 November 2023
Revised: 25 December 2023
Accepted: 28 December 2023
Published: 30 December 2023

1. Introduction

Steels for large forgings undergo temper embrittlement during the heat treatment process at temperatures ranging from 250 °C to 400 °C and 500 °C to 650 °C. Temper embrittlement typically manifests in two types: reversible and irreversible. Research on both types of temper embrittlement has primarily focused on the segregation of harmful elements such as phosphorus, sulfur, tin, antimony, and arsenic at the grain boundaries during tempering or aging processes. This segregation reduces the bonding strength of iron atoms at the grain boundaries, making cracks prone to initiate and propagate along the grain boundaries, ultimately leading to intergranular fracture [1]. The sensitivity of elements in steel to temper embrittlement is in the order: P > Sn > Sb ≈ As. Additionally, alloying elements such as Ni, Cr, and Mn are significant contributors to temper embrittlement. In the absence of these elements, temper embrittlement is generally not induced, and the order of alloying elements in terms of embrittlement capability is Mn ≈ Si > Cr > Ni. The impact of a single alloying element on temper embrittlement in steel is not significant, but the combined addition of alloying elements greatly promotes the occurrence of temper embrittlement. Attempts have been made to synthesize the effects of alloying elements influencing temper embrittlement into a single coefficient to assess the sensitivity of steel to temper embrittlement. In the 1970s, Bruscato [2] introduced a brittleness factor,

X = (10P + 5Sb + 4Sn + As) × 102, which can be used to predict the brittleness sensitivity of metals. Watanabe [3], in conjunction with experiments on plates and forgings, identified a brittleness sensitivity factor, J = (Si + Mn)(P + Sn) × 104. As X and J values increase, steel transitions towards embrittlement. Bandyopadhyay [4] studied the precipitation behavior of carbides during the tempering process of Ni-Cr-V and Ni-Cr-Mo-V steels. They explained that molybdenum enhances the cohesion of grain boundaries, while phosphorus is less prone to segregate to grain boundaries. Begley [5] investigated the temper embrittlement sensitivity and crack propagation rate characteristics of Ni-Cr-Mo-V steel, noting a sharp increase in fracture toughness at room temperature. Sang-Gyu Park [6] employed thermodynamic calculations to assess the influence of Cr, Mn, and Ni on temper embrittlement in low-alloy steel for nuclear power applications from the perspectives of P diffusion rate and C activity. To suppress reversible temper embrittlement, alloying with Mo and W has long been considered the most effective method. Briant [7] described two primary mechanisms of temper embrittlement: delayed effects during P segregation and increased boundary cohesion strength with the addition of Mo. Petrov and Tsukanov [8] associated irreversible temper embrittlement with the precipitation of carbide elements at grain boundaries, proposing that alloying with Mo and other carbide-forming elements (e.g., Cr) shifts the temperature range of irreversible temper embrittlement from 250 °C to 400 °C. Yang [9] investigated M152 martensitic heat-resistant steel with slow quenching and found that the continuous distribution of $M_{23}C_6$ along the original austenite grain boundaries and M_2C along the residual austenite film is the cause of a sharp decrease in toughness. Lei [10] determined, through the measurement of internal friction temperature curves, that high-temperature temper embrittlement belongs to the category of α-phase aging and exhibits reversibility. Kim [11] studied the effects of vanadium and carbides on the temper embrittlement of Cr-Mo steel.

This paper investigates the embrittlement phenomenon occurring during the high-temperature tempering of a newly developed medium-carbon, medium-alloy Cr-Ni-Mo-V steel by our research team. This study employs optical microscopy and scanning electron microscopy to observe the structural characteristics and utilizes electron backscatter diffraction for quantitative analysis of grain boundary orientation differences; the impact of microstructure on the temper embrittlement phenomenon in large forgings of Cr-Ni-Mo-V steel was evaluated from the perspective of grain boundary characteristics. Additionally, the phenomenon of reduced susceptibility to temper embrittlement due to the increase in the volume fraction of martensite was analyzed by altering the tempering cooling rate, and we explored the fundamental mechanisms of how the tempering cooling rate affects the organizational state for enhancing impact toughness.

2. Experimental Materials and Methods

The experimental material was obtained from the cross-section of a Φ396 mm Cr-Ni-Mo-V steel. The specimens were initially in the as-forged and annealed state. The compositions of the sample steel used in this study are listed in Table 1. The cross-sectional samples were subjected to quenching and tempering processes, as illustrated in Figure 1. For both quenching and tempering heat treatment processes, the samples were placed in the furnace once the desired temperature was reached, with a heating rate of 10 °C/min. After tempering, specimens were sampled at half the radius of the cross-section for both air cooling (TAC) and water cooling (TWC) conditions, and these samples were mechanically processed to determine the strength and Charpy impact toughness at −40 °C. V-notch impact specimens with dimensions of 10 mm × 10 mm × 55 mm were utilized for this purpose. During the tensile testing, strain was measured using an extensometer with a gauge length of 25 mm, and the strain rate was 1 mm/min. The size of the tensile specimen in the experiment is shown in Figure 2. Samples with dimensions of 20 mm × 20 mm × 20 mm were mechanically polished, corroded in a 4% nitric acid ethanol solution, and observed using an optical microscope (Carl Zeiss Axio Imager.M2m, CarlZeiss, Jena, Germany) produced by Leica. The microstructure and fracture analysis of the specimens

under both conditions were collected using a Apreo 2S HiVac scanning electron microscope (SEM) produced by FEI (Thermo Fisher Scientific, Waltham, MA, USA). To investigate the relationship between crack initiation, crack propagation, and microstructure, the fracture surfaces of the −40 °C Charpy impact specimens were studied below the area of the fracture surface, as shown in Figure 2, and subjected to electron backscatter diffraction (EBSD) analysis. Samples for EBSD studies were vibratory polished using 0.02 µm colloidal silica polishing solution. EBSD data were obtained using the Oxford EBSD system equipped with Channel 5 software (Oxford-HKL) and AZtecCrystal v2.1 for post-processing-oriented data analysis to assess the differences in the segregation behavior of tempered martensite under different tempering cooling rates. For the observation of carbide precipitation at grain boundaries under the two tempering cooling conditions, a JEM-2010F (JEOL, Tokyo, Japan) transmission electron microscope (TEM) was employed.

Table 1. Chemical compositions of the sample steels used in this study (in wt.%).

C	Si	Mn	P	S	Ni	Cr	Mo	V	As	Sn	Pb	Sb	Bi
0.26	0.2	0.6	0.005	0.006	3.0	1.0	0.6	0.2	<0.008	<0.006	<0.005	<0.006	<0.005

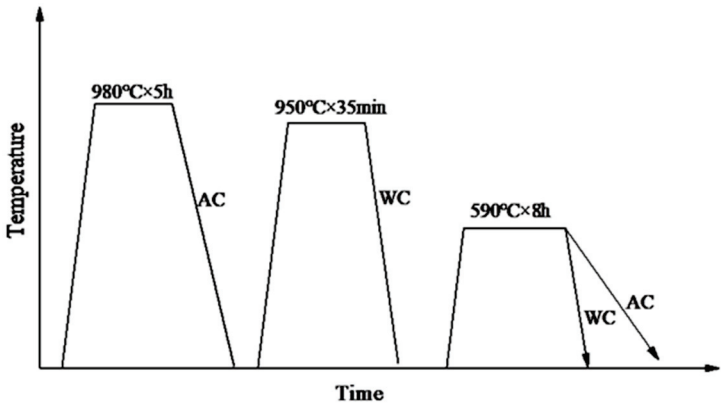

Figure 1. The diagrammatic sketch of heat treatment process.

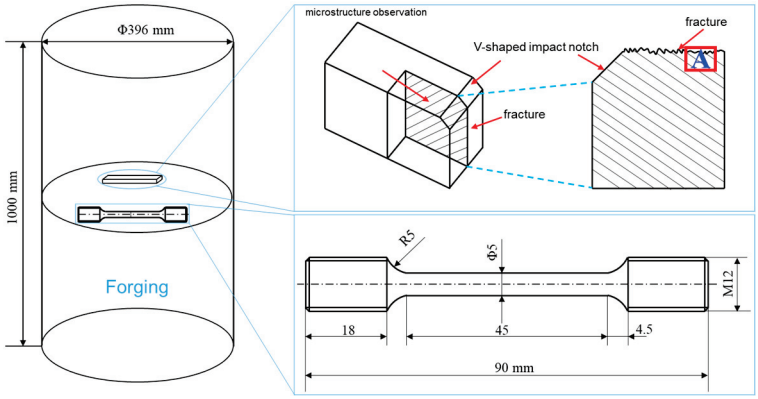

Figure 2. Forging size and sampling position and size of tensile specimen and impact specimen.

3. Results and Discussion

3.1. Mechanical Properties and Microstructure of Tempering Cooling Methods

The mechanical properties of the cross-sectional samples of the experimental steel after heat treatment are presented in Table 2. The air-cooled specimen exhibited a yield strength and tensile strength of 1145 MPa and 1422 MPa, respectively. For the water-cooled and tempered specimen, the yield strength and tensile strength were 1245 MPa and 1480 MPa, respectively. The strengths under both conditions are comparable. However, the impact energy of the water-cooled and tempered specimen is significantly higher than that of

the air-cooled specimen, confirming the reversibility of temper embrittlement in this steel. The Charpy impact energy for the air-cooled specimen at −40 °C is 19 J, lower than the 29 J observed for the water-cooled and tempered state, indicating a substantial change in toughness. To understand the factors influencing toughness, it is essential to consider the pattern of crack propagation within the crystal lattice.

Table 2. Mechanical properties after different tempering cooling methods.

Heat Treatment Process	$R_{p0.1}$/MPa	R_m/MPa	A(%)	Z(%)	KV_2@−40 °C (J)
980 °C × 5 h, AC + 950 °C × 35 min, WC + 590 °C × 8 h, AC	1145 ± 23	1422 ± 28	11 ± 0.4	53 ± 1.5	19 ± 3
980 °C × 5 h, AC + 950 °C × 35 min, WC + 590 °C × 8 h, WC	1245 ± 8	1480 ± 10	12 ± 1.2	54 ± 0.6	29 ± 5

Figure 3 depicts the microstructure of the experimental steel after tempering at 590 °C, followed by air cooling and water cooling. Figure 3a displays the SEM morphology for air cooling, while Figure 3b presents the SEM morphology for water cooling. Upon observing the microstructure, it is evident that both air-cooled and water-cooled structures consist of a mixture of tempered martensite and bainite. In the air-cooled condition, the martensite laths mainly appear as long needle-shaped structures within the microstructure, with larger grain size. Scanning electron microscopy reveals that the carbides precipitated after air cooling are primarily located at the grain boundaries. In contrast, the water-cooled microstructure is more uniform, with martensite laths arranged in a plate-like manner. Fine carbides are observed to be dispersed within the lath matrix, as shown in Figure 4. The average block width of martensite is 0.6 μm for air cooling (TAC) and 1 μm for water cooling (TWC), as measured under SEM.

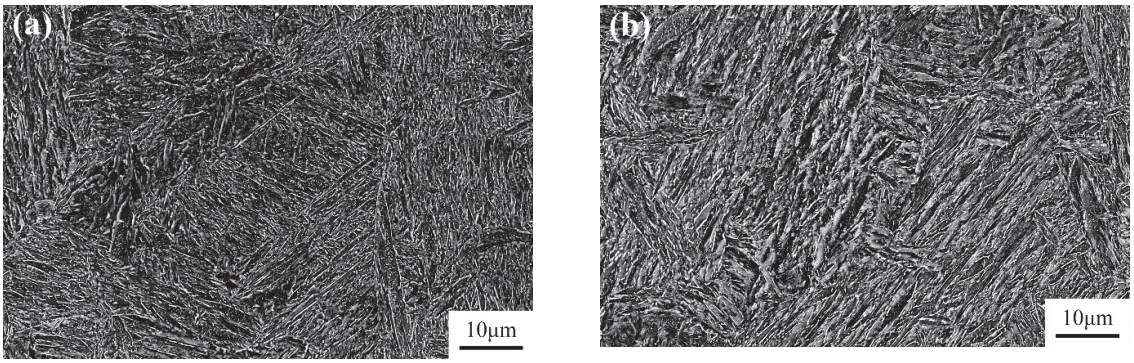

Figure 3. Two cooling methods' SEM microstructure: (**a**) air cooling and (**b**) water cooling.

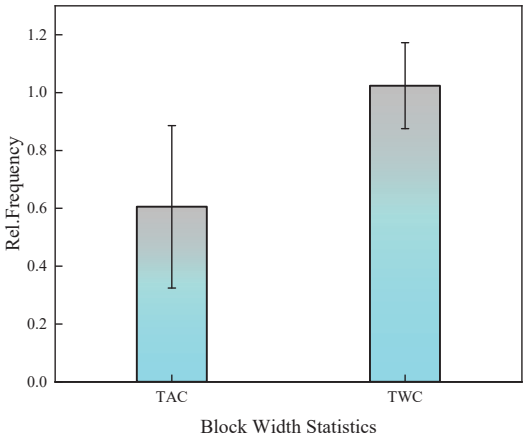

Figure 4. Comparison of block widths in air-cooled and water-cooled martensite.

Figure 5 shows the stress–strain curves after tensile testing under two different cooling methods. It can be observed that after water cooling, there is a slight increase in yield strength, tensile strength, and elongation. Specifically, the tensile strength increased by about 58 MPa, and the yield strength increased by approximately 100 MPa. Figure 6 illustrates the macroscopic and SEM morphology of the fracture surfaces at −40 °C after tempering and subsequent air cooling and water cooling of the experimental steel. By comparing the macroscopic morphology, it is evident that the air-cooled fracture surface (Figure 6a) appears bright white, with a relatively narrow shear lip. Under SEM, the fracture initiation zone (Figure 6c) exhibits intergranular fracture, and in the fibrous region (Figure 6e), both intergranular and cleavage fractures are observed. The impact toughness is significantly low, measuring 19 J.

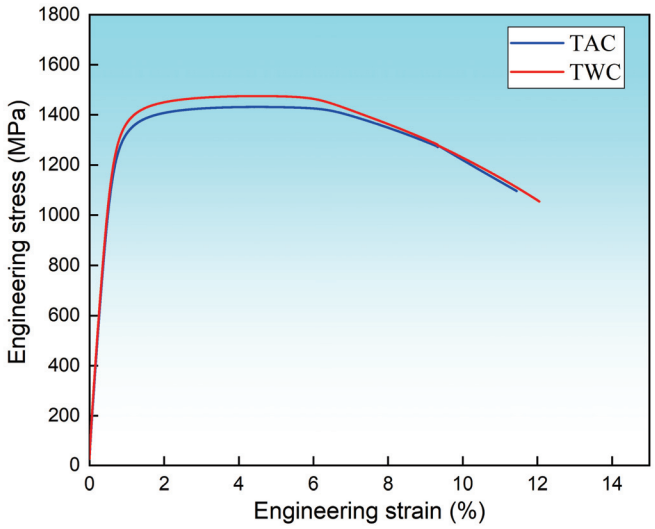

Figure 5. Stress–strain curves under two different cooling methods.

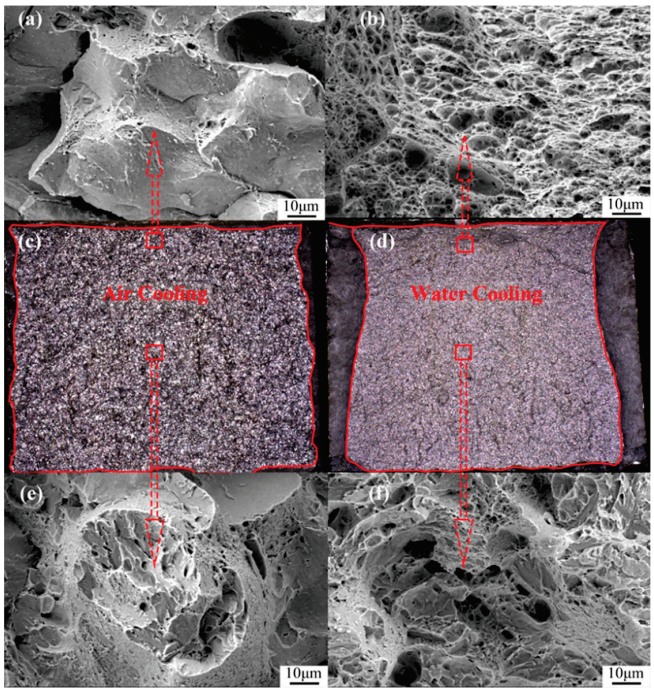

Figure 6. Different tempering cooling methods' −40 °C low-temperature impact fracture morphology: (**a**) air-cooled fracture initiation zone SEM, (**b**) water-cooled fracture initiation zone SEM, (**c**) air-cooled macrofracture zone, (**d**) water-cooled macrofracture zone, (**e**) air-cooled fracture extension zone SEM, and (**f**) water-cooled fracture extension zone SEM.

In contrast, the macroscopic morphology of the water-cooled fracture surface (Figure 6b) shows a typical wider shear lip. Moreover, under SEM, the fracture initiation zone (Figure 6d) displays ductile dimples, and in the fibrous region (Figure 6f), ductile dimples and cleavage facets are observed, indicating quasi-cleavage. The toughness is improved by 10 J compared to air cooling, reaching 29 J. Figure 7 presents the EBSD results of the microstructure after tempering and subsequent air cooling and water cooling, reconstructed using the AZtecCrystal v2.1 software. It can be observed that after air cooling, the cracks propagate along the grain boundaries, while after water cooling, the cracks propagate transgranularly.

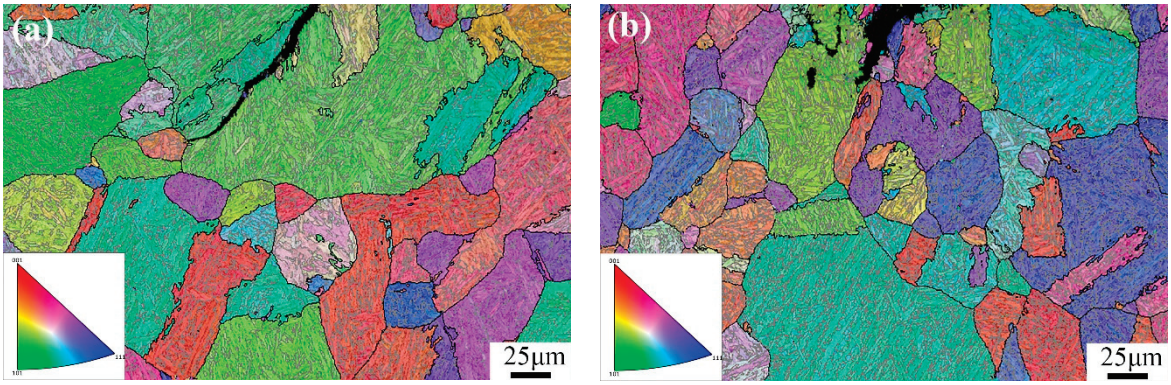

Figure 7. EBSD micrograph of protoaustenite grain reconstruction for (**a**) tempering air cooling and (**b**) tempering water cooling.

3.2. Impact of Cooling Rate on Crack Propagation

For large forgings, in order to reduce the thermal stress during the tempering process in the temperature range of 400 °C to 650 °C, a slow cooling method is generally employed, corresponding to the temper-embrittlement-sensitive zone of steel. The cooling rate significantly influences crack propagation. At slower cooling rates, cracks tend to propagate along grain boundaries, and the propagation of intergranular fractures is related to the weakening of interfaces. The preferred path for crack propagation is at defect locations or areas of interface weakening. Fine needle-shaped martensite can lead to unstable intergranular structures, reducing the energy required for crack absorption. In contrast, at faster cooling rates, martensite exists in a plate-like form, and the aspect ratio of the laths decreases, increasing the probability of crack transgranular propagation and improving toughness [12].

The AZtecCrystal software was utilized to analyze the distribution of grain boundaries near the cracks. Figure 7 shows the misorientation distribution of grain boundaries near the cracks under two conditions. Low-angle grain boundaries (LAGBs) with misorientation angles from 2° to 15° are represented by red lines, while high-angle grain boundaries (HAGBs) with misorientation angles from 15° to 45° are represented by black lines, indicating a minimal difference between air-cooled and water-cooled tempering conditions. Boundaries with angles greater than 45° are denoted by green lines. Figure 8 compares the relative frequencies of LAGBs and HAGBs under two different tempering cooling rates, revealing a similar frequency for both low- and high-angle grain boundaries. Previous studies have suggested that HAGBs hinder crack propagation [13–15]. Additionally, research has indicated that LAGBs play a crucial role in both strength and toughness. The high dislocation density generated in the overcooled austenite during processing can be inherited by martensite, forming sub-grains through dynamic recovery. Such low-angle grain boundaries have an inhibiting effect on crack propagation. In the yellow dashed box in Figure 8, low-angle grain boundaries are concentrated at the crack arrest position. The frequency of grain boundaries does not change significantly under different tempering cooling rates for the experimental steel. However, after water cooling and tempering, as the martensite lath bundles widen, the position of low-angle grain boundaries changes.

Compared to the air-cooled state, more low-angle grain boundaries appear between the lath bundles rather than around the original austenite grain boundaries. Figure 9 shows the relative frequency of grain boundary structure by different tempering cooling methods; no significant changes were observed in the boundary frequency under the two different cooling methods.

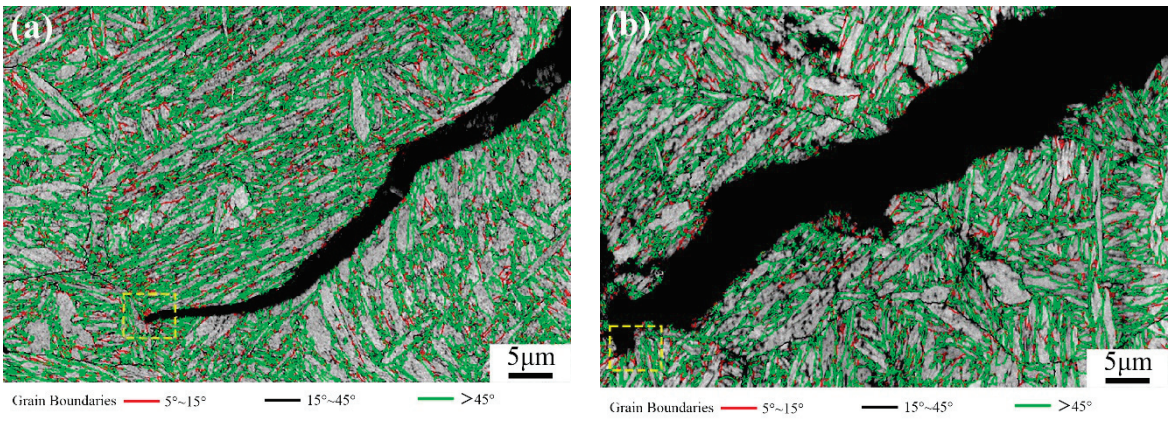

Figure 8. Band contrast (BC) maps depicting boundary distribution in (**a**) TAC and (**b**) TWC (red line: 15° > θ > 5°, black line: 45° > θ > 15°, green line: θ > 45°).

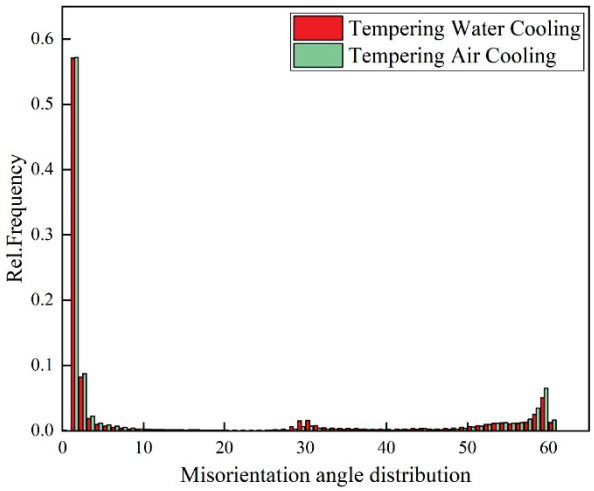

Figure 9. Relative frequency of grain boundary structure by different tempering cooling methods.

Geometrically necessary dislocations (GNDs) can provide quantitative information about localized plastic deformation. In some studies, this method can also be used to characterize the distribution of orientation deviations in cracks. Through the AZtecCrystal software, GND distributions under different tempering cooling rates are color-coded, as shown in Figure 9. Blue represents regions with lower dislocation orientation deviations, while green represents regions with high geometrically necessary dislocation densities. Larger GNDs are distributed near the crack, and at the crack tip in Figure 10a, there is a higher density of geometrically necessary dislocations. It can be observed that GNDs tend to be distributed at many low-angle grain boundaries, as low-angle grain boundaries hinder the slip of dislocations, leading to the accumulation of GNDs. In contrast, high-angle grain boundaries do not have a significant distribution of GNDs, indicating a strong ability to absorb dislocations. They are potential locations for crack initiation, and when cracks coincide with regions of high stress concentration and high-angle boundaries, crack initiation and propagation are accelerated [16]. Using the HKL Channel 5 software, GNDs were geometrically calculated for the two conditions, as shown in Figure 11. It can be seen that the frequency of GNDs is lower after tempering and water cooling, indicating more

stable low-angle and low-energy grain boundaries. These boundaries resist sliding, thereby enhancing toughness.

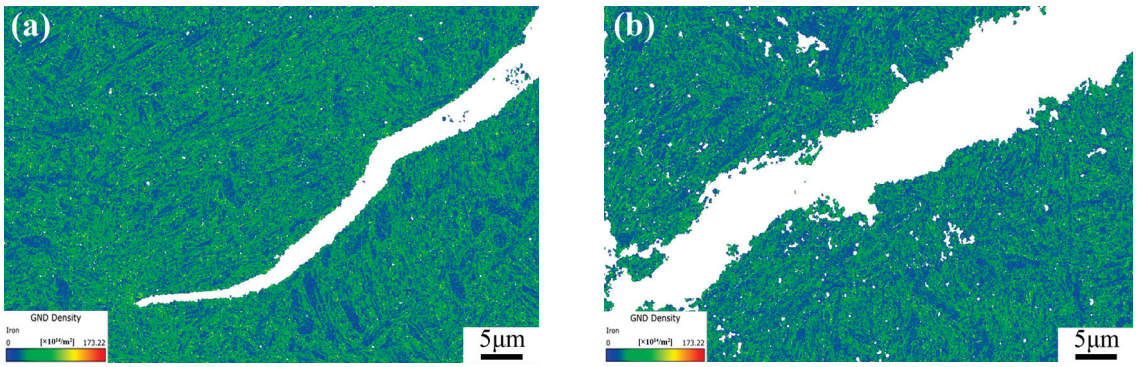

Figure 10. GND density micrographs for (**a**) TAC and (**b**) TWC.

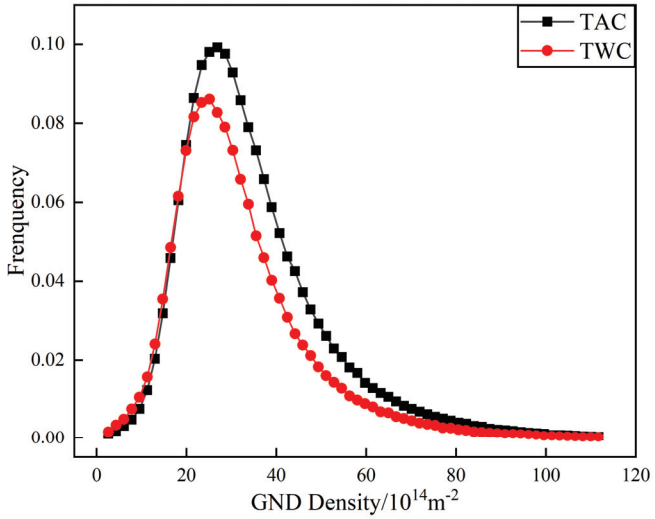

Figure 11. Geometrically necessary dislocation (GND) density distribution.

On the other hand, during the tempering process, the precipitation of Fe_3C at grain boundaries and the segregation of impurity atoms lead to interface weakening and brittle fracture, as depicted in Figure 12. Fe_3C exists in a rod-like form along the grain boundaries, and Table 2 provides the EDS analysis of Fe_3C at the grain boundaries. The diffusion rate of impurity atoms at the grain boundaries is higher than that of iron atoms because there are more vacancies at the grain boundaries, which can promote dislocation migration. Consequently, there is a higher density of dislocations and impurity content at the grain boundaries, and the pinning effect of impurities can easily result in temper embrittlement [17,18]. McMahon proposed that during tempering in the embrittlement temperature range, Fe_3C precipitates along the grain boundaries, and since impurities have low solubility in Fe_3C, impurities are rejected and concentrated at the interface during carbide precipitation. This creates favorable pathways for crack propagation along the interface, constituting a non-equilibrium segregation process [19,20]. Rapid cooling after tempering suppresses the process of impurity element enrichment and segregation. The rod-like Fe_3C transforms into a spherical shape, as shown in Figure 12. Table 3 shows the EDS of Fe_3C in the yellow box in Figure 12. Figure 13a illustrates the rod-like Fe_3C near the grain boundaries observed using TEM in the air-cooled state, while Figure 13b displays the spherical Fe_3C near the grain boundaries observed using TEM in the water-cooled state. This process helps avoid the occurrence of the second type of temper embrittlement or eliminates already-formed temper embrittlement.

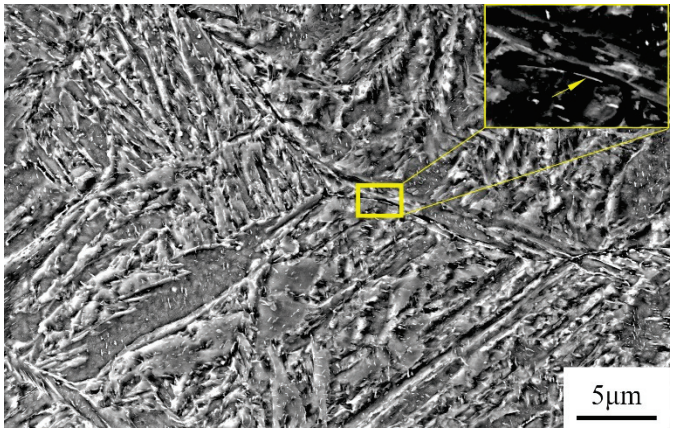

Figure 12. Microstructure with points of intergranular particle analyzed with EDS (see results in Table 2).

Table 3. EDS analysis results of position in Figure 9.

Element	Mass Fraction/%
C	6.91
Cr	2.09
Ni	3.52
Fe	Bal.

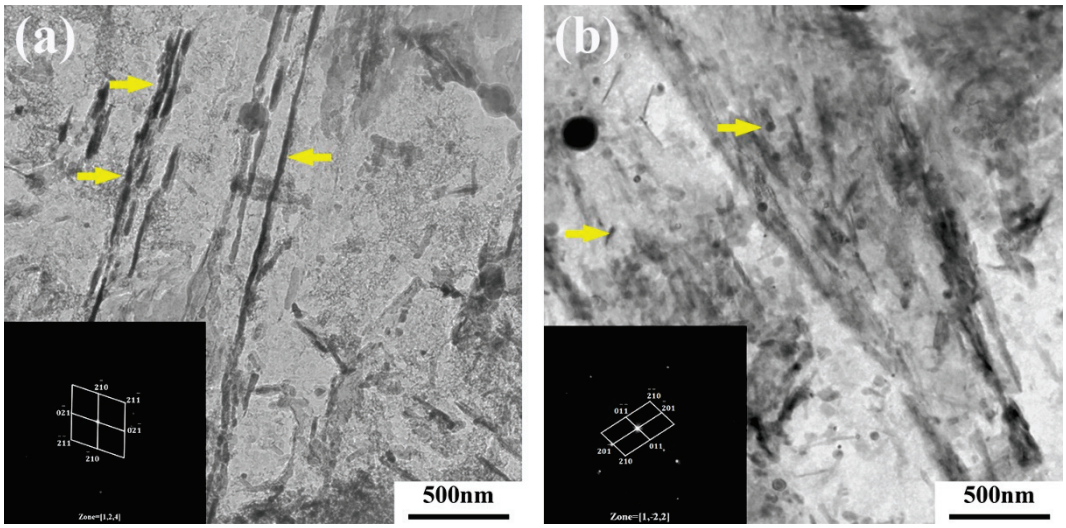

Figure 13. (**a**) Air-cooled and (**b**) water-cooled TEM characterization of Fe_3C.

3.3. Influence of Cooling Rate on M/B Microstructure

The samples after two tempering cooling methods were characterized using EBSD, and quantitative analysis of the BCC phase was performed. Based on the BC values from the Kikuchi model and using Gaussian multi-peak fitting, the fraction distribution of martensite and bainite was analyzed [21–23]. The thresholds for differentiating martensite and bainite were set in the Gaussian plot by intersecting the Gaussian curves, as shown in Figure 14. Combining the BC plot to calculate the proportions of each phase, Table 4 indicates that in the microstructure of the air-cooled sample after tempering, martensite occupies approximately 60 vol%, and bainite occupies about 40 vol%. After tempering and water cooling, the microstructure comprises approximately 67% martensite and 33% bainite. Research by Edwards suggests that the martensite–bainite mixed structure in medium-carbon Cr-Ni-Mo-V steel exhibits good toughness. Additionally, when the martensite

comprises ≤25% bainite on the martensite matrix, the toughness improves under the same strength conditions. This is because when cracks propagate through the two-phase structure, the different toughness of the phases causes a change in the direction of crack expansion. The optimal microstructure state, where bainite accounts for close to 25% after tempering and water cooling, leads to an improvement in toughness compared to the air-cooled tempering state. This is attributed to the fact that during rapid tempering and cooling, bainite forms before martensite, pre-dividing the grains and effectively refining the grain structure, resulting in improved toughness.

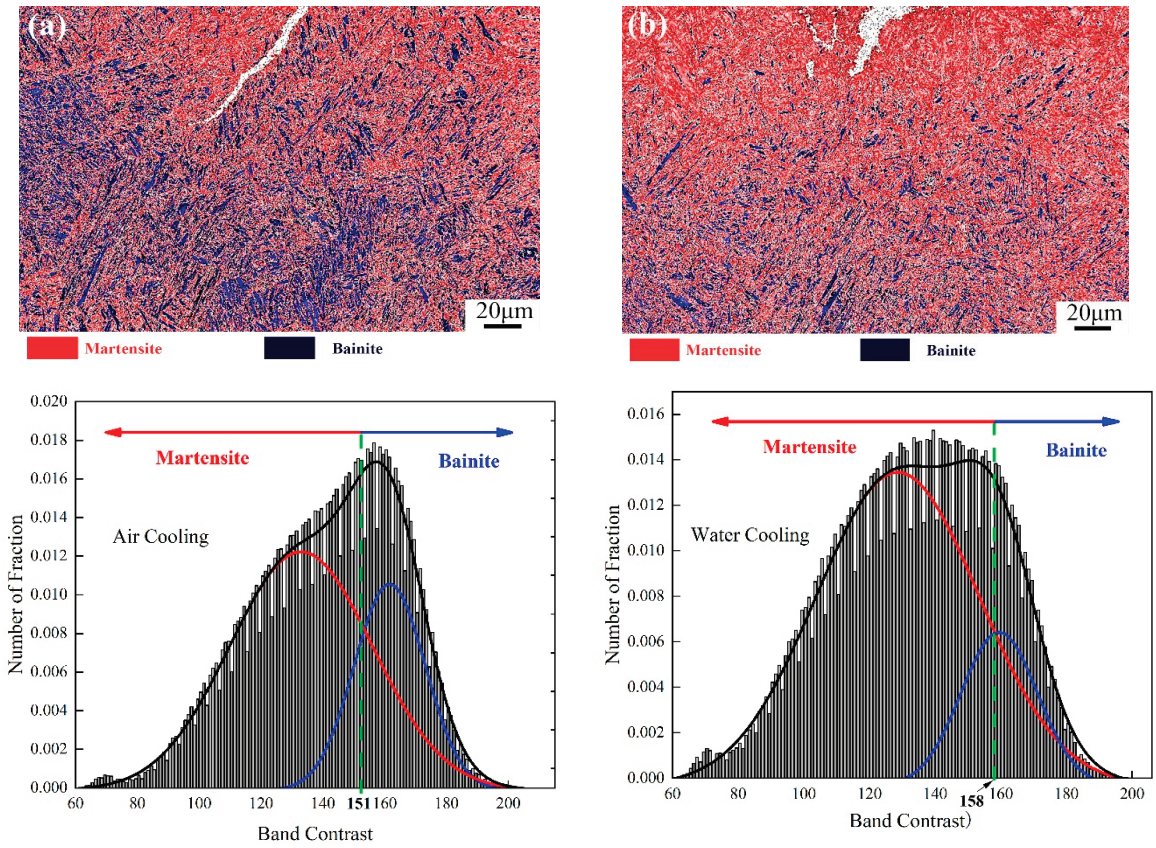

Figure 14. (**a**) Distribution of martensite and bainite complex structures in air-cooled and (**b**) water-cooled states.

Table 4. Quantitative and qualitative phase fraction of martensite/bainite via EBSD for TAC and TWC.

Tempering Cooling Method	Martensite	Bainite
Tempering air cooling	60%	40%
Tempering water cooling	67%	33%

4. Conclusions

This study investigated temper embrittlement in medium-carbon alloy steel during the production of large forgings, focusing on both mechanical properties and microstructural aspects. The results can be summarized as follows:

1. After air-cooling tempering, the fracture surface is dominated by intergranular fracture, while after tempering and water cooling, quasi-cleavage fracture is predominant. The distribution of high- and low-angle grain boundaries shows minimal differences between the two states. However, tempering and water cooling result in lower dislocation density, and the improvement in toughness is related to the decrease in dislocation density.

2. The second type of temper embrittlement observed in medium-carbon alloy steel large forgings during high-temperature tempering at 590 °C is attributed to the concentration of impurities near the grain boundaries, especially around Fe_3C. Tempering and water cooling suppress this segregation, thereby eliminating the already-occurring temper embrittlement. At the same time, with an increase in tempering rate, the morphology of Fe_3C transforms from elongated rods to granular.
3. The impact toughness is higher after tempering and water cooling compared to air-cooling tempering. The microstructure in both states consists of a mixture of martensite and bainite. In the air-cooled state, martensite plates exist in the form of long needles, while in the water-cooled state, the structure consists of uniformly distributed martensite plates. The reduction in bainite content during tempering and water cooling approaches the optimal ratio for martensite–bainite mixed structures, contributing to the enhanced toughness.
4. For the reversible temper brittleness issue that occurs in large forgings, it can be mitigated by using water cooling, i.e., increasing the cooling rate during tempering, to enhance toughness. This method is applicable to large Cr-Ni-Mo-V forgings.

Author Contributions: Conceptualization, C.H. and H.D.; methodology, H.D.; software, C.Y.; validation, C.Y. and C.H.; formal analysis, C.Y.; investigation, T.X.; resources, T.X.; data curation, T.X.; writing—original draft preparation, C.Y.; writing—review and editing, C.H.; visualization, H.Z.; supervision, C.H.; project administration, C.H. All authors have read and agreed to the published version of the manuscript.

Funding: This research received no external funding.

Institutional Review Board Statement: Not applicable.

Informed Consent Statement: Not applicable.

Data Availability Statement: Data are contained within the article.

Conflicts of Interest: Author Tingting Xu was employed by the company Zhongyuan Special Steel Co., Ltd. The remaining authors declare that the research was conducted in the absence of any commercial or financial relationships that could be construed as a potential conflict of interest.

References

1. Chen, G.H. Temper embrittlement of steels for heavy forging. *Spec. Steel* **1995**, *16*, 8–14.
2. Robert, B. *High Temperature Embrittlement Phenomena of 2-1/4Cr-1Mo Weldments*; ASME: New York, NY, USA, 1971.
3. Murakami, Y.; Nomura, T.; Watanabe, J. *Heavy-Section 21/4Cr-1Mo Steel for Hydrogenation Reactors*; ASTM International: West Conshohocken, PA, USA, 1982.
4. Bandyopadhyay, N.; Briant, C.L.; Hall, E.L. Carbide precipitation, grain boundary segregation, and temper embrittlement in NiCrMoV rotor steels. *Metall. Trans.* **1985**, *A16*, 721–737. [CrossRef]
5. Begley, J.A.; Toolin, P.R. Fracture toughness and fatigue crack growth rate properties of a Ni-Cr-Mo-V steel sensitive to temper embrittlement. *Int. J. Fract.* **1973**, *9*, 243–253. [CrossRef]
6. Park, S.-G.; Lee, K.-H.; Min, K.-D.; Kim, M.-C.; Lee, B.-S. Influence of the thermodynamic parameters on the temper embrittlement of SA508 Gr. 4N Ni–Cr–Mo low alloy steel with variation of Ni, Cr and Mn contents. *J. Nucl. Mater.* **2012**, *426*, 1–8. [CrossRef]
7. Messmer, R.P.; Briant, C.L. The Role of Chemical Bonding in Grain Boundary Embrittlement. *Acta Metall.* **1982**, *30*, 457–467. [CrossRef]
8. Petrov, G.M.; Tsukanov, V.V. Temper brittleness of complex-alloyed structural steels. In *Metallovedenie i Termicheskaya Obrabotka Metallov*; Springer: Berlin/Heidelberg, Germany, 1977; pp. 17–20.
9. Wang, C.; Liu, X.-Q.; Liu, Z.-D. Embrittlement mechanism due to slow cooling during quenching for M152 martensitic heat resistant steel. *J. Iron Steel Res. Int.* **2010**, *17*, 60–66.
10. Lei, T.; Tang, Z.; Su, M. A Study on High Temperature Temper Brittleness by Internal Friction Measurements. *Acta Metall. Sin.* **1982**, *18*, 485–492.
11. Kim, J.T.; Kim, B.H.; Kong, B.O.; Kim, D.J. Effects of V and Carbides on the Temper Embrittlement of the 2.25 Cr-1Mo Steel. In *ASME Pressure Vessels and Piping Conference, Proceedings of the ASME 2006 Pressure Vessels and Piping/ICPVT-11 Conference, Vancouver, BC, Canada, 23–27 July 2006*; ASME: New York, NY, USA, 2006; Volume 47578, pp. 501–510.
12. Liang, Y.; Long, S.; Xu, P.; Lu, Y.; Jiang, Y.; Liang, Y.; Yang, M. The important role of martensite laths to fracture toughness for the ductile fracture controlled by the strain in EA4T axle steel. *Mater. Sci. Eng. A* **2017**, *695*, 154–164. [CrossRef]

13. Wang, X.L.; Wang, Z.Q.; Ma, X.P.; Subramanian, S.V.; Xie, Z.J.; Shang, C.J.; Li, X.C. Analysis of impact toughness scatter in simulated coarse-grained HAZ of E550 grade offshore engineering steel from the aspect of crystallographic structure. *Mater. Charact.* **2018**, *140*, 312–319. [CrossRef]
14. Terasaki, H.; Shintome, Y.; Komizo, Y.-I.; Ohata, M.; Moriguchi, K. Effect of close-packed plane boundaries in a bain zone on the crack path in simulated coarse-grained HAZ of bainitic steel. *Metall. Mater. Trans. A* **2015**, *46*, 2035–2039. [CrossRef]
15. Morris, J.W.; Guo, Z. The nature and consequences of coherent transformations in steel. *ISIJ Int.* **2003**, *43*, 410–419. [CrossRef]
16. Wang, C.; Wang, M.; Shi, J.; Hui, W.; Dong, H. Effect of microstructure refinement on the strength and toughness of low alloy martensitic steel. *J. Mater. Sci. Technol.* **2007**, *23*, 659.
17. Hickey, J.J.; Bulloch, J.H. The role of reverse temper embrittlement on some low and high temperature crack extension processes in low carbon, low alloy steels: A review. *Int. J. Press. Vessel. Pip.* **1992**, *49*, 339–386. [CrossRef]
18. Bandyopadhyay, N.; McMahon, C.J. The micro-mechanisms of tempered martensite embrittlement in 4340-type steels. *Metall. Trans. A* **1983**, *14*, 1313–1325. [CrossRef]
19. Wada, T.; Doane, D.V. The effect of an intercritical heat treatment on temper embrittlement of a Ni-Cr-Mo-V rotor steel. *Metall. Mater. Trans. B* **1974**, *5*, 231–239. [CrossRef]
20. Tavares, S.S.M.; da Cunha, R.P.C.; Barbosa, C.; Andia, J.L.M. Temper embrittlement of 9% Ni low carbon steel. *Eng. Fail. Anal.* **2019**, *96*, 538–542. [CrossRef]
21. Chen, K.; Li, H.; Jiang, Z.; Liu, F.; Kang, C.; Ma, X.; Zhao, B. Multiphase microstructure formation and its effect on fracture behavior of medium carbon high silicon high strength steel. *J. Mater. Sci. Technol.* **2021**, *72*, 81–92. [CrossRef]
22. Baek, M.-S.; Kim, K.-S.; Park, T.-W.; Ham, J.; Lee, K.-A. Quantitative phase analysis of martensite-bainite steel using EBSD and its microstructure, tensile and high-cycle fatigue behaviors. *Mater. Sci. Eng. A* **2020**, *785*, 139375. [CrossRef]
23. Breumier, S.; Ostormujof, T.M.; Frincu, B.; Gey, N.; Couturier, A.; Loukachenko, N.; Aba-perea, P.E.; Germain, L. Leveraging EBSD data by deep learning for bainite, ferrite and martensite segmentation. *Mater. Charact.* **2022**, *186*, 111805. [CrossRef]

materials

MDPI

Article

Preparation of Sr_2CeZrO_6 Refractory and Its Interaction with TiAl Alloy

Fuli Bian [1], Zheyu Cai [2], Jian Liu [2], Yu Liu [2], Man Zhang [2], Yixin Fu [2], Kailiang Zhu [1], Guangyao Chen [2,3,4,*] and Chonghe Li [2,3,4,*]

1 Fire Research Institute of Shanghai of MEM, Shanghai 200032, China; bianfuli@shfri.cn (F.B.); zhukailiang@shfri.cn (K.Z.)
2 State Key Laboratory of Advanced Special Steel & Shanghai Key Laboratory of Advanced Ferrometallurgy & School of Materials Science and Engineering, Shanghai University, Shanghai 200444, China; zycai2022@shu.edu.cn (Z.C.); liuzuozuo@shu.edu.cn (J.L.); liuyucumt@shu.edu.cn (Y.L.); manzhang@shu.edu.cn (M.Z.); fyx13194382608@shu.edu.cn (Y.F.)
3 Shanghai Special Casting Engineering Technology Research Center, Shanghai 201605, China
4 Zhejiang Institute of Advanced Materials, Shanghai University, Jiaxing 314100, China
* Correspondence: cgybless1@shu.edu.cn (G.C.); chli@staff.shu.edu.cn (C.L.)

Abstract: Vacuum induction melting in a refractory crucible is an economical method to produce TiAl-based alloys, aiming to reduce the preparation cost. In this paper, a Sr_2CeZrO_6 refractory was synthesized by a solid-state reaction method using $SrCO_3$, CeO_2 and ZrO_2 as raw materials, and its interaction with TiAl alloy melt was investigated. The results showed that a single-phase Sr_2CeZrO_6 refractory could be fabricated at 1400 °C for 12 h, and its space group was Pnma with a = 5.9742(3) Å, b = 8.3910(5) Å and c = 5.9069(5) Å. An interaction layer with a 40μm thickness and dense structure could be observed in Sr_2CeZrO_6 crucible after melting TiAl alloy. Additionally, the interaction mechanism showed that the Sr_2CeZrO_6 refractory dissolved in the alloy melt, resulting in the generation of $Sr_3Zr_2O_7$, $SrAl_2O_4$ and CeO_{2-x}, which attached to the surface of the crucible.

Keywords: Sr_2CeZrO_6; refractory; induction melting; TiAl alloys; interaction

Citation: Bian, F.; Cai, Z.; Liu, J.; Liu, Y.; Zhang, M.; Fu, Y.; Zhu, K.; Chen, G.; Li, C. Preparation of Sr_2CeZrO_6 Refractory and Its Interaction with TiAl Alloy. *Materials* **2023**, *16*, 7298. https://doi.org/10.3390/ma16237298

Academic Editor: Francesco Iacoviello

Received: 18 October 2023
Revised: 10 November 2023
Accepted: 21 November 2023
Published: 23 November 2023

1. Introduction

TiAl alloys have been considered as novel lightweight construction materials due to their low density (approximately 4.0 g/cm^3) and high specific strength [1]. They have the potential to replace heavier Ni-based superalloys, resulting in weight reduction and enhancing the thrust-to-weight ratio [2,3]. Although TiAl alloys have substantial performance advantages, their elevated production costs are a factor limiting their further development [4,5].

Investment casting technology with induction skull melting (ISM) has been the commercial method for the manufacture of TiAl alloy parts [6]. However, the implementation of ISM significantly influences the ultimate cost of the casting products, which has contributed to the elevated levels of casting rejections. This is because this method does not easily achieve suitable superheating. In order to solve this problem, a suitable preheat temperature for the casting mold should be used. This results in the occurrence of the melt–mold interaction, and solidification defects are thus also introduced. Vacuum induction melting (VIM) of TiAl alloys using the refractory crucibles offers a viable approach to attaining optimal superheating and reducing the production expenses. However, the key problems are the selection of exceptionally stable and cost-effective refractory in crucible manufacturing [7–10].

Until now, researchers have explored various oxide materials as refractory crucibles for melting TiAl alloys, such as Y_2O_3 [11], CaO [12], ZrO_2 [13] and Al_2O_3 [14]. However, these refractory materials applied for melting TiAl alloy also have shortcomings [15]. Toshimitsu

demonstrated the feasibility of melting TiAl alloys in crucibles made of Y_2O_3, ZrO_2, and Al_2O_3 [13]. Notably, the oxygen levels in the TiAl alloy were relatively low (0.12 wt.%) using the Y_2O_3 crucible. In contrast, the absorption of oxygen from the ZrO_2 and Al_2O_3 crucibles occurred at a notably higher level (0.96 and 1.57 wt.%, respectively). Koichi's work presented that the oxygen concentration could be controlled at 0.1–0.13 wt.% with a holding smelting time ranging from 5 to 20 min in the CaO crucible [16]. From a thermodynamic perspective, Y_2O_3 and CaO had higher stability than that of Al_2O_3 and ZrO_2. Thus, they were more suitable for melting TiAl alloys. However, there are significant challenges that need to be addressed before industrial-scale manufacture. For instance, Y_2O_3 has an inherent drawback of poor thermal shock resistance, and CaO exhibits a hygroscopic nature [17,18]. Given these considerations, it becomes imperative to explore and develop a new stable refractory for the melting of TiAl alloys.

Novel alkaline earth zirconate materials, such as Sr-Zr oxides, exhibit the essential properties for melting titanium alloys. For example, $SrZrO_3$ was an attractive candidate material due to its exceptional resistance to corrosion, especially in alkaline melts and vapors [19]. Generally, compounds with perovskite ABX_3 structure are very well-known inorganic materials. The A and B sites in perovskite materials possess the capability to accommodate diverse metal cations, providing an avenue to regulate both the chemical compositions and the properties of perovskite materials. Substituting elements on the B sites can lead to the formation of double perovskite $A_2B'B''O_6$ compounds, where A represents an alkaline-earth metal, and B′ and B″ represent two different transition metal elements. The positioning of B′ and B″ cations within the crystal structure can vary, either occupying indistinguishable sites or distinct sites, contingent upon their charge and ionic radii. Double perovskites exhibit a wide array of intriguing properties owing to their diverse compositions and structures, prompting extensive investigations into their structural characteristics [20]. In order to develop an Sr-Zr series perovskite oxide refractory for melting titanium alloys, our group attempted to prepare a novel refractory by doping rare earth elements, followed by evaluating their stability for melting titanium alloys [21]. The rare oxide such as CeO_2 has a high melting point (nearly 1950 °C). It is typically stable at high temperatures, making it potentially useful in high-temperature applications, such as in high-temperature lubricants or coating materials [22]. In this study, CeO_2 was introduced into the preparation of the Sr-Zr oxide refractory. It could be considered that the Ce dopant could replace the position of Zr elements in the Sr-Zr oxides. Thus, a double perovskite structure Sr_2CeZrO_6 refractory was fabricated, and then its interaction with melting TiAl alloys was investigated. Until now, there have not been any prior exploration into utilizing Sr_2CeZrO_6 refractory for preparing TiAl alloys.

In this paper, firstly, the manufacturing process involved the synthesis of a Sr_2CeZrO_6 refractory through a solid-state approach utilizing industrial-grade $SrCO_3$, CeO_2 and ZrO_2 raw materials. Subsequently, the formation of the Sr_2CeZrO_6 crucible was achieved via shaping and sintering. Utilizing XRD and SEM, the synthesized powders were analyzed to ascertain the phase composition and microstructure. The structure of Sr_2CeZrO_6 refractory was investigated through the Rietveld method. Subsequently, TiAl alloy was melted in the Sr_2CeZrO_6 crucible, facilitating an exploration into the interaction between the TiAl alloy and Sr_2CeZrO_6 crucible, along with an investigation into the corresponding interaction mechanism.

2. Experiment

$SrCO_3$ (99.9%), ZrO_2 (99.9%) and CeO_2 (99.9%) raw materials were employed for the preparation of a $SrCeZrO_6$ refractory according to the solid-state reaction. The XRD (Bruker GADDS, Cambridge, MA, USA) patterns for the raw materials are shown in Figure 1. The raw materials were accurately measured following a mole ratio of n($SrCO_3$): n(ZrO_2): n(CeO_2) = 2:1:1. Subsequently, they were subjected to ball milling (MD-2 L, Nanjing, China), followed by drying at 120 °C for 12 h. Then, the discs with φ20 mm × 3 mm were fabricated at 120 MPa, holding for 2 min. Finally, the unfired discs were heat-treated at 1400 °C for 12 h.

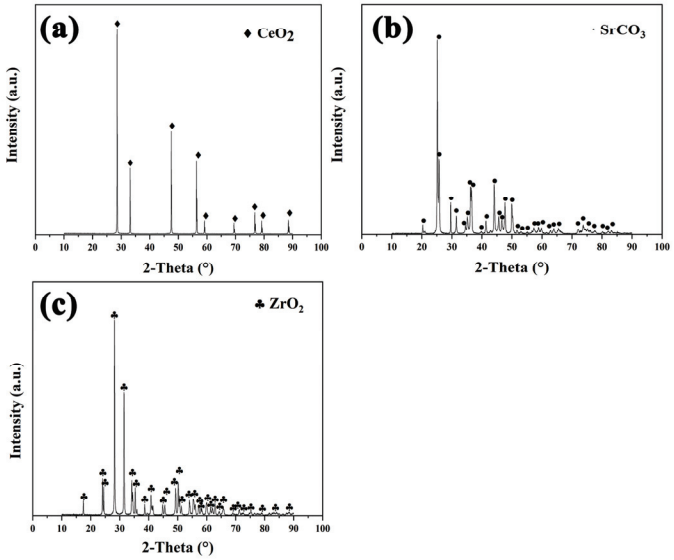

Figure 1. XRD patterns for the raw materials. (**a**) CeO_2; (**b**) $SrCO_3$; (**c**) ZrO_2.

Prior to the phase analysis, the sintered discs were ground into powders and then sieved through a 400-mesh sieve. XRD was used to analyze the phase structure of the powders through Rietveld refinement via GSAS-II software (https://subversion.xray.aps.anl.gov/trac/pyGSAS). Microstructure analysis was carried out using scanning electron microscopy (FEI Nova nano SEM450, Sydney, Austria).

The Sr_2CeZrO_6 refractory material underwent cold isostatic pressing to form crucibles using a U-shaped steel mandrel measuring 3.5 cm in width and 4.5 cm in height. in this shaping process, a pressure of 120 MPa was applied for a duration of 3 min. Then, the crucible biscuits were sintered at 1700 °C and held for 4 h. The slow heating rate of 2 °C/min was carefully controlled to prevent the formation of cracks.

Our goal was to assess the interface stability between the Sr_2CeZrO_6 refractory and the TiAl alloy melt. Before the melting experiment, a TiAl master alloy with an equimolar ratio was prepared using Al pellets (>99.99%) and sponge Ti (>99.9%) in a water-cooled copper crucible. In the VIM furnace, the space surrounding the crucible was filled with Al_2O_3 ramming mass. Then, the master alloy was inserted into the crucible. The furnace chamber was evacuated to 10^{-3} mbar. The high-purity argon gas was backfilled into the chamber at least three times. This effectively prevented oxygen contamination during the melting. As the molten alloy became visible, high-purity argon gas was reintroduced, and the temperature was slowly raised to 1600 °C and maintained for 5 min. Then, the alloy melt was allowed to cool in the crucible. X-ray diffraction was used to analyze the crucible surface in order to examine the interaction products between them. The interaction behavior was investigated after the fabrication of the samples using a buzz saw. Selected sections underwent examination using a digital microscope (VHX-1000). Interaction analyses for the microstructure were conducted using a scanning electron microscope with an energy dispersive spectrometer (EDS).

3. Results and Discussion

3.1. Synthesis of Sr_2CeZrO_6 Powder

Figure 2 shows the powder synthesized using $SrCO_3$, CeO_2 and ZrO_2 after sintering at 1400 °C for 12 h. The sintered powder exhibited a significant sintering phenomenon, as shown in Figure 2a. After the crushing process, the edges of the powder were distinct, indicating that this synthesized condition was sufficient for preparing this refractory. Figure 2b depicts the backscatter electron (BSE) image from Figure 2a. It can be seen that the synthesis degree of this compound was good. Furthermore, chemical element mapping of

Sr, Ce, Zr, and O was carried out (Figure 2b–f). The uniform distribution of these elements is evident, showing no signs of accumulation or segregation.

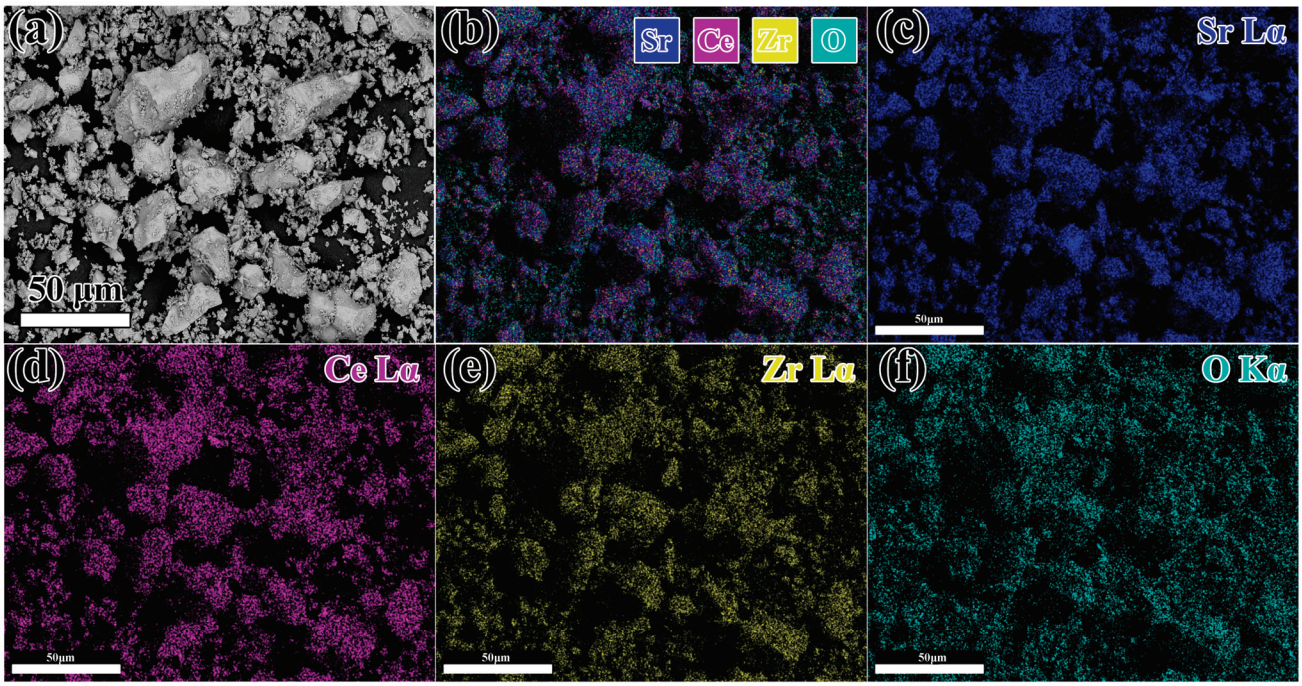

Figure 2. (**a**) The SEM pictures of synthesized powder after maintenance at 1400 °C for 12 h; (**b**–**f**) EDS elemental mapping pictures of Sr Lα, Ce Lα, Zr Lα and O Kα.

To further confirm the crystal structure of Sr_2CeZrO_6, the XRD pattern of the sintered powder was refined by the Rietveld method. The Rietveld refinement of the XRD data of the powder in the 2θ° angle 10~120° is shown in Figure 3. Indexing of the XRD spectra by Jade 6.0 program revealed that Sr_2CeZrO_6 had a similar peak pattern to $SrCeO_3$ (Pnma 62). Therefore, the XRD data of the Sr_2CeZrO_6 sample were refined using the orthogonal structure Pnma space group. In this structural model, Sr atoms occupied the 4c position at coordinates (0.45, 025, 0), while both Ce and Zr atoms occupied the 4a position (0, 0, 0) with an equal occupancy of 0.5:0.5. O atoms were positioned at 4c (0, 0.25, 0) and 8d (0, 0, 0.2). Figure 3 illustrates the refined structural model of the Sr_2CeZrO_6. The experimental intensity (depicted by the green dotted line) of the Sr_2CeZrO_6 coincided with the simulated intensity (shown as the red continuous line). The lattice constants were a = 5.9742(3) Å, b = 8.3910(5) Å, c = 5.9069(5) Å, respectively, with a unit cell volume of 296.11(6) Å3 using the least-squares method. The reliability factors Rwp and GOF stood at 8.94% and 1.57, respectively. This indicated that the Rietveld refinements were conducted at a reasonably high standard. Table 1 outlines the refined structural parameters of the Sr_2CeZrO_6.

Table 1. Refined structural parameters of Sr_2CeZrO_6 by Rietveld refinement of the orthorhombic structure in the Pnma space group (No. 62).

Atom	Wyckoff Position	x	y	z	Site Occ	Biso
Sr	4c	0.46569	0.25000	−0.00795	1.0000	0.1780(7)
Ce	4a	0.00000	0.00000	0.00000	0.5000	0.00805(2)
Zr	4a	0.00000	0.00000	0.00000	0.5000	0.00810(2)
O	4c	0.02400	0.25000	0.09200	1.00000	0.03900(2)
O	8d	0.02874	−0.04360	0.20730	1.00000	0.02960(3)

Crystal structure: orthorhombic; space group (No. 62): Pnma, a = 5.9742(3) Å, b = 8.3910(5) Å, c = 5.9069(5) Å, volume of unit cell = 296.11(6) Å3; Rwp = 8.94%, GOF = 1.57, bond lengths (Å): Sr–O = 2.9809(5) Å × 12, (Sr/Zr)–O = 2.8639(3) Å × 6.

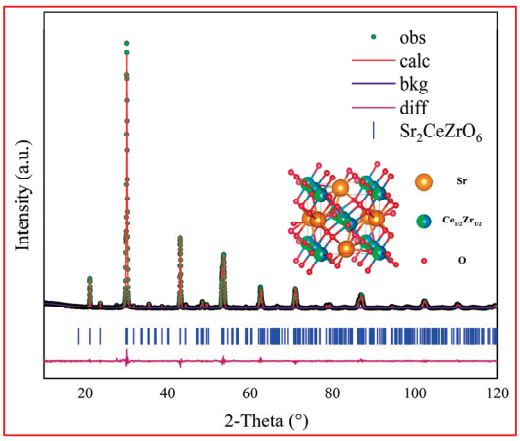

Figure 3. Experimentally observed (dots), Rietveld-calculated (continuous line), and difference (continuous bottom line) profiles for Sr_2CeZrO_6 after Rietveld analysis for the XRD data using the Pnma space group. The vertical tick marks above the difference plot showed the Bragg peak positions.

3.2. Phase Constitution of Sr_2CeZrO_6 Crucible

The SEM picture of the Sr_2CeZrO_6 crucible surface after sintering at 1700 °C and holding for 4 h is shown in Figure 4. The backscatter electron (BSE) picture in Figure 4a showed that the crucible consisted of a single phase. The sintering process of the crucible was undertaken in a silicon molybdenum rod furnace with an air atmosphere. During the prolonged calcination process, substances inside the furnace lining could volatilize and deposit on the surface of the crucible, resulting in the formation of some impurities. Table 2 indicates the EDS results of spots 1 and 2. It can be seen that the grains in the crucible surface consisted of Sr, Ce, Zr and O elements, which was consistent with the theoretical ratio. The XRD pattern in Figure 4b shows that only the Sr_2CeZrO_6 phase could be detected on the crucible surface, confirming the analysis in Figure 4a.

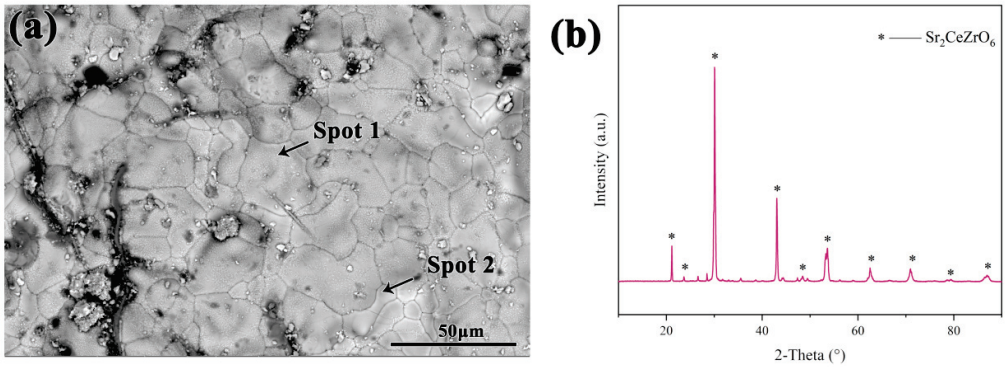

Figure 4. (**a**) The SEM picture of Sr_2CeZrO_6 crucible surface; (**b**) XRD pattern of the crucible surface.

Table 2. EDS results of spots 1 and 2 in Figure 4a.

	Element at%			
	Sr	**Ce**	**Zr**	**O**
Spot 1	13.99	8.56	7.53	69.92
Spot 2	17.36	6.97	7.15	68.52

3.3. Interfacial Interaction

The macroscopic picture of the cooled alloy and the crucible is shown in Figure 5. Evidently, the alloy was separated from the crucible matrix. In the process of the melting, the alloy with its high chemical activity was able to permeate into the crucible refractory, resulting in the generation of a black area (contact layer). Due to the rapid heating rate

during the melting process, some cracks were generated. In the future, decreasing the heating rate should be considered in order to reduce the occurrence of cracks. Additionally, the integrity of the crucible was not changed. The detailed analysis is described below.

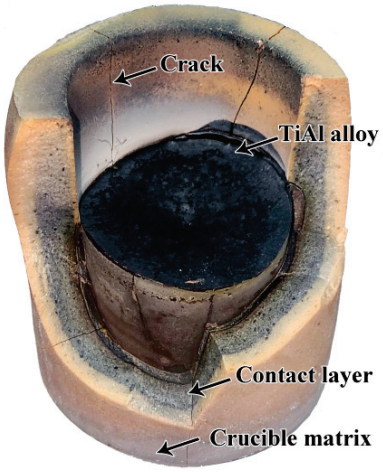

Figure 5. The macroscopic picture of the TiAl alloy cooled in Sr_2CeZrO_6 crucible.

The macroscopic pictures of the cross-sections of the crucibles before and after melting are shown in Figure 6. Before the melting, the crucible displayed a glossy yellow sheen, and the inner wall of the crucible was flat, as shown in Figure 6a. From Figure 6b, it can be seen that the crucible exhibited a black-gray color. Additionally, there was no significant erosion layer observed.

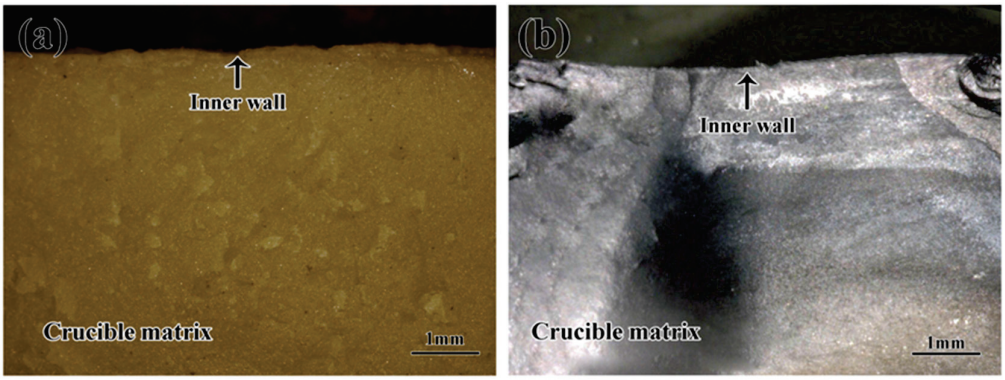

Figure 6. Macroscopic pictures of the crucibles: (**a**) before the melting, (**b**) after the melting.

Figure 7 shows the microstructure of the crucible surface before and after the melting. As shown in Figure 7a, a smooth surface could be observed before the melting, and the boundaries were obvious. However, after the melting, the crucible surface appeared uneven, and the grain boundaries had disappeared. Evidently, during the melting, the crucible surface corroded. Figure 7c shows the magnified picture of area A in Figure 7b. A combination of block and strip grains appeared on the crucible surface, as shown in Figure 7c. Table 3 exhibited that the grains with the block shapes consisted of Sr, Zr, Ce and O elements. The XRD pattern for the crucible surface in Figure 7d shows that it consisted of $Sr_3Zr_2O_7$, CeO_{2-x} and $SrAl_2O_4$ phases. This can be elucidated in conjunction with the suggested interaction model outlined below.

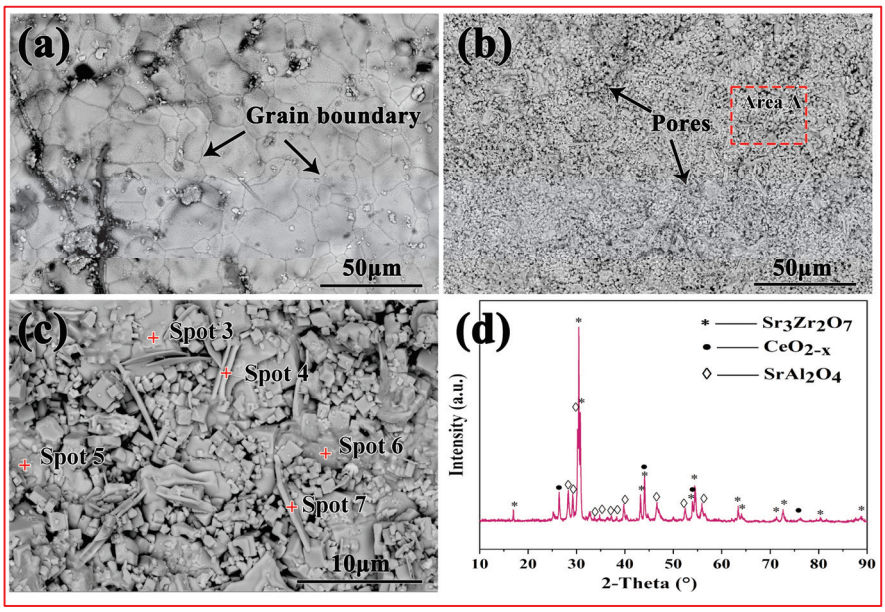

Figure 7. (**a**) SEM pictures of the crucible surface before melting; (**b**) SEM pictures of the crucible surface after melting; (**c**) the magnified picture of area A in (**b**); (**d**) XRD pattern of the crucible surface after melting.

Table 3. EDS results of spots 3–7 in Figure 7.

	Element at%					
	Sr	**Ce**	**Zr**	**O**	**Al**	**Ti**
Spot 3	19.50	9.30	1.95	40.12	26.02	3.11
Spot 4	13.84	13.94	2.61	57.14	11.99	0.48
Spot 5	24.34	1.32	16.07	55.03	3.12	0.12
Spot 6	10.04	6.97	2.05	65.72	14.10	1.12
Spot 7	11.28	7.81	2.16	62.75	13.84	2.16

The SEM pictures of the cross-section of the crucibles before and after melting are shown in Figure 8. As shown in Figure 8a, the inner wall of the crucible was flat, and some pores were observed in the crucible matrix. EDS results in Table 4 show that the crucible matrix (spots 8 and 9) consisted of an Sr_2CeZrO_6 phase. After melting, an interaction layer (~40 μm thickness) and dense structure could be observed in the crucible, as shown in Figure 8b. EDS results indicated that the crucible matrix (spot 10) exhibited a different elementary composition from the interaction layer (spots 11 and 12). As shown in Figure 8d–f, there was a large number of Al elements, which were enriched in the interaction layer. Additionally, the Zr elements exhibited a clear downward trend in the interaction layer in comparison with those in the crucible matrix. It can be concluded that a movement of Al and Zr elements occurred during the interaction between them. Actually, because of the similar structures of the Zr and Ti elements, both of them exhibited excellent compatibility, resulting in the easy dissolution of Zr elements into the alloy melt. From the analysis in Figure 7, it can be seen that the Al reacted with the decomposed refractory to generate $SrAl_2O_4$, resulting in the enrichment of Al elements in the interaction layer. Additionally, there were essentially no Ti elements, which were residual along the crucible sidewall. This indicated that this refractory exhibited a good non-wettability during the alloy melts, consistent with the analysis in Figure 7c.

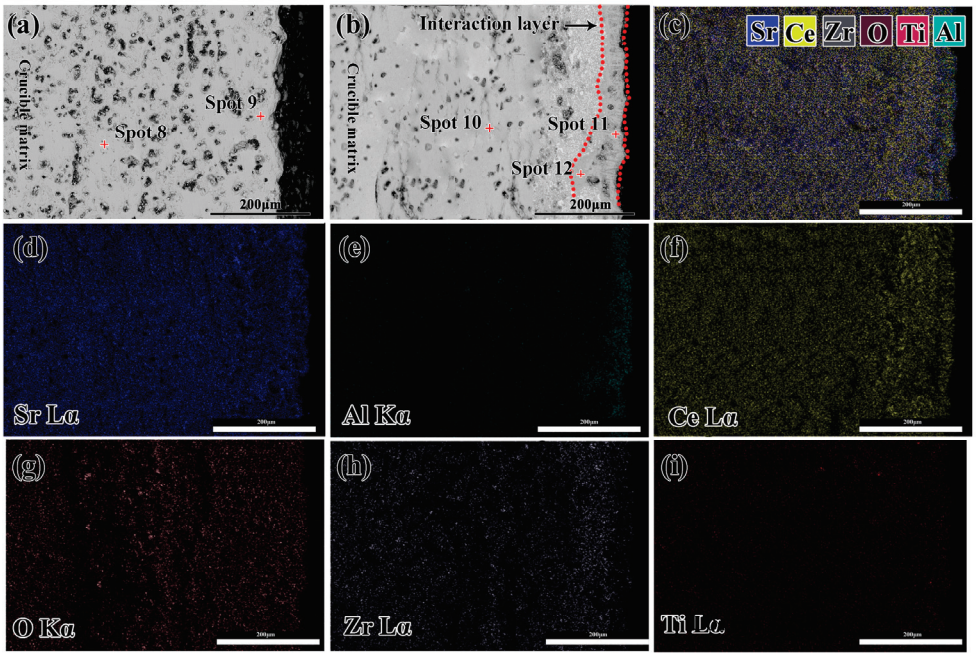

Figure 8. Map scanning image of the sidewall of the crucible before and after melting of the alloy; (**a**) the cross-section of the crucibles before melting; (**b**) the cross-section of the crucible after melting; (**c**) the combination of all elements in (**b**); (**d**–**i**) the EDS element mapping images for Sr, Ce, Zr, O, Zr and Ti.

Table 4. EDS results of spots 8~12 in Figure 8.

	Element at%					
	Sr	**Ce**	**Zr**	**O**	**Al**	**Ti**
Spot 8	19.86	11.31	10.44	58.39	/	/
Spot 9	20.27	10.83	10.86	58.04	/	/
Spot 10	21.61	10.57	11.49	56.33	/	/
Spot 11	10.53	26.40	3.68	59.39	/	/
Spot 12	20.46	3.94	14.48	57.02	4.10	/

The detailed electronic states of the constituent elements in the interaction layer were characterized by X-ray photoelectron spectroscopy (XPS) measurements, as shown in Figure 9. It can be seen that the valence states of Sr and Zr were both in the positive tetravalent state, corresponding to the valence states in $SrTiO_3$ and ZrO_2, respectively. However, the coexistence of Ce^{4+} and Ce^{3+} was observed in this layer. This indicates that there was non-stoichiometric CeO_2 in the interaction layer (i.e., CeO_{2-x}). Evidently, the interaction between the refractory and the alloy melt caused the phase change in the interaction layer. The detailed interaction mechanism is described next.

Figure 10 illustrates the dependence of ΔG^0 vs. the temperature for the formation of TiO_2, TiO, Al_2O_3, CeO, ZrO_2, SrO and $Sr_3Zr_2O_7$, according to results obtained from the HSC software (Version 6.1). The Gibbs free energy of Sr_2CeZrO_6 was not confirmed. Because no interaction products, such as TiO_2 and TiO, could be detected (see Figure 7d), it can be concluded that the interaction mechanism between them was still the dissolution of the crucible refractory in the alloy melt. The dissolution Equation (1) is described below:

$$2Sr_2CeZrO_6 + Ti \overset{\text{in melt}}{\rightarrow} SrO + Sr_3Zr_2O_7 + 2CeO_2 \quad (1)$$

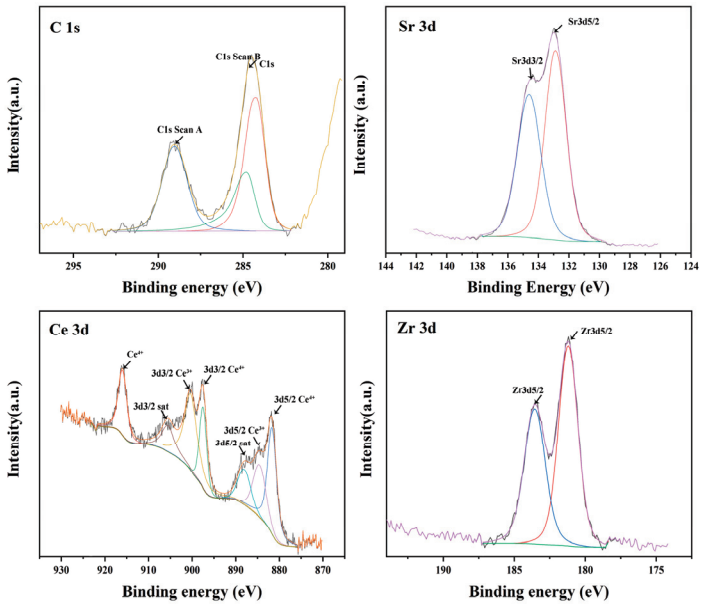

Figure 9. High-resolution X-ray photoelectron spectroscopy (XPS) spectra of C1s, Sr3d, Ce3d and Zr3d for the interaction layer.

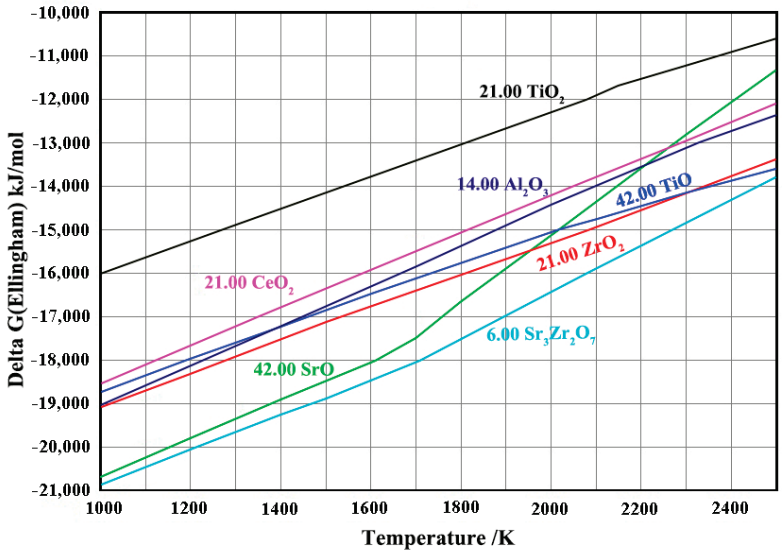

Figure 10. Gibbs free energy for the formation of TiO_2, TiO, Al_2O_3, CeO, ZrO_2, SrO and $Sr_3Zr_2O_7$.

From Figure 10, it can be seen that the decomposed product of $Sr_3Zr_2O_7$ exhibited a better stability than that of TiO_2 and TiO. Thus, due to the high chemical activity of the TiAl alloy melt, it further dissolved in the alloy melt, leading to the generate of SrO and the solution of Zr and O elements into the alloy melt. Additionally, CeO_2 exhibited a worse stability than that of TiO. It reacted with the alloy melt, resulting in the generation of TiO. However, this reaction occurred along the solid–liquid interface, and the Ti melt exhibited a relatively high solubility with the O elements. Thus, no TiO could be detected in the crucible. The Equations (2) and (3) were showed as follows.

$$Sr_3Zr_2O_7 \overset{\text{in melt}}{\rightarrow} SrO + [Zr] + [O] \quad (2)$$

$$CeO_2 + Ti \overset{\text{in melt}}{\rightarrow} Ti[O] + CeO_{2-x} \quad (3)$$

As the O elements dispersed along the interface between the crucible and the alloy melt, it further combined with the Al elements to generate Al_2O_3 products. Then, Al_2O_3 reacted with SrO, resulting in the generation of $SrAl_2O_4$. The reaction Equations (4) and (5) are presented below.

$$[O] + [Al] \overset{\text{in melt}}{\rightarrow} [Al_2O_3] \quad (4)$$

$$SrO + Al_2O_3 \overset{\text{in melt}}{\rightarrow} SrAl_2O_4 \quad (5)$$

4. Conclusions

In this study, a novel perovskite $SrCeZrO_6$ refractory was synthesized using the solid-state method. The interaction of the $SrCeZrO_6$ refractory with a TiAl alloy melt was investigated. Conclusions were obtained as follows:

(1) The pure compound Sr_2CeZrO_6 was successfully synthesized by a solid-state reaction after sintering at 1400 °C for 12 h. The Sr_2CeZrO_6 phase showed Pnma space group symmetry with a = 5.9742(3) Å, b = 8.3910(5) Å, c = 5.9069(5) Å.

(2) The Sr_2CeZrO_6 refractory crucible maintained an intact shape after contacting with the TiAl alloy melt, and the thickness of the interaction layer was about 40 μm.

(3) The Sr_2CeZrO_6 refractory decomposed into $Sr_3Zr_2O_7$, $SrAl_2O_4$ and CeO_{2-x}. The products were generated by the dissolution of the Sr_2CeZrO_6 refractory in the alloy melt, which was the main factor responsible for the interaction mechanism between them. This study provides some theoretical guidance for the development of new refractory materials for melting titanium alloys in the future.

Author Contributions: Conceptualization, K.Z., G.C. and C.L.; formal analysis, Z.C.; investigation, J.L.; resources, Y.L. and M.Z.; data curation, Y.F.; writing—original draft preparation, F.B.; writing—review and editing, F.B.; supervision, G.C.; project administration, F.B. All authors have read and agreed to the published version of the manuscript.

Funding: This research was supported by Science and Technology plan projects of Fire Research Institute of Shanghai (No. 22SX34), National Natural Science Foundation of China (Nos. 52001297; 52104305).

Institutional Review Board Statement: Not applicable.

Informed Consent Statement: Not applicable.

Data Availability Statement: Data are contained within the article.

Conflicts of Interest: The authors declare no conflict of interest.

References

1. Wu, X. Review of alloy and process development of TiAl alloys. *Intermetallics* **2007**, *14*, 1114–1122. [CrossRef]
2. Clemens, H.; Mayer, S. Design, Processing, Microstructure, Properties, and Applications of Advanced Intermetallic TiAl Alloys. *Adv. Eng. Mater.* **2013**, *15*, 191–215. [CrossRef]
3. Chen, S.H.; Schumacher, G. The application of transformation matrices on the determination of γ/γ interface types in a γ-TiAl alloy. *Scr. Mater.* **2004**, *50*, 31–34. [CrossRef]
4. Kim, Y.W. Trends in the development of gamma TiAl alloys. In *Gamma Titanium Aluminides*; Kim, Y.W., Ed.; Minerals, Metals and Materials Society: Warrendale, PA, USA, 1995; pp. 637–652.
5. Yamaguchi, M. High temperature intermetallics—With particular emphasis on TiAl. *Mater. Sci. Technol.* **1992**, *8*, 299–307. [CrossRef]
6. Noda, T. Application of cast gamma TiAl for automobiles. *Intermetallics* **1998**, *6*, 709–713. [CrossRef]
7. Liu, K.; Ma, Y.C.; Gao, M.; Rao, G.B.; Li, Y.Y.; Wei, K.; Wu, X.H.; Loretto, M.H. Single step centrifugal casting TiAl automotive valves. *Intermetallics* **2005**, *13*, 925–928. [CrossRef]
8. Sung, S.Y.; Kim, Y.J. Economic net-shape forming of TiAl alloys for automotive parts. *Intermetallics* **2006**, *14*, 1163–1167. [CrossRef]
9. Lan, L.; Xin, R.Y.; Jin, X.Y.; Gao, S.; He, B.; Rong, Y.H.; Min, N. Effects of Laser Shock Peening on Microstructure and Properties of Ti–6Al–4V Titanium Alloy Fabricated via Selective Laser Melting. *Materials* **2020**, *13*, 3261. [CrossRef] [PubMed]
10. Cristescu, N.D.; Craciun, E.M.; Soós, E. *Mechanics of Elastic Composites*; Chapman and Hall/CRC: Boca Raton, FL, USA, 2004.

11. Cui, R.J.; Tang, X.X.; Gao, M.; Zhang, H.; Gong, S.K. Interactions between TiAl alloys and ytrria refractory material in casting process. *J. Mater. Process. Technol.* **2010**, *210*, 1190–1196.
12. Barbosa, J.; Ribeiro, C.S.; Monteiro, A.C. Influence of superheating on casting of γ-TiAl. *Intermetallics* **2007**, *15*, 945–955. [CrossRef]
13. Tetsui, T.; Kobayashi, T.; Mori, T.; Kishimoto, T.; Harada, H. Evaluation of Ytrria Applicability as a Crucible for Induction Melting of TiAl Alloy. *Mater. Trans.* **2010**, *51*, 1656–1662. [CrossRef]
14. Zhang, H.R.; Tang, X.X.; Zhou, C.G.; Zhang, H.; Zhang, S.W. Comparison of directional solidification of TiAl alloys in conventional Al_2O_3 and novel Y_2O_3-coated Al_2O_3 crucibles. *J. Eur. Ceram. Soc.* **2013**, *33*, 925–934. [CrossRef]
15. Tetsui, T.; Kobayashi, T.; Ueno, T.; Hiroshi, H. Consideration of the influence of contamination from oxide crucibles on TiAl cast material, and the possibility of achieving low-purity TiAl precision cast turbine wheels. *Intermetallics* **2012**, *31*, 274–281. [CrossRef]
16. Sakamoto, K.; Yoshikawa, K.; Kusamichi, T.; Onoye, T. Changes in Oxygen Contents of Titanium Aluminides by Vacuum Induction, Cold Crucible Induction and Electron Beam Melting. *Trans. Iron Steel Inst. Jpn.* **1992**, *32*, 616–624. [CrossRef]
17. Tetsui, T.; Kobayashi, T.; Kishimoto, A.; Harada, H. Structural optimization of an yttria crucible for melting TiAl alloy. *Intermetallics* **2012**, *20*, 16–23. [CrossRef]
18. Li, Z.H.; Wang, Y.; Xu, K.; Yang, J.Z.; Niu, S.B.; Yao, H. Effect of steam on CaO regeneration, carbonation and hydration resistance for CO_2 capture. *Fuel Process. Technol.* **2016**, *151*, 101–106. [CrossRef]
19. Uwanyuze, R.S.; Yavas, B.; Zhang, J.Y.; Kanyo, J.E.; Frame, L.D.; Hebert, R.J.; Schaffoner, S.; Al, S.P. High-temperature interactions between titanium alloys and strontium zirconate refractories. *J. Mater. Eng. Perform.* **2023**, *32*, 1–11. [CrossRef]
20. Zhang, Y.; Xu, X.J. Modeling oxygen ionic conductivities of ABO3 Perovskites through machine learning. *Chem. Phys.* **2022**, *558*, 111511. [CrossRef]
21. Xiao, Y.B.; Chen, G.Y.; Yu, F.H.; Hou, X.; Zhang, Y.; Zou, X.L.; Lu, X.G.; Li, C.H. Preparation of a novel Sr-Zr oxide refractory for induction melting of high-activity alloy. *J. Eur. Ceram. Soc.* **2021**, *41*, 6738–6743. [CrossRef]
22. Zhou, B.; Ke, Q.L.; Wen, M.J.; Ying, T.B.; Cui, G.K.; Gu, Z.Y.; Lu, H.F. Catalytic combustion of toluene on Pt/Al_2O_3 and Pd/Al_2O_3 catalysts with CeO_2, CeO_2-Y_2O_3 and La_2O_3 as coatings. *J. Rare Earths* **2023**, *41*, 1171–1178. [CrossRef]

materials

MDPI

Communication

Dissolution Behavior of Eutectic Carbides in Medium-Alloy Steels for Heavy Forgings

Yu Ji [1], Tingting Xu [2], Caiyan Zhao [2], Guangyao Chen [1,*], Hongshan Zhao [1,3,*], Chundong Hu [1,3] and Han Dong [1,3]

[1] School of Materials Science and Engineering, Shanghai University, Shanghai 200444, China; jiyu@shu.edu.cn (Y.J.); huchundong99@163.com (C.H.); donghan@shu.edu.cn (H.D.)
[2] Zhongyuan Special Steel Co., Ltd., Jiyuan 459000, China; xuting_1@163.com (T.X.); zcy8775@163.com (C.Z.)
[3] Zhejiang Institute of Advanced Materials, Shanghai University, Jiaxing 314100, China
* Correspondence: cgybless1@shu.edu.cn (G.C.); boyushankf@126.com (H.Z.)

Abstract: In this study, we investigate the dissolution behavior of eutectic carbides in heavy forgings. High-temperature diffusion treatment was conducted on 35Cr3Ni3MoVW2 (MoVW2) and 35Cr2Ni3MoV (MoV) steels at 1230 °C for a duration ranging from 0 to 100 h. The dissolution of eutectic carbides and its effects on the microstructure and hardness of the steels were characterized and analyzed via SEM+EBSD, ImageJ, and Thermo-Calc. The results show that the coarse eutectic carbides in both steels gradually dissolved. The distribution and morphology tend to be uniform and spherical, respectively. For holding 50 h, the hardness of both steels significantly exhibited an increasing trend, and it was attributed to the combined effects of solid solution strengthening. Thermodynamic calculations indicated that the higher W content in MoVW2 steel promoted the precipitation of M_6C eutectic carbides. Moreover, both MoVW2 and MoV steels exhibited the precipitation of M_7C_3 eutectic carbides in the final stage of solidification, facilitated by the enrichment of C and Cr in the liquid steels.

Keywords: heavy forging; high-temperature diffusion; Cr-Ni-Mo-V alloy steel; eutectic carbides; hardness

Citation: Ji, Y.; Xu, T.; Zhao, C.; Chen, G.; Zhao, H.; Hu, C.; Dong, H. Dissolution Behavior of Eutectic Carbides in Medium-Alloy Steels for Heavy Forgings. *Materials* **2023**, *16*, 6763. https://doi.org/10.3390/ma16206763

Academic Editor: Andrea Di Schino

Received: 17 September 2023
Revised: 12 October 2023
Accepted: 17 October 2023
Published: 19 October 2023

1. Introduction

Heavy forgings are widely used in fields such as nuclear power rotors and high-pressure vessel equipment. They are the foundational parts of significant technological equipment, and the quality is an important indicator for evaluating China's manufacturing level [1]. To date, the heavy forgings used in high-end equipment have been made from Cr-Ni-Mo-V alloy steels. However, due to the large size of these forgings, the uneven temperature distribution can cause the formation of carbon-rich regions and areas enriched with alloy elements during the final solidification. Thus, it could further cause the formation of eutectic carbides [2]. Generally, the carbide, which acts as an important alloy phase, can directly influence the high-temperature strength and heat resistance of alloy steels through quantity, morphology, size, and distribution [3]. Coarse eutectic carbides not only disrupt the continuity of the steel matrix but also facilitate the formation of cracks, thereby reducing the workability and usability of alloy steel [4,5]. Therefore, it is important to investigate the characteristics of carbides in steel forgings as well as the controlling factors.

Recently, researchers conducted several studies on how to control the formation of eutectic carbides in alloy steels. A study by Zhang et al. revealed that M_7C_3 eutectic carbides could be refined by adjusting the sequence of Nb and Ti additions and optimizing the element distributions in (Nb,Ti)C [6]. Li et al. showed that it was possible to obtain eutectic carbides with smaller size and more uniformly dispersed distribution by increasing the solidification cooling rate [7]. Qu et al. revealed that the morphology of eutectic carbides could be refined by using rare-earth metals [8]. By comparison with techniques such as adjusting steel smelting processes and compositions, high-temperature diffusion

treatment could be considered as an effective way to reduce the content of eutectic carbides and improve the thermal-processing performance of steels. This is primarily because this treatment did not alter the alloy composition or production procedures [9].

High-temperature diffusion treatment for alloy steels was primarily influenced by heating temperature and holding time. A study revealed that a suitable heat-treatment temperature for carbon steels and alloy steels was about 1100~1200 °C and 1200~1300 °C, respectively [10]. Also, increasing the heat-treatment temperature was more effective at improving structural uniformity and reducing eutectic carbides than extending the holding time [11]. Previous studies only focused on the effect of the heating temperature on the diffusion processes for eutectic carbides. There are very few investigations into the holding time [12,13]. Therefore, the effect of the holding time on eutectic carbides in alloy steels still requires in-depth theoretical and experimental research.

In this study, the effect of high-temperature diffusion time on the microstructure and hardness of as-forged Cr-Ni-Mo-V alloy steels was studied, and the precipitation behavior of the eutectic carbides was also investigated using Thermo-Calc v2015a software. The aim is to reduce the eutectic carbides in the steels and enhance their high-temperature performance. The findings provide a valuable reference and guidance for the industrial production and utilization of alloy steels.

2. Materials and Methods

The experimental Cr-Ni-Mo-V steels were obtained from industrial productions of heavy forgings. The chemical compositions of the steels were 35Cr3Ni3MoVW2 (referred to as MoVW2) and 35Cr2Ni3MoV (referred to as MoV), as shown in Table 1. After forging, the steels were subjected to high-temperature diffusion annealing at 1230 °C for 0, 10, 20, 30, 50, 70, 80, and 100 h, separately. Then, the steels were cooled in the air. The steel specimens were sectioned using a cutting machine (Biaole Abrasimet M, Buehler, Lake Bluff, IL, USA), polished using the abrasive papers, and subsequently etched in a solution of nitric acid and ethanol (with a nitric acid concentration of 4 wt.%) for a duration of 10 to 15 s. Simultaneously, 10 mm × 10 mm × 5 mm samples were taken, and vibratory polishing was performed using 0.02 μm colloidal silica suspension for microstructural analysis (EBSD) (Bruker QUANTAX EBSD 400i e-Flash^{FS}, Bruker, Billerica, MA, USA). This analysis was further complemented with AZtecCrystal v2.1 software for post-processing orientation relationships within the microstructure.

Table 1. Chemical composition of the two Cr-Ni-Mo-V experimental steels (mass fraction, %).

Sample	C	Cr	Ni	Mo	V	W	Nb	Ti	Al	Fe
MoVW2	0.33	3.01	3.20	0.62	0.35	2.20	0.028	0.010	0.026	Bal.
MoV	0.36	1.82	3.12	1.10	0.22	/	/	0.003	0.018	Bal.

The metallographic microstructure of the steel specimens was observed using an upright fully automated metallurgical microscope (Carl Zeiss Axio Imager.M2m, Carl Zeiss, Jena, Germany), while the microstructural morphology was examined using a field emission scanning electron microscope (FEI Apreo 2S HiVac, Thermo Fisher Scientific, Waltham, MA, USA). The ImageJ 1.53c software was employed for statistical analysis of the volume percentage and diameter dimensions of the eutectic carbides in the steels (with 20 observations of 5000× fields for each sample). The hardness of the steels was detected using a semi-automatic Brinell hardness tester (Wilson WHBH3000, Bruker, Billerica, MA, USA) with 750 kg load. Additionally, Thermo-Calc thermodynamic software using the Scheil model was utilized to investigate the precipitation behavior of eutectic carbides in the steels after the non-equilibrium solidification.

3. Results and Discussion

Figure 1 shows the microscopic images of MoVW2 and MoV steels after holding at 1230 °C for 0, 50, and 100 h. From Figure 1a,b, it can be seen that the average diameter of the eutectic carbides in MoVW2 and MoV steels were 14.25 and 8.57 μm after holding for 0 h, and the eutectic carbides in the steels exhibited an uneven distribution and irregular shapes. As the holding time increased to 50 h, the morphology of eutectic carbides transformed into a chain-like or block-like structure, and its sizes exhibited a decrease trend, as shown in Figure 1c,d. It was for this reason that the heat treatment for the steels could cause the dissolution of eutectic carbides. Upon extending the holding time to 100 h, the average diameter of the eutectic carbides in MoVW2 and MoV steels was 5.02 and 5.44 μm, respectively. Additionally, the coarse chain-like or block-like eutectic carbides were mostly eliminated and transformed into a spherical shape, as shown in Figure 1e,f. A study by Mao showed that the spherical carbides had a minor impact on the properties of the steels [14]. It indicated that a long holding time for the steels contributed to the dissolution of the carbides and reduced the effects of large-sized and irregular eutectic carbides on the steels.

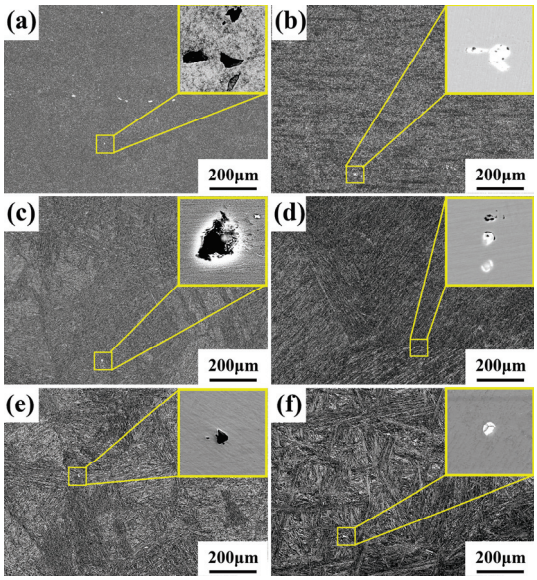

Figure 1. SEM images of eutectic carbides in MoVW2 and MoV steels after holding at 1230 °C for 0, 50, and 100 h. (**a**,**c**,**e**) MoVW2, 0, 50, 100 h; (**b**,**d**,**f**) MoV, 0, 50, 100 h.

Figure 2 shows the SEM images of MoVW2 and MoV steels after holding at 1230 °C for 0 h, 50 h, and 100 h. From Figure 2a,b, it can be seen that the carbides in MoVW2 steel exhibited a uniformly distributed granular pattern after holding for 0 h. However, in MoV steel, the carbides exhibited an irregular shape and uneven distribution. After holding for 50 h, the original austenite grains were coarse, and they could suppress the nucleation of the ferrite. Additionally, a small amount of bainite could also be observed during the cooling [15,16]. From Figure 2c,d, it can be seen that the size of the grains in the steels increased with the increasing holding time, and the carbides along the grain boundaries gradually disappeared. It was for this reason that the dissolution of carbides weakened the pinning effect on the grain boundaries, facilitating the growth of grains. As the holding time increased to 100 h, it was difficult to observe the carbides, indicating that they were mostly completely dissolved, as shown in Figure 2e,f.

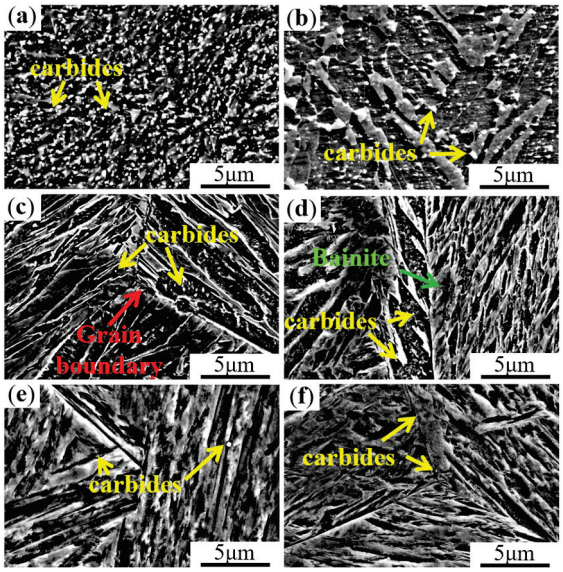

Figure 2. SEM images of MoVW2 and MoV steels after holding at 1230 °C for 0, 50, and 100 h. (**a**,**c**,**e**) MoVW2, 0, 50, 100 h; (**b**,**d**,**f**) MoV, 0, 50, 100 h.

Figure 3 shows the inverse pole figure (IPF) of MoVW2 and MoV steels for holding at 1230 °C for 0 and 100 h. From Figure 3a, it can be seen that grain A had a (101) orientation, and other grains had a relatively single orientation. After holding for 100 h, multiple orientations appeared, because the small grains were absorbed by the large grains during the high-temperature diffusion process, resulting in the grain coarsening, as shown in Figure 3b [17]. Apparently, the growth rates of various grains were uneven, resulting in the appearance of mixed crystallization [18]. Additionally, a long holding time was effective in the generation of a fine needle-like and disordered microstructure in the steels.

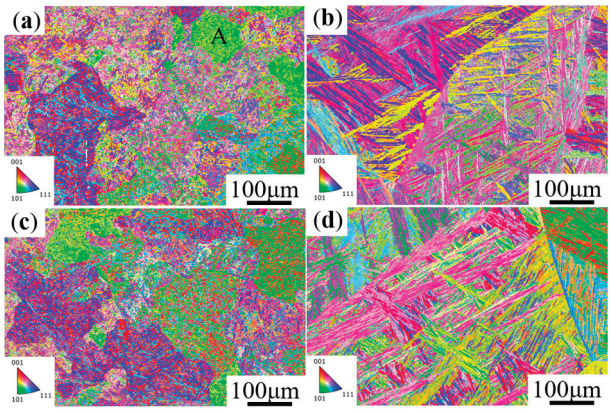

Figure 3. IPF images of MoVW2 and MoV steels after holding at 1230 °C for 0 and 100 h. (**a**,**b**) MoVW2, 0, 100 h; (**c**,**d**) MoV, 0, 100 h.

Figure 4 illustrates the variation in volume percentage of eutectic carbides in MoVW2 and MoV steels for different holding times. The alloy element content in MoVW2 and MoV steels, separated from the C content, was 9.444% and 6.281%, respectively, as indicated in Table 1. Thus, it can be seen that the volume percentage of eutectic carbides in MoVW2 steel was higher than that in MoV steel. Additionally, the volume percentage of the eutectic carbides in both steels exhibited a decreasing trend with the increasing of holding time from approximately 0 to 80 h. The augmented migration rate of carbon and alloy elements was attributed to the prolonged holding time, which could promote the dissolution of the carbides. After holding for 80 h, the volume percentage of eutectic carbides in both

steels was about 0.40%, which indicated that the content of eutectic carbides in both steels was relatively low at this holding time. In this regard, there was a slight difference in the variation in carbides between MoVW2 and MoV steels. In MoVW2 steel, the volume percentage of eutectic carbides was decreased from 3.31% to 1.50% after holding for 0~30 h, and then slightly increased by 0.10% after holding for 50 h. With the increase in holding time, the volume percentage of eutectic carbides was decreased to 0.38% after holding for 100 h. For MoV steel, the volume percentage of eutectic carbides also exhibited a decreasing trend, and it was decreased from 1.18% to 0.47% after holding for 0~100 h.

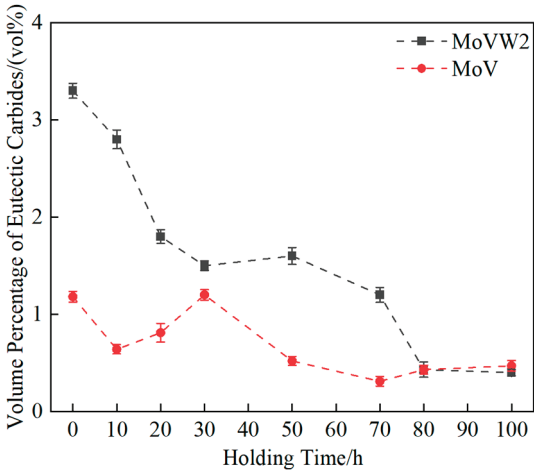

Figure 4. Change curve of volume fraction for the eutectic carbides.

Figure 5 shows the variation in Brinell hardness values with different holding times for MoVW2 and MoV steels. It can be seen that the hardness of MoVW2 steels increased from 286 to 524 HBW after holding for 0~10 h. During the heat treatment, the diffusion of carbides into MoVW2 steel matrix could cause the solid solution strengthening and the reduction of eutectic carbides, which was effective at increasing the hardness. After holding for 20~80 h, the hardness of the steels became stable. This was because the strengthening effect and the dissolution of carbides reached a dynamic balance. However, after holding for 100 h, the hardness rapidly decreased to 300 HBW, due to the grain coarsening and the decrease in the volume percentage of eutectic carbides. In addition, the hardness of MoV steel exhibited the same changing trend as MoVW2 steel. However, it had a higher hardness than that of MoVW2 steel, which was attributed to the higher content of W and Cr elements. The W element was effective at solid solution strengthening, and it could be combined with the C element to form different types of secondary carbides. It could hinder the movement of the dislocations and improve the performance of the steels [19]. Also, the Cr element contributed to the hardness of M_7C_3 carbides [20,21]. Conversely, the presence of bainite in MoV steel could reduce its hardness. Therefore, in the initial stage of holding, both steels exhibited a significant increase in hardness due to the dissolution of eutectic carbides and solid solution strengthening from secondary carbides. With the increase in holding time, the grain sizes were increased, resulting in less significant changes in the hardness. After holding for 50 h, the hardness was generally higher, which indicated that a long holding time was not unfavorable to the improvement of the hardness of the steels. In addition, the consumption of alloying elements by eutectic carbides could weaken the strengthening effect and reduce the precipitation-strengthening effect of eutectic carbides, resulting in a decrease in matrix strength and a noticeable decrease in hardness.

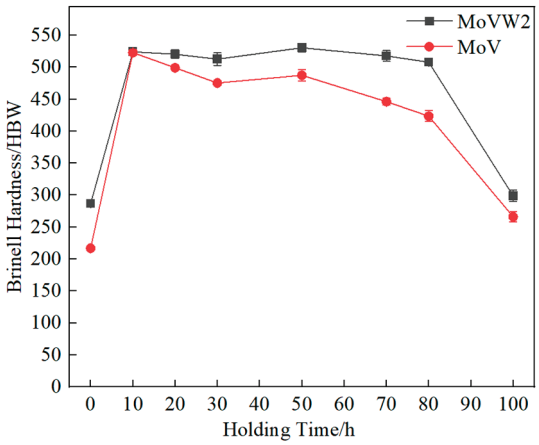

Figure 5. Variation in hardness for MoVW2 and MoV steels at different holding times.

The researchers lacked a shared comprehension of the structure and reaction mechanism involved in the precipitation of eutectic carbides during the solidification of molten steel. However, it was generally believed that the eutectic carbides were formed near the endpoint during the solidification, and the formation of the composition of eutectic carbides had different phase constitution. Thus, Thermo-Calc software was utilized to investigate the non-equilibrium solidification phase diagrams in MoVW2 and MoV steels, as shown in Figure 6. The solidification sequence of MoVW2 steel is shown below:

$$L \rightarrow L + \gamma\text{-Fe} \rightarrow L + \gamma\text{-Fe} + M_6C \rightarrow L + \gamma\text{-Fe} + M_6C + MC \rightarrow L + \gamma\text{-Fe} + M_6C + MC + M_7C_3$$

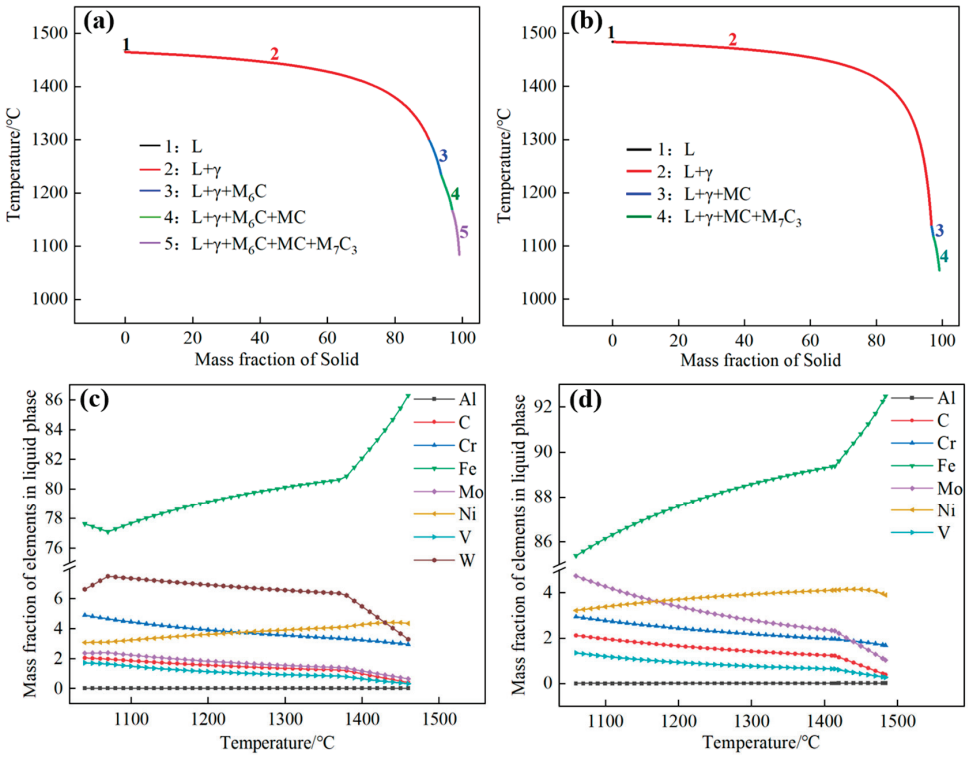

Figure 6. Solidification diagram of MoVW2 and MoV steels and elemental mass fraction in liquid phase as a function of temperature. (**a**,**c**) Nonequilibrium property diagrams of MoVW2, MoV; (**b**,**d**) Mass fraction of elements in liquid phase of MoVW2, MoV.

Apparently, during the solidification process, M_6C, MC, and M_7C_3 eutectic carbides could be precipitated from the liquid phase at the solidification front. In addition, the solidification sequence of MoV steel is shown as follows:

$$L \rightarrow L + \gamma\text{-Fe} \rightarrow L + \gamma\text{-Fe} + MC \rightarrow L + \gamma\text{-Fe} + MC + M_7C_3$$

During the solidification process, MC and M_7C_3 eutectic carbides could be precipitated from the liquid phase at the solidification front. Generally, MC eutectic carbides are carbides enriched in V, Ti, or Nb, and M_6C eutectic carbides contain a large amount of Mo, Fe, and W, and small amounts of V and Cr elements. M_7C_3 eutectic carbides contain a large amount of Cr and Fe, and small amounts of V and Mo elements.

Figure 7 shows the element-mapping analysis for the eutectic carbides. Through the EDX analysis of eutectic carbides after a long holding time, the atomic mass fraction of each element of the eutectic carbides of MoVW2 steel and MoV steel was obtained. It can be seen that the content of each element is different after the diffusion and dissolution of eutectic carbides. From Figure 7, it can be seen that the eutectic carbides in MoVW2 steel were enriched with Cr, V, Mo, and W elements, confirming that it was easy to form composite eutectic carbides such as MC, M_6C, and M_7C_3. Additionally, the eutectic carbides in MoV steel were enriched with Cr, V, and Ti elements, belonging to composite eutectic carbides of MC and M_7C_3. During the early stage of solidification, the amount of C, Cr, Mo, V, and W elements in the liquid phase could be increased with the decreasing temperature due to the precipitation of M_6C and MC eutectic carbides, along with the dissolution of a certain amount of Cr, Mo and other elements. The concentration of Mo elements exhibited a relatively stable condition during solidification; however, the concentration of Ni element was decreased due to the precipitation. The concentration of Al elements in the liquid phase were relatively low, and its variation trend was not significant.

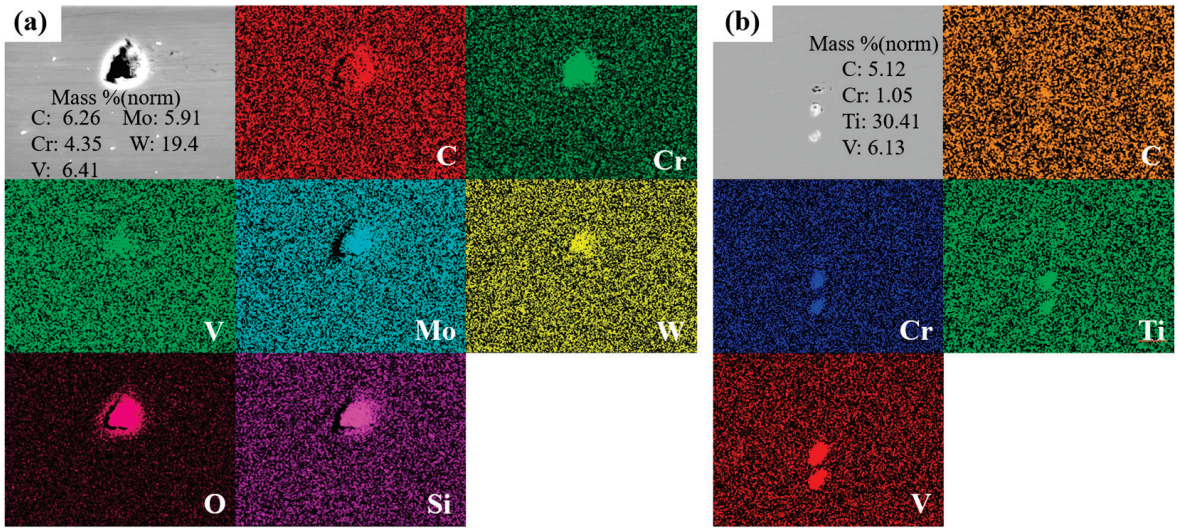

Figure 7. EDS element-mapping images for eutectic carbide: (**a**) MoVW2; (**b**) MoV.

The mass fractions of Fe and W elements in MoVW2 steel exhibited completely opposite trends. This could be because the W element was relatively stable during the early stage of solidification. As the solidification was carried out, the concentration of W element decreased due to the precipitation of M_6C-type eutectic carbides containing W. During the prolonged solidification process of large-sized castings, the W element settled to the bottom of the liquid steel, resulting in its enrichment and providing compositional conditions for the formation of M_6C carbides [22].

The high content of C and Cr in the liquid steel could promote the precipitation of Cr_7C_3 eutectic carbides. However, it could consume a large amount of alloying elements.

Generally, the formation of MC carbides in steel was related to its purity. In the production process, there were small amounts of alloying elements such as V, Nb, and Ti, making the formation of (V, Nb, Ti) (C,N) eutectic carbides quite probable. Additionally, MC carbides often acted as heterogeneous nucleation sites, promoting the nucleation and refinement of M_7C_3 eutectic carbides' size [23–25].

4. Conclusions

1. After high-temperature diffusion at 1230 °C for 0~100 h, the volume percentage of eutectic carbides in MoVW2 and MoV steels gradually decreased. Extending the holding time aids carbide dissolution, leading to a spherical shape and reducing the impact of large, irregular eutectic carbides on the steel. In MoVW2 steel, the volume percentage of eutectic carbides decreased from 3.31% to 0.38%, while in MoV steel, it decreased from 1.18% to 0.47%.
2. The hardness of both MoVW2 and MoV steels was relatively high after holding for 50 h, with MoVW2 steel at 524 HBW and MoV steel at 488 HBW. This was attributed to the solid solution strengthening caused by the dissolution of carbides and the decrease in eutectic carbides. However, after holding for 80~100 h at 1230 °C, the weakening of precipitation strengthening and grain coarsening could significantly result in a decrease in the hardness of both steels.
3. The high W content could promote the precipitation of M_6C-type eutectic carbides in MoVW2 steel. Additionally, due to the enrichment of C and Cr in both MoVW2 and MoV steels, the preferential precipitation of M_7C_3 eutectic carbides occurred in the final stage of solidification from the liquid steel.

Author Contributions: Conceptualization, C.H. and H.D.; methodology, H.D.; software, Y.J.; validation, Y.J., C.H. and H.Z.; formal analysis, Y.J.; investigation, T.X.; resources, C.Z.; data curation, T.X.; writing—original draft preparation, Y.J.; writing—review and editing, G.C.; visualization, G.C.; supervision, C.H.; project administration, C.H.; funding acquisition, G.C. and C.H. All authors have read and agreed to the published version of the manuscript.

Funding: This research was supported by the Shanghai Education Commission 2019 Science and Technology Education 01-44, the Natural Science Foundation of China (No. 52104305).

Institutional Review Board Statement: Not applicable.

Informed Consent Statement: Not applicable.

Data Availability Statement: Not applicable.

Conflicts of Interest: The authors declare no conflict of interest.

References

1. Firrao, D.; Matteis, P.; Scavino, G.; Ubertalli, G.; Ienco, M.G.; Pinasco, M.R.; Ghidini, A. Relationships between tensile and fracture mechanics properties and fatigue properties of large plastic mould steel blocks. *Mater. Sci. Eng. A* **2007**, *468*, 193–200. [CrossRef]
2. Wang, M.; Ma, D.; Liu, Z.; Zhou, J.; Chi, H.; Dai, J. Effect of Nb on segregation, primary carbides and toughness of H13 steel. *Acta Met. Sin.* **2014**, *50*, 285–293.
3. Li, J.; Shi, C.; Li, J.; Shi, C. *Carbide in Special Steel: Formation Mechanism and Control Technology*; Metallurical Industry Press: Beijing, China, 2021; pp. 1–57.
4. Bombač, D.; Terčelj, M.; Fazarinc, M.; Kugler, G. On the increase of intrinsic workability and hot working temperature range of M42 ledeburitic super high steel in as-cast and wrought states. *Mater. Sci. Eng. A* **2017**, *703*, 438–450. [CrossRef]
5. Jiao, W.C.; Li, H.B.; Feng, H.; Jiang, Z.H.; Xia, L.F.; Zhang, S.C. Evolutions of micro-and macrostructure by cerium treatment in as-cast AISI M42 high-speed steel. *Metall. Mater. Trans. B* **2020**, *51*, 2240–2251. [CrossRef]
6. Zhang, Y.; Song, R.; Pei, Y.; Wen, E.; Zhao, Z. The formation of TiC–NbC core-shell structure in hypereutectic high chromium cast iron leads to significant refinement of primary M_7C_3. *J. Alloys Compd.* **2020**, *824*, 153806. [CrossRef]
7. Li, S.; Chen, Y.; Gong, T.; Chen, X.; Fu, P.; Li, D. Effect of cooling rate on the precipitation mechanism of primary carbide during solidification in high carbon-chromium bearing steel. *Acta Met. Sin.* **2021**, *58*, 1024–1034.
8. Qu, Y.; Xing, J.; Zhi, X.; Peng, J.; Fu, H. Effect of cerium on the as-cast microstructure of a hypereutectic high chromium cast iron. *Mater. Lett.* **2008**, *62*, 3024–3027. [CrossRef]

9. Kwon, K.Y.; Kim, Y.D.; Na, Y.S.; Seo, S.M.; Yang, J.K. Microstructural changes and variations of hot deformation stability with homogenization treatment of 1Cr-1.25 Mo-0.25 V Steel before hot forging. *J. Korean Inst. Met. Mater.* **2013**, *51*, 883–892. [CrossRef]
10. Wang, X.; Li, G.; Liu, Y.; Cao, Y.; Wang, F.; Wang, Q. Investigation of primary carbides in a commercial-sized electroslag remelting ingot of H13 steel. *Metals* **2019**, *9*, 1247. [CrossRef]
11. Luo, Y.; Guo, H.; Sun, X.; Mao, M.; Guo, J. Effects of austenitizing conditions on the microstructure of AISI M42 high-speed steel. *Metals* **2017**, *7*, 27. [CrossRef]
12. Liu, X.G.; Nie, S.M.; Ren, Y.L. Experimental study on diffusion annealing before forging of Cr-Mo low-alloy steel. *J. Plast. Eng.* **2007**, *12*, 49–56.
13. Totten, G.E. *Steel Heat Treatment Handbook*, 2nd ed.; 2 Volume Set; CRC Press: Boca Raton, FL, USA, 2006.
14. Mao, M.; Guo, H.; Wang, F.; Sun, X. Effect of cooling rate on the solidification microstructure and characteristics of primary carbides in H13 steel. *ISIJ Int.* **2019**, *59*, 848–857. [CrossRef]
15. Yang, W.Y.; Hu, A.M.; Sun, Z.Q. Effect of austenite grain size on strain enhanced transformation in a low carbon steel. *Acta Met. Sin.* **2000**, *36*, 1055–1060.
16. Yin, Y.; Sun, Z. Microstructure Control of Hot Rolled Trip Steel Based on Dynamic Transformation of Undercooled Austenite II. Cooling Rate after Dynamic Transformation of Undercooled Austenite. *Acta Met. Sin.* **2010**, *46*, 161–166. [CrossRef]
17. Han, R.; Yang, G.; Sun, X.; Zhao, G.; Liang, X.; Zhu, X. Austenite Grain Growth Behavior of Vanadium Microalloying Medium Manganese Martensitic Wear-Resistant Steel. *Acta Met. Sin.* **2022**, *58*, 1589–1599.
18. Hong, S.H.; Lee, D.N. Grain coarsening in IF steel during strain annealing. *Mater. Sci. Eng. A* **2003**, *357*, 75–85. [CrossRef]
19. Huang, B.; Xiong, W.; Zhang, M.; Jing, Y.; Li, B.; Luo, H.; Wang, S. Effect of W content in solid solution on properties and microstructure of (Ti, W) C-Ni_3Al cermets. *J. Alloys Compd.* **2016**, *676*, 142–149. [CrossRef]
20. Zhang, Y.; Li, J.; Zhou, L.; Xiang, S. A theoretical study on the chemical bonding of 3d-transition-metal carbides. *Solid State Commun.* **2002**, *121*, 411–416. [CrossRef]
21. Xie, J.Y.; Chen, N.X.; Shen, J.; Teng, L.; Seetharaman, S. Atomistic study on the structure and thermodynamic properties of Cr_7C_3, Mn_7C_3, Fe_7C_3. *Acta Mater.* **2005**, *53*, 2727–2732. [CrossRef]
22. Fedoseeva, A.; Dudova, N.; Glatzel, U.; Kaibyshev, R. Effect of W on tempering behaviour of a 3% Co modified P92 steel. *J. Mater. Sci.* **2016**, *51*, 9424–9439. [CrossRef]
23. Chung, R.J.; Tang, X.; Li, D.Y.; Hinckley, B.; Dolman, K. Effects of titanium addition on microstructure and wear resistance of hypereutectic high chromium cast iron Fe–25wt.% Cr–4wt.% C. *Wear* **2009**, *267*, 356–361. [CrossRef]
24. Zhou, Y.; Yang, Y.; Yang, J.; Hao, F.; Li, D.; Ren, X.; Yang, Q. Effect of Ti additive on $(Cr, Fe)_7C_3$ carbide in arc surfacing layer and its refined mechanism. *Appl. Surf. Sci.* **2012**, *258*, 6653–6659. [CrossRef]
25. Chung, R.J.; Tang, X.; Li, D.Y.; Hinckley, B.; Dolman, K. Microstructure refinement of hypereutectic high Cr cast irons using hard carbide-forming elements for improved wear resistance. *Wear* **2013**, *301*, 695–706. [CrossRef]

materials

MDPI

Article

Achieving High Strength and Creep Resistance in Inconel 740H Superalloy through Wire-Arc Additive Manufacturing and Thermodynamic-Guided Heat Treatment

Soumya Sridar [1], Luis Fernando Ladinos Pizano [1], Michael A. Klecka [2] and Wei Xiong [1,*]

[1] Physical Metallurgy and Materials Design Laboratory, Department of Mechanical Engineering and Materials Science, University of Pittsburgh, Pittsburgh, PA 15261, USA; sos57@pitt.edu (S.S.); lul58@pitt.edu (L.F.L.P.)
[2] RTX Technology Research Center, 411, Silver Lane, East Hartford, CT 06118, USA; michael.klecka@rtx.com
* Correspondence: weixiong@pitt.edu; Tel.: +1-(412)-383-8092 or +1-(412)-624-4846

Abstract: Inconel 740H superalloy is commonly used in advanced ultra-supercritical power plants since it possesses excellent strength and creep resistance. This study investigates the microstructure and mechanical properties of Inconel 740H superalloy fabricated using wire-arc additive manufacturing. The as-printed microstructure consisted of columnar γ grains with the Laves phase and (Nb, Ti)C carbides as secondary phases. The anisotropy in grain structure increased from the bottom to the top regions, while the hardness was highest in the middle portion of the build. To guide the post-heat treatment design, thermodynamic and kinetic simulations were employed to predict the temperature and time. Complete recrystallization with the Laves phase dissolution occurred throughout the build after homogenization at 1200 °C for 2 h. The peak hardness was achieved after aging at 760 °C for 12 h with the $M_{23}C_6$ carbides decorating the grain boundaries and γ′ precipitates in the grain interior. The yield strength (655 MPa) and ductility (29.5%) in the post-heat treated condition exceeded the design targets (620 MPa, 20%). Stress rupture tests at 750 °C showed that the high-temperature performance was at par with the wrought counterparts. The fracture mode after rupture was identified to be intergranular with the presence of grain boundary cavities along with grain boundary sliding.

Keywords: CALPHAD; recrystallization; stress rupture; anisotropy; diffusion

Citation: Sridar, S.; Ladinos Pizano, L.F.; Klecka, M.A.; Xiong, W. Achieving High Strength and Creep Resistance in Inconel 740H Superalloy through Wire-Arc Additive Manufacturing and Thermodynamic-Guided Heat Treatment. *Materials* **2023**, *16*, 6388. https://doi.org/10.3390/ma16196388

Academic Editor: Xianfei Ding

Received: 20 August 2023
Revised: 15 September 2023
Accepted: 19 September 2023
Published: 25 September 2023

1. Introduction

Inconel 740H is a γ′ strengthened Ni-base superalloy developed by Special Metals Corporation [1], which is primarily used in advanced ultra-supercritical (AUSC) power plants as superheater and reheater tubes that are subjected to high pressure (35 to 45 MPa) and temperatures upto 800 °C. This material is suitable for high-temperature applications owing to its excellent creep and oxidation resistance, as well as microstructure stability and high strength at elevated temperatures [2]. This alloy is derived from its predecessor, Inconel 740, with adjustments in the Al/Ti ratio to avoid the formation of a deleterious η (Ni_3Ti) phase during service [3]. Moreover, the reduction in the silicon, boron, and niobium content in Inconel 740H compared to the parent alloy maximized the weldability by decreasing the susceptibility to liquation cracking [4]. This alloy has been considered a suitable candidate for several power generation applications, such as thermal power plants with super-critical CO_2 [5] and concentrated solar power plants [6]. Inconel 740H in its wrought form has been investigated to determine several critical properties such as corrosion, oxidation, and fatigue resistance for its use in these applications [7–10].

To the best of our knowledge, no reports are available in the literature for the fabrication of monolithic Inconel 740H superalloy by additive manufacturing. Since this alloy possesses superior weldability and is available in wire form, it is a potential candidate to be fabricated using wire-arc additive manufacturing (WAAM). WAAM is a directed energy

deposition (DED) based additive manufacturing technique that uses a plasma or electric arc to melt the wire feedstock for layer-by-layer deposition. This technique is capable of fabricating large-sized components due to its high deposition rate and heat input. The material costs are lesser than any powder-based DED process as the wire feedstock is cheaper than metal powders [11]. However, the microstructure in the as-printed condition might not be suitable for high-temperature applications due to the anisotropy in the matrix due to the columnar grains and lack of adequate strengthening precipitates, which necessitates the design of a post-heat treatment. The standard post-heat treatment for wrought Inconel 740H superalloy is homogenization at 1150 °C for 30 min followed by water quenching and aging at 800 °C for 16 h [3]. The mechanical properties reported for wrought Inconel 740H are yield strength of 724 MPa, ultimate tensile strength of 1066 MPa, and elongation of 28.1% [12]. Though a standard post-heat treatment is available for traditionally manufactured Inconel 740H superalloys, it may not be suitable to apply them for additively manufactured alloys due to the microstructure complexity owing to heating and cooling cycles experienced during deposition as it has been demonstrated for several other additively manufactured alloys [13,14].

To assess the feasibility of fabricating Inconel 740H superalloy using WAAM along with the design of post-heat treatment, a systems design chart [15] was formulated that links the processing steps, macro/microstructure, and target properties for good performance, as shown in Figure 1. The effect of each processing step on the microstructure and the influence of this resultant structure on the mechanical properties, as well as the printability, is depicted concisely in this chart. A two-step post-heat treatment consisting of homogenization to recrystallize the microstructure, relieve the residual stresses, and dissolve the secondary phases, followed by aging to precipitate the strengthening phases is essential for improving the properties. The intended microstructure of Inconel 740H superalloy fabricated using WAAM after post-heat treatment will be a γ matrix consisting of γ′ precipitates for strengthening and continuous $M_{23}C_6$ carbides along the grain boundaries to enhance the creep resistance. MX (M = Ti, Nb; X = C, N) phase will act as pinning particles to avoid excessive grain coarsening during homogenization. It is to be noted that the design targets for the tensile properties were obtained from the ASME Code Case 2702, which certifies Inconel 740H superalloys for service in AUSC power plants in 2011 [16].

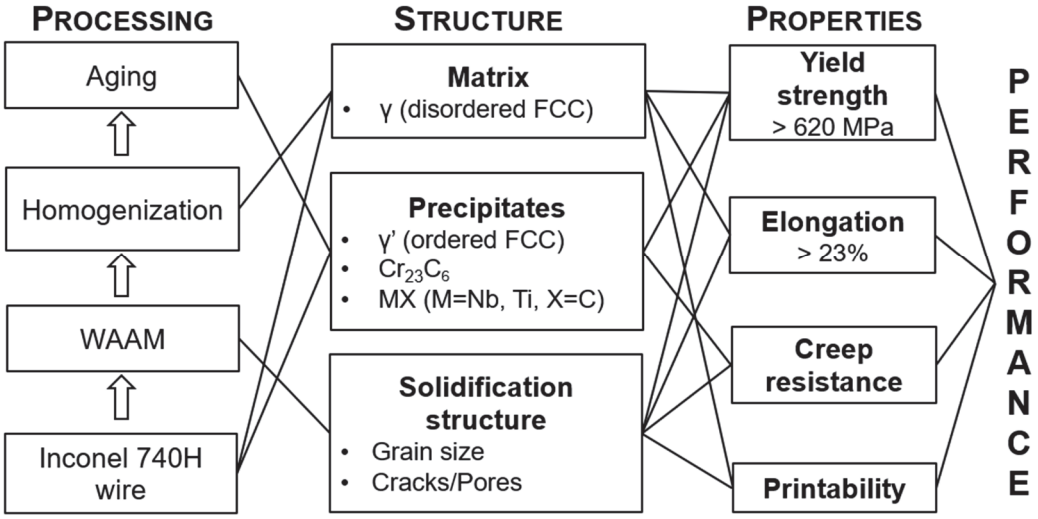

Figure 1. Systems design chart for fabrication of Inconel 740H superalloy using wire-arc additive manufacturing along with post-heat treatment. The microstructural features and desired mechanical properties are listed.

The fabrication of Inconel 740H superalloy using WAAM has been explored for the first time in this work. Since WAAM is capable of fabricating large builds, there is a need to study the variation in the microstructure and properties along the build direction due to the

difference in thermal history for the as-printed Inconel 740H superalloy. Thermodynamic and kinetic simulations guided the design of the post-heat treatment, and its efficacy was determined by evaluating the tensile properties in as-built and post-heat treated conditions. This work will provide an understanding of the applicability of WAAM for fabricating large builds of Inconel 740H superalloy and the mitigation measures required for improving the mechanical properties.

2. Materials and Methods

2.1. Experimental Details

The composition (in wt.%) of Inconel 740H (denoted as 740H hereafter) superalloy wire with 1 mm diameter as specified by the vendor (Special Metals Welding Products Co., Huntington, WV, USA) is listed in Table 1. The sample was built over a mild steel substrate in Raytheon Technologies Development Centre with an ABB robotic WAAM system with a plasma torch connected to a six-axis robot. An average voltage of 20.9 V, layer height of 3 mm, and wire feed rate of 2.5 m/min was maintained throughout the deposition of 50 layers of 740H superalloy. Argon gas with a flow rate of 1.2 L/min was used for producing plasma and shielding the welding torch. The wire feed angle was maintained as 30° and a 12 mm distance was maintained between the torch and the build. An overall deposition rate of 0.9 kg/h was maintained throughout the deposition. The substrate temperature was maintained at 100 °C before the start of the deposition. A higher current (220 and 200 A) and lower travel speed (3.5 and 4 mm/s) was used for the first and second layers to ensure good adhesion with the substrate. Subsequently, a constant current of 166 A and travel speed of 5 mm/s was employed from the 3rd to 50th layer to complete the build. A square raster or lawnmower-type fill pattern with a width of 16 mm and step-over of 3 mm was used for the deposition of all the layers to achieve high stability of the melt pool without any bulging, sagging, or overflow. The dimensions of the final deposit are 180 mm in length, 24 mm in width, and approximately 100 mm in height, as shown in Figure 2a. A two-step post-heat treatment consisting of homogenization and aging steps was designed to improve the mechanical performance of the WAAM 740H superalloy. The homogenization temperature and time were designed based on thermodynamic and kinetic simulations (described in Section 2.2). After the application of the designed homogenization heat treatment, aging time was further optimized with the aging temperature identified from thermodynamic calculations.

The builds deposited using WAAM were sectioned along the build direction using electric discharge machining (Mitsubishi MV2400S, Tatebayashi, Japan) to view the XZ plane for further characterization. As shown in Figure 2b, the extracted sample was divided into three regions namely, top, middle, and bottom to investigate the variation in properties at different locations along the build direction. The sample surfaces were mechanically ground from 600 to 1200 grit emery papers and polished using diamond (3 and 1 μm particles) and silica (0.04 μm particles) suspensions. To reveal the precipitates that formed after aging heat treatment and stress rupture testing, electrolytic etching was carried out using chromic acid (H_2CrO_4) prepared from 15 g of chromium oxide (CrO_3) and 10 mL of concentrated sulfuric acid (H_2SO_4) dissolved in 150 mL of 85% phosphoric acid (H_3PO_4) at a voltage of 5 V for 20 s. The as-polished and etched surface was viewed under FEI Scios Dual Beam focused ion beam—scanning electron microscope (SEM) attached with a field emission gun source. The elemental composition was determined using the OctaneElite energy dispersive spectroscope (EDS) system. The grain structure analysis was carried out using electron backscattered diffraction (EBSD) with a EDAX Hikari EBSD camera and analyzed using the TSL-OIM software (version 8).

Hardness measurements were carried out using the automated Vickers microhardness tester (AMH55 with LM310AT Microindenter, LECO Corporation, St. Joseph, MI, USA) with a 300 g load and 10 s dwell time. For generating the hardness maps, ~600 indentations were performed in the top, middle, and bottom portions of the sample. For determining the hardness after aging heat treatment, an average of 20 hardness readings was considered.

The room temperature tensile tests were carried out using a 500 kN servo-mechanical load frame with a crosshead speed of 1.3 mm/min with the loading direction parallel to the build direction. Flat dog bone-shaped samples were machined with dimensions according to the ASTM E8 standard [17] from the build, as shown in Figure 2c, and three tests were performed for as-built and post-heat treated conditions. Each sample was marked with reflective tags such that the elongation could be monitored in a non-contact mode using a laser-based extensometer during the test. Stress rupture tests were performed at 750 °C with applied stresses of 375, 400, 425, and 450 MPa for the bars extracted from the WAAM builds with dimensions shown in Figure 2d.

Table 1. Composition (in wt.%) of the Inconel 740H wire used for WAAM as specified by the vendor.

Al	C	Co	Cr	Cu	Fe	Mn	Mo	Nb	Si	Ti	Ni
1.4	0.03	20.3	24.6	0.02	0.2	0.24	0.5	1.49	0.1	1.5	Bal.

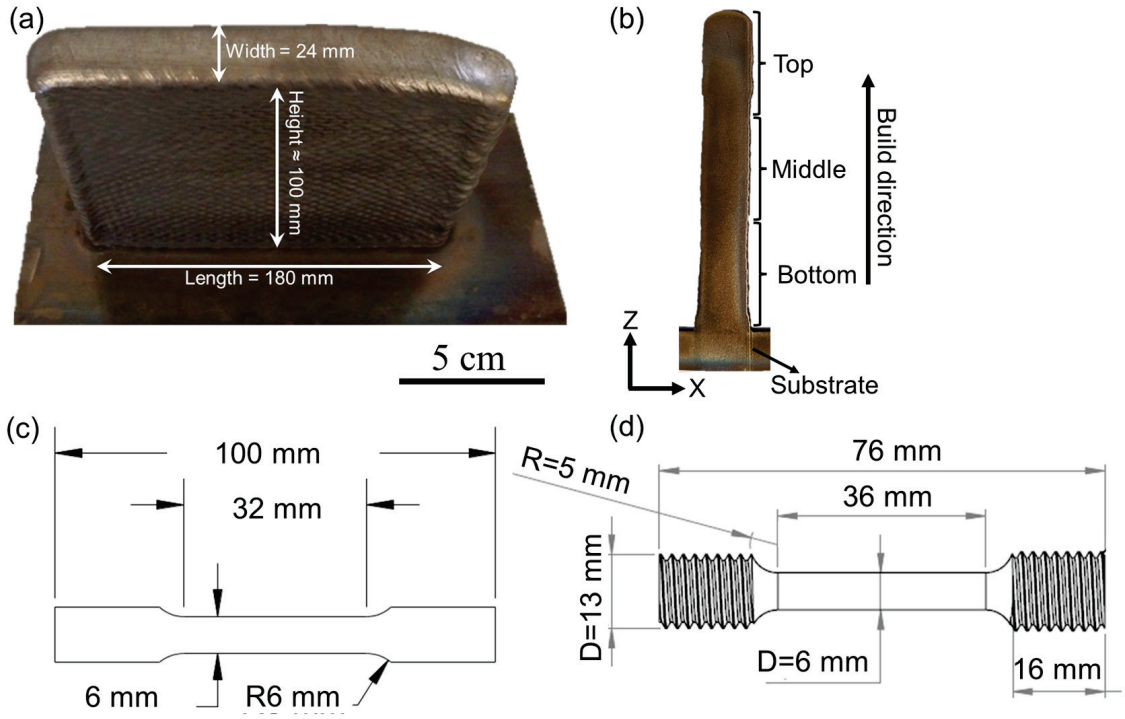

Figure 2. (**a**) Final Inconel 740H superalloy build fabricated using WAAM with the dimensions marked, (**b**) A slice of XZ plane extracted from the final build showing the different portions into which the sample was partitioned to study the variation in properties along the build direction and schematic of the sample used for (**c**) tensile and (**d**) stress rupture tests with its dimensions.

2.2. Computational Details

The kinetic simulations were performed using the DICTRA module of Thermo-Calc software (version 2021b) with TCNI8 and MOBNI4 as thermodynamic and mobility databases, respectively. EDS line scan was performed in the region with the Laves phase in the γ (FCC) matrix of the as-built 740H superalloy to obtain the required inputs for the DICTRA simulations. Two different areas in the matrix, namely, the interdendritic regions and the regions with the Laves phase were probed using line EDS to identify the region with maximum inhomogeneity (Figure 3a,b). Based on the composition variation as a function of distance obtained from the EDS line scan, it was found that the maximum inhomogeneity in composition occurs in the region of the matrix containing the Laves phase. Therefore, it was considered as input for obtaining the optimum homogenization temperature and time using the kinetic simulations. The calculated equilibrium phase fraction as a function

of temperature for the 740H superalloy wire composition using Thermo-Calc is shown in Figure 3c. This calculation was performed using the commercial multicomponent thermodynamic database for Ni-based superalloys namely, TCNI8, available in the Thermo-Calc software (version 2021b). From this plot, it was identified that the homogenization temperature can be either 1100 or 1200 °C due to the absence of deleterious secondary phases, and hence, kinetic calculations were performed for both temperatures. The presence of NbC particles at these temperatures is not considered deleterious since they act as pinning particles to arrest the grain growth during the homogenization heat treatment.

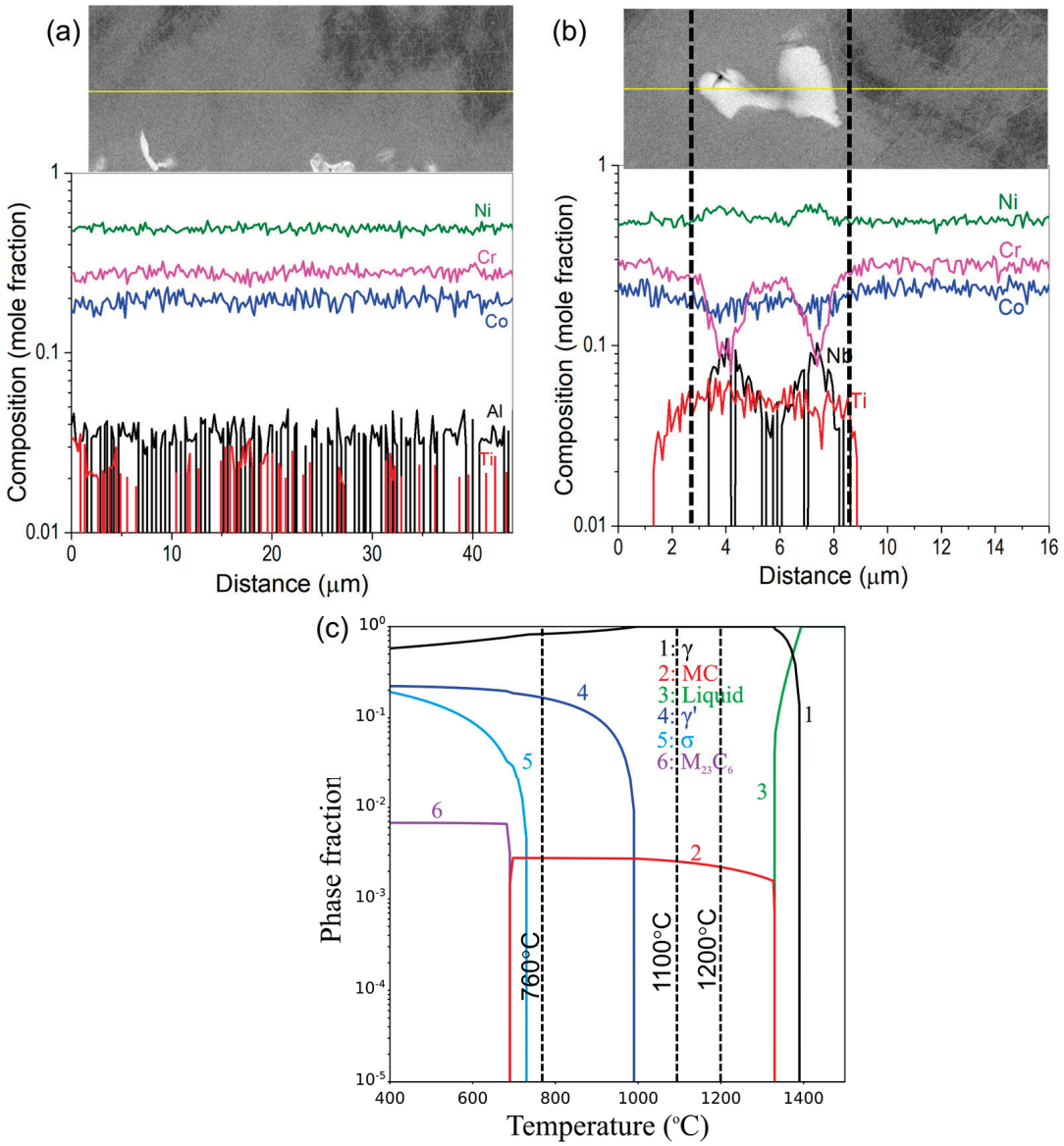

Figure 3. (**a**) Composition of the matrix in the interdendritic region showing negligible composition inhomogeneity, (**b**) Composition of the matrix with the Laves phase determined using EDS which will serve as input for the DICTRA simulations (yellow line indicates the line along with the EDS scan was performed) and (**c**) Calculated equilibrium phase fractions as a function of temperature for the 740H superalloy wire composition to identify the homogenization and aging temperatures for post-heat treatment.

To design the homogenization heat treatment, CALPHAD-based kinetic simulations were performed using the DICTRA module of Thermo-Calc software (version 2021b) to predict the time required to dissolve the Laves phase into the matrix. The simulation

cell was considered as a single-phase FCC where the Laves phase region was considered as an FCC phase with higher Nb and Ti content rather than incorporating a two-phase moving boundary problem with FCC and Laves phases described separately to model the dissolution. The moving boundary problem could not be implemented due to the lack of reliable mobility expressions for the Laves phase in the commercial mobility database (MOBNI4) and in the literature. Hence, a single-phase FCC was considered, which was found to estimate the homogenization time closer to the experimental value for the Inconel 718 superalloy, as reported in our previous work [18]. The simulations were performed for 10^6 s with 200 grid points. Additional inputs such as the width of the cell (total length of the line EDS), number and position of each grid point within the cell (the total number of points and spacing between them in the line EDS), and composition at each grid point (composition at each point of the line EDS) were chosen from the line scan obtained using EDS.

3. Results and Discussion

3.1. As-Built WAAM Inconel 740H Superalloy

Since a large build of Inconel 740H superalloy was fabricated using WAAM in this work, the sample needs to be investigated in different regions to understand the location-specific variation in properties along the build direction in as-built condition. No visible cracks were found in the build, owing to the excellent weldability of the 740H superalloy. The SEM micrographs were obtained in backscattered electron mode from the top, middle, and bottom portions of the sample, as shown in Figure 4(a1–a6). A matrix with a columnar grain structure with secondary phases, such as the Laves phase and (Nb, Ti)C precipitates can be observed. The composition of the secondary phases were confirmed using the EDS line scans (Figure 4(b1–b3)) and also indicating that the Laves phase is rich in Nb. The Laves phase was predominantly found in the interdendritic region, indicating the strong segregation of Nb and Ti in these regions during the solidification. It is also to be noted that several gas pores in spherical shape can be noticed throughout the sample. The possible source for the formation of gas pores could be the dissolution of the shielding gas during the deposition. The average fraction of gas pores was calculated to be 0.32% using ImageJ software (version 1.54f) from the SEM micrographs.

Figure 5 shows the inverse pole figure (IPF) maps and pole figure (PF) intensity maps for (001), (101), and (111) planes obtained using EBSD from the top, middle, and bottom portions of the sample. The grains in the bottom region are found to be less columnar in comparison with the top and middle portions of the sample. This is because the bottom region of the build is close to the mild steel substrate with a higher thermal conductivity than the 740H superalloy, and hence, the substrate acts as an efficient heat sink to dissipate the heat from the deposited material. On the contrary, in the top and middle portions of the build with higher deposition heights, the previously deposited 740H superalloy with lower thermal conductivity acts as the substrate for the freshly deposited material, and hence, the heat dissipation will be slower, leading to the formation of columnar grains. From the maximum intensity of the PF intensity maps for different planes, it is evident that the degree of anisotropy increases from the bottom to the top portion of the sample. A higher maximum intensity indicated higher anisotropy, which is found in the top portion of the sample, and the grains are mostly oriented in the (001) planes, as observed from the PF intensity maps. Due to the high heat input in WAAM, the deposition of a fresh layer leads to remelting of the already solidified layers beneath it. This leads to the same grain growing over several layers with identical orientations leading to anisotropy because of the inhomogeneous heat dissipation triggered by the migrating arc during the deposition [19].

The microhardness maps from different regions of the sample are shown in Figure 6a. In the bottom portion of the sample, a region with very low hardness (195–275 $HV_{0.3}$) was identified, which forms due to the diffusion of iron from the mild steel substrate, which was confirmed using an EDS line scan as shown in Figure 6b. The diffusion is found to be rapid as the effect of the Fe diffusion on the hardness can be found up to nearly 5 mm away

from the substrate. This suggests that the compatibility between the substrate and alloy to be deposited using WAAM is important, and a Ni alloy substrate can be employed to avoid the Fe diffusion in the 740H superalloy. Moreover, the hardness in the middle portion (320–400 $HV_{0.3}$) was higher than the top portion (240–275 $HV_{0.3}$) of the sample. This is because as the deposition progresses, heat accumulation occurs in the building. Since the top portion is farther away from the mild steel substrate, the heat transfer must happen through the previously deposited layers that will be slower, leading to grain coarsening with slower cooling rates and reduced hardness [20]. Accordingly, it has been observed from the grain structure analysis using EBSD (Figure 5) that the average grain size in the top portion of the build is 405 µm whereas the corresponding value in the bottom portion is 285 µm indicating coarsening of grains in the top portion of the build. It has also been reported that remelting during WAAM leads to inhomogeneous heat dissipation with increased nucleation rate and reduced growth rate, and this results in fine grains forming along the melt pool boundaries [19]. Since the middle portion experiences a higher number of remelting and solidification cycles when compared to the top region, the finer grains at the melt pool boundaries result in higher average hardness. With this observation, the middle portion is expected to possess higher residual stresses compared to the top and bottom regions.

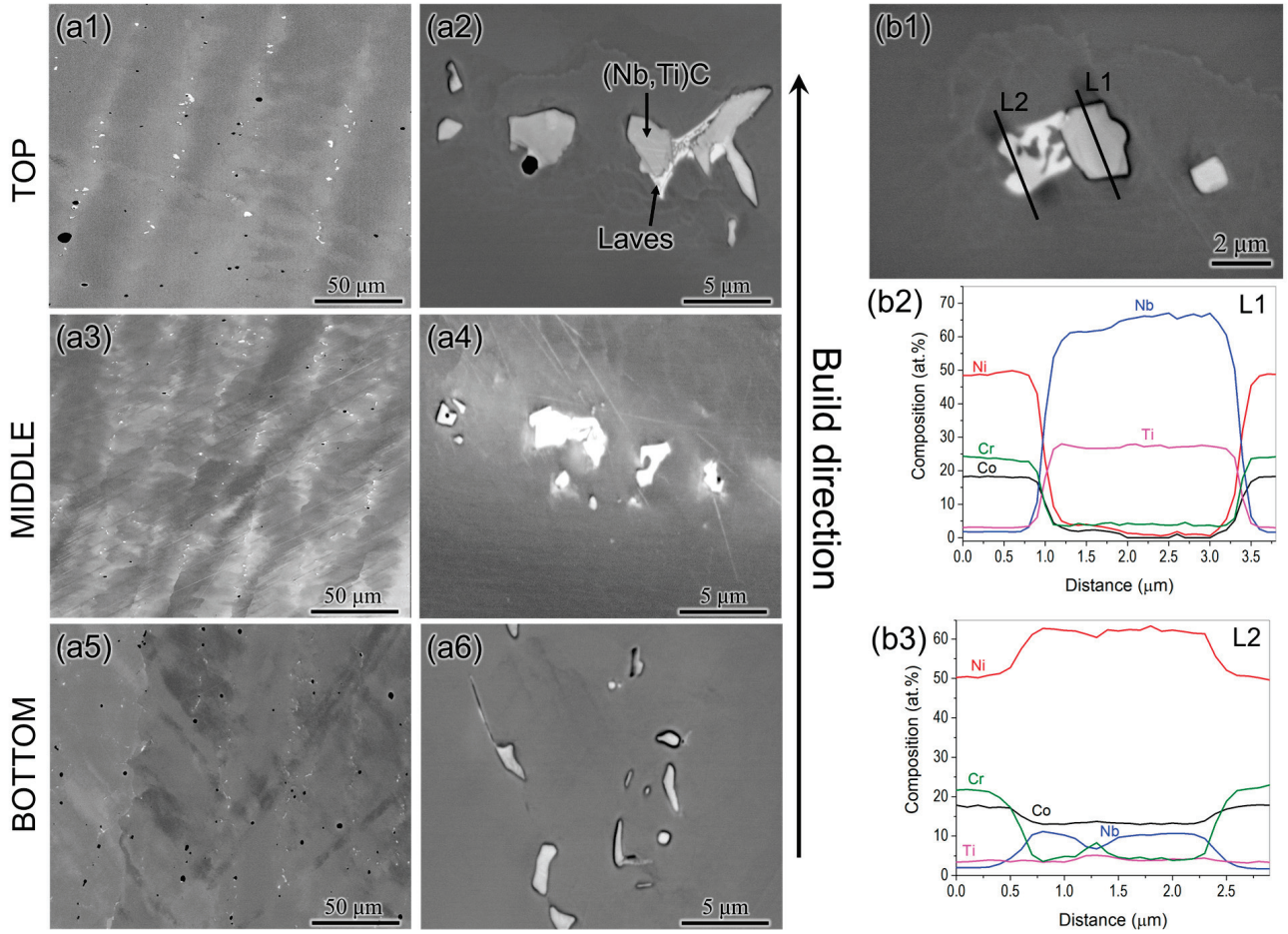

Figure 4. SEM micrographs from (**a1**,**a2**) top, (**a3**,**a4**) middle and (**a5**,**a6**) bottom portions of the WAAM 740H superalloy build in as -built condition showing a γ matrix with columnar grains and secondary phases such as the Laves phase and (Nb, Ti)C and (**b1**–**b3**) SEM micrograph of the second phases in the build and the corresponding EDS line scans confirming their composition. Li corresponds to (Nb,Ti)C phase and L2 denotes the Laves phase rich in Nb.

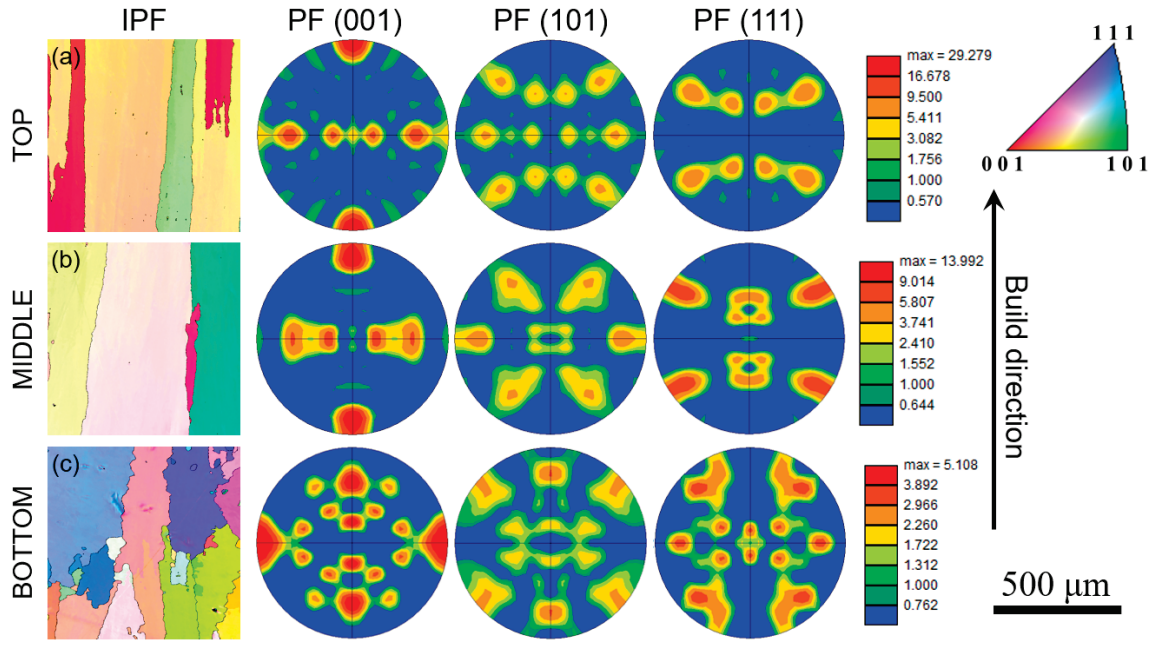

Figure 5. Inverse pole figure and pole figure intensity maps for (001), (101) and (111) planes obtained using electron backscattered diffraction from (**a**) top, (**b**) middle and (**c**) bottom portions of the WAAM 740H superalloy build in as-built condition showing the variation in anisotropy along the build direction.

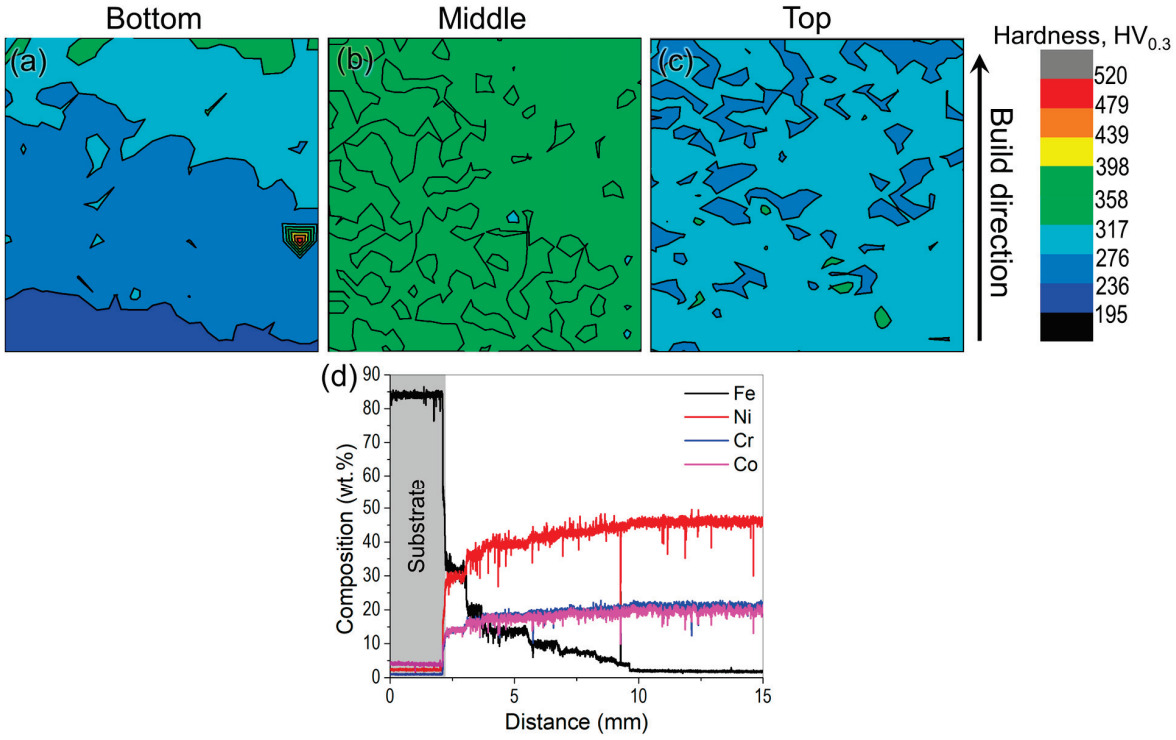

Figure 6. (**a**) Microhardness maps obtained from the (**a**) top, (**b**) middle and (**c**) bottom portions of the WAAM 740H superalloy build in as-built condition showing the drastic variation in microhardness in different regions along the build direction (area for each microhardness map is 3 × 3 cm^2) and (**d**) Composition as a function of distance from the substrate to the bottom portion of the build showing the diffusion of Fe into the 740H superalloy build for ~5 mm height of the build.

3.2. Post-Heat Treatment Design for WAAM Inconel 740H Superalloy

A two-step post-treatment will be designed for Inconel 740H superalloy fabricated using WAAM due to the microstructural heterogeneities in the as-built condition as elaborated in the previous sub-section. The anisotropic grains in the as-built WAAM 740H superalloy need to be recrystallized to obtain an isotropic equiaxed matrix, and the secondary precipitates, such as the Laves phase need to be dissolved into the matrix using the homogenization step. The aging step is required to induce the precipitation of strengthening phases, such as γ′, along with $M_{23}C_6$, to improve the mechanical performance. The standard heat treatment for Inconel 740H superalloy, as recommended by Special Metals Co., is homogenization above 1100 °C followed by air cooling or water quenching and aging in the temperature range of 760–816 °C for longer than 4 h [1]. The common practice for wrought Inconel 740H superalloy is homogenization at 1150 °C for 30 min, followed by water quenching and aging at 800 °C for 16 h [3].

3.2.1. Homogenization

As mentioned earlier, the homogenization temperatures were chosen based on the equilibrium phase fraction vs. temperature plot for the wire feedstock composition in Figure 3b. Since the standard heat treatment for wrought Inconel 740H superalloy needs homogenization at 1150 °C for 30 min, we chose the homogenization temperature around the standard heat treatment temperature to deduce the optimum time to avoid deviating excessively from it. The change in composition of Nb and Ti as a function of time obtained from the DICTRA simulations at 1100 and 1200 °C are shown in Figure 7. The flattening of the composition indicates that the precipitate has dissolved into the matrix. It is evident from this figure that the composition of Nb and Ti almost flattens close to 60 and 30 min at 1100 and 1200 °C, respectively. It is to be noted that the predicted time is only for dissolving the Laves phase into the matrix, however, recrystallization of microstructure is additionally required during homogenization.

Therefore, the homogenization heat treatment for the as-built WAAM 740H superalloy was performed at 1100 and 1200 °C for 1, 2, and 3 h, followed by water quenching. The SEM micrographs from the top, middle, and bottom portions of the samples homogenized at 1100 and 1200 °C for different times are shown in Figure 8. The homogenization heat treatments were performed at 1100 °C for 1, 2, and 3 h, however, it was found that the sample did not recrystallize completely, even after 3 h. The microstructure, after homogenization at 1100 °C for 3 h, retained the columnar microstructure (Figure 8a–c), indicating that this temperature is not sufficient to recrystallize the microstructure throughout the build. After homogenization for 1 h at 1200 °C, the matrix was recrystallized only in the middle portion and still retains the columnar grain structure in the top and bottom portions of the sample. However, no dominant Laves phase was found in the matrix, indicating its complete dissolution. This proves that the predicted homogenization time from the kinetic simulations is in good agreement with the experimental observations. It is also interesting to note that the microstructure in the middle region gets recrystallized faster than the top and bottom portions. This can be correlated with the higher residual stress in the middle region leading to higher hardness as observed from the hardness maps for the as-built WAAM 740H superalloy (Figure 6b). Since residual stresses are the major driving force for recrystallization, the higher residual stress in the middle portion promotes faster recrystallization than other regions. After homogenization at 1200 °C for 2 and 3 h, the matrix is completely recrystallized throughout the build accompanied by the formation of annealing twins (Figure 8g–l). It can be found that the grain size and annealing twins in the sample homogenized for 3 h are coarser than the 2 h homogenized sample. After homogenization at 1200 °C for 2 h, the average grain size was measured to be 600 μm while the corresponding value in as-built condition is 380 μm. Therefore, to avoid further grain coarsening after recrystallization, the optimum homogenization time was determined to be 2 h at 1200 °C.

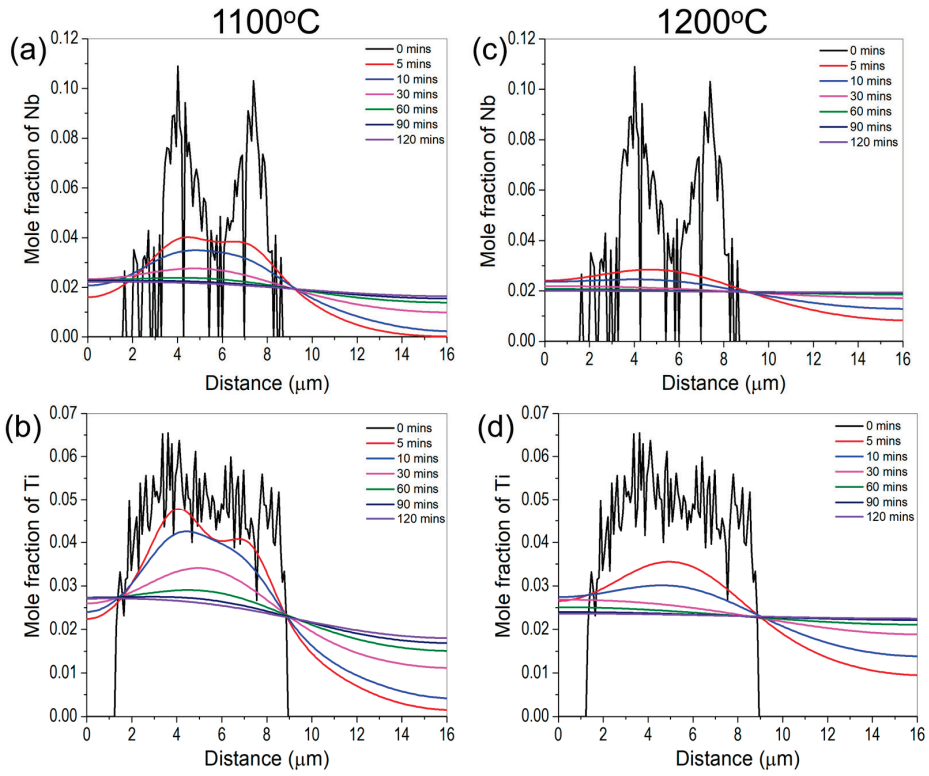

Figure 7. Calculated variation in composition of Nb and Ti as a function of distance for different times obtained from DICTRA at (**a**,**b**) 1100 °C and (**c**,**d**) 1200 °C showing the flattening of composition corresponding to the dissolution of the Laves phase.

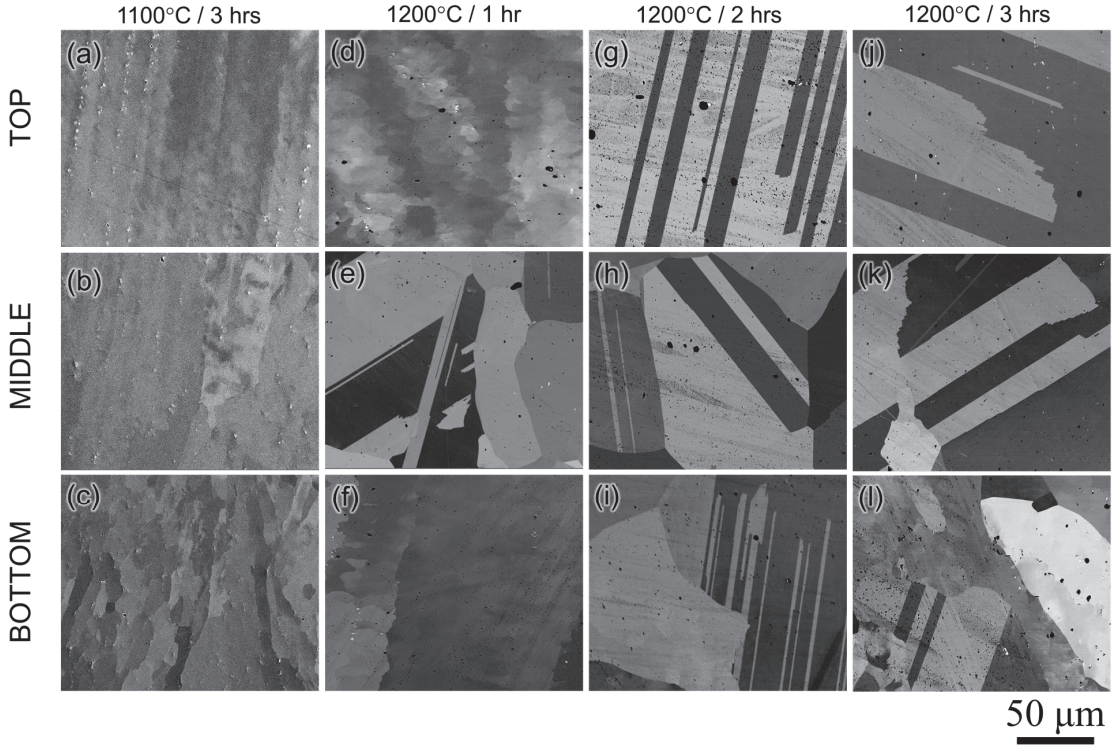

Figure 8. SEM micrographs from the top, middle and bottom regions of the sample homogenized at 1100 °C for (**a**–**c**) 3 h and 1200 °C for (**d**–**f**) 1 h, (**g**–**i**) 2 h and (**j**–**l**) 3 h showing complete recrystallization along with the formation of annealing twins for samples homogenized at 1200 °C for 2 and 3 h.

3.2.2. Aging

The aging temperature for WAAM 740H superalloy was identified as 760 °C, which is slightly lesser than the aging schedule from the standard heat treatment for wrought Inconel 740H superalloy, which is 800 °C for 16 h. This aging temperature was chosen for two reasons. Firstly, at 760 °C the maximum γ′ phase fraction was predicted according to the equilibrium phase fraction vs. temperature plot (Figure 3b). Secondly, this work is part of a project proposed for joining P91 steel with 740H superalloy using WAAM, and hence, we wanted to ensure the same post-heat treatments for both materials. Since aging at 800 °C leads to the formation of α-ferrite in P91 steel, the aging temperature was reduced by 40 °C for better compatibility. The aging heat treatment was performed after homogenization at 1200 °C for 2 h. The microhardness as a function of aging time (Figure 9a) shows that the peak hardness is achieved after aging at 760 °C for 12 h. The optimum aging time is found to be 4 h less than the standard aging time of 16 h, even though the standard aging temperature is higher than that chosen in this work. This observation can be attributed to the effective homogenization of the matrix at higher temperatures and longer time for WAAM 740H superalloy (1200 °C/2 h) compared to standard homogenization (1150 °C/30 min). The designed homogenization heat treatment has effectively dissolved the secondary phase, leading to higher supersaturation in the matrix, and hence, peak aging is achieved with shorter aging time at lower temperatures when compared to the standard aging heat treatment (800 °C/16 h).

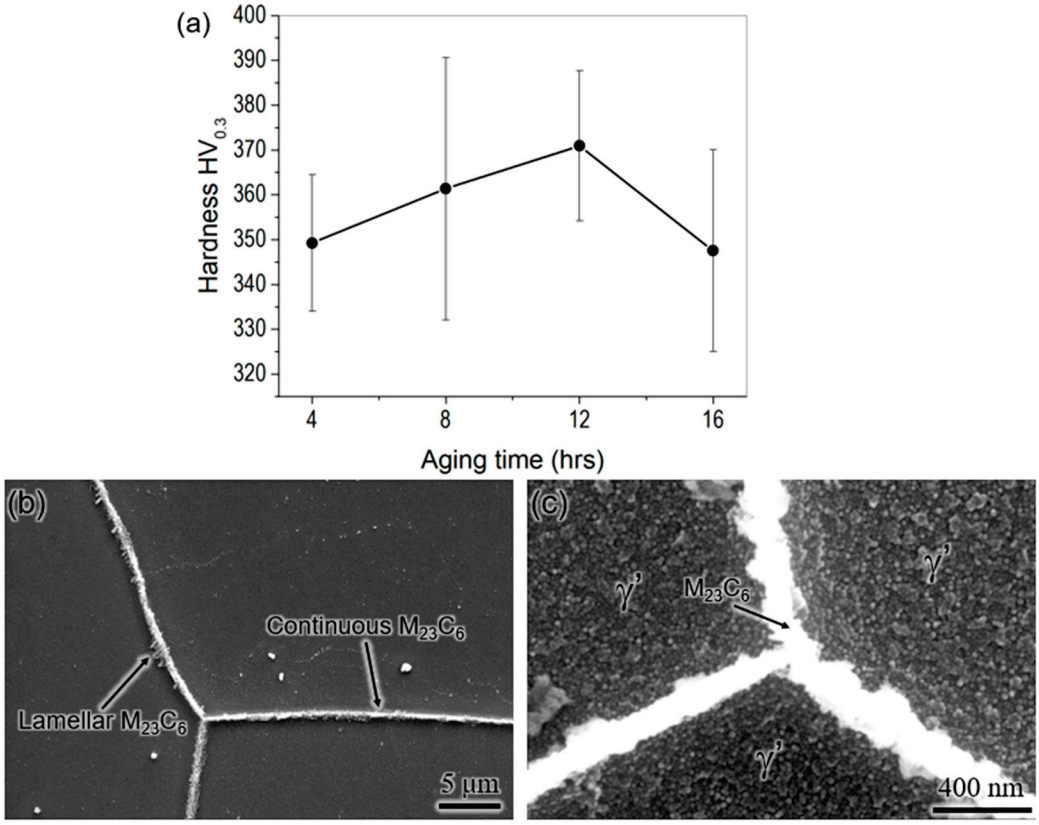

Figure 9. (**a**) Microhardness of aged WAAM 740H superalloy as function of aging time showing the peak hardness being achieved after 12 h of aging at 760 °C and (**b**,**c**) SEM micrographs from WAAM 740H superalloy aged at 760 °C for 12 h after etching indicating the presence of continuous and lamellar $M_{23}C_6$ in the grain boundaries and γ′ phase in the grain interior.

Figure 9b,c show the SEM micrographs of WAAM 740H superalloy aged at 760 °C for 12 h after etching. The grain boundaries were decorated with continuous and thin $M_{23}C_6$ precipitates, along with few lamellar $M_{23}C_6$ precipitates protruding away from the grain

boundary. Moreover, the grain interior was completely filled with the γ′ precipitates, which will lead to the strengthening of the material. Both phases are important for achieving excellent creep resistance in Inconel 740H superalloy, which has been precipitated in desired morphology using the post-heat treatment. The γ′ size was not measured from the SEM micrographs since it could not be resolved clearly. Therefore, an optimum post-heat treatment has been designed for WAAM 740H superalloy with homogenization at 1200 °C for 2 h and aging at 760 °C for 12 h. Its effectiveness will be evaluated by evaluating the mechanical properties, as explained in the upcoming section.

3.3. Mechanical Properties of WAAM Inconel 740H Superalloy

The engineering stress-strain curves, along with the tensile properties of WAAM 740H superalloy, in as-built and post-heat-treated conditions are shown in Figure 10a. The yield strength increases, and consequently, the ductility decreases with the application of the designed post-heat treatment. These quantities are well above the target in both as-built and post-heat treated conditions. However, the yield strength obtained in this work is lower than the corresponding values obtained for wrought 740H superalloy (~724 MPa) reported by Special Metals Co [1]. This can be attributed to the presence of gas pores throughout the build in the as-built condition and after applying the homogenization heat treatment. The fracture surface after the tensile test for post-heat treated WAAM 740H superalloy was observed using SEM, as shown in Figure 11a. It can be found that a ductile mode of fracture has occurred, which is confirmed by the presence of the dimples whereas small pores were also present, which could be gas pores. It has been reported that micropores and undetectable inhomogeneities in as-built conditions can coalesce to reduce the surface energy during the heat treatment to increase the porosity [21]. This emphasizes the application of hot isostatic pressing (HIP) to promote pore closure along with recrystallization of the microstructure. There are reports available in the literature that highlight the importance of HIP in improving the mechanical properties of alloys processed using different additive manufacturing techniques [22–24]. Hence, to improve the mechanical properties of WAAM 740H superalloy, HIP is necessary since the traditional furnace heat treatment without applied external pressure cannot induce pore closure. Another possible method to coalesce the gas pores is by fabricating Inconel 740H superalloy using hot forging WAAM [25], which is a new variant of WAAM that is capable of closing the pores during the deposition.

Stress rupture tests were performed under different stresses (375, 400, 425, and 450 MPa) at 750 °C for WAAM 740H superalloy after application of the designed post-heat treatment and compared with the performance of wrought Inconel 740H superalloy as shown in Figure 10b. Firstly, the applied stress (σ) and rupture time were collected from literature [26–29] for wrought Inconel 740H superalloy tested at 750 °C to evaluate the Larson-Miller (LM) parameter. From the plotted data available in the literature, excessive scatter in data points were observed for the LM parameters. A linear equation ($\sigma = -0.05735 \times LM + 1925$) was fitted to the LM parameter vs. applied stress plot and further extrapolated to the high-stress regime where the tests were performed in this work. On superimposing the LM parameters evaluated from the test results for post-heat treated WAAM 740H superalloy, it was found to coincide closely with the fitted line, as can be seen in Figure 10b. This proves that the stress rupture performance of WAAM 740H superalloy is comparable with its wrought counterparts. However, there is still scope for improving this property for the WAAM 740H superalloy by replacing the homogenization step with HIP to promote gas pore closure.

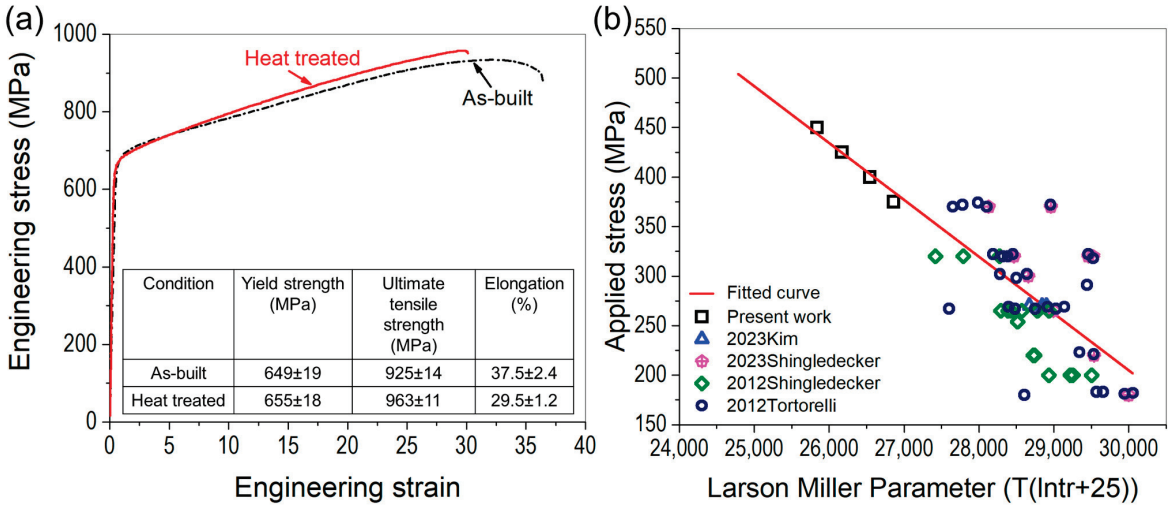

Figure 10. (**a**) Engineering stress-strain curves for WAAM 740H superalloy in as-built and post-heat treated conditions along the list of tensile properties compared with the design targets and (**b**) Larson-Miller parameter vs applied stress curve for the stress rupture performance showing that the post-heat treated WAAM 740H superalloy is at par with its wrought counterparts reported in literature.

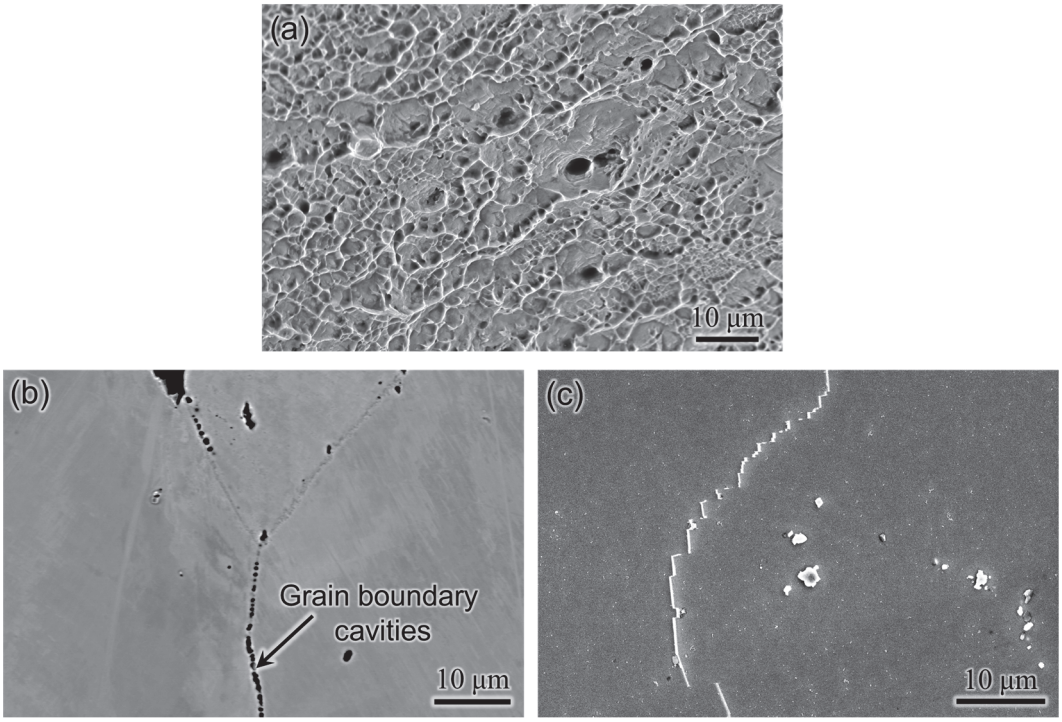

Figure 11. (**a**) Fractography after tensile testing for post-heat treated WAAM 740H superalloy showing a ductile mode of fracture with the presence of dimples along with small gas pores. SEM micrographs after stress rupture tests for WAAM 740H superalloy; (**b**) Grain boundary cavities close to the fracture surface indicating an intergranular mode of fracture and (**c**) Serrated grain boundaries showing grain boundary sliding during the application of stress at high-temperature.

The microstructural features after stress rupture tests were probed using SEM to understand the mechanism. No deleterious phases, such as the η phase, were observed after the stress rupture tests for the WAAM 740H superalloy. Near the fractured surface, cavities were observed along the grain boundaries, proving an intergranular mode of fracture, as shown in Figure 11b. Based on the reports available in the literature [27,30,31],

grain boundary cavities form mainly in the γ′ denuded zone region close to the grain boundary. The mechanism for the formation of γ′ denuded zone in the 740H superalloy has been identified as the discontinuous coarsening of the γ′ phase that is catalyzed by grain boundary migration and sliding during creep [32]. In support of this mechanism, grain boundary migration was confirmed with the presence of serrated grain boundaries after stress rupture tests in this work, as shown in Figure 11c. It is worth mentioning that no significant coarsening of γ′ precipitates was observed after the stress rupture tests.

4. Conclusions

In this work, a crack-free build of Inconel 740H superalloy was fabricated successfully using wire arc additive manufacturing along with post-heat treatment design. The as-printed microstructure comprised of columnar γ grains as the matrix along with the Laves and (Nb, Ti) C as secondary phases. The anisotropy in grain structure increased from the bottom to the top portion of the build. The hardness of the middle portion was the highest, while the bottom was lowest due to the diffusion of iron from the mild steel substrate. For the post-heat treatment design, homogenization and aging temperatures were identified from the thermodynamic calculation, while the homogenization time was predicted using kinetic simulations. The optimum homogenization temperature and time were identified as 1200 °C for 2 h due to the complete recrystallization of microstructure along the build and dissolution of the Laves phase. The optimum aging time at 760 °C with peak hardness (~370 HV) was found to be 12 h. The designed post-heat treatment was significantly different from the standard heat treatment available for wrought Inconel 740H superalloy. The microstructure in peak aged condition consisted of thin and continuous as well as protruding lamellar $M_{23}C_6$ along the grain boundaries and grain interiors filled with the γ′ precipitates. The yield strength (655 MPa) and ductility (29.5%) were above the design targets (620 MPa and 20%) after post-heat treatment. The stress rupture performance of the WAAM Inconel 740H superalloy was at par with its wrought counterpart with an intergranular mode of fracture along with grain boundary migration and fractured MC carbides. The mechanical performance of this alloy can be further improved by replacing the homogenization step with hot isostatic pressing to promote gas pore closure, which is the scope for future work.

Author Contributions: Conceptualization, W.X.; methodology, W.X.; software, S.S. and L.F.L.P.; validation, S.S. and L.F.L.P.; formal analysis, S.S. and L.F.L.P.; investigation, S.S., L.F.L.P., M.A.K. and W.X.; resources, W.X. and M.A.K.; data curation, S.S. and L.F.L.P.; writing—original draft preparation, S.S.; writing—review and editing, S.S., L.F.L.P., M.A.K. and W.X.; visualization, S.S. and L.F.L.P.; supervision, W.X.; project administration, W.X.; funding acquisition, W.X. and M.A.K. All authors have read and agreed to the published version of the manuscript.

Funding: This research was funded by National Energy Technology Laboratory, Department of Energy, United States, grant number DE-FE0031637.

Institutional Review Board Statement: Not applicable.

Informed Consent Statement: Not applicable.

Conflicts of Interest: The authors declare no conflict of interest.

References

1. De Barbadillo, J.J. INCONEL alloy 740H. In *Materials for Ultra-Supercritical and Advanced Ultra-Supercritical Power Plants*; Di Gianfrancesco, A., Ed.; Woodhead Publishing: Sawston, UK, 2017; pp. 469–510.
2. Brittan, A.M.; Mahaffey, J.; Anderson, M.; Sridharan, K. Effect of supercritical CO_2 on the performance of 740H fusion welds. *Mater. Sci. Eng. A* **2019**, *742*, 414–422. [CrossRef]
3. Chong, Y.; Liu, Z.D.; Godfrey, A.; Wang, L.; Liu, W.; Weng, Y.Q. Heat Treatment of a Candidate Material for 700 °C A-USC Power Plants. *J. Iron Steel Res. Int.* **2015**, *22*, 150–156. [CrossRef]
4. Ye, J.S.; Dong, J.X.; Zhang, M.C.; Yao, Z.H.; Zheng, L. Microstructure characteristics of TIG welding joint of 740H pipe for ultra-supercritical power plant boilers. *Mater. Sci. Forum* **2015**, *816*, 662–668. [CrossRef]
5. Xiao, B.; Zhang, N.; Li, K.; Zhu, Z.; Zhang, T.; Zhou, M. Corrosion behaviour of Ni-based alloy Inconel 740H in supercritical carbon dioxide at 650–700 °C. *Corros. Eng. Sci. Technol.* **2023**, *58*, 180–189. [CrossRef]
6. Gore, P.; Singh, M.P.; Suryateja, D.; Basu, B.; Chattopadhyay, K. Early-stage corrosion of IN 740H alloy in eutectic NaCl-KCl molten salt at high temperatures. *Sol. Energy* **2023**, *252*, 330–341. [CrossRef]
7. Mondal, B.; Gao, M.; Palmer, T.A.; DebRoy, T. Solidification cracking of a nickel alloy during high-power keyhole mode laser welding. *J. Mater. Process. Technol.* **2022**, *305*, 117576. [CrossRef]
8. Kopec, M.; Gorniewicz, D.; Kukla, D.; Barwinska, I.; Jóźwiak, S.; Sitek, R.; Kowalewski, Z.L. Effect of plasma nitriding process on the fatigue and high temperature corrosion resistance of Inconel 740H nickel alloy. *Arch. Civ. Mech. Eng.* **2022**, *22*, 57. [CrossRef]
9. Shingledecker, J.; de Barbadillo, J.; Gollihue, R.; Griscom, E.; Purdy, D.; Bridges, A. Development and performance of INCONEL® alloy 740H®seam-welded piping. *Int. J. Press. Vessel. Pip.* **2023**, *202*, 104875. [CrossRef]
10. Gore, P.; Gosain, O.P.; Singh, M.P.; Basu, B.; Chattopadhyay, K. Towards Understanding the Oxide Evolution in Inconel 740H and Haynes 282 in Ambient Pressure Steam Oxidation. *Oxid. Met.* **2022**, *97*, 509–525. [CrossRef]
11. Ali, Y.; Henckell, P.; Hildebrand, J.; Reimann, J.; Bergmann, J.P.; Barnikol-Oettler, S. Wire arc additive manufacturing of hot work tool steel with CMT process. *J. Mater. Process. Technol.* **2019**, *269*, 109–116. [CrossRef]
12. Rozman, K.A.; Detrois, M.; Jablonski, P.D.; Hawk, J.A. Mechanical performance of various INCONEL®740/740H alloy compositions for use in A-USC castings. In *Proceedings of the 9th International Symposium on Superalloy 718 & Derivatives: Energy, Aerospace, and Industrial Applications, The Minerals, Metals & Materials Series*; Springer International Publishing: Cham, Switzerland, 2018; pp. 611–627.
13. Zhao, Y.; Li, K.; Gargani, M.; Xiong, W. A comparative analysis of Inconel 718 made by additive manufacturing and suction casting: Microstructure evolution in homogenization. *Addit. Manuf.* **2020**, *36*, 101404. [CrossRef]
14. Li, K.; Sridar, S.; Tan, S.; Xiong, W. Effect of homogenization on precipitation behavior and strengthening of 17-4PH stainless steel fabricated using laser powder bed fusion. *arXiv* **2021**, arXiv:2112.06289.
15. Olson, G.B. Computational Design of Hierarchically Structured Materials. *Science* **1997**, *277*, 1237–1242. [CrossRef]
16. De Barbadillo, J.J.; Baker, B.A.; Gollihue, R.D.; Patel, S.J. Alloy 740H Component Manufacturing Development. In Proceedings of the Energy Materials 2014: Conference Proceedings, Xi'an, China, 4–6 November 2014; pp. 203–210.
17. *ASTM E8/E8M22*; Standard Test Methods for Tension Testing of Metallic Materials-Designation. American Society for Testing and Materials: West Conshohocken, PA, USA, 2004.
18. Sridar, S.; Zhao, Y.; Xiong, W. Phase Transformations During Homogenization of Inconel 718 Alloy Fabricated by Suction Casting and Laser Powder Bed Fusion: A CALPHAD Case Study Evaluating Different Homogenization Models. *J. Phase Equilibria Diffus.* **2021**, *42*, 28–41. [CrossRef]
19. Hassel, T.; Carstensen, T. Properties and anisotropy behaviour of a nickel base alloy material produced by robot-based wire and arc additive manufacturing. *Weld. World* **2020**, *64*, 1921–1931. [CrossRef]
20. Zuback, J.S.; DebRoy, T. The hardness of additively manufactured alloys. *Materials* **2018**, *11*, 2070. [CrossRef]
21. Hirsch, S.J.; Winter, L.; Grund, T.; Lampke, T. Heat Treatment Influencing Porosity and Tensile Properties of Field Assisted Sintered AlSi7Mg0.6. *Materials* **2022**, *15*, 2503. [CrossRef]
22. Sridar, S.; Zhao, Y.; Li, K.; Wang, X.; Xiong, W. Post-heat treatment design for high-strength low-alloy steels processed by laser powder bed fusion. *Mater. Sci. Eng. A* **2020**, *788*, 139531. [CrossRef]
23. Kumar, A.Y.; Bai, Y.; Eklund, A.; Williams, C.B. The effects of Hot Isostatic Pressing on parts fabricated by binder jetting additive manufacturing. *Addit. Manuf.* **2018**, *24*, 115–124.
24. Gussev, M.N.; Sridharan, N.; Thompson, Z.; Terrani, K.A.; Babu, S.S. Influence of hot isostatic pressing on the performance of aluminum alloy fabricated by ultrasonic additive manufacturing. *Scr. Mater.* **2018**, *145*, 33–36. [CrossRef]
25. Duarte, V.R.; Rodrigues, T.A.; Schell, N.; Miranda, R.M.; Oliveira, J.P.; Santos, T.G. Hot forging wire and arc additive manufacturing (HF-WAAM). *Addit. Manuf.* **2020**, *35*, 101193. [CrossRef]
26. Kim, D.M.; Kim, C.; Yang, C.H.; Park, J.U.; Jeong, H.W.; Yim, K.H.; Hong, H.U. Heat treatment design of Inconel 740H superalloy for microstructure stability and enhanced creep properties. *J. Alloys Compd.* **2023**, *946*, 169341. [CrossRef]
27. Shingledecker, J.P.; Pharr, G.M. The role of eta phase formation on the creep strength and ductility of inconel alloy 740 at 1023 k (750 °C). *Metall. Mater. Trans. A Phys. Metall. Mater. Sci.* **2012**, *43*, 1902–1910. [CrossRef]
28. Shingledecker, J.; Griscom, E.; Bridges, A. Relationship between Grain Size and Sample Thickness on the Creep-Rupture Performance of Thin Metallic Sheets of INCONEL Alloy 740H. *J. Mater. Eng. Perform.* **2023**. [CrossRef]

29. Tortorelli, P.F.; Yamamoto, Y.; Maziasz, P.J.; Moser, J.L.; Stevens, C.O.; Santella, M.L.; Shingledecker, J.P. Materials for Advanced Ultra-Supercritical (A-USC) Steam Boilers. In Proceedings of the 26th Annual Conference on Fossil Energy Materials, Oak Ridge, TN, USA, 17–19 April 2012.
30. Tortorelli, P.F.; Wang, H.; Unocic, K.A.; Santella, M.L.; Shingledecker, J.P.; Cedro, I.V. Long-Term creep-rupture behavior of Inconel 740 and Haynes 282. In Proceedings of the ASME Symposium on Elevated Temperature Application of Materials for Fossil, Nuclear, and Petrochemical Industries, Seattle, WA, USA, 25–27 March 2014; pp. 1–8.
31. Shingledecker, J.P.; Evans, N.D.; Pharr, G.M. Influences of composition and grain size on creep–rupture behavior of Inconel alloy 740. *Mater. Sci. Eng. A* **2013**, *578*, 277–286. [CrossRef]
32. Bechetti, D.H.; DuPont, J.N.; de Barbadillo, J.J.; Baker, B.A.; Watanabe, M. Microstructural Evolution of Inconel Alloy 740H Fusion Welds During Creep. *Metall. Mater. Trans. A* **2015**, *46*, 739–755. [CrossRef]

materials

MDPI

Article

Hot Deformation Behavior and Dynamic Softening Mechanism in 7B50 Aluminum Alloy

Ming Li [1], Yong Li [2,3,*], Yu Liu [2,3], Zhengbing Xiao [2,3] and Yuanchun Huang [1,2,3,*]

[1] School of Mechanical and Electrical Engineering, Central South University, Changsha 410083, China
[2] Research Institute of Light Alloy, Central South University, Changsha 410083, China
[3] State Key Laboratory of High Performance Complex Manufacturing, Central South University, Changsha 410083, China
* Correspondence: 18774826634@163.com (Y.L.); ychuang@csu.edu.cn (Y.H.)

Abstract: The hot deformation behavior and dynamic softening mechanism of 7B50 aluminum alloy were studied via isothermal compression experiments in the range of 320–460 °C/0.001–1.0 s^{-1}. According to the flow curves obtained from the experiments, the flow behavior of this alloy was analyzed, and the Zener–Hollomon (Z) parameter equation was established. The hot processing maps of this alloy were developed based on the dynamic material model, and the optimal hot working region was determined to be 410–460 °C/0.01–0.001 s^{-1}. The electron backscattered diffraction (EBSD) microstructure analysis of the deformed sample shows that the dynamic softening mechanism and microstructure evolution strongly depend on the Z parameter. Meanwhile, a correlation between the dynamic softening mechanism and the lnZ value was established. Dynamic recovery (DRV) was the only softening mechanism during isothermal compression with $\ln Z \geq 20$. Discontinuous dynamic recrystallization (DDRX) becomes the dominant dynamic recrystallization (DRX) mechanism under deformation conditions of $15 < \ln Z < 20$. Meanwhile, the size and percentage of DDRXed grains increased with decreasing lnZ values. The geometric dynamic recrystallization (GDRX) mechanism and continuous dynamic recrystallization (CDRX) mechanism coexist under deformation conditions with $\ln Z \leq 15$.

Keywords: 7B50 aluminum alloy; hot processing map; DRX mechanism; microstructure evolution

Citation: Li, M.; Li, Y.; Liu, Y.; Xiao, Z.; Huang, Y. Hot Deformation Behavior and Dynamic Softening Mechanism in 7B50 Aluminum Alloy. *Materials* **2023**, *16*, 5590. https://doi.org/10.3390/ma16165590

Academic Editor: Frank Czerwinski

Received: 18 July 2023
Revised: 9 August 2023
Accepted: 10 August 2023
Published: 12 August 2023

1. Introduction

7B50 aluminum alloy is particularly suitable for the production of high-performance large thick plates and large forgings due to its high strength, high toughness, and excellent hardenability [1–6]. With the development of large-scale and integrated structural components in the aerospace field, the 7B50 aluminum alloy with high comprehensive performance will also be further used widely [2,7].

High-temperature plastic deformation is often used to change the geometric shape and optimize the microstructure of 7××× series aluminum alloy materials. The thermal deformation parameters (such as strain, strain rate, and deformation temperature) during high-temperature plastic deformation can significantly affect the flow stress and microstructure evolution of the alloy [8–10]. Isothermal compression experiments are often used to investigate the thermal deformation behavior of metals by accurately controlling deformation temperature, strain rate, and deformation amount, and have been used widely in Al-Zn-Mg-Cu aluminum alloys [11–13]. Zhao et al. [14] discussed the influence of strain rate on the recrystallization behavior of 7050 aluminum alloy via isothermal compression experiments. The relevant research results indicated that a low strain rate is conducive to the development of DDRX, while CDRX dominates the deformation process of a high strain rate. Zhao et al. [15] developed two different constitutive models based on the influence of strain rate. Furthermore, Zhao et al. [16] investigated the effect of the forging rate on 7050 aluminum alloy bracket forgings. Li et al.'s study [17] on hot compression experiments

of Al-Zn-Mg-Cu alloy showed that CDRX under low temperature and high strain rates is mainly composed of micro-shear band assist and progressive lattice rotation near grain boundaries. Xu et al.'s research [18] on Al-Zn-Mg-Cu alloy showed that the increase of Z parameter will lead to an increase in the number of misorientation angles and low angle grain boundaries (LAGBs), while the dislocation density will decrease gradually.

Compared with 7050 aluminum alloy, 7B50 aluminum alloy appropriately increases the content of Zn and Mg elements, and further reduces the content of impurity elements, such as Fe and Si, by improving the melting and casting processes. Related studies [19–21] have confirmed that increasing the content of Zn and Mg elements can simultaneously improve the strength of 7××× aluminum alloy. In addition, the decrease in Fe and Si impurity element content can reduce the formation of hard and brittle second phase and improve the plastic formability of 7××× aluminum alloy [22]. 7B50 aluminum alloy for aviation is usually prepared into thick plates or large forgings via hot deformation processing methods such as hot rolling or hot forging. Therefore, the experimental research of the hot deformation behavior of 7B50 aluminum alloy can help to control the microstructure and improve the performance of the product. However, there are currently few reports on the hot deformation behavior of 7B50 aluminum alloy and the influence of Z parameters on microstructure evolution. Therefore, an in-depth understanding of the effects of the deformation parameters on the deformation behavior and microstructure of 7B50 aluminum alloys is required to manufacture 7050 aluminum alloy components with microstructure and properties that meet the requirements.

In order to investigate the hot deformation behavior and microstructure evolution of 7B50 aluminum alloy, isothermal compression experiments were conducted on the 7B50 aluminum alloy using a Gleeble-3800 isothermal simulation machine in the temperature range of 320–460 °C and the strain rate range of 0.001–1.0 s^{-1}. In this paper, the influence of deformation parameters on flow behavior is discussed using isothermal compression experiments on 7B50 aluminum alloy. Based on the Arrhenius constitutive model, the thermal deformation activation energy of 7B50 aluminum alloy was obtained, and the Z parameter equation of the alloy was established. The optimum hot processing parameter range of 7B50 aluminum alloy was determined by constructing its hot processing maps. Based on the EBSD microstructure analysis, the influence of Z parameters on microstructure was discussed and the relationship between Z parameters and the dynamic softening mechanism was established. The research work in this paper provides a basis for reasonably formulating the hot working process of 7B50 aluminum alloy and controlling the microstructure and properties of the product.

2. Materials and Methods

2.1. Experimental Materials and Isothermal Compression Tests

The experimental material was commercial 7B50 aluminum alloy produced by Chinalco Southwest Aluminum Co., Ltd. (Chongqing, China) The specific chemical composition is shown in Table 1.

Table 1. Chemical compositions of 7B50 aluminum alloy (wt. %).

Zn	Mg	Cu	Zr	Ti	Fe	Si	Al
6.35	2.15	2.10	0.10	0.02	0.06	0.03	Bal.

In order to reduce the composition segregation and improve the uniformity of the ingot microstructure, the as-cast 7B50 aluminum alloy was subjected to a two-step homogenization treatment at 400 °C/10 h + 470 °C/48 h. Hot compression standard specimens with a dimension of ϕ10 × 15 mm were machined via wire cutting. The Gleeble-3800 isothermal simulation machine (as shown in Figure 1b) was used for isothermal compression experiments, and the schematic diagram of isothermal compression is depicted in Figure 1. The temperature range was 320–460 °C, the strain rate range was 0.001–1.0 s^{-1},

and the compression deformation of the sample was 60% for the isothermal compression experiments. Graphite sheets were placed between the two end faces of the experimental sample and the moLd for lubrication. Before isothermal compression, the experimental sample was heated to the required temperature at a rate of 5 °C/s and held for 2 min to eliminate the temperature gradient. Water cooling was carried out immediately after compression to retain the deformed microstructure.

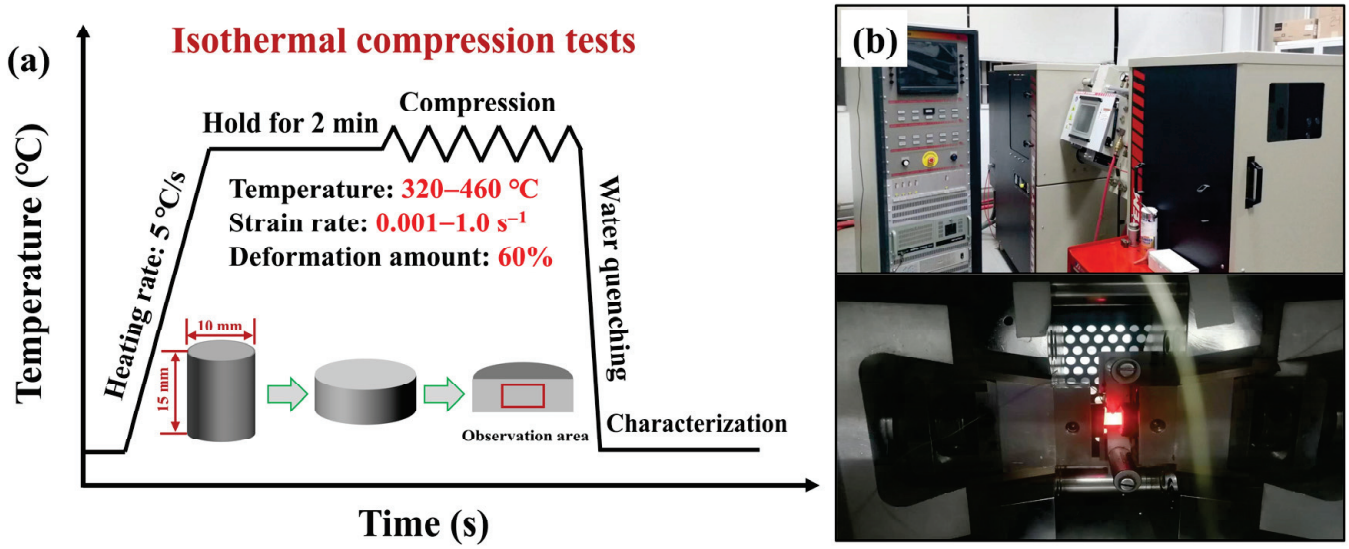

Figure 1. (**a**) Schematic diagram of isothermal compression and (**b**) the Gleeble isothermal simulation machine.

2.2. Microstructure Characterization

The sample after isothermal compression was symmetrically split along the compression direction (CD), and the microstructure at the center of the sample thickness position was characterized. The specimens used for observation were sequentially ground with sandpaper to 2000 grit and then mechanically polished. After mechanical polishing, the samples for EBSD observation were subjected to electropolishing treatment on a double-jet thinning instrument. The electropolishing solution was a mixture of 70% alcohol and 30% nitric acid. The temperature and voltage of electropolishing were −25 °C and 15V, respectively. The scanning electron microscope used for microstructure detection was the TESCAN MIRA3 equipped with an electron backscatter diffraction (EBSD) system. EBSD data was processed via channel5 software.

3. Results and Discussion

3.1. Initial Microstructures

The SEM and EBSD images of 7B50 aluminum alloy before hot deformation are displayed in Figure 2. The eutectic structure of as-cast 7B50 aluminum alloy partially dissolves during the two-step homogenization heat treatment (400 °C/10 h + 470 °C/48 h). Subsequently, a large number of fine $Mg(Al, Cu, Zn)_2$ phases precipitated inside the grains during the slow cooling process. Based on the inverse pole figure (IPF) diagram obtained by the EBSD system (Figure 2b), the microstructure before deformation is composed of coarsely equiaxed grains. The average grain size of as-homogeneous 7B50 aluminum alloy was calculated to be ~174 μm using the line intercept method.

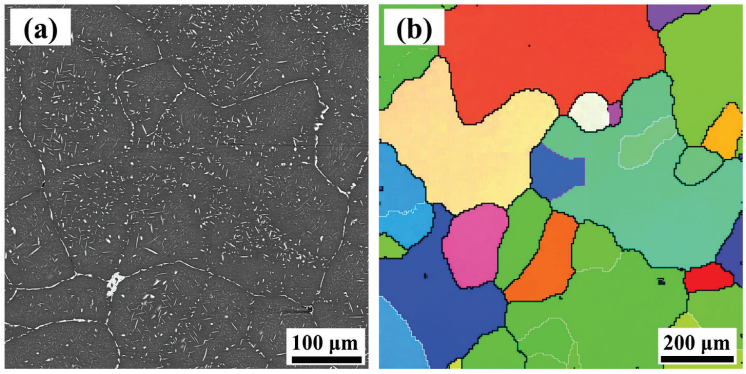

Figure 2. The initial microstructures of as-cast 7B50 alloy: (**a**) SEM image, (**b**) EBSD map.

3.2. Flow Behavior

3.2.1. Flow Stress Curves

Figure 3 displays the flow stress curves of 7B50 aluminum alloy during hot compression at 320–460 °C/0.001–1.0 s^{-1}. In the early stage of deformation, all flow curves rise rapidly, which is a typical work-hardening phenomenon caused by the proliferation of dislocation density [23]. However, the subsequent flow behavior is highly sensitive to the strain rate and deformation temperature. At low temperatures and high strain rates, the flow curves increase slowly with deformation, and there is no peak phenomenon in the flow stress curves. At high temperatures and low strain rates, the flow curves quickly reach their peaks and then slowly decrease and stabilize. The differences in flow stress curves are closely related to the dynamic softening mechanisms (DRV and DRX) during deformation [23,24]. As is well known, the decrease in dislocation density during hot deformation is caused by the dynamic softening behavior of the alloy. The different softening mechanisms mediated by the deformation temperature and strain rate differ in the rate and method of eliminating dislocation density, ultimately leading to significant differences in the flow stress curves.

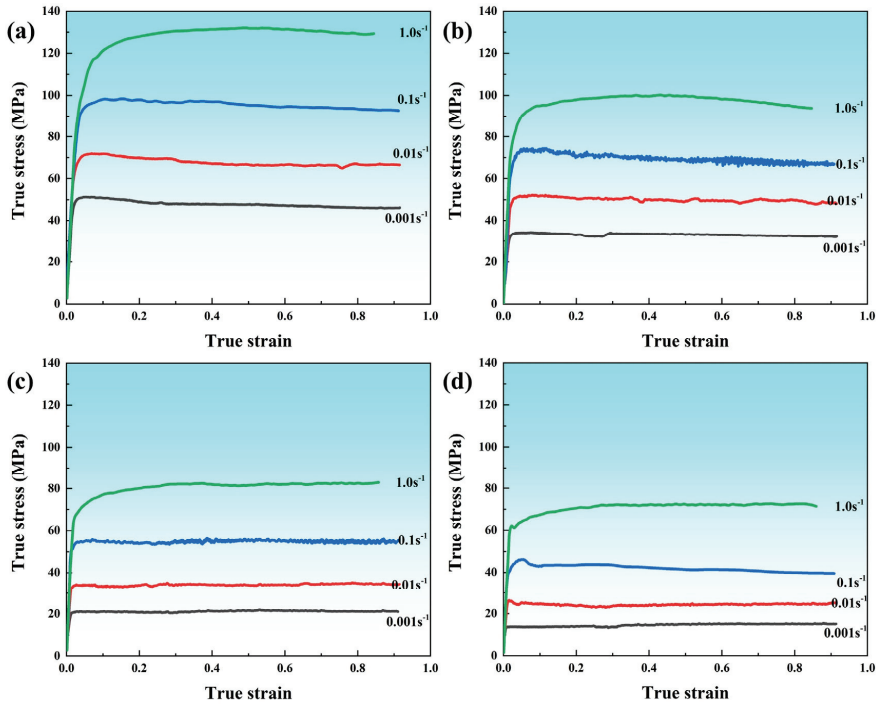

Figure 3. True stress-strain curves under different deformation conditions during isothermal compression: (**a**) 320 °C, (**b**) 370 °C, (**c**) 420 °C, (**d**) 460 °C.

3.2.2. The Zener–Hollomon Parameter

Zener and Hollomon jointly proposed using an exponential equation to describe the comprehensive effect of strain rate and deformation temperature and the equation of Z parameter is as follows [18]:

$$Z = \dot{\varepsilon} exp\left(\frac{Q}{RT}\right) \tag{1}$$

where $\dot{\varepsilon}$ (s^{-1}) and T (K) are the strain rate and deformation temperature, R represents the gas constant (8.314 kJ/moL), and Q (kJ/moL) represents the activation energy of deformation, which describes the difficulty of deformation. Furthermore, the Arrhenius constitutive model commonly used to describe the flow curves can be represented as follows:

$$\dot{\varepsilon} = AF(\sigma)exp\left(-\frac{Q}{RT}\right) \tag{2}$$

$$F(\sigma) = \begin{cases} \sigma^N & (\alpha\sigma < 0.8) \\ exp(\beta\sigma) & (\alpha\sigma \geq 0.8) \\ [sin(\alpha\sigma)]^n & (For\ all) \end{cases} \tag{3}$$

where N, β, α ($\alpha = \beta/N$), A, and n are material constants. According to Equation (3), the values of N and β are the slope values of the $ln\dot{\varepsilon}$-$ln\sigma$; and $ln\dot{\varepsilon}$-σ, which can be obtained by linearly fitting the data of Figure 4a,b when the strain is 0.8.

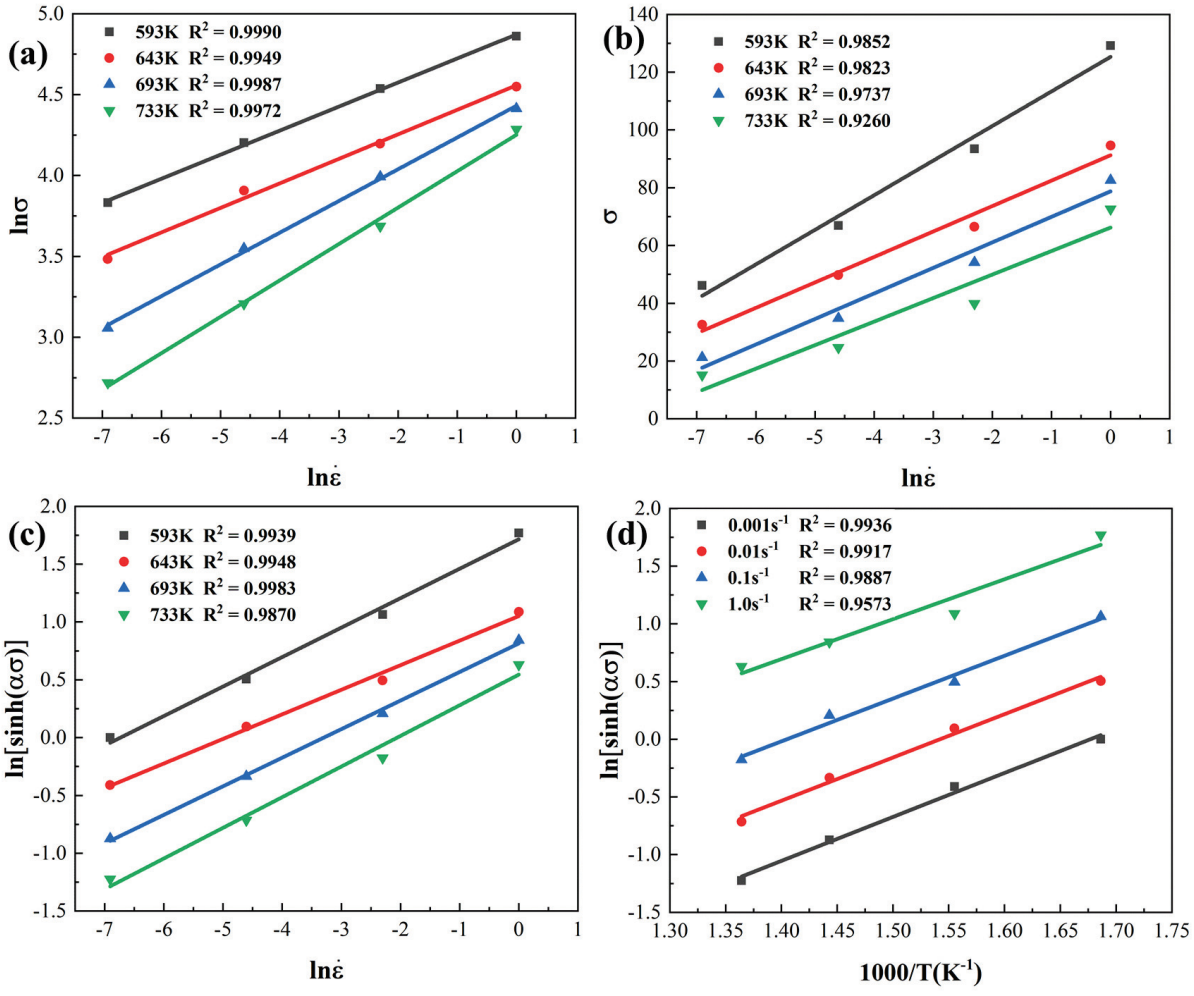

Figure 4. Linear fitting of the relationship between (**a**) $ln\dot{\varepsilon}$-$ln\sigma$, (**b**) $ln\dot{\varepsilon}$-σ, (**c**) $ln\dot{\varepsilon}$-$ln[sinh(\alpha\sigma)]$, and (**d**) $ln[sinh(\alpha\sigma)] - 1/T$ under different deformation conditions.

According to Equation (3), the deformation activation energy Q can be expressed as:

$$Q = R\left[\frac{\partial ln\dot{\varepsilon}}{\partial ln[sinh(\alpha\sigma)]}\right]_T\left[\frac{\partial ln[sinh(\alpha\sigma)]}{\partial(1/T)}\right]_{\dot{\varepsilon}} = Rns \tag{4}$$

Therefore, based on the obtained α value, the slope values of $ln\dot{\varepsilon}$-$ln[sinh(\alpha\sigma)]$ and $ln[sinh(\alpha\sigma)] - 1/T$ are obtained by linear fitting. The calculated average thermal activation energy Q using the same method is only 130.85 kJ/moL. Numerous scholars have studied the heat deformation behavior of 7050 aluminum alloy (the alloy composition is basically the same as that of 7B50 aluminum alloy). Deng et al. [25] calculated that the Q value of 7050 aluminum alloy after two-step homogeneous heat treatment was 160.3 kJ/moL. The Q value of the solid solution 7050 aluminum alloy after extrusion was confirmed to be 179.53 kJ/moL by Zhao et al. [14]. In addition, Wang et al. [26] investigated the thermal deformation behavior of the Al-6.32Zn-2.10Mg-0.1Cu alloy and showed that the Q value of the alloy after reducing Cu content was still as high as 147.81 kJ/moL. The above data indicate that the 7B50 aluminum alloy in this study has better processing performance compared to the traditional 7050 aluminum alloy. Based on the calculated Q value, the lnZ values under different conditions can be obtained using Equation (1) and are shown in Figure 5. There is a close correlation between the Z parameter and the dynamic softening mechanism and microstructure. Xu et al. [18] proposed that the Geometric DRX dominated at $\ln Z \leq 23.44$, CDRX dominated at $23.4 < \ln Z < 33.33$, and DDRX dominated at $\ln Z \geq 33.33$ for Al-Zn-Mg-Cu alloy. The results of thermal deformation studies on 7050 aluminum alloy conducted by Zhao et al. [15] showed that the DDRX mechanism gradually transformed into the CDRX mechanism with increasing Z parameter. Next, the effects of Z parameter on the hot working behavior, microstructure evolution, and dynamic softening mechanism were investigated by focusing on hot processing maps and microstructure analysis.

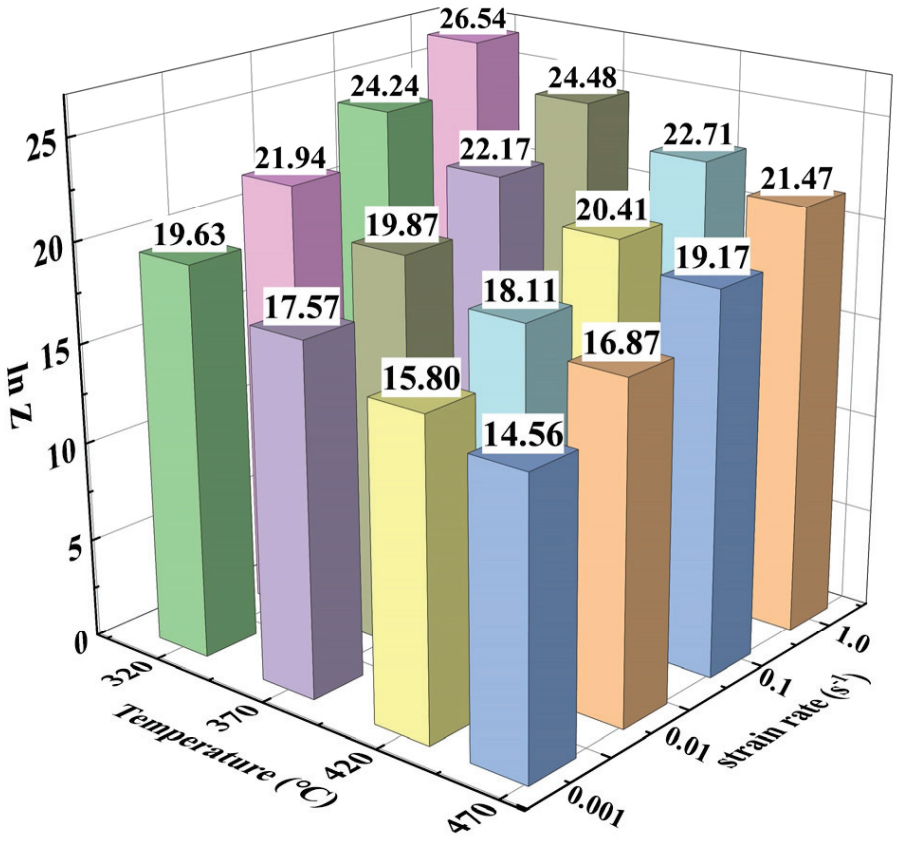

Figure 5. LnZ values under different deformation conditions.

3.2.3. Hot Processing Map

Hot processing maps based on the dynamic material model are widely used to guide the hot plastic working of aluminum alloys [26,27]. Figure 6 illustrates the hot processing maps under different strain conditions, and the details of establishing the hot processing maps can be referred to in the literature [18,28–31]. In the figure, the blue area represents the unstable processing domains that should be avoided during hot plastic processing. The blue unstable domains are mainly distributed in the high strain rate range and increase progressively with increasing strain. The contour lines in the figure are the power dissipation efficiency (η), which represents the percentage of energy used for microstructure evolution. The optimum processing conditions for the experimental 7B50 aluminum alloy can be seen in the hot processing maps as 410–460 °C/0.01–0.001 s^{-1}.

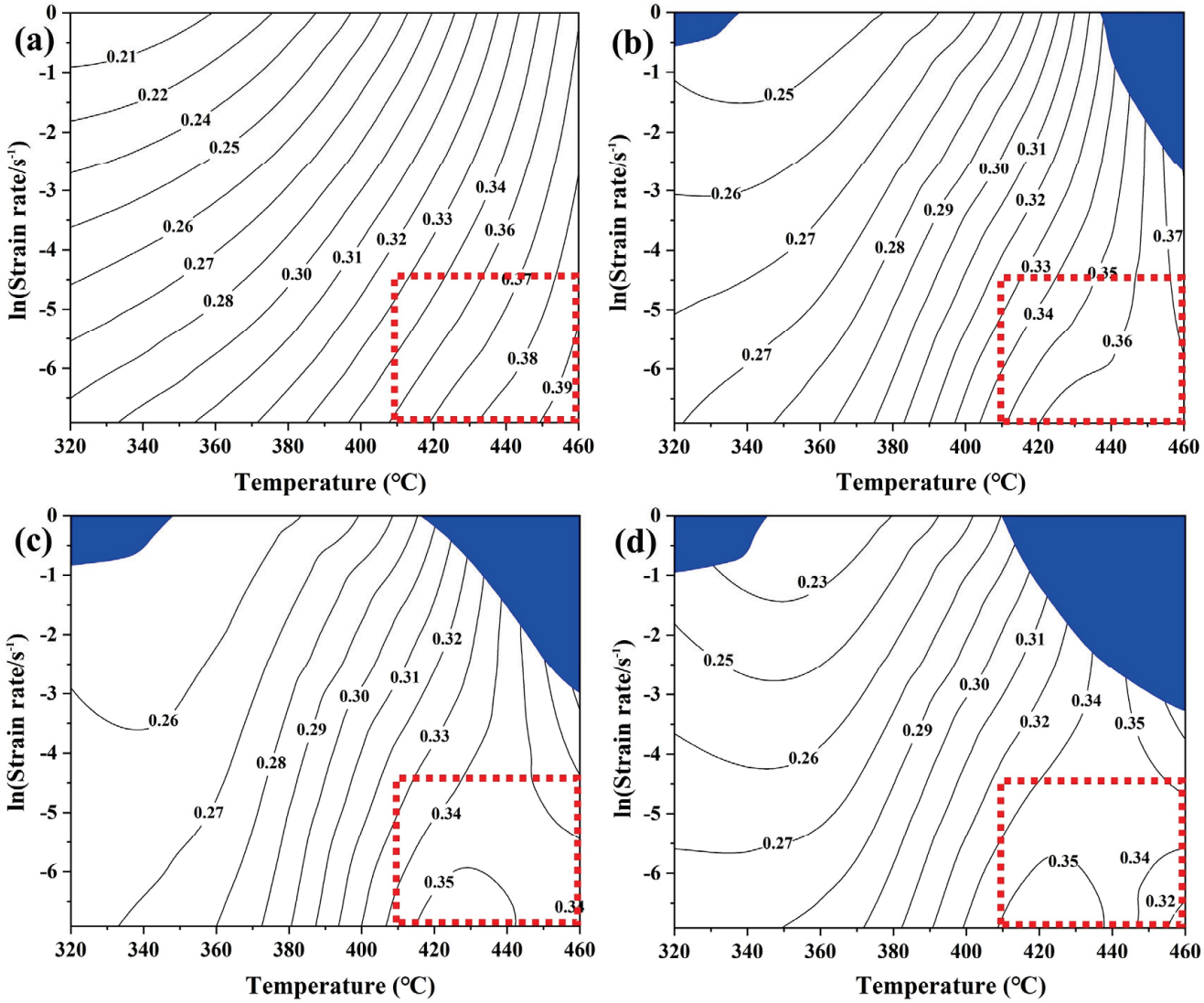

Figure 6. Hot processing maps of 7B50 alloy under different strains: (**a**) 0.2, (**b**) 0.4, (**c**) 0.6, (**d**) 0.8.

It is well known that aluminum alloys belong to high stacking fault energy metals, which are prone to dislocation climb and cross-slip due to the narrow expansion width of dislocations. Therefore, DRV, rather than DRX, usually dominates the thermal deformation process of aluminum alloys. However, the significant dynamic recrystallization behavior of 7××× aluminum alloy has also been reported in much of the literature due to the addition of large numbers of various alloying elements [32–36]. Ren et al.'s research [37] shows that the dynamic softening mechanism of 7055 aluminum alloy gradually changes from DRV to

DRX as the η value increases. When the η value is greater than 50%, the microstructure is composed of fully dynamic recrystallized grains. The range of power dissipation efficiency values in this study is 0.22–0.36, which may lead to the occurrence of DRV and partial DRX.

3.3. Microstructural Evolution and Dynamic Softening Behavior

3.3.1. At High lnZ Values (lnZ ≥ 20)

Figure 7 shows the IPF maps and grain boundary misorientation angle distribution diagrams under the deformation conditions of 420 °C/1.0 s^{-1} and 420 °C/0.1 s^{-1} (lnZ ≥ 20). In the IPF maps, the high-angle grain boundaries (HAGBs) with a misorientation angle greater than 10° is represented by a black solid line, while the white solid line is the low-angle grain boundaries (LAGBs) with a misorientation angle of 2–10°. As can be seen, the microstructure under high lnZ values exhibits typical deformation characteristics. The coarse original grains are elongated perpendicular to the compression direction. There are a large number of distributions of discontinuous and staggered LAGBs within the matrix, which have not formed obvious sub-grains. The grain boundary misorientation angle distributions in Figure 7c,d show that the proportion of LAGBs is as high as 72.4% and 72.2%, which is much higher than the proportion of LAGBs before deformation (18.2%). Meanwhile, the uniform distribution of LAGBs within the matrix indicates that the experimental alloy undergoes uniform deformation during isothermal compression.

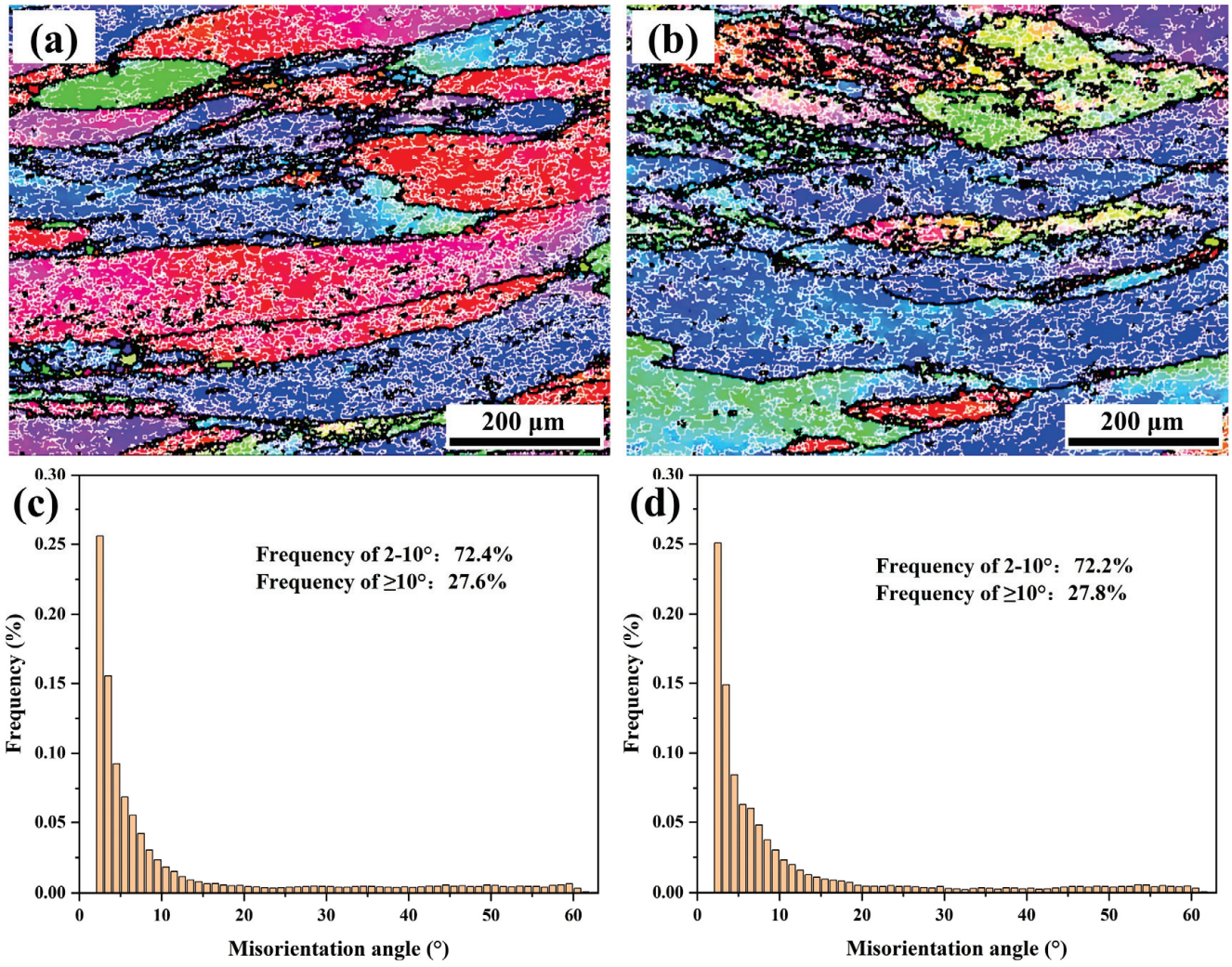

Figure 7. IPF maps and misorientation angle distributions at high lnZ values: (**a**,**c**) lnZ = 22.71 (420 °C, 1 s^{-1}), (**b**,**d**) lnZ = 20.41 (420 °C, 0.1 s^{-1}).

The deformation behavior of individual grains under the deformation condition of lnZ = 22.71 (420 °C, 1 s^{-1}) is presented in Figure 8. The IPF map and crystal orientation models in Figure 8a show that there are orientation differences within the deformed grains. The continuous fluctuation of the relative misorientation angle along arrow L1 in Figure 8b indicates that there are a large number of sub-structures with different orientations within the deformed grains. The corresponding cumulative misorientation angle is close to 20°, manifesting that this grain accommodates large plastic deformation [38]. The {001} pole figure (PF) in Figure 8c shows that the {011} < 100 > direction of this grain is parallel to the CD. Dislocation slip causes the distribution of the {001} PF of this grain to shift along the CD after plastic deformation. Therefore, 7B50 aluminum alloy mainly undergoes dynamic recovery softening under the condition of lnZ $\geq$ 20.

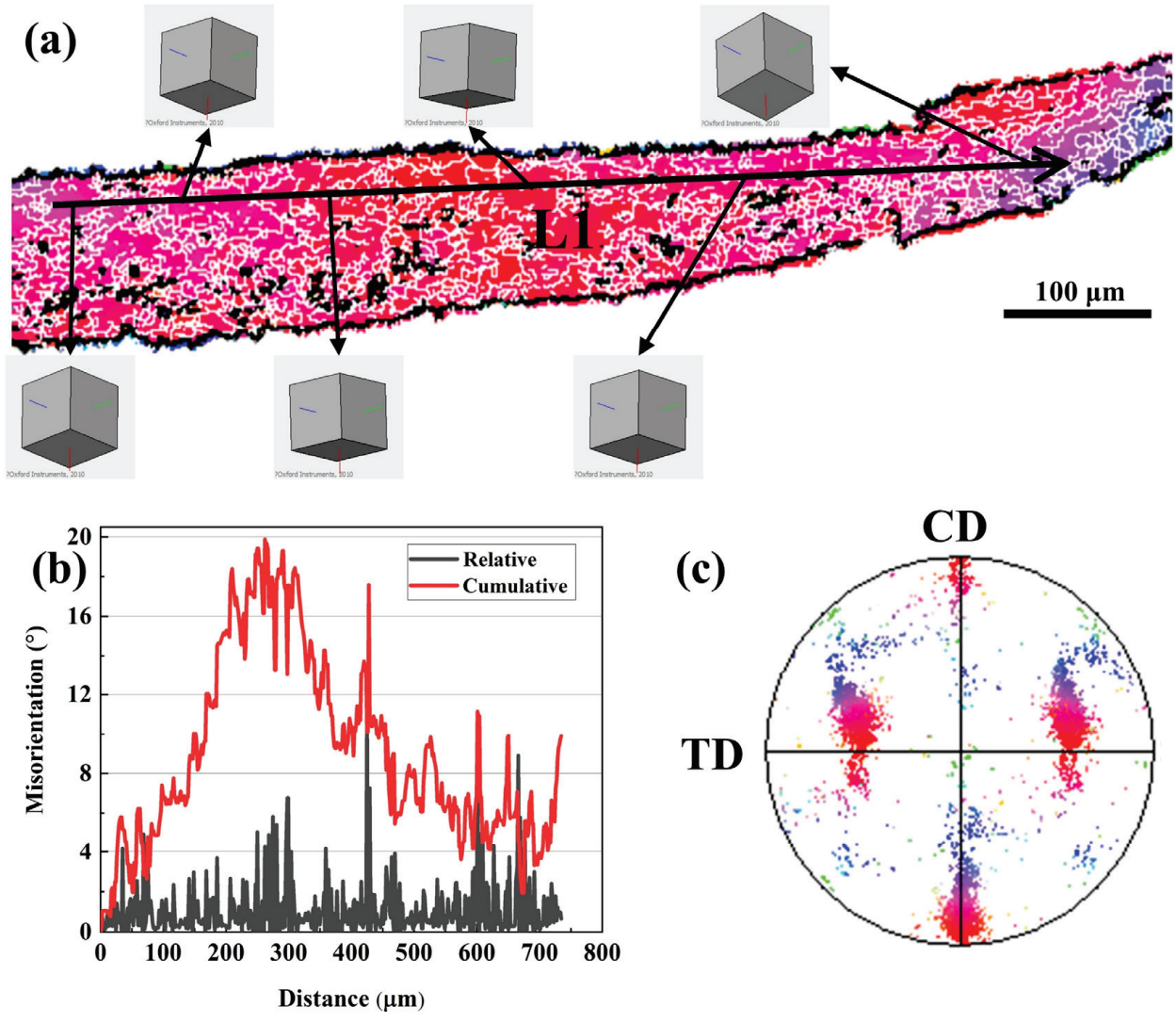

Figure 8. Deformation behavior of individual grain at lnZ = 22.71 (420 °C, 1 s^{-1}): (**a**) IPF map and crystal orientation model, (**b**) relative and cumulative misorientation angle, and (**c**) {001} PF.

3.3.2. At Middle lnZ Values (15 < lnZ < 20)

Figure 9 shows the IPF maps, misorientation angle distributions, and relative and cumulative misorientation angle of lnZ between 15 and 20. Careful observation of Figure 9a–d shows that there are fine DRXed grains at the initial grain boundary (as shown by the yellow arrows). The formation of these DRXed grains is related to the original grain boundary bulging, which is a typical DDRX [39]. The number and size of fine DRXed grains at the initial grain boundaries gradually increase with the decrease in lnZ value. In Figure 9e–h,

the proportion of HAGBs increases from 30.0% to 42% as the lnZ value decreases from 19.63 to 15.8. Therefore, 7B50 aluminum alloy mainly exhibits discontinuous dynamic recrystallization under conditions of 15 < lnZ < 20. Another significant feature is that the number of LAGBs inside the grains decreases rapidly with the decreasing in lnZ value, and the distribution of LAGBs gradually changes from discontinuous to continuous. The relative and cumulative misorientation angles of the straight lines L2–L5 within the grains under different lnZ values are shown in Figure 9i–l. The cumulative misorientation angles all exceed 10°, but the fluctuation of relative misorientation angles gradually weakens with the decrease in lnZ value. This indicates that dynamic recovery softening still exists under middle lnZ values.

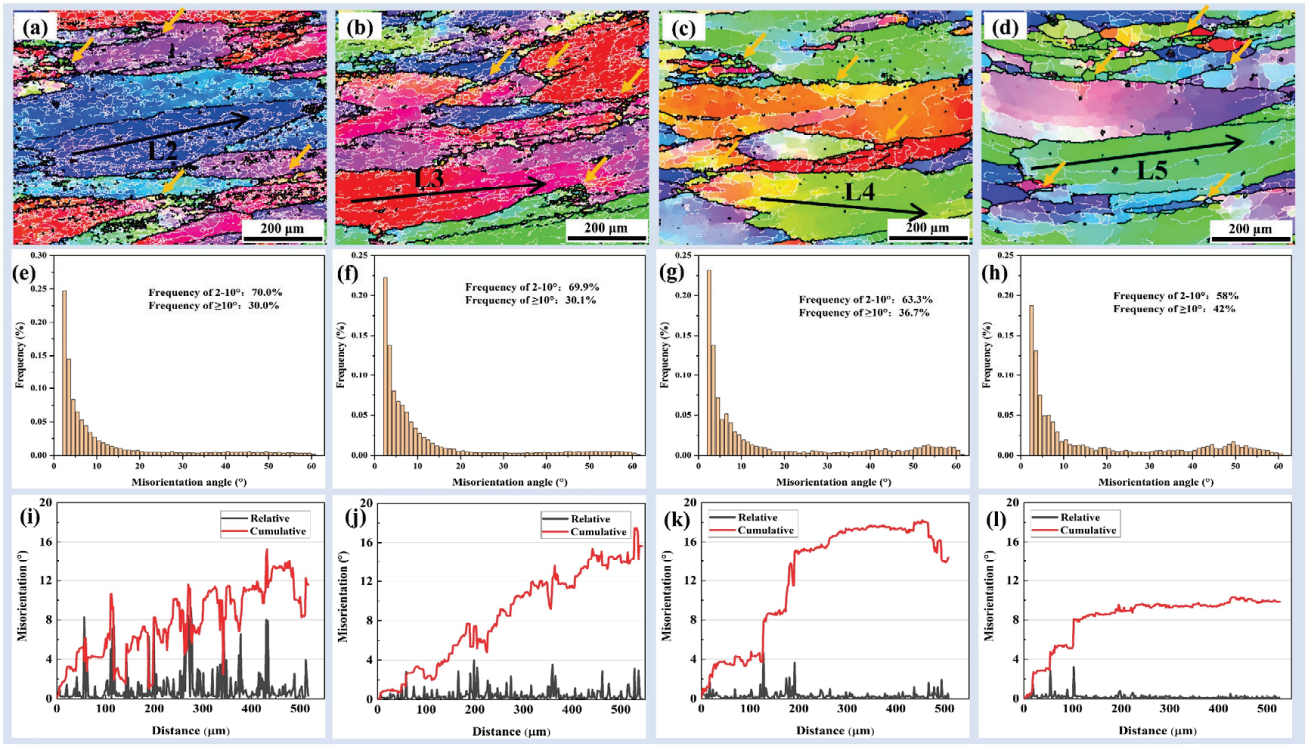

Figure 9. IPF maps, misorientation angle distributions and relative and cumulative misorientation angle at middle lnZ values: (**a**,**e**,**i**) lnZ = 19.63 (320 °C, 0.001 s^{-1}); (**b**,**f**,**j**) lnZ = 18.11 (420 °C, 0.01 s^{-1}); (**c**,**g**,**k**) lnZ = 17.57 (370 °C, 0.001 s^{-1}); (**d**,**h**,**l**) lnZ = 15.80 (420 °C, 0.001 s^{-1}).

3.3.3. At Low lnZ Values (lnZ ≤ 15)

Figure 10 shows the IPF map and misorientation angle distribution diagram at lnZ ≤ 15. The microstructure after deformation at 460 °C/0.001 s^{-1} is composed of partial dynamic recrystallization as shown in Figure 10a. The proportion of DRX and the size of DRXed grains are higher than the deformation condition of 15 < lnZ < 20. The proportion of corresponding HAGBs increases to 46.8%. Meanwhile, the LAGBs inside the grains become flat and continuous, and the corresponding proportion of the LAGBs decreases to 53.2%. In addition, a large number of sub-grains composed of LAGBs were formed inside the initial grains. These phenomena indicate that there is a remarkable difference between the DRX mechanism under the condition of lnZ ≤ 15 and 15 < lnZ < 20.

To investigate the DRX mechanism under deformation conditions of lnZ ≤ 15, the typical regions in Figure 10a were enlarged and displayed in Figure 11a,b,e. As shown in Figure 11a,b, a large number of elongated grains perpendicular to the compression direction are present in the deformation condition of 460 °C/0.001 s^{-1} (Figure 10a). The HAGBs in the sample before deformation are close to each other and almost parallel under compression. Meanwhile, LAGBs perpendicular to HAGBs are formed under the dynamic recovery effect. The elongated deformed grains are divided into brick-like sub-grains by

LAGBs as shown in Figure 11a. The relative and cumulative misorientation angles along L6 indicate that the orientation within the sub-grain is basically consistent under the effect of dynamic recovery, while the misorientation angles near the sub-grain boundary are 5.3° (point A) and 2.5° (point B), respectively. In the subsequent deformation process, LAGBs gradually transform into HAGBs as shown in Figure 11b by absorbing the deformation dislocations and sub-grain rotation. The relative misorientation angles along L7 show that the misorientation angles of HAGBs perpendicular to the original grain boundary are 10–20°, which indicate that these HAGBs are transformed by LAGBs [23,27]. These characteristics are consistent with the typical GDRX phenomenon [40–43]. Therefore, GDRX is the main dynamic softening mechanism under the condition of $\ln Z \leq 15$.

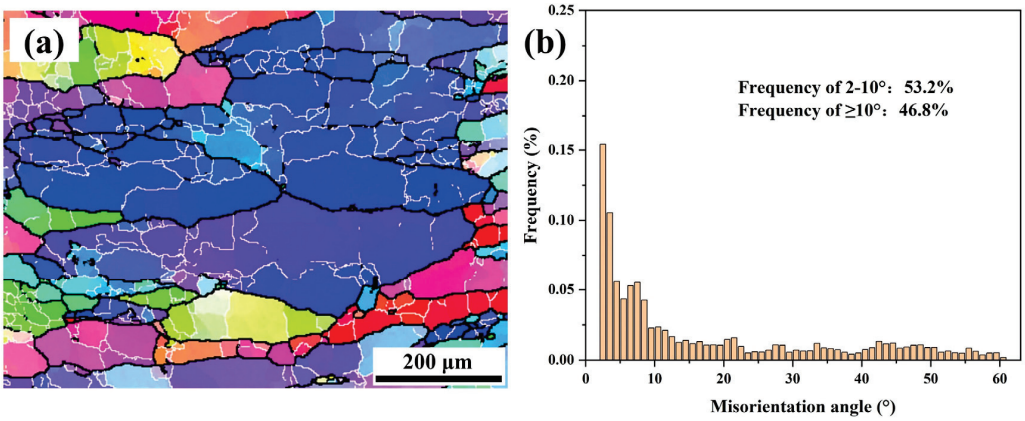

Figure 10. IPF map (**a**) and misorientation angle distributions (**b**) at low lnZ values (lnZ = 14.56, 460 °C/0.001 s^{-1}).

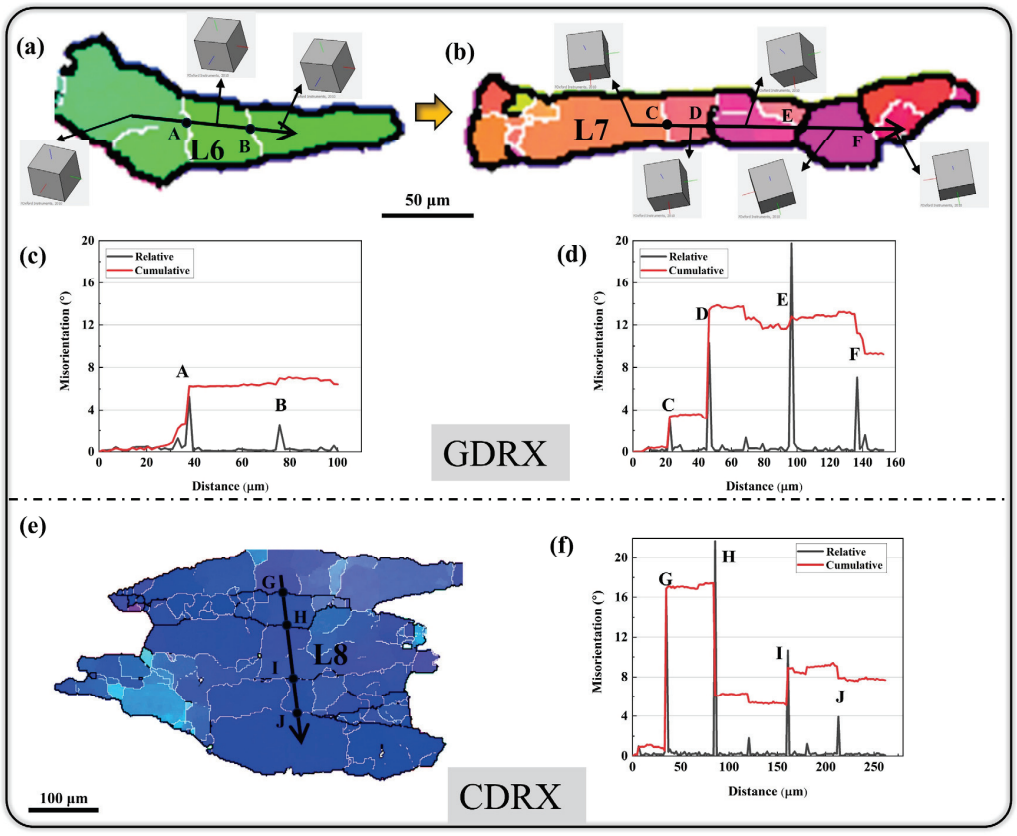

Figure 11. GDRX (**a**–**d**) and CDRX (**e**,**f**) mechanisms at low lnZ values (lnZ = 14.56, 460 °C/0.001 s^{-1}).

Furthermore, some CDRX phenomena also exist under the deformation condition of $\ln Z \leq 15$ as shown in Figure 11e. The CDRX mechanism involves the formation and rotation of sub-grains, which is clearly different from the grain boundary bulging behavior in DDRX mechanism. A large number of sub-grains consisting of LAGBs are present in Figure 11e. There is a small misorientation between sub-grains as shown in the crystal orientation model. During the subsequent deformation process, the sub-grains are transformed into DRXed grain via rotation, and the low-angle sub-grain boundaries are also transformed into HAGBs (as shown in Figure 11f). Therefore, both GDRX and CDRX mechanisms exist under low lnZ values.

4. Conclusion

In this paper, the hot deformation behavior and dynamic softening mechanism of 7B50 aluminum alloy were systematically studied via isothermal compression experiments at 320–460 °C/0.001–1.0 s^{-1}. The main research findings are as follows:

1. Based on the Arrhenius conservative equation, the deformation activation energy of 7B50 aluminum alloy was calculated to be 130.85 kJ/moL. Meanwhile, the Z parameter equation of this alloy was established.
2. Based on the dynamic material model, the hot processing maps of 7B50 aluminum alloy were established. The optimal processing parameter range for 7B50 aluminum alloy was determined to be 410–460 °C/0.01–0.001 s^{-1}.
3. The DRV softening phenomenon exists in all deformation conditions of 7B50 aluminum alloy. However, DRV is the only softening mechanism at $\ln Z \geq 20$. DDRX is the dominant dynamic recrystallization mechanism under deformation conditions of $15 < \ln Z < 20$. The size and proportion of DDRXed grains increased with decreasing lnZ values. Both GDRX and CDRX mechanisms exist under deformation conditions of $\ln Z \leq 15$.

Author Contributions: Investigation, M.L. and Y.L. (Yong Li); methodology, M.L.; data curation, M.L.; data acquisition, M.L. and Y.L. (Yong Li); writing—original draft, M.L.; writing—review and editing, Y.L. (Yong Li) and Z.X.; visualization, Y.L. (Yu Liu) and Y.H.; supervision, Z.X. and Y.L. (Yu Liu); conceptualization, Y.H. All authors have read and agreed to the published version of the manuscript.

Funding: This research received no external funding.

Institutional Review Board Statement: Not applicable.

Informed Consent Statement: Not applicable.

Data Availability Statement: The raw/processed data required to reproduce these findings cannot be shared at this time due to legal or ethical reasons.

Conflicts of Interest: The authors declare that they have no known competing financial interests or personal relationships that could have appeared to influence the work reported in this paper.

References

1. Kang, L.; Zhao, G.; Tian, N.; Zhang, H.-T. Computation of synthetic surface heat transfer coefficient of 7B50 ultra-high-strength aluminum alloy during spray quenching. *Trans. Nonferrous Met. Soc. China* **2018**, *28*, 989–997. [CrossRef]
2. Dursun, T.; Soutis, C. Recent developments in advanced aircraft aluminium alloys. *Mater. Des.* **2014**, *56*, 862–871. [CrossRef]
3. Wang, H.; Xu, W.; Lu, H.; Liu, Y. Effect of microstructure inhomogeneity on creep behavior of friction stir welding 7B50-T7451 aluminum alloy thick plate joint. *Mater. Charact.* **2022**, *193*, 112292. [CrossRef]
4. Xu, X.; Liu, D.; Zhang, X.; Liu, C.; Liu, D. Mechanical and corrosion fatigue behaviors of gradient structured 7B50-T7751 aluminum alloy processed via ultrasonic surface rolling. *J. Mater. Sci. Technol.* **2019**, *40*, 88–98. [CrossRef]
5. Xu, X.; Liu, D.; Zhang, X.; Liu, C.; Liu, D.; Zhang, W. Influence of ultrasonic rolling on surface integrity and corrosion fatigue behavior of 7B50-T7751 aluminum alloy. *Int. J. Fatigue* **2019**, *125*, 237–248. [CrossRef]
6. Xu, X.; Liu, D.; Zhang, X.; Liu, C.; Liu, D.; Ma, A. Effects of Ultrasonic Surface Rolling on the Localized Corrosion Behavior of 7B50-T7751 Aluminum Alloy. *Materials* **2020**, *13*, 738. [CrossRef]

7. Heinz, A.; Haszler, A.; Keidel, C.; MoLdenhauer, S.; Benedictus, R.; Miller, W.S. Recent development in aluminium alloys for aerospace applications. *Mater. Sci. Eng. A* **2000**, *280*, 102–107. [CrossRef]
8. Huang, C.-Q.; Liu, J.-X.; Jia, X.-D. Effect of thermal deformation parameters on the microstructure, texture, and microhardness of 5754 aluminum alloy. *Int. J. Miner. Met. Mater.* **2019**, *26*, 1140–1150. [CrossRef]
9. Zhao, X.; Zhang, Q.; Yang, X.; Chu, Z.; Li, Y.; Qin, F. Flow Behavior and Microstructure Characterization of 7085 Aluminum Alloy Under Various Deformation Conditions. *Met. Mater. Trans. A* **2021**, *52*, 4865–4876. [CrossRef]
10. Wu, S.; Zhu, B.; Jiang, W.; Qiu, H.; Guo, Y. Hot Deformation Behavior and Microstructure Evolution of a Novel Al-Zn-Mg-Li-Cu Alloy. *Materials* **2022**, *15*, 6769. [CrossRef]
11. Lin, Y.C.; Li, L.T.; Xia, Y.C.; Jiang, Y.Q. Hot deformation and processing map of a typical Al-Zn-Mg-Cu alloy. *J. Alloys Compd.* **2013**, *550*, 438–445. [CrossRef]
12. Yan, L.; Shen, J.; Li, Z.; Li, J.; Yan, X. Microstructure evolution of Al-Zn-Mg-Cu-Zr alloy during hot deformation. *Rare Met.* **2010**, *29*, 426–432. [CrossRef]
13. Jiang, Y.; Ding, H. Hot Deformation Behavior of Al-Zn-Mg-Cu Alloy during Compression Tests. *J. Mater. Eng. Perform.* **2022**, *32*, 4585–4596. [CrossRef]
14. Zhao, J.; Deng, Y.; Tang, J.; Zhang, J. Influence of strain rate on hot deformation behavior and recrystallization behavior under isothermal compression of Al-Zn-Mg-Cu alloy. *J. Alloys Compd.* **2019**, *809*, 151788. [CrossRef]
15. Zhao, J.; Deng, Y.; Tan, J.; Zhang, J. Effect of strain rate on the recrystallization mechanism during isothermal compression in 7050 aluminum alloy. *Mater. Sci. Eng. A* **2018**, *734*, 120–128. [CrossRef]
16. Zhao, J.H.; Deng, Y.L.; Zhang, J.; Tang, J.G. Effect of forging speed on the formability, microstructure and mechanical properties of isothermal precision forged of Al-Zn-Mg-Cu alloy. *Mat. Sci. Eng. A* **2019**, *767*, 138366. [CrossRef]
17. Li, H.; Huang, Y.C.; Liu, Y. Dynamic recrystallization mechanisms of as-forged Al–Zn–Mg-(Cu) aluminum alloy during hot compression deformation. *Mat. Sci. Eng. A* **2023**, *878*, 145236. [CrossRef]
18. Xu, C.; Huang, J.; Jiang, F.; Jiang, Y. Dynamic recrystallization and precipitation behavior of a novel Sc, Zr alloyed Al-Zn-Mg-Cu alloy during hot deformation. *Mater. Charact.* **2022**, *183*, 111629. [CrossRef]
19. Chen, Z.Y.; Mo, Y.K.; Nie, Z.R. Effect of Zn Content on the Microstructure and Properties of Super-High Strength Al-Zn-Mg-Cu Alloys. *Metall. Mater. Trans. A* **2013**, *44*, 3910–3920. [CrossRef]
20. Zou, Y.; Wu, X.; Tang, S.; Zhu, Q.; Song, H.; Guo, M.; Cao, L. Investigation on microstructure and mechanical properties of Al-Zn-Mg-Cu alloys with various Zn/Mg ratios. *J. Mater. Sci. Technol.* **2021**, *85*, 106–117. [CrossRef]
21. Graf, G.; Spoerk-Erdely, P.; Staron, P.; Stark, A.; Martin, F.M.; Clemens, H.; Klein, T. Quench rate sensitivity of age-hardenable Al-Zn-Mg-Cu alloys with respect to the Zn/Mg ratio: An in situ SAXS and HEXRD study. *Acta Mater.* **2022**, *227*, 117727. [CrossRef]
22. Fan, X.G.; Jiang, D.M.; Meng, Q.C.; Li, N.K.; Sun, Z.X. Evolution of intermetallic phases of Al-Zn-Mg-Cu alloy during heat treatment. *Trans. Nonferr Met. Soc. China* **2006**, *16*, S1247–S1250. [CrossRef]
23. Huang, K.; Logé, R. A review of dynamic recrystallization phenomena in metallic materials. *Mater. Des.* **2016**, *111*, 548–574. [CrossRef]
24. Raja, N.; Daniel, B. Microstructural evolution of Al-7.3Zn-2.2Mg-2Cu (Al7068) alloy in T6 condition during isothermal compression using 3-dimensional processing map. *J. Alloys Compd.* **2022**, *902*, 163690. [CrossRef]
25. Deng, Y.; Yin, Z.; Huang, J. Hot deformation behavior and microstructural evolution of homogenized 7050 aluminum alloy during compression at elevated temperature. *Mater. Sci. Eng. A* **2011**, *528*, 1780–1786. [CrossRef]
26. Xiao, Z.B.; Wang, Q.; Huang, Y.C.; Hu, J.W.; Li, M. Hot Deformation Characteristics and Processing Parameter Optimization of Al-6.32Zn-2.10Mg Alloy Using Constitutive Equation and Processing Map. *Metals* **2021**, *11*, 360. [CrossRef]
27. Li, J.; Wu, X.; Cao, L.; Liao, B.; Wang, Y.; Liu, Q. Hot deformation and dynamic recrystallization in Al-Mg-Si alloy. *Mater. Charact.* **2021**, *173*, 110976. [CrossRef]
28. Jenab, A.; Taheri, A.K. Experimental investigation of the hot deformation behavior of AA7075: Development and comparison of flow localization parameter and dynamic material model processing maps. *Int. J. Mech. Sci.* **2014**, *78*, 97–105. [CrossRef]
29. Cheng, W.; Bai, Y.; Ma, S.; Wang, L.; Wang, H.; Yu, H. Hot deformation behavior and workability characteristic of a fine-grained Mg–8Sn–2Zn–2Al alloy with processing map. *J. Mater. Sci. Technol.* **2019**, *35*, 1198–1209. [CrossRef]
30. Wang, X.; Liu, Z.; Luo, H. Hot deformation characterization of ultrahigh strength stainless steel through processing maps generated using different instability criteria. *Mater. Charact.* **2017**, *131*, 480–491. [CrossRef]
31. Xu, C.; Pan, J.; Nakata, T.; Qiao, X.; Chi, Y.; Zheng, M.; Kamado, S. Hot compression deformation behavior of Mg-9Gd-2.9Y-1.9Zn-0.4Zr-0.2Ca (wt%) alloy. *Mater. Charact.* **2017**, *124*, 40–49. [CrossRef]
32. Zhao, J.; Deng, Y.; Zhang, J.; Ma, Z.; Zhang, Y. Effect of temperature and strain rate on the grain structure during the multi-directional forging of the Al Zn Mg Cu alloy. *Mater. Sci. Eng. A* **2019**, *756*, 119–128. [CrossRef]
33. Sakai, T.; Miura, H.; Goloborodko, A.; Sitdikov, O. Continuous dynamic recrystallization during the transient severe deformation of aluminum alloy 7475. *Acta Mater.* **2009**, *57*, 153–162. [CrossRef]
34. Sitdikov, O.; Sakai, T.; Goloborodko, A.; Miura, H. Grain fragmentation in a coarse-grained 7475 Al alloy during hot deformation. *Scr. Mater.* **2004**, *51*, 175–179. [CrossRef]
35. Yang, X.; Miura, H.; Sakai, T. Continuous Dynamic Recrystallization in a Superplastic 7075 Aluminum Alloy. *Mater. Trans.* **2002**, *43*, 2400–2407. [CrossRef]

36. Yang, Q.; Deng, Z.; Zhang, Z.; Liu, Q.; Jia, Z.; Huang, G. Effects of strain rate on flow stress behavior and dynamic recrystallization mechanism of Al-Zn-Mg-Cu aluminum alloy during hot deformation. *Mater. Sci. Eng. A* **2016**, *662*, 204–213. [CrossRef]
37. Ren, J.; Wang, R.; Feng, Y.; Peng, C.; Cai, Z. Hot deformation behavior and microstructural evolution of as-quenched 7055 Al alloy fabricated by powder hot extrusion. *Mater. Charact.* **2019**, *156*, 109833. [CrossRef]
38. Miao, J.; Sutton, S.; Luo, A.A. Deformation microstructure and thermomechanical processing maps of homogenized AA2070 aluminum alloy. *Mater. Sci. Eng. A* **2022**, *834*, 142619. [CrossRef]
39. Wang, K.; Zhang, C.; Meng, Z.; Cheng, Z.; Chen, L.; Zhao, G. Precipitation behavior and its effect on the dynamic recrystallization of a novel extruded Al-Cu-Li alloy. *Mater. Des.* **2022**, *223*, 111135. [CrossRef]
40. Hornbuckle, B.; Luckenbaugh, T.; Fudger, S.; Roberts, A.; Jannotti, P.; Byun, T.; Hoelzer, D.; Solanki, K.; Darling, K. Role of geometric dynamic recrystallization in nanocrystalline alloys. *Materialia* **2023**, *30*, 101807. [CrossRef]
41. Li, D.; Liu, H.; Du, S.; Li, X.; Gao, Y.; Zuo, Y. Investigation on material flow and microstructural evolution mechanism in non-thinning and penetrating friction stir welded Al–Cu aluminum alloy. *Mater. Sci. Eng. A* **2023**, *864*, 144572. [CrossRef]
42. Chaudry, U.M.; Han, S.-C.; Jun, T.-S. Effect of welding speed on the microstructure and texture development in the individual weld zone of friction stir welded DP780 steel. *J. Mater. Res. Technol.* **2023**, *23*, 4976–4989. [CrossRef]
43. Zhang, X.; Luo, Z.; Xie, G.; Yu, H.; Liu, Z.; Yang, J. Interface microstructure and bonding mechanisms of 7050 aluminum alloy thick plates produced by vacuum roll cladding. *Mater. Sci. Eng. A* **2022**, *850*, 143582. [CrossRef]

materials

MDPI

Article

He-ion Irradiation Effects on the Microstructures and Mechanical Properties of the Ti-Zr-Hf-V-Ta Low-Activation High-Entropy Alloys

Huanzhi Zhang [1], Qianqian Wang [1], Chunhui Li [1], Zhenbo Zhu [2], Hefei Huang [2,*] and Yiping Lu [1,*]

[1] Key Laboratory of Solidification Control and Digital Preparation Technology (Liaoning Province), School of Materials Science and Engineering, Dalian University of Technology, Dalian 116024, China; 18842603762@mail.dlut.edu.cn (H.Z.)
[2] Shanghai Institute of Applied Physics, Chinese Academy of Sciences (CAS), Shanghai 201800, China
* Correspondence: huanghefei@sinap.ac.cn (H.H.); luyiping@dlut.edu.cn (Y.L.); Tel.: +86-411-8470-9400 (Y.L.); Fax: +86-411-8470-8940 (Y.L.)

Abstract: High-entropy alloys (HEAs) have shown promising potential applications in advanced reactors due to the outstanding mechanical properties and irradiation tolerance at elevated temperatures. In this work, the novel low-activation $Ti_2ZrHf_xV_{0.5}Ta_{0.2}$ HEAs were designed and prepared to explore high-performance HEAs under irradiation. The microstructures and mechanical properties of the $Ti_2ZrHf_xV_{0.5}Ta_{0.2}$ HEAs before and after irradiation were investigated. The results showed that the unirradiated $Ti_2ZrHf_xV_{0.5}Ta_{0.2}$ HEAs displayed a single-phase BCC structure. The yield strength of the $Ti_2ZrHf_xV_{0.5}Ta_{0.2}$ HEAs increased gradually with the increase of Hf content without decreasing the plasticity at room and elevated temperatures. After irradiation, no obvious radiation-induced segregations or precipitations were found in the transmission electron microscope results of the representative $Ti_2ZrHfV_{0.5}Ta_{0.2}$ HEA. The size and number density of the He bubbles in the $Ti_2ZrHfV_{0.5}Ta_{0.2}$ HEA increased with the improvement of fluence at 1023 K. At the fluences of 1×10^{16} and 3×10^{16} ions/cm^2, the irradiation hardening fractions of the $Ti_2ZrHfV_{0.5}Ta_{0.2}$ HEA were 17.7% and 34.1%, respectively, which were lower than those of most reported conventional low-activation materials at similar He ion irradiation fluences. The $Ti_2ZrHfV_{0.5}Ta_{0.2}$ HEA showed good comprehensive mechanical properties, structural stability, and irradiation hardening resistance at elevated temperatures, making it a promising structural material candidate for advanced nuclear energy systems.

Keywords: high-entropy alloys; mechanical properties; helium bubbles; irradiation tolerance; low-activation materials

Citation: Zhang, H.; Wang, Q.; Li, C.; Zhu, Z.; Huang, H.; Lu, Y. He-ion Irradiation Effects on the Microstructures and Mechanical Properties of the Ti-Zr-Hf-V-Ta Low-Activation High-Entropy Alloys. *Materials* **2023**, *16*, 5530. https://doi.org/10.3390/ma16165530

Academic Editor: S. Joseph Poon

Received: 12 July 2023
Revised: 1 August 2023
Accepted: 7 August 2023
Published: 9 August 2023

1. Introduction

It is an irresistible trend to obtain clean, low-carbon, and safe energy generated from next generation fission and future fusion energy reactors to meet the needs of human society and industrial development in the long term [1–5]. The absence of compatible structural materials for extreme environments of high temperature, high neutron flux, and chemical reactivity hinders the development of advanced reactors [6,7]. The evolution of microstructures caused by high-energy particles (neutrons, ions, and electrons) irradiation leads to the degradation of mechanical properties, such as embrittlement, hardening, swelling, etc., which eventually threaten the safety and reliability of the reactors [8,9]. Considering one of the significant goals for the advanced reactors is to produce economically clean energy with no long-lived high-radioactivity waste [10–12], the low-activation criteria should be included in the structural materials' design of advanced reactors. Certain achievements have been made in the research of qualified low-activation materials, including oxide dispersion strengthened (ODS) steels [13,14], V-based alloys [15,16], reduced activation

ferritic/martensitic (RAFM) steels [17,18], and China low activation martensitic (CLAM) steels [19,20].

In the process of pursuing high-performance materials, the high-entropy alloys (HEAs) [21] were introduced. The preeminent properties (such as high strength [22,23], good corrosion resistance [24–26], fine tribological properties [27,28], remarkable softening resistance [29,30], and outstanding irradiation tolerance [1,2,5,31], etc.) enhance the application competitiveness of HEAs under extreme environments. Among them, refractory high-entropy alloys (RHEAs) [32], which are characterized by a high melting point and prepared by methods such as vacuum arc melting, suspension melting, spark plasma sintering [33], and wire electric discharge machining [34], are expected to play a role in future high-temperature applications [35]. Compared with conventional alloys, HEAs, especially the body-centered cubic (BCC) structured ones composed of refractory elements, exhibit better irradiation tolerance for the extreme lattice distortions and chemical complexity, such as prominent resistance to hardening [1,36], suppressed dislocation evolution [11,36,37], low volume swelling rate [38,39], and reduced radiation-induced segregation [40–42], etc. Hence, the HEAs are considered to be a promising candidate for nuclear structural materials [1,43] and the corresponding irradiation resistance mechanism has been revealed to a certain extent [2,5,44,45]. The irradiation tolerance of the HEAs could be improved by selecting the appropriate elements and adjusting the chemical complexity [2,46]. Nevertheless, the HEAs designed for nuclear industry applications are limited [36,42].

In this work, by introducing the concept of low-activation materials to the design of HEAs, a novel series of RHEAs with BCC structure were proposed, with the expectation to explore high-performance HEAs under irradiation. In addition, good comprehensive mechanical properties at room and elevated temperatures should also be equipped for the potential application. The basic parameters [47] (melting point (T_m), atomic radius (r), density (ρ), and valence electron concentration (VEC)) of some commonly used low-activation elements in the nuclear industry are displayed in Table 1. However, not all the elements mentioned are suitable for the design of BCC-structured RHEAs. The high VEC value of Fe element is not conducive to the formation of single-phase BCC structure, and its low melting point could reduce the working temperature of the materials after alloying. The negative mixing enthalpy between Cr and other refractory elements contributes to the appearance of intermetallic compounds, which deteriorates the plasticity of the HEAs. In the as-cast samples, W element with a high melting point is usually seriously segregated, worsening the mechanical and irradiation tolerance. The five refractory elements of Ti, Zr, Hf, V, and Ta were chosen to prepare the low-activation HEAs after considering the basic physical and chemical properties and the alloying characteristics of each element in HEAs. The $Ti_2ZrHf_xV_{0.5}Ta_{0.2}$ (x values in molar ratio, x = 0.25, 0.5, 0.75 and 1, denoted as Hf0.25Ta, Hf0.5Ta, Hf0.75Ta and Hf1Ta, respectively) low-activation HEAs were designed, and the effects of Hf element on the microstructures and mechanical properties were investigated. As shown in Table 2, according to the phase formation rules of HEAs [48–50], all the empirical parameters predicted the formation of single BCC solid solution phase in the $Ti_2ZrHf_xV_{0.5}Ta_{0.2}$ HEAs.

Table 1. The values of T_m (K), r (nm), ρ (g/cm^3), and VEC of some reduced-activation elements.

Elements	Fe	Ti	Zr	Cr	V	Hf	Ta	W
T_m (K)	1811	1941	2128	2180	2183	2506	3290	3695
r (nm)	0.126	0.147	0.160	0.128	0.134	0.159	0.146	0.139
ρ (g/cm^3)	7.87	4.51	6.51	7.14	6.11	13.31	16.65	19.25
VEC	8	4	4	6	5	4	5	6

Ordinarily, the He atoms produced by transmutation reaction would aggregate and form large-scale He bubbles for the limited solubility in the metals, which strongly deteriorated the mechanical properties of the alloys after irradiation [51]. The embrittlement and hardening induced by He atoms were considered as the primary concerns of the stability of structure materials around the half melting temperature (T_m) regime in the

nuclear reactors [52]. Therefore, the performance of HEAs under He ion irradiation at elevated temperature is definitely worth investigating. In this work, the evolutions of the microstructures and mechanical properties of the novel low-activation $Ti_2ZrHfV_{0.5}Ta_{0.2}$ HEA with He ions implantation at 1023 K (0.47 T_m) were studied in detail.

Table 2. Values of VEC, δ (%), Ω, ΔH_{mix} (kJ mol^{-1}), and ΔS_{mix} (J K^{-1} mol^{-1}) of the $Ti_2ZrHf_xV_{0.5}Ta_{0.2}$ HEAs.

Alloys	VEC	Δ	Ω	ΔH_{mix}	ΔS_{mix}
Hf0.25Ta	4.18	5.51	27.52	−0.82	10.64
Hf0.5Ta	4.17	5.54	32.09	−0.83	11.20
Hf0.75Ta	4.16	5.54	36.17	−0.69	11.48
Hf1Ta	4.15	5.52	283.96	−0.63	11.60

2. Experimental Section

2.1. Materials

The $Ti_2ZrHf_xV_{0.5}Ta_{0.2}$ HEAs were manufactured by vacuum arc melting under Ar atmosphere. The purity of each raw elemental metal used in this study was higher than 99.9 wt%. All raw metals were purchased from the instrumental and research center of Shanghai Yanku. The furnace chamber was vacuumed to below 5×10^{-3} Pa and then protective high-purity argon was reverse charged to 0.05 Pa before starting the melting process. The raw metals were melted on a water-cooled copper crucible. In order to improve the quality of ingots, Ti ingot was melted before melting HEA ingots to remove excess oxygen. For obtaining better homogenization, the ingots were re-melted a minimum of seven times. Each smelting time was 2 min, and the smelting current was approximately 500 A. The acquired samples were button-shaped with a diameter of ~28 mm and a thickness of ~11 mm.

2.2. Characterization of Microstructure and Mechanical Properties of As-Cast Samples

The crystal structures of the as-cast samples were characterized by an EMPYREAN X-ray diffractometer (Malvern Panalytical, Almelo, Netherlands) with the 2θ scanning from 20 to 100 degrees. The scanning electron microscopy (SEM, Zeiss supra55, ZEISS, Carl Zeiss AG, Jena, Germany) with an energy-dispersive spectrometer (EDS) was introduced to analyze the morphology and chemical compositions. The Φ 5 × 10 mm cylindrical specimens prepared by wire electrical discharge machining were used to test the mechanical properties at room temperature (RT) using a Wippermann materials testing machine. A thermal simulation machine of Gleeble-3500 (Data Science International, Sao Paulo City, Brazil) was adopted for the compressive tests at elevated temperature (873 K) with Φ 6 × 9 mm cylindrical specimens.

2.3. Irradiation Experiment and Characterization of Microstructure of Irradiated Samples

The irradiation tolerance of the selected representative alloy (Hf1Ta) was identified by He ion irradiation at 1023 K. The prepared specimens were irradiated with 1 MeV He ions to the fluences of 1×10^{16} and 3×10^{16} ions/cm^2 at the Shanghai Institute of Applied Physics, Chinese Academy of Sciences (SINAP-CAS, Shanghai, China) using a 4 MV Pelletron accelerator. The sheets (sized 1 mm × 6.5 mm × 10 mm) for the irradiation experiments were taken from the as-cast Hf1Ta HEA. Then, mechanical polishing and electro-polishing were used to optimize the irradiated surface of the samples. At the fluence of 3×10^{16} ions/cm^2, the irradiation damage and He concentration along the depth direction were predicted by Stopping and Range of Ions in Matter (SRIM-2008, http://www.srim.org/, accessed on 3 March 2022), as shown in Figure 1. The displacement energies were set as 30, 40, 90, 40, and 91 eV for the Ti, Zr, Hf, V, and Ta elements, respectively. Simulation results showed that the peak irradiation dose and He concentration were ~1.2 displacements per atom (dpa) and 3.0 at.%, respectively. For observing the microstructures and He bubbles characteristics, the transmission electron microscopy (TEM, Themis

Z G3, Thermo Fisher Scientific, Waltham, MA, USA) was employed. Thin films with a thickness of ~60 nm were fabricated by the focused ion beam (FIB, Helios G4UX, Thermo Fisher Scientific, Waltham, MA, USA).

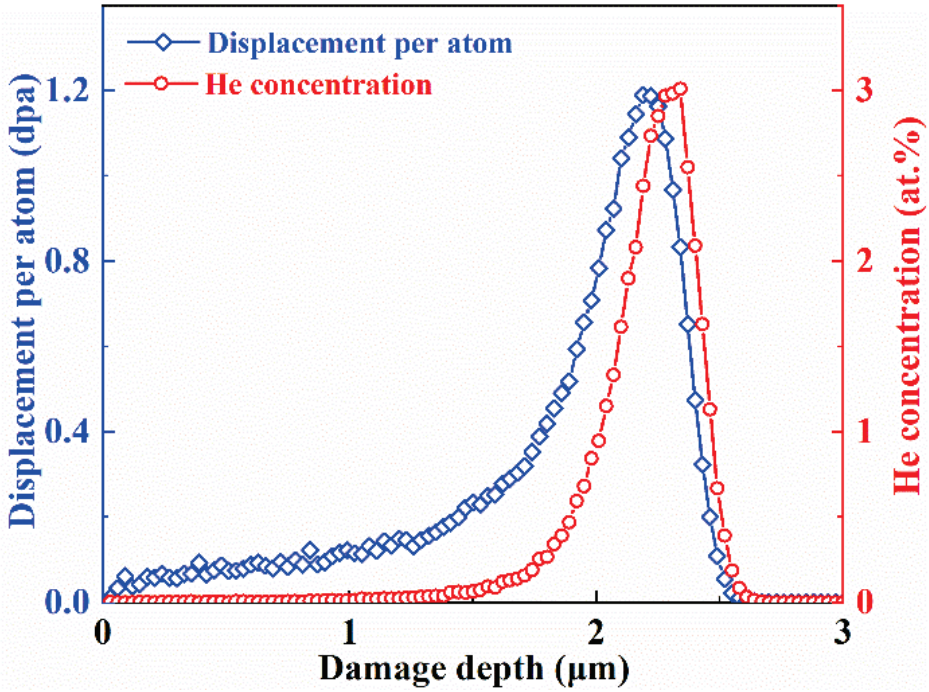

Figure 1. The depth distribution of He concentration and displacement damage in the Hf1Ta HEA at the fluence of 3×10^{16} ions/cm^2.

2.4. Nanoindentation Test

The hardening behaviors of the samples with He ions implantation were determined by nanoindentation tests (G200 nano-indenter, Technologies, Palo Alto City, CA, USA). More than 8 measurements were adopted to calculate the average hardness of each depth. The size and density of He bubbles in the Hf1Ta HEA were calculated by the Image Pro software (Version 6.0), and more than 2 areas (100 nm × 100 nm) selected from the peak damage regions were chosen to count.

3. Results and Discussion

3.1. Microstructures of the As-Cast $Ti_2ZrHf_xV_{0.5}Ta_{0.2}$ HEAs

The XRD patterns of the as-cast $Ti_2ZrHf_xV_{0.5}Ta_{0.2}$ HEAs are exhibited in Figure 2a, in which only the diffraction peaks of BCC phase can be observed. The absence of other phase diffraction peaks in the patterns suggested that the increase of Hf content had little effect on the structure of the $Ti_2ZrHf_xV_{0.5}Ta_{0.2}$ HEAs.

The shift of the (110) diffraction peaks of BCC phases are displayed in Figure 2b. As can be detected, the (110) peak shifted to a lower 2θ angle (decreased from 37.96° in the Hf0.25Ta to 37.28° in the Hf1Ta) as the Hf content increased, implying that tensile strain out-plane was created due the compressive in-plane stress induced by Hf [53,54]. According to Bragg's law, the values of the lattice constants were calculated to be 0.3349, 0.3387, 0.3398, and 0.3408 nm for $Ti_2ZrHf_xV_{0.5}Ta_{0.2}$ HEAs corresponding to x = 0.25, 0.5, 0.75, and 1, respectively. The addition of Hf element with the second largest atomic radius could improve the lattice distortion, which contributed to the increase of lattice constants.

Figure 3 displays the SEM images of the as-cast $Ti_2ZrHf_xV_{0.5}Ta_{0.2}$ HEAs. All the HEAs exhibited typical dendritic structure and no significant microstructure evolution can be observed in the HEAs with different Hf content. Combined with the XRD results, the $Ti_2ZrHf_xV_{0.5}Ta_{0.2}$ HEAs exhibited a single BCC solid solution structure. The increase

of Hf content could hardly change the microstructures of the $Ti_2ZrHf_xV_{0.5}Ta_{0.2}$ HEAs significantly, indicating the complete dissolution of Hf element in the matrix. Through EDS analysis, the chemical composition of different regions in the $Ti_2ZrHf_xV_{0.5}Ta_{0.2}$ HEAs are listed in Table 3. Dendritic regions in the $Ti_2ZrHf_xV_{0.5}Ta_{0.2}$ HEAs were enriched with higher melting point elements of Hf and Ta elements, while interdendritic regions were enriched with lower melting point elements of Zr and V elements, which could be attributed to the behaviors of elements with different melting points during solidification. It should be noted that the addition of Hf element could mitigate the segregations of the elements and the relatively uniform microstructure was obtained in the Hf1Ta HEA.

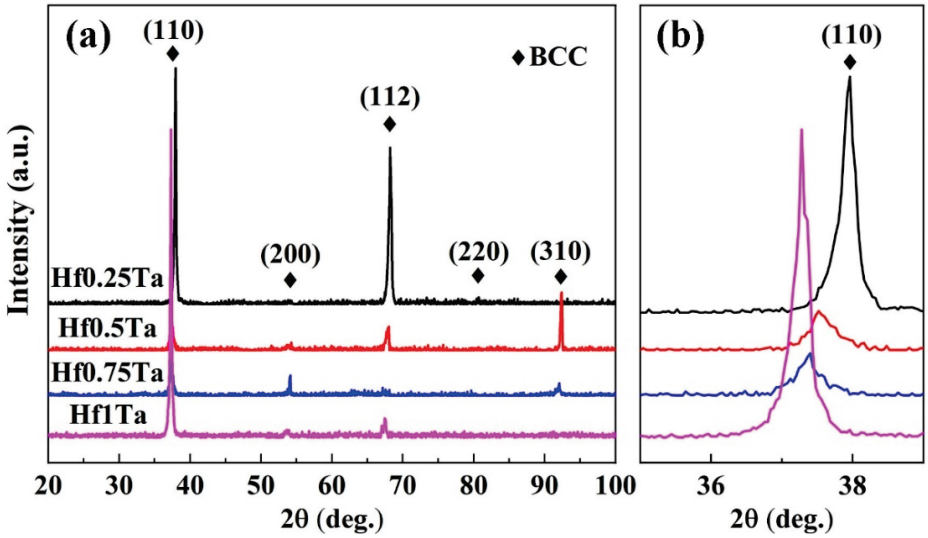

Figure 2. (**a**) The X-ray diffraction patterns of the $Ti_2ZrHf_xV_{0.5}Ta$ HEAs; (**b**) corresponding detailed scans of the (110) peaks of the BCC phase.

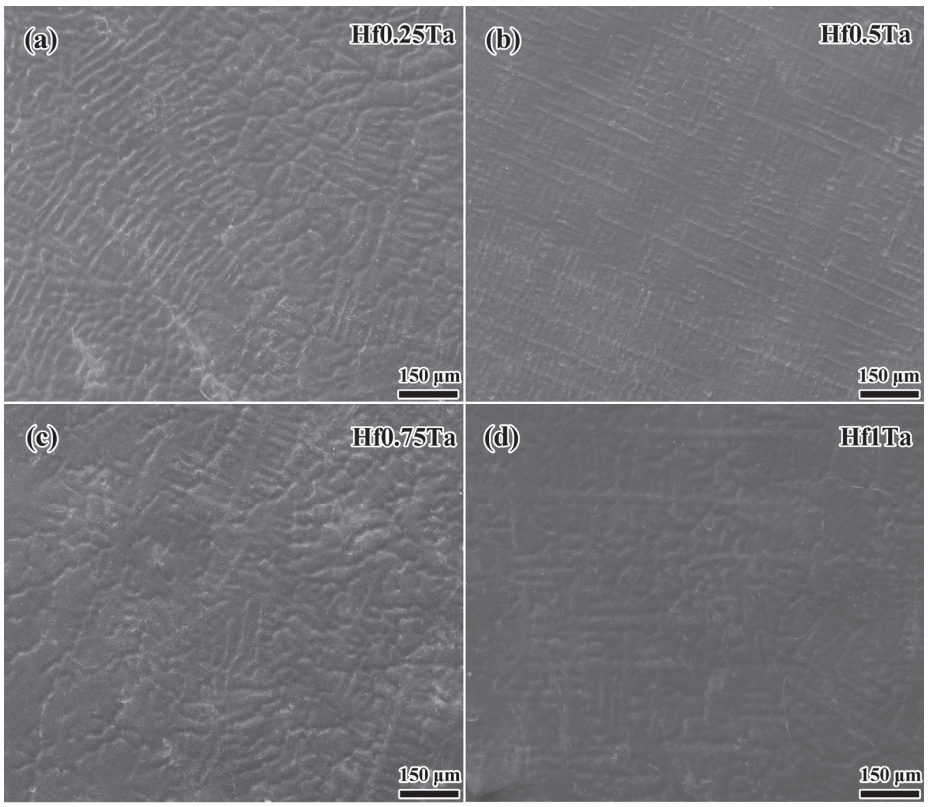

Figure 3. Microstructures of the as-cast (**a**) Hf0.25Ta, (**b**) Hf0.5Ta, (**c**) Hf0.75Ta, and (**d**) Hf1Ta HEAs.

Table 3. Chemical composition of dendritic (D) and interdendritic (ID) regions of the $Ti_2ZrHf_xV_{0.5}Ta_{0.2}$ HEAs in atomic percentage.

Alloys	Regions	Ti	Zr	V	Hf	Ta
Hf0.25Ta	D	45.65	24.43	9.76	14.04	6.12
	ID	45.35	25.39	11.83	12.96	4.47
Hf0.5Ta	D	45.18	23.50	9.70	15.81	5.81
	ID	45.31	24.02	10.56	14.72	5.40
Hf0.75Ta	D	44.11	22.39	9.53	18.37	5.60
	ID	44.02	22.80	10.31	17.60	5.26
Hf1Ta	D	42.24	21.01	9.04	23.26	4.45
	ID	42.42	21.53	9.58	22.54	4.11

3.2. Mechanical Properties of the As-Cast $Ti_2ZrHf_xV_{0.5}Ta_{0.2}$ HEAs

Figure 4 exhibits the engineering stress–strain curves of $Ti_2ZrHf_xV_{0.5}Ta_{0.2}$ HEAs gained by the compression test at RT. The values of yield strength σ and plastic strain ε are summarized in Table 4. The plastic strain of the $Ti_2ZrHf_xV_{0.5}Ta_{0.2}$ HEAs was more than 50% and no fracture could be detected during the compression test. Although the changes of Hf content have no obvious effect on the plasticity, the yield strength of the $Ti_2ZrHf_xV_{0.5}Ta_{0.2}$ HEAs improved from 745 to 873 MPa as the Hf content increased. The advances in mechanical properties were predominantly attributed to the variation in lattice distortion of this series of HEAs. The addition of Hf element with second largest atomic radius intensified the lattice distortion and raised the resistance to dislocation motion, and thus the yield strength was enhanced.

The mechanical properties of the $Ti_2ZrHf_xV_{0.5}Ta_{0.2}$ HEAs at 873 K have been investigated, and the compressive stress–strain curves are exhibited in Figure 5a. It can be observed from all the flow curves that apparent softening emerged after the appearance of stress peaks at the initial deformation stage, which was a typical manifestation of dynamic recrystallization. The yield strength of the Hf0.25Ta-Hf1Ta HEAs at 873 K was 480, 553, 601, and 662 MPa, respectively. Figure 5b shows the comparison of yield strength of the $Ti_2ZrHf_xV_{0.5}Ta_{0.2}$ HEAs at different temperatures. As the compression test temperature increased from RT to 873 K, the yield strength decreased by 265, 236, 231, and 211 MPa for the Hf0.25Ta-Hf1Ta HEAs, respectively, and the corresponding decline percentages were 34.4%, 29.9%, 27.8%, and 24.2%, respectively. The compression results indicated that the increase of Hf content played a positive role in enhancing yield strength of the $Ti_2ZrHf_xV_{0.5}Ta_{0.2}$ HEAs at RT and 873 K. Generally, the alloy melting point was crucial to the softening resistance at elevated temperatures. The melting points of the $Ti_2ZrHf_xV_{0.5}Ta_{0.2}$ HEAs increased from 2122 K to 2183 K by the increase of Hf content, which was conducive to the softening resistance improvement. On the other hand, the influence of solid solution strengthening caused by the increase of Hf content on the strength cannot be ignored. Under the dual effect, at 873 K the yield strength of $Ti_2ZrHf_xV_{0.5}Ta_{0.2}$ HEAs improved with the increase of Hf content.

The novel low-activation $Ti_2ZrHf_xV_{0.5}Ta_{0.2}$ HEAs, especially Hf1Ta HEA, exhibited fine comprehensive mechanical properties at RT and 873 K, which contributed to the industrial application potential in extreme conditions. The He ion irradiation experiment was introduced to preliminarily evaluate irradiation resistance of the Hf1Ta alloy, which was selected as the representative of the designed low-activation $Ti_2ZrHf_xV_{0.5}Ta_{0.2}$ HEAs due to the high yield strength at RT, elevated temperatures, and high melting point.

Table 4. Values of melting temperature and mechanical properties of the $Ti_2ZrHf_xV_{0.5}Ta_{0.2}$ HEAs at RT.

Alloys	σ (MPa)	ε (%)	T_m (K)
Hf0.25Ta	745	>50	2122
Hf0.5Ta	789	>50	2145
Hf0.75Ta	832	>50	2165
Hf1Ta	873	>50	2183

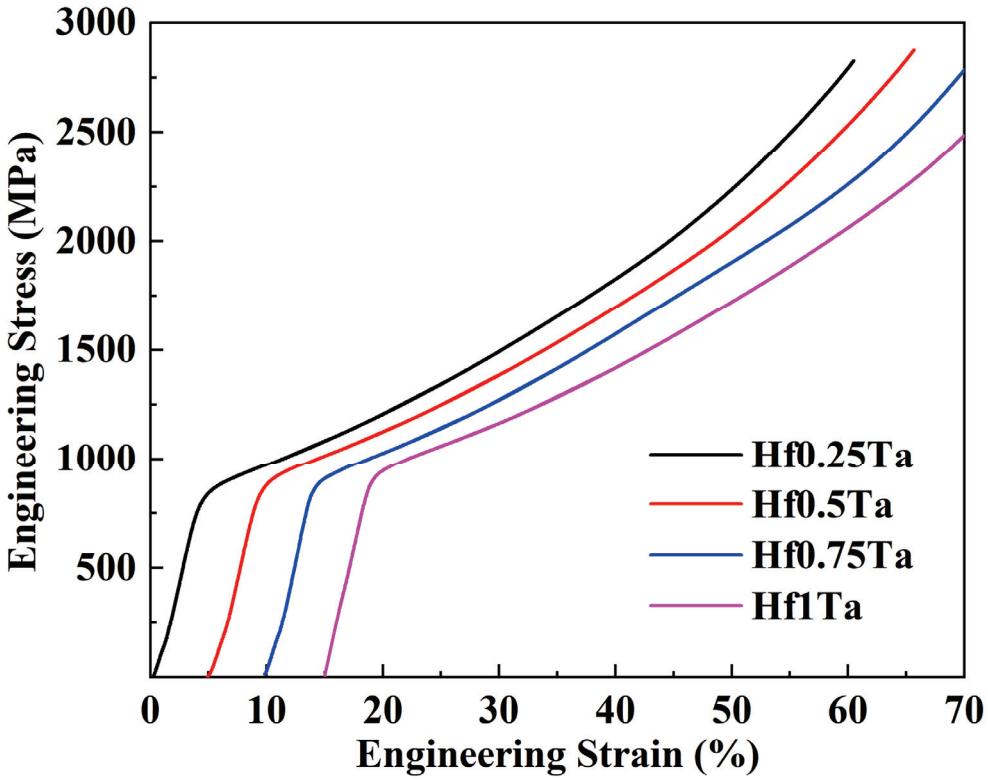

Figure 4. Compressive engineering stress–strain curves of $Ti_2ZrHf_xV_{0.5}Ta_{0.2}$ HEAs at RT.

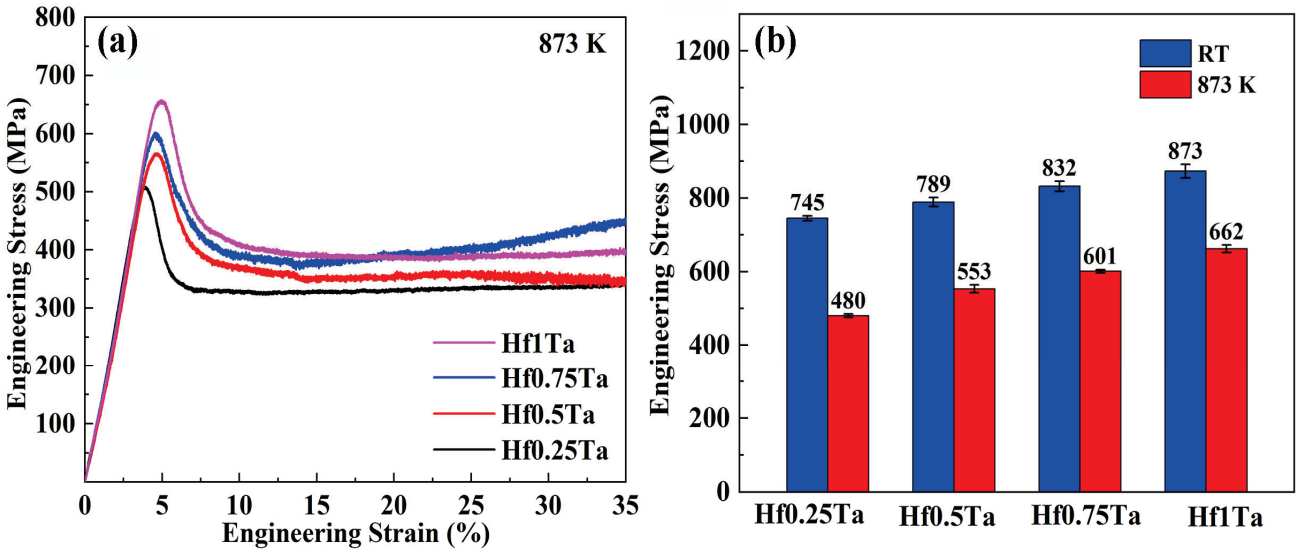

Figure 5. (**a**) Compressive engineering stress–strain curves at 873 K, (**b**) linear graphs of temperature and strength of $Ti_2ZrHf_xV_{0.5}Ta_{0.2}$ HEAs.

3.3. TEM Characterization of the Irradiated $Ti_2ZrHfV_{0.5}Ta_{0.2}$ HEA

The characterizations of He bubbles, such as distribution range, shape, size, and number density, were primarily analyzed in this work. Based on the SRIM simulation results (shown in Figure 1), the peaks of irradiation damage and He concentration emerged at the depth of ~2200 and 2300 nm, respectively. Therefore, at different fluences, the cross-sectional TEM images containing peak damage regions at depths of 1700 to 2700 nm are shown in Figure 6a,b, presenting the He bubbles' distribution characterizations. For the sample irradiated to a fluence of 1×10^{16} ions/cm^2, the He bubbles emerged at the depth

of ~2000 nm and extended to 2500 nm, and no bubbles could be identified beyond this range. A wider spatial distribution of He bubbles was detected in the sample irradiated to a higher fluence of 3×10^{16} ions/cm^2. As can be detected in Figure 6b, larger bubbles were observed in the depth range of 1850~2550 nm, which was roughly consistent with the simulation results shown in Figure 1.

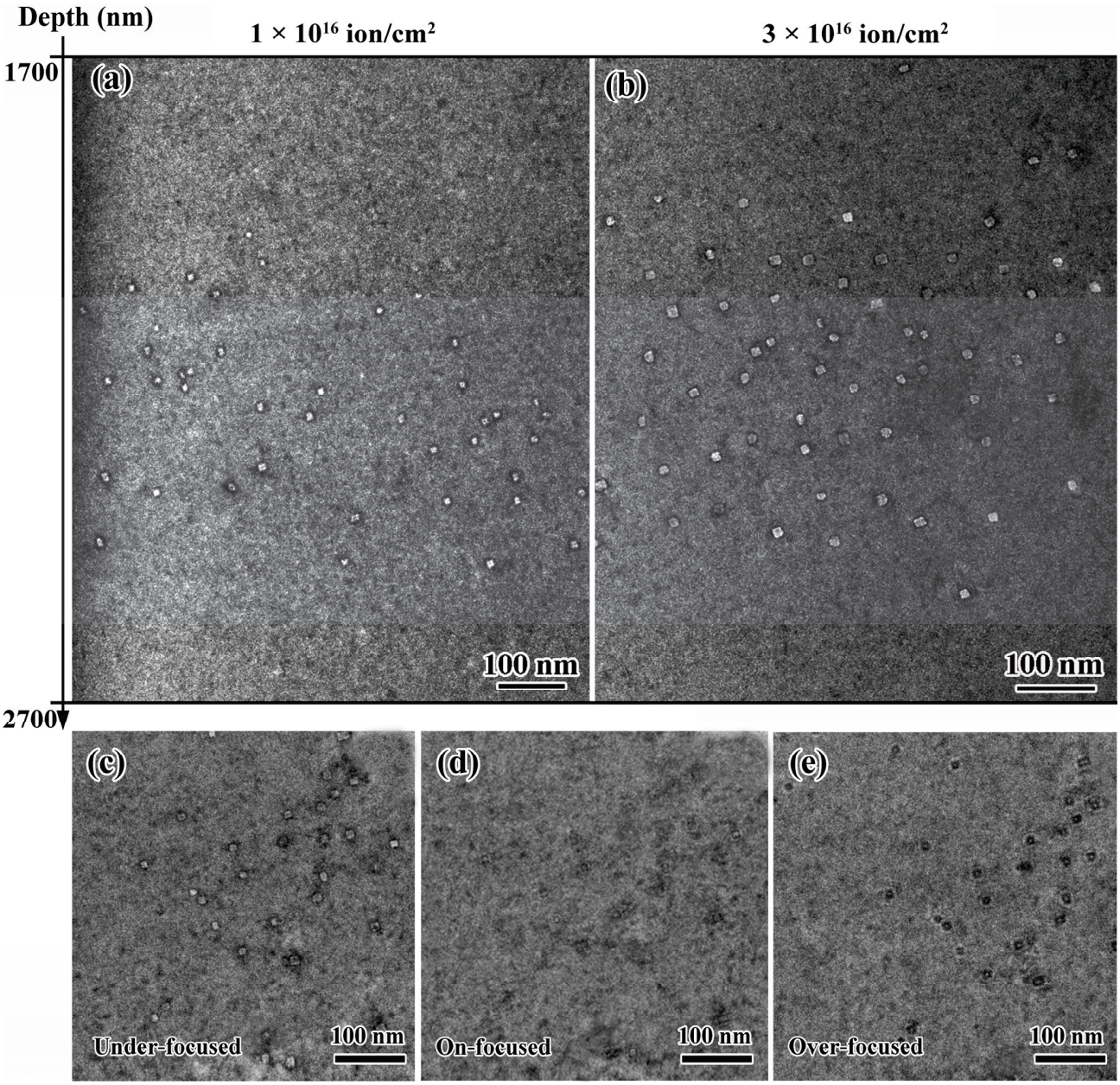

Figure 6. (**a**,**b**) Distribution of He bubbles at 1700~2700 nm depth in irradiated samples at different fluences; (**c**–**e**) the under-, on-, and over-focused images of He bubble characterization obtained at the same position.

The features of He bubbles in the TEM bright field images taken in the same position under different focusing states are presented in Figure 6c–e, in which white and black spots were found in under- and over-focused conditions, respectively. Under different focusing states, no precipitates could be observed in the peak damage regions.

The characterizations of the He bubbles at high magnification are displayed in Figure 7a,b, in which faceted bubbles were observed in the Hf1Ta alloy at different fluences. The He bubbles in BCC-structured conventional materials usually evolved into

polygons at elevated temperatures to maintain a more stable state and faceted bubbles formed in the Nb-Zr and Fe-Cr alloys [55]. The shape of He bubbles in materials can be influenced by several factors, including crystal structure, surface energy, strain effects, volume energy, etc. The extra elastic strain energy was generated by vacancy and He atoms flowing into He bubbles at high temperatures. For maintaining a more stable state of He bubbles, large areas of surfaces were formed and developed on low-energy planes [56], which resulted in the formation of faceted bubbles in the $Ti_2ZrHf_xV_{0.5}Ta_{0.2}$ HEA at 1023 K. The morphology of the bubbles in the Hf1Ta alloy in this study, Ti-Zr-Nb-V-Mo [46], and Ti-V-Nb-Ta RHEAs [57] was similar to that found in the conventional materials with He ions implantation, suggesting that the formation of faceted bubbles at elevated temperature may be a feature of BCC-structured RHEAs.

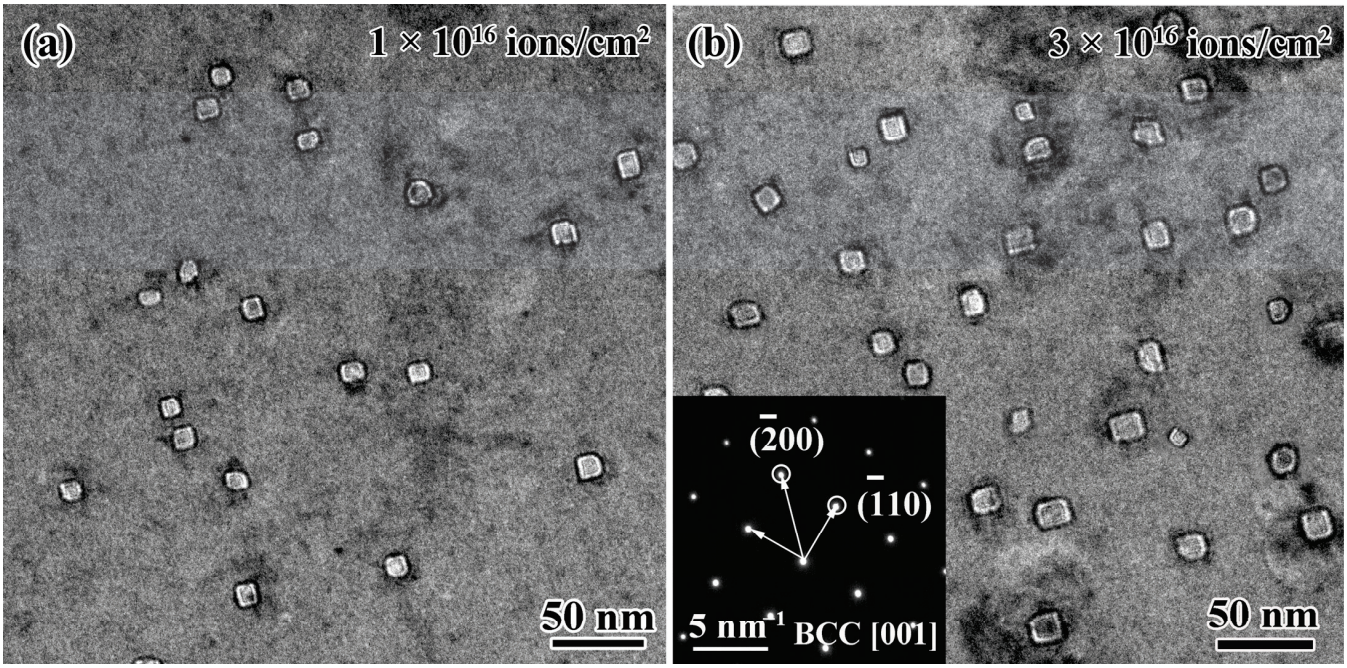

Figure 7. Comparison of He bubble characterizations in the peak damage regions of the Hf1Ta HEA at the fluences of (**a**) 1×10^{16} and (**b**) 3×10^{16} ions/cm^2.

At different fluences, no precipitations could be found in the peak damage regions of the irradiated Ha1Ta HEA and only the diffraction spots of BCC phase were detected in the selected area's electron diffraction patterns obtained from different irradiation damage regions, and they suggested preeminent phase stability of the Hf1Ta HEA under He ion irradiation at 1023 K. The bubbles' distributions in peak damage regions were determined to be random and uniform under different fluences, and the He bubble sizes presented normal-like distributions (as displayed in Figure 8), meaning that the nucleation and growth process of He bubbles in the Hf1Ta HEA was homogeneous under irradiation [57].

Figure 9 exhibits the elemental distributions near the bubbles in the Hf1Ta HEA irradiated to a fluence of 3×10^{16} ions/cm^2. No obvious elemental enrichment regions were detected in the images and the distribution of each element was relatively uniform. Recent studies [40,57] on the HEAs indicated that the atomic size difference dominated the elements segregation under irradiation. In those cases, the vacancies away from the He bubbles were preferentially coupled with the oversized elements, resulting in the enrichment of the undersized elements at the bubbles. Significantly, the radiation-induced segregation may affect the behavior of dislocations/He bubbles and induce stress corrosion cracking, thereby degrading the mechanical properties and putting a negative impact on the irradiation performance of the alloys. The uniform distribution of elements near the He bubbles suggested the good structural stability of the Hf1Ta HEA under the given irradiation condition.

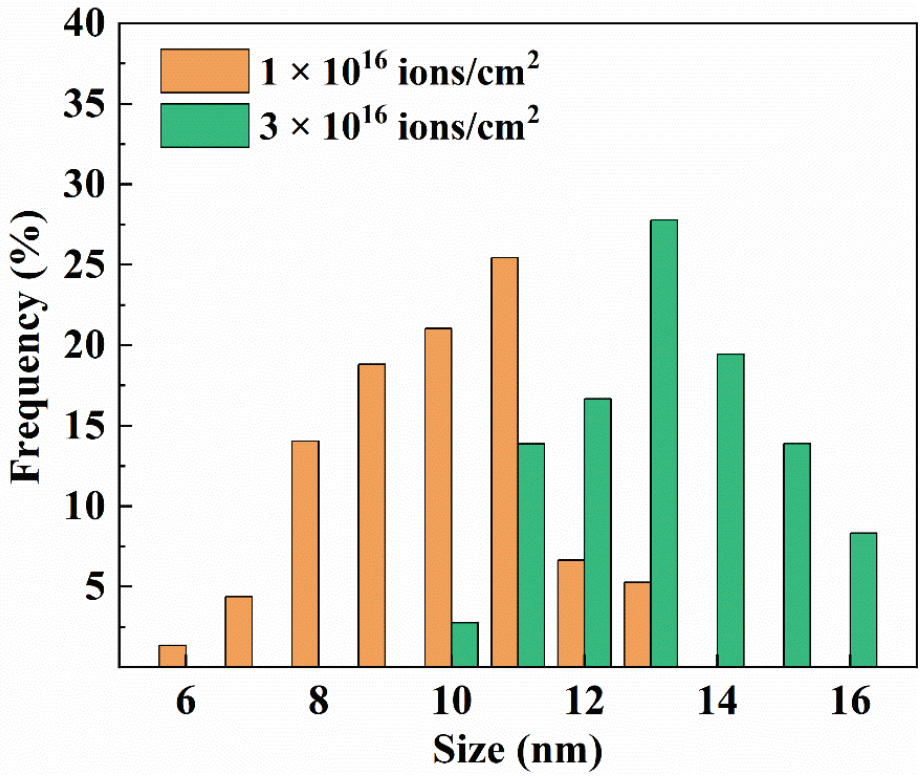

Figure 8. Size distributions of He bubbles in the Hf1Ta HEA at different fluences.

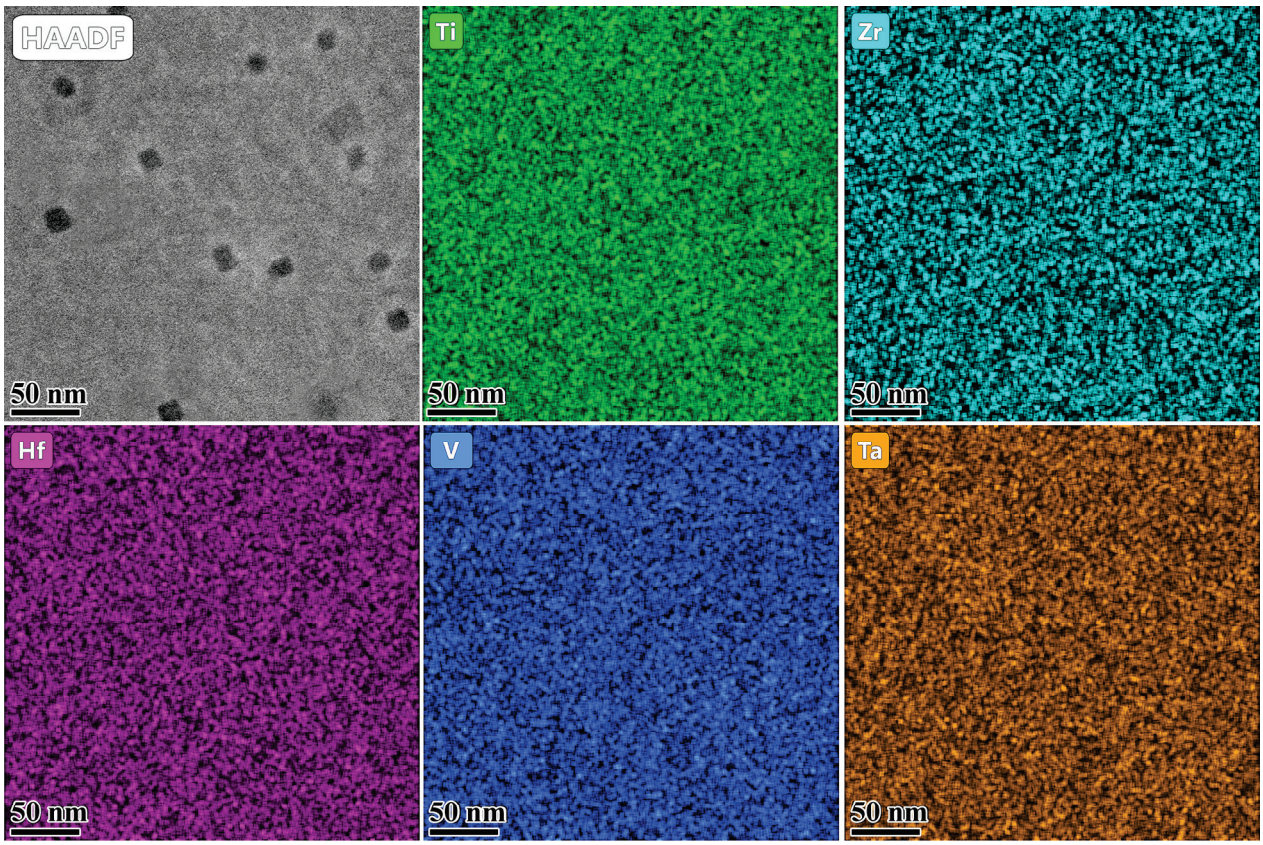

Figure 9. Elemental distribution near the He bubbles in the Hf1Ta HEA irradiated to the fluence of 3×10^{16} ions/cm^2.

The size distributions of the He bubbles in the peak damage regions are shown in Figure 8. At each fluence, the He bubble sizes in the Hf1Ta HEA presented a unimodal distribution. The average sizes (d) and number densities (N) of the He bubbles in the Hf1Ta HEA at different fluences are listed in Table 5. The average size increased from 10.5 nm to 13.7 nm and number density increased from 9.09×10^{20} m^{-3} to 2.42×10^{21} m^{-3} as the fluence improved.

Table 5. Average size and density of He bubbles in the Hf1Ta HEA at different fluences.

Fluence (ions/cm^2)	Average Size (nm)	Number Density ($\times 10^{20}$ m^{-3})
1×10^{16}	10.5	9.09
3×10^{16}	13.7	24.21

Generally, the growth of He bubbles was temperature sensitive and larger He bubbles were found at elevated temperature [58]. The average sizes of He bubbles in the conventional materials were summarized in Table 6. Owing to the limitation of melting point, the temperature of irradiation experiments applied to conventional materials was restricted, which was no more than 973 K. Therefore, the He bubble sizes in the Hf1Ta HEA were larger than those in conventional materials [59–63] due to the higher experiment temperature (1023 K), while He bubble density was one to two orders of magnitude lower. Significantly, the He bubble sizes in the Hf1Ta HEA were between 5–17 nm, which were close to those found in the reported Ti-Zr-Nb-V-Mo [46] at 1023 K and Ti-V-Nb-Ta RHEAs [57] at 973 K. However, the average sizes of He bubbles in tens of nanometers (34.1–85.6 nm) were found in FCC-structured NiCoFeCrMn HEAs and its derivatives [58] at 973 K.

Table 6. Average sizes of He bubbles in the conventional materials (CMs) and typical HEAs and their derivatives at elevated temperatures.

	Alloys	Temperature (K)	Fluence (ions/cm^2)	Peak He Concentration (at.%)	Average Size (nm)
HEAs	TiVTa [57]	973	1×10^{17}	5.0	13.4
	TiVNbTa [57]	973	1×10^{17}	5.0	8.1
	TiZrNbV [46]	1023	6×10^{16}	3.9	12.5
	TiZrNbVMo [46]	1023	6×10^{16}	3.9	10.4
	NiCo [58]	973	6.4×10^{16}	3.6	25.1
	NiCoCr [58]	973	6.4×10^{16}	3.6	34.1
	NiCoFeCrMn [58]	973	6.4×10^{16}	3.6	85.6
CMs	V-4Cr-4Ti [59]	573	5×10^{16}	4.0	2.7
	ODS [60]	723	1×10^{17}	5.6	3.9
	RAFM [63]	773	3×10^{16}	5.7	5.1
	GH3535 [62]	923	1×10^{17}	5.0	2.3
	Ni-SiC [64]	923	6×10^{16}	3.5	8.1

3.4. Irradiation Hardening

Nano-indentation tests were employed to assess the mechanical properties of the Hf1Ta HEA after He ions' irradiation. Figure 10a shows the average hardness dependence of indentation depths of the unirradiated and irradiated Hf1Ta alloy. Due to the surface effect on the measurement accuracy, hardness values measured at the depths less than 80 nm were not reliable and omitted. At the same depth, the irradiated sample possessed higher hardness values than the unirradiated one, which suggested the hardening of irradiated Hf1Ta HEA. For the indentation size effect, the hardness decreased slightly with increasing the indentation depth as shown in Figure 10a, which could be described by the model proposed by Nix and Gao [61]:

$$H = H_0 \sqrt{1 + (h^*/h)} \quad (1)$$

where H represents the measured hardness, H_0 represents the hardness at infinite depth, h^* represents a characteristic length which depends on the material and the shape of indenter tips, and h represents the indentation depth.

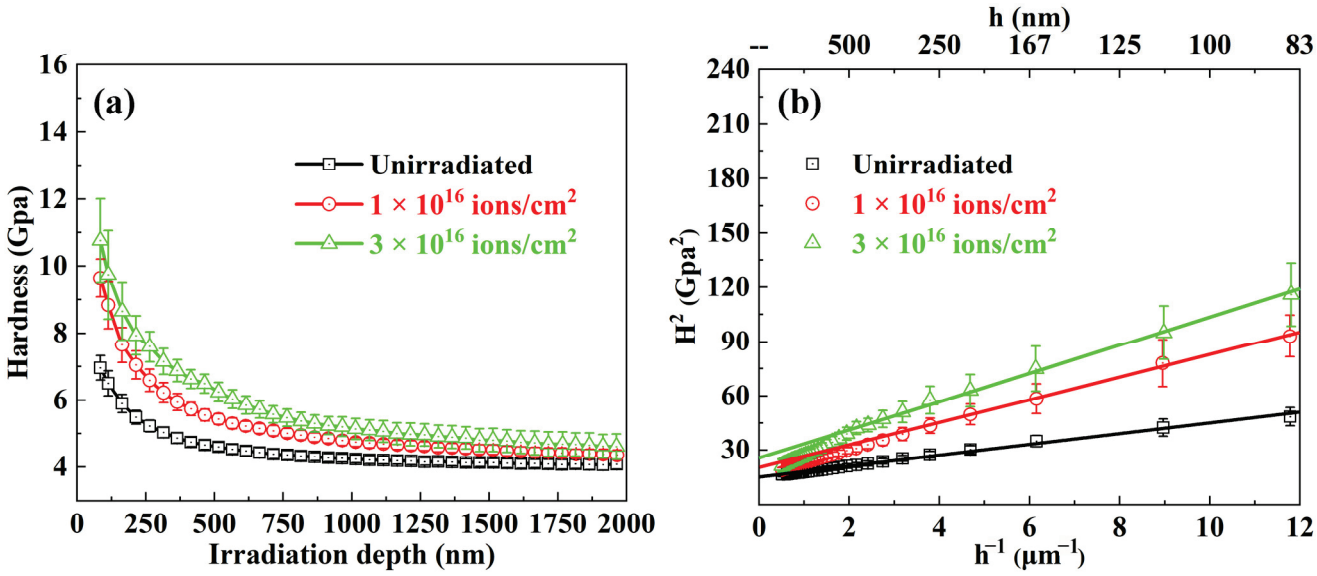

Figure 10. (**a**) The average nano-hardness measurements as a function of depth of the unirradiated and irradiated Hf1Ta HEA; (**b**) corresponding profiles of H^2 versus h^{-1}.

For the uniform material, such as the unirradiated alloys, there was no deviation away from linearity in the profiles of H^2 versus h^{-1} based on the Nix–Gao model. As shown in Figure 10b, the hardness curves of the unirradiated Hf1Ta HEA exhibited a good linear relationship in the irradiation depth range of 80–2000 nm. The irradiated alloy was heterogeneous, with a hard and thin damaged layer near the surface. The volume of the plastic zone generated by the indenter pressing into the surface of the sample is usually much larger than that of the indenter. As the plastic zone extended to the lower undamaged region, the measured hardness value could be affected. In this case, the measured hardness value decreased with the increase of depth and finally approached the hardness of the unirradiated area, which was named as softer substrate effect (SSE) [61]. Therefore, there was a deviation away from linearity when the depth value was large enough (deeper than ~350 nm for the Hf1Ta HEA in this study). The values corresponding to the linearity were usually used for fitting to compare and study the hardness changes of the alloy before and after irradiation to a certain extent. In this study, due to indentation size effect and soft substrate effect, the values of hardness measured in the depth range of 80–350 nm in the irradiated Hf1Ta HEA and 80–2000 nm in the unirradiated Hf1Ta HEA were used for fitting to evaluate the hardness change.

The hardness value of the unirradiated sample was calculated as 3.78 GPa and the hardness increment (ΔH, hardness difference between unirradiated and irradiated samples) and hardening fraction ($\Delta H/H_0$, the ratio of the hardness increment to the hardness of unirradiated sample) are summarized in Table 7. As the irradiation fluence increased from 1×10^{16} to 3×10^{16} ions/cm^2, the hardness increment increased from 0.67 to 1.34 GPa, and the hardening fraction increased from 17.7% to 34.1%. Remarkably, the irradiation hardening fraction of the Hf1Ta HEA was equivalent to that of the BCC structured Ti-Zr-Nb-V-Mo HEAs, which was lower than those of most reported conventional low-activation materials at similar He ions' irradiation fluences (shown in Table 8). RHEAs of different systems showed good irradiation hardening resistance under He ion irradiation, and the selected elements could greatly affect the irradiation resistance of the HEAs, which is worthy of further study in the future.

Table 7. Nanoindentation test results of the Hf1Ta HEA at different fluences.

Fluence (ions/cm^2)	H_0 (GPa)	ΔH (GPa)	$\Delta H/H_0$ (%)
0	3.78	-	-
1×10^{16}	4.45	0.67	17.7
3×10^{16}	5.07	1.34	34.1

Table 8. The hardening fraction of some He-irradiated conventional low-activation materials and HEAs.

Alloys		Temperature (K)	Fluence ($\times 10^{16}$ ions/cm^2)	Hardening Fraction (%)
HEAs	TiZrNb [46]	1023	6	17.3
	TiZrNbV [46]	1023	6	41.3
	TiZrNbVMo [46]	1023	6	23.6
CMs	ODS [60]	723	5	48.1
	V-Cr-Ti [59]	573	5	52.0
	RAFM [65]	773	3	85.9
	CLAM [19]	773	3	61.1

Irradiation-induced defects, including dislocation loops, He bubbles, and stacking faults, could act as the barrier of sliding dislocations, and have a significantly negative impact on the mechanical properties of the irradiated alloys. It was reported that the obstacle strength of He bubble defects was strongly related to their sizes [66–68]. Compared to the smaller defects, the probability of interaction with dislocations was enhanced due to the large cross section of the oversized bubbles [46]. The maximum He bubble size in Hf1Ta HEA can reach more than 16 nm with average sizes of 10.5 and 13.7 nm at different fluences, which was conducive to enhancing the interaction between He bubbles and dislocations and improving the hardness. Thus, the formation of large He bubbles in the irradiated Hf1Ta HEA could be considered as the main cause of hardening. Compared with the sample irradiated at low fluence, the larger and denser He bubbles generated in the sample irradiated at high fluence can interact with the dislocations more effectively, which led to the higher hardness increment and hardening fraction in the Hf1Ta HEA irradiated at the fluence of 3×10^{16} ions/cm^2. Additionally, Zhao [33] and Shi [34] proposed that residual density of vacancies and interstitials produced by irradiation could be greatly reduced by the effective recombination in the HEAs. The severe lattice distortion in HEAs could impose restrictions on the formation and growth of defect clusters, resulting in small size defects with low density in the matrix. For those reasons, the force on dislocation movement could be weakened and the degradation of mechanical properties of the Hf1Ta HEA after irradiation was mitigated. Fine structural stability, limited radiation-induced segregation, and low residual defect density contributed to the good irradiation tolerance of the Hf1Ta HEA.

4. Conclusions

The novel low-activation $Ti_2ZrHf_xV_{0.5}Ta_{0.2}$ HEAs were designed and prepared. He ion irradiation experiments were employed to preliminarily evaluate irradiation tolerance of the representative Hf1Ta HEA. The microstructures and mechanical properties of the as-cast and irradiated samples were investigated. The main conclusions are as follows:

(1) The as-cast $Ti_2ZrHf_xV_{0.5}Ta_{0.2}$ HEAs exhibited BCC solid solution structure and the plastic strain exceeded 50%. Due to the solid solution strengthening caused by the increase of Hf content, the yield strength of the $Ti_2ZrHf_xV_{0.5}Ta_{0.2}$ HEAs enhanced from 745 to 873 MPa at room temperature and from 480 to 662 MPa at 873 K.

(2) No obvious radiation-induced element segregations or precipitations were found in the He-implanted Hf1Ta HEA, which reflected fine structural stability under He ion irradiation at 1023 K.
(3) The morphology of the He bubbles in the Hf1Ta HEA was faceted, which was similar to that found in the BCC structured conventional materials, Ti-Zr-Nb-V-Mo, and Ti-V-Nb-Ta RHEAs at elevated temperatures.
(4) As the irradiation fluence increased from 1×10^{16} to 3×10^{16} ions/cm^2, the average size of the He bubbles in Hf1Ta HEA increased from 10.5 to 13.7 nm and number density increased from 9.09×10^{20} to 2.42×10^{21} m^{-3}.
(5) With improving fluence, the irradiation hardness increment increased from 0.67 to 1.34 GPa, and the hardening fraction increased from 17.7% to 34.1%. Due to the low residual defect density and fine structural stability, the hardening fraction of the irradiated Hf1Ta HEA was lower than those of most reported conventional low-activation materials at similar He ions' irradiation fluences. The experimental results indicated that the novel low-activation RHEA may be one of the promising candidate structural materials for advanced nuclear energy system.

Author Contributions: H.Z., Investigation, Methodology, Data curation, Writing-Original draft preparation. Q.W., Formal Analysis and Software. C.L., Formal Analysis. Z.Z., Writing–Reviewing and Editing. H.H., Writing–Reviewing and Editing. Y.L., Writing–Reviewing and Editing, Visualization, Supervision. All authors have read and agreed to the published version of the manuscript.

Funding: Supported by the National Key Research and Development Program of China (Nos. 2019YFA0209901 and 2018YFA0702901), Liao Ning Revitalization Talents Program (No. XLYC1807047).

Institutional Review Board Statement: Not applicable.

Informed Consent Statement: Not applicable.

Data Availability Statement: Not applicable.

Conflicts of Interest: The authors declare no conflict of interest.

References

1. Lu, Y.P.; Huang, H.F.; Gao, X.; Ren, C.; Gao, J.; Zhang, H.Z.; Zheng, S.; Jin, Q.; Zhao, Y.; Lu, C.Y.; et al. A promising new class of irradiation tolerant materials: $Ti_2ZrHfV_{0.5}Mo_{0.2}$ high-entropy alloy. *J. Mater. Sci. Technol.* **2019**, *35*, 369–373. [CrossRef]
2. Lu, C.Y.; Niu, L.; Chen, N.; Jin, K.; Yang, T.; Xiu, P.; Zhang, Y.; Gao, F.; Bei, H.; Shi, S.; et al. Enhancing radiation tolerance by controlling defect mobility and migration pathways in multicomponent single-phase alloys. *Nat. Commun.* **2016**, *7*, 13564. [CrossRef] [PubMed]
3. Hussain, A.; Khan, S.A.; Sharma, S.K.; Sudarshan, K.; Sharma, S.K.; Singh, C.; Kulriya, P.K. Influence of defect dynamics on the nanoindentation hardness in NiCoCrFePd high entropy alloy under high dose Xe^{+3} irradiation. *Mater. Sci. Eng. A* **2023**, *863*, 144523. [CrossRef]
4. Griffiths, M. Effect of neutron irradiation on the mechanical properties, swelling and creep of Austenitic stainless steels. *Materials* **2021**, *14*, 2622. [CrossRef] [PubMed]
5. Zhang, Y.W.; Stocks, G.M.; Jin, K.; Lu, C.Y.; Bei, H.; Sales, B.C.; Wang, L.; Beland, L.K.; Stoller, R.E.; Samolyuk, G.D.; et al. Influence of chemical disorder on energy dissipation and defect evolution in concentrated solid solution alloys. *Nat. Commun.* **2015**, *6*, 8736. [CrossRef]
6. Ullah, M.W.; Aidhy, D.S.; Zhang, Y.; Weber, W.J. Damage accumulation in ion-irradiated Ni-based concentrated solid-solution alloys. *Acta Mater.* **2016**, *109*, 17–22. [CrossRef]
7. Moschetti, M.; Burr, P.A.; Obbard, E.; Kruzic, J.J.; Hosemann, P.; Gludovatz, B. Design considerations for high entropy alloys in advanced nuclear applications. *J. Nucl. Mater.* **2022**, *567*, 153814. [CrossRef]
8. Hussain, A.; Dhaka, R.S.; Ryu, H.J.; Sharma, S.K.; Kulriya, P.K. A critical review on temperature dependent irradiation response of high entropy alloys. *J. Alloys Compd.* **2023**, *948*, 169624. [CrossRef]
9. Amanzhulov, B.; Ivanov, I.; Uglov, V.; Zlotski, S.; Ryskulov, A.; Kurakhmedov, A.; Koloberdin, M.; Zdorovets, M. Composition and structure of NiCoFeCr and NiCoFeCrMn high-entropy alloys irradiated by helium ions. *Materials* **2023**, *16*, 3695. [CrossRef]
10. Ayyagari, A.; Salloom, R.; Muskeri, S.; Mukherjee, S. Low activation high entropy alloys for next generation nuclear applications. *Materialia* **2018**, *4*, 99–103. [CrossRef]
11. Sadeghilaridjani, M.; Ayyagari, A.; Muskeri, S.; Hasannaeimi, V.; Salloom, R.; Chen, W.Y.; Mukherjee, S. Ion irradiation response and mechanical behavior of reduced activity high entropy alloy. *J. Nucl. Mater.* **2020**, *529*, 151955. [CrossRef]

12. Carruthers, A.W.; Li, B.S.; Rigby, M.; Raquet, L.C.; Mythili, R.; Ghosh, C.; Dasgupta, A.; Armstrong, D.E.J.; Gandy, A.S.; Pickering, E.J. Novel reduced-activation TiVCrFe based high entropy alloys. *J. Alloys Compd.* **2021**, *856*, 157399. [CrossRef]
13. Klimenkov, M.; Jäntsch, U.; Rieth, M.; Dürrschnabel, M.; Möslang, A.; Schneider, H.C. Post-irradiation microstructural examination of EUROFER-ODS steel irradiated at 300 °C and 400 °C. *J. Nucl. Mater.* **2021**, *557*, 153259. [CrossRef]
14. Šćepanović, M.; de Castro, V.; García-Cortés, I.; Sánchez, F.J.; Gigl, T.; Hugenschmidt, C.; Leguey, T. Characterisation of open volume defects in Fe–Cr and ODS Fe–Cr alloys after He^+ and Fe^+ ion irradiations. *J. Nucl. Mater.* **2020**, *538*, 152230. [CrossRef]
15. Mandal, S.; Sharma, S.K.; Gayathri, N.; Sudarshan, K.; Mukherjee, P.; Pujari, P.K.; Menon, R.; Nabhiraj, P.Y.; Sagdeo, A. Synchrotron GIXRD and slow positron beam characterisation of Ar ion irradiated pure V and V-4Cr-4Ti alloy: Candidate structural material for fusion reactor application. *Fusion Eng. Des.* **2020**, *154*, 111518. [CrossRef]
16. Miyazawa, T.; Saito, H.; Hishinuma, Y.; Nagasaka, T.; Muroga, T.; Shen, J.; Okuno, Y.; Yu, H.; Kasada, R.; Hasegawa, A. Effect on impact properties of adding tantalum to V-4Cr-4Ti ternary vanadium alloy. *Nucl. Mater. Energy* **2022**, *31*, 101198. [CrossRef]
17. Ramachandran, R.; Julie, S.; Rajaraman, R.; Govindaraj, R.; David, C.; Amarendra, G. High-temperature radiation damage studies of Reduced Activation Ferritic/Martensitic (RAFM) steel at fusion relevant He/dpa ratio using positron beam based doppler broadening spectroscopy. *J. Nucl. Mater.* **2021**, *544*, 152697. [CrossRef]
18. Kachko, O.; Puype, A.; Terentyev, D.; Bonny, G.; Renterghem, W.V.; Petrov, R.H. Development of RAFM steels for high temperature applications guided by thermodynamic modelling. *Nucl. Mater. Energy* **2022**, *32*, 101211. [CrossRef]
19. Fu, Z.Y.; Liu, P.P.; Wan, F.R.; Zhan, Q. Helium and hydrogen irradiation induced hardening in CLAM steel. *Fusion Eng. Des.* **2015**, *91*, 73–78. [CrossRef]
20. Wei, Y.P.; Liu, P.P.; Zhu, Y.M.; Wang, Z.Q.; Wan, F.R.; Zhan, Q. Evaluation of irradiation hardening and microstructure evolution under the synergistic interaction of He and subsequent Fe ions irradiation in CLAM steel. *J. Alloys Compd.* **2016**, *676*, 481–488. [CrossRef]
21. Gao, M.C.; Liaw, P.K.; Yeh, J.W.; Zhang, Y. *High-Entropy Alloys: Fundamentals and Applications*; Springer: Berlin/Heidelberg, Germany, 2016. [CrossRef]
22. Ferreirós, P.A.; von Tiedemann, S.O.; Parkes, N.; Gurah, D.; King, D.J.M.; Norman, P.; Gilbert, M.R.; Knowles, A.J. VNbCrMo refractory high-entropy alloy for nuclear applications. *Int. J. Refract. Met. Hard Mat.* **2023**, *113*, 106200. [CrossRef]
23. Iroc, L.K.; Tukac, O.U.; Tanrisevdi, B.B.; El-Atwani, O.; Tunes, M.A.; Kalay, Y.E.; Aydogan, E. Design of oxygen-doped TiZrHfNbTa refractory high entropy alloys with enhanced strength and ductility. *Mater. Des.* **2022**, *223*, 111239. [CrossRef]
24. Thorhallsson, A.I.; Fanicchia, F.; Davison, E.; Paul, S.; Olafsson, D. Erosion and corrosion resistance performance of laser metal deposited high-entropy alloy coatings at hellisheidi geothermal site. *Materials* **2021**, *14*, 3071. [CrossRef] [PubMed]
25. Quiambao, K.F.; McDonnell, S.J.; Schreiber, D.K.; Gerard, A.Y.; Freedy, K.M.; Lu, P.; Saal, J.E.; Frankel, G.S.; Scully, J.R. Passivation of a corrosion resistant high entropy alloy in non-oxidizing sulfate solutions. *Acta Mater.* **2019**, *164*, 362–376. [CrossRef]
26. Mehmood, K.; Umer, M.A.; Munawar, A.U.; Imran, M.; Shahid, M.; Ilyas, M.; Firdous, R.; Kousar, H.; Usman, M. Microstructure and corrosion behavior of atmospheric plasma sprayed NiCoCrAlFe high entropy alloy coating. *Materials* **2022**, *15*, 1486. [CrossRef]
27. Miao, J.W.; Li, T.X.; Li, Q.; Chen, X.H.; Ren, Z.; Lu, Y.P. Enhanced surface properties of the $Al_{0.65}$CoCrFeNi high-entropy alloy via laser remelting. *Materials* **2023**, *16*, 1085. [CrossRef]
28. Nagarjuna, C.; Sharma, A.; Lee, K.; Hong, S.-J.; Ahn, B. Microstructure, mechanical and tribological properties of oxide dispersion strengthened CoCrFeMnNi high-entropy alloys fabricated by powder metallurgy. *J. Mater. Res. Technol.* **2023**, *22*, 1708–1722. [CrossRef]
29. Kumar, P.; Kim, S.J.; Yu, Q.; Ell, J.; Zhang, M.; Yang, Y.; Kim, J.Y.; Park, H.K.; Minor, A.M.; Park, E.S.; et al. Compressive vs. tensile yield and fracture toughness behavior of a body-centered cubic refractory high-entropy superalloy $Al_{0.5}Nb_{1.25}Ta_{1.25}TiZr$ at temperatures from ambient to 1200 °C. *Acta Mater.* **2023**, *245*, 118620. [CrossRef]
30. Chakraborty, P.; Sarkar, A.; Ali, K.; Jha, J.; Jothilakshmi, N.; Arya, A.; Tewari, R. Design and development of low density, high strength ZrNbAlVTi high entropy alloy for high temperature applications. *Int. J. Refract. Met. Hard Mat.* **2023**, *113*, 106222. [CrossRef]
31. Kumar, N.A.P.K.; Li, C.; Leonard, K.J.; Bei, H.; Zinkle, S.J. Microstructural stability and mechanical behavior of FeNiMnCr high entropy alloy under ion irradiation. *Acta Mater.* **2016**, *113*, 230–244. [CrossRef]
32. Senkov, O.N.; Wilks, G.B.; Miracle, D.B.; Chuang, C.P.; Liaw, P.K. Refractory high-entropy alloys. *Intermetallics* **2010**, *18*, 1758–1765. [CrossRef]
33. Razumov, N.; Makhmutov, T.; Kim, A.; Shemyakinsky, B.; Popovich, A.J.M. Refractory CrMoNbWV high-entropy alloy manufactured by mechanical alloying and spark plasma sintering: Evolution of microstructure and properties. *Materials* **2021**, *14*, 621. [CrossRef]
34. Ceritbinmez, F.; Kanca, E.; Yünlü, L.; Patel, K.; Akhtar, M.A.; Mukherjee, S.; Günen, A. Wire electric discharge machining and its effect on the surface finish of HfNbTaTiZr refractory high-entropy alloy. *Int. J. Adv. Manuf. Technol.* **2023**, *125*, 1419–1427. [CrossRef]
35. Günen, A.; Ceritbinmez, F.; Patel, K.; Akhtar, M.A.; Mukherjee, S.; Kanca, E.; Karakas, M.S. WEDM machining of MoNbTaTiZr refractory high entropy alloy. *CIRP J. Manuf. Sci. Technol.* **2022**, *38*, 547–559. [CrossRef]
36. El-Atwani, O.; Li, N.; Li, M.; Devaraj, A.; Martinez, E.J.S.A. Outstanding radiation resistance of Tungsten-based high entropy alloys. *Sci. Adv.* **2019**, *5*, eaav2002. [CrossRef] [PubMed]
37. Levo, E.; Granberg, F.; Fridlund, C.; Nordlund, K.; Djurabekova, F. Radiation damage buildup and dislocation evolution in Ni and equiatomic multicomponent Ni-based alloys. *J. Nucl. Mater.* **2017**, *490*, 323–332. [CrossRef]
38. Jin, K.; Lu, C.Y.; Wang, L.M.; Qu, J.; Weber, W.J.; Zhang, Y.; Bei, H. Effects of compositional complexity on the ion-irradiation induced swelling and hardening in Ni-containing equiatomic alloys. *Scr. Mater.* **2016**, *119*, 65–70. [CrossRef]

39. Chang, S.; Tseng, K.K.; Yang, T.Y.; Chao, D.S.; Yeh, J.W.; Liang, J.H. Irradiation-induced swelling and hardening in HfNbTaTiZr refractory high-entropy alloy. *Mater. Lett.* **2020**, *272*, 127832. [CrossRef]
40. He, M.R.; Wang, S.; Shi, S.; Jin, K.; Bei, H.; Yasuda, K.; Matsumura, S.; Higashida, K.; Robertson, I.M. Mechanisms of radiation-induced segregation in CrFeCoNi-based single-phase concentrated solid solution alloys. *Acta Mater.* **2017**, *126*, 182–193. [CrossRef]
41. Lu, C.Y.; Yang, T.; Jin, K.; Gao, N.; Xiu, P.; Zhang, Y.; Gao, F.; Bei, H.; Weber, W.J.; Sun, K.; et al. Radiation-induced segregation on defect clusters in single-phase concentrated solid-solution alloys. *Acta Mater.* **2017**, *127*, 98–107. [CrossRef]
42. Zhang, Z.; Han, E.H.; Xiang, C. Irradiation behaviors of two novel single-phase bcc-structure high-entropy alloys for accident-tolerant fuel cladding. *J. Mater. Sci. Technol.* **2021**, *84*, 230–238. [CrossRef]
43. Abhaya, S.; Rajaraman, R.; Kalavathi, S.; David, C.; Panigrahi, B.K.; Amarendra, G. Effect of dose and post irradiation annealing in Ni implanted high entropy alloy FeCrCoNi using slow positron beam. *J. Alloys Compd.* **2016**, *669*, 117–122. [CrossRef]
44. Zhao, S.J. Defect properties in a VTaCrW equiatomic high entropy alloy (HEA) with the body centered cubic (bcc) structure. *J. Mater. Sci. Technol.* **2020**, *44*, 133–139. [CrossRef]
45. Shi, T.; Su, Z.; Li, J.; Liu, C.; Yang, J.; He, X.; Yun, D.; Peng, Q.; Lu, C. Distinct point defect behaviours in body-centered cubic medium-entropy alloy NbZrTi induced by severe lattice distortion. *Acta Mater.* **2022**, *229*, 117806. [CrossRef]
46. Zhang, H.Z.; Huang, H.F.; He, T.; Yan, H.W.; Zhang, Y.A.; Lu, Y.P.; Wang, T.M.; Li, T.J. Microstructures, mechanical properties, and irradiation tolerance of the Ti–Zr–Nb–V–Mo refractory high-entropy alloys. *Intermetallics* **2023**, *157*, 107873. [CrossRef]
47. WebElements. The Periodic Table of the Elements. Available online: https://www.webelements.com (accessed on 1 March 2023).
48. Guo, S.; Ng, C.; Lu, J.; Liu, C.T. Effect of valence electron concentration on stability of fcc or bcc phase in high entropy alloys. *J. Appl. Phys.* **2011**, *109*, 103505. [CrossRef]
49. Zhang, Y.; Zhou, Y.J.; Lin, J.P.; Chen, G.L.; Liaw, P.K. Solid-solution phase formation rules for multi-component alloys. *Adv. Eng. Mater.* **2008**, *10*, 534–538. [CrossRef]
50. Yang, X.; Zhang, Y. Prediction of high-entropy stabilized solid-solution in multi-component alloys. *Mater. Chem. Phys.* **2012**, *132*, 233–238. [CrossRef]
51. Duemmler, K.; Zheng, C.; Baumier, C.; Gentils, A.; Kaoumi, D. Helium bubble nucleation and growth in alloy HT9 through the use of in situ TEM: Sequential he-implantation and heavy-ion irradiation versus dual-beam irradiation. *J. Nucl. Mater.* **2021**, *545*, 152641. [CrossRef]
52. Chen, D.; Tong, Y.; Li, H.; Wang, J.; Zhao, Y.L.; Hu, A.; Kai, J.J. Helium accumulation and bubble formation in FeCoNiCr alloy under high fluence He^+ implantation. *J. Nucl. Mater.* **2018**, *501*, 208–216. [CrossRef]
53. Daghbouj, N.; Sen, H.S.; Callisti, M.; Vronka, M.; Karlik, M.; Duchoň, J.; Čech, J.; Havránek, V.; Polcar, T. Revealing nanoscale strain mechanisms in ion-irradiated multilayers. *Acta Mater.* **2022**, *229*, 117807. [CrossRef]
54. Daghbouj, N.; Li, B.S.; Callisti, M.; Sen, H.S.; Karlik, M.; Polcar, T. Microstructural evolution of helium-irradiated 6H–SiC subjected to different irradiation conditions and annealing temperatures: A multiple characterization study. *Acta Mater.* **2019**, *181*, 160–172. [CrossRef]
55. Yan, Z.; Yang, T.; Lin, Y.; Lu, Y.; Su, Y.; Zinkle, S.J.; Wang, Y. Effects of temperature on helium bubble behaviour in Fe–9Cr alloy. *J. Nucl. Mater.* **2020**, *532*, 152045. [CrossRef]
56. Ofan, A.; Zhang, L.; Gaathon, O.; Bakhru, S.; Bakhru, H.; Zhu, Y.; Welch, D.; Osgood, R.M. Spherical solid He nanometer bubbles in an anisotropic complex oxide. *Phys. Rev. B* **2010**, *82*, 104113. [CrossRef]
57. Jia, N.; Li, Y.; Huang, H.; Chen, S.; Li, D.; Dou, Y.; He, X.; Yang, W.; Xue, Y.; Jin, K. Helium bubble formation in refractory single-phase concentrated solid solution alloys under MeV He ion irradiation. *J. Nucl. Mater.* **2021**, *550*, 152937. [CrossRef]
58. Liu, S.; Lin, W.; Chen, D.; Han, B.; Zhao, S.; He, F.; Niu, H.; Kai, J.J. Effects of temperature on helium cavity evolution in single-phase concentrated solid-solution alloys. *J. Nucl. Mater.* **2021**, *557*, 153261. [CrossRef]
59. Jiang, S.; Yu, C.; Zheng, P.; Guo, L.; Zhou, X.; Rao, W.F. Bubbles and precipitates formation and effects on the hardening of irradiated vanadium alloys. *J. Nucl. Mater.* **2021**, *544*, 152712. [CrossRef]
60. Wu, Z.F.; Xu, L.D.; Chen, H.Q.; Liang, Y.X.; Du, J.L.; Wang, Y.F.; Zhang, S.L.; Cai, X.C.; Sun, B.R.; Zhang, J.; et al. Significant suppression of void swelling and irradiation hardening in a nanograined/nanoprecipitated 14YWT-ODS steel irradiated by helium ions. *J. Nucl. Mater.* **2022**, *559*, 153418. [CrossRef]
61. Zhu, Z.; Huang, H.; Muránsky, O.; Liu, J.; Zhu, Z.; Huang, Y. On the irradiation tolerance of nano-grained Ni–Mo–Cr alloy: 1 MeV He^+ irradiation experiment. *J. Nucl. Mater.* **2021**, *544*, 152694. [CrossRef]
62. Bai, J.; Li, J.; Fu, C.; Ren, C.; Chen, S.; Li, Y.; Li, Z.; Chen, Q.; Zhu, Z.; Lin, J. Effect of helium bubbles on the irradiation hardening of GH3535 welded joints at 650 °C. *J. Nucl. Mater.* **2021**, *557*, 153241. [CrossRef]
63. Cui, M.; Wang, J.; Wang, Z.; Shen, T.; Wei, K.; Yao, C.; Sun, J.; Gao, N.; Zhu, Y.; Pang, L.; et al. Helium irradiation induced hardening in MNHS steels. *Nucl. Instrum. Methods Phys. Res. Sect. B Beam Interact. Mater. Atoms* **2017**, *406*, 611–617. [CrossRef]
64. Zhou, X.L.; Huang, H.F.; Xie, R.; Thorogood, G.J.; Yang, C.; Li, Z.J.; Xu, H.J. Helium ion irradiation behavior of Ni-1wt.%SiC_{NP} composite and the effect of ion flux. *J. Nucl. Mater.* **2015**, *467*, 848–854. [CrossRef]
65. Liu, P.P.; Han, W.T.; Yi, X.O.; Zhan, Q.; Wan, F.R. Effect of He and H synergy on mechanical property of ion-irradiated Fe-10Cr alloy. *Fusion Eng. Des.* **2018**, *129*, 221–229. [CrossRef]
66. Wang, Q.; Judge, C.D.; Howard, C.; Mattucci, M.; Rajakumar, H.; Hoendermis, S.; Dixon, C.; Daymond, M.R.; Bickel, G. Investigation on the deformation mechanisms and size-dependent hardening effect of He bubbles in 84 dpa neutron irradiated Inconel X-750. *Nucl. Mater. Energy* **2021**, *28*, 101025. [CrossRef]

67. Simar, A.; Voigt, H.J.L.; Wirth, B.D. Molecular dynamics simulations of dislocation interaction with voids in nickel. *Comput. Mater. Sci.* **2011**, *50*, 1811–1817. [CrossRef]
68. Sobie, C.; Bertin, N.; Capolungo, L. Analysis of obstacle hardening models using dislocation dynamics: Application to irradiation-induced defects. *Metall. Mater. Trans. A* **2015**, *46*, 3761–3772. [CrossRef]

materials

MDPI

Article

Characterization of Complex Concentrated Alloys and Their Potential in Car Brake Manufacturing

Ioana Anasiei [1,†], Dumitru Mitrica [1,†], Ioana-Cristina Badea [1,†], Beatrice-Adriana Șerban [1,*], Johannes Trapp [2], Andreas Storz [3], Ioan Carcea [4], Mihai Tudor Olaru [1,*], Marian Burada [1], Nicolae Constantin [5], Alexandru Cristian Matei [1], Ana-Maria Julieta Popescu [6] and Mihai Ghiță [1]

[1] National R&D Institute for Non-Ferrous and Rare Metals, 102 Biruinței, 077145 Bucharest, Romania; ianasiei@imnr.ro (I.A.); dmitrica@imnr.ro (D.M.); cristina.banica@imnr.ro (I.-C.B.); mburada@imnr.ro (M.B.); alex.matei@imnr.ro (A.C.M.); mihai@imnr.ro (M.G.)
[2] Fraunhofer Institute for Manufacturing Technology and Advanced Materials—IFAM, Winterbergstr. 28, 01277 Dresden, Germany; johannes.trapp@ifam-dd.fraunhofer.de
[3] Sigma Materials GmbH, Wupperstrasse 36a, 40699 Erkrath, Germany; andreas.storz@sigma-materials.de
[4] Rancon S.R.L., 25 G. Coșbuc St., 70293 Iași, Romania; ioan.carcea@yahoo.com
[5] Faculty of Materials Science and Engineering, University Politehnica of Bucharest, 313 Splaiul Independentei, 060042 Bucharest, Romania; nctin2014@yahoo.com
[6] Romanian Academy, "Ilie Murgulescu" Institute of Physical Chemistry, 202 Splaiul Independenței, 060021 Bucharest, Romania; popescuamj@yahoo.com
* Correspondence: beatrice.carlan@imnr.ro (B.-A.Ș.); o.mihai@imnr.ro (M.T.O.)
† These authors contributed equally to this work.

Abstract: The paper studies new materials for brake disks used in car manufacturing. The materials used in the manufacturing of the brake disc must adapt and correlate with the challenges of current society. There is a tremendous interest in the development of a material that has high strength, good heat transfer, corrosion resistance and low density, in order to withstand high-breaking forces, high heat and various adverse environment. Low-density materials improve fuel efficiency and environmental impact. Complex concentrated alloys (CCA) are metallic element mixtures with multi-principal elements, which can respond promisingly to this challenge with their variety of properties. Several compositions were studied through thermodynamic criteria calculations (entropy of mixing, enthalpy of mixing, lambda coefficient, etc.) and CALPHAD modeling, in order to determine appropriate structures. The selected compositions were obtained in an induction furnace with a protective atmosphere and then subjected to an annealing process. Alloy samples presented uniform phase distribution, a high-melting temperature (over 1000 °C), high hardness (1000–1400 HV), good corrosion resistance in 3.5 wt.% NaCl solution (under 0.2 mm/year) and a low density (under 6 g/cm^3).

Keywords: complex concentrated alloys; structural characterization; corrosion resistance; transportation applications; materials design

Citation: Anasiei, I.; Mitrica, D.; Badea, I.-C.; Șerban, B.-A.; Trapp, J.; Storz, A.; Carcea, I.; Olaru, M.T.; Burada, M.; Constantin, N.; et al. Characterization of Complex Concentrated Alloys and Their Potential in Car Brake Manufacturing. *Materials* **2023**, *16*, 5067. https://doi.org/10.3390/ma16145067

Academic Editor: Xianfei Ding

Received: 20 June 2023
Revised: 6 July 2023
Accepted: 12 July 2023
Published: 18 July 2023

1. Introduction

The braking system plays a crucial role in stopping or slowing down a vehicle by creating frictional resistance [1].

The braking system mainly consists of a disk bolted to the wheel hub and a caliper containing pads connected to the axle stationary housing. The caliper applies a braking force to the disk through the braking pads to slow down or stop the vehicle. The brake disk is the main component that makes the connection between the wheels and the car. High-mechanical forces are developing at this stage and friction produces high local heat (up to 1000 °C). Due to the importance and necessity of the brake disc, the material requirements have to be established and defined very clearly. High strength at low and higher temperatures, high-friction coefficient, good heat capacity and corrosion resistance

are the main characteristics of brake disk materials [2]. On the other hand, the automotive industry is in continuous development, and it is important to consider a series of additional competitive factors, specifically, lightweight and low particulate emissions.

Several types of materials are used to manufacture the components of the braking system, such as cast iron, aluminum alloys, titanium alloys, composite materials and carbon fibers [3]. From all the materials, the most used is grey cast iron, due to its high strength, high-temperature stability and low-manufacturing costs [4]. Although grey cast iron has been used extensively, it has several disadvantages. Grey cast iron has a high density of 7.25 kg/cm^3, and low-corrosion resistance, which determine high-fuel consumption, short maintenance intervals and significant particulate pollution. The most important disadvantage of using cast iron for the brake disk is environmental pollution. Recent studies show that 16–55 mass% of non-exhaust PM10 emissions are caused by brake wear [5]. Above all, size is an important aspect, as it determines how deep the particles can penetrate the human body. Using the PM10, PM2.5, PM1, and PM0.1 classifications, the average brake dust particle diameter is about 2 μm, well within the 2.5 range. Additionally, some sources show a second distribution peak around PM0.1, indicating the severity of the respirable dust and particulate matter problem. Small particles in the air can be inhaled and penetrate deep into the lung tissue, causing serious lung disease. Small particles are produced as a result of the disc and the brake pads friction. These particles remain in suspension in the atmosphere, being a source of pollution and a human health hazard [6–9]. Seo et al. [7] studied the suspended particle pollution of four types of brake discs made from three types of cast iron (FC170, FC200 FC250) and a ceramic material, in order to analyze the particle size and mass concentration. The study showed that cast iron generates the most airborne particles. Ghouri et al. [8] studied the influence of corrosion on particle pollution for grey cast iron disk brakes. It was found that corroded disks increase the particle emissions by double and also inhibited braking performance by reducing the coefficient of friction. The effect of temperature on particulate emissions was calculated by Seo et al. in [9]. It was found that the thermal conductivity is one of the main depending factors and that cast iron disks produce the highest amounts of particulate matter.

Complex concentrated alloys (CCAs) represent a promising solution to this challenge, due to the high versatility of their properties [10]. These new materials have the advantage of having a high number of component elements that can form complex combinations, which leads to a series of favorable properties. CCAs are including the high-entropy alloy (HEA) family by allowing a larger compositional domain, formation of intermetallic phases and without a minimum number of elements. Alloys from this group of materials generally have a higher configurational entropy than conventional alloys. Due to this characteristic, CCAs tend to form disordered and compositionally complex solid solution structures. The large number of component elements allows for a higher degree of freedom in alloy compositions and properties.

Several alloy compositions, containing low-density elements, have been investigated by several research teams [10–14]. In order to induce the high-entropy effect, some authors maintained the group of elements that are found in most of the studied HEA and added, in a controlled manner, lighter elements. A light weight HEA based on the Cr-Fe-Mn system, with gradual additions of Al and Ti, was studied by Feng et al. [11]. A dominant BCC structure was obtained at low additions of Ti; still, the alloy brittleness and relatively high density can be detrimental in several applications. Kushnerov and Bashev [12] investigated the Al and Si additions to the main Cu-Fe-Mn-Ni system and found that cooling rates strongly influence the phase constitution of the alloy. Most of the alloy compositions formed a single-phase FCC structure in the as-cast state, but the density of the material was over 4 g/cm^3. A LWHEA with a high proportion of low-density elements was developed by TSENG et al. [13]. The alloy presented a predominant BCC-type solid solution structure and a lower level of intermetallic phases. The Al20Be20Fe10Si15Ti35 alloy delivered good mechanical properties and oxidation resistance. Still, Be is a safety hazard element and may raise the production costs. Recently, a research in the field

of LWCCAs was performed by Gondhalekar [14], aiming to design and develop new light-weight aluminium based CCAs. Empirical rules from HEA design were applied in the process, alongside with thermodynamic modeling. Several compositions containing Ag were found to have good potential, but the alloy cost may restrict the use for light weight applications. Other compositions have been proposed by Mitrica et al. [15,16] but improvements need to be made for the reduction of intermetallic phase content and for particle distribution improvements.

The development of complex light alloys with higher strength and high-temperature stability has been researched by several authors.

A new alloy system, Al-Fe-Mn-Si, was designed and researched by O'Brien et al. [17], intended to deliver good corrosion resistance and mechanical properties. The new multi-phase, CCA, has equimolar composition and is based on four principal elements, AlFeMnSi. The results showed that the developed alloy exhibited excellent corrosion resistance and high hardness due to the presence of Fe in high proportion; therefore, the alloy is less expensive with 46% than stainless steel 304 L, and has a lower density of 4.5 g/cm^3.

The idea for the substitution of Ni with Ti for lowering the density in the well-known high-entropy alloy system, Al-Cr-Fe-Mn-Ni, was investigated by Rui Feng et al. in [11]. The authors investigated the phase formation in AlxCrFeMnTiy alloy system through the assessment of various empirical rules pertaining to light-weight HEAs. A comparison between experimental and modeling results showed significant differences. CALPHAD modeling was also performed on Al-Cr-Nb-Ti-V and Cr-Nb-Ti-V-Zr systems, producing enthalpies of mixing values at higher temperatures.

A medium-entropy alloy (MEA) system, based on the Al-Ti-Cr-Mn-V system, was developed by Liao et al. [18] using a nonequiatiomic approach, maintaining Al concentration at 50 at.%, and the main group (TiCrMn) between 30 and 45 at.%. The results showed great mechanical properties before and after annealing, meaning a compression strength of 1940 MPa, while producing a ductility of 30%.

Several research pathways were followed in the past for replacing the well-known and widely applied cast-iron brakes. Different materials were trialed but they lack one of more of the cast iron main properties: high resistance, high-temperature stability and a high-friction coefficient. The aluminum matrix composite materials became the most promising materials, as they are relatively inexpensive to produce, have good mechanical resistance, a good friction coefficient, lower density and lower particulate emissions. The main impediment is the resistance at higher temperatures that is limited by the aluminum alloy matrix.

The present work focuses on the development of new alloys for the manufacturing of disk brakes with low density, high hardness, high-temperature stability and corrosion resistance. The main goal is to provide comparative analyses between two promising alloy systems, i.e., the modeling approach, and to investigate the influence of heat treatment on the structure and properties of the materials and the degree of predictability of the structure offered by the investigated methods. Another important aspect of this study is the applicability potential of the new materials to replace gray cast iron in the manufacture of the brake discs.

2. Materials and Methods

Obtaining a material that meets the requirements imposed by the transport industry and society requires a careful and elaborate selection between the possible CCAs systems. Considering that the particularities of each component element of the alloy have an impact on the final properties of the CCA, selected metals must have a positive effect on the desired characteristics. To obtain a material with a low density, elements such as aluminum, iron and silicon were selected. Cr, Fe and Mn have a relatively high density, but they can be used to increase the melting temperature of the alloy. Also, some of these elements, such as Al and Fe, have attracted attention due to their affordable cost and favorable contributions to the economic impact of the material.

To obtain the most suitable composition of the alloys, there are several useful tools, including the semi-empirical criteria. The criteria with significant effects over the structure and the properties of the alloys are: mixing entropy (ΔS_{mix}), enthalpy of mixing (ΔH_{mix}), atomic size difference (δ), parameter Ω, Allen electronegativity difference (Δ_χ), valence electron concentration (VEC) and the geometrical parameter (Λ).

In this study, the degree of formation of solid solutions was analyzed by calculating Allen electronegativity difference and the geometrical parameter Λ.

The parameter Λ has a high-predictive power on the alloy structure, as mentioned by Anil Kumar Singh et al. [19]. If it has a lower value than 0.24, it will form a multiphase structure containing intermetallic phases. Otherwise, if the aim is to obtain a structure with a single phase of solid solution type, then this parameter must have a value greater than 0.96. If Λ values fall between these two values, then two phase mixtures can be formed.

The parameter Λ depends on the mixing entropy and the atomic size difference of the mixture. The mixing entropy is also an important parameter that characterizes the ability to form a solid solutions structure, and it is determined using Boltzmann's equations [20]:

$$\Delta S_{mix} = -R \cdot \sum c_i \cdot \ln c_i \quad (1)$$

where R is the gas constant and c_i is the molar fraction of the element i.

The atomic radius difference is considered the parameter with the strongest influence on the structure, and is preferable so that the component elements of the alloy have appropriate values [20]. The difference in atomic radius was calculated with Equation (2) [21].

$$\delta = 100 \cdot \sqrt{\sum c_i \cdot \left(1 - \frac{r_i}{\bar{r}}\right)^2} \quad (2)$$

where r_i is the atomic radius of the element i and $\bar{r}$ is the atomic radius average.

Knowing the difference in atomic radius and mixing entropy, the parameter Λ can be determined through Equation (3) [19]:

$$\Lambda = \Delta S_{mix} / \delta^2 \quad (3)$$

To calculate the Allen electronegativity difference ($\Delta\chi$), it is important to know the electronegativity after Pauling for element i (χ_i) and the electronegativity average ($\overline{\chi}$). For the alloy to form solid solutions, its value must be between 3–6%. The Allen electronegativity difference was calculated using Equation (4) [22]:

$$\Delta\chi = 100 \cdot \sqrt{\sum c_i \cdot \left(1 - \frac{\chi_i}{\overline{\chi}}\right)^2} \quad (4)$$

The thermodynamic and kinetic simulation of alloy structures is very useful in the optimization of CCAs systems. This was performed through the Matcalc Pro edition software, version 6.02. The CALPHAD method (CALculation of PHAse Diagrams) analysis is the basis of thermodynamic modeling, while the kinetic evaluation was achieved through the use of specialized modules that study solid-state phase transformations.

The selected alloys were prepared using raw materials of technical purity and mixed to obtain a charge of 250 g of each individual alloy composition. The primary metals were Al, Fe, Mn and Si for the AlFeMnSi alloy, and Al, Cr, Fe, Mn and Ti for $Al_4CrFeMnTi_{0.25}$. The charge for each composition was placed in an alumina–zirconia crucible, in an induction furnace, Linn MFG, 300 type-, with argon atmosphere. After melting, the alloys were cast in a cylindrical copper mold and cooled in the furnace under vacuum. In order to increase the degree of homogeneity, the alloys were remelted several times. The as-cast samples were subjected to heat treatment in an electrical furnace, LHT 04/17 Nabertherm GMBH (Lilienthal, Germany). The heat treatment stage was conducted at 700 °C for 50 h with a slow cooling rate.

The obtained samples, before and after the heat treatment process, were characterized by chemical, structural, mechanical and corrosion analyses.

The chemical composition of the samples was analyzed by inductively coupled plasma spectrometry (ICP-OES) using an Agilent 725 spectrometer (Santa Clara, CA, USA). The structure of the samples was also investigated by SEM-EDAX characterization, with a scanning electron microscope, FEI Quanta 250 (FEI Europe B.V., Eindhoven, The Netherlands). It is equipped with an X-ray spectrometer (EDS), which provides information about the chemical composition of the sample phases.

For a better understanding of the configuration of the phases, XRD analysis was also performed. The sample was analyzed by using a BRUKER D8 ADVANCE powder X-ray diffractometer (CuKα1 radiation, Johannson Ge (111) monochromator) equipped with a PSD Lynx-Eye detector in Θ–2Θ reflection configuration. Data acquisition was performed using DIFFRACplus XRD Commander (Bruker AXS) software in the 2Θ-Region 20–120 with step size 0.020, holding time 8.7 s/step, and sample rotation speed 15 rot/min. The powder sample was mounted on a zero background sample holder. The collected data were processed using a Bruker® Diffracplus EVA Release 2018 software and the database ICDD® Powder Diffraction File (PDF4+, 2019 edition) was used for the phase identification.

The corrosion tests were achieved using Voltalab 80 PGZ 402, with a Volta Master software, version 7.0.8. The tests were performed in a sodium chloride solution of 3.5%, according with the method presented in [23].

Designing an alloy that has the highest melting temperature is of great importance, because the higher it is, the higher the working temperature and the better the thermal resistance. The temperature at which the reactions with heat exchange took place were determined by the thermal analysis equipment Setsys Evolution, Setaram.

Vickers microhardness of the samples were ascertained using a micro-indenter attachment Anton Paar MHT10 (Anton Paar, Graz, Austria, at 25 C, by an applied load of 2 N and a slope of 0.6 N/s. The microhardness was performed using a Zeiss Axio Imager A1m microscope (Zeiss, Jena, Germany).

3. Results and Discussions

3.1. CCAs Structure Design Depending on the Element Concentation

Considering the phase concentration variation in the AlCrFeMnTi and AlFeMnSi alloys systems, the Matcalc simulation program was used to study phase redistribution in the solidification process.

The calculated phase distribution of the AlCrFeMnTi alloy system is shown in Figure 1. The variation of the elements has a significant influence on the phases that can form in the structure. At 200 °C temperature, the variation of eight phases was observed: BCC_A2, BCC_B2, Cub_A13, $AlCr_2$, Al_2Ti, Cr_3Mn_5, FeTi and H_Sigma. Figure 1a shows that a high concentration of BBC_B2 phase is found when the Al content exceeds 13 wt.%, while Cr_3Mn_5 and Cub_A13 phases suffer a decrease in phase fraction. Increasing the aluminum content in the alloy does not have a strong influence on obtaining the $AlCr_2$ phase, which reaches a peak of 0.05 phase fraction between 11 wt.% and 13%. It was also observed that the increase in the Al content leads to a decrease in the concentration of the BCC_A2 and FeTi phases, and after 15 wt.% Al these phases are not found any more in the structure. On the other hand, from Figure 1b, it can be observed that the BCC_B2 phase decreases in proportion to the increase in Cr content. The solid solution BCC_A2 reaches the peak of 0.2 phase fraction at 12%Cr. To obtain a structure composed of the intermetallic compound Cr_3Mn_5, it is necessary for the Cr content to exceed 11%. Between 12 wt.% and 17 wt.%, the variation of the $AlCr_2$ phase can be observed. The proportion of the H_Sigma phase increases after 15 wt.% Al, while FeTi increases after 22 wt.%. The variation of Cr in the alloy does not have a significant influence on FeTi and Cub_A13, which no longer appear in the structure after 1 wt.%, and, respectively, 7 wt.%. The variation of Fe on the phases can be seen in Figure 1c. As in the case of Cr, increasing the Fe content leads to a reduction in the proportion of the BCC_B2 phase, which reaches a peak of 0.8 phase fraction at 10 wt.%

Fe. A significant proportion of the BCC_A2 phase can be observed between 13 wt.% and 19 wt.% Fe. This element has an inconstant influence on the $AlCr_2$ and Cr_3Mn_5 phases, noting that at 15 wt.% Fe, the two phases no longer appear. On the other hand, FeTi and H_Sigma phases increased in proportion after 25 wt.% Fe and, respectively, 18 wt.% Fe. In Figure 1d, it can be observed that the presence of Mn influenced the formation of the phase's structure by favoring the increasing of the BCC_B2 phase, until 24 wt.% Mn. Also, after 23 wt.% Mn, the FeTi phase starts to increase in proportion. When up to 13% wt.% Cr, the Al_2Ti phase decreases in concentration, while the H_Sigma phase increases. The $AlCr_2$ phase reaches a peak of 0.3 phase fraction at 13 wt.% Mn, after which it decreases. Figure 1e shows the influence of Ti concentration on the phases variation. BCC_B2 is the predominant phase in the structure at a content of less than 20 wt.% Mn. The BCC_A2 solid solution is found in high proportions in the alloy structure at a low Ti content, but after 13 wt.%, this will no longer be present. On the other hand, after 13 wt.% Ti, the H_Sigma phase increases in proportion, reaching approximately 0.25 phase fraction at 16 wt.% Ti. The $AlCr_2$ phase is observed to reach 0.2 phase fraction at 15 wt.% Ti, after which, it decreases in proportion. On the other hand, it was observed that the Cr_3Mn_5 phase has an inconstant growth with the increase of Ti.

The phase evolution, depending on element concentration, was calculated for AlFeMnSi alloy system (Figure 2). A higher concentration of Al has a strong influence over the formation of Al_2Fe, which becomes more stable over 15 wt.% Al (Figure 2a). The influence of Al content is shown also by the transition between Al_2Fe and BCC_B2 at higher Al concentrations. After 26% wt.% Al, Al_2Fe phase increases in proportion, while the other phases decrease. The aluminum concentration has a minor influence on the formation of the BCC_A2_#01 phase: a variation of the BCC_A2 phase.

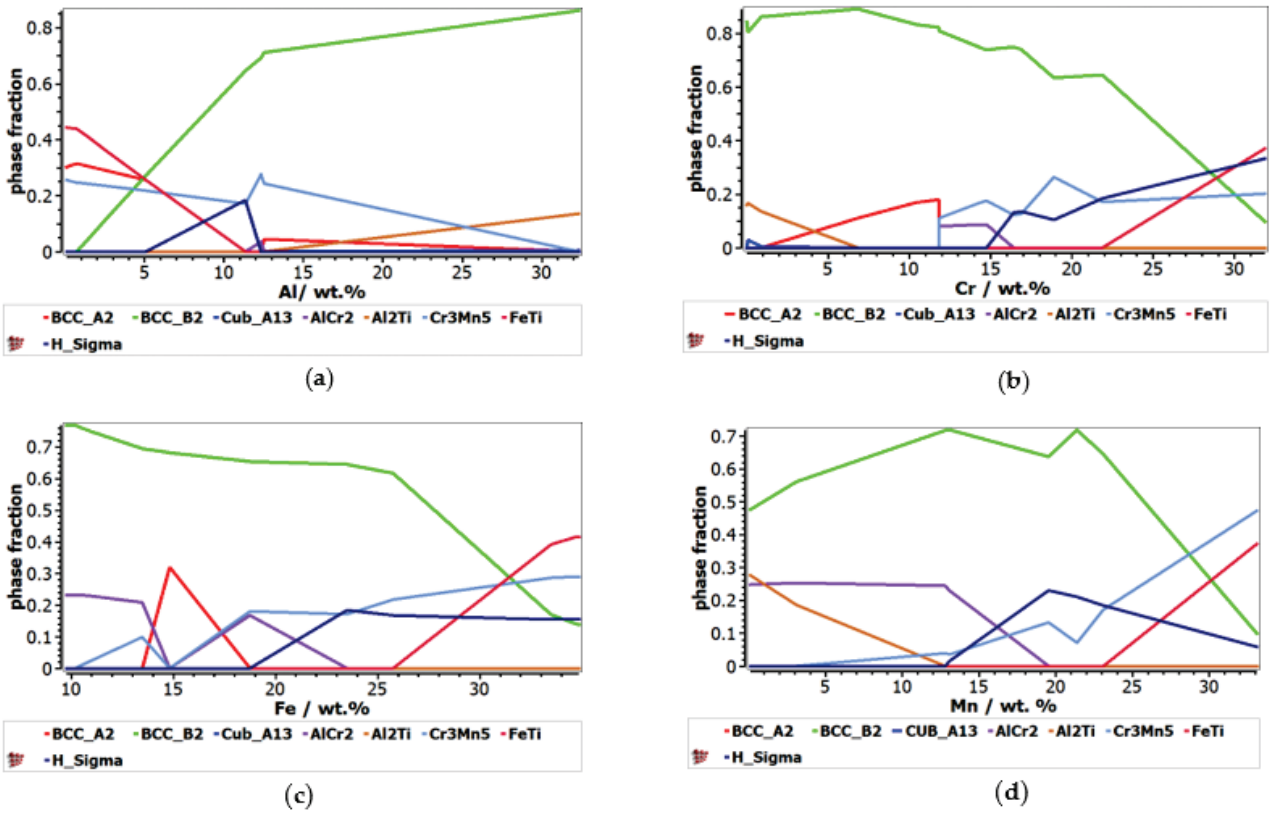

Figure 1. *Cont.*

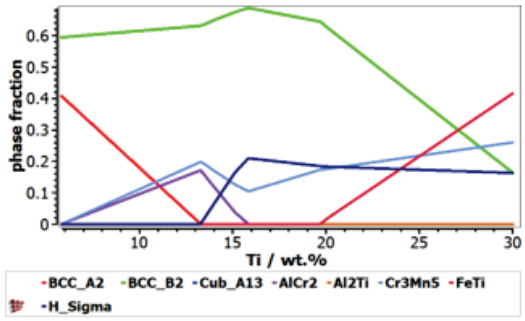

(**e**)

Figure 1. The impact of the alloying element on the phase stability for the AlCrFeMnTi alloy system: (**a**) Al influence; (**b**) Cr influence; (**c**) Fe influence; (**d**) Mn influence; (**e**) Ti influence.

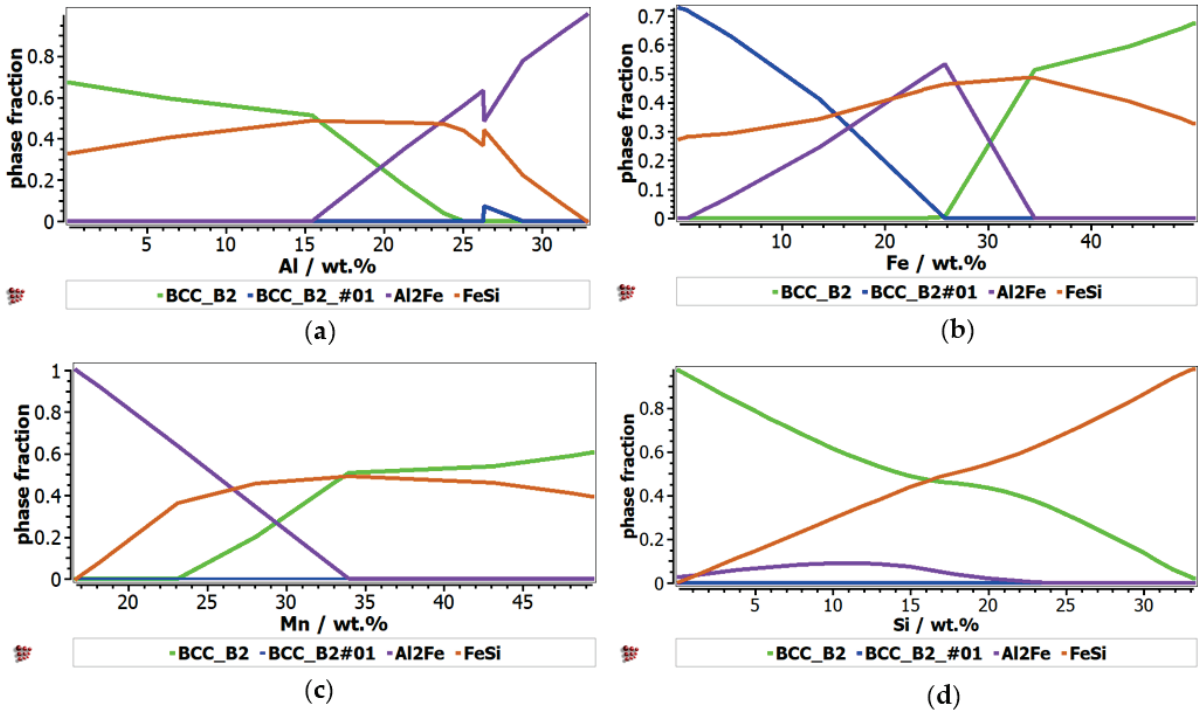

Figure 2. The proportions of phases that can be found in the Al-Fe-Mn-Si alloy system, at 400 °C, depending on the variation of the component elements: (**a**) Al; (**b**) Fe (**c**) Mn; (**d**) Si.

The proportion of the FeSi phase suffers a major decrease at 26 wt.% Al. Figure 2b shows the influence of Fe content over the formation of solid solution and intermetallic compound phases in the selected alloy. The proportion of the solid solution phases varies with the increase of Fe content; a transition between BCC_B2 and BCC_B2#01 phases occurred at 26 wt.% Al. Another transition was observed at 16%wt.% Al, between BCC_A2_#01 and Al_2Fe. The presence of Fe has a significant contribution to the stability of FeSi phase, which reaches a peak of 0.5 phase fraction at 35 wt.% Fe. By increasing the Fe content, the concentration of Al_2Fe has the higher peak of 0.6 at 25 wt.% and then decreases. The alloy structure is also defined by the presence of Mn, which has an important contribution to the stabilization of the complex compound-based phases (Figure 2c). Increasing Mn proportion has an important influence on the stability of BCC_B2 and FeSi. Si content has a strong influence over the formation of the FeSi phase, which reaches the highest peak at 30 wt.% Si (Figure 2d). This element content has also a high influence over the formation of the BCC_B2 solid solution phase, which is inversely proportional to the increase of the

component proportion. On the other hand, the Al_2Fe phase is insignificantly affected by the silicon content.

3.2. Thermodynamic and Kinetic Criteria Calculation

In the case of CCAs, the elements' proportion has a high impact on the alloy structure. Based on the criteria calculation results, the optimal composition of the selected alloy's systems can be designed, varying the proportions of each element from 0.5 to 2.5 molar concentration. Table 1 shows the criteria calculation for the AlCrFeMnTi alloy system and Table 2 for AlFeMnSi alloy system.

Table 1. Criteria calculation results for AlCrFeMnTi system.

No.	Alloy	$\Delta\chi_{Allen}$ %	Λ (J/mol·K)	ρ (g/cm^3)	Melting Temperature (°C)
1	$Al_{0.5}$CrFeMnTi	9.35	0.29	6.01	1474.48
2	AlCrFeMnTi	8.90	0.30	5.62	1393.06
3	$Al_{1.5}$CrFeMnTi	8.51	0.30	5.31	1326.45
4	Al_2CrFeMnTi	8.17	0.31	5.06	1270.94
5	$Al_{2.5}$CrFeMnTi	7.87	0.31	4.85	1223.97
6	$AlCr_{0.5}$CrFeMnTi	9.39	0.31	5.47	1341.52
7	AlCrFeMnTi	8.90	0.30	5.62	1393.06
8	$AlCr_{1.5}$FeMnTi	8.48	0.29	5.74	1435.24
9	$AlCr_2$FeMnTi	8.12	0.28	5.84	1470.39
10	$AlCr_{2.5}$FeMnTi	7.80	0.28	5.93	1500.13
11	$AlCrFe_{0.5}$MnTi	8.81	0.31	5.41	1377.29
12	AlCrFeMnTi	8.90	0.30	5.62	1393.06
13	$AlCrFe_{1.5}$MnTi	8.87	0.28	5.79	1405.97
14	AClrlFe_2MnTi	8.78	0.27	5.94	1416.72
15	$AlCrFe_{2.5}$MnTi	8.65	0.27	6.07	1425.82
16	$AlCrFeMn_{0.5}$Ti	9.14	0.26	5.44	1409.52
17	AlCrFeMnTi	8.90	0.30	5.62	1393.06
18	$AlCrFeMn_{1.5}$Ti	8.66	0.32	5.76	1379.60
19	$AlCrFeMn_2$Ti	8.42	0.35	5.89	1368.39
20	$AlCrFeMn_{2.5}$Ti	8.19	0.36	6.00	1358.90
21	$AlCrFeMnTi_{0.5}$	7.45	0.31	5.77	1362.52
22	AlCrFeMnTi	8.90	0.30	5.62	1393.06
23	$AlCrFeMnTi_{1.5}$	9.76	0.29	5.50	1418.06
24	$AlCrFeMnTi_2$	10.29	0.28	5.40	1438.89
25	$AlCrFeMnTi_{2.5}$	10.63	0.28	5.32	1456.51

Table 2. Criteria calculation results for AlFeMnSi system.

No.	Alloy	$\Delta\chi_{Allen}$ %	Λ (J/mol·K)	ρ (g/cm^3)	Melting Temperature (°C)
1	$Al_{0.5}$FeMnSi	5.48	0.19	4.83	1292.62
2	AlFeMnSi	6.21	0.17	4.54	1213.58
3	$Al_{1.5}$FeMnSi	6.56	0.16	4.32	1152.11
4	Al_2FeMnSi	6.73	0.16	4.15	1102.93
5	$Al_{2.5}$FeMnSi	6.80	0.16	4.00	1062.69
6	$AlFe_{0.5}$MnSi	6.61	0.15	4.18	1167.66
7	AlFeMnSi	6.21	0.17	4.54	1213.58
8	$AlFe_{1.5}$MnSi	5.87	0.18	4.84	1249.29
19	$AlFe_2$MnSi	5.58	0.19	5.08	1277.86
10	$AlFe_{2.5}$MnSi	5.32	0.20	5.29	1301.24
11	$AlFeMn_{0.5}$Si	6.61	0.15	4.21	1209.09
12	AlFeMnSi	6.21	0.17	4.54	1213.58
13	$AlFeMn_{1.5}$Si	5.87	0.19	4.81	1217.07
14	$AlFeMn_2$Si	5.58	0.20	5.03	1219.86
15	$AlFeMn_{2.5}$Si	5.33	0.21	5.22	1222.15

Table 2. *Cont.*

No.	Alloy	$\Delta\chi_{Allen}$ %	Λ (J/mol·K)	ρ (g/cm^3)	Melting Temperature (°C)
16	$AlFeMnSi_{0.5}$	5.79	0.20	4.98	1184.95
17	AlFeMnSi	6.21	0.17	4.54	1213.58
18	$AlFeMnSi_{1.5}$	6.35	0.16	4.23	1235.85
19	$AlFeMnSi_2$	6.36	0.15	3.99	1526.81
20	$AlFeMnSi_{2.5}$	6.32	0.14	3.81	1268.24

Figures 3 and 4 illustrate the influence of each element composition on the most representative parameters for the AlCrFeMnTi and AlFeMnSi alloy system. The optimal range for solid solution formation is represented by $\Lambda > 24$ J/mol·K and $\Delta\chi < 6\%$, as it is presented in Section 2. To design a material with potential application in the manufacture of the brake disc, the influence of the elements compositions on density and melting temperature was analyzed. The dotted line in the diagrams represent the range limit.

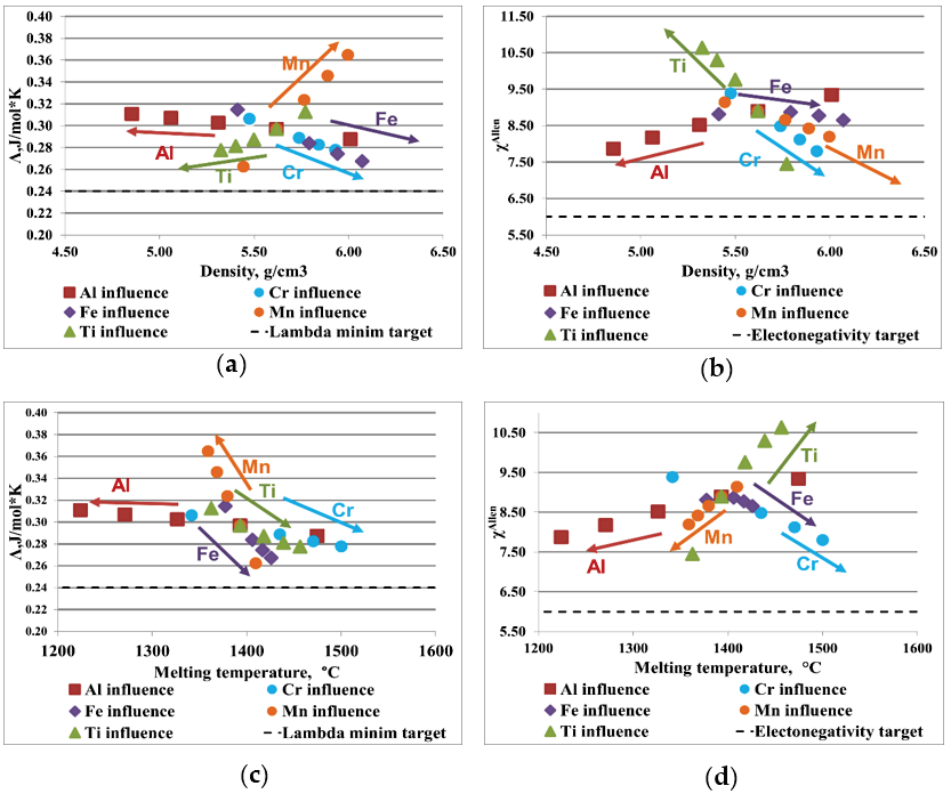

Figure 3. Graphical representation of the elemental influence over the criteria values for AlCrFeMnTi alloy system: (**a**) density, ρ, and the parameter Λ; (**b**) density, ρ, and the Allen electronegativity difference, Δχ; (**c**) the melting temperature and the parameter Λ; (**d**) the melting temperature and Allen electronegativity difference, Δχ.

The relationship between the parameter Λ and density for the AlCrFEMnTi alloy system is shown in Figure 3a. Al does not have a significant influence on the formation of solid solution phases. On the other hand, the use of aluminum in high concentration contributes to reducing the density. By analyzing the graphic representation of Al influence, it was observed that the melting temperature is inversely proportional to the increase in aluminum content (Figure 3c,d). It was also observed that Al has a positive influence on the alloy electronegativity (Figure 3b,d). Ti has a positive influence on decreasing the alloy density and improves the resistance to high temperatures. Analyzing the variation of Λ with density and with melting temperature, it can be observed that Ti is not a good solid

solution former. Cr and Fe influence the structural characteristics of the alloy in a similar way, contributing favorably to the increase of the melting temperature. These elements are rather heavy and increase the alloy density, considerably. It was observed that increasing the proportions of Cr and Fe has a negative influence on the formation of solid solutions. On the other hand, it was observed that increasing the Mn content influences, positively, the formation of the solid solution phases. But it also affects the increasing of the alloy density and reduces the melting temperature.

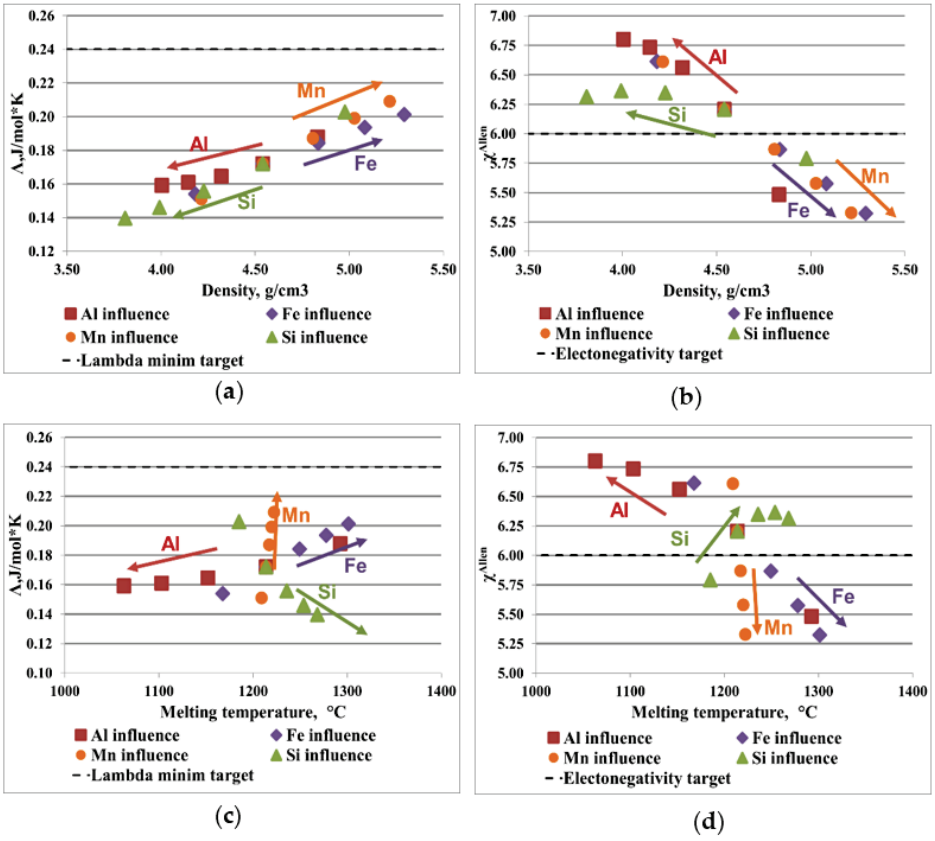

Figure 4. Graphical representation of the elemental influence over the criteria values for AlFeMnSi alloy system: (**a**) density, ρ, and the parameter Λ; (**b**) density, ρ, and the Allen electronegativity difference, Δχ; (**c**) the melting temperature and the parameter Λ; (**d**) the melting temperature and Allen electronegativity difference, Δχ.

Figure 4a shows the ratio between the alloy density and the parameter Λ, where Mn and Fe have a positive influence on the formation of solid solution. The tendency of forming solid solutions was observed by analyzing the ratio between electronegativity and density and melting temperature (Figure 4b,d). Mn and Fe are elements with a moderate melting temperature and increasing their concentration contributes to obtaining an alloy with potential application on manufacturing brake discs (Figure 4c,d). Increasing Al and Si content does not stimulate the formation of a solid solution, as observed by analyzing the parameter Λ and Δχ. An advantage of these elements is that they are light, which has a positive effect on reducing the density of the alloy

3.3. CCA Selection Using CALPHAD Method and Criteria Calculation

The information obtained through the Calphad method, regarding the complex materials design and optimization, establish an efficient approach to determine multicomponent phase diagrams using the mathematical determination of Gibbs free energies and diffusion mobility for each system phase [24]. The phase stability parameters and the effect of the composition on the phase formation are determined by the Calphad calculated composition-

temperature diagram for the alloy. Therefore, the relation between the empirical criteria and the alloy composition is highlighted by the interpretation of those type of diagrams [25].

By analyzing the CALPHAD modeling results for the AlCrFeMnTi alloy system it was observed that a high percentage of Al contributes to obtaining a structure based on solid solutions. To obtain a suitable material for the brake disc, the density, melting temperature and the criticality of the elements were considered in the selection process.

The criteria calculation results provide information about the positive and negative influence of the elements over the formation of solid solutions. For the AlCrFeMnTi alloy system, it was observed that Mn has a favorable effect on the evolution of the parameter Λ. Regarding the Allen electronegativity difference, the increase of Cr, Fe and Mn tend to bring the alloy to the optimal zone. For the material to have potential application in the manufacture of the brake disc, the increasing of Al content contributes to the reduction of alloy density. Ti has the same effect over the alloy weight and improves the melting temperature. In the selection process, the reduction of its content was taken into account, because Ti is a critical raw material.

The CALPHAD modeling and the empirical calculation show that the AlCrFeMnTi alloy system has a promising capability to form structures preponderantly based on solid solutions. It was observed that a high content of Al favors the formation of BCC_B2, while Cr, Fe and Ti have a strong influence over the formation of BCC_A2. On the other hand, the criteria calculation results show that a high percentage of Fe and Mn has a favorable influence over the formation of a solid solution structure. Considering that the material weight is an important characteristic of the brake disk, Al content is increased to reduce the alloy density. Ti has positive influence over the alloy structure, but is using a lower percentage because it is a critical material. Several preliminary trials were made in order to meet all the proposed requirements. After analyzing the modeling and the preliminary trials results, a complex concentrated alloy was selected: $Al_4CrFeMnTi_{0.25}$ (Table 3).

Table 3. Optimization results for AlCrFeMnTi and AlFeMnSi systems.

Nr	Optimised Composition							$\Delta\chi_{Allen}$ %	Λ (J/mol·K)	ρ (g/cm^3)	Melting Temperature (°C)
	Alloy	at %									
		Al	Cr	Fe	Mn	Ti	Si				
1	$Al_4CrFeMnTi_{0.25}$	55	14	14	14	3	-	5.37	0.29	4.39	1061.42
2	AlFeMnSi	16	-	34	33	-	17	6.21	0.17	4.54	1213.58

The CALPHAD modeling results of AlFeMnSi alloy system show that a high percentage of Fe and Mn contributes to the obtaining of a preponderantly based on a solid solution structure. Otherwise, the Al and Si have a negative influence over the formation of hard intermetallic compounds: FeSi and Al_2Fe.

Criteria calculation provide useful information for the selection of the alloy compositions. For the AlFeMnSi alloy system, Fe and Mn have a positive influence on the evolution of the parameter Λ and the Allen electronegativity difference. The increasing of these elements also contributes to obtaining a higher melting temperature. On the other hand, Al and Si have a favorable influence over the alloy density.

The modeling results of the AlFeMnSi alloy system show that the system can provide alloys with majorly solid solution structures. The CALPHAD modeling and the criteria calculation show that high percentages of Mn and Fe favors the formation of the solid solution structure, BCC_B2, while increasing Al and Si content has a negative influence on the formation of intermetallic compounds. Because the material weight is an important requirement of the brake disc, Al's and Si's influence over the alloy density allows to analyze the selected alloy's compositions. A suitable composition was selected in order to satisfy the proposed requirements of the brake disc after several preliminary trials. The selected composition is AlFeMnSi (Table 3).

In order to predict the behavior of the selected composition in specific solidification conditions, the equilibrium and Scheil–Gulliver diagrams of the alloys (Figures 5 and 6)

were calculated. In the $Al_4CrFeMnTi_{0.25}$ phase diagram (Figure 5), it can be observed that the complex concentrated alloy has a high content of BCC_B2, Al_8Fe_3, $AlCr_2$ and Al_8Mn_5_D810 phases at room temperature. Also, the intermetallic compound Al_3Ti_L is also present in the structure, but in a smaller proportion. The equilibrium diagram shows that the BCC_B2 phase has a higher concentration in the structure until approximately 750 °C, after which, it decreases. After the temperature of 100 °C, the BCC_A2 solid solution becomes the majority, reaching approximately 0.6 phase fraction, but it reduces significantly at almost 750 °C. The Al_5Fe_2-based phase has a high proportion between 300 and 500 °C.

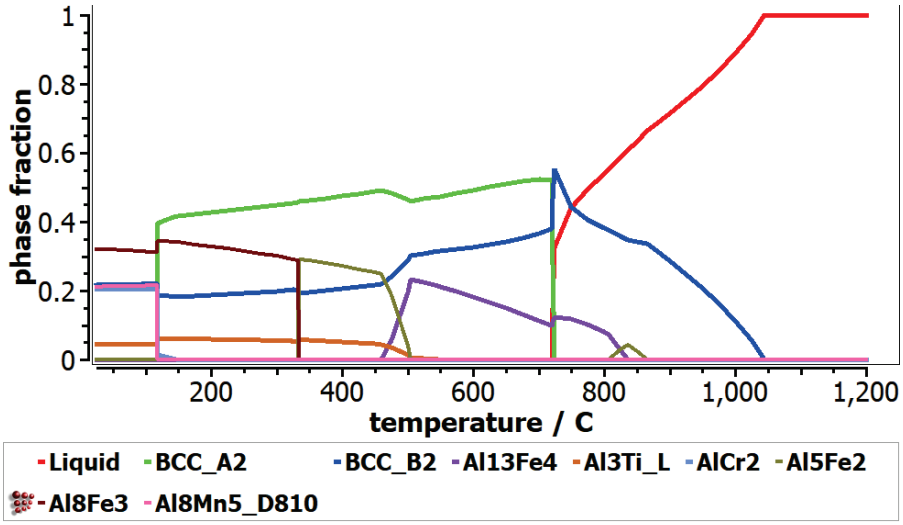

Figure 5. Equilibrium diagrams for $Al_4CrFeMnTi_{0.25}$ alloy.

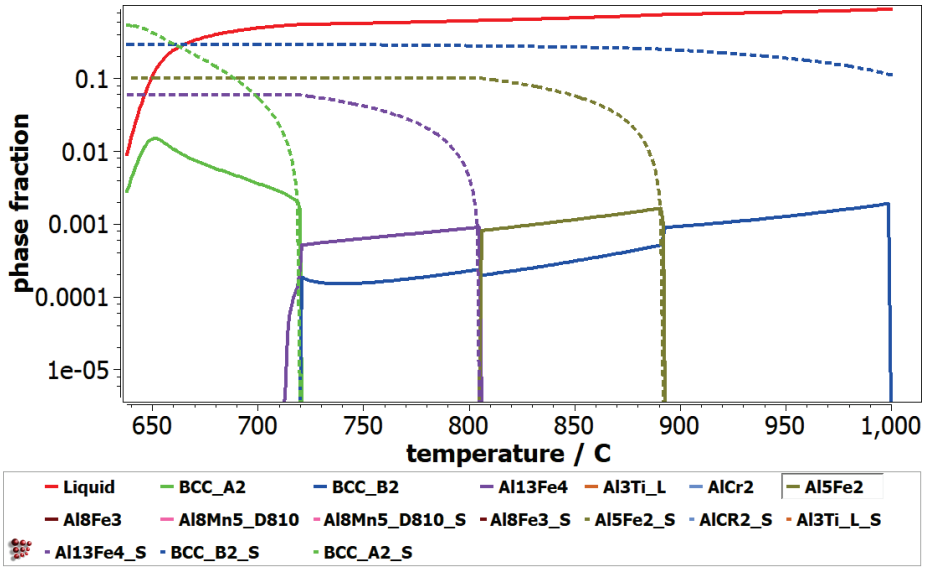

Figure 6. Scheill-Gulliver diagram for $Al_4CrFeMnTi_{0.25}$ alloy.

The non-equilibrium solidification phases predicted by the Scheil–Gulliver diagram are presented in Figure 6. The phases with S termination on the name define the equilibrium and non-equilibrium values of the cumulative solidification patterns. It can be observed that the BCC_B2 phase is formed first during the solidification process. After, it can be observed that the BCC_A2, Al_5Fe_2 and $Al_{13}Fe_4$ phases are formed, which are stable. The Al_3Ti_L, $AlCr_2$, Al_8Fe_3 and Al_8Mn_5_D810 phases do not show up in the Scheil-Gulliver diagram, since their formation occurs at temperatures below 650 °C. In the Scheil-Gulliver diagram

of the $Al_4CrFeMnTi_{0.25}$ alloy, the melting temperature is lower than in the equilibrium phase diagram (Figure 5).

The equilibrium diagram of AlFeMnSi alloy shows the formation of three phases: BCC_B2, Al_2Fe and FeSi (Figure 7). BCC_B2 and FeSi are the preponderant phases until the melting process begins at 800 °C. The equilibrium diagram shows that the Al_2Fe phase has a lower concentration and decreases significantly after approximately 500 °C. The Scheil-Gulliver diagram provides useful information regarding the behavior of the alloy upon solidification (Figure 8). The non-equilibrium solidification shows differences between solidification temperatures of the phases. The FeSi phase solidifies first in the AlFeMnSi alloy, followed by the BCC_B2 phase, which has the solidification starting point at around 930 °C. The Al_2Fe phase is not shown in the Scheil diagram, as its formation occurs at lower temperatures.

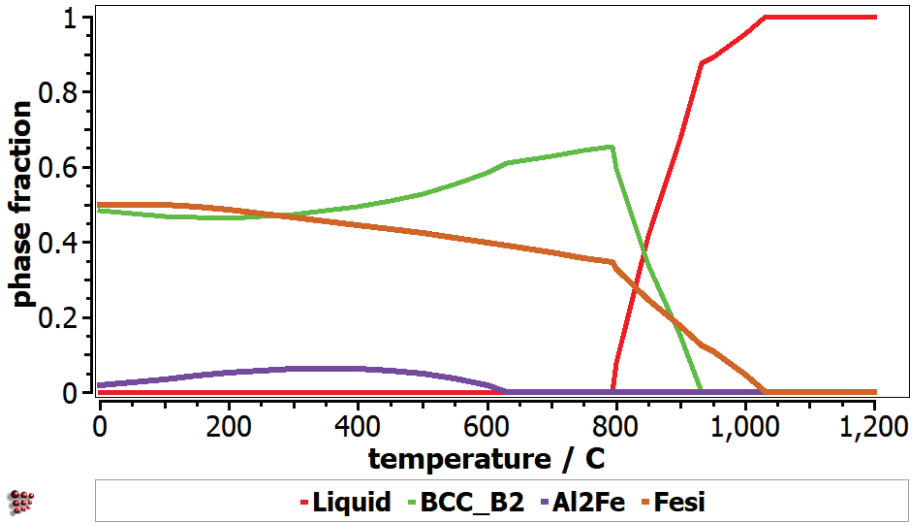

Figure 7. Equilibrium diagram for AlFeMnSi alloy.

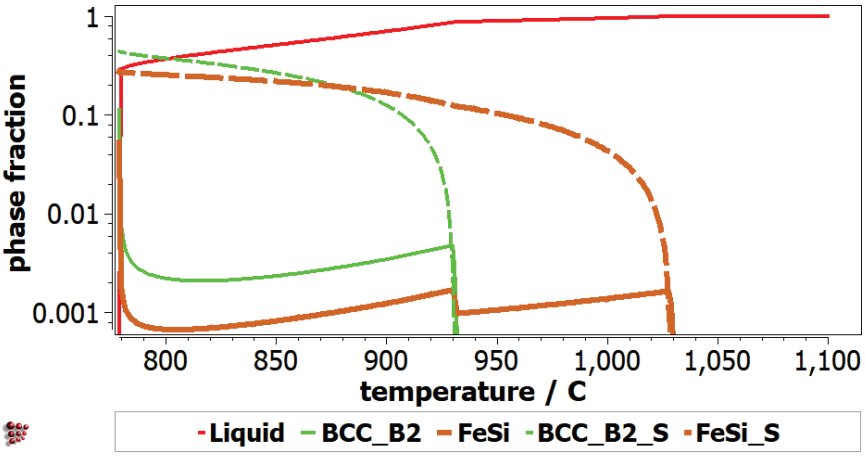

Figure 8. Scheill-Gulliver diagram for AlFeMnSi alloy.

3.4. The Experimental Results of the Studied Alloys

The as-cast and annealed samples were chemically, thermally, and structurally analyzed in order to reveal the experimental characteristics. Corrosion tests were also performed on the resulting alloys' specimens, along with density and microhardness measurements.

The chemical analysis of the samples in the as-cast state demonstrated that the products were obtained with a composition close to the nominal one (Table 4).

Table 4. The chemical composition of the as-cast alloys.

Alloy	Composition Type	Al	Cr	Fe	Mn	Ti	Si
$Al_4CrFeMnTi_{0.25}$	Nominal	38.20	18.39	19.75	19.43	4.23	-
	Experimental	39.04	20.94	14.97	21.51	3.54	-
AlFeMnSi	Nominal	16.3	-	33.7	33	-	17
	Experimental	18.58	-	34.14	28.19	-	19.09

The optical micrograph analysis showed that there are no significant differences between the as-cast and quenched states (Figure 9). Usually, after solidification, the alloys present a dendritic-type structure, while in the case of the $Al_4CrFeMnTi_{0.25}$ as-cast alloy, it is observed that the structure has a polygonal aspect (Figure 9a). The grains are well defined, equiaxial in shape, and finer in the marginal area than in the central part. The thermal treatment implied the rapid cooling of the structure, which inevitably led to the reduction of the grain size, which can be seen in Figure 9b.

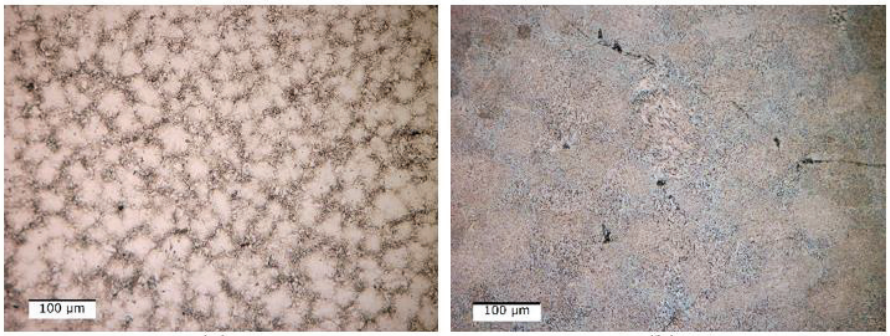

Figure 9. Optical micrographs of (**a**) as-cast and (**b**) quenched $Al_4CrFeMnTi_{0.25}$ alloy.

Figure 10 shows the scanning electron microscopy results where it can be observed that there are no differences regarding the morphology of the structure or the number of phases. The as-cast alloy (Figure 10a) has a polygonal structure with finer grains in the marginal area. After analyzing the SEM results of the cast alloy, hard lamellar phases were observed inside the grains. After the thermal treatment, the polygonal structure is preserved, as can be seen from Figure 10b. On the other hand, the lamellar hard phase is better distributed inside the grains. The EDS-mapping analysis (Figures 11 and 12), performed on the two states of the alloy, provided new information about the structure of the material, especially about the distribution of the elements in the phase. For the as-cast alloy, it was observed that the elements are distributed approximately uniformly.

Regarding the composition of the lamellar phase, it can be observed that it has a composition similar to that of the matrix phase. However, in the case of the heat-treated alloy, it was observed that the distribution of the elements is mostly uniform, with the exception of Ti, which is concentrated in the marginal area of the grains (Figure 12).

The phases of the as-cast alloy were studied using the XRD method and it is shown in Figure 13. The results of the analysis showed that the structure of the as-cast alloy is mostly composed of a $D8_{10}$ type phase, which is an intermetallic compound ($Al_{14.79}Mn_{10.71}$) that crystallizes in the trigonal system. The as-cast sample also contains a solid solution phase, BCC_B2 type ($Ti_{1.04}Fe_{0.862}Mn_{0.096}$) and a $D0_{22}$ type phase (Al_3Ti) in reduced proportions. The heat-treated sample consists of the same phases as the cast one: $D8_{10,}$ BCC_B2 and $D0_{22}$.

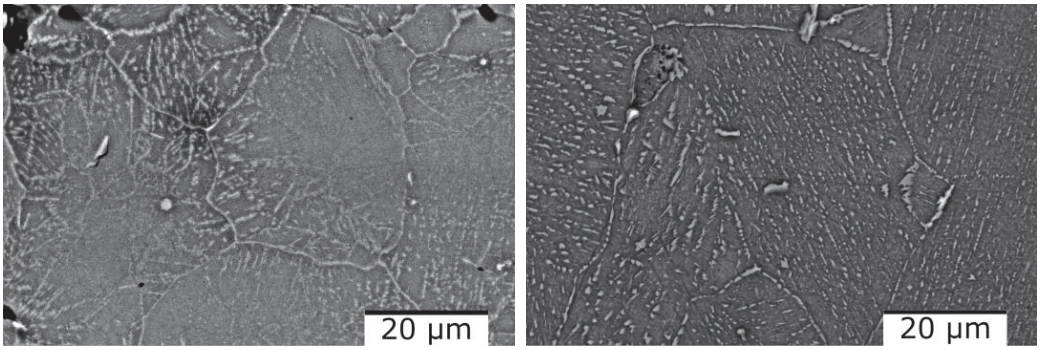

(**a**) (**b**)

Figure 10. SEM images of the $Al_4CrFeMnTi_{0.25}$ alloy in as-cast (**a**) and heat treated (**b**) states.

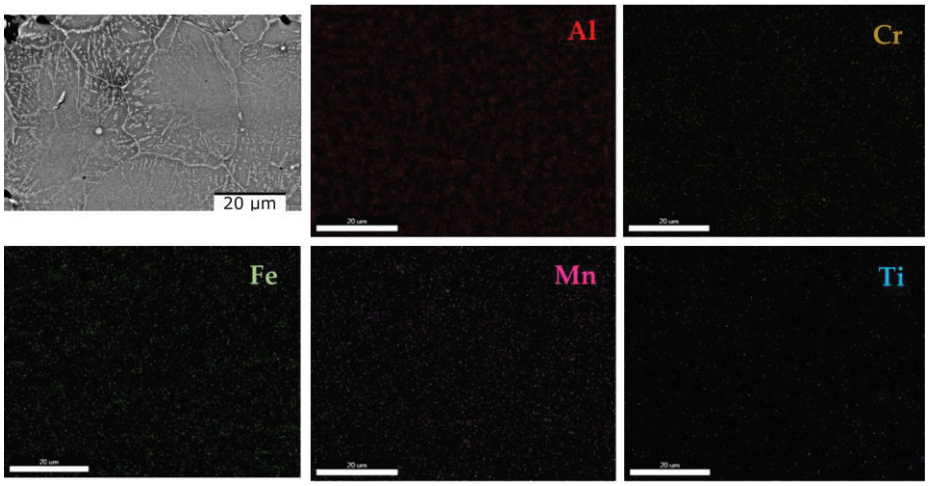

Figure 11. EDS mapping of the as-cast $Al_4CrFeMnTi_{0.25}$ alloy.

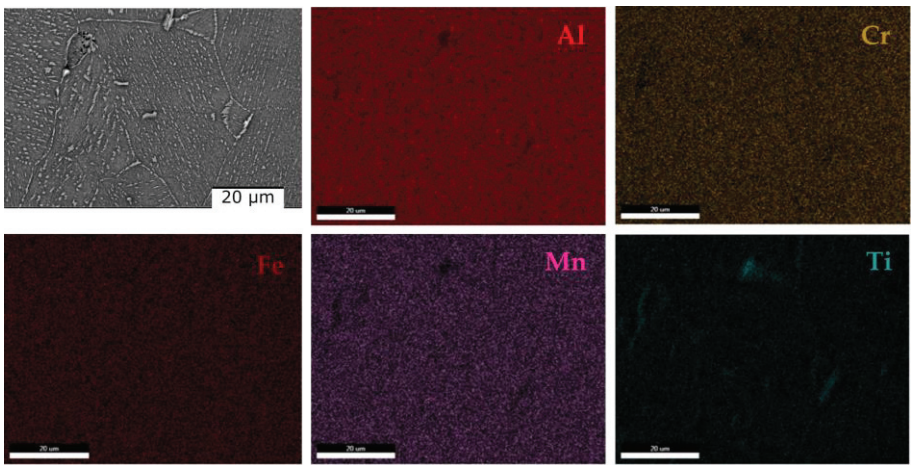

Figure 12. EDS mapping of the quenched $Al_4CrFeMnTi_{0.25}$ alloy.

Regarding the composition of the lamellar phase, it can be observed that it has a composition similar to that of the matrix phase. However, in the case of the heat-treated alloy, it was observed that the distribution of the elements is mostly uniform, with the exception of Ti, which is concentrated in the marginal area of the grains (Figure 12).

The phases of the as-cast alloy were studied using the XRD method and it is shown in Figure 13. The results of the analysis showed that the structure of the as-cast alloy is mostly

composed of a $D8_{10}$ type phase, which is an intermetallic compound ($Al_{14.79}Mn_{10.71}$) that crystallizes in the trigonal system. The as-cast sample also contains a solid solution phase, BCC_B2 type ($Ti_{1.04}Fe_{0.862}Mn_{0.096}$) and a $D0_{22}$ type phase (Al_3Ti) in reduced proportions. The heat-treated sample consists of the same phases as the cast one: $D8_{10,}$ BCC_B2 and $D0_{22}$.

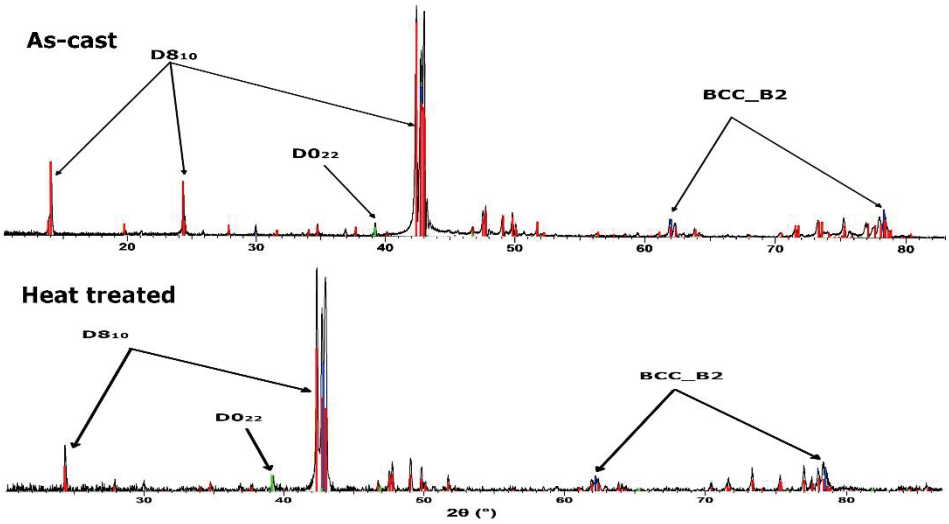

Figure 13. X-ray diffraction pattern for the as-cast and heat treated $Al_4CrFeMnTi_{0.25}$ alloy.

The determination of the phase transformations and the melting temperature for $Al_4CrFeMnTi_{0.25}$ alloy was determined by differential thermal analysis. Figure 14 shows an exothermic phase transformation that takes place between 1000 and 1050 °C. But the solid–liquid transformation takes place at a higher temperature, between 1100–1200 °C. During the modeling stage, it was calculated that the melting temperature of the alloy would be approximately 1400 °C, but it was experimentally proven that the material melts at a lower temperature.

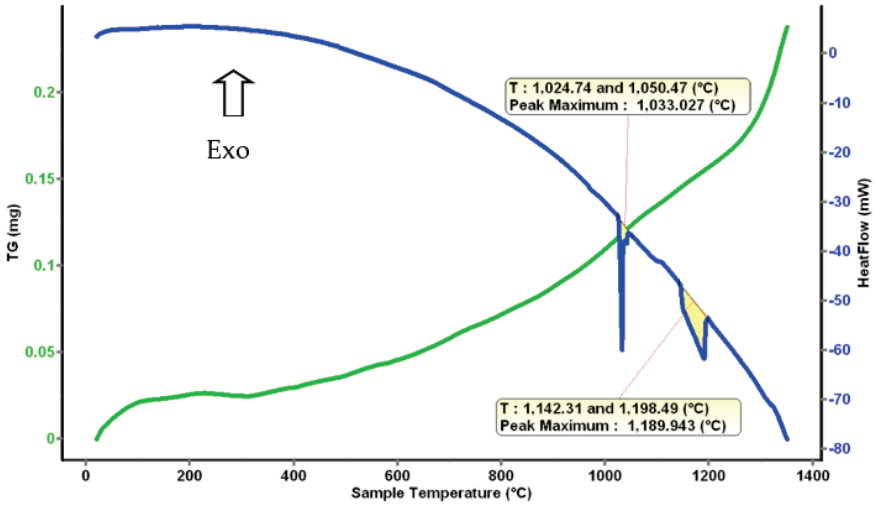

Figure 14. Thermal Analysis diagram for $Al_4CrFeMnTi_{0.25}$.

Optical analyses of the as-cast and quenched AlFeMnSi alloy samples (Figure 15) revealed that there are no significant differences between the structure of the two states. The as-cast sample has two phases, one dendritic and one interdendritic, well delimited between them (Figure 15a). The structure of the alloy does not show significant changes following the quenched treatment, which can be seen in Figure 15b. But the results for the optical micrographs analyses of as-cast and quenched samples showed that the application of thermal treatment contributed to the reduction of the grain size.

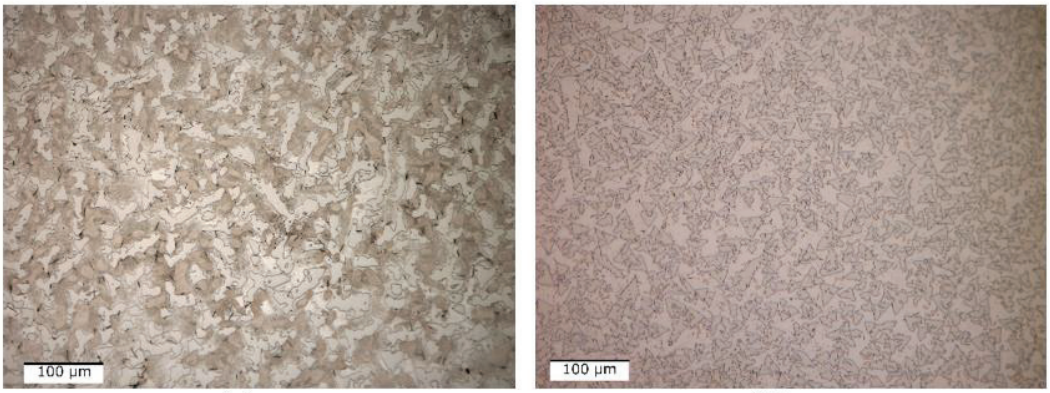

Figure 15. Optical micrographs of as-cast (**a**) and quenched (**b**) AlFeMnSi alloy.

The dendritic structure of the as-cast AlFeMnSi alloy was highlighted by SEM analysis (Figure 16a). The interdendritic and dendritic phases are well defined, which can also be observed in the case of the quenched sample (Figure 16b). The EDS-mapping results show no large differences in terms of element distribution (Figures 17 and 18). The as-cast alloy presented a dendritic structure with a higher concentration of Fe, Mn and Si. Al was observed to compose the majority in the interdendritic area. The two phases are well defined, which was also observed after the analysis of the quenched sample. EDS-mapping analysis showed that there are significant differences regarding the size of the phases.

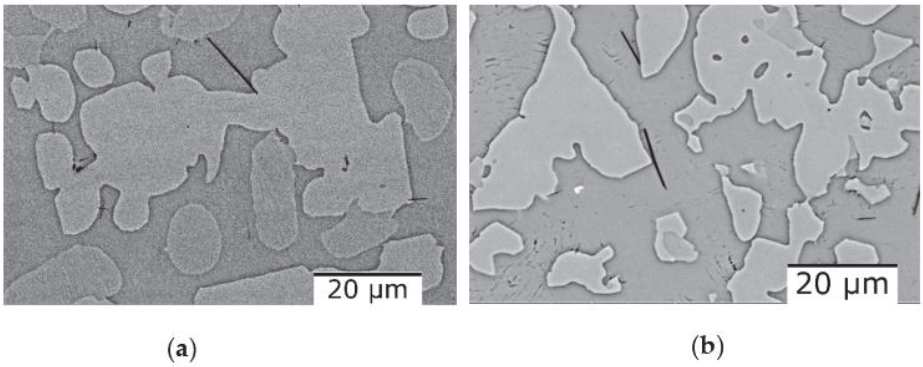

Figure 16. SEM-EDS image of the AlFeMnSi alloy in as-cast (**a**) and quenched (**b**) states.

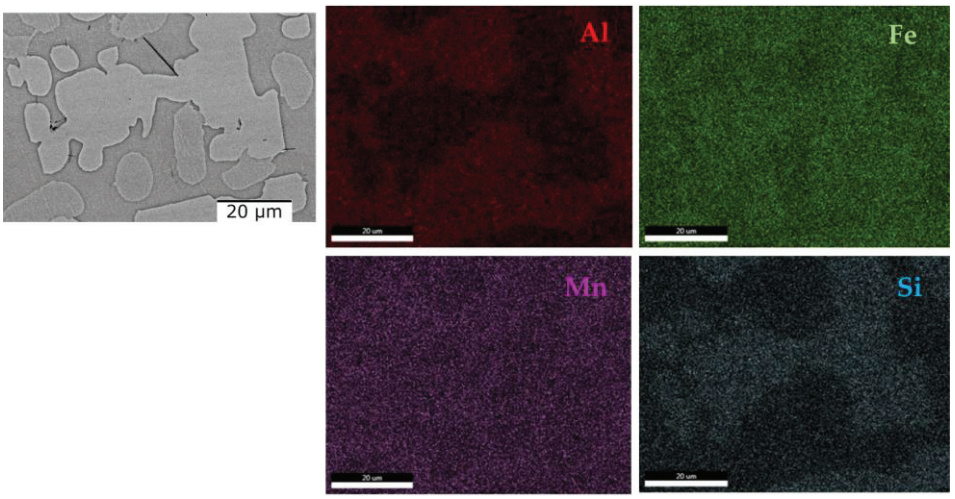

Figure 17. EDS mapping of the as-cast AlFeMNSi alloy.

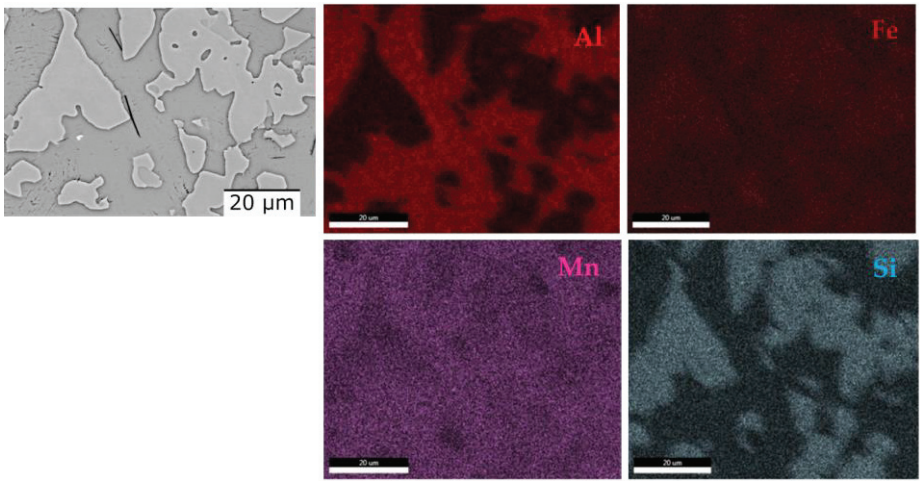

Figure 18. EDS mapping of the quenched AlFeMnSi alloy.

XRD phase analysis of the as-cast and heat treated (Figure 19) AlFeMnSi alloys demonstrated that the samples have similar structure configuration, showing two phases: BCC_B2 and B20 types. Analyzing the results, it was observed that the as-cast sample is mostly made up of the B20 phase, while the BCC_B2 solid solution is in a smaller proportion. After quenching and natural aging, there were no differences in terms of the type of phases or their number, only the B20 phase increased in proportion.

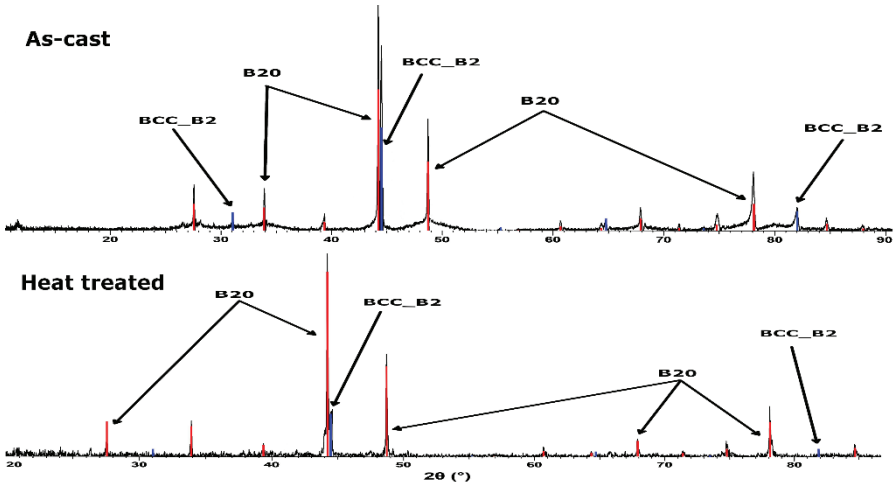

Figure 19. X-ray diffraction pattern for the as-cast and heat treatment AlFeMnSi alloy.

Differential thermal analysis offers information about the temperature at which a phase change occurs. From the theoretical calculation, the melting temperature of the AlFeMnSi alloy was predicted to be around 1200 °C, but the thermal analysis shows that the solid–liquid transformation is between 1026 and 1074 °C (Figure 20).

Heat treatment has been one of the most convenient and economical ways of enhancing the mechanical properties of a material. In the case of aluminum alloys, it was observed that the application of a natural aging treatment after quenching contributes significantly to the increase of the hardness. For the AlFeMnSi alloy, it was observed that the sample increases in hardness after the application of quenching and natural aging by approximately 15% (Table 5). But for the $Al_4CrFeMnTi_{0.25}$ alloy, a decrease in hardness by more than 10% was observed. Although after the thermal treatment no significant differences were observed, the type of phases and their number remained the same; the redistribution of the elements led to the modification of the hardness of the material.

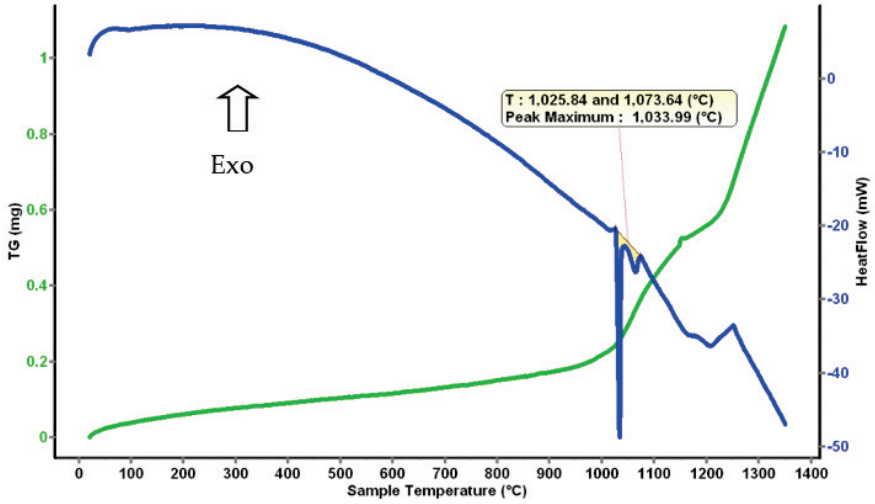

Figure 20. Thermal Analysis diagram for the AlFeMnSi alloy.

Table 5. Microhardness results for the obtained alloy.

	Specimen	HV
$Al_4CrFeMnTi_{0.25}$	as-cast	1131.10
	Annealed	1008.20
AlFeMnSi	as-cast	1164.10
	Annealed	1368.70

Corrosion resistance is an important property for the material used in the manufacturing of brake discs. The samples were tested by potentiodynamic polarization measurements (linear polarization resistance (LPR), Tafel plots) and performed in an aerated 3.5 wt.% NaCl solution. For a better interpretation, the results were compared with those of grey cast iron, the material that is usually used in the manufacturing of brake discs. Table 6 shows the corrosion potential (E_{corr}), corrosion current density (i_{corr}), polarization resistance (R_p) and corrosion rate (CR). It is observed that the values obtained for the CCA alloys are superior to the conventional cast iron material. The heat treatment process has little influence on the corrosion resistance for $Al_4CrFeMnTi_{0.25}$ alloy but has a larger influence on the AlFeMnSi alloy. The values obtained of 0.013 mmpy and 0.003 mmpy, respectively, represent great improvements in materials used for brake disc manufacturing.

Table 6. The corrosion parameters of the tested samples in 3.5 wt.% NaCl at 25 °C.

Samples	E_{OCP} (v)	Rp ($\Omega \cdot cm^2$)	E_{corr} (V)	i_{corr} (A/cm^2)	CR (mm/Year)
Grey cast iron	−0.622	29.68	−0.646	4.82×10^2	0.334
$Al_4CrFeMnTi_{0.25}$ as cast	−0.504	1566.17	−0.478	13.88	0.012
$Al_4CrFeMnTi_{0.25}$ annealed	−0.575	-	−0.522	39.28	0.013
AlFeMnSi as cast	−0.531	502.13	−0.499	2.27×10^2	0.164
AlFeMnSi annealed	−0.539	2422.26	−0.515	2.60	0.003

Rp = polarization resistance; Ecorr = corrosion potential; icorr = corrosion current density; CR = corrosion rate.

4. Conclusions

This paper presents the selection and characterization process of two CCA alloys to determine their potential use in brake disc material manufacturing. In the current study, the AlFeMnSi and AlCrFeMnTi alloy systems were proposed. To design the optimal composition, the Matcalc program was used, which provided information about the redistribution of solid solutions during the solidification process. Also, to determine the right composition, the thermodynamic and kinetic criteria were calculated, varying the concentration of each element.

In the case of the AlCrFeMnTi alloy system, it was found that the density decrease and the formation of the BCC_B2 solid solution are favored by increasing the Al content. The increase in the concentration of Cr in the alloy contributes to the increase in the phase fraction of intermetallic compounds, such as FeTi and Cr3Mn5, but also to the decrease in the proportion of solid solutions. A concentration of Cr and Fe higher than 20 wt.% leads to a reduction in the proportion of the BCC_B2 solid solution. Also, increasing the Cr and Fe content increases the density and melting temperature of the alloy. Mn has a significant influence on the increase in density, melting temperature and the formation of solid solutions. Increasing the Ti content has a positive effect on the density and melting temperature of the alloy, but does not facilitate the formation of solid solutions. However, at a content lower than 20 wt.% Ti, the phase fraction for the BCC_B2 phase is high.

Several possible compositions were tried to determine an alloy with high potential to be used in the manufacture of the brake disc. The selected complex concentrated alloy was: $Al_4CrFeMnTi_{0.25}$.

In order to predict the type of phases and their number for the $Al_4CrFeMnTi_{0.25}$ alloy, the equilibrium diagram was created. The modeling results predicted that the alloy structure at ambient temperature will consist of five phases: Al_8Fe_3, BCC_B2, $AlCr_2$, Al_8Mn_5_D810 and Al_3Ti_L. The XRD analysis showed that the structure of the cast sample consists of only three phases, but these were also found in the equilibrium diagram: D810, BCC_B2 and Al_3Ti. Modeling by the CALPHAD method provides indicative information about the possible phases that can form, which means that there may be differences between the predicted results and those obtained experimentally. Also, the database that was used is not specialized on multi-component alloys.

The two selected alloys were obtained using an induction furnace. In order to improve the mechanical and physical characteristics, the samples were subjected to an annealing process.

Following the optical, SEM and XRD analysis of the $Al_4CrFeMnTi_{0.25}$ alloy (as-cast and annealed) and AlFeMnSi alloy (as-cast and annealed) samples, the presence of solid solution phases and intermetallic compounds was observed.

The $Al_4CrFeMnTi_{0.25\ a}$s-cast alloy is characterized by a polygonal structure, which is preserved even after applying the natural aging treatment, but a decrease in the size of the grains is observed. Following the ESD analysis, it was found that the constituent phases are uniformly dispersed in the structure with an agglomeration of titanium in the marginal area of the grains. After the simulation through the Matcalc program, it resulted that three phases will form in the alloy. Through XRD analysis, the presence of a BCC-type solid solution phase was observed, which was also determined through modeling. Through the Scheill–Gulliver diagram for the $Al_4CrFeMnTi_{0.25}$ alloy, it was found that the BCC_A2 phase is formed after the solidification of the alloy and that it is a stable one. Following the simulation obtained through the Matcalc program, a composition close to the empirical one was not obtained in terms of the phases of the intermetallic compound. Following the structural analysis, the results were: $Mn_{6.32}Al_{6.68}$ and $Mn_{10}Al_{16}$. The melting temperature of the alloy is approximately 1200 °C, but following the thermal analysis a phase change of around 1000 °C was observed. The thermal aging treatment influenced the mechanical characteristics of the sample, resulting in a decrease in microhardness after the analysis. And corrosion resistance was influenced by natural aging, but not significantly.

Through optical microscopy and SEM, it was observed that the AlFeMnSi alloy has a dendritic structure. In the interdendritic area, the presence of acicular compounds was

highlighted. This structure showed slight changes after the application of the thermal treatment, but a reduction of the grain sizes was observed. The EDS analysis showed an increase in the number of phases in the alloy after the natural aging thermal treatment. The modeling showed that the alloy will have four constituent phases: BCC_B2, BCC_B2_#01, Al_2Fe and FeSi. The empirical results showed that the cast alloy has two main phases: BCC ($Fe_{0.95}Al_{0.89}Si_{0.16}$) and cubic ($MnAl_{0.05}Si_{0.95}$). The heat treated phase distribution showed a smaller proportion of the BCC phase. The samples were also thermally analyzed. After the analysis, it was determined that the AlFeMnSi alloy has a melting temperature of approximately 1000 °C, more than what was predicted by the equilibrium diagram obtained through the Matcalc program. In comparison with the previously studied alloy, an increase in the microhardness of the sample was observed for the AlFeMnSi alloy after applying the heat treatment. Also, corrosion resistance has improved and is superior to cast iron.

The two studied alloys presented great properties and have the potential to be used in the manufacture of brake disc material. However, further studies are necessary for the development of the disk brakes based on these materials, where reliable alloy production, processing and process integration are crucial.

Author Contributions: Conceptualization, I.A., D.M. and I.-C.B.; methodology, M.T.O.; software, D.M. and B.-A.Ș.; validation, J.T., A.S. and I.C.; formal analysis, I.-C.B. and M.B.; investigation, I.A., A.C.M., A.-M.J.P. and M.G.; resources, D.M.; data curation, N.C.; writing—original draft preparation, I.A.; writing—review and editing, B.-A.Ș. and M.B.; visualization, A.S.; supervision, D.M.; project administration, J.T.; funding acquisition, I.C. All authors have read and agreed to the published version of the manuscript.

Funding: This research was funded by the University Politechnica of Bucharest-PubArt Programme supporting scientific articles and communications publication.

Institutional Review Board Statement: Not applicable.

Informed Consent Statement: Not applicable.

Data Availability Statement: Not applicable.

Acknowledgments: This work was supported by the European Social Fund from the Sectoral Operational Programme Human Capital 2014–2020, through the Financial Agreement with the title "Training of PhD students and postdoctoral researchers in order to acquire applied research skills-SMART" Contract no. 13530/16 June 2022—SIMIS code: 153734"and by research grants from the Romanian National Authority for Scientific Research and Innovation, CNCS/CCCDI–UEFISCDI, project numbers: ERANET-M-COMPTRANS-1, within PNCDI III and PN-III-P2-2.1-PED-2019-2022, within PNCDI III and with the supported by a grant from the Ministry of Research and Innovation, Program Nucleu, contract no. 6N/2019 (Project number PN 19 19 02 01/2019) and also the authors would want to thank University "Politechnica" of Bucharest for the chance to publish this paper.

Conflicts of Interest: The authors declare no conflict of interest. The funders had no role in the design of the study; in the collection, analyses, or interpretation of data; in the writing of the manuscript, or in the decision to publish the results.

References

1. Shanker, P.S. A review on properties of conventional and metal matrix composite materials in manufacturing of disc brake. *Mater. Today Proc.* **2018**, *5*, 5864–5869. [CrossRef]
2. Rashid, A. Overview of disc brakes and related phenomena—A review. *Int. J. Veh. Noise Vib.* **2014**, *10*, 257. [CrossRef]
3. Maleque, M.A.; Dyuti, S.; Rahman, M.M. Materials selection method in design of automotive disc. In Proceedings of the World Congress on Engineering, London, UK, 30 June–2 July 2010; Volume III, ISBN 978-988-18210-8-9.
4. Shinde, H.S. Structural Analysis of Disc Brake Rotor for Different Materials. *Int. Res. J. Eng. Technol. (IRJET)* **2017**, *4*, 2129–2135. Available online: https://www.irjet.net/archives/V4/i7/IRJET-V4I7440.pdf (accessed on 20 June 2023).
5. Grigoratos, T.; Martini, G. Non-Exhaust Traffic Related Emissions. Brake and Tyre Wear PM, European Commission Joint Research Centre Report, Institute of Energy and Transport. 2014. Available online: https://publications.jrc.ec.europa.eu/repository/bitstream/JRC89231/jrc89231-online%20final%20version%202.pdf (accessed on 20 June 2023).

6. Ingo, G.M.; Riccucci, C.; Pisani, G.; Pascucci, M.; D'Ercole, D.; Guerriero, E.; Boccaccini, F.; Falso, G.; Zambonini, G.; Paolini, V.; et al. The vehicle braking systems as main source of inhalable airborne magnetite particles in trafficked areas. *Environ. Int.* **2022**, *158*, 106991. [CrossRef] [PubMed]
7. Seo, H.; Park, J.; Kim, Y.C.; Lee, J.J.; Jang, H. Effect of disc materials on brake emission during moderate-temperature braking. *Tribol. Int.* **2021**, *163*, 107185. [CrossRef]
8. Ghouri, I.; Barker, R.; Brooks, P.; Kosarieh, S.; Barton, D. The Effects of Corrosion on Particle Emissions from a Grey Cast Iron Brake Disc. *SAE Tech. Pap.* **2022**, *1*, 1178. [CrossRef]
9. Seo, H.; Joo, B.; Park, J.; Kim, Y.C.; Lee, J.J.; Jang, H. Effect of disc material on particulate matter emissions during high-temperature braking. *Tribol. Int.* **2021**, *154*, 106713. [CrossRef]
10. Gorsse, S.; Couzinié, J.-P.; Miracle, D.B. From high-entropy alloys to complex concentrated alloys. *Comptes Rendus Phys.* **2018**, *19*, 721–736. [CrossRef]
11. Feng, R.; Gao, M.C.; Lee, C.; Mathes, M.; Zuo, T.; Chen, S.; Hawk, J.A.; Zhang, Y.; Liaw, P.K. Design of Light-Weight High-Entropy Alloys. *Entropy* **2016**, *18*, 333. [CrossRef]
12. Kushnerov, O.I.; Bashev, V.F. Effect of Al and Si additions and cooling rates on phase composition and properties of CuFeMnNi alloy. *Bull. Dnipropetr. Univ.* **2016**, *24*, 68–74.
13. Tseng, K.; Yang, Y.; Juan, C.; Chin, T.; Tsai, C.; Yeh, J. A light-weight high-entropy alloy Al20Be20Fe10Si15Ti35. *Sci. China Technol. Sci.* **2018**, *61*, 184–188. [CrossRef]
14. Gondhalekar, A.A. Design and Development of Light Weight High Entropy Alloys. Dissertation, 2019, Jönköping University, School of Engineering, JTH, Materials and Manufacturing. Available online: https://urn.kb.se/resolve?urn=urn:nbn:se:hj:diva-45551 (accessed on 20 June 2023).
15. Mitrica, D.; Badea, I.C.; Olaru, M.T.; Serban, B.A.; Vonica, D.; Burada, M.; Geanta, V.; Rotariu, A.N.; Stoiciu, F.; Badilita, V.; et al. Modeling and Experimental Results of Selected Lightweight Complex Concentrated Alloys, before and after Heat Treatment. *Materials* **2020**, *13*, 4330. [CrossRef]
16. Mitrica, D.; Badea, I.C.; Serban, B.A.; Olaru, M.T.; Vonica, D.; Burada, M.; Piticescu, R.-R.; Popov, V.V. Complex concentrated alloys for substitution of critical raw materials in applications for extreme conditions. *Materials* **2021**, *14*, 1197. [CrossRef] [PubMed]
17. O'brien, S.P.; Christudasjustus, J.; Esteves, L.; Vijayan, S.; Jinschek, J.R.; Birbilis, N.; Gupta, R.K. A low-cost, low-density, and corrosion resistant AlFeMnSi compositionally complex alloy. *NPJ Mater. Degrad.* **2021**, *5*, 12. [CrossRef]
18. Liao, Y.-C.; Chen, P.-S.; Li, C.-H.; Tsai, P.-H.; Jang, J.S.C.; Hsieh, K.-C.; Chen, C.-Y.; Lin, P.-H.; Huang, J.C.; Wu, H.-J.; et al. Development of Novel Lightweight Dual-Phase Al-Ti-Cr-Mn-V Medium-Entropy Alloys with High Strength and Ductility. *Entropy* **2020**, *22*, 74. [CrossRef]
19. Singh, A.K.; Kumar, N.; Dwivedi, A.; Subramaniam, A. A geometrical parameter for the formation of disordered solid solutions in multi-component alloys. *Intermetallics* **2014**, *53*, 112–119. [CrossRef]
20. Yang, X.; Zhang, Y. Prediction of high-entropy stabilized solid-solution in multi-component alloys. *Mater. Chem. Phys.* **2012**, *132*, 233–238. [CrossRef]
21. Zhang, Y.; Zhou, Y.J.; Lin, J.P.; Chen, G.L.; Liaw, P.K. Solid-Solution Phase Formation Rules for Multi-component Alloys. *Adv. Eng. Mater.* **2008**, *10*, 534–538. [CrossRef]
22. Poletti, M.; Battezzati, L. Electronic and thermodynamic criteria for the occurrence of high entropy alloys in metallic systems. *Acta Mater.* **2014**, *75*, 297–306. [CrossRef]
23. Popescu, A.-M.J.; Branzoi, F.; Burada, M.; Atkinson, I.; Constantin, I.; Moreno, J.C.; Miculescu, F.; Mitrica, D.; Badea, I.-C.; Olaru, M.T.; et al. Influence of Heat Treatment on the Corrosion Behavior of Electrodeposited CoCrFeMnNi High-Entropy Alloy Thin Films. *Coatings* **2022**, *12*, 1108. [CrossRef]
24. Chen, H.-L.; Mao, H.; Chen, Q. Database development and Calphad calculations for high entropy alloys: Challenges, strategies, and tips. *Mater. Chem. Phys.* **2017**, *210*, 279–290. [CrossRef]
25. Liang, S.-M.; Schmid-Fetzer, R. Evaluation of Calphad Approach and Empirical Rules on the Phase Stability of Multi-principal Element Alloys. *J. Phase Equilibria Diffus.* **2017**, *38*, 369–381. [CrossRef]

materials

MDPI

Article

Effects of Homogenization Heat Treatment on the Fe Micro-Segregation in Ti-1023 Titanium Alloy

Jian-Bo Tong [1], Chao-Jie Zhang [2,*], Jun-Shu Chen [1], Meng-Qi Yan [1], Rui-Lin Xu [1] and Li-Jun Huang [1]

[1] Aviation Key Laboratory of Science and Technology on Advanced Titanium Alloys, AECC Beijing Institute of Aeronautical Materials, Beijing 100095, China
[2] School of Metallurgical Engineering, Anhui University of Technology, Ma'anshan 243002, China
* Correspondence: zhangcj@ahut.edu.cn

Abstract: The segregation of the Fe element in Ti-10V-2Fe-3Al titanium alloy (Ti-1023) can lead to the generation of beta flecks, which seriously affects the performance of Ti-1023 products. During the heat treatment (HT) process at a high temperature, the Fe element in Ti-1023 ingots will migrate, making its distribution more uniform and reducing the segregation index. In this paper, the control of Fe micro-segregation in Ti-1023 ingots by homogenization HT was investigated. Firstly, dissection sampling and SEM-EDS analysis methods were used to study the distribution pattern of the Fe element in the equiaxed grains in the core of Ti-1023 ingots. It was found that the Fe content in the grain gradually increased along with the radial direction from the core to the grain boundary. Then, the homogenization HT experiments and numerical simulations of Ti-1023 at different HT temperatures from 1050 °C to 1200 °C were carried out. The results showed that the uniformity of Fe element distribution within grain can be significantly improved by the homogenization HT. With increasing HT temperature, Fe atoms migration ability increases, and the uniformity of Fe element distribution improves. Homogenization HT at 1150 °C and 1200 °C for 12 h can effectively reduce the degree of Fe element segregation.

Keywords: Ti-1023 titanium alloy; homogenization heat treatment; diffusion; micro-segregation

Citation: Tong, J.-B.; Zhang, C.-J.; Chen, J.-S.; Yan, M.-Q.; Xu, R.-L.; Huang, L.-J. Effects of Homogenization Heat Treatment on the Fe Micro-Segregation in Ti-1023 Titanium Alloy. *Materials* **2023**, *16*, 4911. https://doi.org/10.3390/ma16144911

Academic Editor: Jan Haubrich

Received: 30 May 2023
Revised: 6 July 2023
Accepted: 7 July 2023
Published: 9 July 2023

1. Introduction

Ti-1023 is a typical near-beta Ti alloy with a beta transit temperature of 795 °C and has high fracture toughness, deep hardening potential and inherent ductility [1–3]. It is mainly used in the manufacturing of large load-bearing components such as aircraft fuselages, helicopter rotors and landing gears [4–8]. Due to the small equilibrium distribution constant of Fe during solidification of Ti-1023, which is as low as 0.3, it has a high tendency of segregation [9–12]. The low partition ratios of Fe, combined with the relative movement of liquid and solid phases in the two-phase zone caused by buoyancy and Lorentz force, large differences of Fe content at different areas and β-flecks are likely to occur in the ingot [13–17] result in the precipitation of brittle phase. The β-flecks usually deteriorate the plasticity and fatigue properties of Ti-1023 forgings [14].

At the microscopic scale, there is a possibility of relatively significant compositional differences within individual grains due to different solidification sequences, which could be inherited in bars and forgings [18–22]. It has been found that there is a certain degree of segregation of Fe elements in Ti-1023. Zhao Yongqing et al. [23] studied the distribution of Fe elements in Ti-3Fe and Ti-6Al-1.7Fe within isometric crystals, and the results proved that the two alloys have a high Fe element content in the ingot near the grain boundary. For the Ti-3Fe alloy with a high Fe element content, the elevated Fe element content near the grain boundary was more obvious. Jing Zhenquan et al. [24] examined the heredity law of macrosegregation of the easily segregated Fe element between the primary and secondary ingots by numerical simulation of the interaction between temperature and solute fields during the process of vacuum arc remelting.

Multiple smelting, homogenization HT and other methods are required to prevent and control the segregation of Fe in Ti-1023 [25–28]. HT can relieve macro-segregation and micro-segregation of many kinds of alloys to a certain degree [29–33]. However, at present, there are limited reports on the intragranular distribution of Fe in Ti-1023, and there is little research on the improvement of intragranular segregation by annealing. It is important to reveal the distribution pattern of Fe content in the grains of Ti-1023 ingots to study the formation and control of β-flecks. Therefore, this paper uses energy spectroscopy to study the distribution pattern of Fe content at the grain scale in large-size Ti-1023 ingots. Various homogenization HT processes were used to eliminate or reduce the gradient of Fe content within the grains.

2. Materials and Methods

2.1. Sampling and Corrosion of Ti-1023 Ingots

Ti-1023, with the composition shown in Table 1, was smelted using a vacuum smelting furnace and cast into an ingot with the size of ϕ360 mm × 1300 mm. A pie-shaped sample with the size of ϕ360 mm × 10 mm was cut from the middle part of the Ti-1023 ingot.

Table 1. Composition of Ti-1023, wt.%.

Element	Al	V	Fe	O	N	H	Ti
Content	3.02 ± 0.03	10.25 ± 0.05	1.92 ± 0.10	0.08 ± 0.01	0.009 ± 0.001	0.0012 ± 0.0003	Bal.

Note: The Al and V contents were measured using the method of inductively coupled plasma atomic emission spectroscopy. The Fe content was measured using the method of atomic absorption spectroscopy. The O, N and H contents were measured using the methods of inert gas melting and infrared detection.

Considering the segregation in the axial part of the ingot is obvious [17], four cylindrical samples with a size of ϕ30 mm × 10 mm were cut from the center of the pie-shaped sample, as shown in Figure 1.

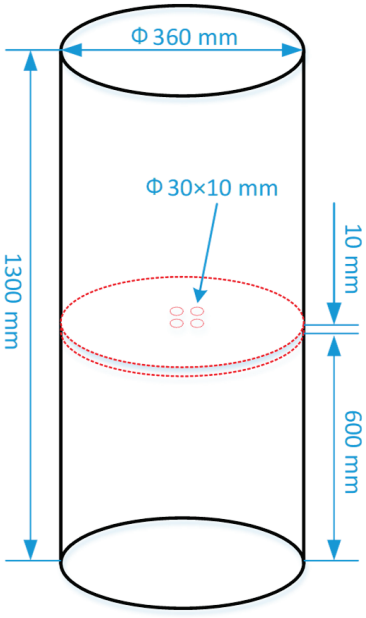

Figure 1. Schematic of sampling from the Ti-1023 ingot.

In order to observe the grain distribution of the Ti-1023 sample, the sample was ground using silicon carbide abrasive paper, polished using the diamond polishing paste, and finally etched using 4% nitric acid alcohol solution.

2.2. Detection of Fe Element Content Distribution in Sample Grains

The microstructure of the four samples mentioned above were observed using SEM (JSM-6510LV). In each sample, three grains with a regular shape were chosen to detect the Fe element content. The distances between the parallel edges of the grains were measure as D, and then several micro-areas with the size of 10 μm × 10 μm were selected from the midpoint of one of the parallel edges along the direction of the grain center at intervals of $D/20$, as shown in Figure 2a. The compositions of each micro-area were detected using an energy spectrum analyzer (JSM-6510LV, manufacturer is Hitachi, Tokyo, Japan).

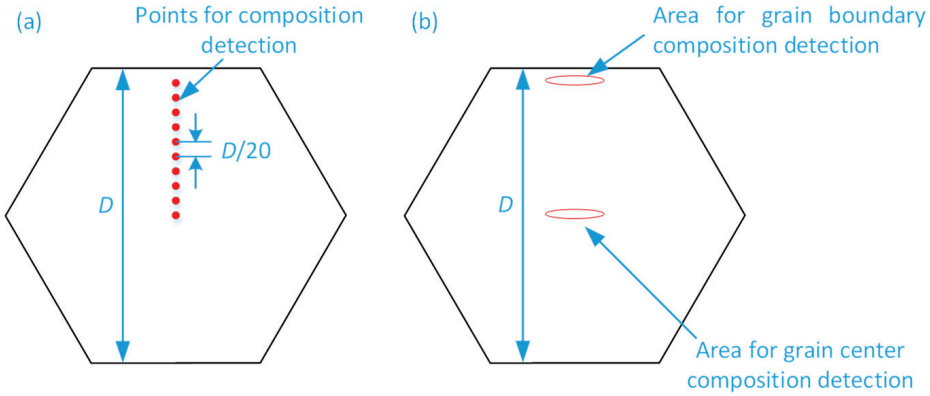

Figure 2. Schematic of composition detection areas (**a**) Micro-areas chosen in one grain for composition detection, (**b**) Composition detection areas in grain center and near grain boundary.

2.3. Homogenization HT of Sample

Before the homogenization HT, select three grains with large size about 6 mm to 10 mm in each sample. For each grain, the composition was detected using an energy spectrum analyzer at the grain center and near grain boundary, as shown in Figure 2b.

The four samples, numbered 1# to 4#, were encapsulated in different quartz tubes filled with argon as a protective atmosphere. Keep the four quartz tubes at different temperatures of 1050 °C, 1100 °C, 1150 °C and 1200 °C for 12 h, and then cooled to room temperature in the furnace.

After the homogenization HT, the four samples were taken out of the quartz tubes. In the same way, the samples were etched using Carroll solution after being ground and polished. Three grains with a large size about 6 mm to 10 mm were chosen in each sample, and their compositions were detected using an energy spectrum analyzer at the grain center and near the grain boundary, as shown in Figure 2b.

3. Numerical Simulation of Fe Diffusion Intragranular of Ti-1023 during Homogenization HT

In order to establish a mathematical model for the diffusion and transport of Fe in Ti-1023, the following assumptions were made:

1. Grain boundary and dislocation have no influences on diffusion.
2. The diffusion rate of Fe is equal in all directions.
3. The diffusion coefficient of Fe is a constant value when the temperature and composition are determined.

Based on Fick's law, the mathematical model of Fe diffusion in Ti alloy was established, and the main governing equation is the component transfer equation, as shown in Formula (1):

$$\frac{\partial C}{\partial t} = \frac{\partial}{\partial x_i}\left(D\frac{\partial C}{\partial x_i}\right) \quad (1)$$

where C is the concentration of Fe, mol·m^{-3}, x is the coordinate of i direction, m, D is the diffusion coefficient, m^2·s^{-1}, which can be calculated via Formula (2):

$$D = D_0 \exp\left(-\frac{Q}{RT}\right) \quad (2)$$

The diffusion constant D_0 and the activation energy of the Fe element in Ti-1023 are obtained through diffusion couple test, which are 5.45 × 10^{-5} m^2·s^{-1} and 249,940 J·mol^{-1}, respectively. Figure 3 shows the diffusion coefficients of the Fe element in Ti-1023 at different temperatures during the homogenization HT.

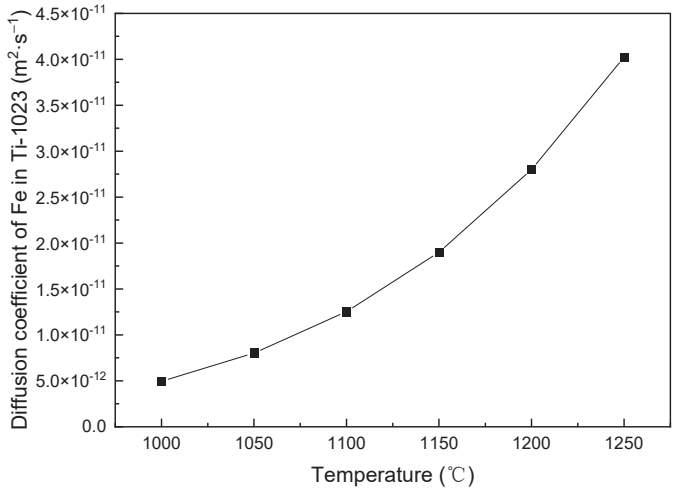

Figure 3. Diffusion coefficients of Fe element in Ti-1023 during homogenization HT.

The mathematical forms of the unsteady diffusion mass transfer and unsteady heat conduction equations are similar. Therefore, the heat transfer module in the finite element software ProCAST can be used for the numerical simulation of Fe diffusion during the Ti-1023 homogenization HT process. A two-dimensional geometric model of a single grain of Ti-1023 was established, assuming the grain to be hexagonal with a side length of 4 mm. The finite element mesh of the grain consisted of 10,704 nodes and 9142 triangular elements, which were selected based on several mesh refinements, as shown in Figure 4.

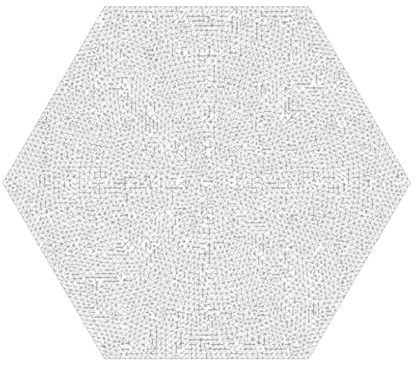

Figure 4. Geometric model and mesh of a single grain of Ti-1023.

The initial distribution of Fe contents is shown in Figure 5. The Fe contents in the grain center and grain boundary are set according to the results of detection of Fe element content distribution in sample grains, which are about 1.9% and 2.2%, respectively. The boundary edges of the single grain are considered walls, meaning that no Fe atoms moving in or out of the single grain through these six edges.

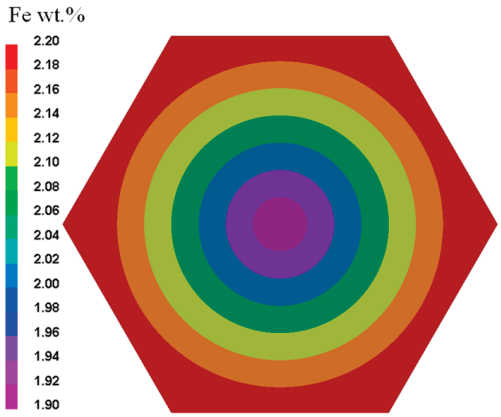

Figure 5. Initial distribution of Fe element content.

4. Results and Discussion

4.1. Characterization of Intragranular Fe Content Distribution of Ti-1023 Ingot

Macrographs of the grain distributions of the four samples from the Ti-1023 ingot are shown in Figure 6. It can be seen that the shape of the grains is irregular polygon, and the measured sizes of the grains using area method are ranging from about 3 mm to 8 mm.

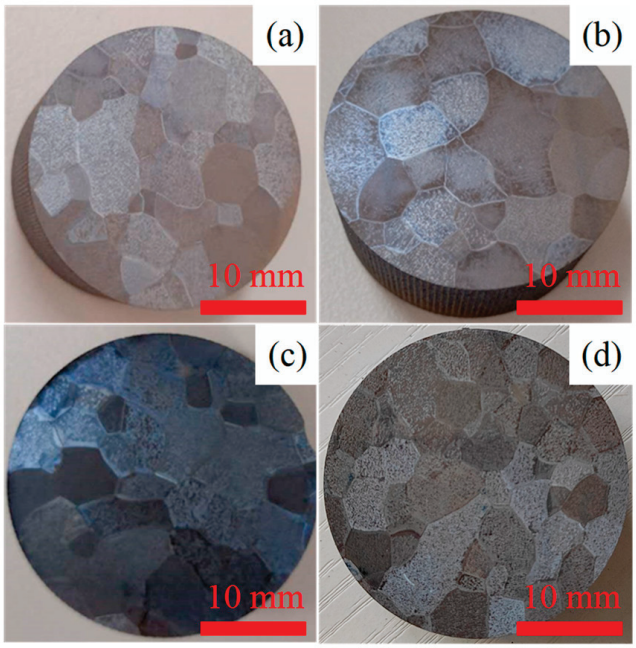

Figure 6. Macrographs of grain distributions of the four samples from the Ti-1023 ingot, (**a**–**d**) are 1# sample to 4# sample, respectively.

The distributions of Fe content in the grains of the Ti-1023 samples are shown in Table 2. It can be seen that the distribution of Fe content in the grains is uneven, and in most of the grains, the Fe content is low in the grain center and high near the grain boundary. The average distribution of Fe content in the grains along the radial direction is obtained by averaging the Fe content at the corresponding position of all grains, as shown in Figure 7. It can be seen that the Fe content in the grain increases gradually from the center to the boundary along the radial direction. Put differently, there is positive segregation of Fe content near the grain boundary and negative segregation near the grain center. The average Fe content increases from 1.90% near the center to 2.15% near the grain boundary.

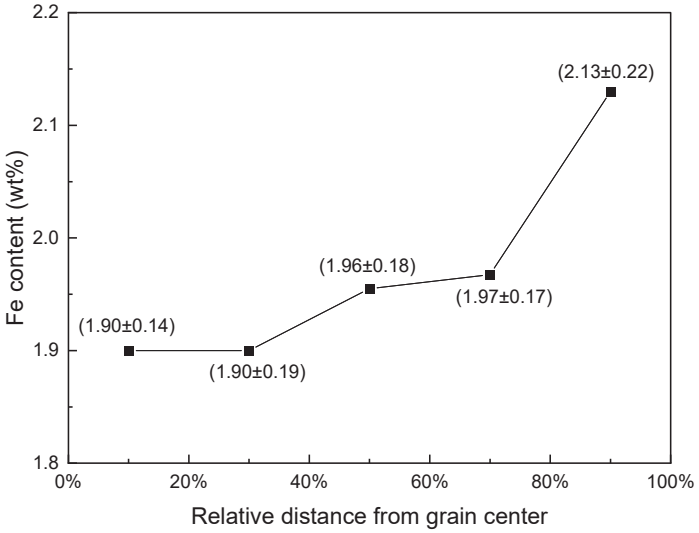

Figure 7. Average distribution of Fe content in the grains along the radial direction.

Table 2. Distributions of Fe content in grains of the Ti-1023 samples, wt%.

Relative Distance from Grain Center	Sample1#-Grain1#	Sample1#-Grain2#	Sample2#-Grain1#	Sample2#-Grain2#	Sample3#-Grain1#	Sample3#-Grain2#	Sample4#-Grain1#	Sample4#-Grain2#
0%	1.81	2.15	1.95	1.69	1.93	1.92	2.20	2.10
10%	2.04	1.94	2.15	1.78	1.67	2.02	1.80	1.80
20%	1.97	1.91	2.12	1.58	1.83	1.84	1.90	1.80
30%	1.84	1.89	2.16	1.87	1.69	1.55	2.00	2.20
40%	1.89	1.89	2.22	1.84	1.80	1.71	2.10	2.00
50%	1.76	2.28	2.10	1.82	1.65	2.13	1.90	2.00
60%	1.66	1.97	2.13	1.86	1.96	1.79	1.80	1.80
70%	1.77	2.29	2.11	1.92	1.68	1.87	2.00	2.10
80%	2.10	2.48	2.07	1.68	1.68	1.92	1.70	1.60
90%	1.98	2.49	2.23	1.81	2.04	1.99	2.50	2.00
100%	1.90	2.28	2.25	1.59	1.99	2.13	2.50	1.50

The segregation of the Fe element in Ti-1023 is caused by the small equilibrium distribution constant K_0 of the Fe element during solidification. K_0 is the ratio of Fe content in the solid and liquid phases at equilibrium, that is, $K_0 = C_S/C_L$, where C_S and C_L are the concentration of solute in the solid and liquid phases, respectively. The difference in Fe content between the grain center and the grain boundary has an important influence on the formation of β-freckle, which would appear during the subsequent forging process.

4.2. Effect of Homogenization HT on the Distribution of Fe Content in the Grains

The Fe contents in the grain center and boundary of the Ti-1023 ingot before and after homogenization HT were measured, and the Fe content distributions in the grain center and near the grain boundary of 1# to 4# samples before and after HT were obtained, as shown in Table 3. The Fe content deviation is used to characterize the difference in Fe content between at the grain center and grain boundary, which is calculated with the formula $(C_{boundary} - C_{center})/C_{boundary} \times 100\%$, where $C_{boundary}$ and C_{center} represent the Fe contents in grain boundary and grain center, respectively. For the samples before HT, according to the statistical results of 36 pairs of Fe contents in the grain boundary and in the center of 12 grains, it can be seen that there is a difference of 3.8–13.3% between the Fe content in the grain center and the grain boundary. In other words, the Fe element exhibits positive segregation at the grain boundary of the Ti-1023 ingot.

Table 3. Fe content in the grain center and boundary before and after homogenization HT.

Sample#	Before HT			After HT			HT Temperature, °C
	Grain Boundary	Grain Center	Difference	Grain Boundary	Grain Center	Difference	
1#	2.16	1.96	9.3%	2.10	1.98	5.7%	1050
1#	2.22	2.04	8.1%	2.18	1.90	12.8%	1050
1#	2.36	2.15	8.9%	2.14	2.02	5.6%	1050
2#	2.20	1.96	10.9%	2.08	2.01	3.4%	1100
2#	2.17	2.01	7.4%	2.40	2.29	4.6%	1100
2#	2.20	2.09	5.0%	2.15	1.95	9.3%	1100
3#	2.12	2.01	5.2%	2.27	2.21	2.6%	1150
3#	2.17	1.91	12.0%	2.38	2.29	3.8%	1150
3#	2.25	1.95	13.3%	2.20	2.09	5.0%	1150
4#	2.24	2.02	9.8%	2.11	2.03	3.8%	1200
4#	2.38	2.29	3.8%	2.14	2.07	3.3%	1200
4#	2.40	2.26	5.8%	2.46	2.45	0.4%	1200

Then, the 1#–4# Ti-1023 samples were subjected to homogenization HT at different temperatures of 1050 °C, 1100 °C, 1150 °C and 1200 °C for 12 h, respectively. During the homogenization HT process, Fe atoms are capable of diffusing against the concentration gradient, reducing the chemical segregation to a certain extent [34,35]. The results show that after homogenization HT at 1050 °C for 12 h, the Fe content deviations in the Ti-1023 ingot are 5.7%, 12.8% and 5.6%, respectively, which are not significantly lower than before HT. These results indicate that at 1050 °C, the diffusivity of the Fe element is lower, and the diffusion rate is lower, resulting in an insignificant homogenization effect of the Fe content after 12 h. When the homogenization HT temperature is increased to 1100 °C, the Fe content deviations in the ingot are 3.4%, 4.6% and 9.3%, respectively, which are slightly improved compared to before HT. This indicates that significant homogenization and diffusion of the Fe element cannot be achieved within 12 h under 1100 °C. When the homogenization HT temperature is increased to 1150 °C, the Fe content deviations in the ingot are 2.6%, 3.8% and 5.0%, respectively. The uniformity of the Fe content distribution in the grains is improved to a certain extent compared to before HT. After 12 h of homogenization HT at 1200 °C, the Fe content deviations in the ingot reaches 0.4–3.8%, and the distribution uniformity of the Fe content is further improved with the increase in temperature, as shown in Figure 8.

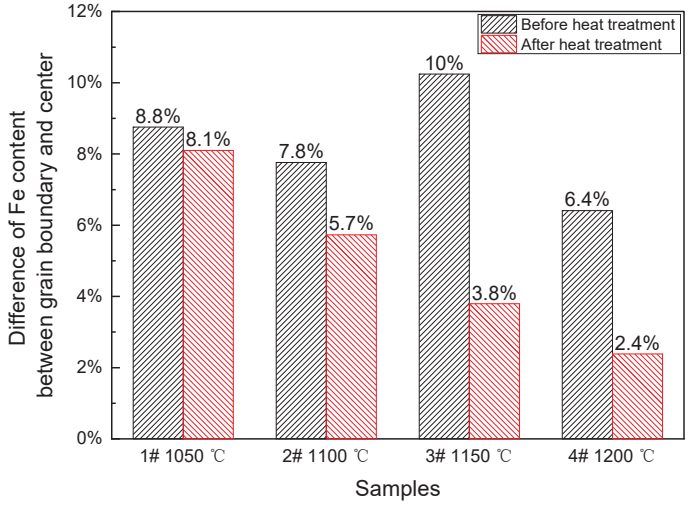

Figure 8. Fe content deviations before and after homogenization HT.

According to the above analysis of the experimental data, the Fe content deviations of the Ti-1023 samples after HT decrease gradually with the increase in HT temperature. The homogenization HT above 1150 °C for 12 h can make more sufficient Fe diffusion. With the increase in HT temperature, the atomic diffusion energy is gradually activated, and atomic

mobility is gradually improved [36–38]. The diffusion coefficient of the Fe element in the Ti alloy matrix increases exponentially with the increase in temperature, thus increasing the HT temperature can improve the diffusion of the Fe element effectively and improves the uniformity of its distribution.

However, in actual industrial production of Ti-1023, the oxidation of the ingot during the HT process would cause the loss of the metal and reduce the yield of the Ti alloy. Therefore, the homogenization HT temperature should be determined according to the degree of oxidation and the effect of the Fe content deviation.

4.3. Homogenization Factors of Fe Content in Ti-1023 Grains during HT

4.3.1. Effect of HT Temperature on Homogenization of Fe in Grains

Both HT temperature and time have significant effect on the homogenization of alloys [39,40]. Increased homogenization treatment temperature and extended holding time can significantly alleviate the segregation of the alloying element [41]. In other words, a reasonable high HT temperature and long HT time will result in a uniform distribution of alloy elements. The distributions of Fe content in Ti-1023 grains after homogenization HT for 12 h at different temperatures are shown in Figure 9, it can be seen that: (1) For a single grain, the higher the homogenization HT temperature, the more uniform the distribution of Fe element content would be after a certain HT time. (2) Homogenization HT temperature has a great influence on the homogenization of Fe content in a single grain. For example, after homogenization HT at 1000 °C and 1250 °C for 12 h, the differences in Fe contents between the grain center and grain boundary are 0.21% and 0.04%, respectively, and the Fe content deviations are 10.9% and 1.8%, respectively.

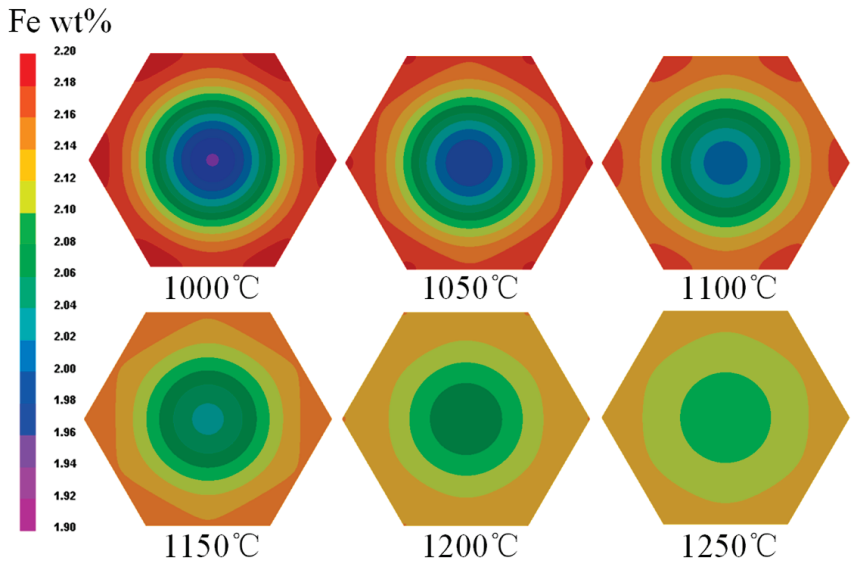

Figure 9. Distributions of Fe content in Ti-1023 grains after homogenization HT for 12 h at different temperatures.

In order to further clarify the effect of homogenization HT temperature on the distribution of Fe content within the grains of Ti-1023, a characteristic line passing through the core of the grain was selected, and the Fe content distribution curve along this characteristic line after homogenization HT at different temperatures are plotted, as shown in Figure 10. It can be seen that when the homogenization HT time is fixed, the higher the temperature, the more uniform the Fe content distribution along the characteristic line. For example, when the homogenization HT time is 12 h, the extreme difference in Fe content along the characteristic line at 1000 °C is 0.19%, while at 1250 °C is 0.01%.

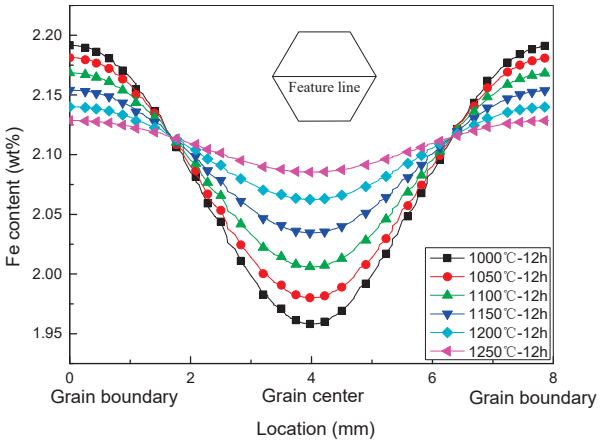

Figure 10. Fe content distribution curve along the characteristic line after homogenization HT at different temperatures, 12 h.

Three characteristic points were selected within the grain of Ti-1023: the core, the middle and the grain boundary, as shown in Figure 11a. The Fe contents of these three characteristic points at different homogenization HT temperatures with time are shown in Figure 11b–d. It can be seen that: (1) The Fe content in the core and middle of the grain increases with increasing homogenization HT time. The higher the homogenization HT temperature, the faster the initial increase in Fe element content, and the slower the subsequent increase at the end of the HT. (2) The Fe content at the grain boundaries decreases with increasing homogenization HT time. During homogenization HT, the high temperature accelerates the diffusion rate of atoms, making the dendritic segregation gradually disappear [42]. The higher the homogenization HT temperature, the faster the initial decrease in Fe content, and the slower the subsequent decrease at the end of the HT.

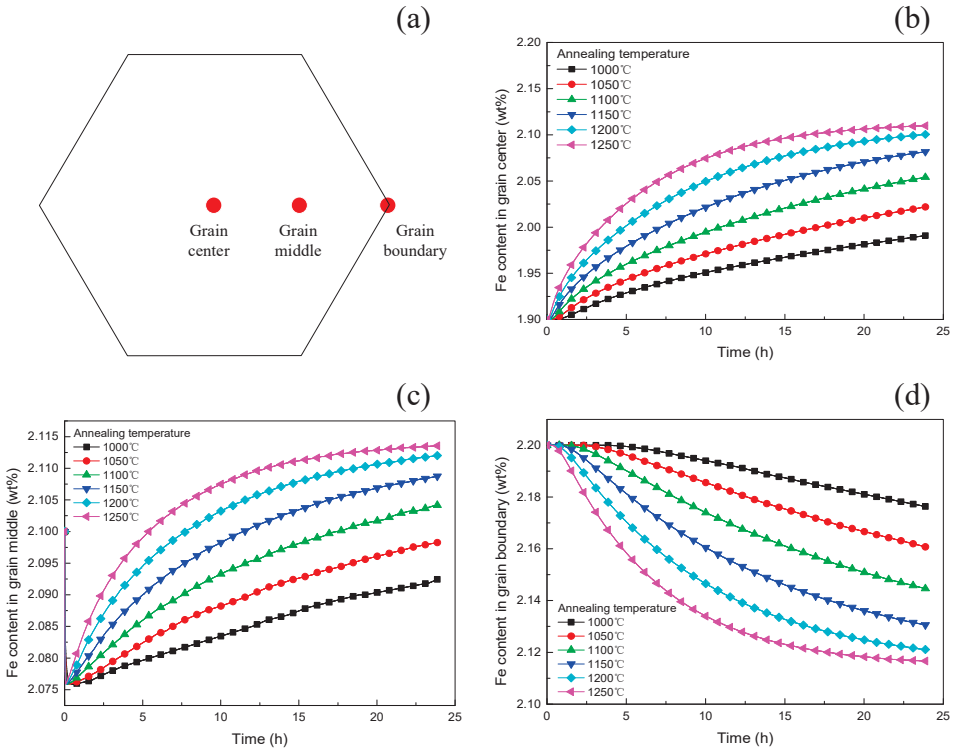

Figure 11. Fe content of characteristic points at different homogenization HT temperatures, (**a**) Schematic of three characteristic points selected within the grain of Ti-1023, (**b**–**d**) Fe contents at different homogenization HT temperatures with time of the core, the middle, and the grain boundary, respectively.

4.3.2. Effect of HT Time on Homogenization of Fe in Grain

At a reasonable homogenization temperature, the alloy elements gradually tend to distribute uniformly with an increase in homogenization time [42]. Distributions of Fe content in the grain during homogenization HT of Ti-1023 were obtained at different temperatures of 1000 °C, 1050 °C, 1100 °C, 1150 °C, 1200 °C and 1250 °C, respectively. Figure 12 shows distributions of Fe content in the grain during homogenization HT of Ti-1023 at a temperature of 1200 °C. During homogenization HT of Ti-1023, the Fe content in the grain tends to become more uniform gradually with an increase in time. When the HT time is 24 h at 1200 °C, the Fe content in the Ti-1023 grains can reach a nearly complete uniformity.

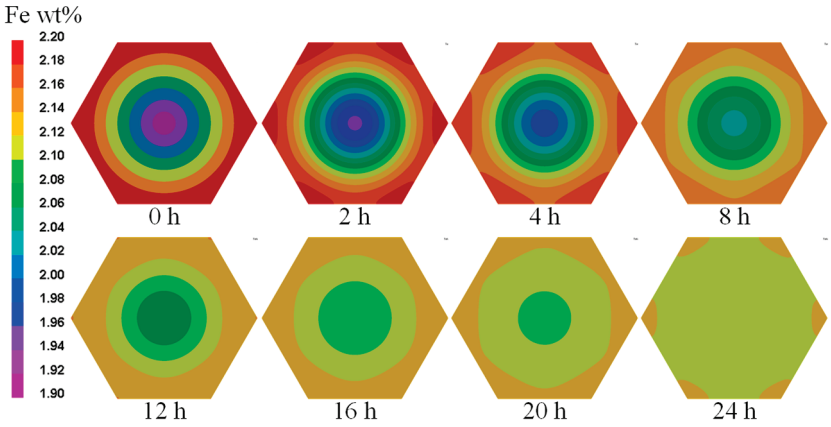

Figure 12. Distributions of Fe content in grain during homogenization HT of Ti-1023 at the temperature of 1200 °C.

Fe content distributions at different positions in the grain during homogenization HT of Ti-1023 are shown in Figure 13. It can be seen that: (1) At a certain HT temperature, the Fe content at different distances from the grain center approaches the average value over time. (2) When the HT temperature is high, such as 1200 °C, the Fe content at different distances from the grain center exhibits a nonlinear change with time, following a concave curve.

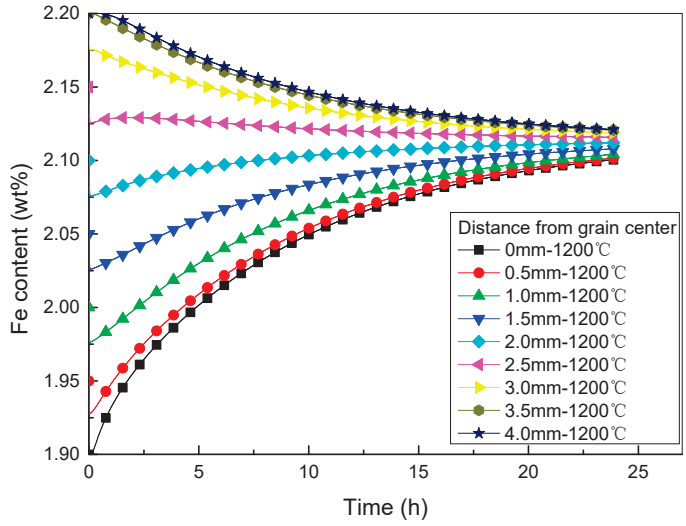

Figure 13. Fe content distributions at different positions in the grain during homogenization HT at 1200 °C.

5. Conclusions

In this paper, the distribution of Fe content in the grains of Ti-1023 ingots smelted by vacuum self-consumption was investigated. The distribution pattern of Fe contents

along the radial direction of the grains in the Ti-1023 ingot was obtained. The effect of homogenization HT temperature on reducing Fe segregation in the microscopic region was investigated by conducting homogenizing HT at temperatures ranging from 1050 °C to 1200 °C for 12 h. Combined with the numerical simulation, the Fe diffusion during the homogenization HT of Ti-1023 was investigated to explore the Fe diffusion law within the grain. The influences of the homogenization HT temperature and time on the distribution of Fe content in Ti-1023 were clarified and the following conclusions were drawn:

1. The Fe content in the Ti-1023 ingots near the grain boundary is higher than that in the core of the grain.
2. The degree of uniform distribution of Fe content within the grain can be improved by homogenization HT. As the HT temperature increases, the Fe element migration capacity improves and the degree of uniform distribution of Fe elements increases.
3. Homogenization HT time has a great influence on the distribution of Fe content within the grain. The longer the HT time, the more uniform the distribution of Fe content. Fe content can achieve complete uniformity within the grain of Ti-1023 after homogenization HT at 1200 °C for 12 h.
4. Homogenization HT of Ti-1023 at 1150 °C to 1200 °C for 12 h can reduce the Fe content deviation from about 10% to less than 4%.

In order to save heat treatment costs and maximize material performance, further research will be conducted on the plasticity and fatigue properties of Ti-1023 with different degrees of Fe segregation after homogenization HT. In addition, methods for controlling Fe segregation during the solidification process of Ti-1023 ingots will also be investigated in future studies.

Author Contributions: Methodology, C.-J.Z. and L.-J.H.; Software, C.-J.Z. and J.-S.C.; Formal analysis, J.-B.T.; Investigation, C.-J.Z. and M.-Q.Y.; Writing—review & editing, J.-B.T., C.-J.Z. and R.-L.X. All authors have read and agreed to the published version of the manuscript.

Funding: This work was funded by the National Natural Science Foundation of China under Grant No. 52104317.

Institutional Review Board Statement: Not applicable.

Informed Consent Statement: Not applicable.

Data Availability Statement: Not applicable.

Conflicts of Interest: The authors declare no conflict of interest.

References

1. Neelakantan, S.; San Martin, D.; Rivera-Diaz-del-Castillo, P.; van der Zwaag, S. Plasticity Induced Transformation in a Metastable Beta Ti-1023 Alloy by Controlled Heat Treatments. *Mater. Sci. Technol.* **2009**, *25*, 1351–1358. [CrossRef]
2. Wang, Q.; Yang, C.; Wu, J.; Gao, B.; He, Z.; Wang, K. Phase Transformation Behavior of Ti-1023 Under Static Heat Treatment and Dynamic Thermo-Mechanical Coupling. *Mater. Charact.* **2022**, *192*, 112248. [CrossRef]
3. Yang, H.; Chen, Z.; Zhou, Z. Influence of Cutting Speed and Tool Wear On the Surface Integrity of the Titanium Alloy Ti-1023 During Milling. *Int. J. Adv. Manuf. Technol.* **2015**, *78*, 1113–1126.
4. Lhadi, S.; Purushottam raj purohit, R.r.p.; Richeton, T.; Gey, N.; Berbenni, S.; Perroud, O.; Germain, L. Elasto-Viscoplastic Tensile Behavior of as-Forged Ti-1023 Alloy: Experiments and Micromechanical Modeling. *Mater. Sci. Eng. A* **2020**, *787*, 139491. [CrossRef]
5. Li, L.; Wang, Z.; Ma, W. Experimental Study on the High Temperature Impact Torsional Behavior of Ti-1023 Alloy. *Materials* **2022**, *15*, 3847. [CrossRef]
6. Li, P.; Sun, X.; Zhang, T.; Zhang, H.; Wang, D.; Sun, Q.; Xiao, L.; Sun, J. Adaptive Volume Control in Titanium Alloy for High Temperature Performance. *Materials* **2019**, *12*, 3950. [CrossRef] [PubMed]
7. Quan, F.; Chen, Z.; Zhu, Y.; Zhang, Y. A Method of Assessing the Strength of Metal Surface Using Film Samples On Titanium Alloy Ti-1023. *Strain* **2019**, *55*, e12317. [CrossRef]
8. Storchak, M.; Zakiev, I.; Träris, L. Mechanical Properties of Subsurface Layers in the Machining of the Titanium Alloy Ti10V2Fe3Al. *J. Mech. Sci. Technol.* **2018**, *32*, 315–322. [CrossRef]
9. Bermingham, M.J.; McDonald, S.D.; StJohn, D.H.; Dargusch, M.S. Segregation and Grain Refinement in Cast Titanium Alloys. *J. Mater. Res.* **2009**, *24*, 1529–1535. [CrossRef]

10. Joseph, S.; Kontis, P.; Chang, Y.; Shi, Y.; Raabe, D.; Gault, B.; Dye, D. A Cracking Oxygen Story: A New View of Stress Corrosion Cracking in Titanium Alloys. *Acta Mater.* **2022**, *227*, 117687. [CrossRef]
11. Ng, C.H.; Bermingham, M.J.; Dargusch, M.S. Eliminating Segregation Defects During Additive Manufacturing of High Strength Beta-Titanium Alloys. *Addit. Manuf.* **2021**, *39*, 101855.
12. Ng, C.H.; Bermingham, M.J.; Yuan, L.; Dargusch, M.S. Towards Beta-Fleck Defect Free Additively Manufactured Titanium Alloys by Promoting the Columnar to Equiaxed Transition and Grain Refinement. *Acta Mater.* **2022**, *224*, 117511. [CrossRef]
13. Fan, K.; Wu, L.C.; Li, J.J.; Wang, J.C. Numerical Simulation of Macrosegregation Caused by Buoyancy Driven Flow During Var Process for Titanium Alloys. *Rare Metal Mat. Eng.* **2020**, *49*, 871–877.
14. He, Y.; Hu, R.; Luo, W.; Sun, F.; Wang, K.; Fu, B.; Li, J.; Liu, X. Effect of Stirring Magnetic Field On the Macrostructure and Macrosegregation of Fe Element of Ti-1023 Alloy Ingot. *Rare Metal Mat. Eng.* **2017**, *46*, 3063–3067.
15. Liao, Q.; Ge, P.; Liu, Y.; Wang, R.Q. Fe Elemental Segregation Control of Large Sized Ti70 Alloy Ingot. *Rare Metal Mat. Eng.* **2020**, *49*, 968–972.
16. Liu, X.; Feng, G.; Zhou, Y.; Fan, Q. Macrosegregation and the Underlying Mechanism in Ti-6.5Al-1.0Cr-0.5Fe-6.0Mo-3.0Sn-4.0Zr Alloy. *Prog. Nat. Sci.* **2019**, *29*, 224–230. [CrossRef]
17. Yang, Z.; Kou, H.; Li, J.; Hu, R.; Chang, H.; Zhou, L. Macrosegregation Behavior of Ti-10V-2Fe-3Al Alloy During Vacuum Consumable Arc Remelting Process. *J. Mater. Eng. Perform.* **2011**, *20*, 65–70. [CrossRef]
18. Gao, J.H.; Nutter, J.; Liu, X.G.; Guan, D.K.; Huang, Y.H.; Dye, D.; Rainforth, W.M. Segregation Mediated Heterogeneous Structure in a Metastable Beta Titanium Alloy with a Superior Combination of Strength and Ductility. *Sci. Rep.* **2018**, *8*, 7512. [CrossRef]
19. Huang, S.S.; Ma, Y.J.; Zhang, S.L.; Qi, M.; Lei, J.F.; Zong, Y.P.; Yang, R. Influence of Alloying Elements Partitioning Behaviors On the Microstructure and Mechanical Properties in Alpha Plus Beta Titanium Alloy. *Acta Metall. Sin.* **2019**, *55*, 741–750.
20. Prithiv, T.S.; Kloenne, Z.; Li, D.A.; Shi, R.P.; Zheng, Y.F.; Fraser, H.L.; Gault, B.; Antonov, S. Grain Boundary Segregation and its Implications Regarding the Formation of the Grain Boundary Alpha Phase in the Metastable β-Titanium Ti-5Al-5Mo-5V-3Cr Alloy. *Scr. Mater.* **2022**, *207*, 114320. [CrossRef]
21. Wang, J.; Qin, Z.W.; Xiong, F.H.; Wang, S.S.; Lu, X.G.; Li, C.H. Design and Preparation of Low-Cost Alpha Plus Beta Titanium Alloy Based On Assessment of Ti-Al-Fe-Cr System. *Mater. Sci. Eng. A* **2018**, *732*, 63–69. [CrossRef]
22. Xu, Z.; Wang, H.; Tang, H.; Cheng, X.; Zhu, Y. Microstructure, Microsegregation and Mechanical Properties of Directed Energy Deposited Ti-32Mo Titanium Alloy. *J. Mater. Sci.* **2022**, *57*, 12540–12555. [CrossRef]
23. Zhao, Y.; Liu, J.; Zhou, L. Analysis On the Segregation of Typical Alloying Elements of Cu, Fe and Cr in Ti Alloys. *Rare Metal Mat. Eng.* **2005**, *34*, 531–538.
24. Jing, Z.; Sun, Y.; Song, S. Numerical Simulation of Macrosegregation Heredity On Tc4 Titanium Alloy Ingot by Vacuum Arc Remelting. *Metall. Res. Technol.* **2023**, *120*, 116.
25. Edalati, K.; Daio, T.; Lee, S.; Horita, Z.; Nishizaki, T.; Akune, T.; Nojima, T.; Sasaki, T. High Strength and Superconductivity in Nanostructured Niobium–Titanium Alloy by High-Pressure Torsion and Annealing: Significance of Elemental Decomposition and Supersaturation. *Acta Mater.* **2014**, *80*, 149–158. [CrossRef]
26. Lei, Z.; Chen, Y.; Ma, S.; Zhou, H.; Liu, J.; Wang, X. Influence of Aging Heat Treatment On Microstructure and Tensile Properties of Laser Oscillating Welded Tb8 Titanium Alloy Joints. *Mater. Sci. Eng. A* **2020**, *797*, 140083. [CrossRef]
27. Mitchell, A. Composition Control in Titanium Alloys. In Proceedings of the Ti-2011: 12th World Conference on Titanium, Beijing, China, 19–24 June 2011; Science Press Beijing: Beijing, China, 2012; Volume I, pp. 71–74.
28. Schwaighofer, E.; Schloffer, M.; Schmoelzer, T.; Mayer, S.; Lindemann, J.; Guether, V.; Klose, J.; Clemens, H. Influence of Heat Treatments On the Microstructure of a Multi-Phase Titanium Aluminide Alloy. *Pract. Metallogr.* **2012**, *49*, 124–137. [CrossRef]
29. Dichtl, C.; Zhang, Z.B.; Gardner, H.; Bagot, P.; Radecka, A.; Dye, D.; Thomas, M.; Sandala, R.; Da Fonseca, J.Q.; Preuss, M. Element Segregation and $Alpha_2$ Formation in Primary Alpha of a Near-Alpha Ti-Alloy. *Mater. Charact.* **2020**, *164*, 110327. [CrossRef]
30. Karthik, G.M.; Kim, H.S. Heterogeneous Aspects of Additive Manufactured Metallic Parts: A Review. *Met. Mater. Int.* **2021**, *27*, 1–39. [CrossRef]
31. Lukyanov, A.V.; Pushin, V.G.; Kuranova, N.N.; Svirid, A.E.; Uksusnikov, A.N.; Ustyugov, Y.M.; Gunderov, D.V. Effect of the Thermomechanical Treatment On Structural and Phase Transformations in $Cu–_{14}Al–_3Ni$ Shape Memory Alloy Subjected to High-Pressure Torsion. *Phys. Met. Metallogr.* **2018**, *119*, 374–382. [CrossRef]
32. Xu, M.; Liu, G.-H.; Li, T.-R.; Wang, B.-X.; Wang, Z.-D. Microstructure Characteristics of Ti–43Al Alloy During Twin-Roll Strip Casting and Heat Treatment. *Trans. Nonferrous Met. Soc. China* **2019**, *29*, 1017–1025. [CrossRef]
33. Zheng, S.; Shen, J.; Shang, Z.; Wang, W.; Xiong, Y.; Yue, X. Effects of Multi-Step Heat Treatment On the Microstructure, Segregation and Property of a Directional Solidified Ti-45.5Al–3Nb-0.11C-0.3Si Alloy Produced by Electromagnetic Confinement. *Mater. Sci. Eng. A* **2020**, *794*, 139962. [CrossRef]
34. Mi, Y.; Wang, Y.; Wang, Y.; Dong, Y.; Chang, H.; Alexandrov, I.V. Effect of Heat Treatment On Microstructure and Mechanical Behavior of Ultrafine-Grained Ti-2Fe-0.1B. *Materials* **2023**, *16*, 2955. [CrossRef] [PubMed]
35. Hu, M.; Wang, L.; Li, G.; Huang, Q.; Liu, Y.; He, J.; Wu, H.; Song, M. Investigations On Microstructure and Properties of Ti-Nb-Zr Medium-Entropy Alloys for Metallic Biomaterials. *Intermetallics* **2022**, *145*, 107568. [CrossRef]
36. Gierlotka, W.; Lothongkum, G.; Lohwongwatana, B.; Puncreoburt, C. Atomic Mobility in Titanium Grade 5 (Ti6Al4V). *J. Min. Metall. Sect. B Metall.* **2019**, *55*, 65–77. [CrossRef]

37. Liu, Y.; Ge, Y.; Yu, D.; Pan, T.; Zhang, L. Assessment of the diffusional mobilities in bcc Ti–V alloys. *J. Alloys Compd.* **2009**, *470*, 176–182. [CrossRef]
38. Shi, R.; Luo, A.A. Applications of Calphad Modeling and Databases in Advanced Lightweight Metallic Materials. *Calphad* **2018**, *62*, 1–17. [CrossRef]
39. Guo, X.; Zhou, Y.; Qi, H.; Tang, X. Study On the as-Cast Microstructure and Homogenization Mechanism of Gh3128 Superalloy. *J. Mater. Eng. Perform.* **2023**, 1–12. [CrossRef]
40. Liu, Y.; He, S.; Li, Y.; Liu, Z.; Li, C.; Li, J.; Miao, H.; Zhu, D.; Su, L. In Vitro Degradation Behavior and Microstructural Evolution of a Novel Biodegradable Zn-Mg-Sr Alloy During Homogenization. *J. Mater. Eng. Perform.* **2022**, *32*, 4283–4294. [CrossRef]
41. Wang, T.; Wan, Z.P.; Li, Z.; Li, P.H.; Li, X.X.; Wei, K.; Zhang, Y. Effect of Heat Treatment Parameters On Microstructure and Hot Workability of as-Cast Fine Grain Ingot of Gh4720Li Alloy. *Acta Metall. Sin.* **2020**, *56*, 182–192.
42. He, S.; Li, C.; Ren, J.; Han, Y. Investigation On Alloying Element Distribution in Cr8Mo2Siv Cold-Work Die Steel Ingot During Homogenization. *Steel Res. Int.* **2018**, *89*, 1800148. [CrossRef]

materials

MDPI

Article

Estimation of Cooling Rate of High-Strength Thick Plate Steel during Water Quenching Based on a Dilatometric Experiment

Hyo-Haeng Jo [1], Kyeong-Won Kim [1], Hyungkwon Park [1], Joonoh Moon [2], Young-Woo Kim [3], Hyun-Bo Shim [3] and Chang-Hoon Lee [1,*]

[1] Korea Institute of Materials Science, Changwon 51508, Republic of Korea; jhh4857@kims.re.kr (H.-H.J.)
[2] Department of Materials Convergence and System Engineering, Changwon National University, Changwon 51140, Republic of Korea
[3] Hyundai Steel Company, Dangjin 31719, Republic of Korea
* Correspondence: lee1626@kims.re.kr; Tel.: +82-55-280-3362; Fax: +82-55-280-3599

Abstract: The microstructure and hardness along the thickness direction of a water-quenched, high-strength thick plate with a thickness of 40 mm were investigated with three specimens from the thick plate: surface, 1/4t, and 1/2t (center) thickness, and the phase transformation behavior of the thick plate according to the cooling rate was analyzed through dilatometric experiments. Finally, the cooling rate for each thickness of the thick plate was estimated by comparing the microstructure and hardness of the thick plate along with the thickness with those of the dilatometric specimens. Martensite microstructure was observed on the surface of the water-quenched thick plate due to the fast cooling rate. On the other hand, an inhomogeneous microstructure was transformed inside the thick plate due to the relatively slow cooling rate and central segregation of Mn. A small fraction of bainite was shown at 1/4t thickness. A banded microstructure with martensite and bainite resulting from Mn segregation was developed at 1/2t; that is, the full martensite microstructure was transformed in the Mn-enriched area even at a slow cooling rate due to high hardenability, but a bainite microstructure was formed in the Mn-depleted area owing to relatively low hardenability. A portion of martensite with fine cementite at the surface and 1/4t was identified as auto-tempered martensite with a Bagaryatskii orientation relationship between the ferrite matrix and cementite. The microstructure and hardness as well as dilatation were investigated at various cooling rates through a dilatometric experiment, and a continuous cooling transformation (CCT) diagram was finally presented for the thick plate. Comparing the microstructure and hardness at the surface, 1/4t, and 1/2t of the thick plate with those of dilatometric specimens cooled at various cooling rates, it was estimated that the surface of the thick plate was cooled at more than 20 °C/s, whereas the 1/4t region was cooled at approximately 5~10 °C/s during water quenching. Despite the difficulty in estimation of the cooling rate of 1/2t due to the banded structure, the cooling rate of 1/2t was estimated between 3 and 5 °C/s based on the results of an Mn-depleted zone.

Keywords: thick plate steel; water quenching; cooling rate; microstructure; hardness; dilatometry

Citation: Jo, H.-H.; Kim, K.-W.; Park, H.; Moon, J.; Kim, Y.-W.; Shim, H.-B.; Lee, C.-H. Estimation of Cooling Rate of High-Strength Thick Plate Steel during Water Quenching Based on a Dilatometric Experiment. *Materials* **2023**, *16*, 4792. https://doi.org/10.3390/ma16134792

Academic Editor: Xianfei Ding

Received: 1 June 2023
Revised: 26 June 2023
Accepted: 28 June 2023
Published: 3 July 2023

1. Introduction

As shipbuilding and construction have grown in scale, thick plate steels are increasingly in demand for their high strength and toughness [1–12]. In order for thick plate steels to have high strength and toughness, a thermo-mechanically controlled process (TMCP) is applied during hot rolling, or quenching and tempering (QT) heat treatment is introduced. For TMCP, strength and toughness can be improved by obtaining a low-temperature microstructure such as bainite by controlling the hot rolling temperature and applying accelerated cooling, which has a very high cooling capability, so there is no significant difference in microstructures in the thickness direction of a thick plate with a thickness of 40 mm. The other method for high strength and toughness in thick plates is QT heat

treatment, which is aimed at obtaining a tempered martensite microstructure that provides an excellent combination of strength and toughness. At the surface area, a martensite microstructure can be easily obtained after water quenching due to the fast cooling rate, whereas the slow cooling rate in the center of the thick plate results in a transformation to bainite or ferrite. As the thickness increases, it is difficult to obtain a uniform microstructure in the thickness direction, leading to a complex microstructure composed of various phases such as martensite, bainite, and ferrite inside thick plates after water quenching. Although many researchers have tried to predict cooling rates in the thickness direction of thick plate steels during water quenching, a systematic analysis of cooling rates in thick plates has yet to be reported [13–16]. H. Wang et al. [13] studied the effect of cooling rate on microstructure and mechanical properties in low-carbon, low-alloyed steel plates using a dilatometric experiment. However, the authors focused on how the microstructure and mechanical property relationships of a low-carbon, low-alloyed steel are affected by phase transformations during continuous cooling, not on the estimation of the cooling rate in a thick steel plate. Lv Yanchun et al. [14] reported that temperatures in the core and surface of a steel plate with a thickness of 60 mm were measured by thermocouples embedded in the core and surface of the steel plate during normalizing, and the cooling rate was simulated through a finite element model using the measured temperature data. They did not consider the cooling rate of steel plate metallurgically by investigating microstructure, mechanical properties, etc. Therefore, in this study, our aim was to precisely identify the microstructure and hardness of high-strength thick plate steel with a thickness of 40 mm in the thickness direction as well as specimens from a high-strength thick plate controlled at various cooling rates by a dilatometric experiment. Finally, we estimated the cooling rates in the thickness direction of the thick plate during water quenching based on a comparison of the microstructure and hardness in both specimens from the thick plate and from the dilatometric experiments.

2. Experimental Procedure

Microstructures in the thickness direction of a water-quenched thick plate with a thickness of 40 mm and dilatometric specimens cooled with various cooling rates were carefully characterized by scanning and transmission electron microscopies, and the Vickers hardness of the thick plate and the dilatometric specimens were measured to evaluate mechanical properties.

2.1. Material Preparation and Characterization

The microstructure and hardness were investigated for high-strength thick plate steel with a thickness of 40 mm after austenitization at 900~930 °C for 60~90 min and water quenching (As-Quenched, AQ). The chemical composition is shown in Table 1. Note that details of the compositions of micro-alloying elements cannot be disclosed due to information security. The microstructure of the surface, 1/4t, and 1/2t in the thickness direction of the thick plate was observed using scanning electron microscopy (JSM-7001F, JEOL, Tokyo, Japan) and transmission electron microscopy (JEM-2100F, JEOL, Japan). The samples for scanning electron microscopy (SEM) were prepared using a 1% picral solution (1 g picric acid + 5 mL HCL + 100 mL ethyl alcohol) after mechanical polishing and disc samples with 3 mm diameter for transmission electron microscopy (TEM) were prepared by mechanical polishing to 70~100 μm thickness, followed by electro-chemical polishing using a twin-jet polisher with a solution of 10% perchloric acid and 90% methanol at −30 °C. Vickers hardness (FM-700, Future Tech, Kawasaki, Japan) was measured under a load of 1 kg for 10 s.

Table 1. Chemical composition of thick plate steel.

Specimen	Thickness (mm)	Chemical Compositions (wt%)				
		C	Si	Mn	V + Nb + Ti	Cu + Ni + Cr + Mo
AQ	40	0.28	0.3	0.7	0.05	1.6

2.2. Dilatometric Experiment

Dilatometric specimens with dimensions of 3 mm diameter × 10 mm length were machined from the thick plate using a dilatometer (Dilatronic-III, Theta, San Jose, CA, USA). The heat treatment conditions for the dilatometric experiment are shown in Figure 1. After austenitizing at 950 °C for 5 min, cooling was performed at various cooling rates between 0.5 to 50 °C/s. It is difficult to find any evidence of undissolved cementites or heterogeneity of austenite during this austenitizing condition. A CCT diagram was prepared based on the dilatation results, the microstructure observation, and the Vickers hardness for the specimens controlled with various cooling rates. The specimens were observed by SEM (JSM-7001F, JEOL) and TEM (JEM-2100F, JEOL) and their Vickers hardness was measured under the same conditions as described above. It was confirmed that prior austenite grain sizes of the thick plate and the dilatometric specimen are very similar: 14.9 μm in the thick plate and 15.6 μm in the dilatometric specimen.

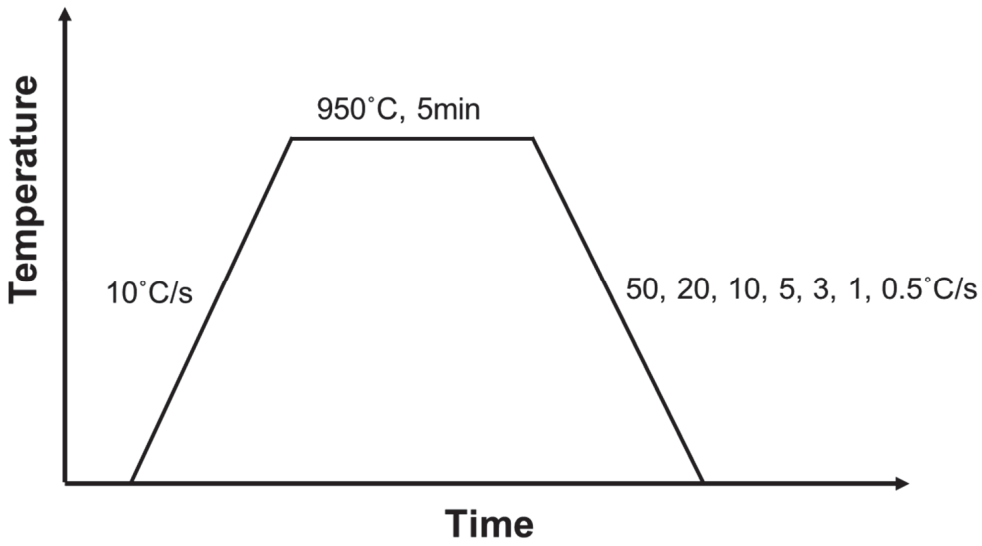

Figure 1. Heat treatment conditions for dilatometric experiment.

3. Results and Discussion

3.1. Investigation of AQ Specimens

Figure 2 shows SEM micrographs of the surface, 1/4t, and 1/2t in the AQ thick plate. The surface area shows a martensite microstructure. Martensite and a small fraction of bainite at austenite grain boundaries and a banded structure with martensite and bainite were observed at 1/4t and 1/2t, respectively. Bainite transformation occurs toward the center in thickness due to a slow cooling rate. It is well known that this banded structure at 1/2t is formed due to the segregation of alloying elements, especially Mn during slab solidification, resulting in Mn-enriched and Mn-depleted regions [17–21]. The Mn-enriched zone at 1/2t of the AQ specimen was transformed to martensite due to high hardenability even at a slow cooling rate, whereas a bainite transformation occurred in the Mn-depleted zone with relatively low hardenability. Table 2 presents the Vickers hardness according to the thickness. The hardness of the surface with martensite was approximately 500 Hv, and that of 1/4t, which contains martensite and a small amount of bainite, was 390 Hv. The hardness of the martensite and bainite in the banded structure of the 1/2t were measured as

507 Hv and 351 Hv, respectively. As a result, the Vickers hardness results are consistent with the microstructural change according to thickness. Figure 3 presents a high-magnification SEM image, a TEM bright field image, and the selected area diffraction pattern at 1/4t. In Figure 3a, martensitic lath and fine particles inside the lath were observed. Through a TEM analysis, this microstructure was identified as auto-tempered martensite with fine cementite, where a Bagayatskii orientation relationship between the ferrite matrix and fine cementite was found in Figure 3b,c. Auto-tempering of martensite is a phenomenon that can occur immediately after martensite transformation for steels with a relatively high martensite transformation start (Ms) temperature [22–24]. The Ms temperature of the AQ specimen is around 400 °C, which is relatively high, resulting in auto-tempering.

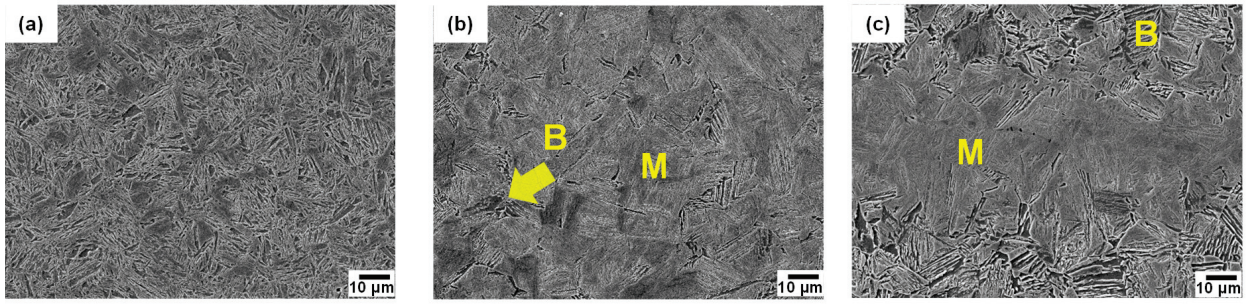

Figure 2. SEM micrographs of AQ specimen: (**a**) surface, (**b**) 1/4t and (**c**) 1/2t in thickness. (M: martensite, B: bainite).

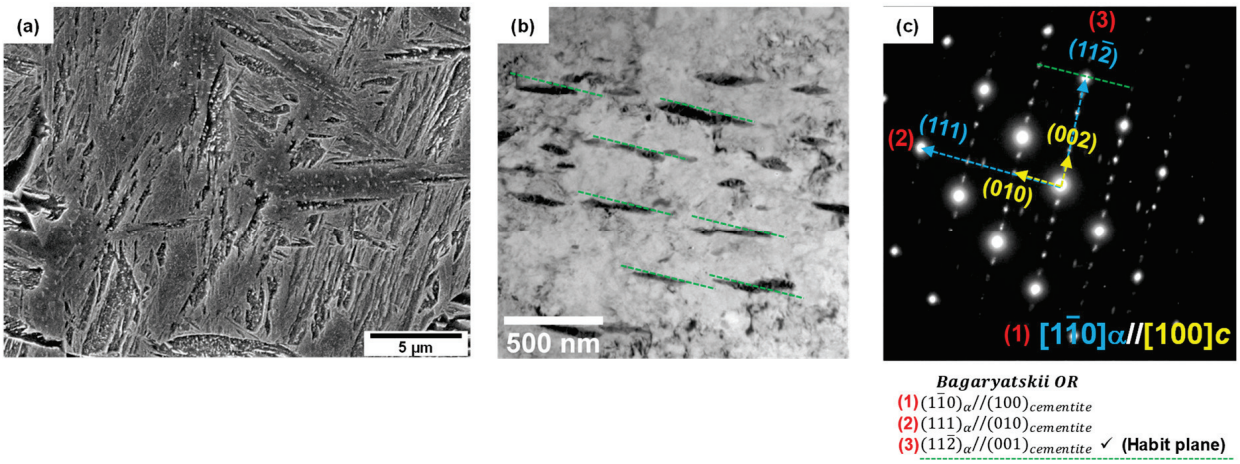

Figure 3. Auto-tempered martensite at 1/4t of AQ specimen: (**a**) SEM micrograph with high magnification, (**b**) TEM micrograph, and (**c**) selected area diffraction pattern showing Bagaryatskii orientation relationship between ferrite and cementite in auto-tempered martensite. (green line: habit plane).

Table 2. Vickers hardness of AQ specimen.

Specimen	Position in Thickness		HV (1 kg)
			Mean (Standard Deviation)
AQ	1/2t (banded structure)	1/2t (1)—Mn-enriched zone	507 (±18.3)
		1/2t (2)—Mn-depleted zone	351 (±16.7)
	1/4t		391 (±17.1)
	surface		503 (±3.5)

3.2. Dilatation Results of AQ Specimens

Figure 4 shows the dilatation behavior of an AQ specimen during heating and cooling. With a decreasing cooling rate, volume expansion occurs at a higher temperature during cooling, which is consistent with the previous studies [11–13]. Therefore, martensite can be transformed at a higher cooling rate, and bainite or ferrite can be transformed as the cooling rate becomes slower in the AQ specimen. The microstructure according to the cooling rate is presented in Figure 5. Full martensite was clearly shown at a cooling rate of 50 °C/s. At 20 °C/s, it was found that a very small amount of bainite was transformed. With a decreasing cooling rate to 3 °C/s, the amount of the transformed bainite increased and the fraction of martensite decreased. At cooling rates of 1 °C/s and 0.5 °C/s, the ferrite phase was found as well as bainite, but martensite was hardly observed. It is determined that auto-tempering of the dilatometric specimen cooled at various cooling rates occurred, as also observed in the AQ thick plate. Figure 6 shows the SEM and TEM micrographs of specimens cooled at 50 °C/s as an example of auto-tempering. It was confirmed again that AQ steel was auto-tempered due to its high MS temperature. Figure 7 shows the Vickers hardness of dilatometric specimens according to the cooling rate. As the cooling rate became slower, the Vickers hardness accordingly became lower, which is consistent with the microstructural change in Figure 5. Full martensite has a hardness of approximately 500 Hv. With an increasing fraction of bainite, the hardness decreases to 322 Hv for the specimen cooled at 3 °C/s. At much slower cooling rates of 1 °C/s and 0.5 °C/s, the hardness is below 300 Hv because of the transformation to ferrite, which is a soft phase.

A CCT diagram of the AQ specimen is presented in Figure 8, based on Figure 4, Figure 5, and Figure 7. It was found that full martensite was transformed at a cooling rate of 50 °C/s, bainite and martensite were transformed at a cooling rate in the range between 3~20 °C/s, and ferrite and bainite and no more martensite were transformed at a cooling rate lower than 1 °C/s. Bainite transformation start (Bs) and martensite transformation start (Ms) temperatures can be calculated by Equations (1) and (2), respectively [25–28]. The calculated Bs and Ms temperatures were 606 °C and 378 °C, respectively, which are similar to those in this CCT diagram.

$$[\text{Bs, °C}] = 830 - 270[\text{C}] - 90[\text{Mn}] - 70[\text{Cr}] - 37[\text{Ni}] - 83[\text{Mo}] \text{ (wt.\%)} \quad (1)$$

$$[\text{Ms, °C}] = 561 - 474[\text{C}] - 33[\text{Mn}] - 17[\text{Cr}] - 17[\text{Ni}] - 21[\text{Mo}] \text{ (wt.\%)} \quad (2)$$

Finally, the actual cooling rate for each thickness of the AQ thick plate during water quenching was estimated by comparing the microstructure and hardness between the AQ thick plate in the thickness direction and dilatometric specimens cooled at various cooling rates, as shown in Figure 9. The hardness of 500 Hv and martensite at the surface of the AQ thick plate show that the surface should be cooled at a cooling rate of 20 °C/s or more. The hardness of 390 Hv and microstructure of martensite and bainite at 1/4t were similar to those of the dilatometric specimens cooled at a cooling rate between 5 and 10 °C/s. In the case of 1/2t, it was difficult to estimate the cooling rate due to the banded structure, but if the results of an Mn-depleted zone are considered, the cooling rate of 1/2t was estimated between 3 and 5 °C/s.

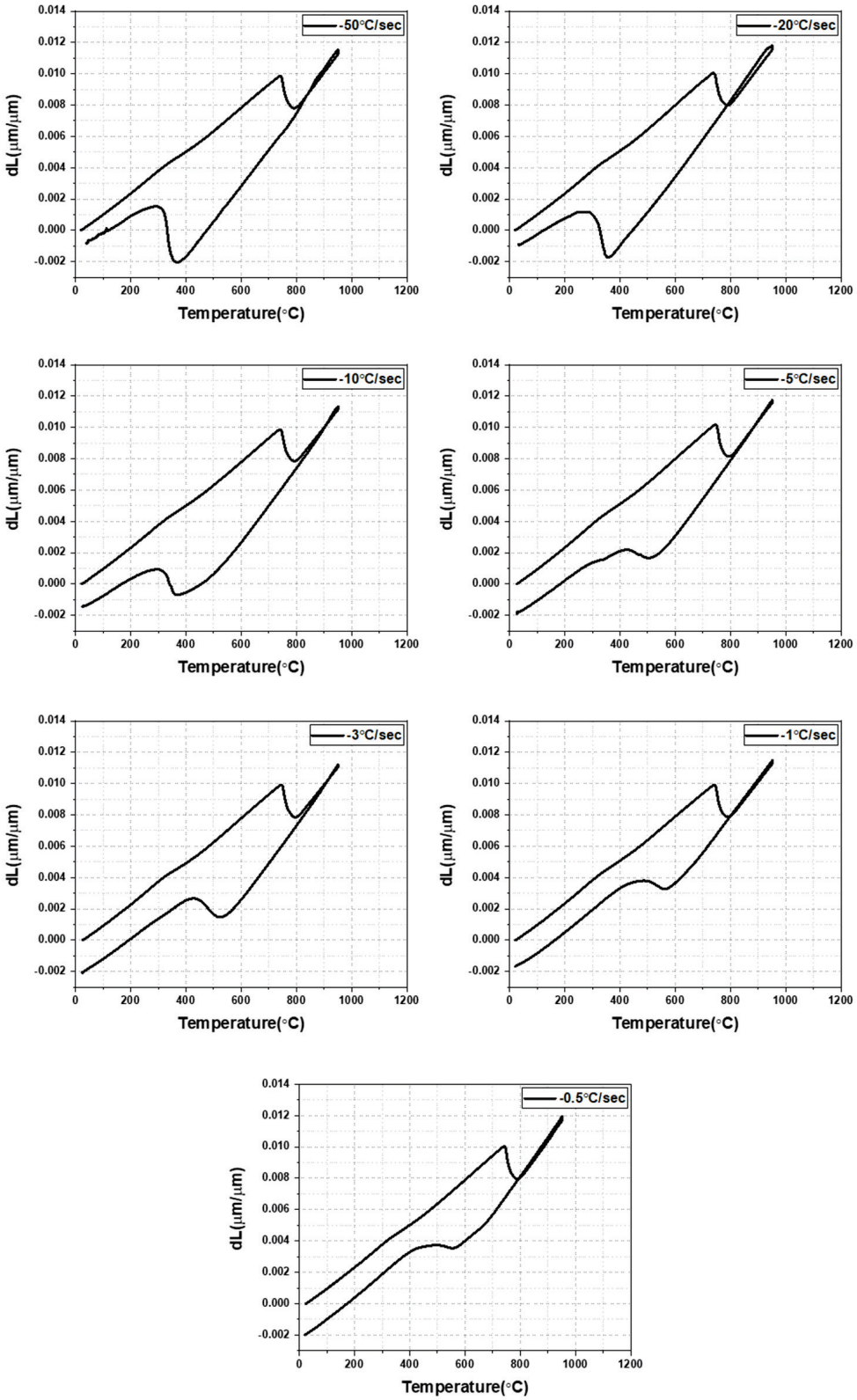

Figure 4. Dilatation results of AQ specimen according to cooling rate.

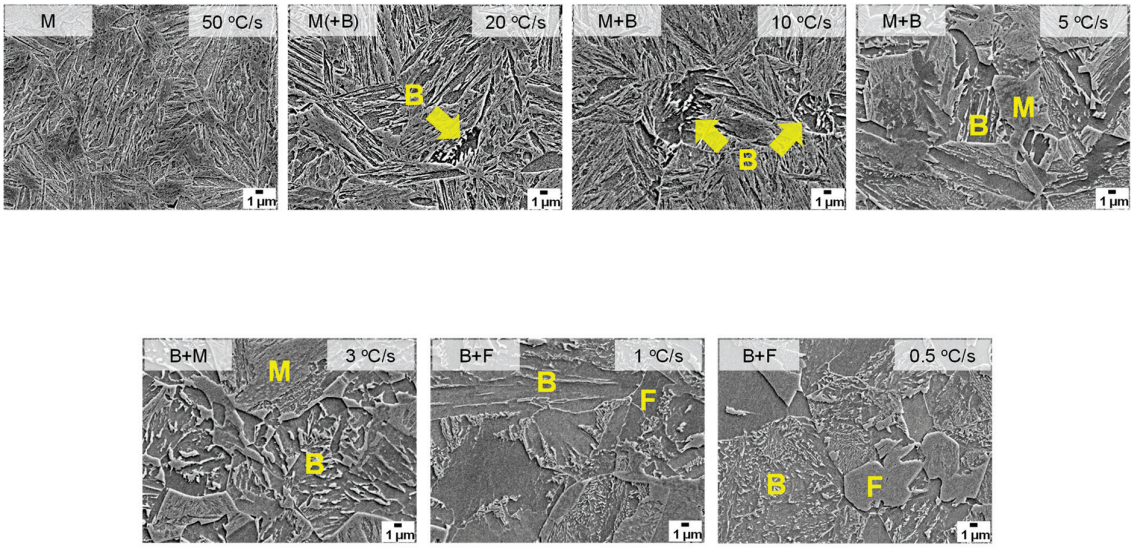

Figure 5. SEM micrographs of dilatometric specimens according to cooling rate. (M: martensite, B: bainite, F: ferrite).

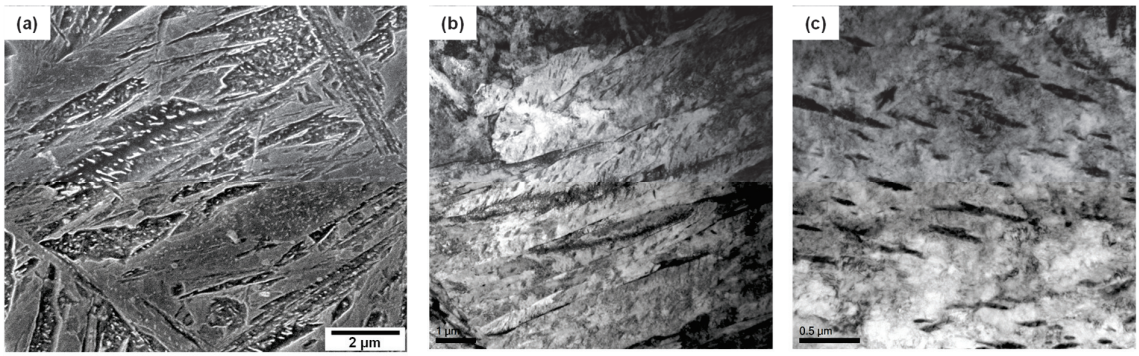

Figure 6. Auto-tempered martensite in dilatometric specimen cooled at 50 °C/s: (**a**) SEM micrograph with high magnification, (**b**,**c**) TEM bright field images.

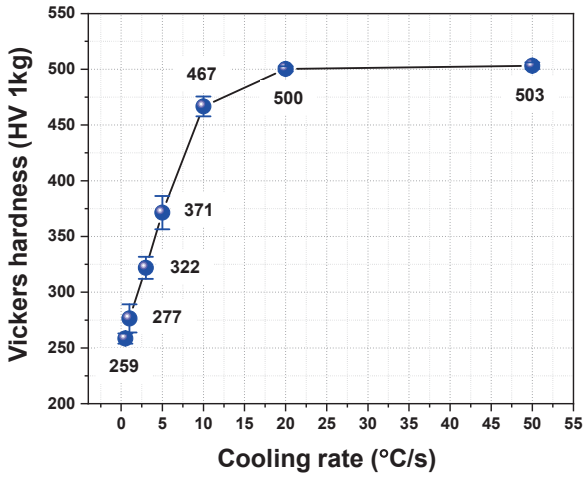

Cooling rate (°C/s)	HV (1kg)	
	Mean	Standard deviation
0.5	259	4.6
1	277	12.7
3	322	9.9
5	371	14.9
10	467	8.9
20	500	2.4
50	503	2.9

Figure 7. Vickers hardness of dilatometric specimens according to cooling rate.

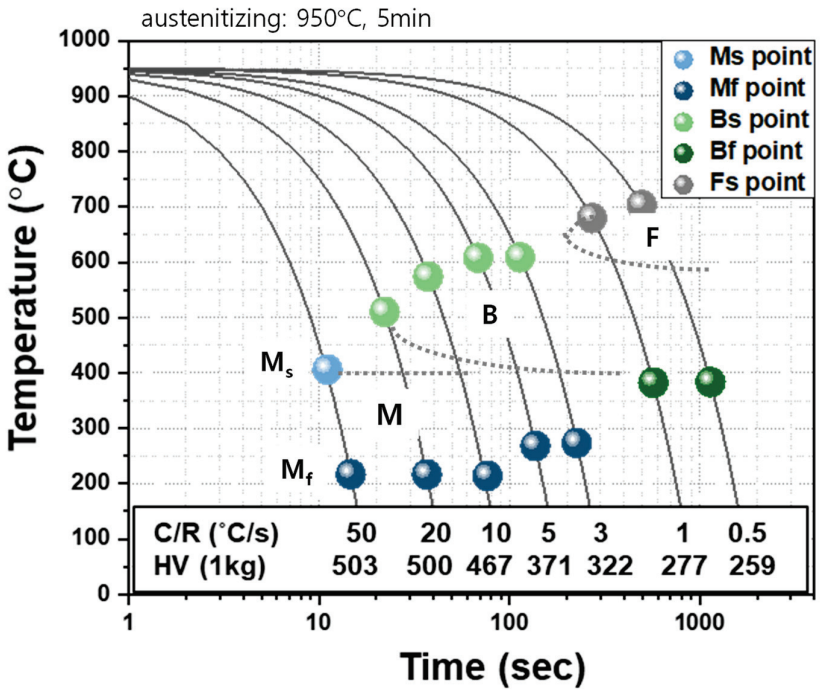

Figure 8. CCT diagram of AQ specimen based on a dilatometric experiment.

Specimen	Position in thickness		HV (1kg) Mean	Microstructure
AQ	1/2t (banded structure)	1/2t (1) – high Mn	507	M
		1/2t (2) – low Mn	351	B+M
	1/4t		391	M+B
	surface		503	M

Cooling rate (°C/s)	HV (1kg) Mean	Microstructure
0.5	259	B+F
1	277	B+F
3	322	B+M
5	371	M+B
10	467	M+B
20	500	M(+B)
50	503	M

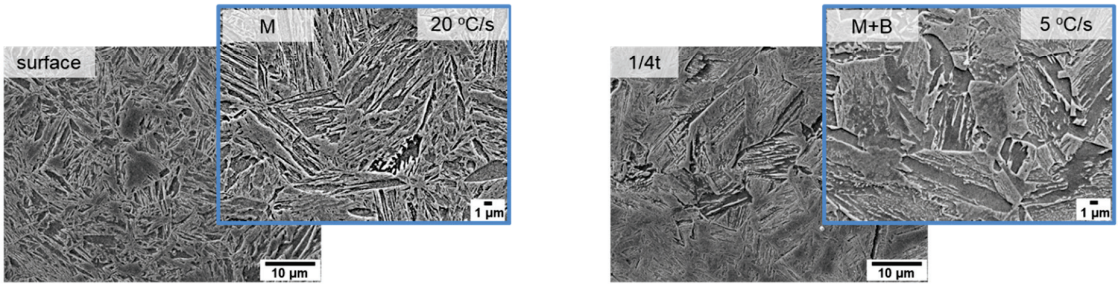

Figure 9. Estimation of cooling rate of AQ thick plate during water quenching by comparison of hardness and microstructure between AQ thick plate and dilatometric specimens.

4. Conclusions

In this study, the microstructure and hardness of an AQ thick plate with 40 mm thickness were investigated in the thickness direction. Dilatometric experiments with specimens from the AQ thick plate were conducted to verify the effect of the cooling rate on the microstructure and hardness and to make a CCT diagram of the AQ steel. Finally, we estimated the cooling rate of the AQ thick plate in the thickness direction during water quenching based on an investigation of the thick plate and dilatometric specimens. The

surface of the thick plate showed a full martensite microstructure due to the fast cooling rate, and the bainite structure was partially transformed at 1/4t due to the slower cooling rate. At 1/2t, a banded structure with martensite and bainite was formed due to a hardenability difference resulting from the central segregation of Mn in the slab. By comparing the microstructure and hardness of dilatometric specimens cooled at various cooling rates, the cooling rates at the surface and at 1/4t of the thick plate during water quenching were more than 20 °C/s and between 5 and 10 °C/s, respectively. The cooling rate at 1/2t was estimated between 3 and 5 °C/s based on the results of an Mn-depleted zone. A portion of martensite in both the AQ thick plate and the dilatometric specimen was identified as auto-tempered martensite in which there is a Bagayatskii orientation relationship between the ferrite matrix and cementite.

Author Contributions: Conceptualization, J.M. and C.-H.L.; Methodology, K.-W.K.; Validation, H.P.; Investigation, H.-H.J.; Writing—original draft, H.-H.J.; Writing—review & editing, Y.-W.K., H.-B.S. and C.-H.L.; Supervision, C.-H.L. All authors have read and agreed to the published version of the manuscript.

Funding: This research was funded by CBMM with grant number PICN190 and the Fundamental Research Program of the Korea Institute of Materials Science with grant number PNK8920.

Institutional Review Board Statement: Not applicable.

Informed Consent Statement: Not applicable.

Data Availability Statement: The data presented in this study are available on request from the corresponding author.

Acknowledgments: This work was financially supported by CBMM and the Fundamental Research Program of the Korea Institute of Materials Science (PNK8920). The authors thank S.-D. Kim in Pukyong National University for help with the TEM analysis.

Conflicts of Interest: The authors declare no conflict of interest.

References

1. Ouchi, C. Development of steel plates by intensive use of TMCP and direct quenching processes. *ISIJ Int.* **2001**, *41*, 542–553. [CrossRef]
2. Liu, D.; Li, Q.; Emi, T. Microstructure and mechanical properties in hot-rolled extra high-yield-strength steel plates for offshore structure and shipbuilding. *Metall. Mater. Trans. A* **2011**, *42*, 1349–1361. [CrossRef]
3. Nishilka, K.; Ichikawa, K. Progress in thermomechanical control of steel plates and their commercialization. *Sci. Technol. Adv. Mater.* **2012**, *13*, 023001. [CrossRef] [PubMed]
4. Uemori, R.; Inoue, T.; Ichikawa, K.; Nose, T.; Fujioka, M.; Minagawa, M.; Shirahata, H. Steels for marine transportation and construction. *Nippon Steel Tech. Rep.* **2012**, *101*, 37.
5. Sun, X.; Yuan, S.; Xie, Z.; Dong, L.; Shang, C.; Misra, R. Microstructure-property relationship in a high strength-high toughness combination ultra-heavy gauge offshore plate steel: The significance of multiphase microstructure. *Mater. Sci. Eng. A* **2017**, *689*, 212–219. [CrossRef]
6. Yoshie, A.; Sasaki, J. Recent development of niobium bearing structural steels for ships and infrastructures in Nippon steel. In *Niobium Bearing Structural Steel*; TMS (The Minerals, Metals & Materials Society): Pittsburgh, PA, USA, 2010.
7. Liu, D.; Cheng, B.; Chen, Y. Strengthening and Toughening of a Heavy Plate Steel for Shipbuilding with Yield Strength of Approximately 690 MPa. *Metall. Mater. Trans. A* **2013**, *44*, 440–455. [CrossRef]
8. Tang, S.; Liu, Z.; Wang, G. Development of High Strength Plates with Low Yield Ratio by the Combination of TMCP and Inter-Critical Quenching and Tempering. *Steel Res. Int.* **2011**, *82*, 772–778. [CrossRef]
9. Guo, K.; Pan, T.; Zhang, N.; Meng, L.; Luo, X.; Chai, F. Effect of Microstructural Evolution on the Mechanical Properties of Ni-Cr-Mo Ultra-Heavy Steel Plate. *Materials* **2023**, *16*, 1607. [CrossRef] [PubMed]
10. Schino, A.; Guagnelli, M. Metallurgical design of high strength/high toughness steels. *Mater. Sci. Forum* **2012**, *706–709*, 2084–2089. [CrossRef]
11. Saxena, A.; Kumar, V.; Datta, R. Influence of Cooling Rate on Transformation Behavior of 0.15% V Microalloyed Steel. *J. Mater. Eng. Perform.* **2011**, *20*, 1481–1483. [CrossRef]
12. Zhao, Y.; Shang, C.; Yang, S.; Wang, X.; He, X. The metastable austenite transformation in Mo-Nb-Cu-B low carbon steel. *Mater. Sci. Eng. A* **2006**, *433*, 169–174. [CrossRef]
13. Wang, H.; Cao, L.; Li, Y.; Schneider, M.; Detemple, E.; Eggeler, G. Effect of cooling rate on the microstructure and mechanical properties of a low-carbon low-alloyed steel. *J. Mater. Sci.* **2021**, *56*, 11098–11113. [CrossRef]

14. Lv, Y.; Zhang, Y.; Wang, H.; Wang, W.; Liu, Y. Temperature Variation of Steel Plate with Different Thickness on Normalizing Process. *J. Phys. Conf. Ser.* **2021**, *1820*, 012127.
15. Stewart, R.; Speer, J.; Thomas, B.; Moor, E.; Clarke, A. Quenching and Partitioning of Plate Steels: Partitioning Design Methodology. *Metall. Mater. Trans. A* **2019**, *50*, 4701–4713. [CrossRef]
16. Fu, T.; Deng, X.; Tian, X.; Liu, G.; Wang, Z. Experimental study on temperature drop during roller quenching process of large-section ultra-heavy steel plate. *Sci. Prog.* **2021**, *104*, 00368504211009330. [CrossRef]
17. Thompson, S.; Howell, R. Factors influencing ferrite/pearlite banding and origin of large pearlite nodules in a hypoeutectoid plate steel. *Mater. Sci. Technol.* **1992**, *8*, 777–784. [CrossRef]
18. Ha, W.; Lee, C.; Park, C. Microstructural control of hot rolled strips and their tensile strengths after hot stamping process. *J. Mech. Sci. Technol.* **2015**, *29*, 209–213. [CrossRef]
19. Slater, C.; Bandi, B.; Dastur, P.; Davis, C. Segregation Neutralised Steels: Microstructural Banding Elimination from Dual-Phase Steel Through Alloy Design Accounting for Inherent Segregation. *Metall. Mater. Trans. A* **2022**, *53*, 2286–2299. [CrossRef]
20. Shi, L.; Yan, Z.; Liu, Y.; Yang, X.; Zhang, C.; Li, H. Effect of acicular ferrite on banded structures in low-carbon microalloyed steel. *Int. J. Miner. Metall. Mater.* **2014**, *21*, 1167–1174. [CrossRef]
21. Ye, Q.; Liu, Z.; Yang, Y.; Wang, G. Effect of Rolling Temperature and Ultrafast Cooling Rate on Microstructure and Mechanical Properties of Steel Plate. *Metall. Mater. Trans. A* **2022**, *47*, 3622–3632. [CrossRef]
22. Honeycombe, R.; Bhadeshia, H. *Steels: Microstructure and Properties*, 4th ed.; Elsevier Ltd.: Amsterdam, The Netherlands, 2017; pp. 238–246.
23. Matsuda, H.; Mizuno, R.; Funakawa, Y.; Seto, K.; Matsuoka, S.; Tanaka, T. Effects of auto-tempering behaviour of martensite on mechanical properties of ultra high strength steel sheets. *J. Alloys Compd.* **2013**, *577*, S661–S667. [CrossRef]
24. Jiang, H.; He, Y.; Lin, L.; Liu, R.; Zhang, Y.; Zheng, W.; Li, L. Microstructures and Properties of Auto-Tempering Ultra-High Strength Automotive Steel under Different Thermal-Processing Conditions. *Metals* **2021**, *11*, 1121. [CrossRef]
25. Bhadeshia, H. *Bainite in Steel*, 3rd ed.; Maney Publishing: Leeds, UK, 2015; p. 142.
26. Lee, Y. Empirical formula of isothermal bainite start temperature of steels. *J. Mater. Sci. Lett.* **2002**, *21*, 1253–1255. [CrossRef]
27. Akyel, F.; Olschok, S.; Reisgen, U. Reduction of distortion by using the low transformation temperature effect for high alloy steels in electron beam welding. *Weld. World* **2021**, *65*, 23–34. [CrossRef]
28. Steven, W.; Haynes, A. The Temperature of Formation of Martensite and Bainite in Low-Alloy Steels. *J. Iron Steel Inst.* **1956**, *183*, 349–359.

materials

MDPI

Article

Microstructure, Mechanical Properties and Oxidation Resistance of Nb-Si Based Ultrahigh-Temperature Alloys Prepared by Hot Press Sintering

Lijing Zhang [1], Ping Guan [2,*] and Xiping Guo [1,*]

[1] State Key Laboratory of Solidification Processing, Northwestern Polytechnical University, Xi'an 710072, China
[2] School of Chemistry and Chemical Engineering, Northwestern Polytechnical University, Xi'an 710129, China
* Correspondence: guanping1113@nwpu.edu.cn (P.G.); xpguo@nwpu.edu.cn (X.G.); Tel./Fax: +86-29-88494873 (X.G.)

Abstract: Nb-Si based ultrahigh-temperature alloys with the composition of Nb-22Ti-15Si-5Cr-3Al (atomic percentage, at. %) were prepared by hot press sintering (HPS) at 1250, 1350, 1400, 1450 and 1500 °C. The effects of HPS temperatures on the microstructure, room temperature fracture toughness, hardness and isothermal oxidation behavior of the alloys were investigated. The results showed that the microstructures of the alloys prepared by HPS at different temperatures were composed of Nbss, βTiss and $\gamma(Nb,X)_5Si_3$ phases. When the HPS temperature was 1450 °C, the microstructure was fine and nearly equiaxed. When the HPS temperature was lower than 1450 °C, the supersaturated Nbss with insufficient diffusion reaction still existed. When the HPS temperature exceeded 1450 °C, the microstructure coarsened obviously. Both the room temperature fracture toughness and Vickers hardness of the alloys prepared by HPS at 1450 °C were the highest. The alloy prepared by HPS at 1450 °C exhibited the lowest mass gain upon oxidation at 1250 °C for 20 h. The oxide film was mainly composed of Nb_2O_5, $TiNb_2O_7$, TiO_2 and a small amount of amorphous silicate. The formation mechanism of oxide film is concluded as follows: TiO_2 forms by the preferential reaction of βTiss and O in the alloy; after that, a stable oxide film composed of TiO_2 and Nb_2O_5 forms; then, $TiNb_2O_7$ is formed by the reaction of TiO_2 and Nb_2O_5.

Keywords: Nb-Si based ultrahigh-temperature alloys; hot press sintering; microstructure; room temperature fracture toughness; hardness; oxidation resistance

Citation: Zhang, L.; Guan, P.; Guo, X. Microstructure, Mechanical Properties and Oxidation Resistance of Nb-Si Based Ultrahigh-Temperature Alloys Prepared by Hot Press Sintering. *Materials* **2023**, *16*, 3809. https://doi.org/10.3390/ma16103809

Academic Editor: Antonino Squillace

Received: 1 April 2023
Revised: 10 May 2023
Accepted: 15 May 2023
Published: 18 May 2023

1. Introduction

The next-generation aero-engines with high thrust-to-weight ratio have put forward requirements on the temperature-enduring capacity of their hot-end components [1,2]. The operating temperature of the most advanced Ni-based single crystal superalloy is about 1150 °C, which is basically close to their limit (85% of their melting temperatures) [3]. Therefore, it has become an urgent task to develop new high-temperature metallic structural materials that can serve for a long time at temperatures above 1200 °C. As Nb-Si based ultrahigh-temperature alloys with additions of alloying elements such as Al and Cr, etc., have a high melting point (above 1750 °C), relatively low density (6.6–7.2 g/cm^3), good high temperature creep strength and good fatigue behavior, they have been considered as a prospective high-temperature structural material and have attracted much attention in recent years [4–8].

At present, non-consumable arc melting or directional solidification are employed frequently to prepare Nb-Si based ultrahigh-temperature alloys, which possess microstructures consisting of Nb solid solution (Nbss) and silicides ($(Nb,X)_5Si_3$ ("X" represents the elements substituting for Nb such as Ti and Cr)) [9–14]. However, there exist some drawbacks such as serious compositional segregation, coarse microstructure and distinct microstructural heterogeneity in Nb-Si based alloy ingots produced by the aforementioned

solidification methods, which would result in poorer mechanical properties. Therefore, seeking a method to prepare Nb-Si based ultrahigh-temperature alloys with uniform composition, even phase distributions and fine microstructure is of great importance. Powder metallurgy can synthesize products with fine microstructure at the micrometer level, which shows excellent high-temperature plastic deformation ability and even superplasticity [15–17]. Due to their extremely high melting temperature, it is reasonable to prepare this kind of ultrahigh-temperature alloy by powder metallurgy. The powder metallurgy route generally consists of two procedures, i.e., first preparing the powder blends by mechanical alloying and then sintering the powder blends using methods such as HPS [18,19]. A few researchers have fabricated Nb-Si based alloys by powder metallurgy methods [20–22]. However, only the microstructure and mechanical properties of Nb-Si binary and Nb-Si-Fe or Nb-Si-Ti ternary alloys have been studied [20–22]. Until now, there is no report in the open literature about the preparation, microstructural characteristics and properties of more practical multicomponent Nb-Si based ultrahigh-temperature alloys through a powder metallurgy route.

Based on the previous research results [10,13,14,23–25], optimized Nb-Si based ultrahigh-temperature alloy powders with a composition of Nb-22Ti-15Si-5Cr-3Al (hereafter, all compositions are given in at. % unless otherwise stated) will be fabricated by powder metallurgy. Temperature is an important parameter in the HPS process. Sintering is a temperature-controlled thermal activation process. As the temperature increases, the temperature-related rate factor (e.g., diffusion rate) in the sintering process increases, resulting in an increase in densification rate [26]. To our best knowledge, up to now, there is no systematic research on the effect of HPS temperature on the microstructure and properties of Nb-Si based ultrahigh-temperature alloys. In the present work, the microstructure, room temperature fracture toughness, microhardness and oxidation behavior at 1250 °C of Nb-22Ti-15Si-5Cr-3Al ultrahigh-temperature alloys prepared by HPS at different temperatures have been integrally evaluated.

2. Experimental Procedures

Nb, Ti, Si, Cr and Al elemental powders were weighed according to the composition of Nb-22Ti-15Si-5Cr-3Al. Mechanical alloying was performed for 20 h in a planetary ball mill using stainless steel jars and milling balls under Ar atmosphere. The ball milling speed and ball-to-powder ratio (BPR) were fixed at 400 rpm and 15:1. A total 1.25 wt.% stearic acid was added as the process control agent. Block Nb-Si based alloys were prepared in a HVHS-2 ultrahigh-temperature and high-vacuum HPS furnace under Ar atmosphere. The furnace was designed and produced by SKY technology development Co., Ltd. (Shenyang, China), Chinese Academy of Sciences; it uses U-shaped tungsten rods as the heating unit and WRW5Z-395 tungsten rhenium thermocouple as the temperature measurement and control device, with a temperature control accuracy of ±1 °C. The evaluated HPS temperatures were 1250, 1350, 1400, 1450 and 1500 °C.

X-ray diffraction analysis (XRD, X'Pert Pro, Cu K_α, PANalytical, Almelo, The Netherlands) was used to identify the constituent phases in the specimens. The microstructure of the specimens was observed by scanning electron microscopy (SEM, MIRA3 XMU, TESCAN, Brno, Czech Republic) and the chemical compositions of their constituent phases were analyzed by energy dispersive spectroscopy (EDS, Inca X-sight, OXFORD Limited, Oxford, United Kingdom). The refined microstructure of the specimens was examined by a Tecnai F30 G2 transmission electron microscope (TEM) equipped with an EELS system (Gatan GIF Tridiem 863, AMETEK, Berwyn, PA, USA) operating at 300 kV. The Image-Pro Plus 7.0 software (IPP 7.0) was used for quantitative analysis of the volume fraction of constituent phases and the area fraction of pores in the alloys. To improve the statistical accuracy, five BSE images with the same magnification (×1000) were used for each alloy.

The single edge notched three-point-bending specimen for room temperature fracture toughness (K_Q) measurement with dimensions of 25 mm × 5 mm × 2.5 mm was prepared by electro-discharge machining (EDM), and the notch is within the depth of 2.5 ± 0.1 mm.

The K_Q value was measured on an electronic universal mechanical testing machine (Instron-3382, INSTRON Corporation, High Wycombe, United Kingdom). Three specimens were tested and the average K_Q value was employed for each specimen condition.

The density of the specimens were measured using Archimedes' drainage method, based on which the relative density of each specimen was calculated [27]. The Vickers hardness (HV) of the specimens was measured using an HMV-2T (Shimadzu, Hitachi Corporation, Japan) hardness machine with a load of 0.98 N. Each employed hardness value was the average of at least 5 indentations.

The specimens used for oxidation tests were 7 mm × 7 mm × 7 mm cubes cut from the sintered plates, 30 mm in diameter and 10 mm in thickness, by EDM. After the six surfaces were ground, the actual dimensions of each specimen were measured using a vernier caliper and its surface area was calculated before oxidation tests. The isothermal oxidation behavior of the specimens was examined in an open-ended tube furnace. After holding them at 1250 °C for 20 h, the specimens were furnace-cooled down to room temperature. The mass changes of the specimens after oxidation tests were obtained using an electronic balance with an accuracy of 0.001 g.

3. Results and Discussion

3.1. Phase Analysis of the Alloys

In order to determine the phase constituents of the Nb-Si based ultrahigh-temperature alloys prepared by HPS at different temperatures, XRD analysis was performed on each alloy prepared, as shown in Figure 1. It can be seen that the alloy has diffraction peaks of three phases, which are calibrated as Nbss, $\gamma(Nb,X)_5Si_3$ ("X" represents Ti, Cr and Al) and βTiss (determination of the diffraction peak of βTiss will be described in the subsequent sections). The $\gamma(Nb,X)_5Si_3$ intermetallic compound that appeared was generated by the in situ reaction during HPS. At the same time, no diffraction peaks of Cr, Si and other components were found in the Nb-Si based ultrahigh-temperature alloy's bulk samples prepared by HPS, indicating that Cr, Si and other components all participated in the reaction during HPS: on one hand, they dissolved into the Nb lattice to form Nbss; on the other hand, the $\gamma(Nb,X)_5Si_3$ silicide was generated due to the chemical reaction among them and other components. In addition, the intensity of the diffraction peak of the $\gamma(Nb,X)_5Si_3$ intermetallic compound in the Nb-Si based ultrahigh-temperature alloys prepared by HPS at 1250 °C was relatively weak, and the Nbss diffraction peak is still the main peak in the patterns. However, when the HPS temperature was higher than 1250 °C, compared with the diffraction peaks of Nbss, those of $\gamma(Nb,X)_5Si_3$ were obviously enhanced, which indicates that an increase in HPS temperature promotes the formation of intermetallic compounds through the reaction among Nb, Ti and Si in the milled powders. The in situ reaction in the milled powders began to occur when the HPS temperature was higher than 1250 °C.

3.2. Microstructure of the Alloys

Figure 2 shows the backscattered electron (BSE) images of the microstructure of the Nb-Si based ultrahigh-temperature alloys prepared by HPS at different temperatures. It can be seen that the alloy consists of three different contrast areas: white, gray and dark gray. Combined with XRD and EDS analysis results, it can be concluded that the white region is Nbss, the gray one is $\gamma(Nb,X)_5Si_3$ and the dark gray one is βTiss.

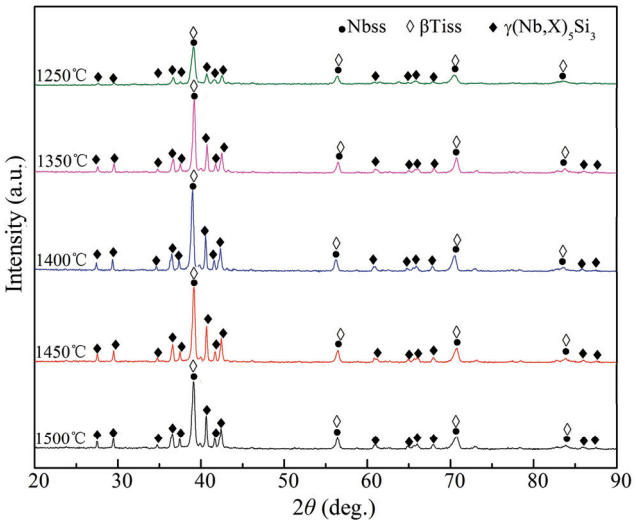

Figure 1. XRD patterns of the Nb-Si based ultrahigh-temperature alloys hot press sintered (HPSed) at different temperatures.

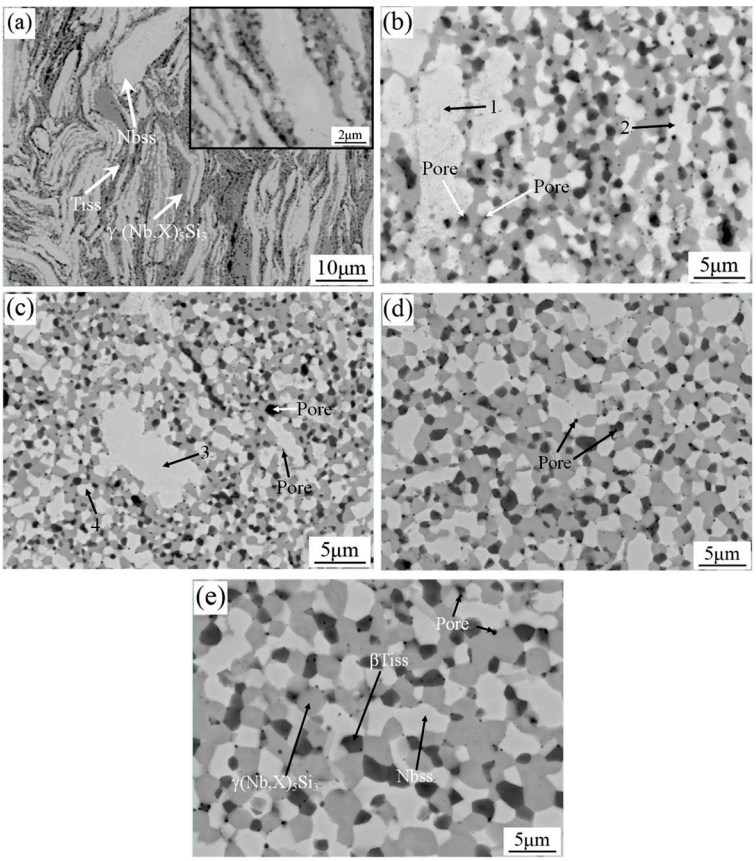

Figure 2. BSE images of the Nb-Si based ultrahigh-temperature alloys HPSed at (**a**) 1250 °C, (**b**) 1350 °C, (**c**) 1400 °C, (**d**) 1450 °C and (**e**) 1500 °C. The arrowhead positions with numerals "1–4" are the locations where EDS analyses were performed.

As can be seen in Figure 2a, when the HPS temperature was 1250 °C, the microstructure of the alloy showed obvious river-like strip morphologies, with the length of the strip structure reaching tens of microns and the width only being about a few microns, wherein the Nbss strips are basically parallel to each other. When HPS was carried out at 1250 °C, the powder particles softened under the simultaneous application of pressure such that the

lamellar microstructure tended to be distributed perpendicular to the direction of press stress, thus forming a river-like microstructure morphology parallel to each other.

As can be seen in the enlarged view in the upper right corner of Figure 2a, $\gamma(Nb,X)_5Si_3$ and βTiss were basically distributed in the interface area of Nbss. From this, it can be inferred that $\gamma(Nb,X)_5Si_3$ and βTiss were precipitated from the decomposition of the supersaturated Nbss in ball-milled powder particles during the HPS process. Table 1 shows the EDS composition analysis results of different phases in Nb-Si based ultrahigh-temperature alloys prepared by HPS at 1250 °C. It can be seen that the content of solid solution elements in Nbss is still very high (especially Si); so, it is still supersaturated Nbss. The gray region is $\gamma(Nb,X)_5Si_3$ and the black region is βTiss, which indicates that the HPS temperature of 1250 °C is too low; therefore, the milled powder particles do not fully react and obvious diffusion does not occur, resulting in a large amount of supersaturated Nbss strips still existing in the sintered alloy bulk.

Table 1. EDS analysis results of each constituent phase in the Nb-Si based ultrahigh-temperature alloys HPSed at 1250 °C shown in Figure 2a, marked by arrowheads.

Constituent Phase	Composition (at. %)				
	Nb	Ti	Si	Cr	Al
Nbss	60.21	17.89	12.80	5.35	3.75
$\gamma(Nb,X)_5Si_3$	47.01	18.71	33.11	0.36	0.81
βTiss	8.50	86.48	3.62	0.57	0.83

Figure 2b,c show the microstructures of Nb-Si based ultrahigh-temperature alloys prepared by HPS at 1350 and 1400 °C, respectively. It can be seen that the morphology of each phase in the microstructure of the alloy changed obviously. In most areas of the alloy, the white, gray and dark gray phases changed from irregular shapes in the alloys HPSed at 1250 °C to nearly equiaxed grain shapes, and the phase interfaces evolved to be clearer and more distinguishable. However, there are still large blocks of Nbss in local areas. Table 2 shows EDS composition analysis results of different phases in Nb-Si based ultrahigh-temperature alloys prepared by HPS at 1350 and 1400 °C. It can be seen that the contents of Ti, Si, Cr and other solute elements in the large blocks of Nbss are higher than those in the Nbss located in the homogeneous microstructural areas, indicating that the large blocks of Nbss are still a supersaturated solid solution. As the HPS temperature increases from 1350 to 1400 °C, the number of large Nbss blocks decreases. It is inferred that the elements in the powders can hardly diffuse with each other and react fully when HPS is performed at a temperature below 1400 °C.

Table 2. EDS analysis results of the phases marked with numerals "1", "2", "3" and "4" in Figure 2b,c.

Sites	Composition (at. %)				
	Nb	Ti	Si	Cr	Al
1	65.96	16.89	8.81	5.25	3.09
2	79.34	8.84	0.93	7.23	3.66
3	68.51	15.33	7.39	5.98	2.79
4	79.98	8.16	0.75	6.91	4.20

Figure 2d,e show the microstructure of the Nb-Si based ultrahigh-temperature alloys prepared by HPS at 1450 and 1500 °C, respectively. It can be seen that the supersaturated Nbss in the microstructure disappeared and the phases are evenly distributed. The white, gray and dark gray phases completely changed from irregular shapes when the HPS temperature was 1250 °C to nearly equiaxed grain morphologies in the alloys HPSed at a temperature above 1450 °C, with clear and distinguishable phase interfaces, fine microstructures and the size of each grain being smaller than 5 μm. From this phenomenon,

it can be concluded that the higher HPS temperature provides a greater driving force for the in situ formation of intermetallic compounds; at the same time, recrystallization is easier to occur at a higher HPS temperature, such that the morphology of each phase grain in the microstructure tends to be regular and their distribution is more uniform. When the HPS temperature continues to increase to 1500 °C, the phase grains in the microstructure of the alloy are still equiaxed, and the morphology and distribution of the constituent phases are basically the same as those prepared by HPS at 1450 °C. However, it can be clearly observed that the microstructure of the alloy prepared by HPS at 1500 °C is significantly coarsened and some silicides have dimensions larger than 5 μm.

From the microstructure of Nb-Si based ultrahigh-temperature alloys prepared by HPS at different temperatures, it was found that the alloy has three phases with different contrasts. Combined with EDS composition analysis, it can be determined that the corresponding three phases are Nbss, $\gamma(Nb,X)_5Si_3$ and βTiss. However, only the diffraction peaks of two phases, namely, Nbss and $\gamma(Nb,X)_5Si_3$, are shown in the corresponding XRD patterns. In order to further determine the crystal structure of Tiss, the microstructure of the Nb-Si based ultrahigh-temperature alloys prepared by HPS at 1450 °C was analyzed by TEM, as shown in Figure 3. Figure 3a is a bright field image of the microstructure, and Figure 3b,c are the selected area electron diffraction (SAED) patterns of the corresponding regions. It can be seen that Nbss and Tiss exist in the microstructure, and the crystal structure of Tiss is body-centered cubic (bcc), indicating that it is beta-type. Since the β-type Tiss and Nbss have the same crystal structure and their lattice constants are very close to each other, the diffraction peaks of Tiss and Nbss are almost overlapped in XRD patterns, which is why there are only two sets of diffraction peaks in the XRD patterns. During HPS process, the supersaturated Nbss in the ball-milled powders reacts in situ to form the equilibrium Nbss, $\gamma(Nb,X)_5Si_3$ and βTiss phases.

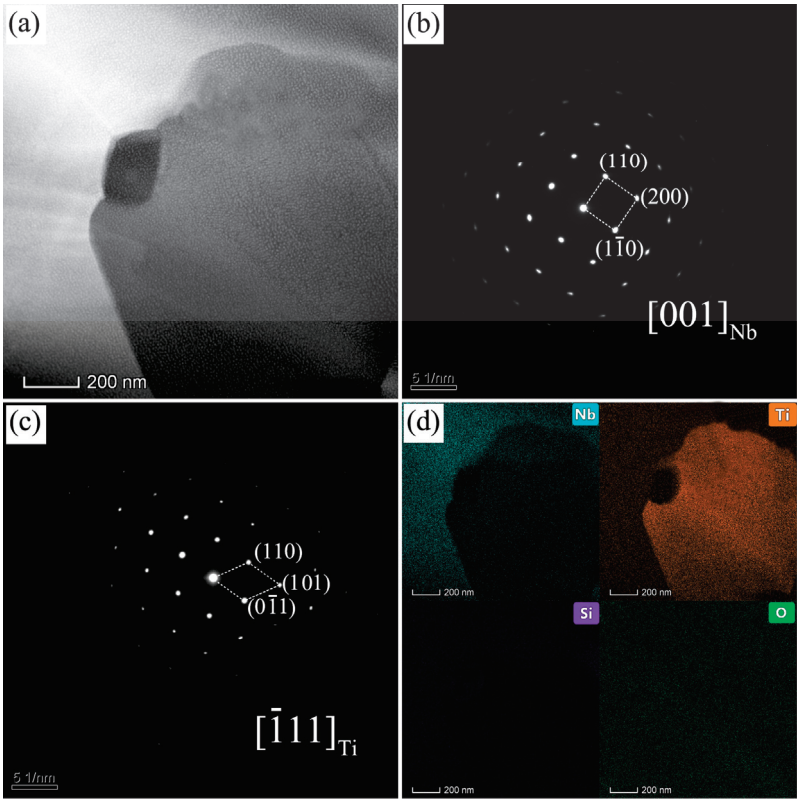

Figure 3. Nb-Si based ultrahigh-temperature alloys HPSed at 1450 °C. (**a**) Bright field image, (**b**) SAED pattern of Nbss, (**c**) SAED pattern of Tiss and (**d**) the element mapping.

Figure 3d is a plane distribution diagram of elements corresponding to TEM bright field images of samples prepared by HPS at 1450 °C. It can be clearly seen that there are voids at the phase interface. Therefore, in addition to the large black region in the microstructure (Figure 2), which is a hole, the small black area at the interface between different phases should also be a hole. However, the reasons for the formation of these two holes are different. The former may be caused by the release of residual gas between powder particles during HPS, while the latter may be caused by the difference in the molar volume of different phases during HPS. As can be seen in Figure 2, as the HPS temperature increases, the porosity in the sintered alloy becomes less. This is due to the increase in recrystallization degree and grain growth of the alloy with the increase in sintering temperature. Quantitative metallography analysis by IPP 7.0 shows that the area fraction of the pores in the HPSed alloys decreases with the increase in HPS temperature from 1.2% at the HPS temperature of 1250 °C to 0.8% at 1350 °C, 0.7% at 1400 °C, 0.4% at 1450 °C and 0.4% at 1500 °C. The area fractions of porosities are the same when the HPS temperature is 1450 °C and 1500 °C.

3.3. Physical Characters of the Alloys

Figure 4 shows the density and relative density changes of Nb-Si based ultrahigh-temperature alloys prepared by HPS at 1250, 1350, 1400, 1450 and 1500 °C, measured by Archimedes drainage method. When sintered at 1250 °C, the density of the alloy is only 6.593 g/cm^3; thus, the densification degree is relatively low. The density of the alloy increases rapidly with the increase in sintering temperature. However, when the HPS temperature is higher than 1400 °C, the increase in density becomes lower, especially after 1450 °C. When the HPS temperature was 1450 °C, the density of the alloy reached 6.905 g/cm^3. The density of the alloy was still 6.907 g/cm^3 when the HPS temperature was increased to 1500 °C, which is nearly the same as that of the alloy sintered at 1450 °C. The variation of the relative density of the alloys also presents an obvious increasing tendency with the increase in HPS temperature, which is consistent with the variation in the alloy's density [27]. The density of the sintered alloys is closely related to the in situ reaction during the sintering process. Increasing the sintering temperature can promote the in situ reaction in the milled powders to form intermetallic compounds, as has been proved by the XRD patterns in Figure 1 and microstructure in Figure 2. Therefore, a higher HPS temperature can lead to higher density and relative density of the alloys. However, when the HPS temperature is increased to 1450 °C, sufficient atomic diffusion and reaction can already occur among the as-milled alloy powders; thus, further increasing the HPS temperature no longer obviously increases the density and relative density of the alloy.

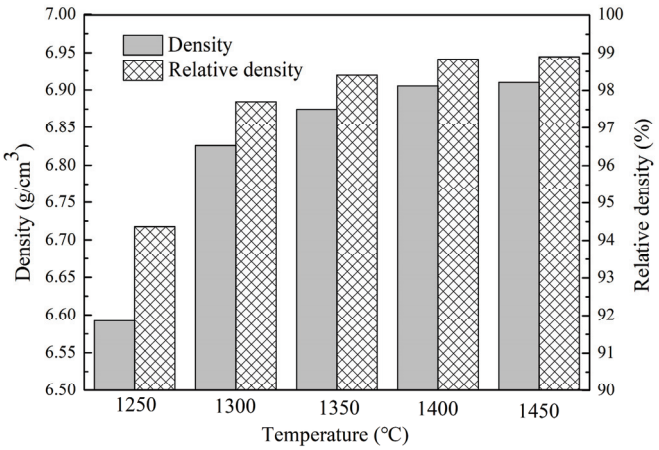

Figure 4. Variation of the density and relative density of the Nb-Si based ultrahigh-temperature alloys vs. HPS temperature.

Figure 5 shows the average size changes of the Nbss, $\gamma(Nb,X)_5Si_3$ and βTiss phase grains in Nb-Si based ultrahigh-temperature alloys prepared by HPS at different temperatures. It can be seen that the Nbss grain size first decreases and then increases with the increase in HPS temperature, and its size is the smallest when the HPS temperature is 1450 °C. This is because the supersaturated Nbss in the ball-milled powders still remains in the alloy sintered at temperatures below 1450 °C. However, when the HPS temperature is higher than 1450 °C, the in situ reaction of the powders and even the recrystallization ability of the alloys are enhanced, resulting in the recrystallization of Nbss grains and the obvious occurrence of Nbss grain growth. Differently from Nbss, the sizes of $\gamma(Nb,X)_5Si_3$ and βTiss phase grains increase with the increase in HPS temperature, because both phases are in situ precipitated from supersaturated Nbss powders during the HPS process and are essentially not affected by the size of the original powders. Therefore, with the increase in HPS temperature, the precipitation rate of both $\gamma(Nb,X)_5Si_3$ and βTiss becomes faster and their grain size increases continuously. The size of these two phases increased obviously in the microstructure of the alloy prepared by HPS at 1500 °C, which may be due to the exponential relationship between recrystallization rate and temperature. On the whole, the microstructure of Nb-Si based ultrahigh-temperature alloys prepared by HPS is significantly finer than that of the arc melted alloy, since the size of Nb_5Si_3 in the arc melted alloy is generally in the tens of microns [10].

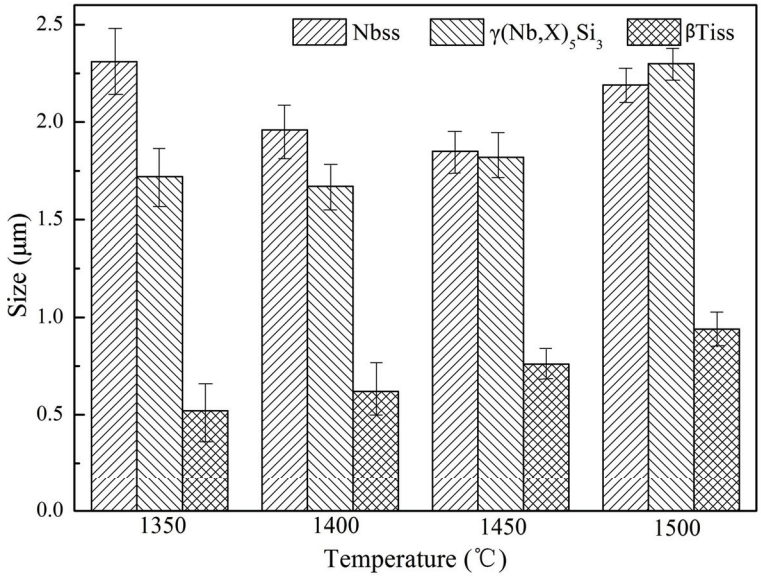

Figure 5. Grain size of the constituent phases in the alloys HPSed at different temperatures.

Figure 6 shows the volume fraction of each phase in the microstructure of Nb-Si based ultrahigh-temperature alloys prepared by HPS at different temperatures. It can be seen that when the HPS temperature is lower than 1450 °C, the volume fraction of Nbss phase decreases continuously from 48.77% at 1350 °C to 38.02% at 1450 °C. The volume fraction of $\gamma(Nb,X)_5Si_3$ phase increased from 38.65% in the alloy sintered at 1350 °C to 44.97% in the alloy sintered at 1450 °C, and that of the βTiss phase from 12.58% to 17.01%, respectively. This further shows that the alloy powders will react more thoroughly with the increase in HPS temperature until 1450 °C. However, when the HPS temperature further increases to 1500 °C, the volume fraction of each phase does not change obviously. This indicates that at 1450 °C, the as-milled Nb-Si based ultrahigh-temperature alloy powders have undergone sufficient atomic diffusion and reaction during the HPS process, and all the final products—namely, Nbss, $\gamma(Nb,X)_5Si_3$ and βTiss phases—have formed.

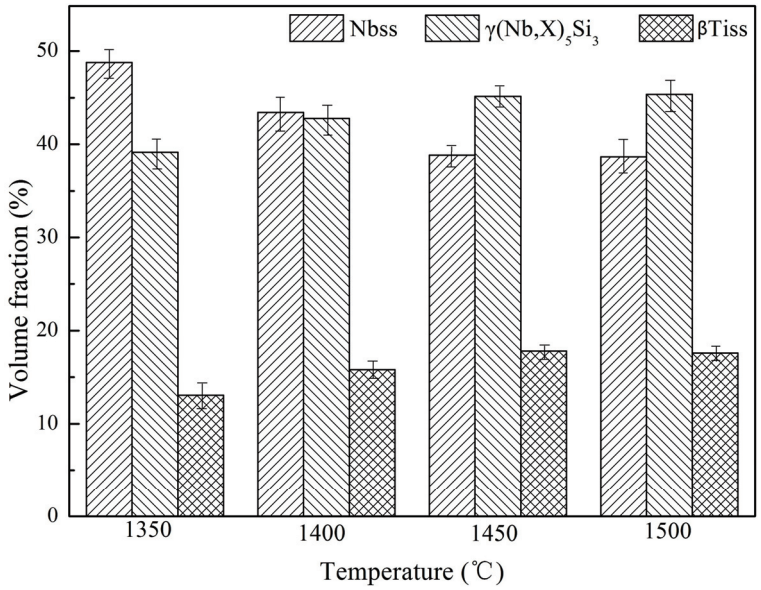

Figure 6. Volume fraction of each phase in the alloys HPSed at different temperatures.

3.4. Room Temperature Fracture Toughness

Table 3 presents the room temperature fracture toughness K_Q values of the Nb-Si based ultrahigh-temperature alloy prepared by HPS at different temperatures. It can be seen that when the HPS temperature is lower than 1450 °C, the K_Q values of the alloy exhibit an increasing trend with the increase in HPS temperature. This should be a comprehensive improvement, including increased alloy density and more uniform and refined grains with the increase in HPS temperature. However, when the HPS temperature further increased to 1500 °C, the K_Q values of the alloy decreased slightly. This can be attributed to the fact that the density of the alloy does not change significantly when the HPS temperature increases from 1450 °C to 1500 °C but the equiaxed grains coarsen a little.

Table 3. Room temperature facture toughness of the Nb-Si based ultrahigh-temperature alloys prepared by HPS at different temperatures.

HPS Temperature (°C)	Average $K_Q \pm$ Error Bar (MPa·m$^{1/2}$)
1350	8.1 ± 0.6
1400	8.7 ± 0.3
1450	10.9 ± 0.4
1500	10.2 ± 0.4

Figure 7 shows the crack propagation paths of the three-point bending specimens of Nb-Si based ultrahigh-temperature alloys prepared by HPS at 1400 and 1450 °C. It can be seen that the crack in the alloy prepared by HPS at 1400 °C propagates straightly. The crack propagation of the specimen of the alloy was not hindered effectively by the microstructure. This may be due to the low density of the alloy prepared by HPS at 1400 °C, meaning the cracks could propagate rapidly along the fine voids in the microstructure. The crack propagation path of the alloy prepared by HPS at 1450 °C is similar to that of the alloy prepared at 1400 °C. However, crack bridging and crack deflection occurs during the crack propagation process of the specimen prepared by HPS at 1450 °C (Figure 7b), which indicates that the microstructure hinders the crack propagation effectively and, thus, improves the room temperature fracture toughness of the alloy obviously.

Figure 8 shows the SEM images of fracture surfaces of the three-point bending specimens of the Nb-Si based ultrahigh-temperature alloys prepared by HPS at different temperatures. It can be seen that the fracture surfaces of the alloys prepared by HPS at 1350 and 1400 °C are smooth. The density of the alloys prepared at these two temperatures is

not high and there are a lot of pores. As a result, the fracture surfaces of the alloys show a honeycomb-like morphology. The existence of pores leads to increased brittleness of the alloys. After HPS at 1450 and 1500 °C, the fracture surfaces of the three-point bending specimens of the alloys show relative fluctuations, indicating that the alloys have undergone a certain degree of plastic deformation. The reason is that the density of the alloys is greatly increased, so there are only a few small-sized pores in the fracture morphology. On the other hand, the Nb-Si based ultrahigh-temperature alloys prepared by HPS at these two temperatures have an equiaxed morphology with a clear interface (as shown in Figure 2). The crack deflects when it propagates to the interface and needs more energy to continue to propagate; so, it has relatively high room temperature fracture toughness values.

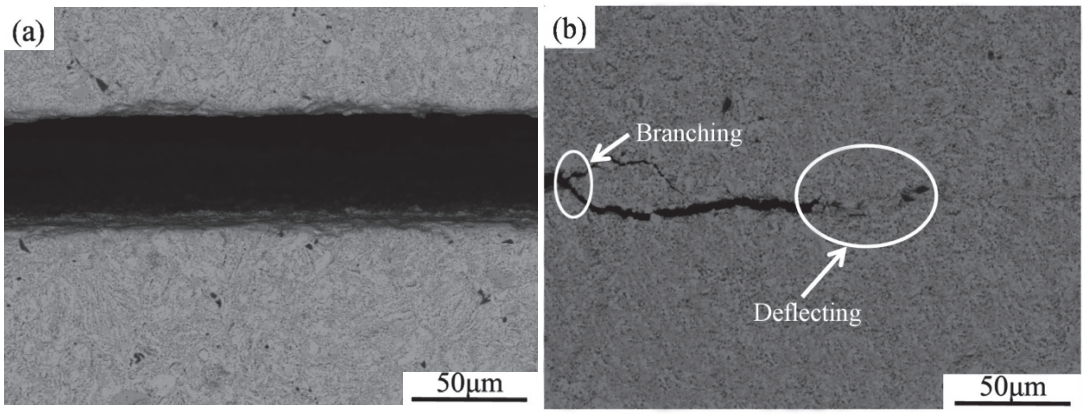

Figure 7. Crack propagation paths of the three-point bending specimens of the Nb-Si based ultrahigh-temperature alloys prepared by HPS at (**a**) 1400 °C and (**b**) 1450 °C.

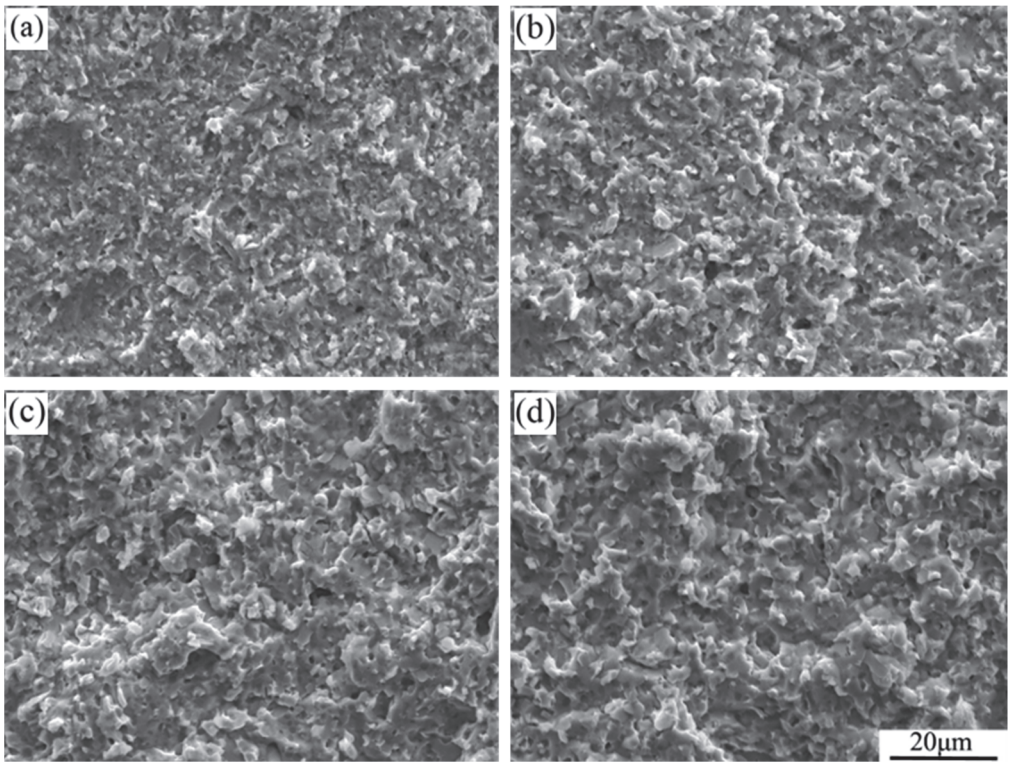

Figure 8. Typical SEM images of the fracture surfaces of the three-point bending specimens of Nb-Si based ultrahigh-temperature alloys prepared by HPS at (**a**) 1350 °C, (**b**) 1400 °C, (**c**) 1450 °C and (**d**) 1500 °C.

3.5. Hardness

The Vickers hardness of Nb-Si based ultrahigh-temperature alloys prepared by HPS at different temperatures is listed in Table 4. It can be seen that the Vickers hardness of the alloys gradually increases with the increase in HPS temperature until 1450 °C. This is due to the low density of the alloys and the existence of a large number of voids when the HPS temperature is lower than 1450 °C. The lower the HPS temperature is, the lower the density of the alloy. The existence of pores seriously weakens the ability of the alloys to resist the indentation, which results in the specimen prepared by HPS at lower temperature having a smaller hardness value. As the amount of porosities decreases with the increase in HPS temperature, the Vickers hardness value of the alloys increases gradually. When the HPS temperature rises to 1450 °C, the Vickers hardness value of the alloys is the largest. The Vickers hardness value of the alloys decreases when the HPS temperature is further increased to 1500 °C. This is mainly due to the coarsening of the alloy's microstructure. The Vickers hardness value of Nb-Si based ultrahigh-temperature alloys prepared by HPS at 1450 °C is about 1138 HV, while the Vickers microhardness of primary silicide in Nb-Si based ultrahigh-temperature alloys prepared by arc melting method is 1083 HV and the microhardness of eutectic structure is only 671 HV [10]. The high hardness value of Nb-Si based ultrahigh-temperature alloys prepared by HPS should be due to grain refinement strengthening caused by the fine grain structure of the HPSed alloys.

Table 4. Vickers hardness of Nb-Si based ultrahigh-temperature alloys prepared by HPS at different temperatures.

HPS Temperature (°C)	Vickers Hardness ± Error Bar (HV)
1350	780 ± 73
1400	885 ± 61
1450	1138 ± 59
1500	979 ± 38

3.6. Oxidation Behavior of the Alloys

Figure 9 shows the weight gain per unit area of Nb-Si based ultrahigh-temperature alloys prepared by HPS at 1250, 1350, 1400, 1450 and 1500 °C after oxidation at 1250 °C for 20 h. It can be seen that the weight gain per unit area of the alloys decreases significantly with the increase in HPS temperature, from about 62.26 mg/cm^2 for the alloy prepared by HPS at 1250 °C to about 40.51 mg/cm^2 for the alloy prepared by HPS at 1450 °C, while the oxidation weight gain per unit area of the alloys HPSed at 1500 °C does not change significantly compared with that of the alloy prepared by HPS at 1450 °C. This indicates that the alloys prepared by HPS at different temperatures have obviously different oxidation performance. When the HPS temperature was 1250 °C, there still remained many microstructural characteristics of the original milled powder particles in the sintered alloys. This indicates that the sintering reaction of the powders is not sufficient at such lower HPS temperature, resulting in the alloy being not dense; thus, its high-temperature oxidation resistance is poor. When the HPS temperature was higher, the sintered alloys had nearly equiaxed grains. The sintering reaction is much more sufficient. The reaction diffusion of each element in the alloys is also sufficient, resulting in a more compact microstructure that is beneficial for forming a denser and more protective oxide scale, thereby improving the high-temperature oxidation resistance of the alloy.

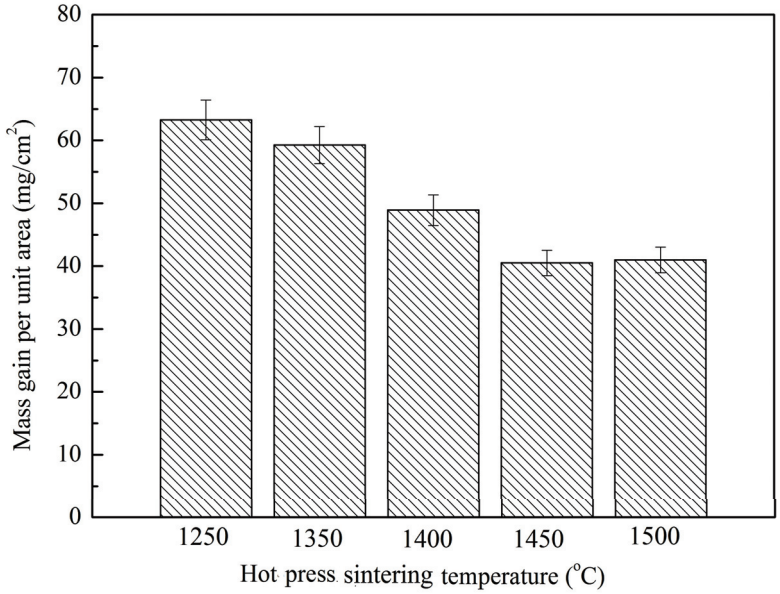

Figure 9. Mass gains per unit area of the Nb-Si based ultrahigh-temperature alloys prepared by HPS at different temperatures upon oxidation at 1250 °C for 20 h.

Figure 10 shows the XRD patterns of the oxide films on the Nb-Si based ultrahigh-temperature alloys prepared by HPS at different temperatures after oxidation at 1250 °C for 20 h. Figure 11 shows the cross-sectional BSE morphology of the oxide film. Table 5 presents the EDS analysis results of the composition of the typical phases observed in Figure 11. It can be seen from Figure 11 that the oxide films of the alloy prepared by HPS at different temperatures possess similar microstructures. The XRD patterns show that the oxide films composed of Nb_2O_5, TiO_2 and $TiNb_2O_7$ form on the surface of each alloy after oxidation. EDS analysis of the typical phases in the oxide films shows that the oxygen content in the gray–white microstructure is higher, and the typical components are 9.40Nb-4.53Ti-0.20Al-2.13Cr-0.73Si-83.01O (at. %), as shown by the compositions of points 1, 8 and 12. Combined with the XRD patterns in Figure 10, it can be seen that these gray–white phases are mainly Nb_2O_5. The content of Si and O in some black-contrast microstructures existing in the oxide films is higher, as shown by the compositions of points 2 and 9, indicating that it is mainly SiO_2 or silicate phases. However, it is difficult to find the diffraction peaks of SiO_2 or silicates in the XRD patterns. The main reason may be that the oxidation products of the silicides exist in amorphous form. Similar XRD patterns of the arc-melted Nb-Si based ultrahigh-temperature alloys after oxidation at 1250 °C were analyzed in our previous research [14]. The atomic ratio of Nb to Ti in gray-contrast microstructure is about 2:1, and the result of XRD analysis on the outer layer of oxide film shows that it is $TiNb_2O_7$. In addition, many fine dark gray phases are dispersed in the outer layer of the oxide film. The Ti content in these dispersed dark gray hues, massive dark gray microstructures with broken surface and continuous dark gray structures at the bottom of the outer layer is high, which are all TiO_2, combined with XRD analysis results. The reason for the formation of continuous TiO_2 layer at the bottom of the outer oxide film will be analyzed and discussed later. Figure 11f summarizes the microstructure of the scales formed on the HPSed alloys upon oxidation at 1250 °C for 20 h. It can be seen that the Si-containing oxides or silicate areas and Nb_2O_5, TiO_2 and $TiNb_2O_7$ areas are separately distributed. More TiO_2 forms at the bottom of the scales.

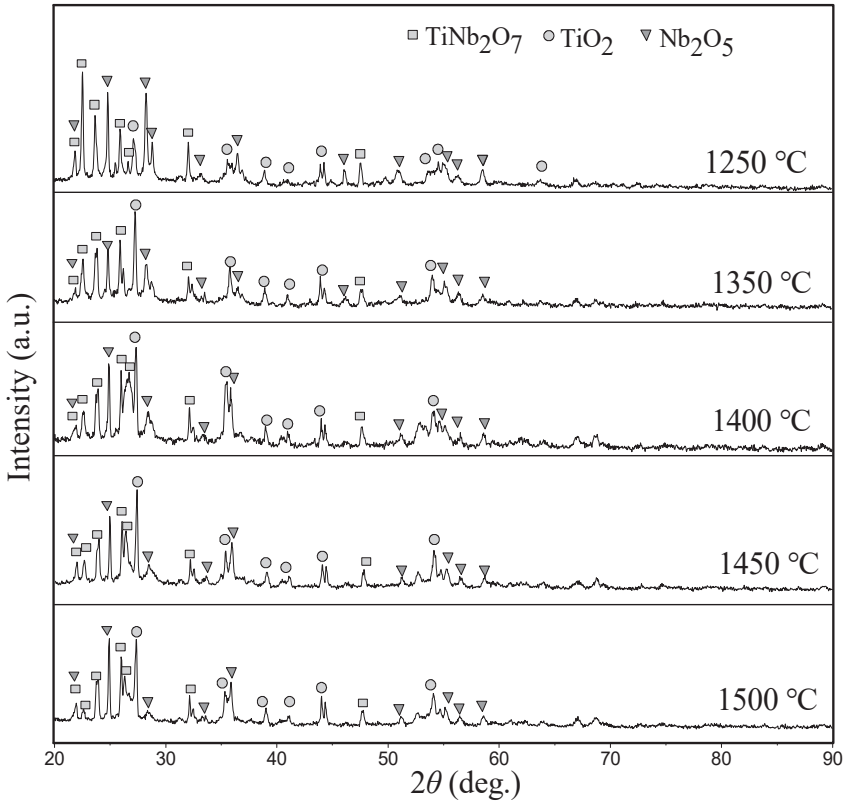

Figure 10. XRD patterns of the outer layers of the scales formed on Nb-Si based ultrahigh-temperature alloys prepared by HPS at different temperature upon oxidation at 1250 °C for 20 h.

Table 5. Composition of the constituent phases marked by arrows with numerals "1–12" in Figure 11, determined by EDS analyses.

Sites	Composition (at. %)					
	Nb	Ti	Al	Cr	Si	O
1	21.28	4.45	/	1.22	0.09	72.97
2	10.96	1.49	0.05	0.15	15.53	71.82
3	9.40	4.53	0.20	2.13	0.73	83.01
4	3.15	21.93	0.10	2.51	0.01	72.30
5	18.40	7.18	0.28	0.09	0.72	73.32
6	/	15.13	0.22	/	1.29	83.37
7	7.05	15.18	0.41	6.50	/	70.87
8	22.49	2.77	0.18	0.23	0.25	74.07
9	0.53	0.33	0.06	0.07	33.14	65.87
10	2.32	28.28	/	0.33	3.11	65.96
11	12.20	9.27	0.96	5.83	0.87	70.87
12	20.93	2.73	0.01	0.24	3.05	73.05

Figure 12 shows the BSE morphology of the internal oxidation zone of the Nb-Si based ultrahigh-temperature alloys prepared by HPS at different temperatures after oxidation at 1250 °C for 20 h. It can be seen that the internal oxidation zone is composed of three typical phases: black (as shown in points 1, 4, 7 and 10), gray (as shown in points 2, 5, 8 and 11) and light gray (as shown in points 3, 6, 9 and 12). However, there are obvious differences in the microstructural morphologies of the internal oxidation zone of the alloys prepared by HPS at different temperatures. The internal oxidation zone of the alloy prepared by HPS at 1250 °C mainly presents a plate-like microstructure, while that of the alloy prepared by HPS at higher temperature presents nearly a equiaxed grains feature. The EDS analysis results of the compositions of the above typical phases are shown in Table 6. It can be seen that Ti and

O contents in the black phase are higher, satisfying the composition of TiO_2, indicating that it is mainly TiO_2. The content of Nb and Si in the dark gray phase satisfies the composition of Nb_5Si_3 phase, indicating that it is mainly Nb_5Si_3 phase in the alloy but there is a certain content of O. However, the content of Nb in the light gray phase is generally higher than 70 at. %, and the rest includes a small content of other elements and a certain content of O, indicating that it is mainly Nbss phase. The results of EDS analysis show that TiO_2 preferentially formed in the alloys during the oxidation process, which is more closely related to the lower formation energy of TiO_2 than that of Nb_2O_5: the Gibbs free energy of formation of TiO_2 and Nb_2O_5 at 1250 °C is −669.8 kJ and −498.9 kJ, respectively (the reaction value is the standard Gibbs free energy of Ti and Nb when they react with 1 mol of O_2 to form their corresponding oxides); according to the selective oxidation theory raised by Wagner, oxygen atoms will preferentially react with elements with stronger affinity to generate corresponding oxides when oxygen is limited [28]. In this study, the inward diffusion of oxygen atoms into the metal substrate is hindered by the outer oxide film, creating an environment for the preferential oxidation of Ti in the internal oxidation zone.

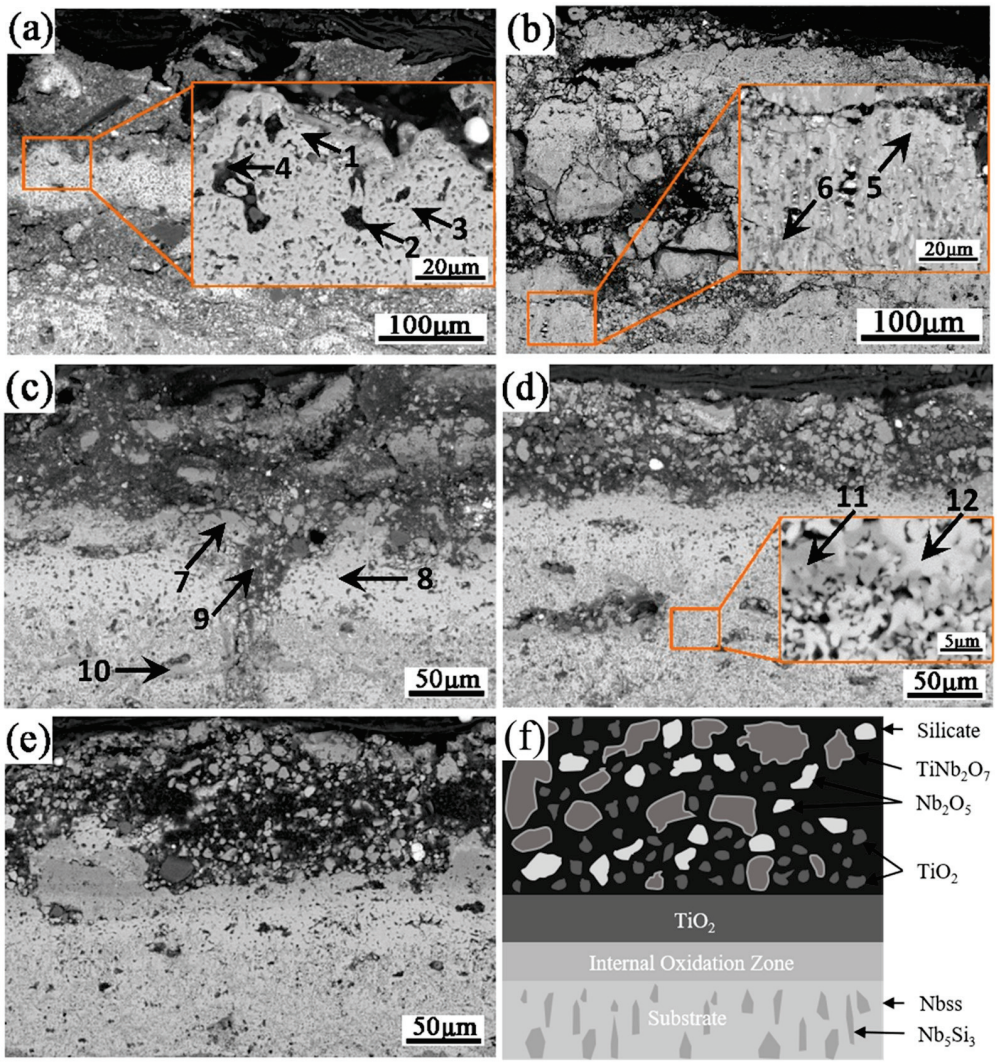

Figure 11. BSE images of the outer layers of the scales formed on Nb-Si based ultrahigh-temperature alloys prepared by HPS at different temperatures upon oxidation at 1250 °C for 20 h. HPSed at (**a**) 1250 °C, (**b**) 1350 °C, (**c**) 1400 °C, (**d**) 1450 °C and (**e**) 1500 °C, and (**f**) is the sketch drawing for the microstructure of the specimen oxidized at 1250 °C for 20 h. The arrowhead positions with numerals "1–12" are the locations where EDS analyses were performed.

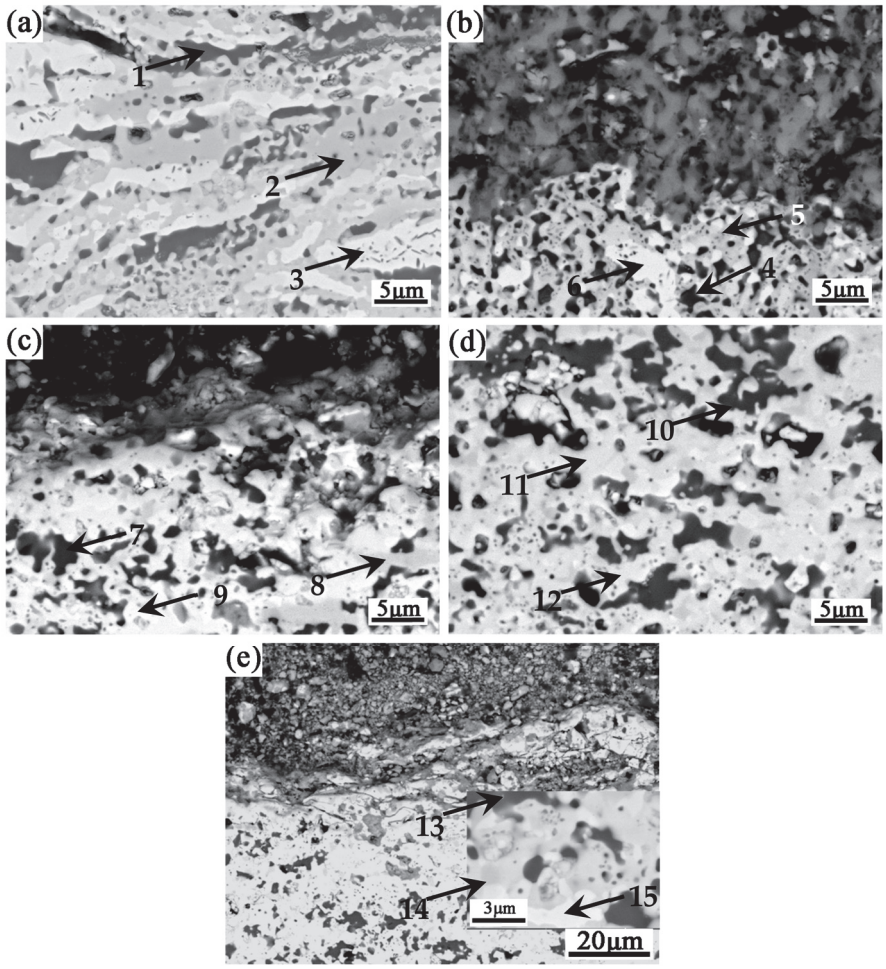

Figure 12. BSE images of the internal oxidation zones of Nb-Si based ultrahigh-temperature alloys prepared by HPS at different temperatures upon oxidation at 1250 °C for 20 h. HPSed at (**a**) 1250 °C, (**b**) 1350 °C, (**c**) 1400 °C, (**d**) 1450 °C and (**e**) 1500 °C. The arrowhead positions with numerals "1–15" are the locations where EDS analyses were performed.

Table 6. Composition of constituent phases marked by arrows with numerals "1–15" in Figure 12, determined by EDS analyses.

Sites	Composition (at. %)					
	Nb	Ti	Al	Cr	Si	O
1	0.16	27.94	0.67	/	0.07	71.16
2	56.38	3.13	0.26	0.44	27.86	11.93
3	75.68	0.30	/	4.22	0.99	18.81
4	8.25	25.59	1.39	0.24	2.61	61.92
5	57.18	3.85	0.30	0.68	21.05	16.95
6	75.05	1.01	/	3.66	0.06	20.22
7	1.60	28.27	0.37	0.20	0.48	69.08
8	54.07	0.45	/	1.11	29.03	15.34
9	72.93	1.86	0.27	3.52	1.30	20.11
10	4.05	28.80	0.55	0.12	0.42	66.06
11	44.71	6.82	0.79	0.41	20.46	26.80
12	78.84	3.27	0.61	0.24	1.38	15.66
13	1.44	29.98	0.32	0.66	0.59	67.01
14	51.17	0.37	/	23.57	3.13	21.75
15	78.64	2.91	2.80	4.95	0.71	14.33

4. Conclusions

(1) The microstructure of Nb-Si based ultrahigh-temperature alloys prepared by HPS at different temperatures consists of Nbss, βTiss and $\gamma(Nb,X)_5Si_3$ phases. The microstructure of the alloys prepared by HPS at 1450 °C is fine and nearly equiaxed. However, there are still supersaturated Nbss in the alloys prepared by HPS below this temperature. The microstructure of the alloys obviously coarsens when the HPS temperature is higher than 1450 °C.

(2) With the increase in HPS temperature, the density of the prepared Nb-Si based ultrahigh-temperature alloys increases continuously, and the density of the alloy prepared at 1450 °C reaches the maximum. With the increase in HPS temperature, the contents of βTiss and $\gamma(Nb,X)_5Si_3$ in the alloy gradually increase.

(3) The room temperature fracture toughness and Vickers hardness of Nb-Si based ultrahigh-temperature alloys prepared by HPS at 1450 °C are the highest.

(4) The oxide films spalled out and there were obvious internal oxidation zones in the alloys prepared by HPS at different temperatures upon oxidation at 1250 °C for 20 h. The oxidation weight gain of the alloy prepared by HPS at 1450 °C is the smallest. The oxide film of the alloy is mainly composed of Nb_2O_5, $TiNb_2O_7$, TiO_2 and a small amount of amorphous silicate.

Author Contributions: Conceptualization, X.G.; Methodology, X.G.; Validation, P.G.; Formal analysis, L.Z., P.G. and X.G.; Investigation, L.Z.; Writing—review & editing, L.Z. and P.G.; Supervision, X.G.; Project administration, X.G.; Funding acquisition, X.G. All authors have read and agreed to the published version of the manuscript.

Funding: This research was funded by the National Natural Science Foundation of China (No. 51971181), the Research Fund of the State Key Laboratory of Solidification Processing (NWPU), China (Grant No. 2020-TZ-01).

Data Availability Statement: Further data can be provided upon request.

Conflicts of Interest: The authors declare no conflict of interest.

References

1. Bewlay, B.P.; Jackson, M.R.; Zhao, J.C.; Subramanian, P.R.; Mendiratta, M.G.; Lewandowski, J.J. Ultrahigh Temperature Nb-Silicide-Based Composites. *MRS Bull.* **2003**, *28*, 646–653. [CrossRef]
2. Bewlay, B.P.; Jackson, M.R.; Lipsitt, H.A. The Balance of Mechanical and Environmental Properties of a Multielement Niobium-Niobium Silicide-Based in situ Composite. *Metall. Mater. Trans. A* **1996**, *27*, 3801–3808. [CrossRef]
3. Subramanian, P.R.; Mendiratta, M.G.; Dimiduk, D.M.; Stucke, M.A. Advanced Intermetallic Alloys—Beyond Gamma Titanium Aluminides. *Mater. Sci. Eng. A* **1997**, *239*, 1–13. [CrossRef]
4. Bewlay, B.P.; Jackson, M.R.; Subramanian, P.R.; Zhao, J.C. A Review of Very-High-Temperature Nb-Sicilide-Based Composites. *Metall. Mater. Trans. A* **2003**, *34*, 2043–2052. [CrossRef]
5. Guo, H.S.; Guo, X.P. Microstructure Evolution and Room Temperature Fracture Toughness of an Integrally Directionally Solidified Nb-Si Based Ultrahigh Temperature Alloy. *Scr. Mater.* **2011**, *64*, 637–640. [CrossRef]
6. Yeh, C.L.; Chen, W.H. A Comparative Study on Combustion Synthesis of Nb-Si Compounds. *J. Alloys Compd.* **2006**, *425*, 216–222. [CrossRef]
7. Geng, J.; Tsakiropoulos, P.; Shao, G.S. A Study of the Effects of Hf and Sn Additions on the Microstructure of Nbss/Nb_5Si_3 Based in situ Composites. *Intermetallics* **2007**, *15*, 69–76. [CrossRef]
8. Lu, Y.Y.; Zhang, J.; Tian, L.X.; Li, Y.L.; Ma, C.L. Microstructural Evolution of Unidirectionally Solidified Nbss-Nb_5Si_3 Eutectic Alloy. *Rare Met.* **2011**, *30*, 335–339. [CrossRef]
9. Ma, R.; Guo, X.P. Composite Alloying Effects of V and Zr on the Microstructures and Properties of Multi-elemental Nb-Si Based Ultrahigh Temperature Alloys. *Mater. Sci. Eng. A* **2021**, *813*, 141175. [CrossRef]
10. Zhang, S.; Guo, X.P. Effects of B Addition on the Microstructure and Properties of Nb Silicide Based Ultrahigh Temperature Alloys. *Intermetallics* **2015**, *57*, 83–92. [CrossRef]
11. Ma, R.; Guo, X.P. Effects of Mo and Zr Composite Additions on the Microstructure, Mechanical Properties and Oxidation Resistance of Multi-elemental Nb-Si Based Ultrahigh Temperature Alloys. *J. Alloys Compd.* **2021**, *870*, 159437. [CrossRef]
12. Guo, X.P.; Guo, H.S.; Yao, C.F. Integrally Directionally Solidified Microstructure of an Niobium Silicide Based Ultrahigh Temperature Alloy. *Int. J. Mod. Phys. B* **2009**, *23*, 1093–1098. [CrossRef]

13. Tsakiropoulos, P. Alloys for Application at Ultra-high Temperatures: Nb-silicide in situ Composites Challenges, Breakthroughs and Opportunities. *Prog. Mater. Sci.* **2022**, *123*, 100714. [CrossRef]
14. Zhang, S.; Guo, X.P. Effects of Cr and Hf Additions on the Microstructure and Properties of Nb Silicide Based Ultrahigh Temperature Alloys. *Mater. Sci. Eng. A* **2015**, *638*, 121–131. [CrossRef]
15. Yi, D.Q.; Li, D.; Li, J.; Zhou, H.M. Powder Metallurgic Process for Preparing Nb-15Ti-11Al-10Si Composites. *Chin. J. Rare Met.* **2007**, *31*, 472–476.
16. Wang, X.L.; Zhang, K.F. Mechanical Alloying, Microstructure and Properties of Nb-16Si Alloy. *J. Alloys Compd.* **2010**, *490*, 677–683. [CrossRef]
17. Wang, T.T.; Guo, X.P. Morphology and Phase Constituents of Mechanical Alloyed Nb-Si Based Ultrahigh Temperature Alloy Powders. *Rare Met.* **2007**, *30*, 427–432. [CrossRef]
18. Fei, T.; Yu, Y.X.; Zhou, C.G.; Sha, J.B. The Deformation and Fracture Modes of Fine and Coarsened Nb-ss Phase in a Nb-20Si-24Ti-2Al-2Cr Alloy with a Nb-ss/Nb_5Si_3 Microstructure. *Mater. Des.* **2017**, *116*, 92–98. [CrossRef]
19. Ahmadi, E.; Malekzadeh, M.; Sadrnezhaad, S.K. Preparation of Nanostructured High-temperature TZM Alloy by Mechanical Alloying and Sintering. *Int. J. Refract. Met. Hard Mater.* **2011**, *29*, 141–145. [CrossRef]
20. Goncharov, I.; Hisamova, L.; Mustafaeva, L.; Razumov, N.; Makhmutov, T.; Kim, A.; Wang, Q.S.; Shamshurin, A.; Popovich, A. Microstructure and Phase Composition of the Nb-Si Based in-situ Composite from Plasma Spheroidized Powder. *Mater. Today Proc.* **2020**, *30*, 545–548. [CrossRef]
21. Wang, X.L.; Wang, G.F.; Zhang, K.F. Effect of Mechanical Alloying on Microstructure and Mechanical Properties of Hot-Pressed Nb-16Si Alloys. *Mater. Sci. Eng. A* **2010**, *527*, 3253–3258. [CrossRef]
22. Li, Z.; Peng, L.M. Microstructural and Mechanical Characterization of Nb-based in situ Composites from Nb-Si-Ti Ternary System. *Acta Mater.* **2007**, *55*, 6573–6585. [CrossRef]
23. Ma, R.; Guo, X.P. Cooperative Effects of Mo, V and Zr Additions on the Microstructure and Properties of Multi-elemental Nb-Si Based Alloys. *J. Mater. Sci. Technol.* **2023**, *132*, 27–41. [CrossRef]
24. Chen, R.R.; Chen, D.Z.; Wang, Q.; Wang, S.; Zhou, Z.C.; Ding, H.S.; Fu, H.Z. Research Progress on Nb-Si Base Ultrahigh Temperature Alloys and Directional Solidification Technology. *Acta Metall. Sin.* **2021**, *57*, 1141–1154.
25. Kommineni, G.; Golla, B.R.; Alam, M.Z.; Sarkar, R.; Prasad, V.V.S. Structure-property Correlation and Deformation Mechanisms in Ductile Phase (Nb-ss) Toughened Cast Nb-Si Alloys. *J. Alloys Compd.* **2021**, *873*, 159832. [CrossRef]
26. Kang, S.J.L. Sintering: Densification, Grain Growth and Microstructure. *Int. J. Powder Metall.* **2005**, *3*, 41.
27. Wang, X.L. *Microstructure Evolution and Properties of Nb-Si Refractory Alloys Fabricated by Powder Metallurgy*; Harbin Institute of Technology: Harbin, China, 2011; p. 42.
28. Wagner, C. Passivity and Inhibition During the Oxidation of Metals at Elevated Temperatures. *Corros. Sci.* **1965**, *5*, 751. [CrossRef]

materials

MDPI

Article

A Modified Constitutive Model and Microstructure Characterization for 2195 Al-Li Alloy Hot Extrusion

Hui Li [1,2], Jian Wang [3,*], Yuanchun Huang [1,2,4,*] and Rong Fu [1,2]

1 College of Mechanical and Electrical Engineering, Central South University, Changsha 410083, China; lih0605@163.com (H.L.)
2 State Key Laboratory of High-Performance Complex Manufacturing, Central South University, Changsha 410083, China
3 Southwest Aluminum (Group) Co., Ltd., Chongqing 400050, China
4 Light Alloy Research Institute, Central South University, Changsha 410083, China
* Correspondence: wjsh601166@163.com (J.W.); ychuang@csu.edu.cn (Y.H.)

Abstract: The quality of extruded profiles depends largely on accurate constitutive models and thermal processing maps. In this study, a modified Arrhenius constitutive model for homogenized 2195 Al-Li alloy with multi-parameter co-compensation was developed and further enhanced the prediction accuracy of flow stresses. Through the processing map and microstructure characterization, the 2195 Al-Li alloy could be deformed optimally at the temperature range of 710~783 K and strain rate of 0.001~0.12 s^{-1}, preventing the occurrence of local plastic flow and abnormal growth of recrystallized grains. The accuracy of the constitutive model was verified through numerical simulation of 2195 Al-Li alloy extruded profiles with large shaped cross-sections. Dynamic recrystallization occurred at different regions during the practical extrusion process, resulting in slight variations in the microstructure. The differences in microstructure were due to the varying degrees of temperature and stress experienced by the material in different regions.

Keywords: 2195 Al-Li alloy; constitutive model; extrusion numerical simulation; microstructure

Citation: Li, H.; Wang, J.; Huang, Y.; Fu, R. A Modified Constitutive Model and Microstructure Characterization for 2195 Al-Li Alloy Hot Extrusion. *Materials* **2023**, *16*, 3826. https://doi.org/10.3390/ma16103826

Academic Editor: Xianfei Ding

Received: 19 March 2023
Revised: 15 May 2023
Accepted: 17 May 2023
Published: 18 May 2023

1. Introduction

Compared with ordinary aluminum alloys, Al-Li alloy components possess lighter weight, higher mechanical properties and fatigue resistance [1,2]. These features make them popular in rail transportation, aircraft, and other industries. Hot extrusion is capable of producing complex shapes with high dimensional accuracy and good mechanical properties, and has become one of the important forming processes [3].

The accuracy of extrusion numerical simulation and the consistency of profiles depend heavily on an accurate constitutive model. Consequently, different types of constitutive models have been developed and have gained some applications. Jonas et al. [4] first established an Arrhenius hyperbolic sinusoidal constitutive model to describe the thermal deformation behavior of alloys. However, this model only considers the effects of deformation temperature and strain rate on flow stress. Therefore, Lin et al. [5] modified the conventional Arrhenius constitutive model using a strain-strain rate compensation method to increase the accuracy of flow stress predictions over wide ranges of strain rate and forming temperature. Subsequently, a new phenomenological model was proposed [6], where the material constants were expressed as functions of strain rate and temperature, enabling the accurate prediction of flow stress in the Al-Cu-Mg alloy. Additionally, a strain-compensated Arrhenius constitutive model was developed by some researchers in order to accurately predict high-temperature flow stresses in different grades of aluminum alloys [7], magnesium alloys [8], steel [9], titanium alloys [10], and other materials. Chen et al. [11] compensated the strain rate and deformation temperature based on the strain-compensated Arrhenius constitutive model, further improving the prediction accuracy.

The work hardening and dynamic softening coincide in the high-temperature rheological process of aluminum alloy, where dynamic recovery (DRV) and dynamic recrystallization (DRX) are the main softening mechanisms. The microstructure of alloys is usually affected by the thermal deformation parameters, and the specific microstructure formed after deformation is the main factor leading to the difference in material properties. The processing map based on the dynamic materials model (DMM) proposed by Prasad et al. [12] can reflect the relationship between the microstructure evolution mechanism and the thermal deformation parameters; therefore a lot of research has been conducted in this field [7,11,13]. Zhang et al. [14] investigated the DRX behavior of 2195 Al-Li alloy at moderate/high temperatures, they evaluated that the primary softening mechanism for deformation at moderate temperatures is discontinuous dynamic recrystallization (DDRX), and it transforms to continuous dynamic recrystallization (CDRX) at high temperatures. Yu et al. [15] found that 2A97 Al-Li alloy exhibited the most elevated power dissipation efficiency in the DRX region using processing maps and indicated that the occurrence of CDRX was related to the dynamic precipitation of the T_1 phase. Wang et al. [16] discovered that the spray-deposited 2195 Al-Li alloy produces high power dissipation efficiency at low temperature and low strain rate, while the lowest power dissipation efficiency was observed at a strain rate of 10 s^{-1} and the material undergoes deformation instability. During thermal deformation, alloys with the same composition in various states will exhibit considerably variable power dissipation efficiencies. Therefore, it is necessary to study the effect of alloy state on the evolution of microstructure.

Currently, significant progress has been made in researching the hot deformation behavior of aluminum alloys. However, there are few successful cases where the obtained constitutive model and hot processing map have been applied to actual industrial production, particularly for Al-Li alloys. Dong et al. [17] simulated the extrusion process of complex cross-section profile by establishing the Arrhenius constitutive model and processing map of AA6N01 aluminum alloy and effectively controlled the distortion and deformation. Xu et al. [18] revealed the cause of abnormal grain growth along the longitudinal weld of the profile in 2196 Al-Cu-Li alloy by finite element method. Zhang et al. [19] used HyperXtrude to build a numerical model of the transverse welds of 7N01 aluminum alloy, and by adjusting the extrusion ratio and die structure, the length of the transverse welds was effectively reduced and high-quality extruded profiles were obtained. In this study, hot compression tests were conducted on the two-stage homogenized 2195 Al-Li alloy, and the modified Arrhenius constitutive model as well as the processing map were established. Then, numerical simulations were carried out using HyperXtrude software to analyze the flow behavior of large shaped cross-sectional profiles of 2195 Al-Li alloy based on the established constitutive model. Finally, practical engineering extrusion tests were conducted and the microstructure in different regions was examined to validate the accuracy of the constitutive model and simulation results. The research strategy of constitutive model, processing map establishment—numerical simulation—actual extrusion test—microstructure analysis will provide strong support for the large-scale industrial production of 2195 Al-Li alloy profiles.

2. Experimental Materials and Methods

2.1. Material and Hot Compression Tests

The 2195 Al-Li Alloy was provided by Southwest Aluminum (Group) Corporation of China Ltd. (Chongqing, China), and the chemical composition of the alloy is 3.98Cu, 0.99Li, 0.32Mg, 0.32Ag, 0.12Zr, 0.08Fe, 0.04Si (wt%) and a balance of Al. The material was sampled at the center of the ingot after a two-stage homogenization treatment of 470 °C/7 h + 525 °C/24 h and machined into a hot compression specimen of Ø8 × 12 mm for diameter and height. Hot compression tests were performed on the Gleeble-3500D thermomechanical simulator with a strain rate range of 0.001–1 s^{-1}, a 60% height depression, and a deformation temperature range of 643–693 K. The specimen was first heated to the required temperature at a rate of 5 K/s, held there for 3 min during the

test, and then hot-compressed at a specific strain rate. Finally, water-cooled quenching was applied immediately after reaching the required reduction to preserve the high-temperature microstructure. Before the hot compression experimental process, graphite foils were placed between the upper and lower ends of the specimen and the contact surface of the WC anvil to reduce friction.

2.2. Establishment of Extrusion Assembly

Figure 1a displays the extrusion assembly diagram of the geometric model, which consists of four components, namely the extrusion container, dummy block, billet and extrusion die. Relevant extrusion process parameters are detailed in Table 1.

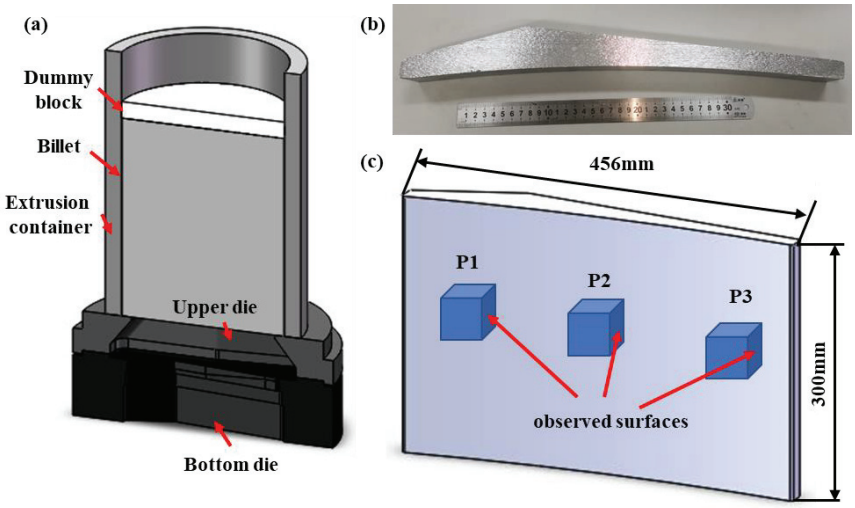

Figure 1. (**a**) Extrusion modeling of assembly diagram, (**b**) The practical 2195 Al-Li alloy extruded profile, (**c**) sampling positions of the profile.

Table 1. Process parameters for extrusion of 2195 Al-Li alloy.

Billet Size/mm	Container Diameter/mm	Billet Temperature/°C	Die Temperature/°C	Extrusion Ratio	Extrusion Velocity/(mm/s)
Ø496 × 600	Ø500	460	450	14.01	0.2

2.3. Microstructure Observation

The as-cast and homogenized microstructures were observed by metallographic microscope (OLYMPOS-DSX500) and scanning electron microscope (SEM, JSM-7800F), respectively, and the chemical composition of the second phase was analyzed by energy dispersive spectrometer (EDS, Xmax-80). In addition, the composition and type of phases contained in the two alloys were identified by X-ray diffractometry (D8 Advance). The microstructural characterization of hot-compressed samples with different process parameters and profiles in different regions after the actual engineering extrusion was carried out using electron backscatter diffraction (EBSD) to investigate the deformation mechanism behind them, which was performed at the Helios Nanolab 600i electron microscope. The sampling position of the hot compressed samples was located in the central area along the compression axis, and the profile was divided into three regions: P1, P2 and P3. The practical 2195 Al-Li alloy extruded profile is shown in Figure 1b, and the observed surfaces are shown in Figure 1c. The specimens used for EBSD analysis were water-ground, mechanically polished, and then placed in electrolytic polishing solutions (90% C_2H_5OH + 10% $HClO_4$) for 5–8 s at room temperature using the parameter of voltage 20 V. The collected EBSD data were analyzed and processed using HKL Channel-5 software.

3. Results and Discussion

3.1. Initial Microstructure

The OM, SEM and XRD diagrams of the as-cast and homogenized 2195 Al-Li alloy are shown in Figure 2. The as-cast alloy shown in Figure 2a has severe dendritic segregation and a sizeable amount of continuously scattered non-equilibrium eutectic organization near to the grain boundary. According to Figure 2b, skeleton coarse second phases are continually dispersed along grain boundaries, whereas a small number of slate-like second phases are scattered throughout the grain. According to the results of the separate EDS analysis of the special second phase's composition, the slate-like second phase is the Al_2Cu phase, while the skeleton second phase is primarily made up of Al, Cu, and Fe elements. Following homogenization, as seen in Figure 2c,d, dendritic segregation is eliminated, leaving only a few sporadic second phases in the matrix. According to the EDS data, these second phases are primarily Al_7Cu_2Fe phases. Based on the results of the XRD analysis of the as-cast and homogenized states shown in Figure 2e, the ingot still contains some $T_1(Al_2CuLi)$, $T_2(Al_6CuLi_3)$ and $S(Al_2CuMg)$ phases. However, after homogenization, these phases are essentially redissolved into the aluminum matrix.

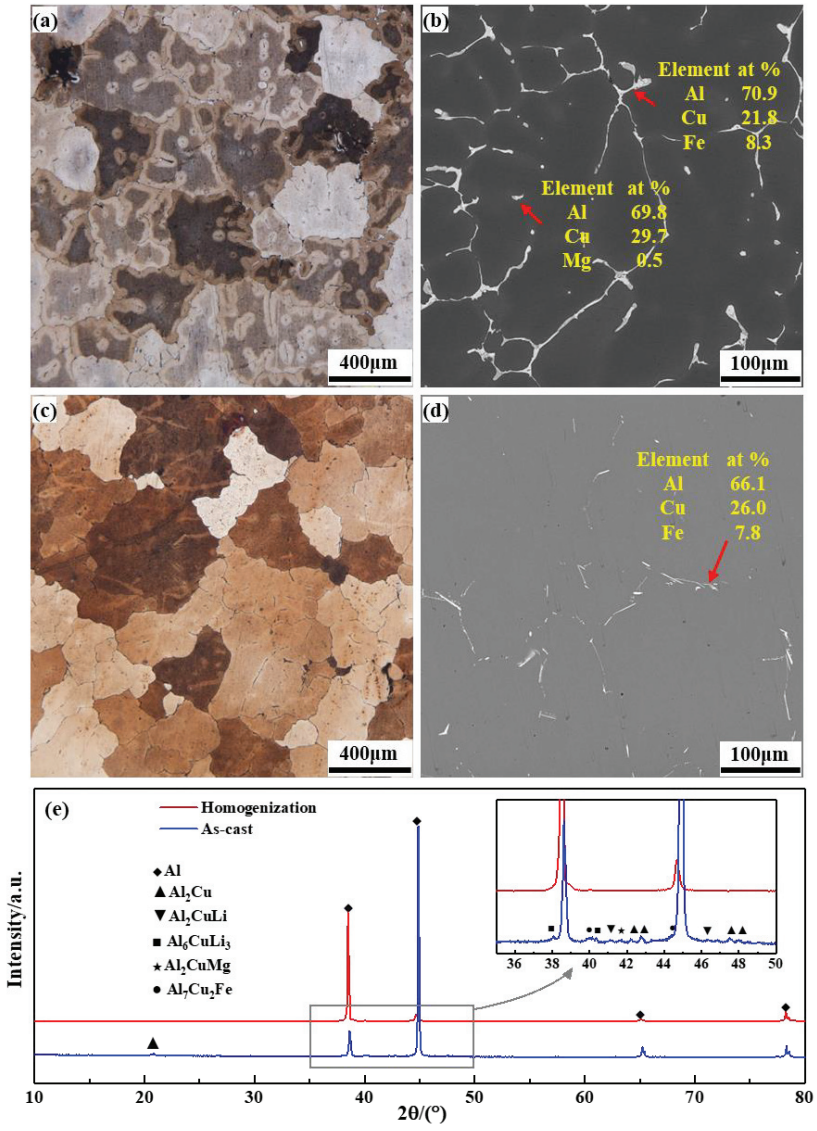

Figure 2. OM, SEM images and XRD pattern of the as-cast and homogenized 2195 Al-Li alloy: (**a**,**b**) as-cast, (**c**,**d**) homogenized, (**e**) XRD pattern.

3.2. Flow Stress Behavior

The true stress-strain curves of the two-stage homogenized 2195 Al-Li alloy obtained by isothermal hot compression tests at different deformation conditions are shown in Figure 3, and the friction and temperature corrections were applied using the method proposed by Ebrahimi and Najafizadeh [20]. As observed in Figure 3, the corrected flow stresses are all smaller than the uncorrected flow stresses, and the average absolute relative error is 6.96%, indicating that the friction between the specimen end face and the indenter increases the real load. It can be seen from the corrected flow stress curves that the flow stress of 2195 Al-Li alloy is significantly affected by the strain rate, deformation temperature and strain.

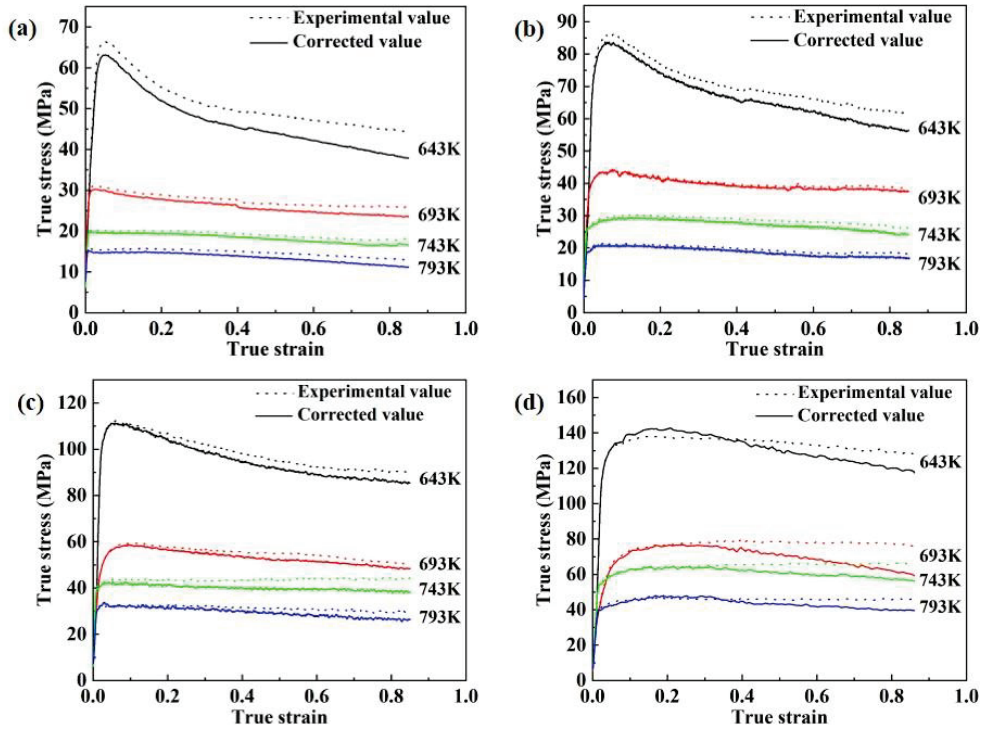

Figure 3. Comparisons of stress-strain curves of 2195 Al-Li alloy before and after friction and temperature corrections: (**a**) 0.001 s^{-1}, (**b**) 0.01 s^{-1}, (**c**) 0.1 s^{-1}, (**d**) 1 s^{-1}.

At the initial stage of deformation, the stress rises rapidly with the increase in strain, and then decreases gradually when the stress reaches the peak, and finally stabilizes. At the fixed deformation temperature, the stress rises with the increase in strain rate because the dislocations caused by the rapid deformation are not ready to eliminate and rearrange in a short time, which leads to an increase in the work hardening rate. Due to the thermal activation of metal atoms being strengthened at higher temperatures and the metal's deformation resistance declining, the stress reduces with increasing deformation temperature at the same strain rate. Additionally, DRV and DRX tend to occur when the alloy is deformed at high temperatures, resulting in alloy softening [21,22].

3.3. Establishment of the Constitutive Model

3.3.1. Arrhenius Constitutive Model with Strain Compensation

The Arrhenius hyperbolic sinusoidal constitutive equation is typically used to depict the connection between flow stress, deformation temperature, and strain rate of metal or alloy during thermal deformation, that is:

$$\dot{\varepsilon} = AF(\sigma)\exp(-\frac{Q}{RT}) \quad (1)$$

$$F(\sigma) = \begin{cases} \sigma^{n_1} & (\alpha\sigma < 0.8) \\ \exp(\beta\sigma) & (\alpha\sigma > 1.2) \\ [\sinh(\alpha\sigma)]^n & (\text{for all } \sigma) \end{cases} \quad (2)$$

where $\dot{\varepsilon}$ is the strain rate (s^{-1}), σ is the flow stress (MPa), R is the universal gas constant (8.314 J mol^{-1} K^{-1}), T is the thermodynamic temperature (K), Q is the deformation thermal activation energy (kJ mol^{-1}), and A, α, n_1, n, *and* β are material constants, where $\alpha = \beta/n_1$. To calculate the value of each constant, Equation (2) is brought into Equation (1) on each side and the logarithm taken to obtain:

$$\ln\dot{\varepsilon} = \begin{cases} \ln A_1 + n_1 \ln\sigma - \frac{Q}{RT} & (\alpha\sigma < 0.8) \\ \ln A_2 + \beta\sigma - \frac{Q}{RT} & (\alpha\sigma > 1.2) \\ \ln A_3 + n\ln[\sinh(\alpha\sigma)] - \frac{Q}{RT} & (\text{for all } \sigma) \end{cases} \quad (3)$$

The solutions for each parameter in this experiment are used for peak stresses with different deformation conditions, and the specific data are shown in Table 2. The relationship between $\ln\dot{\varepsilon} - \ln\sigma$ and $\ln\dot{\varepsilon} - \sigma$ obtained is shown in Figure 4a,b based on the experimental data, and the values of n_1 and β can be regressed to 6.7498 and 0.1357 using the linear fitting method, respectively, then $\alpha = \beta/n_1 = 0.0201$.

Table 2. Peak stress statistics.

Strain Rates/s^{-1}	Temperature/K			
	643 K	**693 K**	**743 K**	**793 K**
0.001	63.17	30.04	19.80	15.33
0.01	83.72	44.18	29.46	20.92
0.1	111.25	58.81	42.65	33.74
1	142.30	76.78	64.64	48.04

For all stress states, combining Equations (1) and (2), and taking partial derivatives on both sides gives:

$$Q = R\left\{\frac{\partial\ln\dot{\varepsilon}}{\partial\ln[\sinh(\alpha\sigma)]}\right\}_T\left\{\frac{\partial\ln[\sinh(\alpha\sigma)]}{\partial(1/T)}\right\}_{\dot{\varepsilon}} \quad (4)$$

Based on the peak stress value, the functional relationship between $\ln[\sinh(\alpha\sigma)] - \ln\dot{\varepsilon}$ and $\ln[\sinh(\alpha\sigma)] - T^{-1}$ can be obtained, as shown in Figure 4c,d. A linear fit to the data in Figure 4c yields n = 4.9057. According to the obtained n and the average value of Q/nR obtained by linear fitting the data in Figure 4d, the average value of Q can be calculated as 249.722 kJ mol^{-1}. Based on obtaining n and Q, combined with Figure 4c, the average value of A can be obtained as 2.5052×10^{16}. Based on the fitted material parameters, the isothermal hot compression constitutive equation is obtained as shown in Equation (5).

$$\dot{\varepsilon} = 2.5052 \times 10^{16}[\sinh(0.0201\sigma)]^{4.9057}\exp\left[-\frac{246386}{RT}\right] \quad (5)$$

Since the strain rate is controlled by the thermal activation energy and temperature during plastic deformation, this coupling relationship can be expressed by the Zener-Hollomon coefficient, which can be rewritten as:

$$Z = \dot{\varepsilon}\exp(\frac{Q}{RT}) = A[\sinh(\alpha\sigma)]^n \quad (6)$$

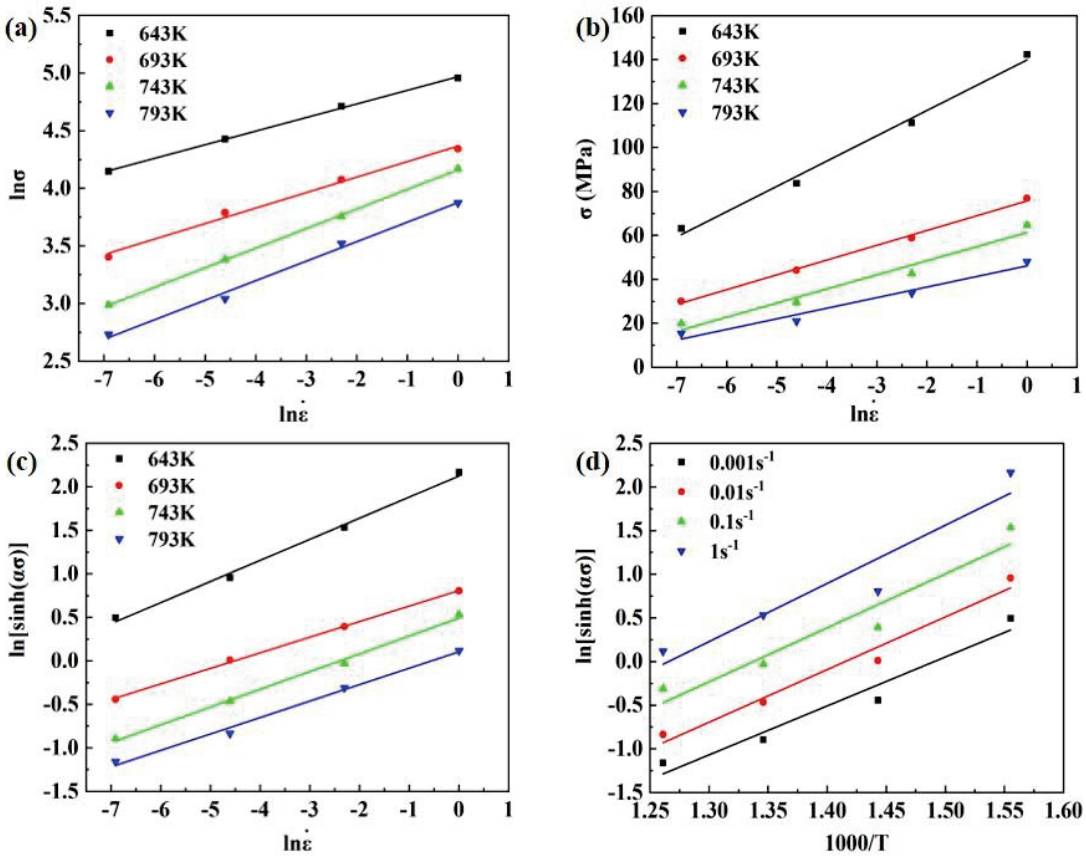

Figure 4. Fitting line of different deformation rate intervals: (**a**) $\ln \dot{\varepsilon} - \ln \sigma$, (**b**) $\ln \dot{\varepsilon} - \sigma$, (**c**) $\ln [sinh(\alpha\sigma)] - \ln \dot{\varepsilon}$, (**d**) $\ln [sinh(\alpha\sigma)] - T^{-1}$.

The expression for the flow stress containing the Zener-Hollomon coefficient can be obtained from the definition of the hyperbolic sine function as follows:

$$\sigma = \frac{1}{\alpha} \ln \left\{ \left(\frac{Z}{A}\right)^{1/n} + \left[\left(\frac{Z}{A}\right)^{2/n} + 1 \right]^{1/2} \right\} \tag{7}$$

The calculated data are brought to the hyperbolic sine function with the Zener-Hollomon coefficient at peak stress, which can be expressed as:

$$\sigma = 49.7193 \ln \left\{ \left(\frac{Z}{2.5052 \times 10^{16}}\right)^{0.2038} + \left[\left(\frac{Z}{2.5052 \times 10^{16}}\right)^{0.4077} + 1 \right]^{1/2} \right\} \tag{8}$$

The Arrhenius model previously established is a function of flow stress on deformation temperature and deformation rate, and does not consider the influence of deformation degree on flow stress. In order to more accurately predict the flow stresses in the alloy during the hot compression process, it is necessary to establish a strain-compensated Arrhenius constitutive model that considers the deformation temperature, deformation rate and deformation degree simultaneously.

The linear regression method can be used to find the values of material parameters such as α, n, Q, and $\ln A$ at different strains (0.05–0.8, with values taken at 0.05 intervals). In this experiment, as shown in Equation (9), a fifth-order polynomial function [15,16] is used for parameter fitting analysis, and the corresponding fitted curves are shown in Figure 5.

The coefficients of the fitted material parameters such as α, n, Q, and ln$A$ are shown in Table 3.

$$\begin{cases} \alpha = B_0 + B_1\varepsilon + B_2\varepsilon^2 + B_3\varepsilon^3 + B_4\varepsilon^4 + B_5\varepsilon^5 \\ n = C_0 + C_1\varepsilon + C_2\varepsilon^2 + C_3\varepsilon^3 + C_4\varepsilon^4 + C_5\varepsilon^5 \\ Q = D_0 + D_1\varepsilon + D_2\varepsilon^2 + D_3\varepsilon^3 + D_4\varepsilon^4 + D_5\varepsilon^5 \\ \ln A = E_0 + E_1\varepsilon + E_2\varepsilon^2 + E_3\varepsilon^3 + E_4\varepsilon^4 + E_5\varepsilon^5 \end{cases} \quad (9)$$

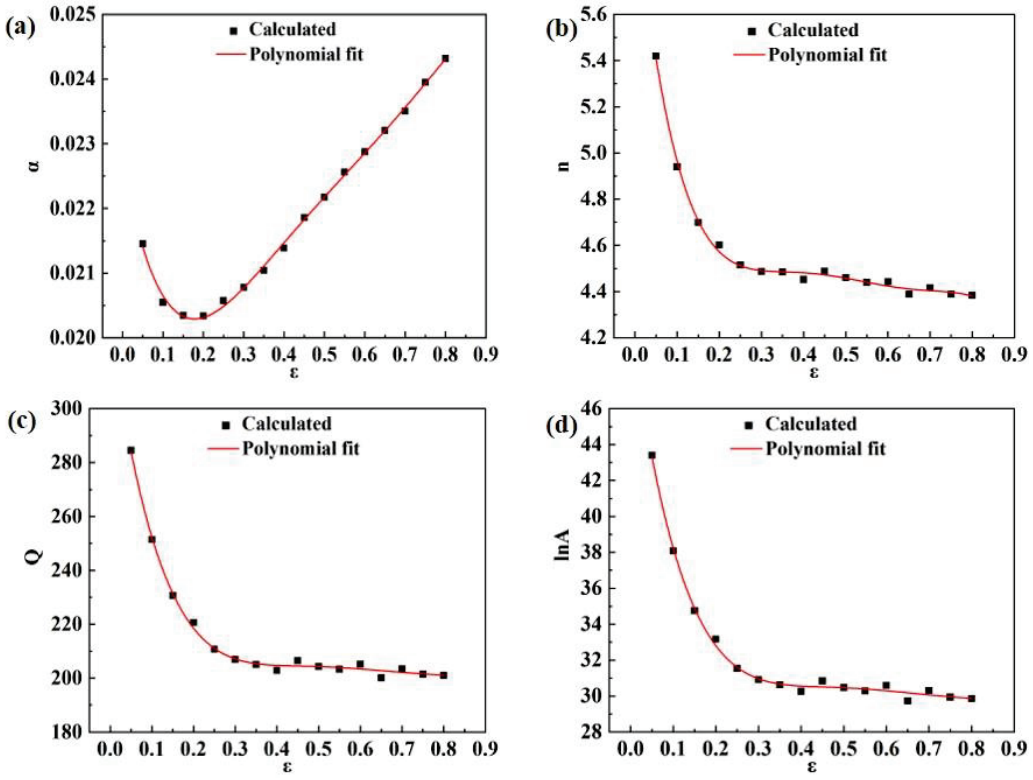

Figure 5. Relationship between material parameters and strain: (**a**) α, (**b**) n, (**c**) Q, (**d**) ln$A$.

Table 3. Coefficients of polynomial fitting material parameters.

α		**n**		**Q**		**lnA**	
B0	0.02277	C0	6.12285	D0	330.50351	E0	50.77187
B1	−0.03474	C1	−17.64282	D1	−1103.31781	E1	−176.75073
B2	0.16345	C2	74.1133	D2	3799.09406	E2	607.48305
B3	−0.30791	C3	−150.3933	D3	−6394.61148	E3	−1021.01887
B4	0.27925	C4	146.24573	D4	5238.73818	E4	834.47043
B5	−0.09768	C5	−54.81721	D5	−1678.4414	E5	−266.50138

The Arrhenius constitutive model of the homogenized 2195 Al-Li alloy considering strain compensation obtained by polynomial fitting of the material parameters can be expressed by Equation (9), which can be used to predict the flow stress for any given deformation condition.

$$\sigma = \frac{1}{\alpha(\varepsilon)} \ln\left\{ \left(\frac{\dot{\varepsilon}\exp(Q(\varepsilon)/RT)}{A(\varepsilon)}\right)^{1/n(\varepsilon)} + \left[\left(\frac{\dot{\varepsilon}\exp(Q(\varepsilon)/RT)}{A(\varepsilon)}\right)^{2/n(\varepsilon)} + 1\right]^{1/2} \right\} \quad (10)$$

To investigate whether the established Arrhenius equation is consistent with the actual flow behavior of 2195 Al-Li alloy at different deformation temperatures and deformation rates, the flow stress values calculated by Equation (10) were compared with those obtained from actual hot compression tests, and the results are shown in Figure 6.

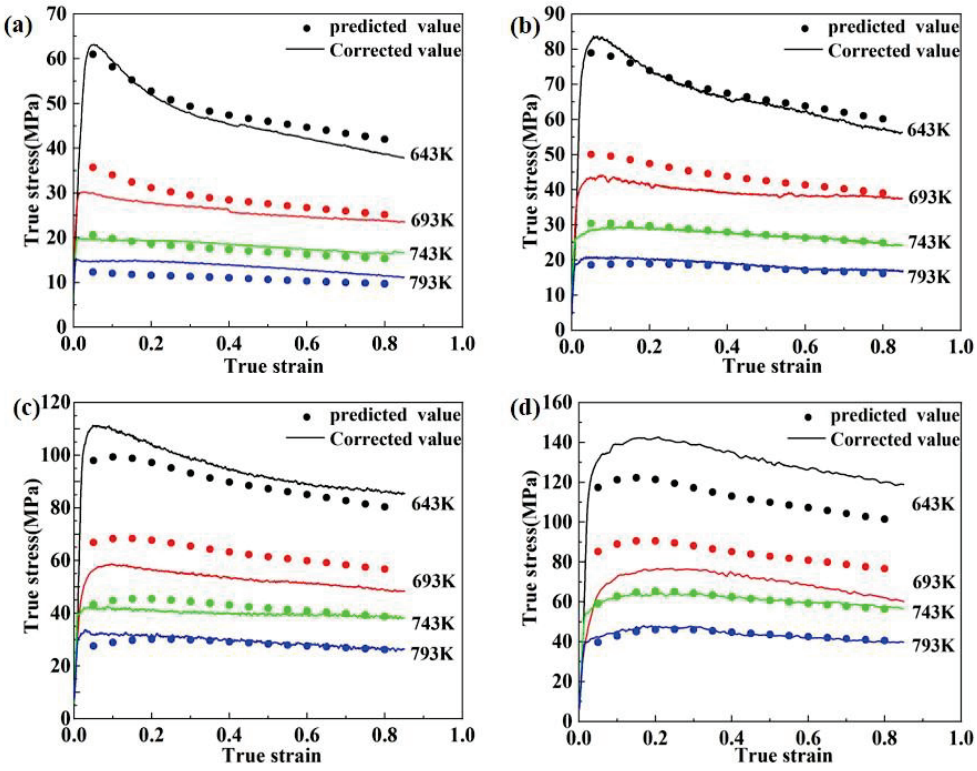

Figure 6. Comparison between the predicted results of flow stress and the corrected test results: (**a**) 0.001 s^{-1}, (**b**) 0.01 s^{-1}, (**c**) 0.1 s^{-1}, (**d**) 1 s^{-1}.

At high temperatures and low strain rates, the strain-compensated Arrhenius constitutive model fits the actual stress-strain curve more accurately, as seen in Figure 6. However, the degree of destabilization is increased at high strain rates (0.1~1 s^{-1}) and deformation temperatures of 643–693 K. The predicted value is only 85.1% of the actual value, especially when the strain rate is 1 s^{-1} and the deformation temperature is 643 K. This implies that the flow stress behavior of 2195 Al-Li alloy cannot be well described by strain compensation correction alone.

The difference between the predicted and test stress values is quantified using the related coefficient (R) and average absolute relative error (AARE), which can be calculated using Equation (11) and Equation (12), respectively. R and AARE have computed values of 0.9758 and 9.51%, respectively. To further correct the Arrhenius constitutive model with strain compensation described previously, it is required to take into account the compensation of the flow stress by strain rate and deformation temperature.

$$R = \frac{\sum_{i=1}^{N} (E_i - \overline{E})(P_i - \overline{P})}{\sqrt{\sum_{i=1}^{N} (E_i - \overline{E})^2 \sum_{i=1}^{N} (P_i - \overline{P})^2}} \tag{11}$$

$$AARE = \frac{1}{N} \sum_{i=1}^{N} \left| \frac{E_i - P_i}{E_i} \right| \tag{12}$$

3.3.2. Arrhenius Constitutive Model Modified by Temperature and Strain Rate

In this section, based on the already established Arrhenius constitutive equation considering strain compensation, a modified function for deformation temperature and strain rate is introduced, to establish an integrated constitutive model considering strain rate, deformation temperature and strain co-compensation, as shown in Equation (13). As

indicated in Table 4, the modified function takes on a polynomial form, the test results obtained under various deformation situations are compared to the expected results first, and then the associated ratios are calculated. The ratio, which measures the difference between actual and predicted values, reflects how well the current constitutive model predicted values; the closer the ratio is to 1, the better. The data in Table 2 were then imported into Matlab software to establish different forms of polynomial functions, from which a function with high fitting accuracy and relatively simple structure was selected as the best-modified function in the form shown in Equation (14), which has a fitting accuracy of 0.9416 and the values of the correlation coefficients are shown in Table 5. A comparison of the correction values obtained from the Arrhenius constitutive model based on the strain rate, temperature and strain corrections with the flow stress values obtained from the actual hot compression tests is shown in Figure 7.

Table 4. The ratio of test stress values to predicted stress values at different strain rates and temperatures.

$\dot{\varepsilon}$	T	Experiment/Predicted	$\dot{\varepsilon}$	T	Experiment/Predicted
0.001	643	0.9635	0.1	643	1.0664
	693	0.9061		693	0.8502
	743	1.0495		743	0.9448
	793	1.2411		793	1.0341
0.01	643	0.9863	1	643	1.1753
	693	0.9044		693	0.8358
	743	0.9845		743	1.0009
	793	1.0568		793	1.0083

Table 5. Values of the coefficients in the modified function.

p_0	p_1	p_2	p_3	p_4	p_5	p_6	p_7	p_8	p_9
168.5	9.543	−0.6904	67.05	-3.203×10^{-2}	9.43×10^{-4}	−69.52	1.423×10^{-2}	1.091×10^{-5}	-4.269×10^{-7}

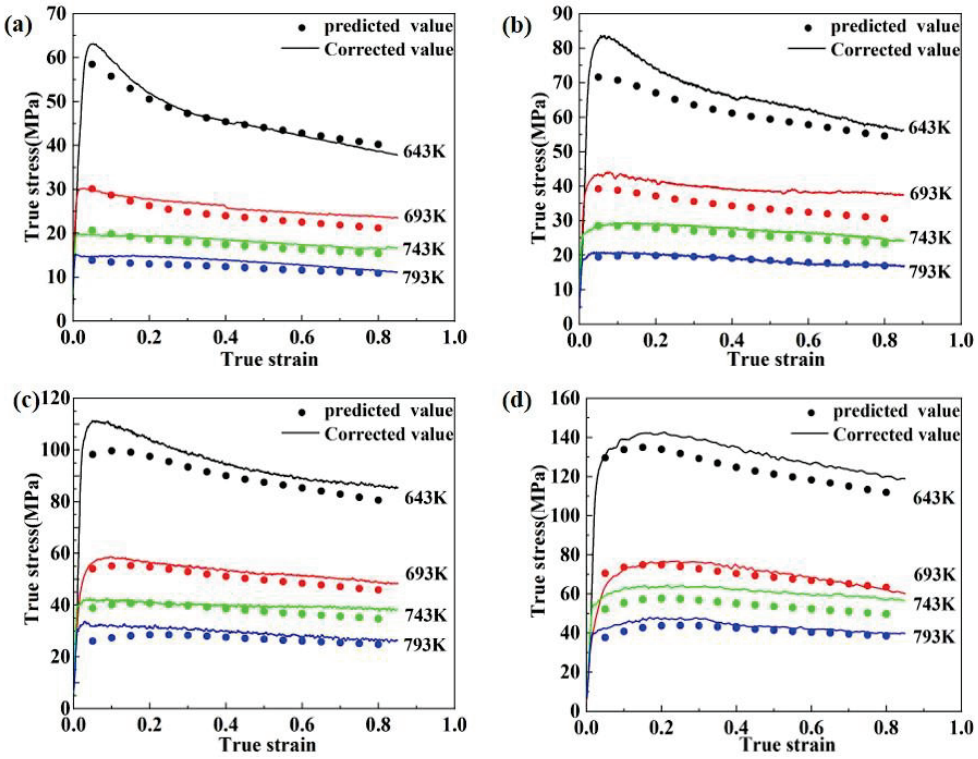

Figure 7. Comparison between the modified function results of flow stress and the corrected test results: (**a**) 0.001 s^{-1}, (**b**) 0.01 s^{-1}, (**c**) 0.1 s^{-1}, (**d**) 1 s^{-1}.

After calculation, the values of R and AARE are 0.9974 and 6.49%, respectively, which are significantly more accurate than the previous model. Therefore, the strain-compensated Arrhenius constitutive model considering strain rate and temperature corrections can accurately describe the flow behavior of 2195 Al-Li alloy.

$$\sigma = f(\dot{\varepsilon}, T) \cdot \frac{1}{\alpha(\varepsilon)} \ln\left\{ \left(\frac{\dot{\varepsilon}\exp(Q(\varepsilon)/RT)}{A(\varepsilon)}\right)^{1/n(\varepsilon)} + \left[\left(\frac{\dot{\varepsilon}\exp(Q(\varepsilon)/RT)}{A(\varepsilon)}\right)^{2/n(\varepsilon)} + 1\right]^{1/2} \right\} \tag{13}$$

$$f(\dot{\varepsilon}, T) = p_0 + p_1\dot{\varepsilon} + p_2 T + p_3\dot{\varepsilon}^2 + p_4\dot{\varepsilon}\cdot T + p_5 T^2 + p_6\dot{\varepsilon}^3 + p_7\dot{\varepsilon}^2\cdot T + p_8\dot{\varepsilon}\cdot T^2 + p_9 T^3 \tag{14}$$

3.4. Processing Map and Microstructure

3.4.1. Establishment of Processing Map

The processing map based on DMM, which comprises a power dissipation efficiency map and an instability map, and contains two portions of the safety domain and instability domain, can reflect the relationship between the microstructure evolution mechanism and the alloy's thermal deformation parameters. During thermal deformation, the material can be regarded as an energy dissipater, and the total dissipated power P can be split into two parts: content G and co-content J. The strain rate sensitivity coefficient m can be used to express the relationship between temperature and strain rate under constant temperature and strain combinations.

$$m = \frac{dJ}{dG} = \frac{d\ln\sigma}{d\ln\dot{\varepsilon}}_{T,\varepsilon} \tag{15}$$

For an ideal linear dissipater, m = 1, and J obtains the maximum value $J_{\max}$. For a nonlinear dissipater, the power dissipation efficiency η can be expressed as the ratio of J to $J_{\max}$ as follows:

$$\eta = \frac{J}{J_{\max}} = \frac{2m}{m+1} \tag{16}$$

However, a larger value of η does not mean better workability of the alloy, because the value of η under the conditions corresponding to the workability instability domain may also be larger [23,24]. Therefore, the instability criterion established by Prasad et al. [12] is used in this paper to determine the instability domain, as shown in Equation (17).

$$\xi(\dot{\varepsilon}) = \frac{\partial\ln\left(\frac{m}{m+1}\right)}{\partial\ln\dot{\varepsilon}} + m < 0 \tag{17}$$

When $\xi < 0$, plastic flow destabilization will occur, that is, it is more likely to produce adiabatic shear bands, flow localizations and other microstructure defects during deformation.

The processing map of the homogenized 2195 Al-Li alloy during hot compression with a strain of 0.8 was plotted in Figure 8, where the white and grey areas indicate the safety domains and the instability domains, respectively, and the numbers of the contour lines represent the values of the power dissipation coefficient η. It has been confirmed that the microstructure of the safety domains is mainly related to DRV, DRX and phase transition [25]. The higher η usually indicates more energy for microstructure evolution and better plastic deformation properties under the corresponding deformation conditions [26]. In general, the increase in the degree of DRX stimulates a raise in the power dissipation efficiency η.

The power dissipation exhibits peak areas in two temperature ranges: one is in the low-temperature range of 673–693 K, where the strain rate is below 0.001 s^{-1}, and the other is in the high-temperature range of 743–793 K with a moderate strain rate of 0.01–0.1 s^{-1}, as depicted in Figure 8. Additionally, a valley area of power dissipation is observed at high strain rates of 0.1–1 s^{-1} and medium temperatures of 673–703 K. Simultaneously, three instability domains are evident in the low-temperature, low-strain-rate region (658–708 K, 0.001–0.01 s^{-1}), the low-temperature, high-strain-rate region (643 K, 1 s^{-1}), and the high-temperature, high-strain-rate region (743–783 K, 0.3–1 s^{-1}). The occurrence

of the peak area of power dissipation at low temperature and low strain rate suggests the occurrence of DRV in the alloy. Meanwhile, the appearance of the peak area of power dissipation at high temperature and medium strain rate may be attributed to CDRX. Generally, alloys tend to undergo destabilization when deformed within the high-temperature and high-strain-rate range, consistent with the findings of Zhang et al. [14] and Wang et al. [16]. However, the alloy also exhibits destabilization at 658–708 K, 0.001–0.01 s^{-1}, which requires verification through microstructural analysis.

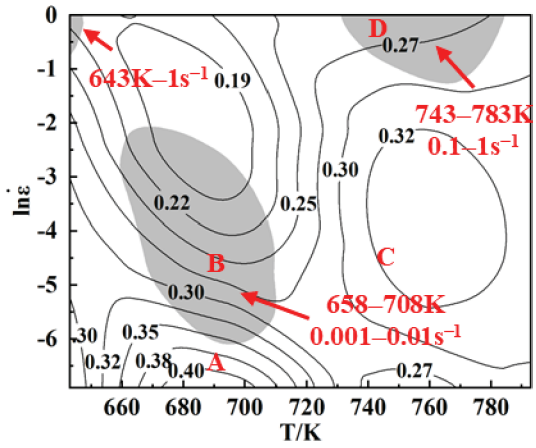

Figure 8. Processing map of the homogenized 2195 Al-Li alloy at the true strain of 0.8.

Therefore, four typical regions were selected in the processing map; regions A (693 K, 0.001 s^{-1}) and C (743 K, 0.01 s^{-1}) are stable and regions B (693 K, 0.01 s^{-1}) and D (743 K, 1 s^{-1}) are unstable. The microstructure of these four regions was tested to analyze and discuss the deformation mechanism under different deformation conditions.

3.4.2. Microstructure Characterization

Figure 9 illustrates the inverse pole figures, grain boundary maps and recrystallization microstructure distributions of the tested alloy under various strain rates and deformation temperatures. Thick black lines are used to indicate high angle grain boundaries (HAGBs, misorientation > 15°), and thin red lines are used to indicate low angle grain boundaries (LAGBs, misorientation 2–15°). In deformation microstructure distribution maps, red represents deformed structure (0–2°), yellow represents substructure (2–15°), and blue represents recrystallized grain (>15°).

As observed in Figure 9, a large number of original equiaxed grains are flattened and elongated along the compression direction, and some of the original flattened grain boundaries are serrated. Figure 9(a1,a2) reveal that in region A, where deformation occurs at a low temperature of 693 K and a low strain rate of 0.001 s^{-1}, clear and uniformly distributed LAGBs can be observed inside the grains. This uniform plastic deformation indicates the occurrence of DRV in the alloy. The presence of partially recrystallized grains on the HAGBs, especially at the trigonal grain boundaries (as shown in the white elliptical box), with a significant difference in misorientation from the adjacent grains, indicates that DRX occurred under this condition [27], which is consistent with the results of the distribution of DRX grains demonstrated in Figure 9(a3), with a DRX degree of 6.0%. In addition, the power dissipation efficiency corresponding to this region in the processing map is also the largest, further confirming the alloy's good workability. The microstructure of the material is displayed in Figure 9(b1–b3) when the strain rate reaches 0.01 s^{-1}. It can be seen that the majority of the grains are distributed with uniform LAGBs inside, while only a small number of deformed grains with distinct grain boundary contours have almost no LAGBs inside. Moreover, adiabatic shear zones appear in specific locations (marked with yellow boxes). Figure 9(b3) reveals fewer recovery microstructures, more pronounced DRX (9.9%), significantly larger average grain size of recrystallized grains, and the presence

of abnormally grown DRX grains (indicated by white arrows). These observations further support the notion that as the strain rate increases, the alloy deforms non-uniformly.

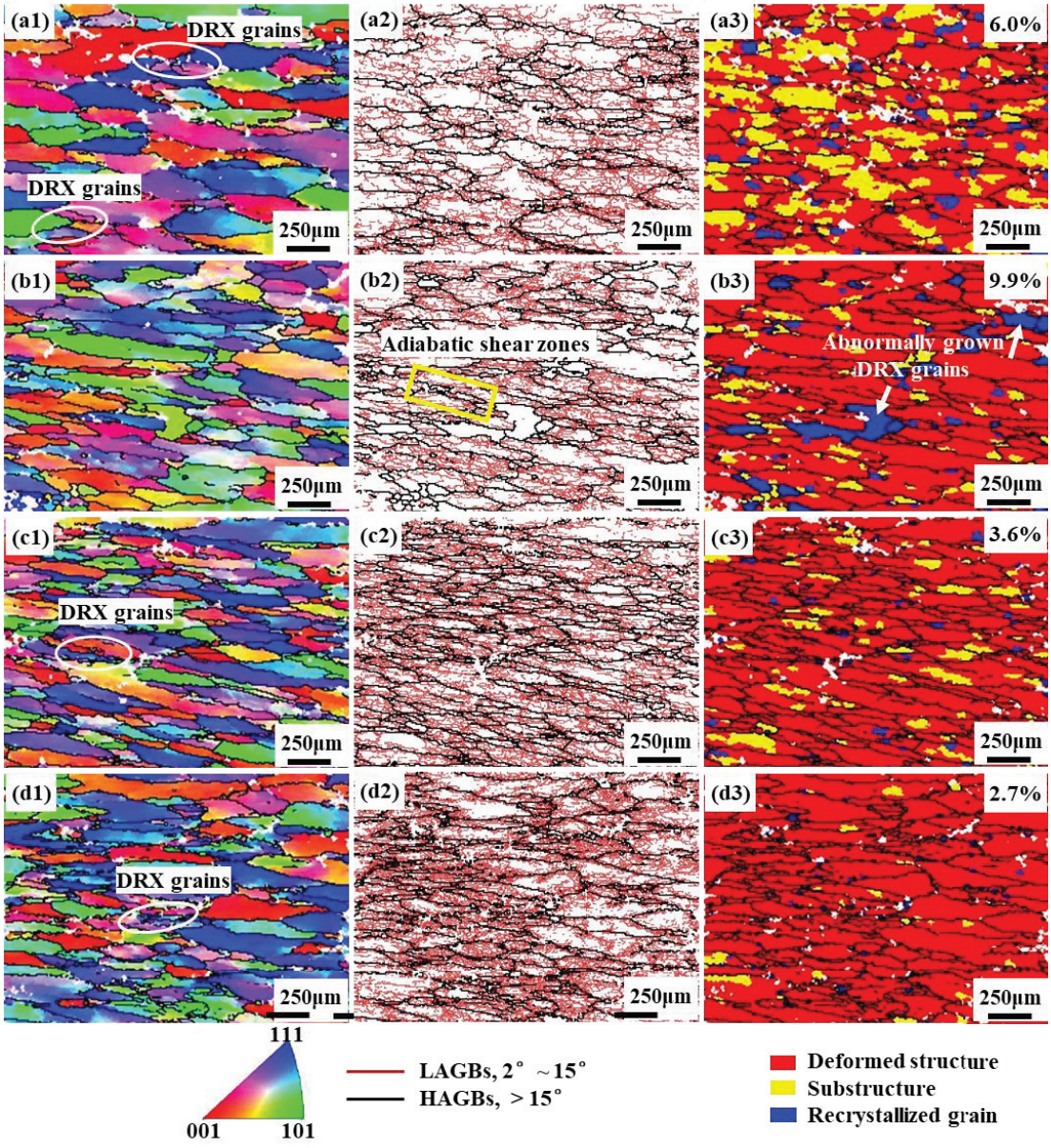

Figure 9. Inverse pole figures, grain boundary maps and recrystallization microstructure distributions of the alloy at (**a1–a3**) A (693 K, 0.001 s^{-1}), (**b1–b3**) B (693 K, 0.01 s^{-1}), (**c1–c3**) C (743 K, 0.01 s^{-1}) and (**d1–d3**) D (793 K, 1 s^{-1}).

When the deformation condition is in the safety domain C, the power dissipation efficiency increases from 0.24 to 0.32. It can be seen from Figure 9(c1,c2) that the original grains undergo a more uniform plastic deformation and a large number of LAGBs are generated inside the grains. Figure 9(c3) shows the formation of fine chain-like recrystallized grains near the original grain boundaries, indicating that the recrystallization mechanism is dominated by DDRX under this deformation condition. In Figure 9(d1–d3), it can be seen that the alloy experiences more severe local plastic deformation when it is in the instability zone D. This can be attributed to the intensified local deformation resulting from higher strain rates and deformation temperatures. Consequently, the grains within the shear deformation zone become significantly elongated along the shear direction and exhibit diverse grain orientations. It is important to note that this condition exhibits the least amount

of recrystallization (2.7%). The numerous small grains already formed near the original grain boundaries are not the result of recrystallization. Furthermore, the entanglement of numerous HAGBs suggests the challenges in coordinating material flow, indicating typical flow localization characteristics [28].

The effects of deformation process parameters on dislocations and substructures were investigated using TEM, and the results are presented in Figure 10. Figure 10(a1,a2) clearly illustrates that the distribution of dislocations among different grains is non-uniform at 693 K and 0.01 s^{-1} (unstable zone B). Numerous dislocations accumulate at certain original HAGBs, forming a mass of dislocation walls and tangles. Conversely, there is no apparent presence of dislocations within another portion of the coarse grains, indicating the alloy's instability under this deformation condition. Furthermore, the formation of DRX grain was observed near the original HAGB, which possess diameter larger than 2 μm. Additionally, a certain number of second phase particles exist at the grain boundaries, effectively pinning them and impeding dislocation movement. In the case of deformation occurring within the stable region C, as depicted in Figure 10(b1,b2), the number of dislocations and second phase particles within the matrix significantly decreases. The (sub)grain boundaries become more distinct, suggesting that higher temperatures promote dislocation climbing and cross-slip migration, as well as the dissolution of second phase particles. Furthermore, the generation of a greater number of subgrains and DRX grains with smaller sizes was observed. This observation demonstrates that most of the dislocations undergo DRV and DRX through rearrangement and annihilation [29], ultimately leading to a decrease in flow stress.

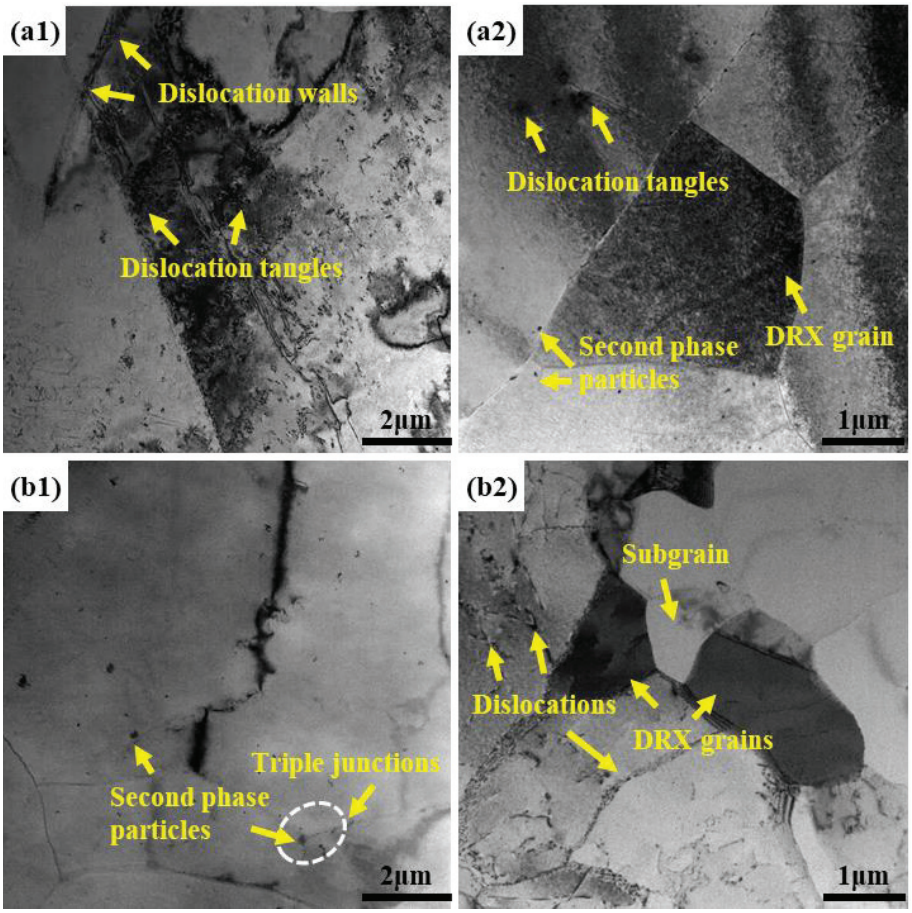

Figure 10. TEM images of the alloy under different deformation parameters: (**a1**,**a2**) region B, (**b1**,**b2**) region C.

Considering the established processing map and the detected microstructure, the optimum deformation parameters of the homogenized 2195 Al-Li alloy were finally identified as 710–783 K and 0.001–0.12 s^{-1}.

3.5. Application of Constitutive Model and Numerical Simulation Verification

This section describes the flow behavior of the material during thermal deformation using the established constitutive model. The model is then applied to the finite element simulation of 2195 Al-Li alloy extruded profiles with large shaped cross-sections in HyperXtrude software, and the extrusion parameters are shown in Table 1. Physical field quantities such as deformation behavior and stress distribution are analyzed to verify the accuracy and reliability of the constitutive model.

The results of the numerical simulation are presented in Figure 11. The small graph at the bottom right of each graph illustrates the distribution of the physical field of the profile section at the exit of the die. Figure 11a indicates that the velocity of the material is non-uniform along the extrusion direction and at the exit of the section. The velocity is significantly higher at the center than at the two ends, with the maximum velocity difference being 1.528 mm/s. Figure 11b shows that the profile reaches a maximum temperature of 765.2 K and a minimum temperature of 745.6 K during the extrusion process, with a maximum temperature difference of 19.6 K. The heat generated by the plastic deformation of the material itself, the friction between the ingot and the die, and the simultaneous heat transfer between the material and the outside lead to the temperature of the deformed material being higher than the initial extrusion temperature [30,31]. As shown in Figure 11c,d, the distribution of the equivalent stress and strain rate exhibit similar characteristics. The stress values on both surfaces at the thickest part of the profile are significantly higher than those at the left and right ends of the profile, reaching 12.48 MPa. This indicates that a stronger frictional effect occurs between the surfaces on both sides of the thickest part of the profile and the bearing of the die, which leads to the climbing of the stress values. Additionally, the profile's irregular cross-section leads to different degrees of deformation in different areas, further increasing the unevenness of deformation.

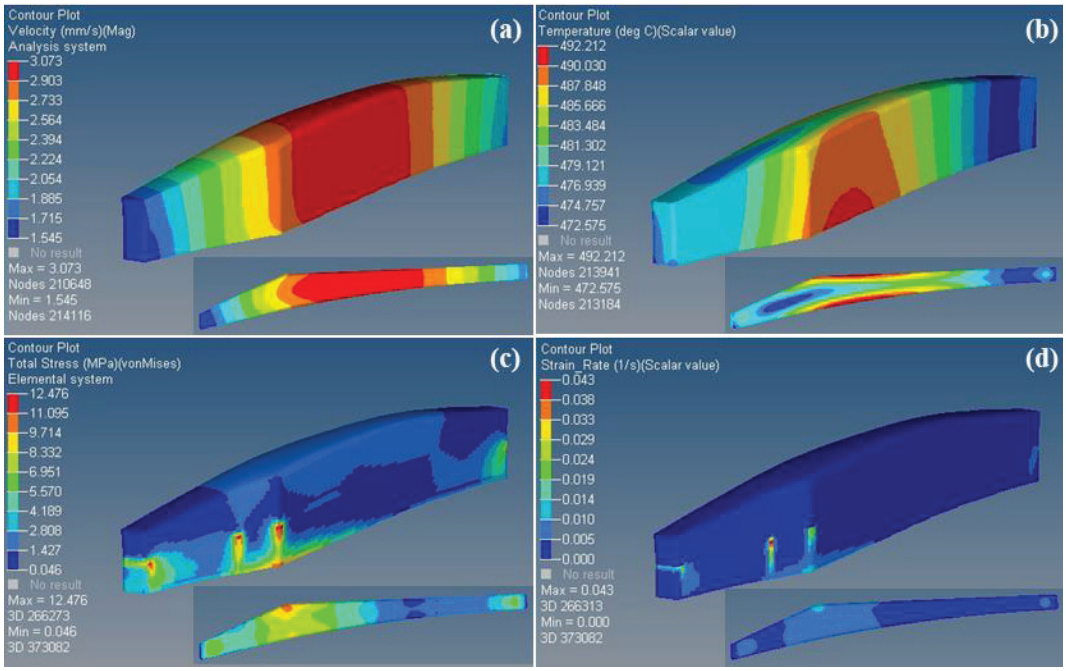

Figure 11. Numerical simulation results: (**a**) velocity field, (**b**) temperature field, (**c**) stress field, (**d**) strain rate field.

In summary, the deformation temperature of the alloy ranges from 745 K to 765 K, and the deformation rate ranges from 0.000034 s^{-1} to 0.043 s^{-1}. The range of value variation falls within the feasible region (710~783 K, 0.001~0.12 s^{-1}) of the processing map established in Section 3.4. This indicates that the entire extrusion deformation occurs within the processing safety zone.

3.6. Confirmation Experiments

Practical extrusion tests were carried out on a 25 MN extruder to verify the accuracy of the constitutive model and numerical simulation, and the extruded profile of 2195 Al-Li alloy with high dimensional accuracy was successfully obtained, as shown in Figure 1b.

To investigate the microstructure evolution during extrusion, EBSD analysis was performed on three observed surfaces of the profile, as shown in Figure 1c. Figure 12 illustrates the IPF maps and the relative frequency of misorientation angles at the three observation points. The deformed grains exhibit a fibrous and dispersed morphology along the extrusion direction (ED), as shown in Figure 12a–c. Notably, the grains in different locations display distinct preferred misorientations, specifically along the ED <001> and <101> crystal directions. Moreover, the microstructure does not display any significant signs of local plastic deformation or adiabatic shear bands, indicating that the chosen process parameters for extrusion fall within the safe processing zone.

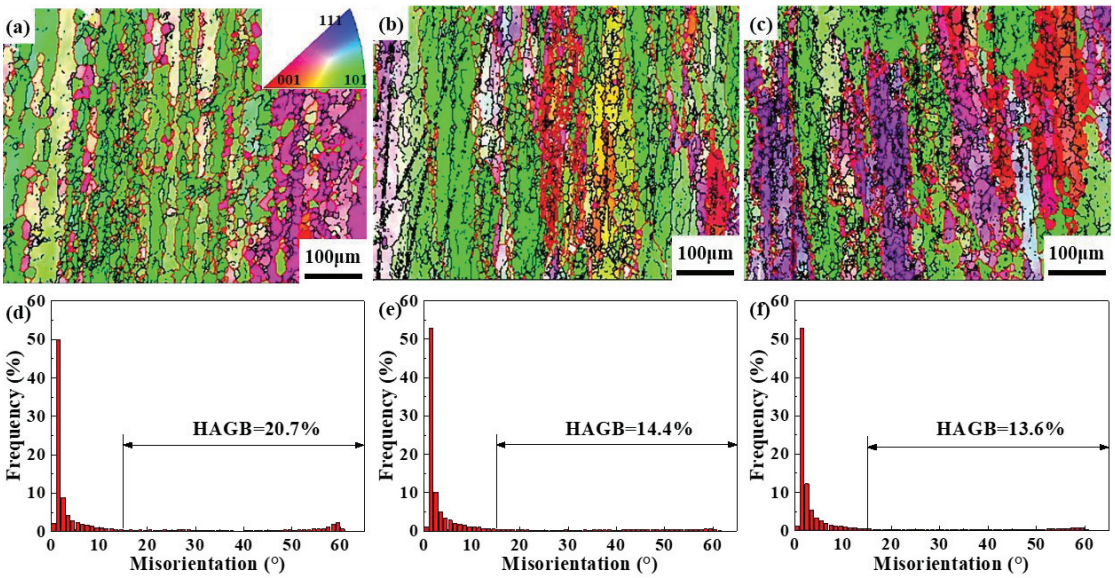

Figure 12. IPF maps and relative frequency of misorientation angles along the ED direction of the profile for different sampling areas: (**a**,**d**) P1, (**b**,**e**) P2, (**c**,**f**) P3.

Further investigation reveals the presence of smaller recrystallized grains exhibiting a chain distribution along the elongated grain boundary, with a small number of recrystallized grains also observed within the original grains, indicating that CDRX and DDRX occur concurrently during extrusion deformation. Figure 12d–f displays a substantial variation in the relative frequencies of misorientation angles among these three regions. The P1 region exhibits the highest proportion of HAGBs at 20.7%, while the P2 and P3 regions display lower proportions of HAGBs at 13.6% and 14.4%, respectively. Considering the physical field distribution in Figure 12, it can be inferred that the P1 region of the material experiences more severe plastic deformation and higher temperatures during the extrusion process, which may account for the increased generation of DRX grains in that region. During the continuous extrusion of 2195 Al-Li alloy, dislocations constantly propagate, with a majority of them climbing and slipping along the slip surface and shear zone. This process leads to the fragmentation of fibrous grains and the formation of numerous LAGBs [11,32].

Storage energy causes LAGBs to constantly rotate while absorbing dislocations, eventually resulting in the formation of recrystallized grains.

By utilizing the established multiparameter compensated constitutive model and processing map, the physical field distribution during the steady-state extrusion deformation stage of 2195 Al-Li alloy was accurately predicted. The microstructure analysis confirmed the production of high-quality extruded profiles. The successful fabrication of extruded profiles from 2195 Al-Li alloy serves as a compelling validation of the extensive applicability of accurate numerical simulations in industrial manufacturing. This approach not only reduces development costs and time but also enhances production efficiency and ensures stability in product quality.

4. Conclusions

In this study, the constitutive model and processing map of 2195 Al-Li alloy were established, and the accuracy of the constitutive model was proved by numerical simulation and practical extrusion test. The main conclusions are as follows:

1. An Arrhenius constitutive model considering deformation temperature, strain rate and strain co-compensation was established based on the true stress-strain data of homogenized 2195 Al-Li alloy after friction and temperature correction. This model significantly improved the accuracy of flow stress prediction during hot compression, with R and AARE values increasing to 0.9974 and 6.49%, respectively;
2. The processing safety zone and instability zone of 2195 Al-Li alloy were identified by employing the hot processing map. During hot compression, the alloy experienced both DRV and DRX. In the instability zone, considerable local plastic deformation bands and abnormally grown recrystallized grains were observed. The optimal deformation parameters for the 2195 Al-Li alloy were determined as 710~783 K and 0.001~0.12 s^{-1};
3. The physical field distribution of 2195 Al-Li alloy extruded profiles with large shaped cross-sections during extrusion was accurately predicted by a modified Arrhenius constitutive model. Practical extrusion tests produced extruded profiles with slight variations in microstructure in different regions. These variations were caused by uneven temperature and stress distributions, with higher temperature and more severe stress promoting the formation of HAGBs and DRX grains.

Author Contributions: Investigation, R.F.; Writing—original draft, H.L.; Writing—review & editing, J.W.; Project administration, Y.H. All authors have read and agreed to the published version of the manuscript.

Funding: National Natural Science Foundation of China, grant number U1837207.

Institutional Review Board Statement: Not applicable.

Informed Consent Statement: Not applicable.

Conflicts of Interest: The authors declare that they have no known competing financial interests or personal relationships that could have appeared to influence the work reported in this paper.

References

1. Williams, J.C.; Starke, E.A. Progress in structural materials for aerospace systems. *Acta Mater.* **2003**, *51*, 5775–5799. [CrossRef]
2. Araullo-Peters, V.; Gault, B.; Geuser, F.D.; Deschamps, A.; Cairney, J.M. Microstructural evolution during ageing of Al–Cu–Li–x alloys. *Acta Mater.* **2014**, *66*, 199–208. [CrossRef]
3. Hales, S.J.; Hafley, R.A. Texture and anisotropy in Al-Li alloy 2195 plate and near-net-shape extrusions. *Mater. Sci. Eng. A* **1998**, *257*, 153–164. [CrossRef]
4. Jonas, J.; Sellars, C.; Tegart, W. Strength and structure under hot-working conditions. *Metall. Rev.* **1969**, *14*, 1–24. [CrossRef]
5. Lin, Y.C.; Chen, M.S.; Zhong, J. Constitutive modeling for elevated temperature flow behavior of 42CrMo steel. *Comput. Mater. Sci.* **2008**, *42*, 470–477. [CrossRef]
6. Lin, Y.C.; Ding, Y.; Chen, M.S.; Deng, J. A new phenomenological constitutive model for hot tensile deformation behaviors of a typical Al–Cu–Mg alloy. *Mater. Des.* **2013**, *52*, 118–127. [CrossRef]

7. Zhao, J.H.; Deng, Y.L.; Tang, J.G.; Zhang, J. Influence of strain rate on hot deformation behavior and recrystallization behavior under isothermal compression of Al-Zn-Mg-Cu alloy. *J. Alloys Compd.* **2019**, *809*, 151788. [CrossRef]
8. Hu, L.; Lang, M.W.; Shi, L.X.; Li, M.G.; Zhou, T.; Bao, C.L.; Yang, M.B. Study on hot deformation behavior of homogenized Mg-8.5Gd-4.5Y-0.8Zn-0.4Zr alloy using a combination of strain-compensated Arrhenius constitutive model and finite element simulation method. *J. Magnes. Alloy.* **2021**, *11*, 1016–1028. [CrossRef]
9. Xiao, X.; Liu, G.Q.; Hu, B.F.; Zheng, X.; Wang, L.N.; Chen, S.J.; Ullah, A. A comparative study on Arrhenius-type constitutive equations and artificial neural network model to predict high-temperature deformation behaviour in 12Cr3WV steel. *Comput. Mater. Sci.* **2012**, *62*, 227–234. [CrossRef]
10. Meng, Q.G.; Bai, C.G.; Xu, D.S. Flow behavior and processing map for hot deformation of ATI425 titanium alloy. *J. Mater. Sci. Technol.* **2018**, *34*, 679–688. [CrossRef]
11. Chen, X.X.; Zhao, G.Q.; Zhao, X.T.; Wang, Y.X.; Xu, X.; Zhang, C.S. Constitutive modeling and microstructure characterization of 2196 Al-Li alloy in various hot deformation conditions. *J. Manuf. Process.* **2020**, *59*, 326–342. [CrossRef]
12. Prasad, Y.V.R.K.; Gegel, H.L.; Doraivelu, S.M.; Malas, J.C.; Morgan, J.T.; Lark, K.A.; Barker, D.R. Modeling of dynamic material behavior in hot deformation: Forging of Ti-6242. *Metall. Trans. A* **1984**, *15*, 1883–1892. [CrossRef]
13. Nayan, N.; Murty, S.V.S.N.; Chhangani, S.; Prakash, A.; Prasad, M.J.N.V.; Samajdar, I. Effect of temperature and strain rate on hot deformation behavior and microstructure of Al-Cu-Li alloy. *J. Alloys Compd.* **2017**, *723*, 548–558. [CrossRef]
14. Zhang, J.J.; Yi, Y.P.; Huang, S.Q.; Mao, X.C.; He, H.L.; Tang, J.G.; Guo, W.F.; Dong, F. Dynamic recrystallization mechanisms of 2195 aluminum alloy during medium/high temperature compression deformation. *Mater. Sci. Eng. A* **2021**, *804*, 140650. [CrossRef]
15. Yu, W.C.; Li, H.Y.; Du, R.; You, W.; Zhao, M.C.; Wang, Z.A. Characteristic constitution model and microstructure of an Al-3.5Cu-1.5Li alloy subjected to thermal deformation. *Mater. Charact.* **2018**, *145*, 53–64. [CrossRef]
16. Wang, Y.X.; Zhao, G.Q.; Xu, X.; Chen, X.X.; Zhang, C.S. Constitutive modeling, processing map establishment and microstructure analysis of spray deposited Al-Cu-Li alloy 2195. *J. Alloys Compd.* **2019**, *779*, 735–751. [CrossRef]
17. Dong, Y.Y.; Zhang, C.S.; Zhao, G.Q.; Guan, Y.J.; Gao, A.J.; Sun, W.C. Constitutive equation and processing maps of an Al–Mg–Si aluminum alloy: Determination and application in simulating extrusion process of complex profiles. *Mater. Des.* **2016**, *92*, 983–997. [CrossRef]
18. Xu, X.; Ma, X.W.; Zhao, G.Q.; Chen, X.X.; Wang, Y.X. Abnormal grain growth of 2196 Al-Cu-Li alloy weld seams during extrusion and heat treatment. *J. Alloys Compd.* **2021**, *867*, 159043. [CrossRef]
19. Zhang, C.S.; Dong, Y.Y.; Wang, C.X.; Zhao, G.Q.; Chen, L.; Sun, W.C. Evolution of transverse weld during porthole extrusion of AA7N01 hollow profile. *J. Mater. Process. Technol.* **2017**, *248*, 103–114. [CrossRef]
20. Ebrahimi, R.; Najafizadeh, A. A new method for evaluation of friction in bulk metal forming. *J. Mater. Process. Technol.* **2004**, *152*, 136–143. [CrossRef]
21. Yang, Q.B.; Wang, X.Z.; Li, X.; Deng, Z.H.; Jia, Z.H.; Zhang, Z.Q.; Huang, G.J.; Liu, Q. Hot deformation behavior and microstructure of AA2195 alloy under plane strain compression. *Mater. Charact.* **2017**, *131*, 500–507. [CrossRef]
22. Yang, G.; Xu, W.; Jin, X.; Wang, Z.; Shan, D.; Guo, B. Hot deformation behavior and microstructure evolution of the spray deposited and secondary hot extruded 2195 Al–Li alloy. *J. Mater. Res. Technol.* **2022**, *20*, 2784–2798. [CrossRef]
23. Park, S.Y.; Kim, W.J. Difference in the Hot Compressive Behavior and Processing Maps between the As-cast and Homogenized Al-Zn-Mg-Cu (7075) Alloys. *J. Mater. Sci. Technol.* **2016**, *32*, 660–670. [CrossRef]
24. Wu, H.; Wen, S.P.; Huang, H.; Gao, K.Y.; Wu, X.L.; Wang, W.; Nie, Z.R. Hot deformation behavior and processing map of a new type Al-Zn-Mg-Er-Zr alloy. *J. Alloys Compd.* **2016**, *685*, 869–880. [CrossRef]
25. Miao, J.S.; Sutton, S.; Luo, A.A. Deformation microstructure and thermomechanical processing maps of homogenized AA2070 aluminum alloy. *Mater. Sci. Eng. A* **2022**, *834*, 142619. [CrossRef]
26. El Mehtedi, M.; Gabrielli, F.; Spigarelli, S. Hot workability in process modeling of a bearing steel by using combined constitutive equations and dynamic material model. *Mater. Des.* **2014**, *53*, 398–404. [CrossRef]
27. Shen, B.; Deng, L.; Wang, X.Y. A new dynamic recrystallisation model of an extruded Al-Cu-Li alloy during high-temperature deformation. *Mater. Sci. Eng. A* **2015**, *625*, 288–295. [CrossRef]
28. Lin, Y.C.; Li, L.T.; Xia, Y.C.; Jiang, Y.Q. Hot deformation and processing map of a typical Al–Zn–Mg–Cu alloy. *J. Alloys Compd.* **2013**, *550*, 438–445. [CrossRef]
29. Wang, Z.Y.; Zhang, K.S.; Song, Y.Q.; Ali, R.A.; Chen, W.L.; Wang, X.X. Constitutive behavior and microstructural evolution of 2060 Al–Li alloy under high strain rate: Experiment and simulation. *Mater. Sci. Eng. A* **2022**, *844*, 143048. [CrossRef]
30. Attarilar, S.; Gode, C.; Mashhuriazar, M.H.; Ebrahimi, M. Tailoring twist extrusion process; the better strain behavior at the lower required loads. *J. Alloys Compd.* **2021**, *859*, 157855. [CrossRef]
31. Yi, J.; Wang, Z.H.; Liu, Z.W.; Zhang, J.M.; He, X. FE analysis of extrusion defect and optimization of metal flow in porthole die for complex hollow aluminum profile. *Trans. Nonferrous Met. Soc. China* **2018**, *28*, 2094–2101. [CrossRef]
32. Jiang, J.F.; Wang, Y.; Liu, Y.Z.; Xiao, G.F.; Li, H. Microstructure and mechanical properties of 7005 aluminum alloy processed by one-pass equal channel reciprocating extrusion. *Trans. Nonferrous Met. Soc. China* **2021**, *31*, 609–625. [CrossRef]

materials

MDPI

Article

In-Situ Synchrotron HEXRD Study on the Micro-Stress Evolution Behavior of a Superalloy during Room-Temperature Compression

Hao Wang [1,*], Ruolan Tong [2], Guangxu Liu [1], Aixue Sha [1], Lin Song [2,*] and Tiebang Zhang [2]

[1] Beijing Institute of Aeronautical Materials, AECC, Beijing 100095, China
[2] State Key Laboratory of Solidification Processing, Northwestern Polytechnical University, Xi'an 710072, China
* Correspondence: whbiam@163.com (H.W.); songlin@nwpu.edu.cn (L.S.)

Abstract: The residual stress generated during heat treatment of nickel-base superalloys will affect their service performance and introduce primary cracks. In a component with high residual stress, a tiny amount of plastic deformation at room temperature can release the stress to a certain extent. However, the stress-releasing mechanism is still unclear. In the present study, the micro-mechanical behavior of the FGH96 nickel-base superalloy during room temperature compression was studied using in situ synchrotron radiation high-energy X-ray diffraction. The in situ evolution of the lattice strain was observed during deformation. The stress distribution mechanism of grains and phases with different orientations was clarified. The results show that at the elastic deformation stage, the (200) lattice plane of γ' phase bears more stress after the stress reaches 900 MPa. When the stress exceeds 1160 MPa, the load is redistributed to the grains with their <200> crystal directions aligned with the loading direction. After yielding, the γ' phase still bears the main stress.

Keywords: FGH96 superalloy; in situ synchrotron HEXRD; load partitioning; room-temperature compression

Citation: Wang, H.; Tong, R.; Liu, G.; Sha, A.; Song, L.; Zhang, T. In-Situ Synchrotron HEXRD Study on the Micro-Stress Evolution Behavior of a Superalloy during Room-Temperature Compression. *Materials* **2023**, *16*, 3761. https:// doi.org/10.3390/ma16103761

Academic Editor: Daniela Kovacheva

Received: 16 April 2023
Revised: 8 May 2023
Accepted: 15 May 2023
Published: 16 May 2023

1. Introduction

Nickel-based superalloys are widely used in aerospace and aeronautical industry for their high strength, excellent creep resistance, fatigue resistance, and corrosion resistance [1,2]. Powder metallurgy (PM) nickel-based superalloys with a high volume fraction of γ' strengthening phase are used for the turbine disks on aero-engines. However, in the large-scale components, the uneven temperature distribution during heat treatment causes significant residual stress, which has a significant impact on the dimensional stability of disks during the subsequent machining and service process. Therefore, the distribution and evolution mechanisms of internal stress in PM superalloy components have always been a concern of researchers.

There are three types of residual stress [3]. Type I is macro residual stress, which is caused by uneven plastic deformation within the whole part. Type II is intergranular residual stress and type III is intragranular residual stress, both of which are micro-stresses. They are related to the deformation incompatibility between grains and lattice defects (vacancies, interstitial atoms, dislocations, etc.). PM nickel-based superalloy components usually contain a high level of residual stress after forging and heat treatment [4–6], which has a negative effect on the dimension stability and fatigue life of the component. However, pre-deformation could improve fatigue performance of the materials. Through the evolution of different types of texture in the pre-deformed Al-Cu-Li alloy, the strong Gaussian texture aided the reduction of the fatigue crack growth rate and increased the damage tolerance [7]. In magnesium alloy AZ31, $\{10\bar{1}2\}$ twins were introduced by pre-compression deformation, which improved the fatigue performance of the sample [8]. The residual

compressive stress increased the effective fatigue threshold, inhibited crack propagation, and prolonged the fatigue life of the material [9]. Since annealing (which will introduce uneven cooling as well) cannot effectively lower the residual stresses inside the γ/γ' alloy turbine disk, pre-spinning is usually used in industry to release and redistribute residual stress in order to obtain a better service stability and durability. It was found that the micro plastic deformation during pre-spinning can effectively lower residual stresses of the turbine disk [10], which is due to the internal stress evolution caused by the variation of interplanar spacing during deformation. Therefore, it is necessary to accurately measure the micro stress and strain during cold deformation.

In addition to neutron diffraction, synchrotron X-ray diffraction is a reliable method for accurately measuring the interplanar spacing. In particular, synchrotron radiation high-energy X-ray diffraction has a higher angular resolution, which has irreplaceable advantages in accurate determination of cell parameters. Coakley et al. [11] measured the lattice strain evolution during tensile tests of a polycrystalline nickel-base superalloy and found that the strain transferred to {220}γ after initial yielding of {200}. In the meantime, the strain was transferred from γ phase to γ' phase. The two phases deformed together afterwards. Ma et al. [12] evaluated the load distribution of grains/phases with different orientations using in situ loading of a superalloy and obtained the critical shear stress of each phase. Goodfellow et al. [13] found that the stress had an intergranular distribution under low loads and an interphase distribution under high loads. The large lattice misfit resulted in the initiation of interphase load distribution under low stress. Prasad et al. [14] analyzed the diffraction data of six {hkl} planes during tensile deformation and found that the dislocation density in the additive-manufactured crack-free Hastelloy was higher than that in the forged alloy. The proportion of screw dislocation was higher. Stress distribution behavior is closely related to the microstructures and volume fraction of γ' strengthening phases, which is of great significance for revealing the deformation mechanism of precipitation strengthening superalloys. However, the relevant reports are still insufficient.

In this paper, compression experiments of a PM nickel-base superalloy at room temperature were carried out. The behavior of internal stress accumulation and stress distribution during micro plastic deformation was revealed by in situ synchrotron radiation X-ray diffraction. This work can offer a useful reference for improving the dimension stability and fatigue life of superalloy turbine disk by revealing the internal stress distribution.

2. Experiment

The FGH96 superalloy billet was prepared through the PM method. The chemical composition (in wt. %) of FGH96 superalloy is shown in Table 1. The FGH96 alloy powders (<270 mesh) were consolidated by hot isostatic pressing (HIP) at 1170 °C and a stress condition of 140 MPa/5 h. The HIPed ingot was then hot extruded and isothermal forged at subsolvus temperatures. After forging, the pancake was heat treated at 1160 °C for 4 h for solid solution treatment, and then aged at 760 °C for 16 h, followed by air cooling. The microstructure of the aged ingot was observed in the optical microscope and scanning electron microscope (SEM). Samples were prepared by grinding and chemical polishing. Cylinders with a diameter of 4 mm and a height of 8 mm were machined from the ingot for in situ compression tests. In situ high energy synchrotron X-ray diffraction (HEXRD) measurement was conducted in the Deutsches Elektronen-Synchrotron (DESY) in Hamburg, utilizing the P07EH3 beamline of Helmholtz- Zentrum Geesthacht at PETRA III, with a beam size of 0.4 × 0.4 mm^2 and a beam energy of 100 KeV (wave length 0.124 Å). The schematic diagram of the experimental device is shown in Figure 1. The longitudinal direction (LD, $\varphi = 0°$) is parallel to the load axis and cylinder axis. The transverse direction (TD, $\varphi = 90°$) is perpendicular to the load axis. At room temperature, the cylinder was compressed, with a strain rate of 10^{-3} s^{-1} and unloaded at 5.4% strain.

Table 1. Chemical composition (wt. %) of the FGH96 superalloy.

Co	Cr	Mo	W	Al	Ti	Nb	C	B	Zr	Ni
12.9	15.7	4.0	4.0	2.1	3.7	0.7	0.05	0.03	0.05	Balance

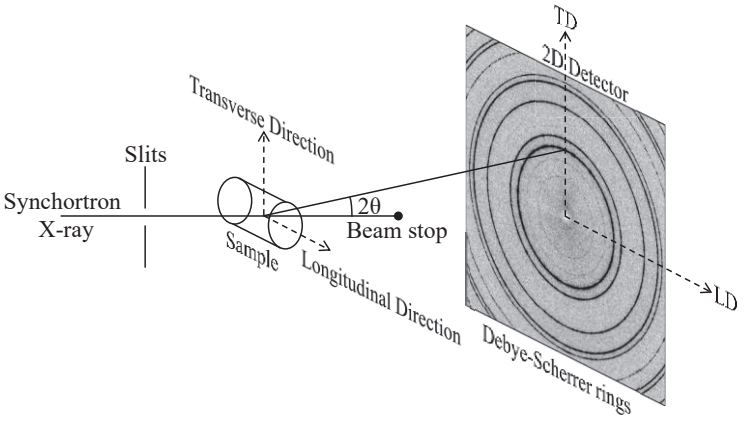

Figure 1. Schematic diagram of the in-situ compression HEXRD experimental device.

The diffraction images were recorded on a two-dimensional detector. Debye–Scherrer diffraction rings were unrolled by FIT2D software and integrated along the LD/TD within the range of $\pm 10^{\circ}$ into a series of one-dimensional XRD patterns. Matlab software was used to fit diffraction peaks according to the pseudo-voigt function, which also calculated the peak position, full width at half maximum (FWHM), and peak intensity of each {hkl} reflection. The corresponding interplanar spacing d_{hkl} was calculated according to Bragg's Law:

$$d_{\mathrm{hkl}} = \lambda / 2 \sin \theta_{\mathrm{hkl}} \tag{1}$$

where λ (0.124 Å) is the wavelength and $2\theta_{\mathrm{hkl}}$ is the diffraction angle of the X-ray. The lattice strain $\varepsilon_{\mathrm{hkl}}$ was then calculated as:

$$\varepsilon_{\mathrm{hkl}} = \left(d^1_{hkl} - d^0_{hkl} \right) / d^0_{hkl} \tag{2}$$

where d^0_{hkl} and d^1_{hkl} are the interplanar spacing d of the {hkl} lattice planes in the conditions of initial stress-free state and loading state, respectively.

The very similar lattice constants of γ and γ′ phases generated overlapped diffraction peaks, which made it difficult to determine the peak positions and lattice misfit. The lattice spacing d_{hkl} of superlattice reflections was used to derive the parallel high exponential fundamental {2h2k2l} reflections. The positions of γ-{2h2k2l} reflections were obtained by fixing the position of γ′-{2h2k2l} reflections and deconvolution. In order to ensure the reliability of the fitting process, the integral intensities of γ and γ′ peaks, which are proportional to the volume fractions of the corresponding phases, were considered as constants, according to the following equation [12]:

$$\frac{I^{\gamma'}_{2h2k2l}}{I^{\gamma}_{2h2k2l}} = \frac{\left| F^{\gamma'}_{2h2k2l} \right|^2}{\left| F^{\gamma}_{2h2k2l} \right|^2} \frac{v_f}{\left(1 - v_f \right)} \tag{3}$$

where I_{hkl} is the intensity of {hkl} peak and v_f is the volume fraction of γ′ phase, measured as 0.4. F_{hkl} is the structural factor determined by Equation (4):

$$F_{hkl} = b_c e^{2\pi \mathrm{i}(0\mathrm{h}+0\mathrm{k}+0\mathrm{l})} + b_f (e^{2\pi \mathrm{i}(0.5\mathrm{h}+0.5\mathrm{k}+0\mathrm{l})} + e^{2\pi \mathrm{i}(0.5\mathrm{h}+0\mathrm{k}+0.5\mathrm{l})} + e^{2\pi \mathrm{i}(0\mathrm{h}+0.5\mathrm{k}+0.5\mathrm{l})}) \tag{4}$$

where b_c and b_f are the scattering lengths of corner atoms (primarily Al atoms) and face atoms (primarily Ni atoms), which are 0.35×10^{-12} cm and 1.03×10^{-12} cm, respectively. For the γ phase, it is assumed that $b_c = b_f = b_{Ni}$. The value of lattice misfit was calculated as:

$$\delta = \frac{2\left(a_{\gamma'} - a_{\gamma}\right)}{a_{\gamma'} + a_{\gamma}} \quad (5)$$

where a_{γ} and $a_{\gamma'}$ are the lattice constants of the γ and γ′ phases, respectively.

3. Results

3.1. Microstructure and Compression Curves of FGH 96 Superalloy

The microstructure of the superalloy sample used for in situ compression tests is shown in Figure 2a,b, which displays the overall grain statistics observed by an optical microscope and the distribution of γ′ precipitates observed by SEM. Figure 2a shows a fine-grain microstructure with an average grain size of approximately 30 μm. Two kinds of γ′ precipitate exist—namely, the secondary γ′ precipitates nucleated during cooling after solution and tertiary γ′ precipitates formed and grown during the aging treatment. However, there was no primary γ′ precipitates phase located at the grain boundary. The volume fraction of γ′ precipitates was approximately 40%. Figure 2c is the diffraction pattern obtained by synchrotron radiation measured before the compression. Since a number of peaks of the $L1_2$-γ′ phase are overlapped with the peaks of fcc-γ, most diffraction rings are labeled as the common reflections of γ′/γ. However, a few superlattice diffractions, such as $(100)_{\gamma'}$ and $(110)_{\gamma'}$, can also be clearly seen on the pattern. Some other peaks exhibit higher intensity, for example (111) and (200), owing to the overlap effect of γ and γ′ phases. The fine grain size of the microstructure can also be reflected by the integrity of the diffraction rings in Figure 2c, indicating a good homogeneity of the microstructure.

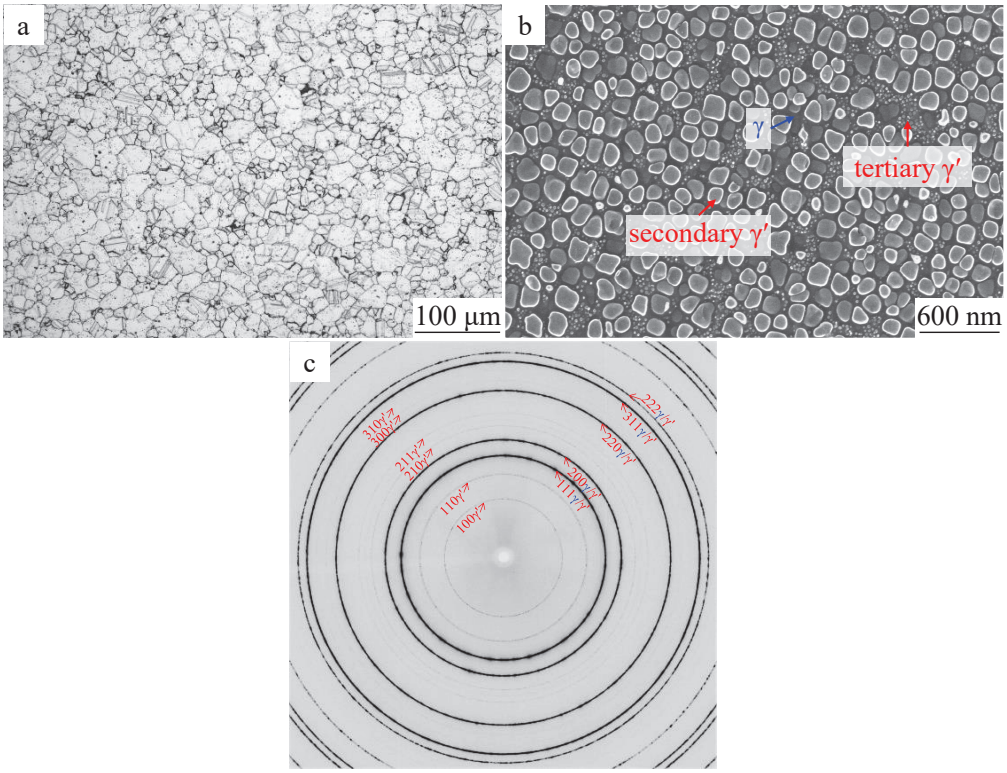

Figure 2. (**a**) Optical image of FGH 96 alloy after forging; (**b**) backscattered electron SEM image of the secondary and tertiary γ′ precipitates; (**c**) synchrotron radiation diffraction pattern of the microstructure before deformation.

The true stress-strain curve of FGH96 superalloy obtained by in situ synchrotron radiation compression is shown in Figure 3. The stress increased rapidly in the elastic stage, while a specific yield point is difficult to obtain. The red curve in Figure 3 shows the evolution of the work hardening rate. When the strain reached 1%, the work hardening rate rapidly decreased, and the sample yielded at about 980 MPa. After that, the strain increased rapidly with the increase in stress while the work hardening rate almost remained constant during the plastic deformation. The maximum true strain was 5.4% and the corresponding true stress was 1435 MPa.

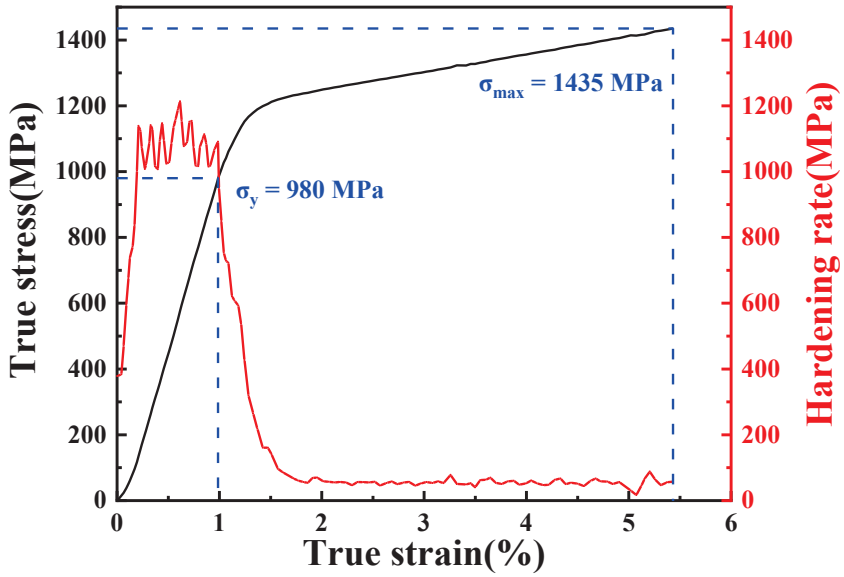

Figure 3. True stress-true strain curve obtained in the in situ compression measurement at room temperature.

3.2. Evolution of the Reflections during the In-Situ Compression Test

The unrolled two-dimensional X-ray diffraction patterns of the alloy before and after compression are shown in Figure 4a,b, respectively. The reflections of (100), (110), (210), and (211) planes are superlattice diffractions, which correspond to the γ′ phase. The intensity of $(210)_{\gamma'}$ and $(211)_{\gamma'}$ diffraction peaks decreased after deformation. The intensity of (111), (200), (220), (311), and (222) diffraction peaks was much higher than the other lattice planes, indicating that the lattice constants of the γ and γ′ phases are almost the same. According to the superlattice diffraction pattern of the γ′ phase and the peak separation processing, the lattice constants of the γ and γ′ phase were determined a_{γ} = 3.587 ± 0.005Å and $a_{\gamma'}$ = 3.589 ± 0.005Å, respectively. Thus, the lattice misfit was 0.056 ± 0.005%. Comparing Figure 4a,b, the width of these diffraction peaks increased significantly after deformation, indicating that plastic deformation caused a large residual strain. It should be noted that the phase constitution (the volume fractions of γ and γ′ phases) had not changed before and after deformation.

Figure 5a shows the evolution of the diffraction peaks during room temperature compression. During loading, an obvious deviation of the peak position from the normal value can be observed. After unloading, the diffraction peaks almost returned to being symmetrical, but the full width at half maximum (FWHM) of the peaks did not return to the original state (Figure 5d). In addition, the 2θ values of peaks also shifted (Figure 5b). Due to the effect of residual stress caused by the plastic strain, the interplanar spacings decreased and the diffraction peaks broadened, which were obviously caused by dislocation movement. A certain number of dislocations made the interplanar spacing of the slip planes unable to fully recover to the initial state, that is, a certain amount of the lattice stress caused by the absence of semi atom plane of edge dislocations remained in the microstructure [15]. Elastic distortion appeared around the dislocation line. When a large number of dislocations were activated, the accumulated lattice distortion caused the

interplanar spacing to deviate from the normal value, and the FWHM increased at the same time. During compression, the shape and position of the diffraction peaks changed significantly, and the asymmetry gradually increased, which is probably due to the increase in the γ/γ' misfit. Specifically, the diffraction peak intensity, 2θ angle, and the FWHM data obtained by fitting in Figure 5b–d are analyzed as follows.

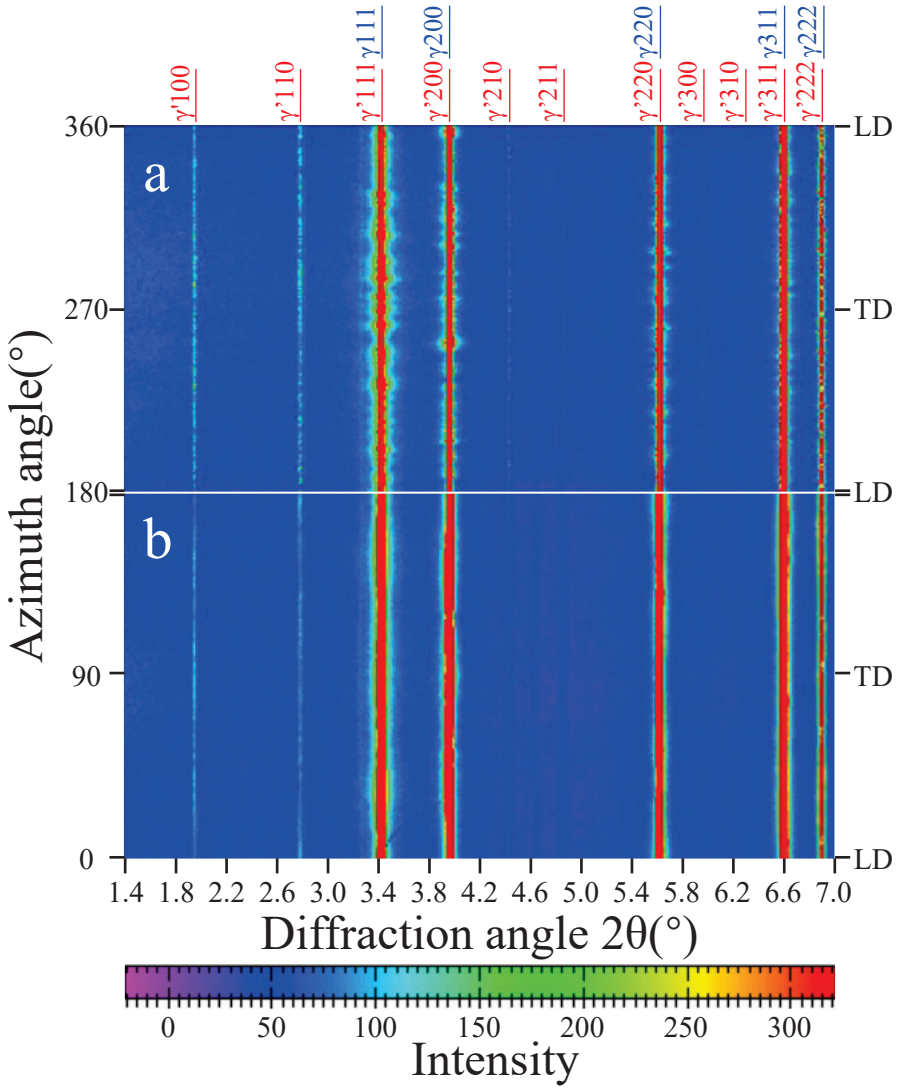

Figure 4. Unrolled two-dimensional diffraction rings of the sample (**a**) before and (**b**) after compression at room temperature.

In the elastic deformation stage, with the increase in stress, the lattice plane spacings decreased while the 2θ angle increased. Meanwhile, the peak position gradually shifted to the right, as shown in Figure 5b. The shift of (220) and (311) diffraction peaks was the largest while the shift of (111) diffraction peaks was relatively small. During the stable plastic deformation stage, the position of the diffraction peak changed gradually, which showed that the influence caused by elastic distortion is increasingly apparent. After unloading, the values of 2θ angle decreased rapidly, whereas it was still higher than that before the deformation. Generally, the diffraction peak intensity is related to the preferred orientation. In Figure 5c, the diffraction intensity decreased at the elastic deformation stage, whereas it fluctuated at the beginning of the plastic deformation, and then continued to decrease slowly at the stable plastic deformation stage. Specifically, the intensity of (111) diffraction peak decreased significantly after unloading while the intensity of other diffraction peaks increased. Due to the different deformation ability of γ and γ' phases, the asymmetry of

diffraction peaks increased rapidly and even double peaks appeared. Therefore, single-peak fitting cannot fully satisfy the practical situation. Thus, further separation of single γ and γ′ diffraction peaks is necessary, which will be discussed in Section 4.2.

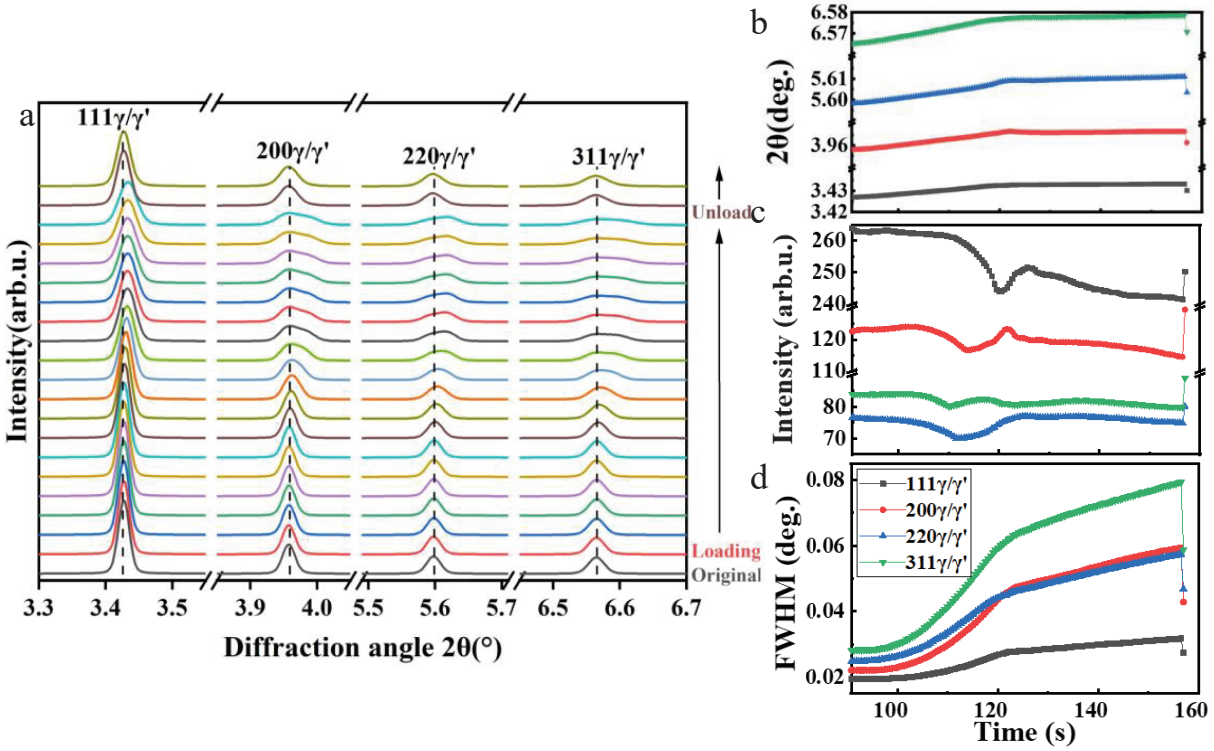

Figure 5. Evolution of one-dimensional diffraction pattern during compression: (**a**) overall one-dimensional HEXRD curve; (**b**) offset 2θ value; (**c**) peak intensity; (**d**) FWHM.

The evolution of FWHM with time during compression is shown in Figure 5d. After plastic deformation, the FWHM values of (111), (200), (220), and (311) planes increased by 21%, 44%, 36%, and 49%, respectively, indicating the dislocation density in the alloy increased rapidly and the defects accumulated continuously [16]. The difference of the widening rate of each lattice plane was obviously caused by the anisotropy of the crystal structure. As the dislocations were fully located on the close-packed lattice plane (111) with the largest slip distance, the increase in FWHM of the (111) plane was not as significant as the other planes. Since the dislocations were partially located on other lattice planes, the misfit degree of the atoms on the adjacent lattice planes was higher than that on the glide plane, resulting in a faster widening rate of the peaks. In addition, the increase in the peak width of (311) lattice plane was the largest, suggesting that the dislocation slip had the strongest influence on its interplanar spacing. This phenomenon can be used as a basis for analyzing the deformation degree of cubic structures.

4. Discussion

4.1. Intergranular Microstress Evolution

The true stress-lattice strain evolution during compression is shown in Figure 6a. The lattice strain value along the longitudinal direction (LD) was negative. For the convenience of the discussion, the absolute value will be considered in the following part. The deformation process can be divided into three stages: the elastic deformation stage, the elasto-plastic transition stage, and the stable plastic deformation stage. In the first stage, the linear response between the lattice strain and true stress was observed for the (111), (200), (220), and (311) planes. Due to the strong anisotropy of the γ′ phase, the <200> direction was the most likely to generate elastic strain, while the <111> direction had the largest stiffness, meaning that its strain was smaller under the same stress conditions. The elastic

stiffness of <220> and <311> directions was moderate, which is consistent with the previous results [13,17]. At the stress level of 900 MPa, the (111) reflection exhibited a downward deviation first and other lattice planes followed immediately, whereas they still remained in the elastic deformation stage.

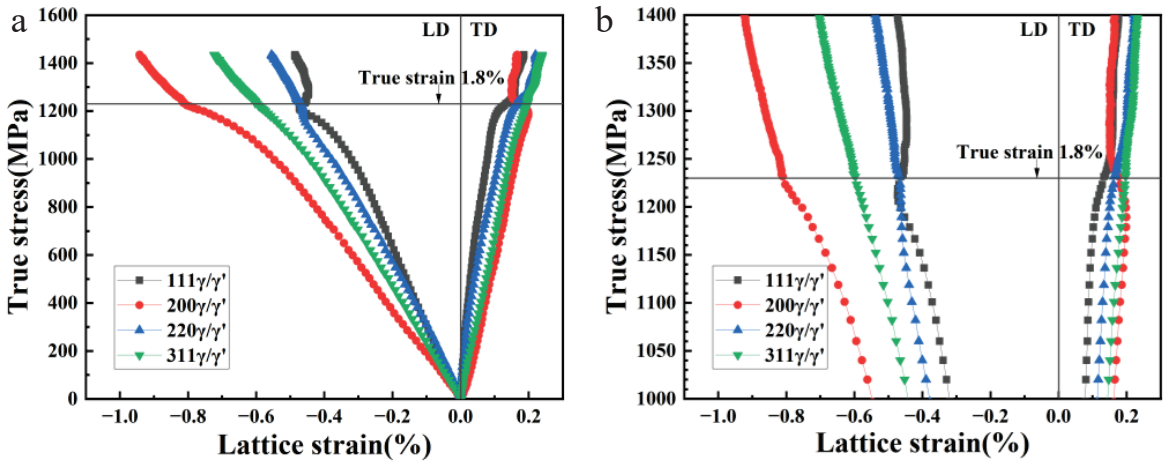

Figure 6. True stress-lattice strain curve during room temperature compression: (**a**) overall evolution of each lattice strain with true stress in the whole deformation process; (**b**) evolution of each lattice strain above 1000 MPa.

In the second stage, the (220) reflection firstly yielded at 1160 MPa and then the (111) reflection yielded at 1200 MPa. The gradient of the curve changed dramatically in this period. Generally, the (111) reflection yielded first because it was subjected to the maximum stress. However, due to the effect of plastic anisotropy, the Schmidt factor for the a/2<110> slip in the grains with their (100) and (110) planes perpendicular to the LD was much larger than those with their (111) planes perpendicular to the LD. Therefore, the latter ones yielded later and bore the transferred load [18]. Figure 6b shows the enlarged view of the lattice plane evolution above 1000 MP. After the yielding of (220) and (111) planes, the (200) plane bore a higher load and the lattice strain increased to a more negative value, showing a downward offset of the (200) curve. The behavior of the (311) reflection always remained close to linear, which was consistent with previous studies [19–21].

The third stage started at 1230 MPa. As shown in Figure 6b, an inflection point appeared in each lattice strain, and the corresponding true strain at this moment was 1.8%. The upward deviation of the curve indicated that obvious plastic deformation occurred. The lattice strain of (111) reflection along the LD direction and the (200) reflection along the transverse direction (TD) showed an obvious decrease. This phenomenon might be due to the fact that the slip systems of the grains in favorable orientations were activated [22]. The dislocations began to slip, and part of the internal stress was released, resulting in lattice strain reduction. Taking the (111) lattice plane as an example, it can be seen from the detour of the strain curve that the absolute value of the lattice strain was about 0.5% when the strain reached 5.4%, which was slightly higher than the absolute value of the maximum elastic strain. This indicates that although the internal stress of the sample decreases for a while at the occurrence of plastic deformation, it soon shifts to an increasing trend. From the perspective of the deformation mechanism, the strain releasing effect caused by dislocation slip only existed at the initial stage of plastic deformation. The subsequent rise of the lattice strain indicated that dislocations were re-blocked and pinned after a certain distance of gliding, which corresponds to the macroscopical work hardening. This is also reflected in the compression stress-strain curve, where obvious work hardening occurs after yielding (Figure 3). Considering the microstructure of the alloy, this is due to the pinning effect of secondary and tertiary γ' particles. Dislocations were blocked at the γ/γ' phase interface and were thus unable to propagate for a long distance. Only when the load continued to

rise to make the dislocations trapped at the interface slip into the interior of the γ' phase could the strain be relaxed again. In addition, when the strain was 0.44%, the absolute value of the γ/γ' lattice strain reached the minimum, which indicated that the lattice strain had been reduced to a lower level by micro-plastic deformation (dislocation slip). The corresponding engineering strain was 2.9%. It can be considered that if the sample was unloaded at this moment, the internal stress in the sample would be released to some extent.

4.2. Interphase Microstress Evolution

Although the diffraction peaks of γ and γ' phases overlapped, different orientations of the phases would bear varying loads, which further complicated the deformation mechanism. Therefore, the diffraction peaks of the γ and γ' phases should be discussed separately. Figure 7a shows the fitted true stress-lattice strain curves of the (200) and (220) diffraction peaks of γ and γ' phases. Since the background has a great influence on the diffraction peaks of $(100)_{\gamma'}$ and $(110)_{\gamma'}$, the fitting results with a confident degree above 99.5% are selected. In the linear–elastic stage, the curves of the γ and γ' phases almost coincided, indicating that γ and γ' had a similar stiffness. As shown in Figure 7a, $(220)_{\gamma}/(220)_{\gamma'}$ yielded first and $(200)_{\gamma}/(200)_{\gamma'}$ bore higher stress, and, thus, the lattice strain with $(200)_{\gamma}/(200)_{\gamma'}$ orientation increased rapidly. When the stress reached 900 MPa, the γ phase in the direction of $(200)_{\gamma}$//LD was more prone to plastic deformation than the γ' phase, indicating that the dislocations were more likely to slip in the softer γ phase. At the same time, the γ' phase bore a higher load and obvious interphase load redistribution occurred. On the (220) lattice plane, γ and γ' phases had a nearly consistent deformation. After yielding, the γ phase shared the load with the γ' phase, and the two phases deformed almost at the same strain rate. In the plastic stage, $(200)_{\gamma}$ yielded first, resulting in an upward migration of true stress-lattice strain curve, while $(200)_{\gamma'}$ bore a higher load and continued to deform. In the TD direction, $(200)_{\gamma}$ yielded at 1200 MPa, and then its lattice strain decreased with the increase in stress, and the curve rebounded. It could be due to this that the dislocations slipped from γ to γ' and then started to slip again, which redistributed the stress [12]. At the stable plastic deformation stage after 1230 MPa, the strain hardly increased and the stress–lattice strain gradient of (220)γ was large, indicating that more load was allocated to the γ' phase.

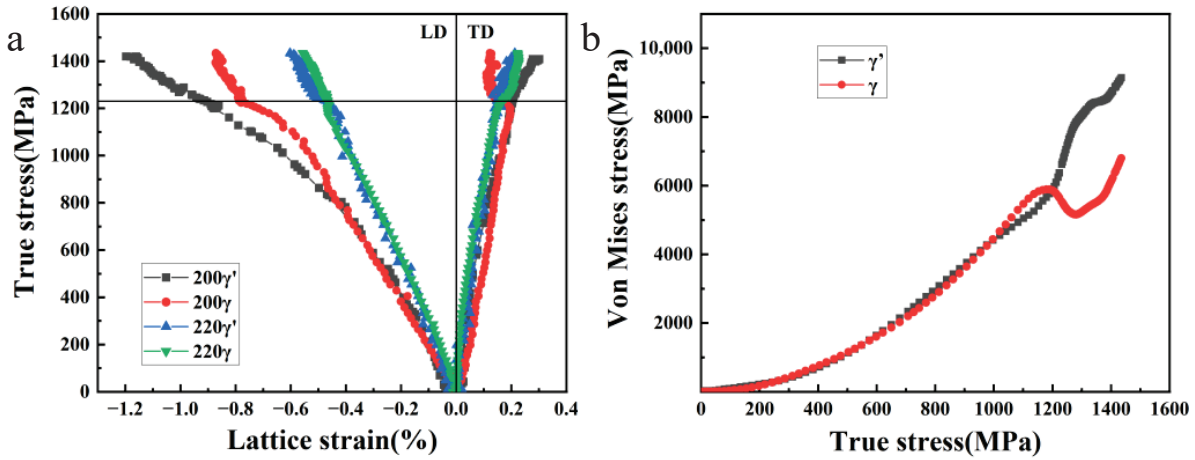

Figure 7. (**a**) True stress–lattice strain curves of (200) and (220) diffraction peaks of the γ and γ' phases; (**b**) relationship between Von Mises equivalent stress and true stress of the γ and γ' phases.

Von Mises equivalent stress [23,24] can be used to observe the stress changes between γ and γ' phases:

$$\sigma_{VM} = \frac{1}{\sqrt{2}}\left[(\sigma_{11}-\sigma_{22})^2 + (\sigma_{22}-\sigma_{33})^2 + (\sigma_{11}-\sigma_{33})^2\right] \quad (6)$$

$$\sigma_{11} = \frac{E}{1+\vartheta}\varepsilon_{11} + \frac{\vartheta E}{(1+\vartheta)(1-2\vartheta)}(\varepsilon_{11}+\varepsilon_{22}+\varepsilon_{33}) \quad (7)$$

$$\sigma_{22} = \sigma_{33} = \frac{E}{1+\vartheta}\varepsilon_{22} + \frac{\vartheta E}{(1+\vartheta)(1-2\vartheta)}(\varepsilon_{11}+\varepsilon_{22}+\varepsilon_{33}) \quad (8)$$

where σ_{VM} is Von Mises effective stress. σ_{11} and σ_{22} are the principal stresses along the LD and TD, respectively. E is the elastic constant of diffraction, ϑ is Poisson's ratio, ε_{22} and ε_{33} is the lattice strain for LD and normal direction (ND), respectively. ε_{22} equals to ε_{33}.

Poisson's ratio is the average value of the lattice strain ratio at TD and LD. The lattice plane (220) was selected to calculate the stress of γ' and γ phases, as shown in Figure 7b. Although fitting error makes the curve fluctuate to some extent, it still reflects the evolution trend of load bearing on the γ and γ' phases. During the elastic stage, there was almost no difference in the load distribution between the two phases. The equivalent stress in the two phases was concordant. When the stress reached 1200 MPa, the stress on the γ phase decreased and transferred to the γ' phase. During the subsequent plastic deformation stage, the γ' phase bore higher stress continuously.

5. Conclusions

The deformation and stress partitioning mechanisms of PM FGH96 nickel-based superalloy during small strain compression at room temperature were investigated using in situ HEXRD technique. It was found that the (111) lattice plane had the maximum stiffness while (200) had the minimum. Between the γ/γ' grains, when the applied stress reached 1160 MPa, the (220) lattice plane yielded first, and then the load was redistributed to grains with the <200> crystal directions aligned with the loading direction. Between the γ and γ' phase, when stress was above 900 MPa, the $(200)_{\gamma'}$ bore the main stress; when the stress reached 1200 MPa, the γ phase yielded first, and the stress was allocated to the γ' phase. When the engineering strain was 2.9%, the lattice strain of (111) reduced to 0.44%, so it can be considered that the large pre-existing internal stress of the superalloy turbine disk can be released if unloaded at this strain.

Author Contributions: Methodology, H.W.; Validation, G.L.; Investigation, G.L.; Resources, L.S.; Data curation, H.W. and R.T.; Writing—original draft, R.T.; Writing—review & editing, H.W.; Visualization, L.S.; Supervision and Review, T.Z.; Project administration and Review, A.S. All authors have read and agreed to the published version of the manuscript.

Funding: This research was funded by the National Natural Science Foundation of China (contract No. 51971175).

Institutional Review Board Statement: Not applicable.

Informed Consent Statement: Not applicable.

Data Availability Statement: Data will be available on request.

Acknowledgments: This work was supported by the National Natural Science Foundation of China (contract No. 51971175). The authors appreciate the kind help of Andreas Stark at PETRA III P07 Hatch in DESY on the in-situ measurements.

Conflicts of Interest: The authors declare no conflict of interest.

References

1. Pollock, T.M. Alloy design for aircraft engines. *Nat. Mater.* **2016**, *15*, 809–815. [CrossRef]
2. Reed, R.C. *The Superalloys Fundamentals and Applications*; Cambridge University Press: Cambridge, UK, 2006.
3. Chen, W.; Voisin, T.; Zhang, Y.; Forien, J.B.; Spadaccini, C.M.; McDowell, D.L.; Zhu, T.; Wang, Y.M. Microscale residual stresses in additively manufactured stainless steel. *Nat. Commun.* **2019**, *10*, 4338. [CrossRef]
4. Zhang, Z.; Feng, Y.; Tan, Q.; Zou, J.; Li, J.; Zhou, X.; Sun, G.; Wang, Y. Residual stress distribution in Ni-based superalloy turbine discs during fabrication evaluated by neutron/X-ray diffraction measurement and thermomechanical simulation. *Mater. Des.* **2019**, *166*, 107603. [CrossRef]

5. Imbrogno, S.; Rinaldi, S.; Umbrello, D.; Filice, L.; Franchi, R.; Del Prete, A. A physically based constitutive model for predicting the surface integrity in machining of Waspaloy. *Mater. Des.* **2018**, *152*, 140–155. [CrossRef]
6. Liu, X.; Luzin, V.; Qin, H.; Bi, Z.; Li, M.; Liu, Y.; Sun, K.; Chen, D. Mapping of three-dimensional residual stresses by neutron diffraction in nickel-based superalloy discs prepared under different quenching conditions. Mater. *Today Commun.* **2022**, *32*, 103876.
7. Liu, F.; Liu, Z.; Liu, M.; Hu, Y.; Chen, Y.; Bai, S. Analysis of empirical relation between microstructure, texture evolution and fatigue properties of an Al-Cu-Li alloy during different pre-deformation processes. *Mater. Sci. Eng. A* **2018**, *726*, 309–319. [CrossRef]
8. Huang, G.S.; Li, J.H.; Han, T.Z.; Zhang, H. Improving low-cycle fatigue properties of rolled AZ31 magnesium alloy by pre-compression deformation. *Mater. Des.* **2014**, *58*, 439–444. [CrossRef]
9. Du, B.P.; Li, N. The influence of microstress on the effective fatigue threshold. *Int. J. Fatigue* **1989**, *11*, 43–50.
10. Longuet, A.; Dumont, C.; Georges, E. Advanced modeling tools for processing and lifing of aeroengine components. In *Superalloys 2020*; The Minerals, Metals & Materials Series; ASM International: Materials Park, OH, USA, 2020; pp. 3–15.
11. Coakley, J.; Dye, D. Lattice strain evolution in a high volume fraction polycrystal nickel superalloy. *Scr. Mater.* **2012**, *67*, 435–438. [CrossRef]
12. Ma, S.; Rangaswamy, P.; Majumdar, B.S. Microstress evolution during in situ loading of a superalloy containing high volume fraction of γ' phase. *Scr. Mater.* **2003**, *48*, 525–530. [CrossRef]
13. Goodfellow, A.J.; Kelleher, J.; Jones, N.G.; Dye, D.; Hardy, M.; Stone, H. The effect of Mo on load partitioning and microstrain evolution during compression of a series of polycrystalline Ni-Based superalloys. *Acta Mater.* **2019**, *176*, 318–329. [CrossRef]
14. Prasad, K.; Horita, Y.; Ito, A.; Torizuka, S. In situ synchrotron diffraction study of a crack-free additively manufactured Ni base superalloy. *Scr. Mater.* **2021**, *200*, 113896. [CrossRef]
15. Grant, B.M.B.; Francis, E.M.; Quinta Da Fonseca, J.; Daymond, M.R.; Preuss, M. Deformation behaviour of an advanced nickel-based superalloy studied by neutron diffraction and electron microscopy. *Acta Mater.* **2012**, *60*, 6829–6841. [CrossRef]
16. Liu, T.K.; Wu, G.L.; Liu, C.K.; Nie, Z.H.; Ungár, T.; Ren, Y.; Wang, Y.D. Interface coherency strain relaxation due to plastic deformation in single crystal Ni-base superalloys. *Mater. Sci. Eng. A* **2013**, *568*, 83–87. [CrossRef]
17. Wagner, J.N.; Hofmann, M.; Wimpory, R.; Krempaszky, C.; Stockinger, M. Microstructure and temperature dependence of intergranular strains on diffractometric macroscopic residual stress analysis. *Mater. Sci. Eng. A* **2014**, *618*, 271–279. [CrossRef]
18. Clausen, B.; Lorentzen, T.; Leffersa, T. Self-consistent modelling of the plastic deformation of FCC polycrystals and its implications for diffraction measurements of internal stresses. *Acta Mater.* **1998**, *46*, 3087–3098. [CrossRef]
19. Jaladurgam, N.R.; Li, H.; Kelleher, J.; Persson, C.; Steuwer, A.; Colliander, M.H. Microstructure-dependent deformation behaviour of a low γ' volume fraction Ni-base superalloy studied by in-situ neutron diffraction. *Acta Mater.* **2020**, *183*, 182–195. [CrossRef]
20. Stone, H.J.; Reed, R.C.; Holden, T.M. Determination of the plane specific elastic constants of waspaloy using neutron diffraction. *Scr. Mater.* **1999**, *40*, 353–358. [CrossRef]
21. Wang, Z.; Stoica, A.D.; Ma, D.; Beese, A.M. Diffraction and single-crystal elastic constants of Inconel 625 at room and elevated temperatures determined by neutron diffraction. *Mater. Sci. Eng. A* **2016**, *674*, 406–412. [CrossRef]
22. Lu, Y.; Ma, S.; Majumdar, B.S. Elastic microstrains during tension and creep of superalloys: Results from in situ neutron diffraction. In Proceedings of the International Symposium on Superalloys 2008, Champion, PA, USA, 14–18 September 2008; pp. 553–562.
23. Mises, R.V. Mechanik der festen Körper im plastisch-deformablen Zustand, Nachrichten von der Königlichen Gesellschaftder Wissenschaften zu Göettingen. *Math.-Phys. Kl.* **1913**, *1913*, 582–592.
24. Dieter, G.E.; Bacon, D. *Mechanical Metallurgy*; McGraw-Hill: New York, NY, USA, 1986.

materials

MDPI

Article

Improving Precipitation in Cryogenic Rolling 6016 Aluminum Alloys during Aging Treatment

Xucheng Wang [1,2], Yu Liu [2,3] and Yuanchun Huang [1,2,3,*]

[1] College of Mechanical and Electrical Engineering, Central South University, Changsha 410083, China
[2] State Key Laboratory of High Performance Complex Manufacturing, Central South University, Changsha 410083, China
[3] Light Alloys Research Institute, Central South University, Changsha 410083, China
* Correspondence: ychuang@csu.edu.cn

Abstract: This study systematically investigated the performance and microstructure characterization of cryogenic rolling (CR) and room-temperature rolling (RTR) Al–Mg–Si alloys. The result showed that the hardness of the CR alloys decreased at the early aging stage, but that the hardness of the RTR alloys increased at the early aging stage. Retrogression phenomena were apparent in the CR alloys at the early aging stage. Despite undergoing the same solid solution treatment, a few substructures were still observed in the CR alloys, and the degree of recrystallization in the CR alloys was significantly inferior to that in the RTR alloys. After aging for 50 h, the strength and precipitates' density in the CR 75 alloy were higher than that in the other alloys; this indicated that the substructures were beneficial to precipitation and precipitate growth. A precipitation strength model was employed to illustrate the precipitation contribution at different aging stages. The results showed that the CR 75 alloy obtained the strongest precipitation strengthening.

Keywords: AA6016 plate; cryogenic rolling; aging treatment; substructures; precipitation strengthening

Citation: Wang, X.; Liu, Y.; Huang, Y. Improving Precipitation in Cryogenic Rolling 6016 Aluminum Alloys during Aging Treatment. *Materials* **2023**, *16*, 3336. https://doi.org/10.3390/ma16093336

Academic Editor: Xianfei Ding

Received: 20 March 2023
Revised: 16 April 2023
Accepted: 19 April 2023
Published: 24 April 2023

1. Introduction

Heat-treatable Al–Mg–Si (6xxx) alloys have been widely used in the automotive industry due to their moderate strength, good formability and light weight [1–3]. With further economic growth, the pursuit of outstanding alloy strength has become the focus of the aluminum industry. Numerous methods have been developed to improve the mechanical properties of Al–Mg–Si alloys, such as equal-channel angular pressing (ECAP) [4,5], high-pressure torsion (HPT) [6,7], accumulative roll bonding (ARB) [8,9], friction stir processing [10] and cryogenic rolling (CR) [11,12]. Among these methods, cryogenic rolling has been the most widely accepted for the production of bulk ultrafine-grained (UFG) materials. Compared to room-temperature rolling (RTR), superior mechanical properties can be obtained by cryogenic rolling—this is due to the suppression of recovery and the reservation of dislocations during cryogenic rolling [11].

Although cryogenic rolling can significantly improve materials' properties, it is widely accepted that precipitation strengthening caused by aging treatments still plays an important role in the strength of Al–Mg–Si alloys. The contribution of precipitation strengthening mainly results from the interaction between nanoscale precipitates and dislocations [13,14]. Various cryogenic rolling processes can result in diverse dislocation densities and dislocation structures that prominently affect precipitation. Researchers have shown that high dislocation densities are apt to reduce the supersaturation of matrices to a level that promotes nucleation, but that the attraction of solutes to dislocations could decrease the driving force for nucleation [15,16]. The precipitation sequence in Al–Mg–Si alloys is generally considered as [17–19]: super-saturated solid solution (SSSS) → atomic clusters → GP zones → β'' → β', *U1*, *U2*, B′ → β, Si. A Mg_2Si phase (i.e., β phase) and β'' phase are widely deemed as efficient strengthening precipitates in Al–Mg–Si alloys [14,20,21].

Therefore, understanding information about precipitates during aging treatments is vital in Al–Mg–Si alloys.

Recently, many experts have focused on the interactions between dislocations and precipitates in Al–Mg–Si alloys [14,20,22]. Dislocations are considered to shear the β'' phase [22,23] but bypass the β' phase [23,24]. In an early study [25], the critical shear radius was used as a vital parameter to establish a yield strength model that included inherent strengthening, solution strengthening and precipitation strengthening; this model has been accepted widely in aging treatments. In recent years, other, similar models have also included the influence of microstructural characteristics [26–28]. Hitherto, the precipitation behaviors in Al–Mg–Si alloys have mainly focused on room-temperature deformation and hot deformation [29–31]. In order to greatly improve alloy strength, researchers have mainly focused on the process of "solution treatment + CR + aging treatment" [32–34], and this process improves alloys strength significantly. Superior mechanical properties obtained by low-temperature deformation in Al alloys have been attributed to the complicated effects of multiple strength mechanisms. For 6016 Al alloys, their main application is in manufacturing high-strength Al alloy automotive plates [3,17]. Although the process of "solution treatment + CR + aging treatment" can increase an alloy's strength, the anisotropy brought on by its texture is difficult to reduce in subsequent aging processes. Krishna's research [12] has shown that cryorolled alloys show an enhanced texture index value and a high IPA value, exhibiting enhanced anisotropic behavior compared to RTR-rolled alloys. Higher anisotropy could be harmful to subsequent manufacture processes [1].

Therefore, it is vital to explore processes that can not only improve the alloy's strength, but also reduce the anisotropy caused by the deformation texture; hence, a process of "CR + solution treatment + aging treatment" was designed. Precipitation strengthening is vital after subsequent aging treatments. When CR alloys undergo solution treatments, partial recrystallization can reduce the anisotropy caused by their texture.

In the present work, the aim was to illustrate the superior mechanical properties of CR alloys after aging treatments, to reduce the anisotropy caused by deformation texture and to employ the precipitation model to discuss precipitation strength during aging treatments.

2. Experimental and Theoretical Methods

2.1. Experimental Methods

The materials were twin-cast rolled 6016 alloy plates (4 mm thickness) that had been annealed. The composition of the 6016 alloy is shown in Table 1.

Table 1. Chemical composition of cast-rolled 6016 aluminum.

Element	Si	Fe	Mn	Mg	Cr	Al
wt.%	1.48	0.34	0.16	0.49	0.1	Bal.

One part of the plates was rolled up to a 50% and 75% reduction in thickness at liquid nitrogen temperature (hereafter labeled CR 50 and CR 75). The rolling process was carried out at 0.05 m/s with a 5% reduction in thickness per pass, as shown in Figure 1a,b. For comparison, another part of the plates was rolled with the same thickness reductions at room temperature (hereafter labeled RTR 50 and RTR 75). The CR alloys were immersed in a liquid nitrogen bath (−195 °C) for 30 min before rolling and were immersed in the liquid nitrogen for 2 min after every intermediate rolling pass. The rolled plates were solution heat-treated at 540 °C for 1 h and quenched in water at room temperature; all alloys were subsequently artificially aged at 160–200 °C for various periods of time. A schematic illustration of the whole process is shown in Figure 1c,d.

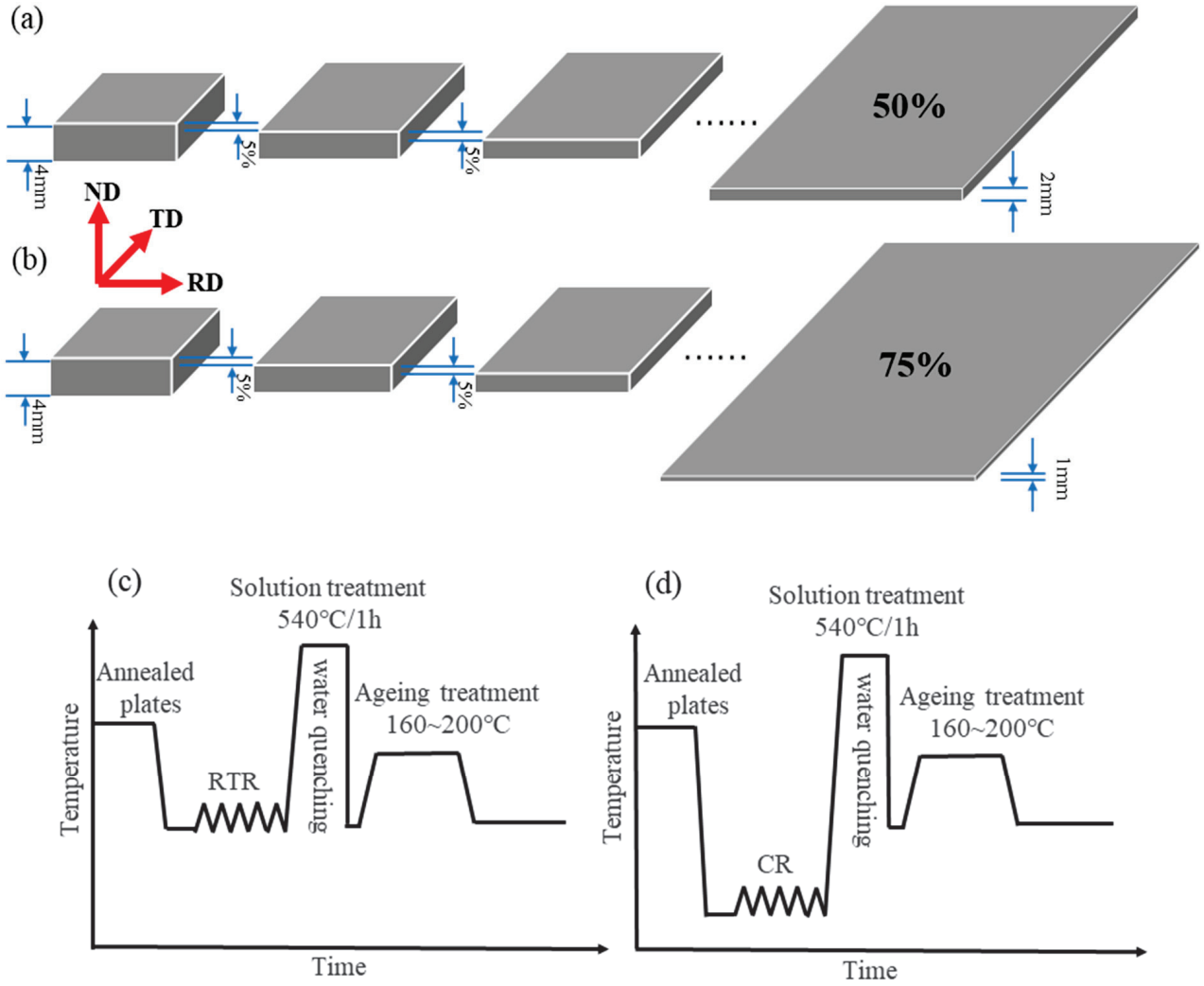

Figure 1. The rolling process of the 6016 aluminum alloy at (**a**) 50 % and (**b**) 75%; The process diagram for the (**c**) RTR and (**d**) CR.

The microhardness of the alloys was tested with a load of 100 g and a dwell time of 15 s, excluding the maximum and minimum values. Quantitative X-ray diffraction (XRD, Cu Kα radiation, scan rate: 5°/min, scan step size: 0.02°, scan angle range: 30°–80°) measurements were performed with a D/max 2550 VB. Transmission electron microscopy (TEM) specimens were polished to a thickness of 50–80 μm and then punched into a Φ3 mm disc. The foil was subjected to twin-jet electropolishing with a mixed solution of 30% nitric acid and 70% methanol at −25 °C, at a subsequent voltage of 20 V. TEM observations were conducted on a Tecnai G2 F20 S-TWIN TMP operated with an accelerating voltage of 200 kV and a variable operating current in the range of 104–108 mA. Electron back-scattered diffraction samples were taken from the ND-RD section of the plate, and the microstructure was characterized by a Sirion 200 field emission scanning electron microscope (FEI Corporation, Valley City, ND, USA). The Electron Back-Scattered Diffraction (EBSD) samples were mechanically ground, followed by electro-polishing in an ethanol–perchloric acid solution (ratio of ethanol to perchloric acid of 9:1) at a temperature of −20 °C and a voltage of 20 V. The EBSD data were analyzed using HKL Channel 5 software.

2.2. Theoretical Methods

Researchers have established a strong obstacle model for the peak aging stage and a weak obstacle model for the under aging stage [35]. This model concluded that the critical resolved shear stress is determined from the interaction of gliding dislocations with point

obstacles, while the average obstacle spacing is estimated by their shapes and orientation relationships with the matrix [25,35]. The strong obstacles model is given by Equation (1):

$$\sigma_{ppt} = \frac{MF_{peak}f_{peak}^{1/2}}{br_{peak}(2\pi)^{1/2}}f_r^{1/2} \tag{1}$$

where M is the Taylor factor, b is the magnitude of the Burgers vector and r_{peak} and F_{peak} represent the average radius cross-section and the average obstacle strength of the precipitates at the peak aging stage, respectively. f_{peak} is the volume fraction of the precipitates at the peak aging stage—this is a constant parameter [25]—and f_r is the relative volume fraction of the precipitates, which is defined as in Equation (2):

$$f_r = \frac{f}{f_{peak}} \tag{2}$$

where f is the volume fraction of the precipitates, and is calculated as follows:

$$f = \frac{4}{3}\pi {r_{eq}}^3 N \tag{3}$$

where N and r_{eq} represent the precipitate number density and the precipitate equivalent radius, respectively. N and r_{eq} are defined as follows:

$$N = \frac{3N_{cs}}{At} \tag{4}$$

$$r_{eq} = \left(\prod_1^n r_n\right)^{1/n} \tag{5}$$

where N_{cs} is the number of precipitate cross-sections in the image, A is the field of view area, t is thickness in the center of the image given in Ref. [28], r_n is the radius of the measured precipitate radius and n is the number of measured precipitates. The weak obstacles model is expressed as Equation (6):

$$\sigma_{ppt} = \frac{MF_{peak}^{3/2}f_{peak}^{1/2}}{b(2\sqrt{3}\pi)^{1/2}\Gamma^{1/2}r_{peak}^{3/2}}r^{1/2}f_r^{1/2} \tag{6}$$

where Γ represents the dislocation line tension—described as $\Gamma = Gb^2/2$—$r = (3/2)^{1/4}r_{acs}$ is the radius of an average equivalent circular and r_{acs} is the average cross-section radius of the precipitates [36].

σ_{dis} is usually assumed to scale with the dislocation density shown as Equation (7) [15,25]:

$$\sigma_{dis} = M\alpha Gb\sqrt{\rho} \tag{7}$$

where b is the Burgers vector, G is the shear modulus, α is a geometric constant, M is the Taylor factor and ρ represents dislocation density, which can be given by Equation (8) [37]:

$$\frac{\beta\cos\theta}{\lambda} = \frac{1}{D_v} + \frac{4\varepsilon\sin\theta}{\lambda} \tag{8}$$

where β is integral breadth, λ is the wavelength, D_v is the volume-weighted average crystallite size and ε is the micro-strain. The slope and intercept of $\beta\cos\theta$ with 4 $\sin\theta$ represent the micro-strain value (ε) and the volume-weighted average crystallite size (D_v), respectively. The basic assumption of the Williamson–Hall technique is that both the size

and strain-broadened profiles are of a Lorentzian shape [38]. The dislocation density can be given by Equation (9) [38,39]:

$$\rho = {\rho_d}^{1/2} \times {\rho_s}^{1/2} \tag{9}$$

where ρ_d is the dislocation density due to the domain size, and ρ_s is the dislocation density due to strain broadening. These are calculated as in Equations (10) and (11):

$$\rho_d = \frac{3}{D_v^2} \tag{10}$$

$$\rho_s = \frac{K\varepsilon^2}{b^2} \tag{11}$$

where $K = 6\pi$ and b is the Burgers vector for the FCC structure.

3. Results

3.1. Mechanical Properties

Figure 2a–c shows the age-hardening curves of the CR alloys and the RTR alloys at various temperatures. Compared to the CR alloys, the RTR alloys reached peak hardness in less time. The hardness of the RTR alloys barely increased when the samples were aged at 160 °C after 20 h; this indicates that the hardness of the RTR alloys nearly reached the peak, but the hardness of the CR alloys still increased when the samples were aged at 160 °C after 20 h. However, the age-hardening capacities (i.e., the increase in hardness during the aging treatment) of the RTR alloys were significantly inferior to those of the CR alloys; this indicates that a prolonged aging time made the CR alloys reach a superior hardness—the hardness of the CR alloys continued to increase when the alloys were aged for 40–50 h.

However, a different phenomenon appeared between the CR alloys and RTR alloys regardless of the aging temperature: the hardness of the CR alloys first decreased in a short amount of time and then increased rapidly, but the hardness of the RTR alloys continuously increased as the aging time increased. Similar phenomena have appeared in many research works [8,17,40], and the results showed that the hardness of the different samples did not increase rapidly at the early stage of artificial aging. As the samples inevitably underwent natural aging (NA) between the quenching and artificial aging, the CR alloys could be more sensitive to NA. The early stage of the artificial aging caused the retrogression phenomenon and reduced the hardness of the CR alloys.

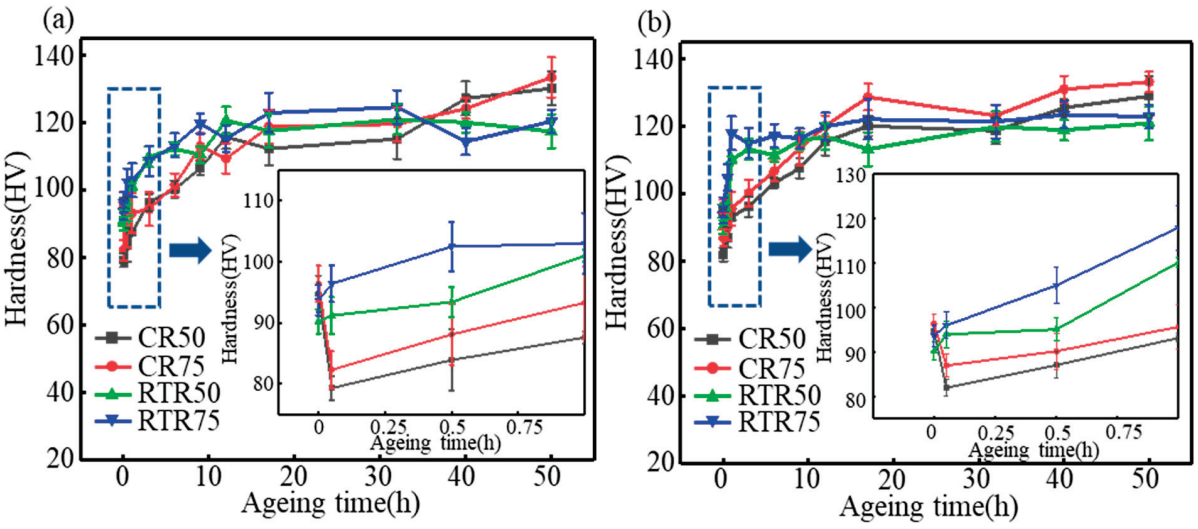

Figure 2. *Cont.*

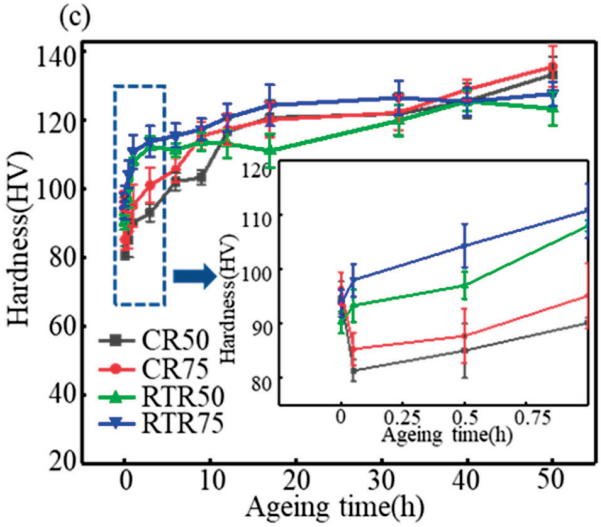

Figure 2. Age-hardening curves of the CR and RTR alloys at (**a**) 160 °C, (**b**) 180 °C and (**c**) 200 °C.

3.2. X-ray Diffraction Analysis

Figure 3 shows the XRD patterns of the CR and RTR alloys before the solution treatment. It was significant that the intensity of the orientation along the (200) crystal plane was mostly higher than that of the other orientations; this was due to the severe accumulation of strain in the rolling direction [41]. According to the Williamson–Hall technique [37], the crystallite size, micro-strain and dislocation density are shown in Table 2. The crystallite sizes in the CR alloys were smaller than those in the RTR alloys, but the micro-strains in the CR alloys were higher than those in the RTR alloys. Large plastic deformations generated high dislocation densities. The dislocation densities of the 50%-reduction alloys were inferior to those of the 75%-reduction alloys. Meanwhile, the dislocation densities in the CR alloys were significantly higher than those in the RTR alloys; this shows that CR improved the dislocation density effectively, and that the deformation energy storage in the CR alloys was higher than that in the RTR alloys. This had a significant influence on the subsequent heat treatment process.

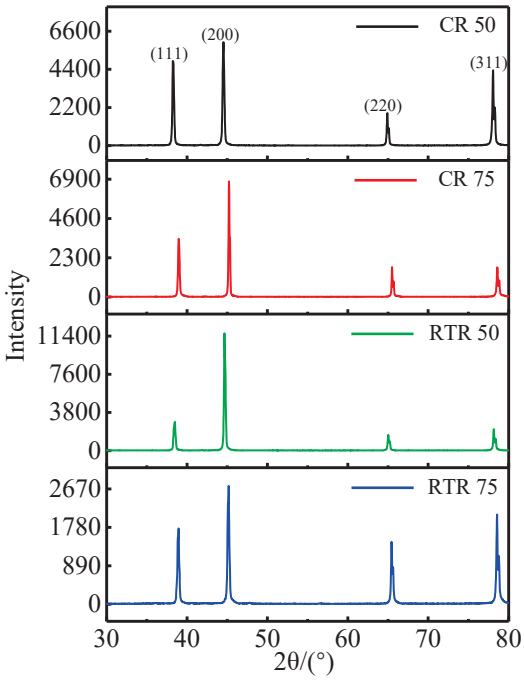

Figure 3. XRD patterns of the samples after CR and RTR, before the solution treatment.

Table 2. Crystallite sizes, micro-strains and dislocation densities of samples.

Process Condition	D_v (nm)	ε ($\times 10^{-3}$)	ρ (m^{-2})
CR 50	177	0.29	2.06×10^{17}
CR 75	105	0.33	3.91×10^{17}
RTR 50	237	0.27	3.40×10^{15}
RTR 75	223	0.31	2.93×10^{15}

3.3. TEM Characterization

Figure 4a–d shows the TEM bright field of the CR and RTR alloys before the solution treatment. It is significant that many dislocations were found in both the RTR and CR samples, and that the dislocation densities in the CR alloys were higher than those in the RTR alloys. Figure 4e,f shows the TEM bright field of the CR and RTR alloys after solution treatment. Subgrains were still observed in the CR alloys, and dislocations surrounded these subgrains. The subgrain size in the CR 75 alloy was less than that of the CR 50 alloy. However, few dislocation structures were found in the RTR alloys after the solution treatment.

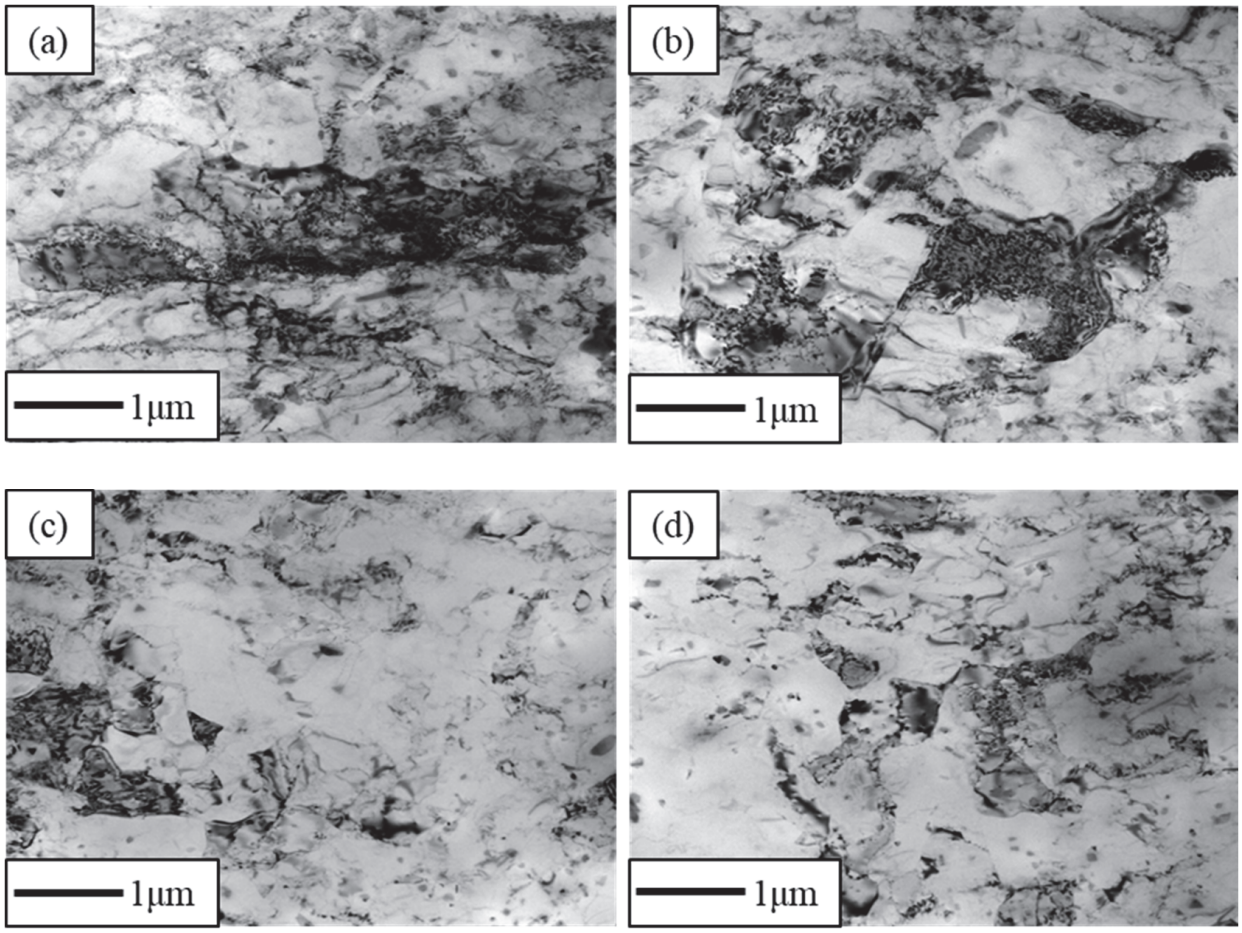

Figure 4. *Cont.*

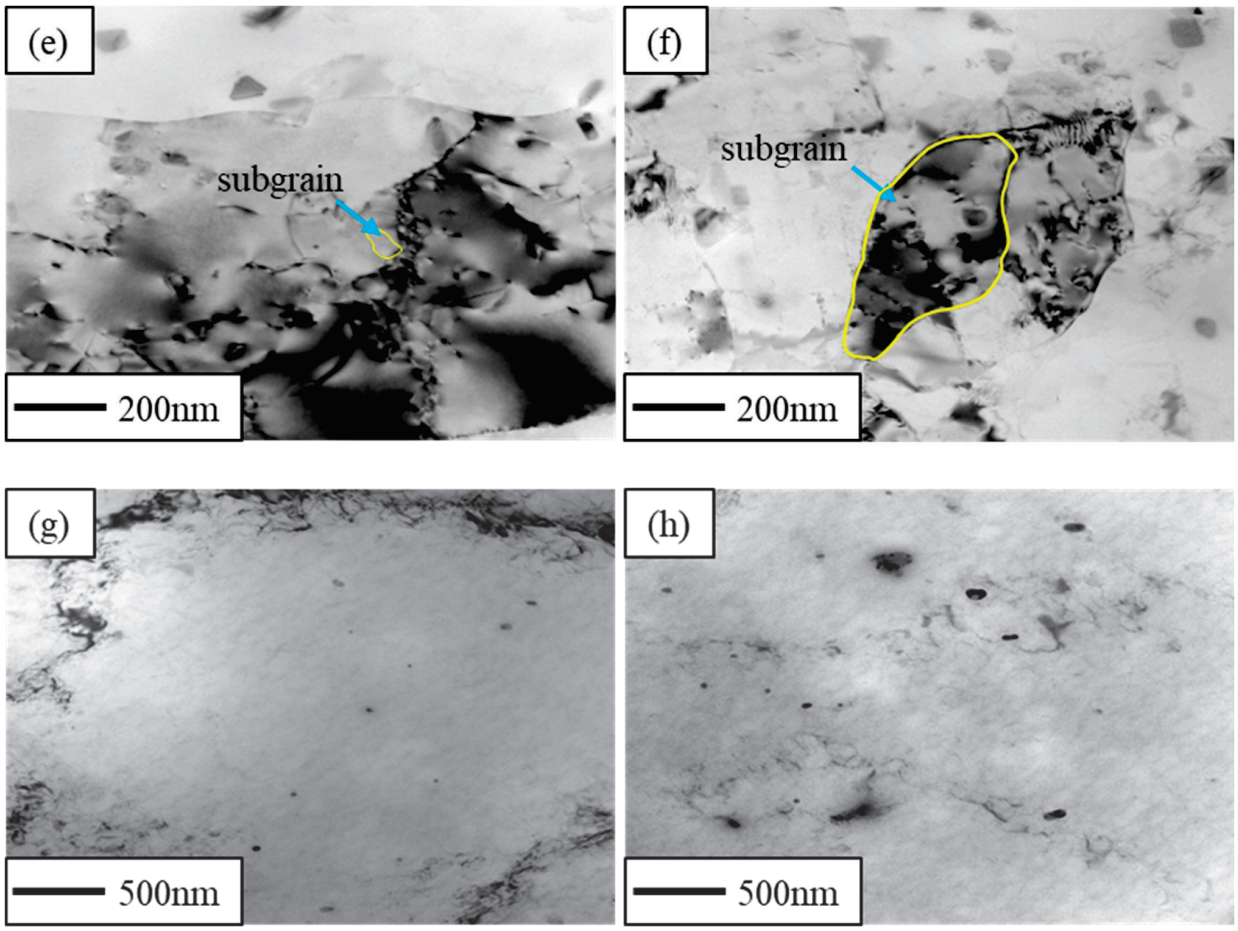

Figure 4. TEM images of alloys before solution treatment: (**a**) CR 75, (**b**) CR 50, (**c**) RTR 75 and (**d**) RTR 50; TEM images of alloys after solution treatment: (**e**) CR 75, (**f**) CR 50, (**g**) RTR 75 and (**h**) RTR 50.

Figure 5a,b shows the TEM bright field of the CR alloys after 3 min of the aging treatment. After 3 min of the aging treatment, there were still a few dislocation structures in the CR alloys, and globular precipitates precipitated near these dislocations to prevent the dislocation from slipping; this indicates that dislocations in the CR alloys did not entirely disappear, although they underwent a short aging treatment. Nevertheless, in the RTR alloys (Figure 5c,d), dislocations were not found—only globular precipitates precipitated in the Al alloys. A previous study [42] confirmed that a large amount of globular Mg_2Si phase is precipitated in Al–Mg–Si alloys, achieving an ultimate tensile strength of 421 MPa —which is greatly improved compared to the conventional T6 state.

Figure 6a–d shows the TEM bright field of the CR and RTR alloys after 50 h of the aging treatment. It was apparent that a mass of globular Mg_2Si phases precipitated in both the CR and RTR alloys. The density of the Mg_2Si phase in the CR 75 alloy was the highest, and the density of the Mg_2Si phase in the RTR 50 alloy was the lowest. The Mg_2Si phase was the main strengthening phase in the 6xxx Al alloy, so the densities of the Mg_2Si phases affected the precipitation strengthening significantly; this indicates that the precipitation strengthening in the CR 75 alloy was superior to other alloys. Meanwhile, the needle-like β'' phase is widely considered another strengthening phase in Al–Mg–Si alloys [14,17,20]. These needle-like β'' phases were found in both of the CR and RTR alloys after 50 h of the aging treatment. However, the density of the needle-like β'' phase had no significant difference, as shown in Figure 7a–d.

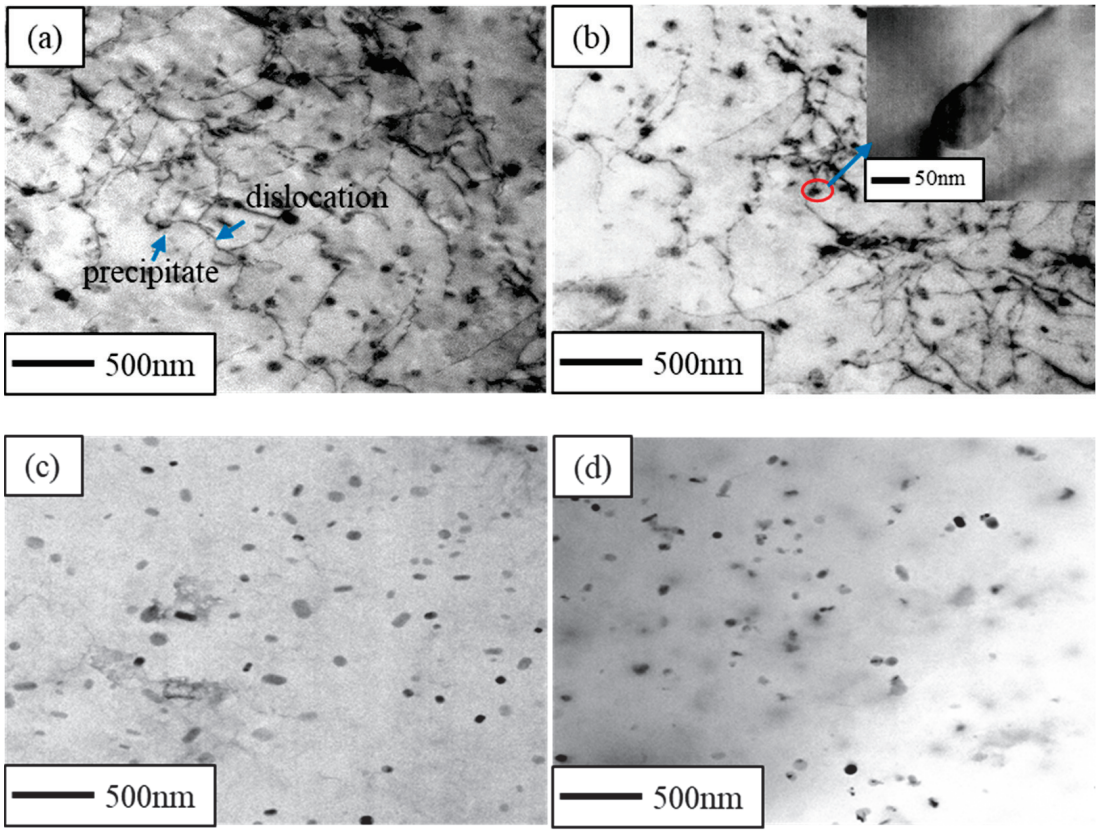

Figure 5. TEM images of alloys aged at 160 °C for 3 min: (**a**) CR 75, (**b**) CR 50, (**c**) RTR 75 and (**d**) RTR 50.

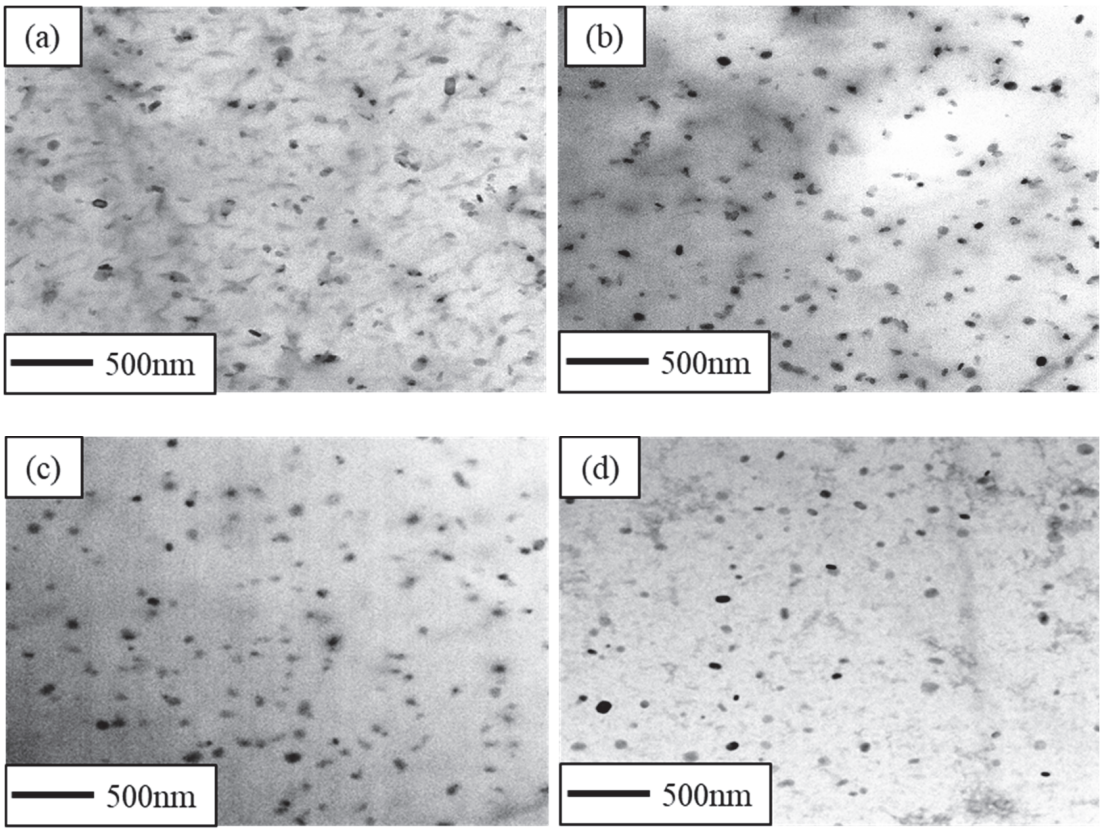

Figure 6. TEM images of alloys aged at 160 °C for 50 h: (**a**) CR 75, (**b**) CR 50, (**c**) RTR 75 and (**d**) RTR 50.

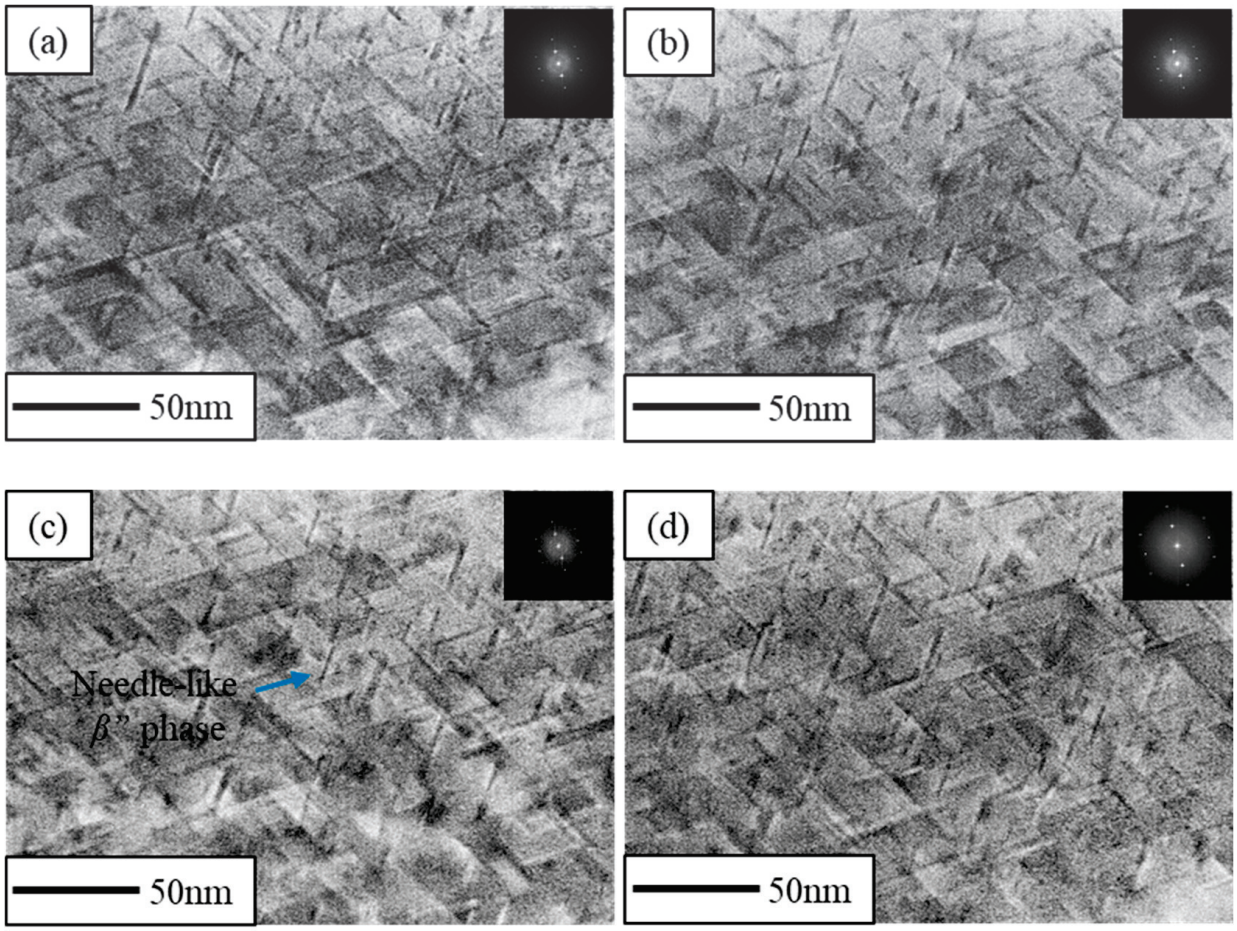

Figure 7. Needle-like β'' phase precipitated in different alloys after 160 °C × 50 h aging treatment: (**a**) CR 75, (**b**) CR 50, (**c**) RTR 75 and (**d**) RTR 50.

3.4. EBSD Characterization

Figure 8a–d shows the IPF of the CR and RTR alloys. It is significant that the average grain size of the RTR 75 alloy was the finest. The average grain sizes of the RTR alloys were finer than those of the CR alloys. The degree of recrystallization and recovery in the CR and RTR alloys is shown in Figure 8e–i. Despite the solid solution treatment, the CR and RTR alloys did not fully recrystallize; there were a few substructures and deformed structures in the alloys. The statistical results show that the degree of recrystallization in the CR alloy was inferior to that in the RTR alloy, but the degree of recovery in the CR alloy was superior to that in the RTR alloy. Substructures (such as dislocation) remained in the CR alloys, which indicated that the CR alloy was prone to recovery during the solution treatment. The recrystallization and the substructure in the RTR 50 alloy were similar to those in the RTR 75 alloy; few deformation structures existed in the RTR alloys. The recrystallization and the substructures in the CR 50 alloy were also similar to those in the CR 75 alloy. However, the deformed structures in the CR 50 alloy were inferior to those in the CR 75 alloy indicating that more deformation energy existed in the CR 75 alloy. Figure 9a–d shows the deformation texture in the different alloys, and the statistical results are shown in Table 3. After the solution treatment, a few deformation textures (Brass {110} <112> and S {123} <634>) still existed in both of the RTR and CR alloys; the proportion of deformation texture in the CR alloys was similar to that in the RTR alloys. Compared with the alloys in Ref. [12], the proportion of deformation texture in the CR alloys was reduced significantly; this resulted in the anisotropy caused by the deformation texture decreasing significantly.

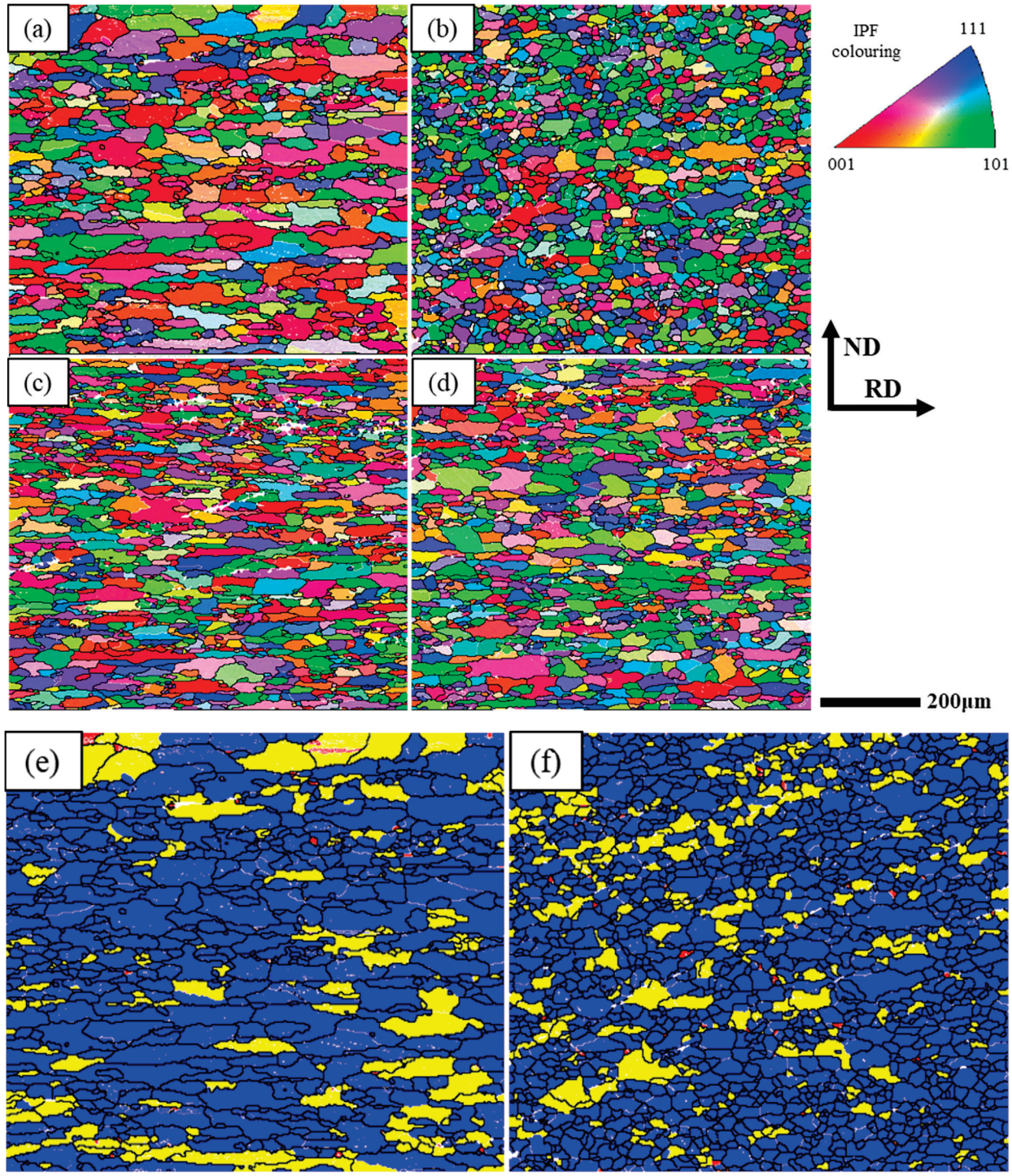

Figure 8. *Cont.*

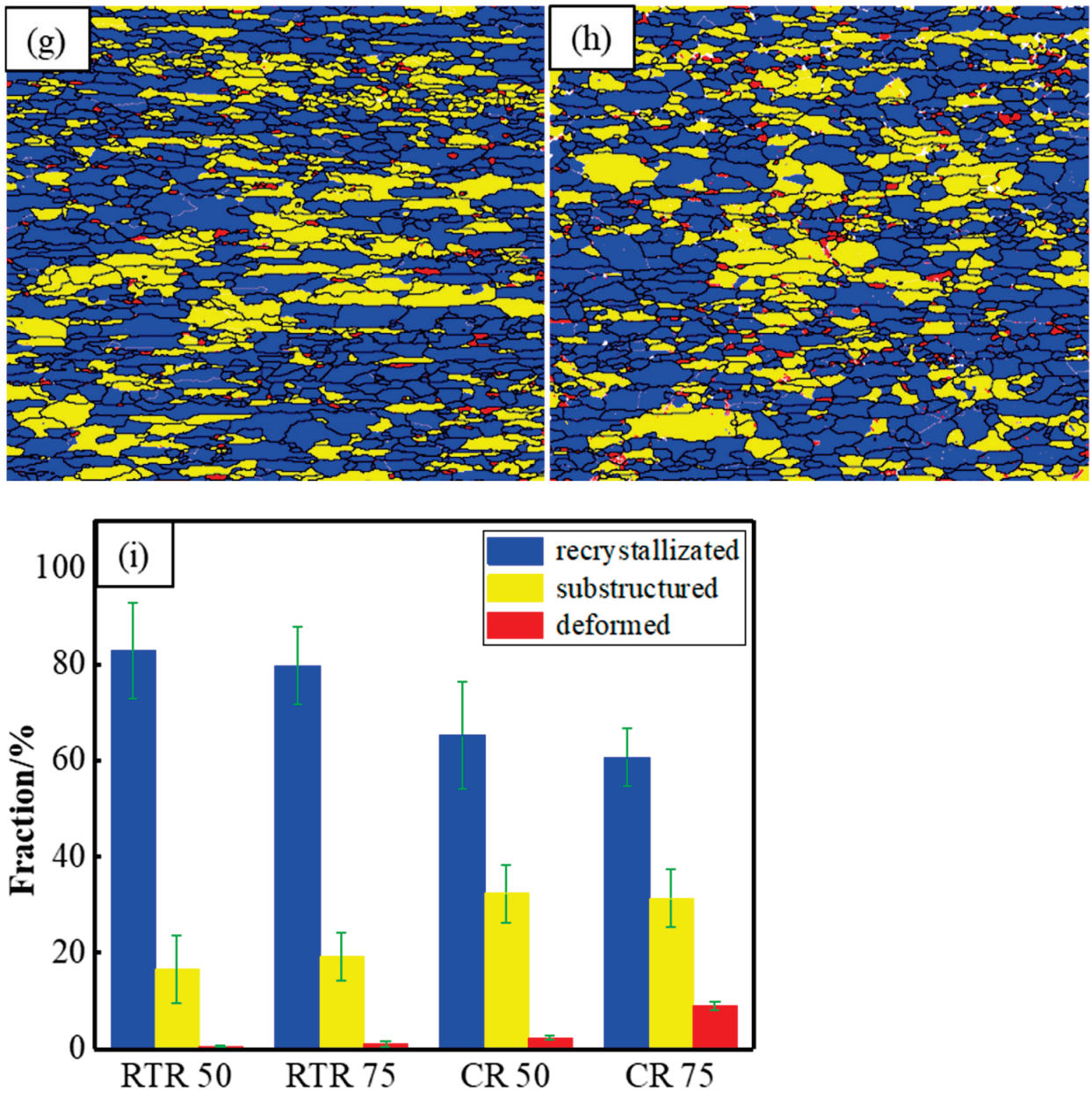

Figure 8. IPF after solution treatment: (**a**) RTR 50, (**b**) RTR 75, (**c**) CR 50 and (**d**) CR 75; degree of recrystallization and recovery: (**e**) RTR 50, (**f**) RTR 75, (**g**) CR 50 and (**h**) CR 75; (**i**) volume fraction.

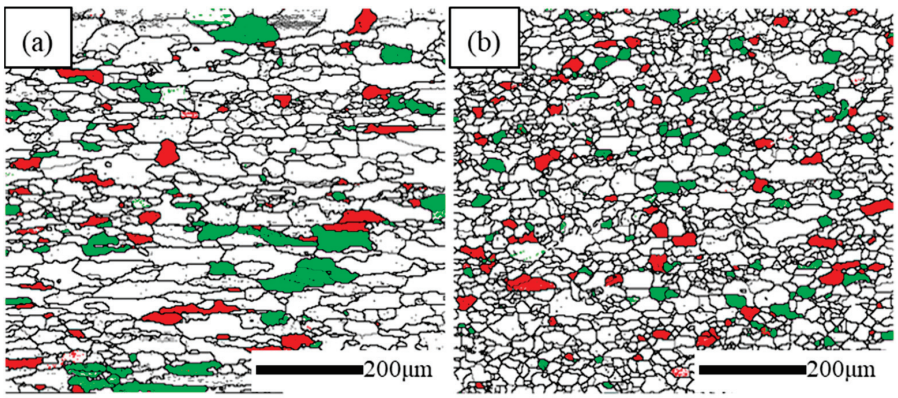

Figure 9. *Cont.*

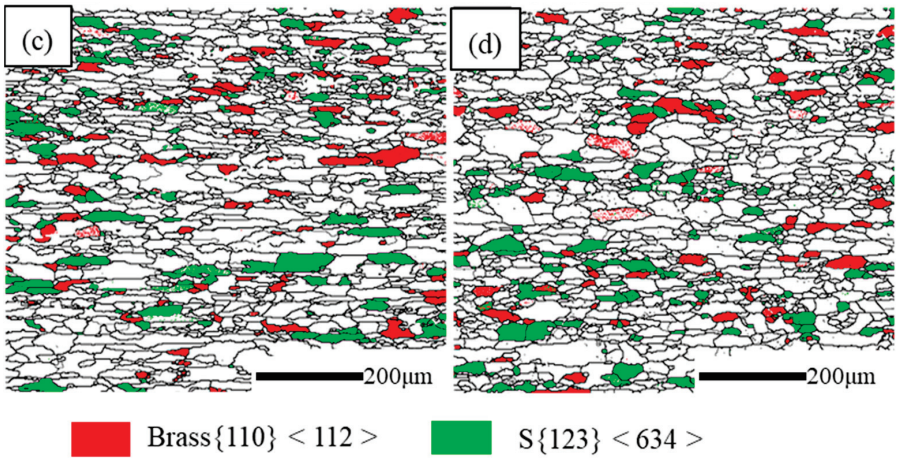

Figure 9. Deformation texture in different alloys: (**a**) RTR 50, (**b**) RTR 75, (**c**) CR 50 and (**d**) CR 75.

Table 3. Texture fraction of different samples.

Process Condition	Brass/%	S/%
RTR 50	8.3	8.2
RTR 75	10.1	10.1
CR 50	10.7	9.8
CR 75	12.5	11.2
LNR 75 [12]	27.99	26.72
RTR 75 [12]	20.96	23.06

4. Discussion

4.1. Microstructure and Precipitate Evolution during Aging Treatment

Compared with the RTR alloys, dislocations in the CR alloys were significantly higher than those in the RTR alloys—as shown in Figure 4a–d. As shown in Figure 4e–h, despite the solution treatment, subgrains were observed in the CR alloys, while these subgrains were not observed in RTR alloys. The hardness variations in the CR and RTR alloys were opposite at the early aging stage: the hardness of the CR alloys decreased, but the hardness of the RTR alloys increased. Researchers [17] found that the hardness, yield strength and tensile strength of the natural aging AA6016 aluminum alloys decreased first, and then increased when the alloys were artificially aged at 185°C. This phenomenon was attributed to the dissolution of clusters formed during natural aging (NA), caused by retrogression and re-aging. A. Serizawa et al. [43] pointed out that the water-quenched alloys were able to form a kind of atomic cluster when alloys were naturally aged; the density gradually increased at the natural aging stage. As a result, supersaturated solute atoms and vacancies in the alloy matrix were consumed in large quantities, and the nucleation growth of the precipitate was delayed. Compared with the RTR alloys, the CR alloys tended to form clusters more easily during NA, due to the substructures formed after the solution treatment (Figure 4e,f).

Grains were broken and elongated during cryogenic rolling, and the work-hardening phenomenon was evident due to the presence of a lot of dislocation tangles. As shown in Figure 8e–h, the proportion of recrystallization in the CR alloys was inferior to that in the RTR alloys. Since the recovery of the CR alloy was inhibited during the rolling process, more dislocations were retained. These irregular dislocations were distributed on different slip planes due to the multiple slip systems in the Al alloy. It was difficult for the Al alloy to recrystallize because of its high layer fault energy; the solution treatment made the edge dislocation climb more easily, which resulted in these dislocation tangles being redistributed on different slip planes to form substructures rather than recrystallization. After the solution treatment, more substructures existed in the CR alloys than in the RTR alloys. The substructures and deformed structures in the CR 75 alloy were higher

than those in the RTR alloys, which indicated that there were more substructures in the CR 75 alloy to provide nucleation for precipitation during the aging treatment. The substructures partly remained after the solution treatment in the CR alloys, which resulted in better substructure strengthening (Figure 4e,f). As shown in Figure 5b, the plate-like Mg_2Si phase was pinned at the dislocation and hindered the dislocation from moving. Supersaturation, substructures and precipitates existed in the CR alloys at the early aging stage. As aging time increased, this supersaturation and the substructures gradually decreased, and the density of precipitates gradually increased; precipitation strengthening was greatly enhanced.

When the aging time reached 20 h, the hardness of both the CR and RTR alloys rose slowly—the reasons were concluded to be as follows:

1. The effect of solution strengthening on alloy strength was nearly exhausted due to the long-time aging treatment.
2. Precipitation strengthening increased slowly. As shown in Equation (12) [15] and Equation (13) [44], when the concentration of alloying elements in the solid solution (C) went down towards the solution equilibrium concentration (C_e)—which resulted in nucleation rate (j) and growth rate(dr/dt) decline—this showed that precipitation had continued to exhaustion, and so precipitation strengthening slowed down.

$$j = j_0 \exp\left[-\left(\frac{A_0}{RT}\right)^3 \left(\frac{1}{\ln(C/C_e)}\right)^2\right] \exp\left(-\frac{Q_d}{RT}\right) \tag{12}$$

$$\frac{dr}{dt} = \frac{\overline{C} - C_i}{C_p - C_i}\frac{D}{r} \tag{13}$$

4.2. Precipitation Strengthening during Aging Treatment

As shown in Figure 5, there were a few dislocations in the CR alloys after aging for 3 min, Mg_2Si phases precipitated in both the CR and RTR alloys. Compared with the RTR alloys, more plate-like Mg_2Si phases precipitated in the CR alloys after aging for 50 h (Figure 6a–d)—in particular, the density in the CR 75 alloy was higher than in the other alloys, indicating that the precipitation strengthening of the CR alloy was higher than that in the RTR alloy. Mg_2Si phase, as the main strengthening phase in Al–Mg–Si alloys, contributes to alloy strength significantly; this contribution is mainly reflected in the prevention of dislocation slipping. A high density of precipitates indicates a strong resistance to dislocations. The substructures retained in the CR alloys after the solution treatment not only brought substructural strengthening, but also benefited precipitation during the aging process. When aging time was increased to 50 h, the dislocations in the CR alloys nearly disappeared; the dislocation removal provided energy for precipitate nucleation and growth during aging treatment. The densities of needle-like β'' phases in the CR and RTR alloys were approximately similar after aging for 50 h (Figure 7a–d); this shows that the difference in strength between the CR and RTR alloys was not related to the β'' phase.

4.3. The Effect of Deformation Texture after Solution Treatment

Texture variation plays an important role in the materials' properties as its effect on anisotropy can be used to improve the formability of Al–Mg–Si autobody sheets [1]. In the "solution treatment + CR + aging treatment" process, the CR sample showed a 27.99% Brass texture and a 26.72% S texture; the anisotropy behavior of the CR sample was enhanced compared with the RTR sample [12]. However, the deformation texture was reduced significantly in the "CR + solution treatment + aging treatment" process, as shown in Table 3. Although the "CR + solution treatment + aging treatment" process sacrificed the partial dislocation strengthening caused by cryorolling, it improved the alloy precipitation strength—reducing the proportion of deformation texture and the anisotropy of the plate.

4.4. The Contributions of Different Strength Mechanisms

Equations (1)–(6) were employed to reveal the precipitation strengthening contributions during the aging treatment, as shown in Figure 10. At the early aging stage, the precipitation strengthening contribution of the CR and RTR alloys showed little difference. However, when alloys were aged at 160 °C for 50 h, the precipitation strengthening contribution of the CR 75 alloy had significant advantages over the others; more substructures remained after the solution treatment in the CR 75 alloy. As aging time increased, these substructures gradually disappeared. The precipitation strengthening in the CR 75 alloy improved more significantly than others due to high precipitate densities (Figure 6a); this resulted in the aging hardening capacity of the CR 75 being superior to the other alloys (Figure 2a–c), and the CR 75 alloy had the highest strength (Figure 6d).

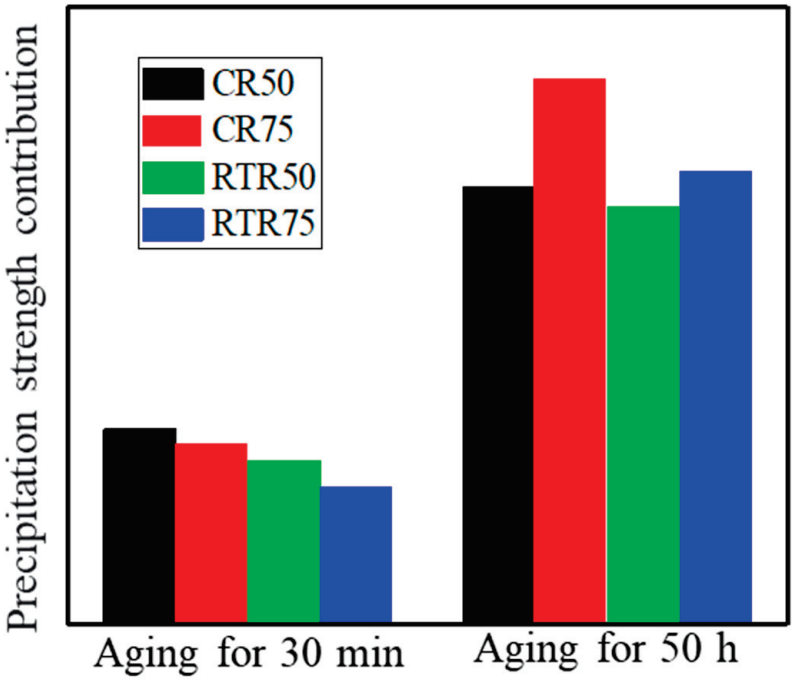

Figure 10. The contribution of precipitation strengthening when alloys were aged at 160 °C for 50 h.

5. Conclusions

The performance and microstructure characterization of CR and RTR alloys were investigated. Compared to RTR, more dislocations existed in alloys after CR due to the suppression of recovery. The hardness of the CR alloys decreased at the early aging stage, but the hardness of the RTR alloys increased at the early aging stage; this is because CR alloys could be more sensitive to NA, and so the retrogression phenomenon was apparent. The proportion of deformation textures was reduced after the solution treatment, which resulted in decreased anisotropy of the plate. After 50 h of the aging treatment, the hardness and the precipitate density of the CR 75 alloy were the highest; this indicates that the residual substructures after the solution treatment promoted precipitation and improved strength during the aging treatment. A precipitation strength model was employed to illustrate the precipitation contribution during the aging treatment; the results show that the CR 75 alloy obtained the strongest precipitation strengthening.

Author Contributions: X.W.: Conceptualization, Methodology, Investigation, Writing—original draft, Y.H.: Funding acquisition, Supervision, Writing—review and editing, Y.L.: Methodology, Supervision. All authors have read and agreed to the published version of the manuscript.

Funding: National Natural Science Foundation of China, Project No. 51575539; Foreign Cooperation Projects of Fujian Province, Project No. 2020I1007.

Institutional Review Board Statement: Not applicable.

Informed Consent Statement: Not applicable.

Conflicts of Interest: The authors declare that they have no known competing financial interests or personal relationships that could have appeared to influence the work reported in this paper.

References

1. Hirsch, J.; Al-Samman, T. Superior light metals by texture engineering: Optimized aluminum and magnesium alloys for automotive applications. *Acta Mater.* **2013**, *61*, 818–843. [CrossRef]
2. Miller, W.S.; Zhuang, L.; Bottema, J.; Wittebrood, A.J.; de Smet, P.; Haszler, A.; Vieregge, A. Recent development in aluminium alloys for the automotive industry. *Mater. Sci. Eng.* **2000**, *280*, 37–49. [CrossRef]
3. Hirsch, J. Recent development in aluminium for automotive applications. *Trans. Nonferrous Met. Soc. China* **2014**, *24*, 1995–2002. [CrossRef]
4. Bochvar, N.R.; Rybalchenko, O.V.; Tabachkova, N.Y.; Rybalchenko, G.V.; Leonova, N.P.; Rokhlin, L.L. Kinetics of phase precipitation in Al–Mg–Si alloys subjected to equal-channel angular pressing during subsequent heating. *J. Alloys Compd.* **2021**, *881*, 160583. [CrossRef]
5. Rochet, C.; Andrieu, E.; Arfaei, B.; Harouard, J.; Laurino, A.; Lowe, T.C.; Odemer, G.; Blanc, C. Influence of equal-channel angular pressing on the corrosion fatigue behaviour of an Al-Mg-Si aluminium alloy for automotive conductors. *Int. J. Fatigue* **2020**, *140*, 105812. [CrossRef]
6. Zhang, X.; Huang, L.K.; Zhang, B.; Chen, Y.Z.; Liu, F. Microstructural evolution and strengthening mechanism of an Al–Si–Mg alloy processed by high-pressure torsion with different heat treatments. *Mater. Sci. Eng. A* **2020**, *794*, 139932. [CrossRef]
7. Bobruk, E.V.; Kazykhanov, V.U.; Murashkin, M.Y. Influence of deformation at elevated temperatures on stability of microstructure and mechanical properties of UFG aluminum alloy. *Mater. Lett.* **2021**, *301*, 130328. [CrossRef]
8. Chrominski, W.; Lewandowska, M. Influence of dislocation structures on precipitation phenomena in rolled Al–Mg–Si alloy. *Mater. Sci. Eng. A.* **2020**, *793*, 139903. [CrossRef]
9. Li, Z.; Jiang, H.; Wang, M.; Jia, H.; Han, H.; Ma, P. Microstructure and mechanical properties of Al-Mg-Si similar alloy laminates produced by accumulative roll bonding. *Materials* **2021**, *14*, 4200. [CrossRef]
10. Jiang, H.J.; Liu, C.Y.; Zhang, B.; Xue, P.; Ma, Z.Y.; Luo, K.; Ma, M.Z.; Liu, R.P. Simultaneously improving mechanical properties and damping capacity of Al-Mg-Si alloy through friction stir processing. *Mater. Charact.* **2017**, *131*, 425–430. [CrossRef]
11. Mei, L.; Chen, X.P.; Huang, G.J.; Liu, Q. Improvement of mechanical properties of a cryorolled Al-Mg-Si alloy through warm rolling and aging. *J. Alloys Compd.* **2019**, *777*, 259–263. [CrossRef]
12. Krishna, N.N.; Ashfaq, M.; Susila, P.; Sivaprasad, K.; Venkateswarlu, K. Mechanical anisotropy and microstructural changes during cryorolling of Al–Mg–Si alloy. *Mater. Charact.* **2015**, *107*, 302–308. [CrossRef]
13. Chen, H.; Lu, J.; Kong, Y.; Li, K.; Yang, T.; Meingast, A.; Yang, M.; Lu, Q.; Du, Y. Atomic scale investigation of the crystal structure and interfaces of the β' precipitate in Al-Mg-Si alloys. *Acta Mater.* **2020**, *185*, 193–203. [CrossRef]
14. Misumi, K.; Kaneko, K.; Nishiyama, T.; Maeda, T.; Yamada, K.; Ikeda, K.; Kikuchi, M.; Takata, K.; Saga, M.; Ushioda, K. Three-dimensional characterization of interaction between β'' precipitate and dislocation in Al–Mg–Si alloy. *J. Alloys Compd.* **2014**, *600*, 29–33. [CrossRef]
15. Myhr, O.R.; Grong, Ø.; Andersen, S.J. Modelling of the age hardening behaviour of Al-Mg-Si alloys. *Acta Mater.* **2001**, *49*, 65–75. [CrossRef]
16. Koster, U.; Liu, W. Phase-transformation of quasi-crystals in aluminum-transition metal-alloys. *Phase Transit.* **1993**, *44*, 137–149. [CrossRef]
17. Engler, O.; Marioara, C.D.; Aruga, Y.; Kozuka, M.; Myhr, O.R. Effect of natural ageing or pre-ageing on the evolution of precipitate structure and strength during age hardening of Al–Mg–Si alloy AA6016. *Mater. Sci. Eng. A* **2019**, *759*, 520–529. [CrossRef]
18. Buchanan, K.; Colas, K.; Ribis, K.; Lopez, J.A.; Garnier, J. Analysis of the metastable precipitates in peak-hardness aged Al-Mg-Si(-Cu) alloys with differing Si contents. *Acta Mater.* **2017**, *132*, 209–221. [CrossRef]
19. Maisonnette, D.; Suery, M.; Nelias, D.; Chaudet, P.; Epicier, T. Effects of heat treatments on the microstructure and mechanical properties of a 6061 aluminium alloy. *Mater. Sci. Eng. A* **2011**, *528*, 2718–2724. [CrossRef]
20. Hasting, H.S.; Frøseth, A.G.; Andersen, S.J.; Vissers, R.; Walmsley, J.C.; Marioara, C.D.; Danoix, F.; Lefebvre, W.; Holmestad, R. Composition of β'' precipitates in Al-Mg-Si alloys by atom probe tomography and first principles calculations. *J. Appl. Phys.* **2009**, *106*, 123527. [CrossRef]
21. Yang, W.; Wang, M.; Sheng, X.; Zhang, Q.; Huang, L. Precipitate characteristics and selected area diffraction patterns of the β' and Q' precipitates in Al-Mg-Si-Cu alloys. *Philos. Mag. Lett.* **2011**, *91*, 150–160. [CrossRef]
22. Poole, W.J.; Wang, X.; Lloyd, D.J.; Embury, J.D. The shearable–non-shearable transition in Al–Mg–Si–Cu precipitation hardening alloys: Implications on the distribution of slip, work hardening and fracture. *Philos. Mag.* **2005**, *85*, 3113–3135. [CrossRef]
23. Yang, M.; Orekhov, A.; Hu, Z.; Feng, M.; Jin, S.; Sha, G.; Li, K.; Samaee, V.; Song, M.; Du, Y.; et al. Shearing and rotation of β'' and β' precipitates in an Al-Mg-Si alloy under tensile deformation: In-situ and ex-situ studies. *Acta Mater.* **2021**, *220*, 117310. [CrossRef]

24. Teichmann, K.; Marioara, C.D.; Andersen, S.J.; Marthinsen, K. TEM study of β′ precipitate interaction mechanisms with dislocations and β′ interfaces with the aluminium matrix in Al–Mg–Si alloys. *Mater. Char.* **2013**, *75*, 1–7. [CrossRef]
25. Esmaeili, S.; Lloyd, D.J.; Poole, W.J. A yield strength model for the Al-Mg-Si-Cu alloy AA6111. *Acta Mater.* **2003**, *51*, 2243–2257. [CrossRef]
26. Nandy, S.; Ray, K.K.; Das, D. Process model to predict yield strength of AA6063 alloy. *Mater. Sci. Eng. A* **2015**, *644*, 413–424. [CrossRef]
27. Hosseini-Benhangi, P.; Mazinani, M.; Haddad-Sabzevar, M. Physically based model of the yield strength for an Al-Mg-Si-Cu-Zn alloy. *Metall. Mater. Trans. A* **2015**, *46*, 5407–5417. [CrossRef]
28. Bahrami, A.; Miroux, A.; Sietsma, J. An age-hardening model for Al-Mg-Si alloys considering needle-shaped precipitates. *Metall. Mater. Trans. A* **2012**, *43*, 4445–4453. [CrossRef]
29. Li, Z.; Chen, L.; Tang, J.; Zhao, G.; Zhang, C.; Chu, X. Microstructure evolution; plastic anisotropy, and intergranular corrosion of Al-Mg-Si sheet processed through a combination of hot extrusion and cold rolling. *Mater. Charact.* **2020**, *164*, 110299. [CrossRef]
30. Wang, Z.; Zhu, F.; Zheng, K.; Jia, J.; Wei, Y.; Li, H.; Huang, L.; Zheng, Z. Effect of the thickness reduction on intergranular corrosion in an under–aged Al–Mg–Si–Cu alloy during cold–rolling. *Corros. Sci.* **2018**, *142*, 201–212. [CrossRef]
31. Jin, S.; Wang, A.; Wang, K.; Li, W.; Wan, B.; Zhai, T. Significant strengthening effect in ultra-fine grained al alloy made by fast solidification and hot extrusion processes. *J. Mater. Res. Technol.* **2021**, *16*, 1761–1769. [CrossRef]
32. Deng, Y.; Huang, G.; Cao, L.; Wu, X.; Huang, L.; Xia, M.; Liu, Q. Improvement of strength and ductility of Al-Cu-Li alloy through cryogenic rolling followed by aging. *Trans. Nonferrous Met. Soc. China* **2017**, *27*, 1920–1927. [CrossRef]
33. He, G.; Li, K.; Yang, Y.; Liu, Y.; Wu, W.; Huang, C. Effect of heat treatment on the microstructure and mechanical properties of cryogenic rolling 2195 Al–Cu–Li alloy. *Mater. Sci. Eng. A* **2021**, *822*, 141682. [CrossRef]
34. Hussain, M.; Rao, P.N.; Singh, D.; Jayaganthan, R. Precipitation hardening behaviour of Al-Mg-Si alloy processed by cryorolling and room temperature rolling. *Mater. Res. Express* **2018**, *5*, 4. [CrossRef]
35. Ardell, A.J. Precipitation hardening. *Metall Mater Trans A* **1985**, *16*, 2131–2165. [CrossRef]
36. Yang, M.; Chen, H.; Orekhov, A.; Lu, Q.; Lan, X.; Li, K.; Zhang, S.; Song, M.; Kong, Y.; Schryvers, D.; et al. Quantified contribution of β′′ and β′ precipitates to the strengthening of an aged Al–Mg–Si alloy. *Mater. Sci. Eng. A* **2020**, *774*, 138776. [CrossRef]
37. Hall, W.H.; Williamson, G.K. Dead time correction for monitored counters. *J. Sci. Instrum.* **1952**, *29*, 132–133. [CrossRef]
38. Krishna, N.N.; Tejas, R.; Sivaprasad, K.; Venkateswarlu, K. Study on cryorolled Al-Cu alloy using X-ray diffraction line profile analysis and evaluation of strengthening mechanisms. *Mater. Des.* **2013**, *52*, 785–790. [CrossRef]
39. Krishna, K.S.V.B.R.; Vigneshwaran, S.; Sekhar, K.C.; Akella, S.S.R.; Sivaprasad, K.; Narayanasamy, R.; Venkateswarlu, K. Mechanical behavior and void coalescence analysis of cryorolled AA8090 alloy. *Int. J. Adv. Des. Manuf. Technol.* **2016**, *93*, 253–259. [CrossRef]
40. Pogatscher, S.; Antrekowitsch, H.; Leitner, H.; Ebner, T.; Uggowitzer, P.J. Mechanisms controlling the artificial aging of Al–Mg–Si alloys. *Acta Mater.* **2011**, *59*, 3352–3363. [CrossRef]
41. Khelfa, T.; Rekik, M.A.; Khitouni, M.; Cabrera-Marrero, J.M. Structure and microstructure evolution of Al–Mg–Si alloy processed by equal-channel angular pressing. *Int. J. Adv. Manuf. Technol.* **2017**, *92*, 1731–1740. [CrossRef]
42. Wang, Y.; Zhao, Y.; Xu, X.; Pan, D.; Jiang, W.; Yang, X.; Wang, Z. Superior mechanical properties induced by the interaction between dislocations and precipitates in the electro-pulsing treated Al-Mg-Si alloys. *Mater. Sci. Eng. A* **2018**, *735*, 154–161. [CrossRef]
43. Serizawa, A.; Hirosawa, S.; Sato, T. Three-dimensional atom probe characterization of nanoclusters responsible for multistep aging behavior of an Al-Mg-Si alloy. *Metall. Mater. Trans. A* **2008**, *39*, 243–251. [CrossRef]
44. Aaron, H.B.; Fainstein, D.; Kotler, G.R. Diffusion-Limited phase transformations: A comparison and critical evaluation of the mathematical approximations. *J. Appl. Phys.* **1970**, *41*, 4404–4410. [CrossRef]

materials

MDPI

Article

On the Role of Microstructure and Defects in the Room and High-Temperature Tensile Behavior of the PBF-LB A357 (AlSi7Mg) Alloy in As-Built and Peak-Aged Conditions

Lavinia Tonelli *, Erica Liverani, Gianluca Di Egidio *, Alessandro Fortunato, Alessandro Morri and Lorella Ceschini

Department of Industrial Engineering (DIN), Alma Mater Studiorum—University of Bologna, Viale del Risorgimento 2, 40136 Bologna, Italy

* Correspondence: lavinia.tonelli2@unibo.it (L.T.); gianluca.diegidio2@unibo.it (G.D.E.)

Abstract: Additive processes like Laser Beam Powder Bed Fusion (PBF-LB) result in a distinctive microstructure characterized by metastability, supersaturation, and finesse. Post-process heat treatments modify microstructural features and tune mechanical behavior. However, the exposition at high temperatures can induce changes in the microstructure. Therefore, the present work focuses on the analyses of the tensile response at room and high (200 °C) temperature of the A357 (AlSi7Mg0.6) alloy processed by PBF-LB and subjected to tailored T5 (direct aging) and T6R (rapid solution treatment, quenching, and aging) treatments. Along with the effect of microstructural features in the as-built T5 and T6R alloy, the role of typical process-related defects is also considered. In this view, the structural integrity of the alloy is evaluated by a deep analysis of the work-hardening behavior, and quality indexes have been compared. Results show that T5 increases tensile strength at room temperature without compromising ductility. T6R homogenizes the microstructure and enhances the structural integrity by reducing the detrimental effect of defects, resulting in the best trade-off between strength and ductility. At 200 °C, tensile properties are comparable, but if resilience and toughness moduli are considered, as-built and T5 alloys show the best overall mechanical performance.

Keywords: additive manufacturing; aluminum alloys; structural integrity; microstructure; mechanical properties; heat treatment

Citation: Tonelli, L.; Liverani, E.; Di Egidio, G.; Fortunato, A.; Morri, A.; Ceschini, L. On the Role of Microstructure and Defects in the Room and High-Temperature Tensile Behavior of the PBF-LB A357 (AlSi7Mg) Alloy in As-Built and Peak-Aged Conditions. *Materials* **2023**, *16*, 2721. https://doi.org/10.3390/ma16072721

Academic Editor: Xianfei Ding

Received: 7 March 2023
Revised: 21 March 2023
Accepted: 26 March 2023
Published: 29 March 2023

1. Introduction

Hypoeutectic Al-Si-Mg conventional cast alloys are widely used in the automotive industry, especially for manufacturing lightweight structural castings that often require complex designs. AlSi7Mg alloys (i.e., A356, A357, and their variations), in particular, are recommended for applications in the power train system (e.g., engine blocks, cylinder heads) due to the high strength and elongation at room temperature achievable after dedicated heat treatment (T6, consisting of solution treatment, quenching, and aging) that promote strengthening due to the precipitation of Mg-Si phases during aging [1,2]. However, for these specific applications, it is crucial to guarantee a high strength at elevated temperatures (up to 200–250 °C) that engine components can commonly experience during their service life [3]. Conventional cast A356 or A357 T6 alloys suffer a non-negligible decrease in mechanical strength if exposed to temperatures close to 200 °C due to coarsening of reinforcing phases related to over-aging [4]. For high-temperature applications, alloys containing a certain amount of Cu assure better thermal stability [4,5]. However, the effect of thermal exposure on the microstructure and mechanical properties of AlSi7Mg alloys processed by innovative additive manufacturing technologies, like laser-based powder bed fusion (PBF-LB), is currently lacking. In recent years, literature has proved that Al-Si-Mg alloys, mostly AlSi10Mg and AlSi7Mg, can be successfully processed with PBF-LB [6–8]. PBF-LB is based on selective melting, layer after layer, of a bed of fine metallic powder and

enables the manufacturing of extremely complex designs with high accuracy. For these reasons, in the automotive field and in the context of promoting more sustainable mobility, PBF-LB can effectively enhance the mass reduction of vehicles by lightweight structural components. In this view, mechanical characterization, even at a temperature consistent with the service life, has to be performed.

From the material point of view, it is worth mentioning that the microstructure resulting from the PBF-LB process is in the unique condition of being supersaturated, metastable, and extremely fine [8]. Consequently, strengthening mechanisms differ substantially from conventional cast alloys and are mostly related to the solid solution, microstructure refinement, and, to a lesser extent, precipitation hardening [9]. Therefore, it is crucial to assess mechanical behavior and its correlation to microstructural features and heat treatment conditions, even when exposed to high temperatures. Furthermore, innovative heat treatments can be optimized on this peculiar microstructure. For example, artificial aging performed directly from the as-built condition promotes the precipitation from the supersaturated solid solution (T5 treatment) [10–15].

Moreover, conventional T6 heat treatment variations can be optimized to induce microstructure homogenization [10–14,16,17]. On the other hand, PBF-LB suffers from typical microstructural defects, such as lack of fusion region, gas, or keyhole porosity, that can also affect the mechanical behavior of the alloy [18]. The role of heat treatment in defining the mechanical response of the A357 PBF-LB alloy has been widely investigated in the literature [10–16]. Some works focused on the correlation between mechanical properties and defects content for the Al-Si PBF-LB alloys can also be found [19,20]. However, the concurrent effect of defects content and heat treatment condition must be addressed. Furthermore, even though a few attempts to assess the high-temperature behavior of AlSi10Mg PBF-LB alloy have been carried out [21–24] to the best of the authors' knowledge, mechanical properties at high temperatures of the A357 PBF-LB alloy have yet to be investigated.

Based on the above, this study aims at (i) investigating tensile behavior at room and high (200 °C) temperature of the A357 PBF-LB in the as-built state and after tailored heat treatments (T5 and T6, optimized in previous work [25]) at peak-aging condition; (ii) correlating tensile behavior to both microstructural features, induced by heat treatments, and defects, induced by the process, by performing the analysis of structural integrity of the alloy with the support of microstructural and fractographic observations.

2. Materials and Methods

2.1. Samples Production and Heat Treatments

Tensile AlSi7Mg0.6 (designated as A357 according to EN1780 standard [26]) samples were produced by PBF-LB, starting from atomized powder supplied by Carpenter Additive (Carpenter Additive, Carpenter Technology Corporation, Philadelphia, PA, USA). Powder chemical composition is reported in Table 1, and its complete characterization can be found in a previous work [27]. In Table 1, the nominal chemical composition of powder was compared to one of the printed samples and checked with a Glow Discharge Optical Emission Spectroscopy (GDOES, GDA-650 Spectrum Analytik GmbH, Hof, Germany). The chemical composition of powder and printed samples satisfied the requirements of the EN 1706 standard for the AlSi7Mg0.6 alloy [28]. More importantly, no deviation in the Mg content was verified in the PBF-LB samples, suggesting that no vaporization of this low melting element occurred during the process.

A total of 24 samples were arranged in four identical building platforms of 8 specimens each to ensure an equivalent in-process thermal cycle. Platforms were designed to enhance the quality of printed parts that, in the absence of pre-heating as in this case, requires limiting the cooling of samples between two subsequent layers (Figure 1a).

Before each job, A357 powder was subjected to a drying pre-treatment, optimized in a previous work [27], at 60 °C for 3 h. A SISMA MySint 100 RM system (SISMA S.p.a, Piovene Rocchette, Italy), equipped with a 200 W fiber laser with a spot diameter of 55 μm,

was used for sample fabrication. The process occurred in a nitrogen environment with residual oxygen content less than 0.1 vol.% and, as previously mentioned, without using a pre-heated platform. Supports, process parameters, and scanning strategy were designed by dedicated software (AutoFab RnD 2.0, Marcam Engineering GmbH, Bremen, Germany) and summarized in Table 2. In addition, process parameters in Table 2 were elaborated based on a previous study [27].

Table 1. The powder's chemical composition (wt.%), given by the supplier [29], and PBF-LB tensile samples were checked by GDOES.

	Al	Si	Mg	Fe	Cu	Mn	Ti	Zn	O	N	Other
Powder	Bal.	6.90	0.55	0.09	<0.05	<0.01	0.09	<0.01	0.1	<0.2	<0.1
PBF-LB tensile samples	Bal.	7.34	0.56	0.08	-	-	0.14	0.07	-	-	0.02

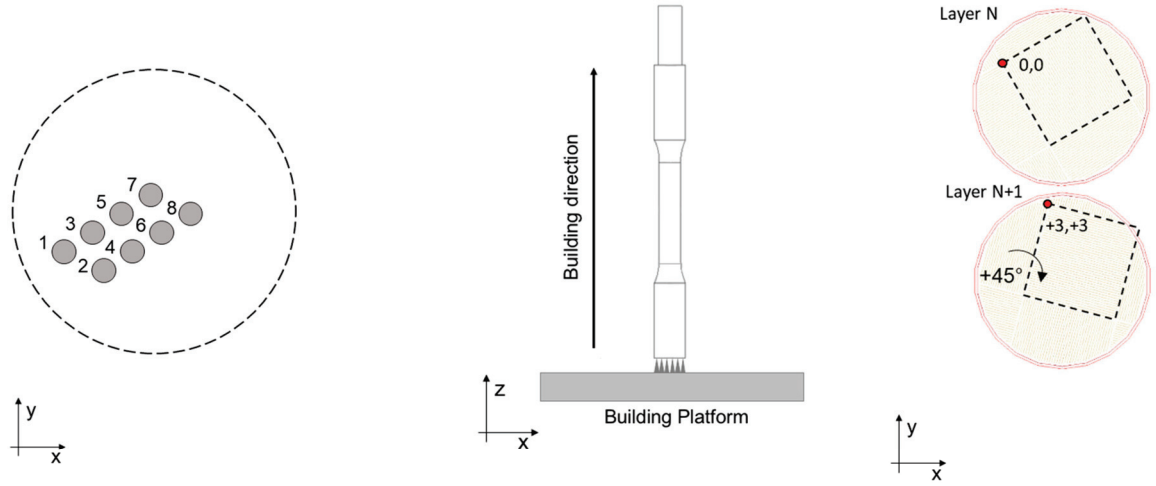

(**a**) (**b**) (**c**)

Figure 1. Tensile samples manufacturing: (**a**) printing position and scanning order; (**b**) building direction, (**c**) chessboard scan strategy.

Table 2. PBF-LB process parameters used for tensile sample manufacturing.

Support Type	Laser Power [W]	Scan Speed [mm/s]	Layer Thickness [μm]	Hatch Space [μm]	Scan Strategy
Cones	175	500	20	80	3×3 mm^2 chessboard

Samples were printed along the direction perpendicular to the platform (along the *z*-axis, Figure 1b), and a roto translating 3×3 mm^2 chessboard scanning strategy (Figure 1c) with an enabled skywriting function was utilized. Round cross-section tensile samples were built with a near-net-shape geometry (Figure 2a) and then machined to final dimensions (Figure 2b); the gripped end geometry was designed to facilitate post-process machining. Tensile samples were proportional (as defined by EN ISO 6892-1 [30]) with a 5 mm final diameter, a 28 mm parallel length, and a 25 mm original gauge length.

Among the 24 produced samples, 8 were tested in the as-built condition, while 16 were subjected to a post-process heat treatment. Direct artificial aging from the as-built condition (T5 temper) and innovative treatment involving a rapid solution treatment, quenching, and artificial aging (T6R temper) was performed [31]. Heat treatment parameters at peak-aged conditions (Table 3) have been tailored to the characteristic microstructure resulting from the PBF-LB process, which diverges substantially from conventional cast alloys. Heat

treatment conditions were optimized in previous work [25] and were performed before machining to the final geometry.

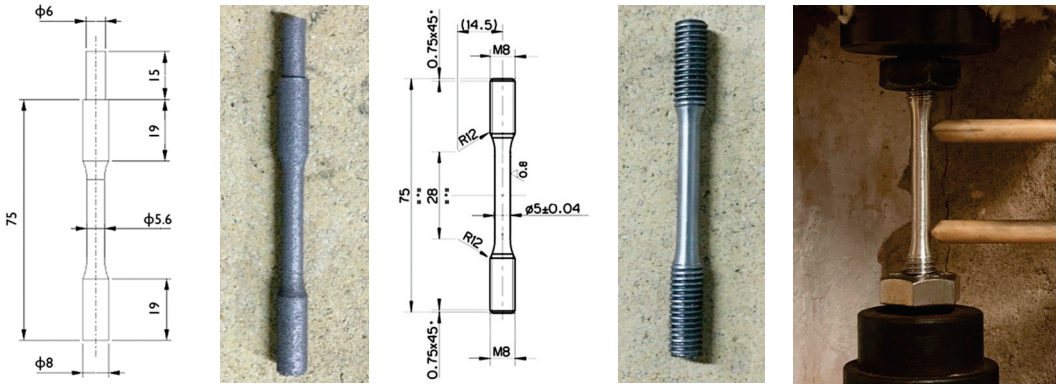

(**a**) (**b**) (**c**)

Figure 2. Tensile samples geometry and dimensions: (**a**) near-net-shape sample obtained by PBF-LB process, (**b**) final sample after machining. In (**c**): equipment for tensile tests.

Table 3. Heat treatments (optimized in [25]) and tensile test conditions.

	Heat Treatment Conditions					**Tensile Test Temperature**	
	Solution Treatment		**Water Quenching**	**Artificial Aging**			
	T [°C]	**t [min]**		**T [°C]**	**t [h]**		
As-built	-	-	-	-	-	Room T	200 °C
T6R	540	10	Warm water (60 °C)	150	4	Room T	200 °C
T5	-		-	170	1	Room T	200 °C

2.2. Tensile and Hardness Tests

Tensile tests were conducted at room and high (200 °C) temperature, following the EN ISO 6892-1 and EN ISO 6892-2 standards [30,32]. Tests were performed on a screw tensile testing machine with a resistance furnace, a 20 kN load cell, and a clip-on extensometer (Figure 1c). Tests were conducted in displacement control mode, with a crosshead speed of 0.007 mm/s. A data acquisition system continuously acquired force and displacement values to compute engineering curves during the tests. All heat treatment conditions were tested at both temperatures, as evidenced in Table 3, and four repetitions were performed for each condition. A soaking time of 30 min was adopted for high-temperature tests to homogenize the sample temperature before the test. The temperature of 200 °C was chosen based on the service life of power-train components and on the threshold temperature at which microstructural coarsening of conventional cast alloys occurs [3,4].

According to the aforementioned standards [30,32], Young modulus (E) is evaluated based on force-extension curves as the slope of the linear portion of the curve, while yield stress is determined as proof strength at 0.2% strain ($Rp_{0.2}$). The tensile strength is defined as Rm, and the percentage elongation after fracture (A%) is determined by deducing the elastic extension. The modulus of resilience (U_R), defined as the area under the engineering stress-strain curve in the elastic region [33], and the modulus of toughness (U_T), defined as the area under the whole engineering stress-strain curve [33], were evaluated for each sample tested. Furthermore, the true stress-true strain curves were computed [33,34]. For tests carried out at room temperature, the structural integrity of samples as a function of the temper condition was evaluated by a detailed analysis of the plastic region of the curve. The Voce equation and Kocks-Mecking model were obtained to describe the work-hardening behavior in as-built, T5, and T6R states. Evaluation of the structural integrity of samples was

performed by computing quality indexes [35–37] and by comparing the experimental tensile strength to the target one that can be reached if no major microstructural discontinuities are present [36,38,39]. Moreover, the strain hardening exponent (n) was evaluated according to the ISO 10275 standard [40].

Sample hardness was evaluated following the Brinell method (HB10, with 2.5 mm ball diameter, 62.5 kgf force, and a force-diameter ratio equal to 10 [41]) before tensile tests and after the tests performed at 200 °C; the latter is defined as residual hardness.

2.3. Microstructural and Fractographic Characterization

After tensile tests, the surface fracture was analyzed at high magnification by a Field Emission Gun Scanning Electron Microscope (FEG-SEM, Tescan Mira 3) to investigate fracture morphology and mechanism.

Microstructural analyses were then devoted to correlate the static mechanical behavior to the microstructural features. To this aim, microstructural characterization was performed on sections extracted from the grip region of samples along the longitudinal (x-z) plane, parallel to the building direction, and along the transversal (x-y) plane, parallel to the building platform and consistent with the cross-section area. Metallographic sections were embedded in a conductive resin and then ground and polished to a mirror finish following standard procedures [42]. Microstructural features were revealed with chemical etching with Keller's reagent (2.5 mL HNO_3, 1.5 mL HCl, 1.0 mL HF and 95 mL distilled water [43]), performed by a 20 s immersion at ambient temperature. Microstructural investigation of etched sections was carried out using optical (OM, Zeiss Axio Imager A1) and FEG-SEM microscopy. Quantitative evaluation of microstructural features (i.e., area% of Si-rich region, as will be later discussed) was conducted with the ImageJ software (National Institutes of Health, version 1.46r, Bethesda, Bethesda, MD, USA) [44].

3. Results and Discussion

3.1. Room Temperature Tensile Behavior: Effect of Temper Condition

Representative engineering and true stress-strain curves of the considered temper conditions (as-built, T5 and T6R) are compared in Figure 3a for room temperature tensile tests and Figure 3b for high temperature (200 °C) tests. Mechanical properties obtained from the analyses of the curves are reported in Figure 4 (yield stress, tensile strength, and elongation) and in Figure 5 (Young, resilience, and toughness modulus). The hardness of the alloy, measured after tensile tests, is reported in Figure 6.

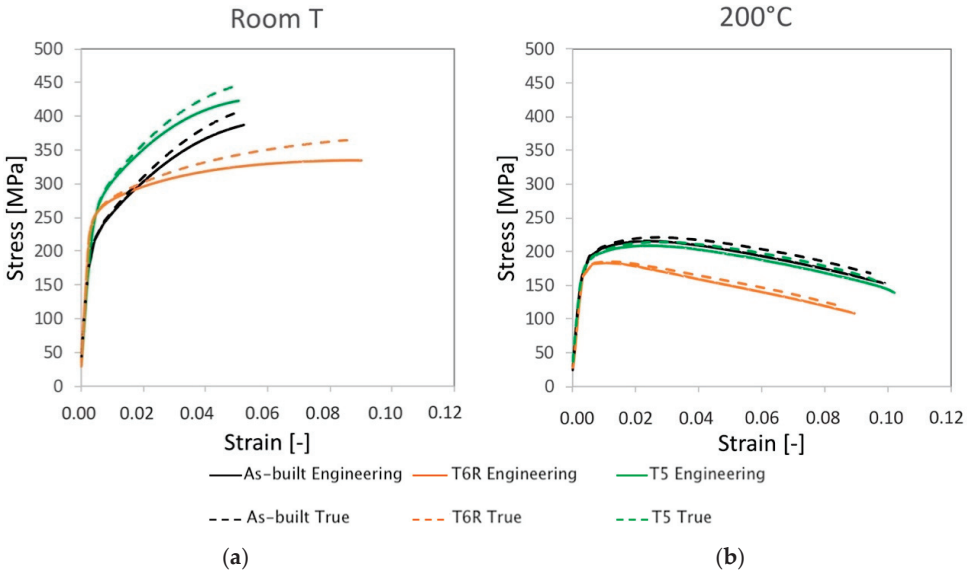

Figure 3. Representative engineering and true stress-strain curves for the as-built, T5, and T6R AlSi7Mg PBF-LB alloy: (**a**) room temperature and (**b**) high temperature (200 °C) tensile tests.

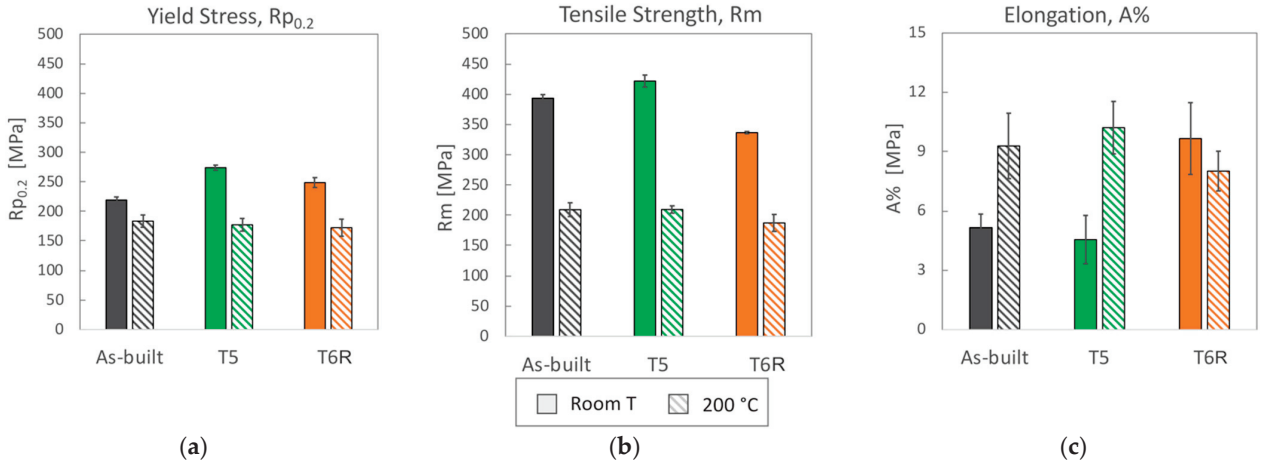

Figure 4. (**a**) Yield stress, (**b**) tensile strength, and (**c**) elongation to failure (mean value and standard deviation) obtained from tensile tests performed at room and high (200 °C) temperature for the as-built, T5, and T6R AlSi7Mg PBF-LB alloy.

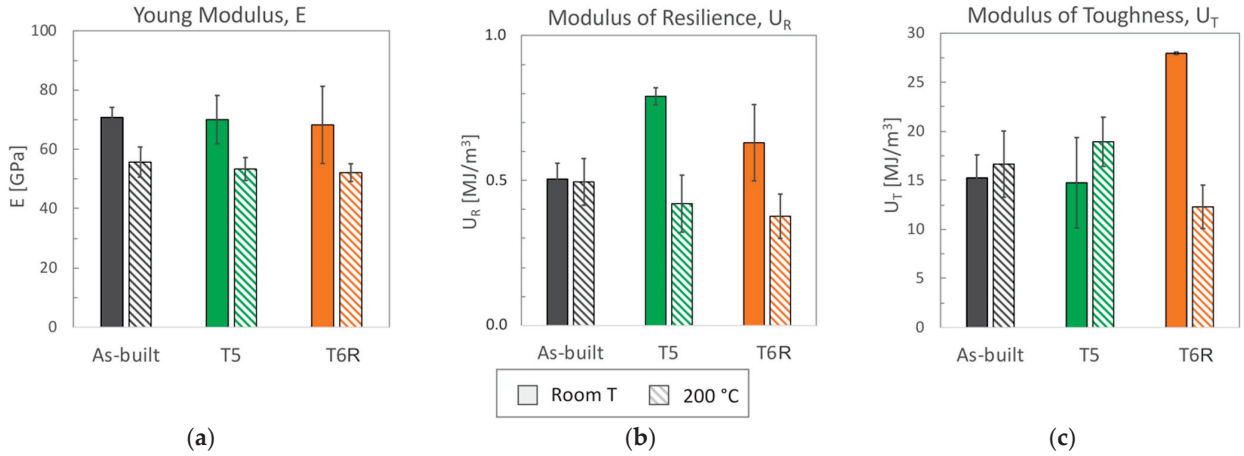

Figure 5. (**a**) Young, (**b**) resilience, and (**c**) toughness modulus (mean value and standard deviation) obtained from tensile tests performed at room and high (200 °C) temperature for the as-built, T5, and T6R AlSi7Mg PBF-LB alloy.

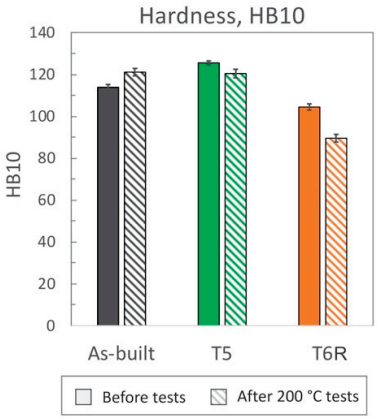

Figure 6. Hardness was evaluated on tensile samples after tests performed at room and high (200 °C) temperature for the as-built, T5, and T6R AlSi7Mg PBF-LB alloy (mean value and standard deviation).

By focusing on room temperature tests, a significant difference in tensile behavior can be noticed according to the temper condition of the alloy. Differences are related to

elastic (yield stress, resilience modulus) and plastic (tensile strength, elongation, toughness modulus) properties, as confirmed by data in Figures 4 and 5. Data are discussed mainly by focusing on mean values, as standard deviations for the given property were comparable among temper conditions. As regards yield stress, the as-built alloy was characterized by $Rp_{0.2}$ = 216 ± 5 MPa and, regarding literature data [10–12,15,16,45], the value is comparable to samples fabricated in similar conditions (vertical building direction and no platform pre-heating), but it is about 30% lower than samples built with a pre-heated platform (temperatures range 100–150 °C). Presumably, samples built with platform pre-heating experienced artificial aging, thus justifying this difference [10,46]. Comparable considerations can also be drawn for ultimate tensile strength that, for the present work, was set at R_m = 394 ± 6 MPa. By also considering the good elongation to failure, equal to A% = 5.2 ± 0.7%, the alloy in the as-built state was characterized by an overall satisfying mechanical behavior.

Both T5 and T6R treatments increased the yield stress of the alloy that reached the highest value after the direct aging (T5) treatment. The yield stress increase compared to the as-built condition was +25% (274 ± 4 MPa) and +13% (249 ± 8 MPa) in the case of T5 and T6R, respectively. As discussed in the following, the increase in yield stress can be correlated to the precipitation of fine reinforcing particles, as evidenced in previous work [25]. An even higher increase was measured for the resilience modulus, which quantifies the material's ability to adsorb energy when subjected to elastic deformation, equal to +56% for T5 (0.79 ± 0.03 MJ/m^3) and +25% for T6R (0.63 ± 0.13 MJ/m^3). By focusing on the plastic region of the stress-strain curves, the effect of the applied heat treatment diverged between T5 and T6R. T5 slightly increased (by 7%, reaching 422 ± 10 MPa) the tensile strength of the as-built alloy without dramatically affecting the elongation (equal to 4.6 ± 1.2%, decreased by 12%). As a result, the modulus of toughness, which quantifies the ability of the material to adsorb energy when subjected to plastic deformation without occurring into the fracture, was comparable for both conditions (15.3 ± 2.3 and 14.8 ± 4.6 MJ/m^3 for as-built and T5, respectively). On the other hand, if compared to the as-built condition, the optimized T6R treatment induced a decrease in the tensile strength (equal to 337 ± 2 MPa, decreased by 14%) and a marked increase in the elongation (by 87%, reaching 9.7 ± 1.8%). Therefore, toughness was maximized by T6R treatment, which reached the value of 28 ± 0.13 MJ/m^3 and increased by 83% compared to the as-built condition. It should be mentioned that toughness is an essential property for a mechanical structural component in all cases where, occasionally, during in-service conditions, the applied stress overcomes the yield. In line with the tensile results, when coming to hardness measurement (Figure 6), T5 treatment induced an increase (from 114 ± 1 of the as-built state to 126 ± 1 HB10). T6R treatment slightly decreased the alloy hardness, reaching 104 ± 1 HB10, even if it improved alloy ductility and the trade-off between strength and ductility.

Microstructural features determine mechanical properties, particularly the involved strengthening mechanisms. Therefore, a modification in the tensile behavior suggests a modification in the strengthening mechanisms, thus on microstructural features. It is well-known that a hierarchical arrangement characterizes the microstructure of PBF-LB Al-Si-Mg alloys, and several microstructural features, with a distinctive scale, can be resolved: (i) layer-by-layer structure formed by solidified melt pools with dimensions up to hundreds of micrometers, (ii) micrometric epitaxial grains passing over layers, (iii) sub-micrometric cellular substructure [8]. According to recent works [9,47–52], the cellular substructure has a crucial role in defining the mechanical properties of Al-Si-Mg alloys. Representative microstructure of as-built, T5, and T6R alloys, observed along the xy (parallel to the building platform) and xz (parallel to the building direction) planes, are reported in Figure 7. The figure shows the characteristic structure formed by sub-micrometric α-Al cells surrounded by a fine network of eutectic-Si. The as-built microstructure suffered from a certain degree of anisotropy. If analyzed in the xy plane, α-Al cells were almost equiaxed (Figure 7a); however, if observed in the xz plane, cells were elongated along the building direction (Figure 7d).

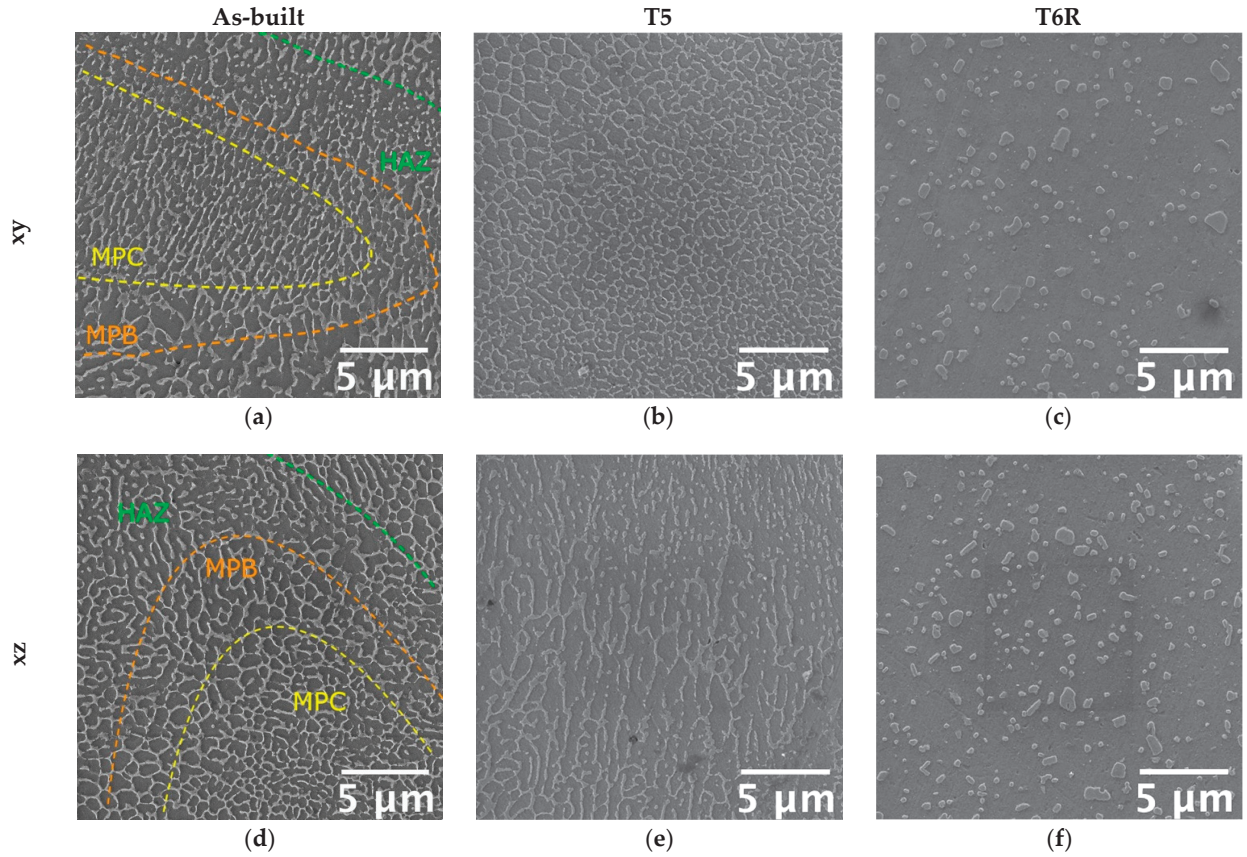

Figure 7. FEG-SEM high magnification micrographs showing the typical microstructure of the as-built, T5, and T6R AlSi7Mg PBF-LB alloy: (**a**–**c**) along the direction parallel to the building platform (xy plane); (**d**–**f**) along the direction parallel to the building one (xz plane).

Furthermore, due to the repeated heat cycles experienced during the PBF-LB process, the morphology of the eutectic-Si network is not homogeneous. In particular, it changes according to the considered region of the melt pool formed due to the interaction between the laser beam and the powder bed [8,53]. If close to the core of the melt pool (MPC in the figure), the network is fine and interconnected; if close to the border (MPB in the figure), it is slightly coarser and partially discontinuous, while in the heat-affected region between consecutive layers (HAZ in the figure), it is almost entirely interrupted. Therefore, in the as-built condition, the peculiar microstructure is extremely inhomogeneous and closely dependent on the process parameters, such as building direction and scanning strategy. The T5 alloy was still characterized by the extremely fine cellular structure in the as-built condition (Figure 7b,e). However, in some regions, the eutectic-Si network appeared slightly fragmented, less defined, and thinner than the as-built one. Finally, the T6R treatments deleted any trace of the manufacturing process (Figure 7c,f). As a result, the eutectic-Si network completely broke down, and the microstructure consisted of a fine distribution of globular and sub-micrometric Si-rich particles dispersed in the α-Al matrix. T6R treatment also succeeded in homogenizing the microstructure, as no difference in morphology was evidenced between the xy and the xz planes.

The definition of strengthening mechanisms involved in the Al-Si-Mg PBF-LB and their relative contribution is still an open field of research, even if several attempts have been made to correlate tensile behavior to microstructure [9]. However, according to the most recent literature, Si plays a significant role in defining the mechanical properties of the alloy, and it can be found in the form of: (i) solid solution; (ii) nanometric-sized Si-particles dispersed within α-Al cells; (iii) eutectic-Si network. Consequently, based on both mechanical and microstructural analyses, as well as literature findings [47–50], it

can be assumed that the main strengthening mechanisms involved in the Al-Si-Mg PBF-LB alloys are: (i) microstructure refinement and solid solution in the as-built condition; (ii) microstructure refinement, solid solution, and precipitation of nanometric-Si from the supersaturated solution in the direct aged (T5) condition; (iii) precipitation of both nanometric-Si and Mg_2Si precursors strengthening phases in the T6R condition. Previous studies on the role of post-process heat treatments of the PBF-LB AlSi7Mg alloy carried out by the authors [25] confirmed that partial precipitation of Si from the supersaturated Al matrix occurred after direct aging. However, more prominent precipitation of Si occurred after the solution treatment and, after artificial aging, also Mg_2Si precursors were detected by XRD analyses. Hence, precipitation strengthening justifies the increase in the yield stress observed for T5 and T6R.

Furthermore, the role of residual stress should also be considered, which can strongly affect mechanical behavior. In the as-built condition, samples were characterized by tensile residual stress, only partially removed by T5 treatment. T6 treatment, on the other hand, succeeded in completely relieving tensile residual stress and presumably induced slight compressive stress [25]. Although, it is worth mentioning that, especially in the case of tensile strength and ductility, strengthening mechanisms and residual stress are not the only ones responsible for defining mechanical properties. Microstructural defects, like porosities, can be detrimental and affect the structural integrity of the alloy. Therefore, the overall mechanical behavior is balanced between these three fundamental aspects.

Work Hardening

Significant differences among the temper conditions were found in the work-hardening behavior. Further analyses were conducted on the plastic region of true stress-strain curves to correlate it to the microstructural features. In the literature, the analysis of the plastic region of stress-strain curves is used to assess the structural integrity of the alloy as the presence of defects, like internal material discontinuities, affects the plastic behavior of the alloy [36,37,54]. While yield stress is marginally affected by defects, Rm and A% strongly depend on it [33]. In the case of PBF-LB, parts are characterized by specific internal defects, such as gas porosities and lack of fusions. Their effect on the mechanical response should be considered. Therefore, the Voce equation and Kock-Mecking model [55,56] investigated the work-hardening behavior of as-built, T5, and T6R samples. Voce equation (Equation (1)) was developed to describe the plastic flow behavior, and it is more effective in the case of fcc-metals than other well-known laws such as Hollomon, Ludwik, and Ludwigson ones [57]. As shown in Figure 8, the Voce equation can be proficiently used also to describe the behavior of the AlSi7Mg PBF-LB alloy.

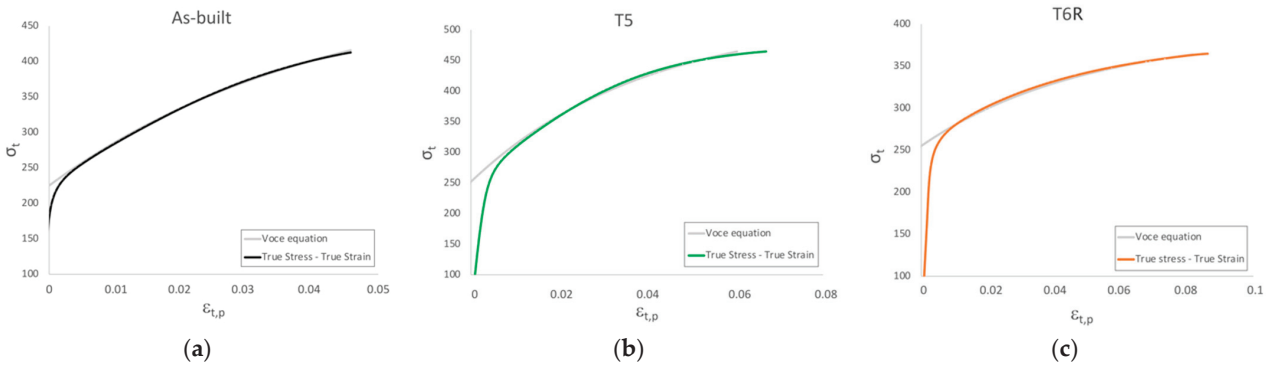

Figure 8. Comparison between true stress-true strain experimental curves and flow curves obtained with Voce equation of representative: (**a**) as-built, (**b**) T5, and (**c**) T6R tensile samples.

Voce equation is expressed as:

$$\sigma_t = \sigma_s + (\sigma_s + \sigma_0)^{-(\varepsilon_{t,p}/\varepsilon_0)} \quad (1)$$

whereσ_s is the saturation stress in case of full plasticity, reached when work hardening rate $\theta = {}^{d\sigma}/_{\varepsilon} = 0$; σ_0 is the threshold stress reached when the true plastic strain $\varepsilon_{t,p} = 0$; ε_0 is the strain characteristic of the Voce equation controlling the shape of the curve.

Based on the Voce equation, the Kocks-Mecking model (Equation (2)) was developed to describe the Stage III of work hardening, characterized by a linear behavior in a diagram representing the work hardening rate θ as a function of the true stress σ_t, termed as Kock-Mecking (KM) diagram (Figure 9).

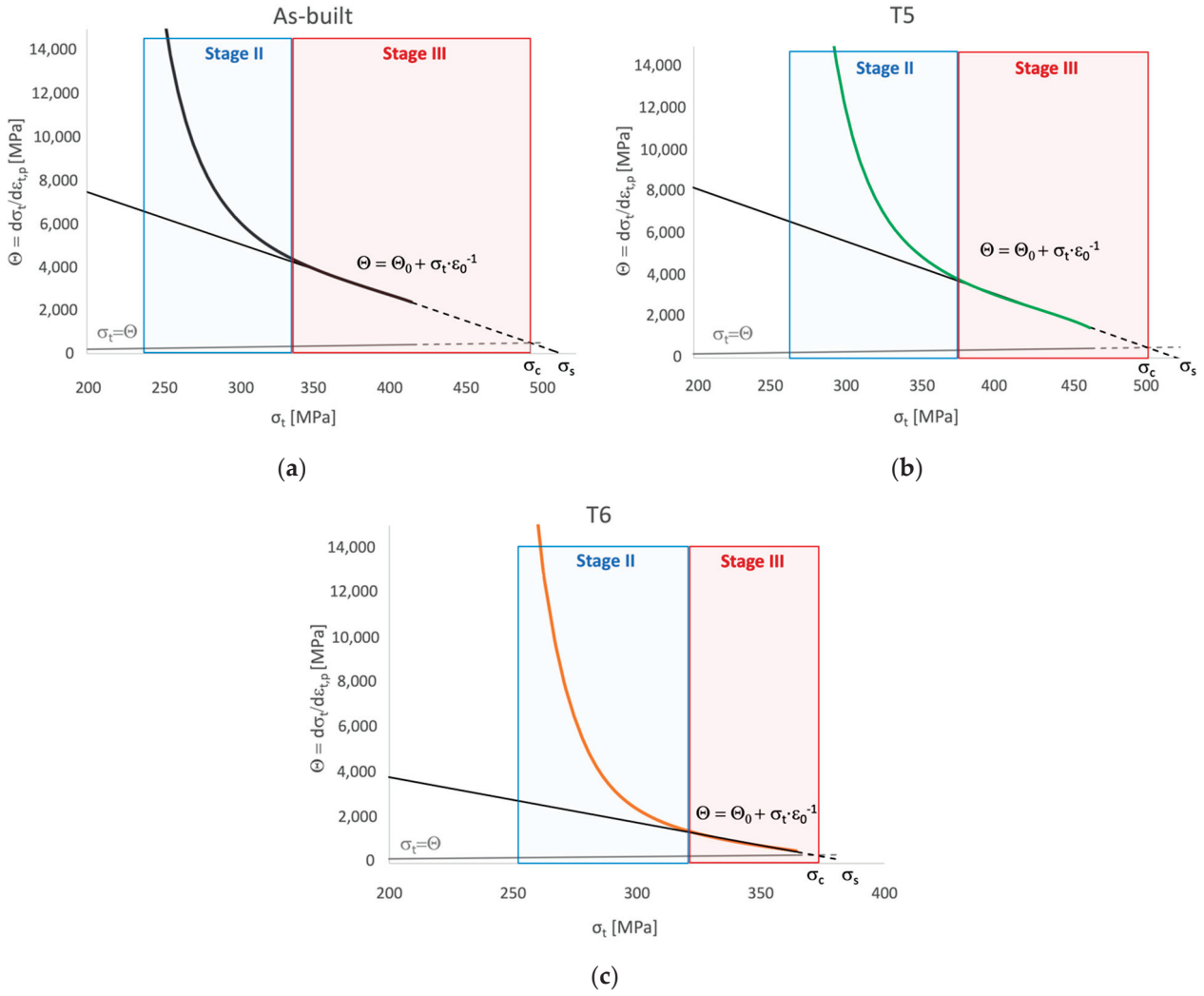

Figure 9. Kocks-Mecking (KM) diagram obtained for the AlSi7Mg PBF-LB alloy in the: (**a**) as-built (black line), (**b**) T5 (green line), and (**c**) T6R temper condition (orange line). Solid lines represent the elaboration of experimental data from tensile tests; dashed lines represent linear extrapolation from experimental data.

The Kocks-Mecking model is expressed as:

$$\theta = {}^{d\sigma}/_{d\varepsilon} = \theta_0 + K\sigma_t \quad (2)$$

where θ_0 work hardening rate when $\sigma = 0$ and is a parameter mainly depending on Stage II work hardening rate and strain rate. According to Angella et al. [54], this parameter can be obtained based on the Voce equation as . From a physical point of view, θ_0 is an athermal constant that describes the dislocation storage rate and is inversely related to the characteristic dimension of the microstructure, while K is a thermal parameter related to the dynamic recovery [54,55,57].

Work hardening behavior of polycrystalline metals can be divided into three stages: (i) non-linear Stage II, where athermal work hardening occurs at a high rate; (ii) linear Stage III, where work hardening and softening mechanisms compete, this region is temperature, and strain-rate sensitive as thermal activation facilitate the dynamic recovery; (iii) non-linear Stage IV where tensile instability is reached. Fracture of samples without major internal defects affecting their structural integrity occurs during Stage IV [37,58,59]. In the same diagram, also the equation characteristic of the onset of the diffusive necking phenomenon $\theta = {}^{d\sigma}/_{d\varepsilon} = \sigma_t$, according to the Considère criterion $\sigma_{t,necking} = \left({}^{d\sigma_t}/_{d\varepsilon_{t,necking}}\right)$, can be represented [60,61]. Therefore, the intersection between the Stage III linear equation and the necking one, which occurs at $\sigma_t = \sigma_c$, can be considered as the threshold between Stage III and Stage IV. As depicted by KM diagrams in Figure 9, samples did not reach Stage IV. Therefore, fracture occurred within Stage III, suggesting a major influence of internal defects in the tensile behavior. Only in the case of the T6R condition, experimental data (solid lines in Figure 9) covered almost entirely Stage III.

This result was also confirmed by comparing the experimental R_m values for each temper condition (already discussed in Figure 4) to the target one, mathematically obtained following the procedure proposed by Tiryakioglu et al. [36] and reported in Figure 10a. As a result, variations among samples are quite reduced. Furthermore, comparing experimental and target data that could be reached in case of the absence of detrimental internal discontinuities shows that only T6R samples reached R_m values close to the target one. Since samples were produced with the same processing conditions, it can be assumed that a comparable content of internal defects characterized them. Therefore, the analysis conducted here suggests that the modification in the microstructure due to the T6R treatment reduced the detrimental effects of internal defects in the plastic behavior of the AlSi7Mg PBF-LB alloy.

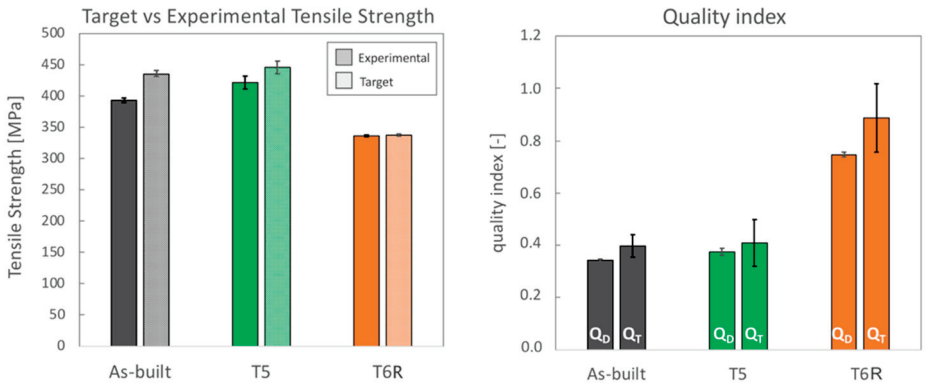

Figure 10. Results from the analyses of the strain hardening behavior AlSi7Mg PBF-LB alloy in the as-built, T5, and T6R temper condition: (**a**) experimental tensile strength obtained from tensile tests compared to the target one; (**b**) quality index (Q_D index is based on ductility, Q_T index is based on toughness).

Analogous results were obtained by comparing quality indexes (Figure 10b). The indexes here considered were elaborated based on the analysis of strain hardening behavior and structural integrity of conventional Al alloys [36–38,54] and derived from the ductility (Q_D) and toughness (Q_T) of the alloy. The quality index Q_D (Equation (3)), also known as the relative ductility parameter q [38], compares the theoretical uniform strain up to the onset of the necking phenomenon ε_{unif}, calculated as proposed by Angella et al. [54], and the strain at fracture ε_f obtained by tensile tests. ε_{unif} represents the maximum practical ductility of the material; therefore, materials that undergo failure before reaching this value ($Q_D < 1$) suffer from internal discontinuities that affect their ductility. The quality index Q_T (Equation (4)), proposed by Tiryakioglu et al. [36], compares the target toughness value ψ_c, that has to be reached during the tensile test in a sample free from major discontinuities,

and the toughness ψ obtained from experimental tensile test. Toughness can be evaluated from the area under the stress-strain curves, as in the present work, or mathematically as a function of the values $R_{p0,2}$, $R_{m,}$ and A%. Q_T index was developed on the concept that the adsorbed energy, thus the toughness, is directly related to the effective crack length produced by discontinuities. Therefore, samples characterized by major internal discontinuities will return $Q_T < 1$.

$$Q_D = \varepsilon_{unif}/\varepsilon_f \tag{3}$$

$$Q_T = \psi_C/\psi \tag{4}$$

Q_D and Q_T indexes obtained for the AlSi7Mg PBF-LB alloy in the as-built, T5, and T6R conditions were lower than 1, thus indicating that internal defects affected the mechanical response of the alloy. However, the T6R state showed the highest quality index, thus confirming that the modifications induced in the microstructure by the tailored T6R treatment, probably also in relieving residual stress as found in previous work [25], reduced the detrimental effect of internal defects.

As previously mentioned, parameters of the Voce equation describing Stage III of strain hardening are closely related to microstructural features. For example, Θ_0 is inversely proportional to the mean free path of mobile dislocation [39]; therefore, it can be correlated to the finesse of the microstructure, like, in the case of PBF-LB, cells dimensions, grain size, and size of Si nanoparticles. On the other hand, ${\varepsilon_0}^{-1}$ is related to dislocation motion, and, in particular, it depends on the crystallographic lattice in which dislocations move [39]. Therefore, a great value of Θ_0 means a fine microstructure and a great ${\varepsilon_0}^{-1}$ value indicates a high tendency to recover dynamically. The strain hardening behavior in Stage III depends on the balance between hindering of dislocation motion and dynamic recovery, so high Θ_0 and ${\varepsilon_0}^{-1}$ are related to high strain hardening ability. The parameters of the Voce equation obtained in the present study are summarized in Table 4. Based on the above, as-built and T5 temper conditions were characterized by the highest values of Voce parameters, thus indicating a very fine microstructure and a significant tendency to strain hardening. In particular, the T5 temper condition was able to maximize both parameters. In the case of T6R, the Θ_0 value was reduced by approximately 50%, suggesting that the heat treatment induced a significant coarsening of the microstructure. On the contrary, the ${\varepsilon_0}^{-1}$ value was comparable to the as-built one, thus suggesting that the ability for dynamic recovery was not affected by the T6R treatment.

Table 4. Parameters of Voce equation, Θ_0 and ${\varepsilon_0}^{-1}$, obtained by the analysis of strain hardening behavior of the AlSi7Mg PBF-LB alloy tested in the as-built, T5 and T6R condition.

Temper Condition	Θ_0 [MPa]	${\varepsilon_0}^{-1}$ [-]
As-built	$12.1 \pm 0.7 \times 10^3$	23.9 ± 1.6
T5	$16.4 \pm 2.1 \times 10^3$	32.3 ± 4.7
T6R	$8.0 \pm 0.6 \times 10^3$	20.4 ± 1.7

Accordingly, strain hardening exponents, n, were evaluated for all the alloy conditions. Results showed that the as-built alloy was characterized by the highest strain hardening exponent (n = 0.26 ± 0.004), which decreased after both T5 (n = 0.21 ± 0.01) and T6R (n = 0.11 ± 0.01) treatments. This result partially confirmed the above outcome and was obtained from the Voce equation. It is known that a change in the strain-hardening behavior suggests a modification in the type or dimension of microstructural features hindering dislocation motion, mostly related to the presence of Si [9,47–50]. In support of these findings, a strong correlation was found in the present work by comparing the area percentage occupied by the eutectic-Si network in as-built and T5 alloy, or Si-rich globular particles in the T6R one, with the hardening exponent n (Figure 11). Area percentage was measured by image analyses of FEG-SEM micrographs analogous to those reported

in Figure 7. By moving from the as-built to the heat-treated condition, the Si-rich area% decreased. Presumably, in the T5 condition, this is due to the shrinkage of the eutectic-Si network because of the precipitation of nanometric Si particles from both the supersaturated matrix and the eutectic network. After T6R treatment, complete precipitation of Si from the supersaturated matrix occurred, along with precipitation of Mg_2Si reinforcing phase precursors [25]. These precipitates are appreciable only at the nanometric scale, so they were not detected by FEG-SEM analyses. As a result, the area% of the Si-rich region after T6R treatment decreased to approximately the 30% of the area occupied by the eutectic-Si network in the case of as-built alloy. Nevertheless, the strong correlation in Figure 11 suggests that the thick and fine eutectic-Si network surrounding the α-Al cells, acting as a two-phase aggregate strengthening mechanism, is primarily responsible for the great strain hardening behavior of the as-built and T5 AlSi7Mg PBF-LB alloy. In the case of T6R alloy, where the eutectic-Si network is no longer present, and the strain hardening behavior is considerably reduced, different microstructural features (i.e., sub-micrometric Si-rich particles or nanometric reinforcing particles) hinder dislocation motion, presumably in relation to precipitate cutting and precipitate looping mechanisms.

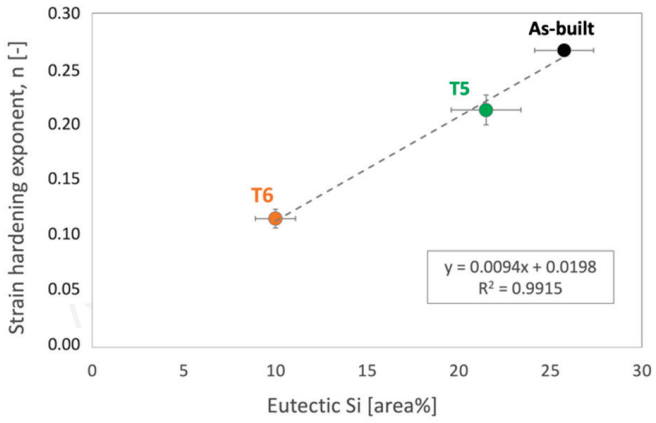

Figure 11. Correlation between strain hardening exponents n measured from true stress-true strain experimental curves and area% of the Si-rich region evaluated on FEG-SEM micrographs for the as-built, T5, and T6R AlSi7Mg PBF-LB tensile samples.

3.2. High-Temperature Tensile Behavior: Effect of Thermal Exposure

When tested at 200 °C, despite the temper condition, samples showed comparable tensile properties (both mean values and standard deviations, Figures 4 and 5). The marked difference in the strain-hardening behavior observed at room temperature was considerably reduced (Figure 3). Based on the previous discussion, it can be argued that the exposition at high temperatures during tensile tests minimized the differences in the structural integrity among temper conditions that, conversely, strongly affected the room temperature behavior. As expected, due to the improved mobility of dislocations at high temperatures, yield stress and tensile strength decreased compared to room temperature tensile tests [23,62]. Accordingly, also Young's modulus decreased from approx. 70 to 50 GPa as a consequence of the exposure to high temperature during the test. The yield stress ranged between 172 and 183 MPa, maximum in the case of as-built samples, while the tensile strength was 209 MPa for as-built and T5 conditions and 187 MPa for T6R. Ductility, on the other hand, for as-built and T5 conditions increased up to 10%, doubling the values obtained at room temperature, while in the case of T6R, it slightly decreased from 9.7 ± 1.8 to 8 ± 1.0%. In terms of modulus of resilience and toughness (Figure 5b,c), the as-built condition was able to preserve the values obtained at room temperature; therefore, its ability to adsorb energy in the elastic and plastic region was not affected by the exposure at high temperature during the tensile test.

On the other hand, this ability was strongly affected in the T6R condition, which showed a significant decrease in both moduli (−40% for U_R and −56% for U_T). T5 condition

exhibited a lower resilience (−47% for U_R) but a higher toughness (+28% for U_T). At the temperature of 200 °C, the as-built condition showed the best overall mechanical behavior, possibly related to its supersaturated solid solution condition. In fact, by observing the residual hardness measured after the test and by comparing it to the values measured before the test (Figure 6), only the as-built condition could increase the hardness after tests. This result presumably relates to the precipitation of nanometric Si particles consequent to the exposition at high temperatures during tests. By observing the microstructure (Figure 12), both as-built and T5 conditions still presented the typical cellular microstructure after high-temperature tests. Compared to the micrographs in Figure 7, it can be noticed that a slight fragmentation occurred due to the high-temperature exposition, as described in [24], even if the phenomenon is more accentuated in the T5 (Figure 12b,e) condition than as-built (Figure 12a,d) one. Mainly if observed on the xy section, the eutectic-Si network on T5 (Figure 12b) samples was almost entirely interrupted, while an overall continuity was maintained on as-built (Figure 12a) ones. Anisotropy in the cellular structure among xy and xz sections was still present in both cases. At the investigated magnification, the T6R microstructure (Figure 12c,f) did not show significant differences due to the high-temperature exposure compared to the microstructure before tests (Figure 7c,f).

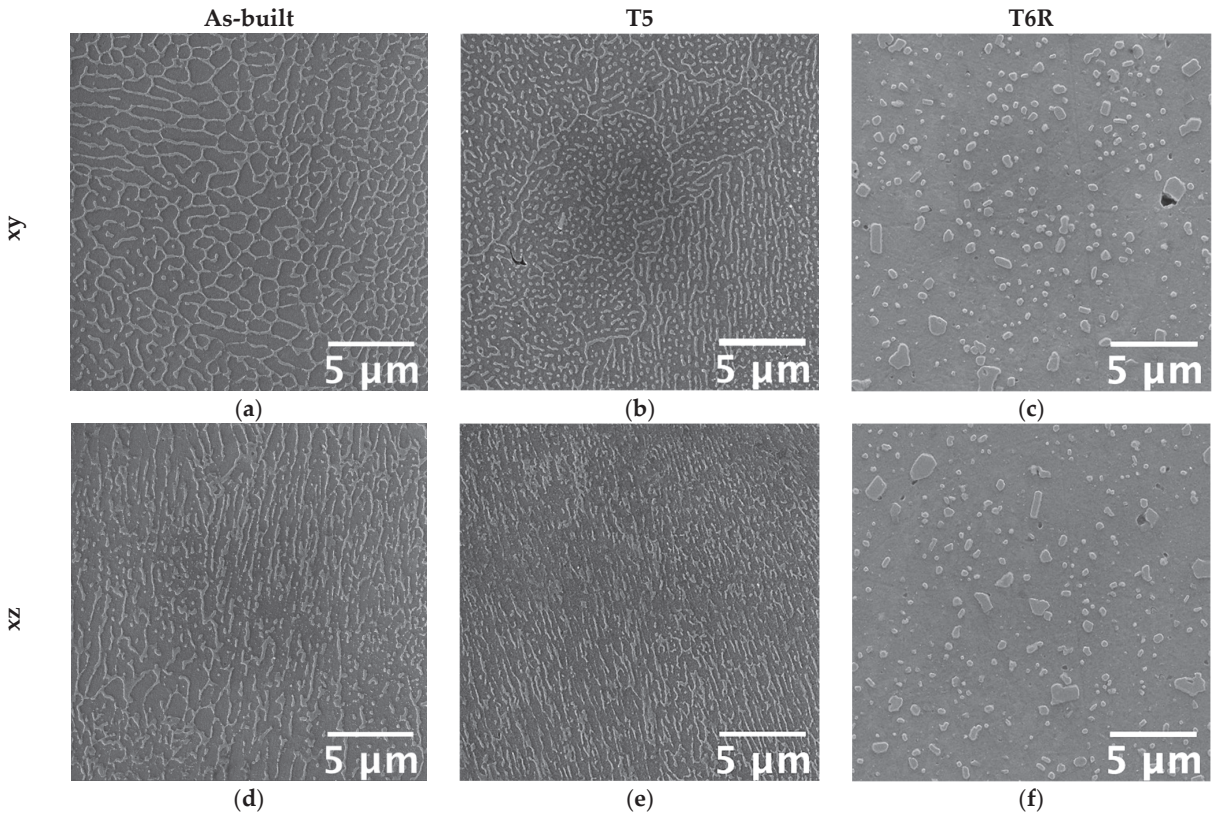

Figure 12. FEG-SEM high magnification micrographs showing the typical microstructure of the as-built, T5, and T6R AlSi7Mg PBF-LB alloy after tensile tests performed at high temperature (200 °C): (**a**–**c**) along the direction parallel to the building platform (xy plane); (**d**–**f**) along the direction parallel to the building one (xz plane).

3.3. Fractographic Analysis

A ductile fracture mode characterized all tested conditions. High magnification analyses of fracture surfaces (Figure 13) revealed the presence of very fine dimples that denote a ductile fracture. Dimples form due to material yielding and usually nucleate in correspondence with material discontinuities. Different microstructural features could be recognized inside dimples based on the temper condition. On as-built samples (Figure 13a,d), a trace of the eutectic-Si network was evidenced, especially on samples tested at room temperature

(Figure 13a), as also observed by Casati and Vedani [12]. After the high-temperature exposure, sub-micrometric particles could be found inside dimples (Figure 13d), confirming the occurrence of Si precipitation from a supersaturated solution. Similarly, sub-micrometric particles were observed inside dimples on T5 samples (Figure 13b,e). By supporting the above-discussed microstructural analyses, traces of the continuous cellular structure were evident only on room-temperature tested samples (Figure 13e).

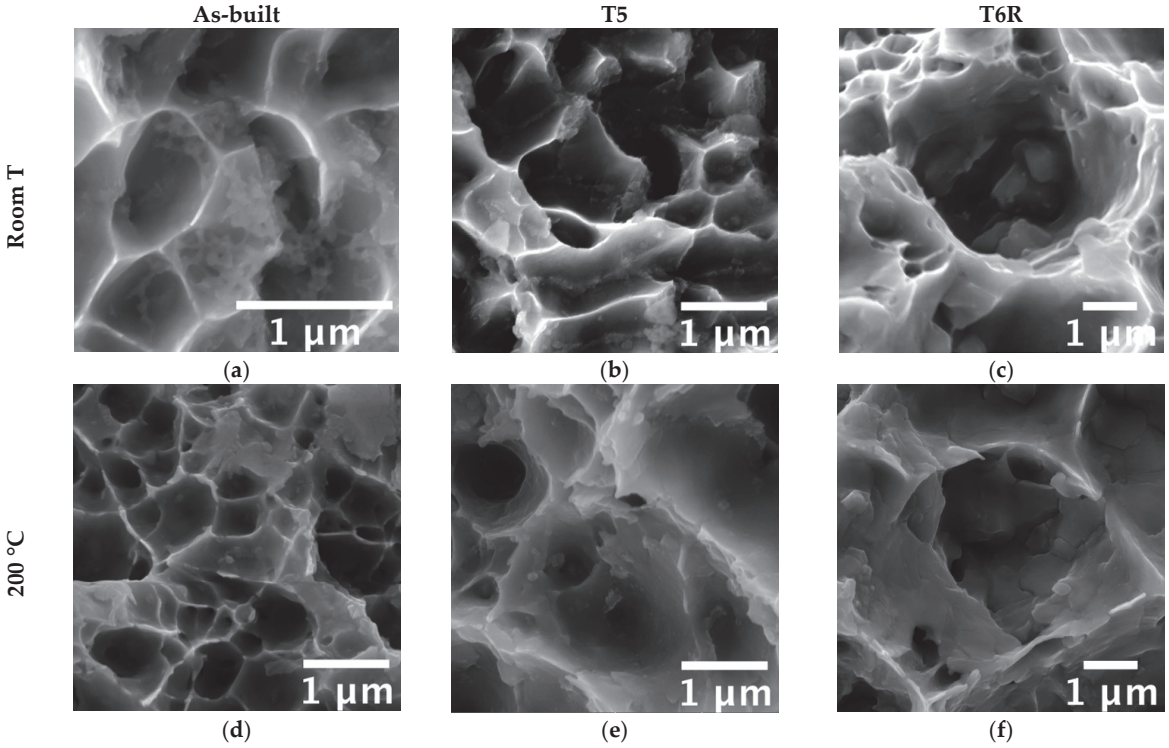

Figure 13. FEG-SEM high magnification fractographic analyses of AB, T5, and T6R AlSi7Mg PBF-LB tensile samples after (**a**–**c**) tests performed at room temperature; (**d**–**f**) tests performed at high temperature (200 °C).

Furthermore, Si particles were found inside dimples in the T6R alloy (Figure 13c,f) that, in most cases, appeared fractured. Due to the flat surfaces of broken Si particles, it can be inferred that a brittle fracture mechanism occurred for them, as also observed by Trevisan et al. [16]. Accordingly to microstructural observations, the finest dimples were observed for the as-built and T5 alloys because of the fine cellular microstructure observed in these conditions. The absence of appreciable microstructural inhomogeneities, as Si-rich particles formed after T6R, delayed dimples nucleation and hindered their growth, as confirmed by the overall fine dimples dimension (approx. 1 µm in the case of as-built alloy). These outcomes agree with the previously discussed tensile results in which both as-built and T5 samples showed greater ultimate tensile strength and hardening than T6 samples. Such finesse was still preserved by the as-built alloy tested at high temperatures, supporting the good overall mechanical behavior discussed in the previous section. It is worth mentioning that only in the case of tests conducted at high temperatures on as-built and T5 samples it was possible to recognize traces of laser scan track on fracture surfaces, as evidenced in Figure 14. Such features evidence the de-cohesion of successive processed layers in correspondence with HAZ regions [63]. Other authors also observed this feature on samples built perpendicularly to the platform, as in the present work [64,65]. However, different from this study, the literature work adopted a platform pre-heating (150–200 °C) for the PBF-LB process and evidenced the presence of scan tracks on surfaces of samples tested at room temperature. Therefore, the de-cohesion of successive processed layers may be promoted by microstructural modifications induced by exposure to high

temperatures during the process or testing. Lastly, the primary defects of this alloy affecting the mechanical behavior, and thus the structural integrity, are represented in Figure 15. Defects found on fracture surfaces of tensile samples, regardless of temper condition or testing temperature, can be divided into two main categories: (i) large and irregular lack of fusion, with dimensions usually greater than 100 µm and an oxidized surface (Figure 15a, highlighted in yellow dashed line); (ii) spherical gas porosities with dimension in the order of tens of micrometers (Figure 15b, highlighted by yellow arrows).

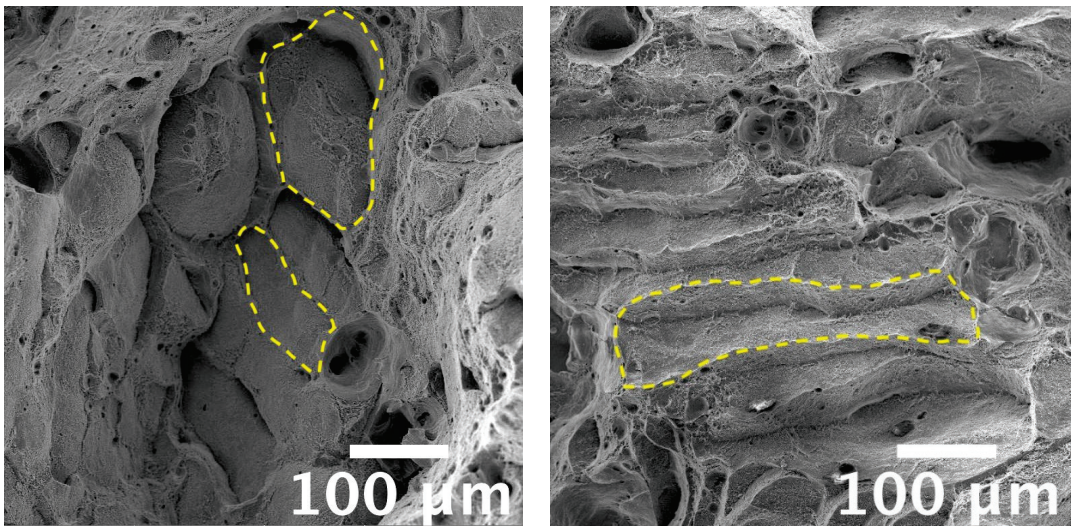

(**a**) (**b**)

Figure 14. FEG-SEM high magnification fractographic analyses, detail of successive layers decohesion on (**a**) AB, (**b**) T5 AlSi7Mg PBF-LB tested at 200 °C. Yellow dashed lines highlight some features related to laser scan tracks.

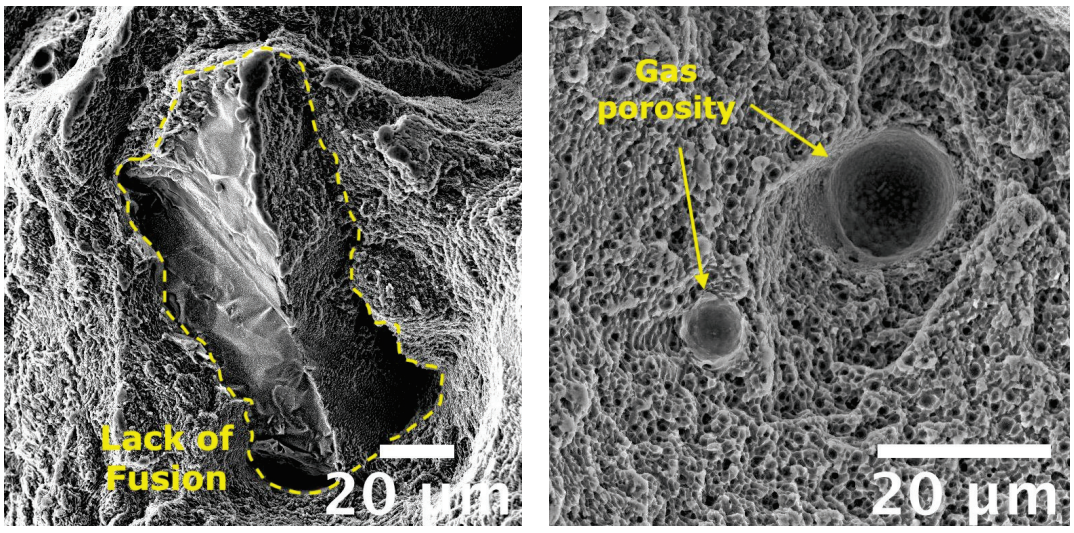

(**a**) (**b**)

Figure 15. FEG-SEM high magnification fractographic analyses of the AlSi7Mg alloy tensile samples show the main defects affecting mechanical behavior: (**a**) lack of fusion and (**b**) gas porosities.

4. Conclusions

The present work aims to characterize the tensile properties at room and high (200 °C) temperature of the A357 (AlSi7Mg0.6) PBF-LB alloy obtained with no platform pre-heating in the as-built condition and after two dedicated heat treatments at peak-aging: direct aging (T5) and rapid solution treatment, quenching and aging (T6R). First, tensile results were

discussed based on both fractographic and microstructural analyses. Concurrently, the effect of typical PBF-LB microstructural defects on the structural integrity of the alloy for each heat treatment condition was evaluated by analyzing the work hardening behavior. Based on the results, the role of microstructural features and defects on tensile behavior can be synthesized as follows:

- As-built alloy showed good overall mechanical behavior at both room and high temperatures, thanks to the distinctive microstructural features (i.e., supersaturated solid solution, cellular structure composed by sub-micrometric α-Al cells surrounded by eutectic-Si network and dispersion of nanometric-sized Si-particles within α-Al cells;) that induced microstructural refinement, solid solution, and two-phase aggregate strengthening mechanisms and high work hardening at room temperature. However, the alloy showed the highest sensitivity to the presence of defects, which strongly affected the tensile response of the alloy.
- T5 alloy preserved the peculiar cellular structure of the as-built alloy along with its strengthening mechanisms and high work hardening. Moreover, due to the induced precipitation strengthening, yield stress and tensile strength increased concerning the as-built alloy without a significant decrease in ductility. Therefore, the resilience of the alloy was enhanced without affecting its toughness. At the same time, when exposed to high temperature, T5 alloy could preserve satisfying mechanical properties, comparable to the as-built one. The sensitivity of the T5 alloy to the presence of defects was slightly lower than the as-built one. However, the structural integrity was still strongly affected by defects.
- T6R alloy was characterized by a coarser but more homogeneous microstructure composed of globular Si-rich particles dispersed in the Al matrix with no trace of cellular structure. T6R resulted in the best trade-off between strength and ductility, with precipitation as the primary strengthening mechanism, and reduced work hardening. Moreover, T6R enhanced the structural integrity of the alloy, which showed an almost negligible sensitivity to internal defects. However, when tested at high temperatures, T6R exhibited the lowest mechanical properties among the tested temper conditions, even if the results are still comparable to as-built and T5 alloys.

Results indicate that post-process heat treatments tailored to the peculiar Al-Si-Mg PBF-LB microstructure can tune the mechanical response, especially at room temperature. Concurrently, for a comparable defect content, the heat treatment positively reduces the detrimental effect of internal defects (e.g., lack of fusion and porosity) on the mechanical behavior. Therefore, both aspects should be considered when designing structural components. However, despite differences evidenced by microstructural analyses, minor deviations in the tensile properties were found among as-built, T5 and T6R conditions when tested at high temperatures. Given the possible application in the automotive or motorbike industry of Al-Si-Mg alloys, especially the AlSi7Mg0.6 one, for components in the power train system, analysis dedicated to the thermal stability will be addressed further in future works.

Author Contributions: Conceptualization, L.T.; methodology, L.T., E.L. and G.D.E.; validation, A.F., L.C. and A.M.; investigation, L.T.; data curation, L.T., E.L. and G.D.E.; writing—original draft preparation, L.T., E.L.; writing—review and editing, L.T., G.D.E. and A.M.; supervision, A.F., L.C. and A.M.; project administration, L.C.; funding acquisition, L.C. All authors have read and agreed to the published version of the manuscript.

Funding: Financed by the European Union-NextGenerationEU (National Sustainable Mobility Center CN00000023, Italian Ministry of University and Research Decree n. 1033-17/06/2022, Spoke 11-Innovative Materials & Lightweighting), and National Recovery and Resilience Plan (NRRP), Mission 04 Component 2 Investment 1.5-NextGenerationEU, Call for tender n. 3277 dated 30 December 2021. The opinions expressed are those of the authors only and should not be considered representative of the European Union or the European Commission's official position. Neither the European Union nor the European Commission can be held responsible for them.

Data Availability Statement: The raw/processed data required to reproduce these findings cannot be shared as the data also forms part of an ongoing study.

Acknowledgments: The authors would like to thank Iuri Boromei at the University of Bologna for his precious contribution to FEG-SEM analyses.

Conflicts of Interest: The authors declare no conflict of interest.

References

1. Sigworth, G. Heat Treatment of Aluminum Alloy Castings, ASM Handbook. In *Aluminum Science and Technology*; Anderson, K., Weritz, J., Kaufman, J.G., Eds.; ASM International: Almere, The Netherlands, 2018.
2. Anderson, K.; Weritz, J.; Kaufman, J.G. (Eds.) 357.0 and Variations A357.0 to F357.0*. In *Properties and Selection of Aluminum Alloys*; ASM International: Almere, The Netherlands, 2019.
3. Ceschini, L.; Morri, A.; Toschi, S.; Seifeddine, S. Room and high temperature fatigue behaviour of the A354 and C355 (Al-Si-Cu-Mg) alloys: Role of microstructure and heat treatment. *Mater. Sci. Eng. A* **2016**, *653*, 129–138. [CrossRef]
4. Banhart, J. Age Hardening of Aluminum Alloys. In *Heat Treating of Nonferrous Alloys*; Totten, G.E., Ed.; ASM International: Almere, The Netherlands, 2016; pp. 214–239.
5. Ceschini, L.; Messieri, S.; Morri, A.; Seifeddine, S.; Toschi, S.; Zamani, M. Effect of Cu addition on overaging behaviour, room and high temperature tensile and fatigue properties of A357 alloy. *Trans. Nonferrous Met. Soc. China* **2020**, *30*, 2861. [CrossRef]
6. Gong, G.; Ye, J.; Chi, Y.; Zhao, Z.; Wang, Z.; Xia, G.; Du, X.; Tian, H.; Yu, H.; Chen, C. Research status of laser additive manufacturing for metal: A review. *J. Mater. Res. Technol.* **2021**, *15*, 855–884. [CrossRef]
7. Kotadia, H.R.; Gibbons, G.; Das, A.; Howes, P.D. A review of Laser Powder Bed Fusion Additive Manufacturing of aluminium alloys: Microstructure and properties. *Addit Manuf.* **2021**, *46*, 102155. [CrossRef]
8. Zhang, J.; Song, B.; Wei, Q.; Bourell, D.; Shi, Y. A review of selective laser melting of aluminum alloys: Processing, microstructure, property and developing trends. *J. Mater. Sci. Technol.* **2019**, *35*, 270–284. [CrossRef]
9. Zhao, L.; Song, L.; Santos Macías, J.G.; Zhu, Y.; Huang, M.; Simar, A.; Li, Z. Review on the correlation between microstructure and mechanical performance for laser powder bed fusion AlSi10Mg. *Addit Manuf.* **2022**, *56*, 102914. [CrossRef]
10. Mauduit, A.; Gransac, H.; Auguste, P.; Pillot, S.; Diószegi, A. Study of AlSi7Mg0.6 Alloy by Selective Laser Melting: Mechanical Properties, Microstructure, Heat Treatment. *J. Cast. Mater. Eng.* **2019**, *3*, 1–13. [CrossRef]
11. Casati, R.; Nasab, M.H.; Tirelli, V.; Vedani, M. Effect of different heat treatment routes on microstructure and mechanical properties of AlSi7Mg, AlSi10Mg and Al-Mg-Zr-Sc alloys produced by selective laser melting. In Proceedings of the European Congress and Exhibition on Powder Metallurgy, European PM Conference Proceedings, Bilbao, Spain, 14–18 October 2018; pp. 1–5.
12. Casati, R.; Vedani, M. Aging Response of an A357 Al Alloy Processed by Selective Laser Melting. *Adv. Eng. Mater.* **2019**, *21*, 1800406. [CrossRef]
13. Rao, J.H.; Zhang, Y.; Zhang, K.; Wu, X.; Huang, A. Selective laser melted Al-7Si-0.6Mg alloy with in-situ precipitation via platform heating for residual strain removal. *Mater. Des.* **2019**, *182*, 108005. [CrossRef]
14. Pereira, J.C.; Gil, E.; Solaberrieta, L.; San Sebastián, M.; Bilbao, Y.; Rodríguez, P.P. Comparison of AlSi7Mg0.6 alloy obtained by selective laser melting and investment casting processes: Microstructure and mechanical properties in as-built/as-cast and heat-treated conditions. *Mater. Sci. Eng. A* **2020**, *778*, 139124. [CrossRef]
15. Oliveira de Menezes, J.T.; Castrodeza, E.M.; Casati, R. Effect of build orientation on fracture and tensile behavior of A357 Al alloy processed by Selective Laser Melting. *Mater. Sci. Eng. A* **2019**, *766*, 138392. [CrossRef]
16. Trevisan, F.; Calignano, F.; Lorusso, M.; Pakkanen, J.; Ambrosio, E.P.; Lombardi, M.; Pavese, M.; Manfredi, D.; Fino, P. Effects of Heat Treatments on A357 Alloy Produced by Selective Laser Melting. In Proceedings of the European Congress and Exhibition on Powder Metallurgy, European PM Conference Proceedings, Hamburg, Germany, 9–13 October 2016; pp. 1–6.
17. Di Egidio, G.; Ceschini, L.; Morri, A.; Martini, C.; Merlin, M. A Novel T6 Rapid Heat Treatment for AlSi10Mg Alloy Produced by Laser-Based Powder Bed Fusion: Comparison with T5 and Conventional T6 Heat Treatments. *Metall. Mater. Trans. B* **2022**, *53*, 284–303. [CrossRef]
18. Mostafaei, A.; Zhao, C.; He, Y.; Reza Ghiaasiaan, S.; Shi, B.; Shao, S.; Shamsaei, N.; Wu, Z.; Kouraytem, N.; Sun, T.; et al. Defects and anomalies in powder bed fusion metal additive manufacturing. *Curr. Opin. Solid State Mater. Sci.* **2022**, *26*, 100974. [CrossRef]
19. Cerri, E.; Ghio, E.; Bolelli, G. Defect-Correlated Vickers Microhardness of Al-Si-Mg Alloy Manufactured by Laser Powder Bed Fusion with Post-process Heat Treatments. *J. Mater. Eng. Perform.* **2022**, *31*, 8047–8067. [CrossRef]
20. Bonneric, M.; Brugger, C.; Saintier, N. Effect of hot isostatic pressing on the critical defect size distribution in AlSi7Mg0.6 alloy obtained by selective laser melting. *Int. J. Fatigue* **2020**, *140*, 105797. [CrossRef]
21. Lehmhus, D.; Rahn, T.; Struss, A.; Gromzig, P.; Wischeropp, T.; Becker, H. High-Temperature Mechanical Properties of Stress-Relieved AlSi10Mg Produced via Laser Powder Bed Fusion Additive Manufacturing. *Materials* **2022**, *15*, 7386. [CrossRef]
22. Tocci, M.; Varone, A.; Montanari, R.; Pola, A. Study of High Temperature Properties of AlSi10Mg Alloy Produced by Laser-Based Powder Bed Fusion. *Mater. Sci. Forum* **2021**, *1016*, 1485–1491. [CrossRef]
23. Di Egidio, G.; Morri, A.; Ceschini, L. Evaluation of High-temperature tensile properties of heat-treated AlSi10Mg alloy produced by Laser-Based Powder Bed Fusion. In Proceedings of the 31st International Conference on Metallurgy and Materials, Brno, Czech Republic, 18–19 May 2022; pp. 580–586.

24. Di Egidio, G.; Morri, A.; Ceschini, L.; Tonelli, L. High-Temperature Behavior of the Heat-Treated and Overaged AlSi10Mg Alloy Produced by Laser-Based Powder Bed Fusion and Comparison with Conventional Al–Si–Mg-Casting Alloys. *Adv. Eng. Mater.* **2023**, 2201238. [CrossRef]
25. Tonelli, L.; Liverani, E.; Morri, A.; Ceschini, L. Role of direct aging and solution treatment on hardness, microstructure and residual stress of the A357 (AlSi7Mg0.6) alloy produced by powder bed fusion. *Metall. Mater. Trans. B* **2021**, *52*, 2484–2496. [CrossRef]
26. *DS/EN 1780-1:2005*; Aluminium and Aluminium Alloys—Designation of Alloyed Aluminium Ingots for Remelting, Master Alloys and Castings–Part 1: Numerical Designation System. Dansk Standard: Nordhavnen, Denmark, 2005.
27. Tonelli, L.; Liverani, E.; Valli, G.; Fortunato, A.; Ceschini, L. Effects of powders and process parameters on density and hardness of A357 aluminum alloy fabricated by selective laser melting. *Int. J. Adv. Manuf. Technol.* **2020**, *106*, 371–383. [CrossRef]
28. *EN 1706:2020*; Aluminium and Aluminium Alloys—Castings—Chemical Composition and Mechanical Properties. European Committee for Standardization (CEN): Bruxelles, Belgium, 2020.
29. Carpenter Technology. (n.d.). Available online: www.carpenteradditive.com (accessed on 15 September 2020).
30. *ISO 6892-1*; Metallic Materials—Tensile testing, Method of Test at Room Temperature. International Organization for Standardization: Geneva, Switzerland, 2019; pp. 1–78.
31. Kaufman, J.G. Aluminum Alloy and Temper Designation Systems of the Aluminum Association. In *Introduction to Aluminum Alloys and Tempers*; ASM International: Almere, The Netherlands, 2000; pp. 9–22.
32. *ISO 6892-2*; Metallic Materials—Tensile Testing, Method of Test at Elevated Temperature. International Organization for Standardization: Geneva, Switzerland, 2019; pp. 1–21.
33. Kuhn, H.; Medlin, D. (Eds.) *Mechanical Testing and Evaluation in ASM Handbook*; ASM International: Almere, The Netherlands, 2000; Volume 8, pp. 124–142.
34. Dieter, G.E.; Bacon, D.J. *Mechanical Metallurgy*; McGraw-Hill: New York, NY, USA, 1986.
35. Angella, G.; Zanardi, F. Validation of a New Quality Assessment Procedure for Ductile Irons Production Based on Strain Hardening Analysis. *Metals* **2019**, *9*, 837. [CrossRef]
36. Tiryakioğlu, M.; Staley, J.T.; Campbell, J. Evaluating structural integrity of cast Al-7%Si-Mg alloys via work hardening characteristics—II. A new quality index. *Mater. Sci. Eng. A* **2004**, *368*, 231–238. [CrossRef]
37. Tiryakioğlu, M.; Campbell, J.; Staley, J.T. Evaluating structural integrity of cast Al-7%Si-Mg alloys via work hardening characteristics—1. Concept of target properties. *Mater. Sci. Eng. A* **2004**, *368*, 205–211. [CrossRef]
38. Cáceres, C.H. A rationale for the quality index of Al-Si-Mg casting alloys. *Int. J. Cast Met. Res.* **2000**, *12*, 385–391. [CrossRef]
39. Angella, G.; Zanardi, F.; Donnini, R. On the significance to use dislocation-density-related constitutive equations to correlate strain hardening with microstructure of metallic alloys: The case of conventional and austempered ductile irons. *J. Alloys Compd.* **2016**, *669*, 262–271. [CrossRef]
40. *ISO 10275:2020*; Metallic Materials—Sheet and Strip—Determination of Tensile Strain Hardening Exponent. International Organization for Standardization: Geneva, Switzerland, 2020; pp. 1–10.
41. *ASTM E10-18*; Standard Test Method for Brinell Hardness of Metallic Materials. ASTM International: West Conshohocken, PA, USA, 2018.
42. *ASTM E3-11(2017)*; Standard Guide for Preparation of Metallographic Specimens. ASTM International: West Conshohocken, PA, USA, 2017.
43. Voort, G.V. (Ed.) *Metallography and Microstructures in ASM Handbook*; ASM International: Almere, The Netherlands, 2004; Volume 9, pp. 294–312.
44. Rueden, C.T.; Schindelin, J.; Hiner, M.C.; DeZonia, B.E.; Walter, A.E.; Arena, E.T.; Eliceiri, K.W. ImageJ2: ImageJ for the next generation of scientific image data. *BMC Bioinform.* **2017**, *18*, 529. [CrossRef]
45. Van Cauwenbergh, P.; Beckers, A.; Thijs, L.; Van Hooreweder, B.; Vanmeensel, K. Heat treatment optimization via thermo-physical characterization of AlSi7Mg and AlSi10Mg manufactured by laser powder bed fusion (LPBF). In Proceedings of the European Congress and Exhibition on Powder Metallurgy, European PM Conference Proceedings, Bilbao, Spain, 14–18 October 2018; pp. 1–7.
46. Casati, R.; Hamidi, M.N.; Coduri, M.; Tirelli, V.; Vedani, M. Effects of Platform Pre-Heating and Thermal-Treatment Strategies on Properties of AlSi10Mg Alloy Processed by Selective Laser Melting. *Metals* **2018**, *8*, 954. [CrossRef]
47. Chen, B.; Moon, S.K.; Yao, X.; Bi, G.; Shen, J.; Umeda, J.; Kondoh, K. Strength and strain hardening of a selective laser melted AlSi10Mg alloy. *Scr. Mater.* **2017**, *141*, 45–49. [CrossRef]
48. Kempf, A.; Hilgenberg, K. Influence of sub-cell structure on the mechanical properties of AlSi10Mg manufactured by laser powder bed fusion. *Mater. Sci. Eng. A* **2020**, *776*, 138976. [CrossRef]
49. Delahaye, J.; Tchuindjang, T.; Lecomte-Beckers, J.; Rigo, O.; Habraken, A.M.; Mertens, M. Influence of Si precipitates on fracture mechanisms of AlSi10Mg parts processed by Selective Laser Melting. *Acta Mater.* **2019**, *175*, 160–170. [CrossRef]
50. Hadadzadeh, A.; Baxter, C.; Amirkhiz, B.S.; Mohammadi, M. Strengthening mechanisms in direct metal laser sintered AlSi10Mg: Comparison between virgin and recycled powders. *Addit. Manuf.* **2018**, *23*, 108–120. [CrossRef]
51. Cao, Y.; Lin, X.; Wang, Q.Z.; Shi, S.Q.; Ma, L.; Kang, N.; Huang, W.D. Microstructure evolution and mechanical properties at high temperature of selective laser melted AlSi10Mg. *J. Mater. Sci. Technol.* **2021**, *62*, 162–172. [CrossRef]
52. Di Egidio, G. Evaluation by nanoindentation of the influence of heat treatments and the consequent induced microstructure on the mechanical response of the heat-treated L-PBF AlSi10Mg alloy. *Metall. Ital.* **2022**, *114*, 8–16.
53. Aboulkhair, N.T.; Everitt, N.M.; Maskery, I.; Ashcroft, I.; Tuck, C. Selective laser melting of aluminum alloys. *MRS Bull.* **2017**, *42*, 311–319. [CrossRef]

54. Angella, G.; Timelli, G.; Bonollo, F. Novel approach based on tensile strain hardening analysis to assess the integrity of an Al alloy produced through High-Pressure Die Casting. *Metall. Ital.* **2021**, *113*, 22–30.
55. Kocks, U.F.; Mecking, H. Physics and phenomenology of strain hardening: The FCC case. *Prog. Mater. Sci.* **2003**, *48*, 171–273. [CrossRef]
56. Kang, S.K.; Kim, Y.C.; Kim, K.H.; Kwon, D.; Kim, J.Y. Constitutive equations optimized for determining strengths of metallic alloys. *Mech. Mater.* **2014**, *73*, 51–57. [CrossRef]
57. Mondal, C.; Singh, A.K.; Mukhopadhyay, A.K.; Chattopadhyay, K. Tensile flow and work hardening behavior of hot cross-rolled AA7010 aluminum alloy sheets. *Mater. Sci. Eng. A* **2013**, *577*, 87–100. [CrossRef]
58. Rollett, A.D.; Kocks, U.F. A Review of the Stages of Work Hardening. *Solid State Phenom.* **1993**, *35–36*, 1–18. [CrossRef]
59. Tu, S.; Ren, X.; He, J.; Zhang, Z. Stress–strain curves of metallic materials and post-necking strain hardening characterization: A review. *Fatigue Fract. Eng. Mater. Struct.* **2020**, *43*, 3–19. [CrossRef]
60. Yasnikov, I.S.; Vinogradov, A.; Estrin, Y. Revisiting the Considère criterion from the viewpoint of dislocation theory fundamentals. *Scr. Mater.* **2014**, *76*, 37–40. [CrossRef]
61. Morales-Palma, D.; Martínez-Donaire, A.J.; Vallellano, C. On the Use of Maximum Force Criteria to Predict Localised Necking in Metal Sheets under Stretch-Bending. *Metals* **2017**, *7*, 469. [CrossRef]
62. Zhao, D.; Lampmam, S. Hot Tension and Compression Testing. In *Mechanical Testing and Evaluation*; Kuhn, H., Medlin, D., Eds.; ASM International: Almere, The Netherlands, 2000; pp. 152–163.
63. Di Egidio, G.; Martini, C.; Börjesson, J.; Ghassemali, E.; Ceschini, L.; Morri, A. Influence of Microstructure on Fracture Mechanisms of the Heat-Treated AlSi10Mg Alloy Produced by Laser-Based Powder Bed Fusion. *Materials* **2023**, *16*, 2006. [CrossRef] [PubMed]
64. Xiong, Z.H.; Liu, S.L.; Li, S.F.; Shi, Y.; Yang, Y.F.; Misra, R.D.K. Role of Melt pool boundary condition in dertermining the mechanical properties of selective laser melting AlSi10Mg alloy. *Mater. Sci. Eng. A* **2019**, *740–741*, 148–156. [CrossRef]
65. Paul, M.J.; Liu, Q.; Best, J.P.; Li, X.; Kruzic, J.J.; Ramamurty, U.; Gludovatz, B. Fracture resistance of AlSi10Mg fabricated by laser powder bed fusion. *Acta Mater.* **2021**, *211*, 116869. [CrossRef]

materials

MDPI

Article

Homogenization of Extrusion Billets of a Novel Al-Mg-Si-Cu Alloy with Increased Copper Content

Antoni Woźnicki [1,*], Beata Leszczyńska-Madej [2], Grzegorz Włoch [2], Jacek Madura [2], Marek Bogusz [2] and Dariusz Leśniak [2]

[1] Aptiv Services Poland S.A., 30-399 Kraków, Poland
[2] Faculty of Non-Ferrous Metals, AGH University of Science and Technology, 30-059 Kraków, Poland
* Correspondence: antoni.woznicki@gmail.com

Abstract: Within the present work the homogenization of DC-cast (direct chill-cast) extrusion billets of Al-Mg-Si-Cu alloy was investigated. The alloy is characterized by higher Cu content than currently applied in 6xxx series. The aim of the work was analysis of billets homogenization conditions enabling maximum dissolution of soluble phases during heating and soaking as well as their re-precipitation during cooling in form of particles capable for rapid dissolution during subsequent processes. The material was subjected to laboratory homogenization and the microstructural effects were assessed on the basis of DSC (differential scanning calorimetry) tests, SEM/EDS (scanning electron microscopy/energy-dispersive spectroscopy) investigations and XRD (X-ray diffraction) analyses. The proposed homogenization scheme with three soaking stages enabled full dissolution of Q-$Al_5Cu_2Mg_8Si_6$ and θ-Al_2Cu phases. The β-Mg_2Si phase was not dissolved completely during soaking, but its amount was significantly reduced. Fast cooling from homogenization was needed to refine β-Mg_2Si phase particles, but despite this in the microstructure coarse Q-$Al_5Cu_2Mg_8Si_6$ phase particles were found. Thus, rapid billets heating may lead to incipient melting at the temperature of about 545 °C and the careful selection of billets preheating and extrusion conditions was found necessary.

Keywords: Al-Mg-Si-Cu alloys; extrusion billets; homogenization soaking; cooling from homogenization

Citation: Woźnicki, A.; Leszczyńska-Madej, B.; Włoch, G.; Madura, J.; Bogusz, M.; Leśniak, D. Homogenization of Extrusion Billets of a Novel Al-Mg-Si-Cu Alloy with Increased Copper Content. *Materials* **2023**, *16*, 2091. https://doi.org/10.3390/ma16052091

Academic Editor: Xianfei Ding

Received: 7 February 2023
Revised: 27 February 2023
Accepted: 1 March 2023
Published: 3 March 2023

1. Introduction

The automotive branch, which is one of the main aluminum alloys consumers, undergoes currently significant transformation resulting from walk towards electromobility. Between year 2018 and 2021, the share of electrically chargeable vehicles (i.e., battery electric vehicles and plug-in hybrids) among new cars registered in the European Union increased from 1.9 to 18% [1]. Considering announced legal restrictions for cars with internal combustion engines one can expect further growth of electric cars share in markets worldwide. This change is an origin of challenges for suppliers of aluminum alloys components, which are used in electric cars. As an example, one may show battery enclosures, in which aluminum alloys extrusions are often used [2,3]. The enclosure must ensure the protection of heavy battery from crashes and strikes as well as enable a thermal management. To provide this, the high-strength extruded profiles with complex shapes, often hollow, are needed. It is worth noticing that high-strength, light components are generally desired in electric cars. Battery increases noticeably vehicle mass, hence there is a need of reducing other components mass, which is very important in terms of range.

The requirement of complex profiles shape causes that among precipitation hardenable aluminum alloys, the 6xxx alloys, in which high strength properties can be combined with good extrudability, are considered as materials of choice. The high-strength 6xxx alloys often have Cu as an essential addition, with its concentrations up to 1.2 wt% [4]. Many of mentioned alloys contain the quaternary Q-phase. Its exact composition is unknown and is reported as $Al_5Cu_2Mg_8Si_6$, $Al_4CuMg_5Si_4$, $Al_4Cu_2Mg_8Si_7$, and $Al_3Cu_2Mg_9Si_7$. In

equilibrium state the Q phase can coexist with (Al) solid solution and two of other three phases: θ-Al_2Cu, β-Mg_2Si, and (Si) [5]. After ageing of Al-Mg-Si-Cu alloys the significant strengthening effects may arise from precursor phases to Q' [5,6]. Despite the fact that Al-Mg-Si-Cu alloys are used since 1950s, since this time grades characterized by tensile strength in T6 temper close to 500 MPa have been elaborated, e.g., 6069 [7], and there are other interesting subjects for investigation in the field of Al and its alloys, e.g., [8–10], the considered alloys are still object of researchers' interest. The works are related to modification of alloys chemical composition as well as application of tailored processing parameters [11–14].

In the case of the Al-Mg-Si-Cu alloys, a solidification comprises several reactions and the microstructure in as-cast state is complex [15–17]. Between (Al) dendrites arms numerous phases can be observed: soluble β-Mg_2Si, θ-Al_2Cu, Q and (Si)—in some cases all of them are reported—as well as Fe-bearing phases e.g., α-Al(FeMn)Si, β-Al(FeMn)Si. The unequilibrium solidus temperature may be even as low as about 485 °C [16].

The homogenization of DC-cast billets is an important part of the extruded products manufacturing cycle, significantly influencing billets extrudability as well as properties of obtained profiles. The primary microstructural process occurring during homogenization heating and soaking is dissolution of soluble phases particles formed during solidification and elimination of microsegregation. At the end of the soaking stage, a maximum attainable enrichment of (Al) solid solution in Mg, Si, and Cu, taking part in subsequent precipitation hardening, shall be obtained. A high soaking temperature facilitates the particles dissolution. However, the low-melting microstructure components (eutectics) present in the as-cast billets need to be removed during the heating stage. In some cases, an intermediate soaking at low temperature (470 °C) is applied, after which a final soaking at high temperature (560–570 °C), may be safely accomplished [16,18].

In 6xxx alloys containing transition metals, usually Mn and/or Cr, during homogenization heating and soaking precipitation of dispersoids takes place. These particles have strong effect on recovery, recrystallization and grain growth processes during hot working and annealing treatments. However, to achieve expected results, the dispersoids need to be fine, densely and uniformly distributed. Thus, the homogenization parameters of high strength 6xxx alloys must be selected with respect to these particles. A slow heating to homogenization or application of intermediate soaking step in course of heating are reported to positively influence dispersoids distribution [19–22]. If final homogenization soaking at high temperature is applied, a stronger tendency of the dispersoids to coarsen is observed, when compared to low temperature soaking, e.g., 560 vs. 500 °C in [11]. On the other hand, low soaking temperature, favorable for dispersoids, may lead to insufficient dissolution of phases, components of which take part in subsequent precipitation hardening [23].

Another microstructural processes occurring during 6xxx alloys homogenization are related to Fe-bearing phases formed during solidification: transformation of undesirable β-Al(FeMn)Si phase into α-Al(FeMn)Si, changes in particles composition and/or morphology. These processes influence the billets extrudability and quality of extruded products surface [24–26].

After completed soaking, the extrusion billets are cooled to the ambient temperature. Within this stage, the phases showing limited solubility in Al matrix re-precipitate. It is of great importance to ensure that the phases will be present in billets structure in form of particles, which are capable for fast dissolution during subsequent billets preheating and extrusion. If the cooling is too slow, the obtained particles are too large to fully dissolve. It results in reduced concentration of alloying additions in (Al) solid solution and in consequence in lowered strength properties of profiles after subsequent quenching on the press output and ageing. Moreover, presence of undissolved particles in the billets microstructure causes an incipient melting of the alloy at a relatively low temperature, as the result of the unequilibrium eutectic reaction between the particles and surrounding matrix. In order to avoid melting, leading to profiles surface defects appearance, the exit temperature of the profile must be kept below the eutectic temperature and the permissible

extrusion speed is reduced [27,28]. On the other hand, too high cooling rates from homogenization temperature are also unfavorable, because of rising supersaturation of the solid solution with alloying additions. It increases flow stress of the material and breakthrough-pressure [29]. The process of cooling billets of Al-Mg-Si alloys is often described in the literature, e.g., [30–32], but there is a lack of similar analyses of 6xxx alloys containing Cu.

The literature data presented above may be summarized as follows: The expected microstructure of homogenized billets is characterized by the presence of soluble phases in the form of fine particles, capable for rapid dissolution during billets preheating and extrusion. In order to achieve this, the homogenization soaking should ensure the maximum possible dissolution of mentioned phases. Due to low melting temperature of the as-cast billets, a multi-step homogenization may be necessary. The conditions of cooling of Al-Mg-Si-Cu billets leading to the refinement of particles precipitated during cooling need to be investigated.

This paper presents the results of investigations of new 6xxx alloy, with higher Cu content than currently applied, intended for application in automotive industry. The work focuses on the analysis of billets homogenization conditions leading to achieving the microstructure as described above.

2. Materials and Methods

The material for investigation came from billet with a diameter of 100 mm, cast in semi-industrial conditions with direct-chill method. The chemical composition of the alloy is presented in Table 1. From the obtained billet, the cuboid specimens with dimensions of $10 \times 20 \times 15$ mm were sectioned. They were intended for examination in the as-cast state as well as for laboratory homogenization experiments.

Table 1. The chemical composition of investigated alloy, mass percentage.

Si	Fe	Cu	Mn	Mg	Cr	Ti	Zr
1.22	0.05	1.41	0.62	0.80	0.38	0.02	0.15

At the first stage of work, the material in the as-cast state was subjected to DSC (differential scanning calorimetry) tests, XRD (X-ray diffraction) analyses, as well as microstructure observations. The DSC tests were performed using a Mettler Toledo 821^e heat flux type calorimeter (Greifensee, Switzerland). The disc-shaped samples were inserted in ceramic pans into the cell with the temperature of 390 °C and heated at 20 °C/min to the temperature of 700 °C in Ar atmosphere. The solidus temperature as well as heat of the incipient melting reactions were determined. The incipient melting reactions heat is given in J/g—the heat value determined from DSC curve was divided by whole specimen mass.

The phase composition of the powdered specimens was analyzed using the Bruker D8 Advance (Karlsruhe, Germany) X-ray diffractometer with Co Kα = 1.79 Å. The analyses were performed in a 2θ angle range of 15° to 100°.

The specimens for microstructure examination were mounted in conductive resin, subsequently mechanically ground and polished using abrasive papers, diamond suspensions and colloidal silica suspension. The billets microstructure was examined using SEM/EDS (scanning electron microscopy/energy-dispersive spectroscopy). The SEM/EDS analyses were performed on non-etched specimens using Zeiss Sigma 300 VP scanning electron microscope (Jena, Germany) equipped with an Oxford Instruments EDS system (Abingdon, England) as well as a Hitachi SU-70 scanning electron microscope (Tokyo, Japan) equipped with a Thermo Scientific EDS system (Waltham, MA, USA). The EDS analyses were applied to determine the chemical composition of the observed eutectic areas or particles and to measure the main alloying elements concentration in the dendrites interiors.

At the second stage of work, soaking parameters were investigated. The homogenization scheme with three soaking stages at 475, 530, and 545 °C was applied (Figure 1a). The temperature of first soaking was selected on the basis of the literature data [16,18,20] and

the results of DSC tests of alloy in the as-cast state showing the solidus (incipient melting) temperature. The temperatures of second and third soaking steps were set at about 15 °C below the solidus temperature obtained after preceding soaking. The specimens were heated from room temperature to 475 °C for 10 h. A similar heating rate, about 40 °C/h, was applied during heating between further soaking stages. After completed soaking, specimens were quenched in water. The heat treatment experiments were accomplished using a Nabertherm forced convection chamber furnace.

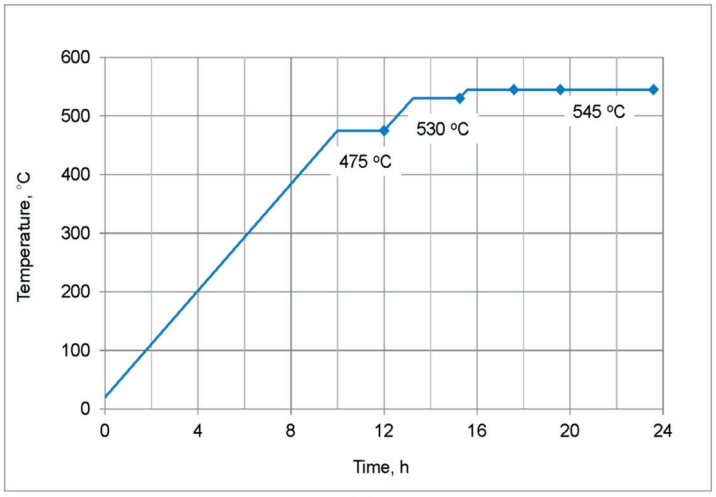

(a)

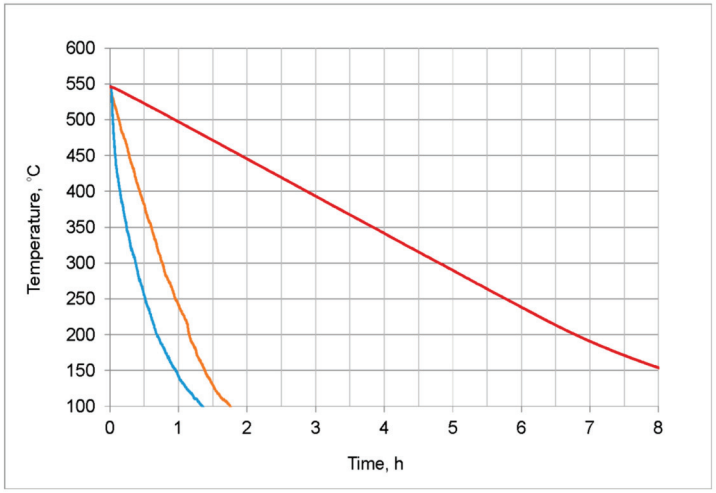

(b)

Figure 1. Laboratory homogenization experiments: (**a**) Heating and soaking conditions with marked sampling points (2nd stage of work); (**b**) cooling curves obtained after homogenization with soaking 475 °C/2 h + 530 °C/2 h + 545 °C/8 h (3rd stage of work). The average cooling rates in the temperature range from 545 to 200 °C, were about 500 (blue line), 300 (orange line), and 50 °C/h (red line).

At the third stage, the influence of cooling rate from the homogenization temperature on the billet microstructure was studied. Specimens were subjected to homogenization with soaking conditions selected on the basis of second stage results, i.e., 475 °C/2 h + 530 °C/2 h + 545 °C/8 h. Then they were cooled to room temperature in three ways (Figure 1b). The average cooling rates in the temperature range from 545 to 200 °C, estimated on the basis of specimens temperature measurements during cooling cycles, were about 500, 300, and 50 °C/h.

Specimens after all homogenization experiments were subjected to DSC tests. In the second stage, the dissolution of low-melting microstructure components was analyzed. In the third stage, the ability of precipitated particles to dissolution during rapid heating was evaluated. On the basis of the obtained DSC results, specimens for XRD analyses and microstructure observations were selected. The examination of homogenized alloy was performed in the manner described above.

The backscattered electron images of specimens cooled after homogenization with different rates were additionally subjected to image analysis procedure. For each specimen, six photographs at magnification of 1000× were acquired in randomly selected areas. Microstructure images were binarized in order to extract β-Mg_2Si particles. Their number and the surface area of particles cross-sections were measured using image analysis software Struktura 1.0, developed at AGH-UST. Based on the obtained surface area, the equivalent diameter of particles cross-sections was calculated and used for particles classification. In the text below, descriptions of particles dimensions or area refer to values determined from observed particles cross-sections.

Similar procedure was not applied to other soluble phases, Q-$Al_5Cu_2Mg_8Si_6$ and θ-Al_2Cu, due to their poor contrast with particles Al(FeMn)Si.

3. Results

3.1. DSC

On the DSC curves in as-cast state, three peaks resulting from incipient melting reactions are observed (Figure 2a). First, denoted as A, has an onset at the temperature of 513 °C, this is unequilibrium solidus temperature of investigated billet. Second peak (B) has an onset at about 539 °C, third peak (C) at about 561 °C. The melting heat values are 0.47, 1.48, and 2.12 J/g respectively (Table 2).

Table 2. DSC test results.

State	Peak A		Peak B		Peak C		Bulk Melting
	Onset, °C	Heat, J/g	Onset, °C	Heat, J/g	Onset, °C	Heat, J/g	Onset, °C
As-cast	513.4	0.47	539.7	1.48	561.3	2.12	
475 °C/2 h–wq			544.8	0.90	560.4	3.77	
475 °C/2 h + 530 °C/2 h–wq					561.3	2.36	
475 °C/2 h + 530 °C/2 h + 545 °C/2 h–wq					562.2	0.79	
475 °C/2 h + 530 °C/2 h + 545 °C/4 h–wq					561.6	[1]	
475 °C/2 h + 530 °C/2 h + 545 °C/8 h–wq							573.4
475 °C/2 h + 530 °C/2 h + 545 °C/8 h–cooling 50 °C/h			542.7	0.02	560.3	5.95	
475 °C/2 h + 530 °C/2 h + 545 °C/8 h–cooling 300 °C/h					558.9	0.78	
475 °C/2 h + 530 °C/2 h + 545 °C/8 h–cooling 500 °C/h			546.7	0.10	562.9	0.14	

[1] Peak C is merged with bulk melting peak and its heat was not determined.

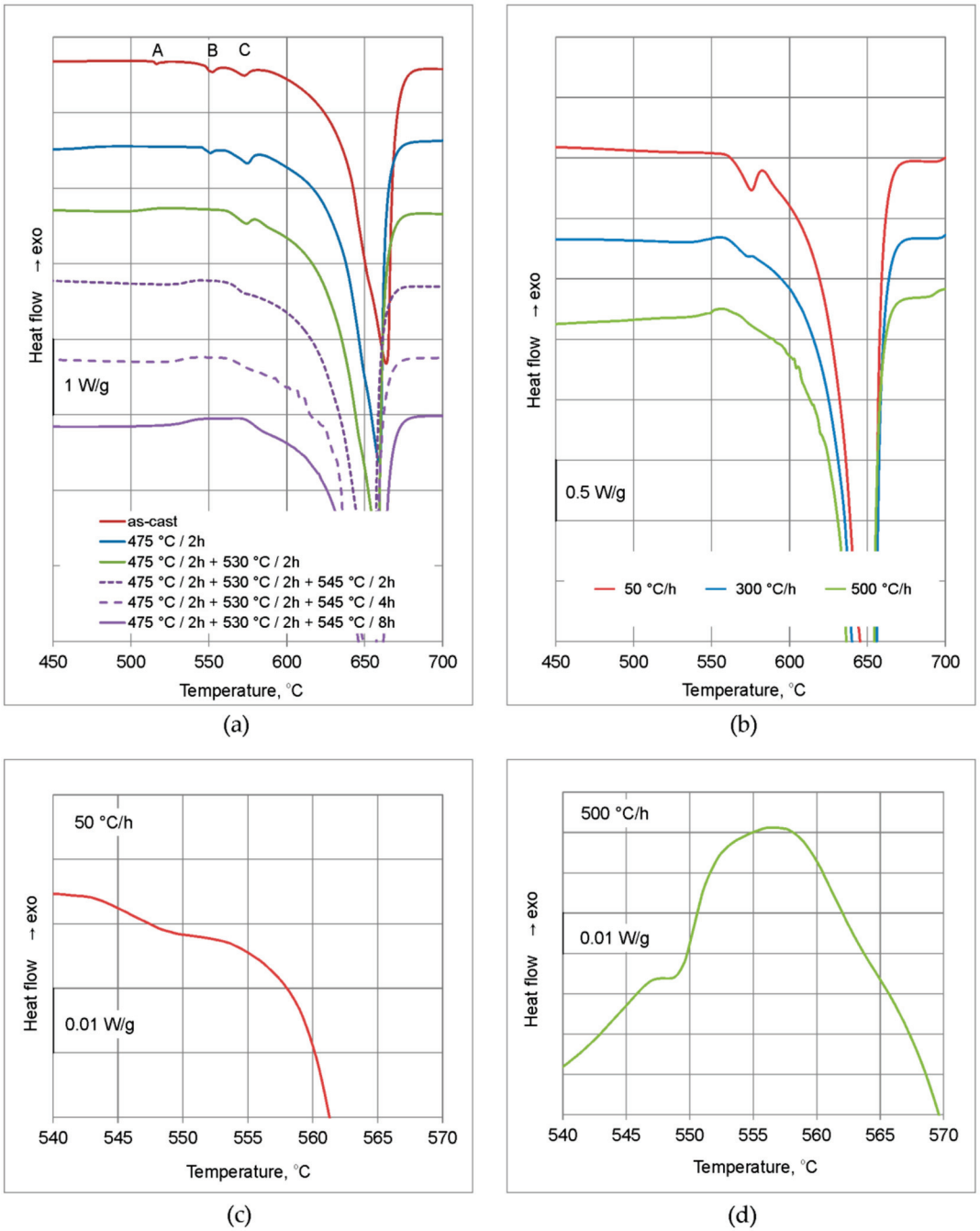

Figure 2. DSC curves: (**a**) As-cast state and after homogenization with differentiated soaking and water quenching; (**b**) after homogenization with soaking 475 °C/2 h + 530 °C/2 h + 545 °C/8 h and differentiated cooling rate; (**c**,**d**) magnified parts of curves from panel **b** showing very small peaks at about 545 °C.

After heating to the temperature of 475 °C, soaking for 2 h and water quenching, peak A is not observed and the solidus temperature rises to about 545 °C. Heat of peak B decreases to about 0.9 J/g, whereas heat of peak C rises to 3.8 J/g. The subsequent heating to the temperature of 530 °C and soaking for 2 h, causes the peak B to vanish and the solidus temperature to rise to about 561 °C. Heat of the peak C decreases to about 2.4 J/g. Owing to the solidus temperature increase another soaking step, at 545 °C, could be accomplished. After 4 h of soaking, the peak C is merged with bulk melting peak, and after 8 h followed by water quenching, it vanishes and solidus temperature rises to about 573 °C (Figure 2a, Table 2).

The DSC curves after three-stage homogenization with final soaking at 545 °C for 8 h and different cooling manners are shown in the Figure 2b. After cooling at 50 and 500 °C/h, on the DSC curves two peaks are observed. First peak has an onset at a temperature of 543–547 °C and its heat is very small: 0.02 and 0.1 J/g respectively for 50 and 500 °C/h (Table 2). After cooling at 300 °C/h this peak is not observed. Second peak has an onset at a temperature 559–563 °C and is visible after all cooling manners. Heat of this peak decreases with cooling rate, values of 5.95, 0.78, and 0.14 J/g are obtained for 50, 300, and 500 °C/h respectively (Table 2). The mentioned peaks correspond to peaks B and C described for as-cast state and during soaking conditions analysis.

3.2. SEM/EDS

The investigated alloy in as-cast state was characterized by dendritic microstructure with numerous particles and eutectic areas located at dendrites/grains boundaries (Figure 3). Microanalyses of the observed particles indicate the presence of phases: β-Mg_2Si, phase containing Al, Mg, Si, and Cu and phase containing primarily Al, Mn, and Si, with Fe, Cr, and Cu also detected. The second mentioned phase was identified as Q-$Al_5Cu_2Mg_8Si_6$, it was done on the basis of spectra quantification results showing that Cu:Si ratio, expressed in at. %, is close to 1:3 [16]. The Fe, Mn, and Si-bearing particles are probably α-Al(FeMn)Si phase, their composition is very close to the particles of this phase described in [12]. The eutectic areas are often multicomponent and the EDS microanalyses results show that besides (Al) they are composed of phases Q-$Al_5Cu_2Mg_8Si_6$, θ-Al_2Cu, and (Si) (Figure 3). The dendrites interiors are noticeably impoverished in main alloying additions, Mg, Si, and Cu (Figure 6).

After heating to 475 °C for 10 h and soaking for 2 h, fraction of particles in the microstructure noticeably decreases (Figure 4a). The β-Mg_2Si, Q-$Al_5Cu_2Mg_8Si_6$, and Al(FeMn)Si particles are observed, phases θ-Al_2Cu and (Si) are not found. At higher magnification, in grains interiors dispersoids are visible. Second soaking step, at 530 °C for 2 h, causes dissolution of phase Q-$Al_5Cu_2Mg_8Si_6$, particles β-Mg_2Si and Al(FeMn)Si are present (Figure 4b). After final soaking, the same particles are observed as after the second one, but amount of β-Mg_2Si is smaller (Figure 4c). The observations at high magnification after second and third soaking reveal a presence of small, elongated particles, bright in the backscattered electron images. Microanalyses show that the particles are rich in Cu and Si, example is shown in the Figure 5. Fraction of this particles in the microstructure can be assessed as very small.

One should notice that after complete soaking, the dispersoids present in the microstructure are uniformly distributed and the tendency of them to coarsen is not found—dimensions of dispersoids are far below 1 μm. The particles of Al(FeMn)Si phase underwent fragmentation and their edges became more rounded (Figures 4c and 5).

The concentration of Mg, Si, and Cu in grains interiors rises in line with particles dissolution (Figure 6). After first soaking stage at 475 °C the concentration of Si and Cu increases noticeably, when compared to as-cast state, which is related to dissolution of θ-Al_2Cu and (Si) observed in eutectic areas, probably to some extent also with dissolution of Q-$Al_5Cu_2Mg_8Si_6$ phase. The second soaking, at 530 °C, causes an increase in all main alloying additions concentration, resulting from of Q-$Al_5Cu_2Mg_8Si_6$ phase dissolution. After final soaking at 545 °C, the Cu content in grains interiors remains unchanged and concentrations of Mg and Si rise due to reduction of β-Mg_2Si phase fraction.

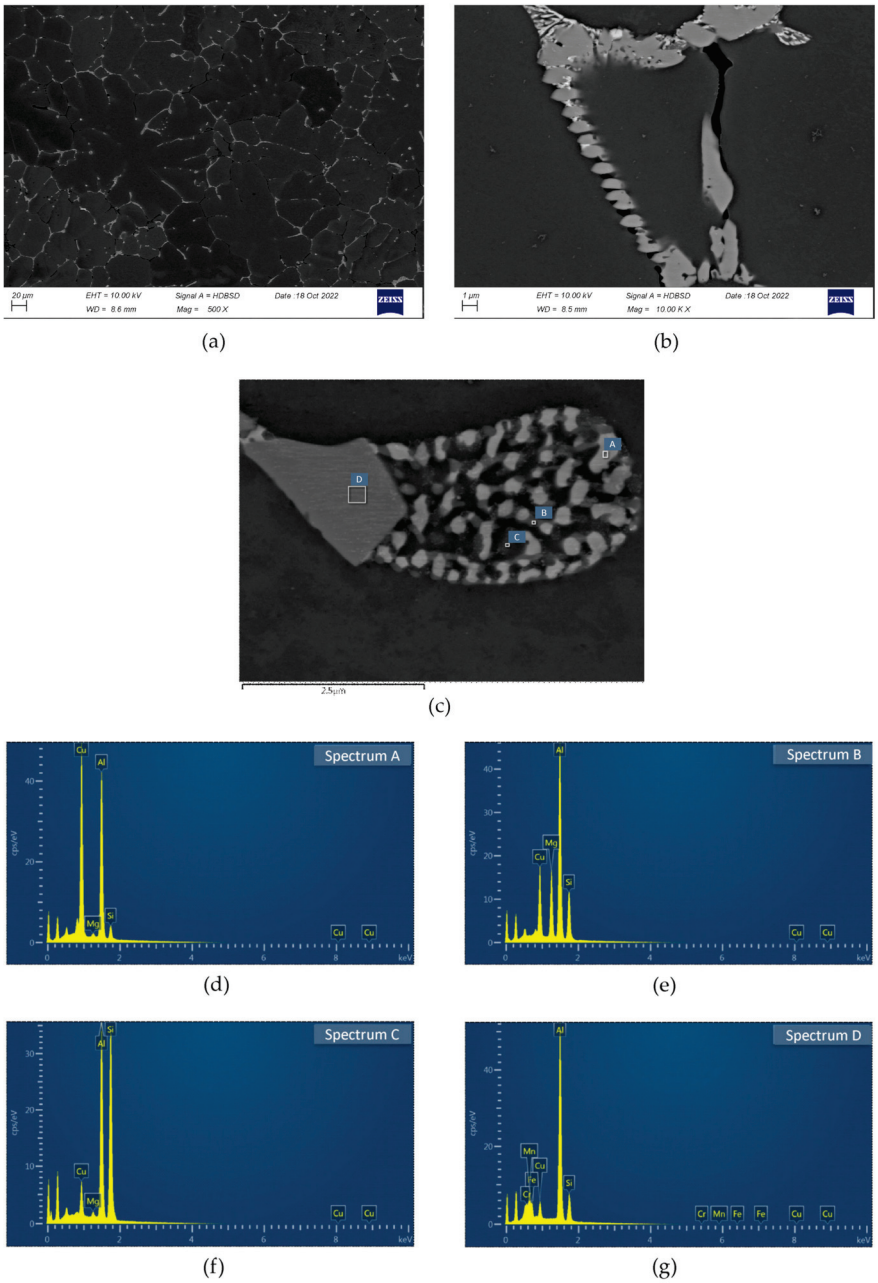

Figure 3. Microstructure of investigated alloy in as-cast state: (**a**) General view of the dendritic microstructure; (**b**,**c**) particles and eutectic areas; (**d**–**g**) spectra from panel c.

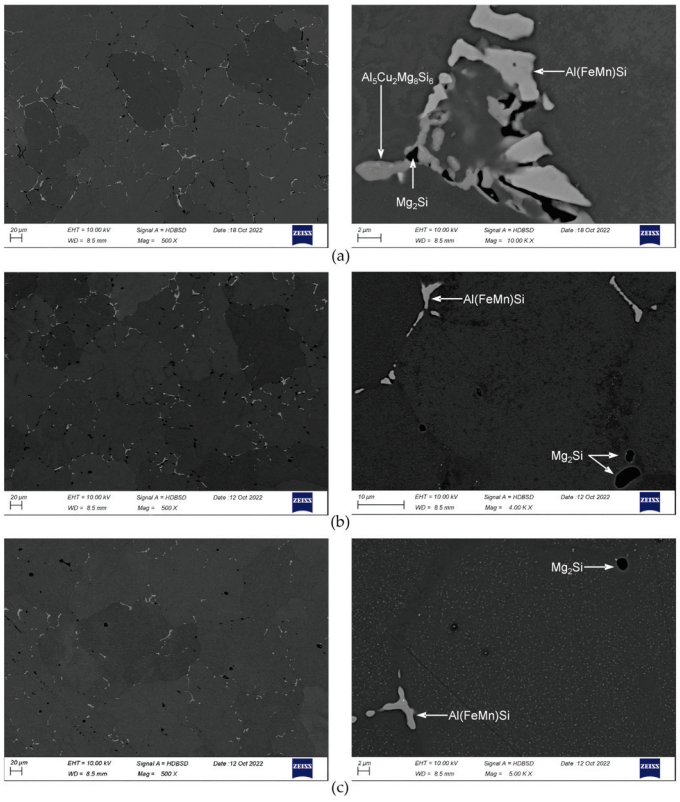

Figure 4. Microstructure of the alloy after heating to 475 °C for 10 h and soaking: (**a**) at 475 °C for 2 h; (**b**) at 475 °C for 2 h + 530 °C for 2 h; and (**c**) at 475 °C for 2 h + 530 °C for 2 h + 545 °C for 8 h. After complete soaking, samples were water quenched.

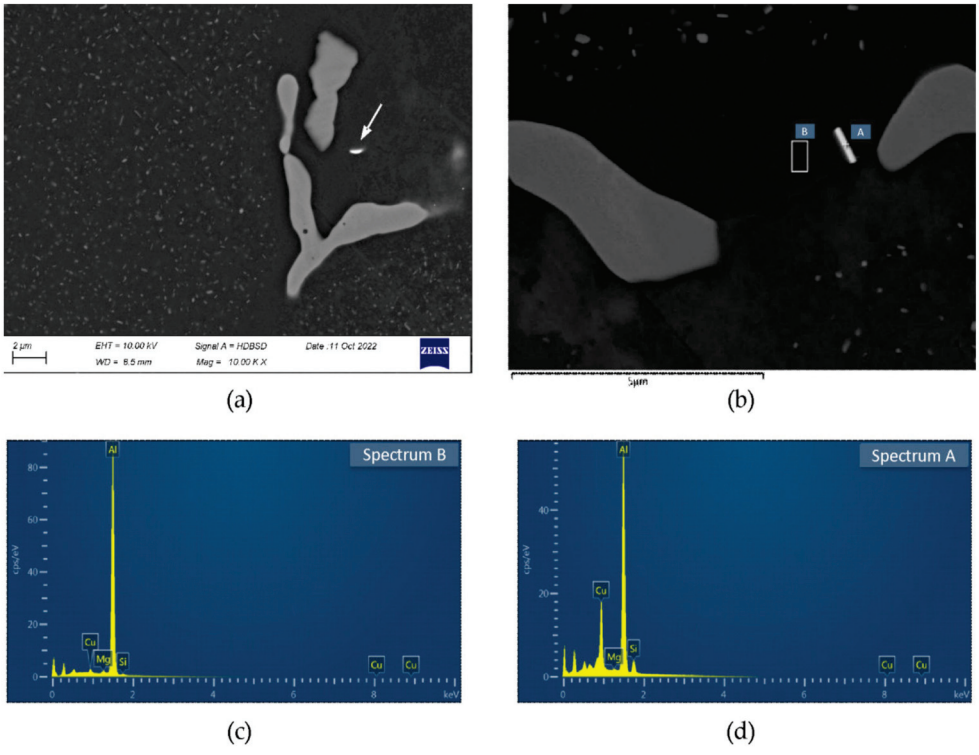

Figure 5. Alloy after homogenization with soaking at 475 °C for 2 h + 530 °C for 2 h + 545 °C for 8 h and water quenching: (**a**,**b**) examples of small particles rich in Cu and Si; (**c**,**d**) spectra from panel b.

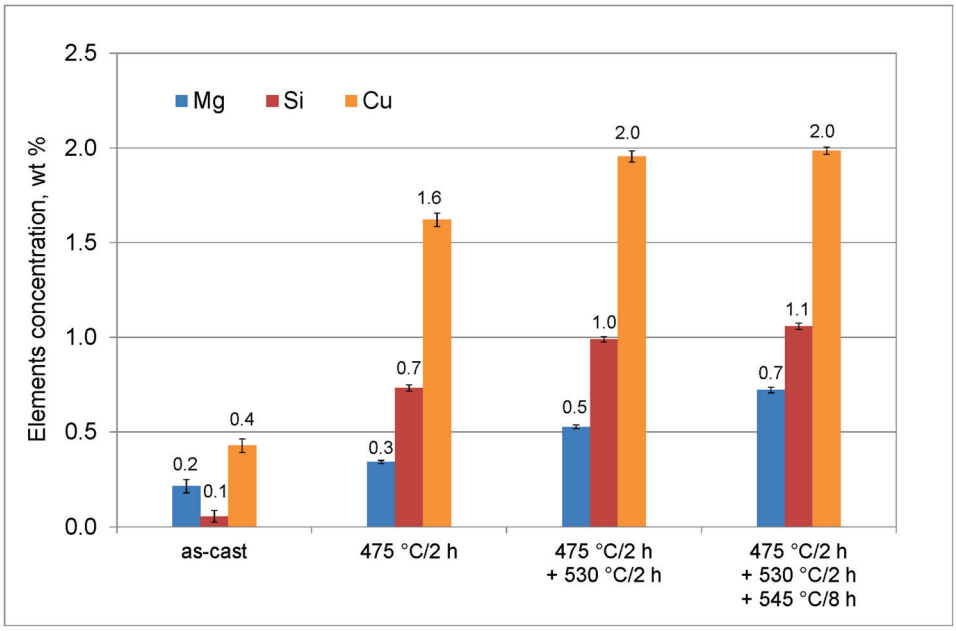

Figure 6. Concentration of Mg, Si, and Cu in dendrites/grains interiors in as-cast state and after each soaking stage (followed by water quenching). Error bars indicate standard deviation of the mean.

Cooling from homogenization temperature at 50 °C/h results in precipitation of coarse particles (Figures 7 and 8). The particles of β-Mg_2Si phase are rather equiaxed, their dimensions are often above 3 μm. Particles of Q-$Al_5Cu_2Mg_8Si_6$ phase are most often elongated. Their length is even above 10 μm and thickness of largest is between 1 and 2 μm. Particles of θ-Al_2Cu phase are also elongated, but noticeably smaller than Q-phase, they have length up to several μm and thickness below 1 μm. With the increase in cooling rate, as expected, the number of large β-Mg_2Si particles clearly decreases and mainly finer ones, with dimensions below 2 μm are observed in the microstructure, although few large particles are also noted. The increase in cooling rate results in lowering of total area of precipitated particles, the (Al) matrix becomes to some extent supersaturated. The θ-Al_2Cu particles also become finer. In the case of Q-$Al_5Cu_2Mg_8Si_6$ phase, results are unexpected. On the one hand the rising cooling rate causes precipitation of fine particles in grains interiors, but on the other hand even after cooling at 500 °C/h large and thick particles are still easily observed. After all examined cooling manners, dimensions of the unfavorable, largest Q-$Al_5Cu_2Mg_8Si_6$ particles found in the microstructure are very similar.

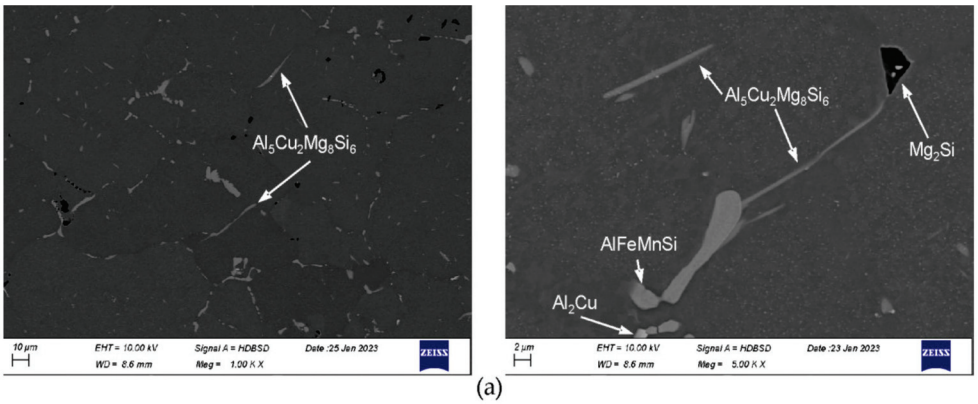

Figure 7. *Cont.*

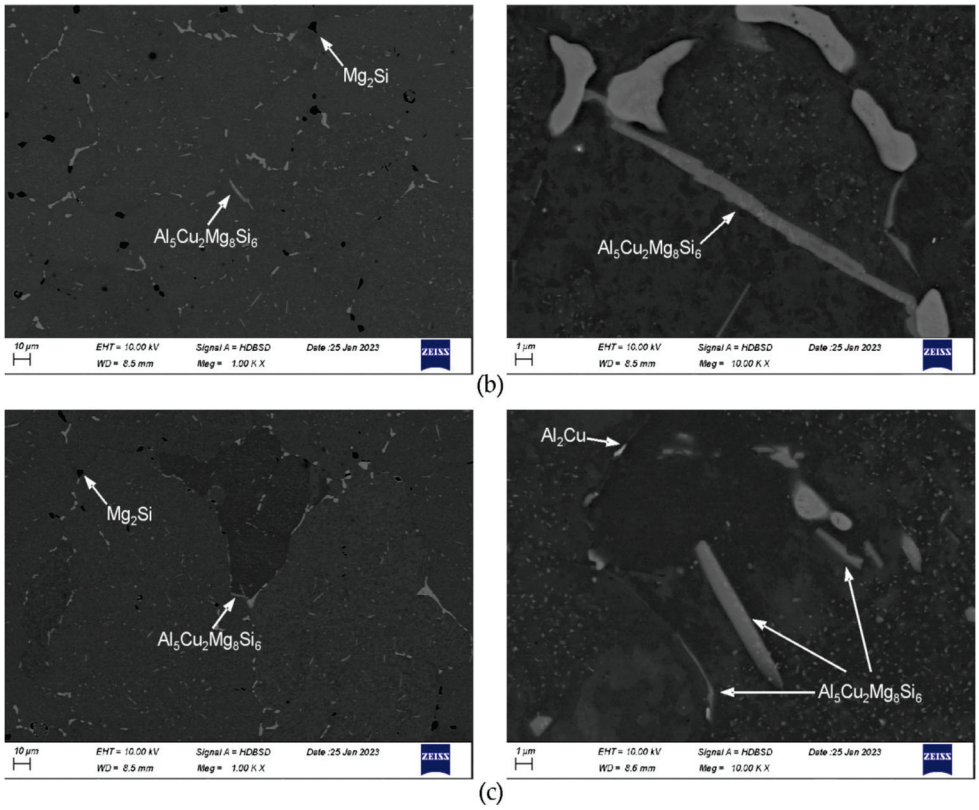

Figure 7. Microstructure after final soaking at 545 °C for 8 h and cooling at: (**a**) 50 °C/h; (**b**) 300 °C/h, and (**c**) 500 °C/h.

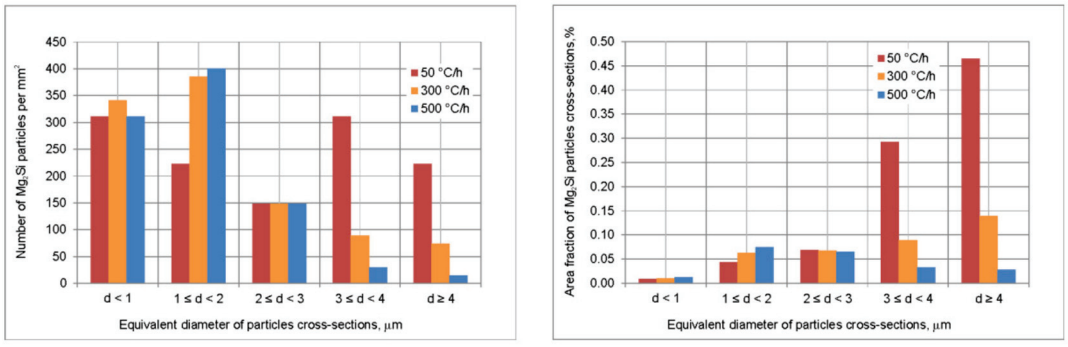

Figure 8. Effect of cooling rate from homogenization temperature on: (**a**) number of β-Mg_2Si particles per mm^2 and (**b**) area fraction of β-Mg_2Si particles cross-sections.

3.3. XRD

XRD spectra for alloy in as-cast state as well as after examined soaking steps are shown in Figure 9. In the spectrum obtained in as-cast state peaks from phases β-Mg_2Si, Q-$Al_5Cu_2Mg_8Si_6$, Si and θ-Al_2Cu are identified; therefore the above presented identification of these phases on the basis of microanalyses results is confirmed. One should note that strong peaks from expected phases often overlap with peaks from Al or from other phases and the analysis of obtained spectra is rather difficult. After first homogenization stage, at 475 °C for 2 h, peak from β-Mg_2Si at 47° slightly grows; during further soaking steps it decreases.

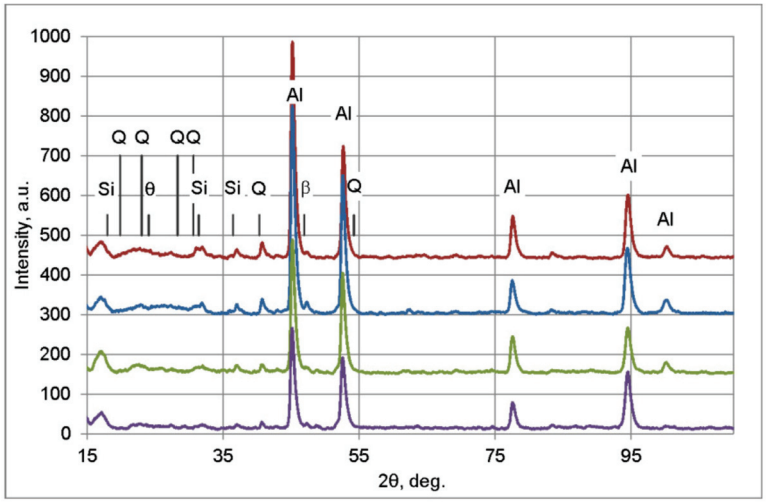

Figure 9. Results of X-ray diffraction phase analysis in as-cast state and after each soaking stage (followed by water quenching). The following JCPDS card was used for peaks identification: 00-004-0787, 00-034-0458, 01-075-0841, 00-041-1068, 03-065-26.95.

4. Discussion

The examined alloy after DC-casting shows dendritic microstructure with depleted (Al) solid solution and large amount of particles and eutectic areas at the dendrites boundaries. Three peaks visible on the DSC curve indicate incipient melting reactions. Based on the presented microstructure observations and the literature data following attempt of reactions identification may be proposed: The peak A, with onset at about 513 °C, can be related to melting of eutectic regions in reaction:

$$(Al) + (Si) + Al_2Cu + Al_5Cu_2Mg_8Si_6 \Rightarrow L \quad (1)$$

In the quaternary Al-Mg-Si-Cu system, this reaction is described to take place at the temperature of 507 °C [33], slightly lower than peak onset temperature. One should note that in [15] the same reaction in commercial alloy 6111 is described to take place at significantly lower temperature, 487 °C.

The peak B in as-cast state has an onset at about 540 °C, and at 545 °C after first soaking at 475 °C. It may be expected that it is related to melting reaction or reactions with the participation of Q-$Al_5Cu_2Mg_8Si_6$ phase:

$$(Al) + Al_5Cu_2Mg_8Si_6 + (Si) \Rightarrow L \quad (2)$$

$$(Al) + Al_5Cu_2Mg_8Si \Rightarrow L \quad (3)$$

It is hard to state unambiguously which of the above mentioned reactions causes peak B occurrence in the examined alloy. However, based on (Si) presence in the eutectic areas as well as slightly lower peak B onset in as-cast state, one may expect that in this state peak is related to reaction (2). After first soaking, (Si) was not found in the microstructure, also probably reaction (3) takes place in this case. According to [17], in quaternary alloy Al—1.0 wt.% Mg—1.1 wt.% Si—0.65 wt.% Cu, these reactions took place at the temperature ranges 519–537 °C and 537–539 °C respectively. Moreover, temperature range for these reactions from quaternary phase diagram is noticeably lower: 507–529 °C [33].

The peak C in as-cast state has an onset at 561 °C. During homogenization it rises, finally is merged with bulk melting peak, and the solidus temperature is 573 °C (Figure 2a, Table 2). One may suppose that this peak is related to melting reaction with the participation of Mg_2Si phase particles and its onset rises due to changes in (Al) solid solution composition. This is based on the microstructure observations showing the presence of Mg_2Si and

Al(FeMn)Si phases, and the literature data indicating that melting of Fe-bearing phases is observed at a higher temperature range [15,33].

The maximum possible dissolution during homogenization of phases contributing to precipitation hardening is essential for obtaining high strength properties of extruded products. This requires high temperature soaking, but due to the presence of three incipient melting peaks on the DSC curve, soaking at 545 °C could be applied after two intermediate soaking stages. The applied soaking enables full dissolution of Q-$Al_5Cu_2Mg_8Si_6$, and θ-Al_2Cu phases resulting in enrichment of solid solution in Cu (Figure 6). Some Cu is detected also in Al(FeMn)Si particles as well as in particles rich in Cu and Si. It is hard to describe the nature of the latter particles. The EDS spectra clearly show peaks from Cu and Si. The ternary phases are not present in aluminum corners of Al-Cu-Si and Al-Mg-Si-Cu phase diagrams. On the other hand, the solubility of Si in θ-Al_2Cu phase is negligible [33]. It is also hard to state if these particles were formed during billet casting or during homogenization. Some microanalyses of eutectic areas constituents in as-cast state showed enrichments in Cu and Si, but it may result from the fact that the volume excited by electron beam is larger than the analyzed eutectic constituent and the X-rays are collected also from neighborhood. These particles should be the subject of further investigations.

Despite the soaking at 545 °C for 8 h, the β-Mg_2Si phase was not dissolved completely, but its amount was significantly reduced. These results indicate that full dissolution of this phase is very difficult or impossible for the examined composition. Rising of homogenization temperature could be possible in laboratory conditions, but application of higher temperature in industrial practice could create the risk of incipient melting (for example due to temperature variation in the furnace). Considering that for the examined composition some part of Mg and Si will not take part in precipitation hardening, a slight reduction in these elements content during further investigations is justified.

As it was already mentioned, the billets cooling from homogenization temperature should cause refinement of precipitated particles making them capable for fast dissolution. As expected, the rising cooling rate contributed to refinement of Mg_2Si particles. After cooling from homogenization at 500 °C/h the precipitated particles dissolved nearly completely within short time (about 9 min) during the DSC test. Although on the DSC curve, peak C was noted and solidus temperature was slightly lower than after water quenching, a small heat of the peak C shows that fraction of remaining particles, which could be dissolved, is very low. Even if in industrial conditions such rapid billet heating was applied, the decrease in solidus temperature and depletion of Mg and Si in (Al) would be rather negligible. The particles of θ-Al_2Cu phase precipitated during cooling are small and do not cause incipient melting. Unexpectedly, even after the fastest examined cooling, in the alloy microstructure coarse particles of Q-$Al_5Cu_2Mg_8Si_6$ phase are observed besides fine ones. The significant variation in Q-phase particles size is hard to explain. The presence of coarse particles lowers the solidus temperature of homogenized alloy to about 545 °C. This is unfavorable because the range of permissible exit temperature during extrusion needs to be noticeably reduced in order to avoid melting. However, the heat of peak B is very small (it is hardly visible on the DSC curves), which indicates that amount of undissolved Q-$Al_5Cu_2Mg_8Si_6$ phase particles at the temperature of about 545 °C (incipient melting) is very small. Thus, one may expect that in industrial process, where billets heating rate will probably be lower and the plastic deformation during extrusion will facilitate diffusion, these particles will be fully dissolved. Nevertheless, this supposition needs to be verified during extrusion trials and conditions of billets preheating and extrusion need to be selected carefully. The results allow to recommend for the examined alloy fast cooling from homogenization temperature, at least at 500 °C/h.

Within future work, the evaluation of proposed homogenization conditions is planned. The homogenized billets are to be extruded in semi-industrial conditions with solution heat treatment on the press. The extruded products, after ageing, will be subjected to detailed examination of microstructure aimed primarily at verification if undissolved particles of phases, components of which are essential in subsequent precipitation hardening, are

present. The solidus temperature will be determined and compared with the value obtained after homogenization with water quenching (within stage 2 of the present work). The mechanical properties tests of extruded products will also be performed.

5. Conclusions

On the basis of the obtained results, the following conclusions can be drawn:

1. The examined alloy in as-cast state was characterized by dendritic microstructure with large amount of particles and eutectic areas at the dendrites boundaries. Besides (Al) solid solution, in the microstructure phases β-Mg_2Si, Q-$Al_5Cu_2Mg_8Si_6$, θ-Al_2Cu, (Si) and Al(FeMn)Si were found. On the DSC curves three peaks resulting from incipient melting reactions were observed, solidus temperature of the alloy in as-cast state was 513 °C.
2. In order to avoid incipient melting, the homogenization scheme with three soaking stages: at 475, 530, and 545 °C was applied. During soaking, full dissolution of Q-$Al_5Cu_2Mg_8Si_6$ and θ-Al_2Cu phases took place. The β-Mg_2Si phase did not dissolve completely during soaking, but its amount was significantly reduced.
3. The alloy needs to be fast cooled from homogenization temperature, at least at 500 °C/h. The β-Mg_2Si and θ-Al_2Cu particles precipitated during cooling were sufficiently refined. Despite such fast cooling, in the microstructure coarse Q-$Al_5Cu_2Mg_8Si_6$ phase particles were found and rapid billets heating may lead to incipient melting at the temperature of about 545 °C. Thus, the careful selection of billets preheating and extrusion conditions was found to be necessary.

Author Contributions: Conceptualization, A.W. and G.W.; methodology, A.W.; investigation, J.M., M.B., B.L.-M., G.W. and A.W.; writing—original draft preparation, A.W.; writing—review and editing, G.W., B.L.-M., J.M., M.B. and D.L.; supervision, D.L. All authors have read and agreed to the published version of the manuscript.

Funding: This research was funded by THE NATIONAL CENTRE FOR RESAERCH AND DEVELOPMENT, grant number TECHMATSTRATEG-III/0040/2019-00 "Development of extrusion technology for sections from ultra-strength AlMgSi(Cu) alloys".

Data Availability Statement: Not applicable.

Conflicts of Interest: The authors declare no conflict of interest.

References

1. Fuel Types of New Passenger Cars in the EU. Available online: https://www.acea.auto/figure/fuel-types-of-new-passenger-cars-in-eu/ (accessed on 29 December 2022).
2. Scamans, G. Electric Vehicles Spike Demand for High Strength Aluminum Extrusions. *Light Met. Age* **2018**, *76*, 6–9.
3. Brown, L.; Nelson, R. The Coming BEV Wave: Implications for Extrusion. *Light Met. Age* **2020**, *78*, 22–24.
4. International Alloy Designations and Chemical Composition Limits for Wrought Aluminum and Wrought Aluminum Alloys. Available online: https://www.aluminum.org/sites/default/files/2021-11/TealSheet.pdf (accessed on 31 December 2022).
5. Chakrabarti, D.J.; Laughlin, D.E. Phase relations and precipitation in Al-Mg-Si alloys with Cu additions. *Prog. Mater. Sci.* **2004**, *49*, 389–410. [CrossRef]
6. Ding, L.; Jia, Z.; Nie, J.-F.; Weng, Y.; Cao, L.; Chen, H.; Wu, X.; Liu, Q. The structural and compositional evolution of precipitates in Al-Mg-Si-Cu alloy. *Acta Mater.* **2018**, *145*, 437–450. [CrossRef]
7. Bergsma, S.C.; Kassner, M.E.; Li, X.; Delos-Reyes, M.A.; Hayes, T.A. The Optimized Mechanical Properties of the New Aluminum Alloy AA 6069. *J. Mater. Eng. Perform.* **1996**, *5*, 111–116. [CrossRef]
8. Guo, S.; Yu, H.; Wang, Z.; Yu, W.; Cheng, W.; Huang, L.; Liu, C.; Yin, F.; Zhao, W.; Qin, C. Microstructural Evolution and Mechanical Properties of Pure Aluminum upon Multi-Pass Caliber Rolling. *Materials* **2022**, *15*, 1206. [CrossRef]
9. Xiong, H.; Wang, Z.; Yu, H.; Chen, T.; Wang, X.; Ye, L. Performances of Al-xLi alloy anodes for Al-air batteries in alkaline electrolyte. *J. Alloys Compd.* **2021**, *889*, 161677. [CrossRef]
10. Liu, H.L.; Li, P.; Xue, K.M.; Qian, C.H.; Hua, R. Microstructural evolution and fracture mechanism of a new Al-Zn-Mg-Cu-Zr alloy processed by equal-channel angular pressing. *Rare Met.* **2022**, *41*, 3546–3551. [CrossRef]
11. Liu, F.; Zhu, X.; Qin, J.; Zhou, W.; Ling, J.; Dong, Q.; Yu, J.; Nagaumi, H.; Zhang, B. Effect of Mn/Cr ratio on precipitation behaviors of α-Al(FeMnCr)Si dispersoids and mechanical properties of Al-Mg-Si-Cu alloys. *Mater. Sci. Eng. A-Struct.* **2022**, *860*, 144269. [CrossRef]

12. Zupanič, F.; Steinacher, M.; Žist, S.; Bončina, T. Microstructure and Properties of a Novel Al-Mg-Si Alloy AA 6086. *Metals* **2021**, *11*, 368. [CrossRef]
13. Žist, S.; Steinacher, M.; Bončina, T.; Albu, M.; Burja, J.; Vončina, M.; Zupanič, F. The Effect of Scandium on the Microstructure of the Aluminium Alloy AA 6086. *Crystals* **2022**, *12*, 973. [CrossRef]
14. Xue, G.; Zhong, G.; Lin, S.; Li, H.-T.; Gui, X.; Zhang, L. Study on Microstructure and Mechanical Properties of Al-Mg-Si-Cu Aluminium Alloy with High Ductility. In Proceedings of the MATEC Web of Conferences Vol. 326 the 17th International Conference on Aluminium Alloys 2020 (ICAA17), Grenoble, France, 26–29 October 2020. [CrossRef]
15. Chen, X.G.; Langlais, J. Solidification behavior of AA6111 Automotive Alloy. *Mater. Sci. Forum* **2000**, *331–337*, 215–222. [CrossRef]
16. Zhang, S.; Xiong, B.; Zhang, Y.; Li, X.; Wang, F.; Li, Z.; Liu, H. The Microstructural Evolution of AA6111 Aluminum Alloy during Homogenization Treatment. *Mater. Sci. Forum* **2013**, *749*, 223–228. [CrossRef]
17. Li, K.; Song, M.; Dua, Y.; Tang, Y.; Dong, H.; Ni, S. Investigation of the as-solidified microstructure of an Al-Mg-Si-Cu alloy. *J. Alloys Compd.* **2014**, *602*, 312–321. [CrossRef]
18. Wu, Y.; Xiong, J.; Lai, R.; Zhang, X.; Guo, Z. The microstructure evolution of an Al-Mg-Si-Mn-Cu-Ce alloy during homogenization. *J. Alloys Compd.* **2009**, *475*, 332–338. [CrossRef]
19. Lodgaard, L.; Ryum, N. Precipitation of dispersoids containing Mn and/or Cr in Al-Mg-Si alloys. *Mater. Sci. Eng. A-Struct.* **2000**, *283*, 144–152. [CrossRef]
20. Han, Y.; Ma, K.; Wang, C.; Nagaumi, H. Precipitation behavior of dispersoids in Al-Mg-Si-Cu-Mn-Cr alloy during homogenization annealing. In Proceedings of the 13th International Conference on Aluminium Alloys ICAA13, Pittsburgh, PA, USA, 3–7 June 2012. [CrossRef]
21. Li, Z.; Qin, J.; Zhang, H.; Wang, X.; Zhang, B.; Nagaumi, H. Improved Distribution and Uniformity of α-Al(Mn,Cr)Si Dispersoids in Al-Mg-Si-Cu-Mn (6xxx) Alloys by Two-Step Homogenization. *Metall. Mater. Trans. A* **2021**, *52*, 3204–3220. [CrossRef]
22. Elasheri, A.; Elgallad, E.M.; Parson, N.; Chen, X.G. Improving the dispersoid distribution and recrystallization resistance of a Zr-containing 6xxx alloy using two-step homogenization. *Philos. Mag. A* **2022**, *102*, 2345–2361. [CrossRef]
23. Mochugovskiy, A.G.; Mosleh, A.O.; Kotov, A.D.; Khokhlov, A.V.; Kaplanskaya, L.Y.; Mikhaylovskaya, A.V. Microstructure Evolution, Constitutive Modelling, and Superplastic Forming of Experimental 6XXX-Type Alloys Processed with Different Thermomechanical Treatments. *Materials* **2023**, *16*, 445. [CrossRef]
24. Cai, Y.; Wang, C.; Zhang, J. Microstructural characteristics and aging response of Zn-containing Al-Mg-Si-Cu alloy. International. *J. Miner. Metall. Mater.* **2013**, *20*, 659–664. [CrossRef]
25. Kuijpers, N.C.W.; Kool, W.H.; Koenis, P.; Nilsen, K.; Todd, I.; Zwaag, S. Assessment of different techniques for quantification of α-Al(FeMn)Si and β-AlFeSi intermetallics in AA 6xxx alloys. *Mater. Charact.* **2002**, *49*, 409–420. [CrossRef]
26. Bayat, N.; Carlberg, T.; Cieslar, M. In-situ study of phase transformations during homogenization of 6005 and 6082 Al alloys. *J. Alloy. Compd.* **2017**, *725*, 504–509. [CrossRef]
27. Reiso, O.; Hafsås, J.E.; Sjothun, O.; Tundal, U. The Effect of Cooling Rate After Homogenization and Billet Preheating Practice on Extrudability and Section Properties. Part 1: Extrudability and Mechanical Properties. In Proceedings of the 6th International Aluminum Extrusion Technology Seminar, Chicago, IL, USA, 14–17 May 1996.
28. Lefstad, M.; Reiso, O. Metalurgical Speed Limitations During the Extrusion of AlMgSi-Alloys. In Proceedings of the 6th International Aluminum Extrusion Technology Seminar, Chicago, IL, USA, 14–17 May 1996.
29. Ricks, R.A.; Parson, N.C.; Yiu, H.L.; Court, S.A. Microstructural Optimisation for Extrusion Of 6063 Alloys, In Proceedings of the 5th International Aluminum Extrusion Technology Seminar, Chicago, IL, USA, 19–22 May 1992.
30. Zając, S.; Bengtsson, B.; Jönsson, C. Influence of cooling after homogenization and reheating to extrusion on extrudability and final properties of AA6063 and AA6082 alloys. *Mater. Sci. Forum* **2002**, *396–402*, 399–404. [CrossRef]
31. Birol, Y. Homogenization of direct chill cast AlSi1MgMn billets. *Int. J. Mater. Res. (Z. Metallkd.)* **2014**, *105*, 75–82. [CrossRef]
32. Qin, J.; Nagaumi, H.; Yu, C.; Liu, F.; Li, Y.; Wang, L. Coarsening behavior of Mg_2Si precipitates during post homogenization cooling process in Al-Mg-Si alloy. *J. Alloy. Compd.* **2022**, *902*, 162851. [CrossRef]
33. Belov, N.A.; Eskin, D.G.; Aksenov, A.A. *Multicomponent Phase Diagrams, Applications for Commercial Aluminum Alloys*; Elsevier: London, UK, 2005.

materials

MDPI

Review

An Overview of Thermal Exposure on Microstructural Degradation and Mechanical Properties in Ni-Based Single Crystal Superalloys

Jian Zhang [1], Fan Lu [2] and Longfei Li [2,3,*]

[1] Science and Technology on Advanced High Temperature Structural Materials Laboratory, AECC Beijing Institute of Aeronautical Materials, Beijing 100095, China
[2] State Key Laboratory for Advanced Metals and Materials, University of Science and Technology Beijing, Beijing 100083, China
[3] Beijing Key Laboratory of Special Melting and Reparation of High-End Metal Materials, University of Science and Technology Beijing, Beijing 100083, China
* Correspondence: lilf@skl.ustb.edu.cn

Abstract: Microstructural stability at elevated temperatures is one of the main concerns for the service reliability of aero-engine turbine blades. Thermal exposure, as an important approach to examine the microstructural degradation, has been widely studied in Ni-based single crystal (SX) superalloys for decades. This paper presents a review on the microstructural degradation induced by high-temperature thermal exposure and the associated damage in mechanical properties in some typical Ni-based SX superalloys. The main factors affecting the microstructural evolution during thermal exposure and the influencing factors in the degradation of mechanical properties are also summarized. Insights into the quantitative estimation of the thermal exposure-affected microstructural evolution and the mechanical properties will be beneficial for the understanding and improvement of reliable service in Ni-based SX superalloys.

Keywords: Ni-based single crystal superalloys; thermal exposure; microstructural evolution; TCP phases; mechanical property

Citation: Zhang, J.; Lu, F.; Li, L. An Overview of Thermal Exposure on Microstructural Degradation and Mechanical Properties in Ni-Based Single Crystal Superalloys. *Materials* **2023**, *16*, 1787. https://doi.org/10.3390/ma16051787

Academic Editor: Elena Villa

Received: 22 January 2023
Revised: 16 February 2023
Accepted: 20 February 2023
Published: 22 February 2023

1. Introduction

Ni-based single crystal (SX) superalloys are the materials of choice for the manufacturing of turbine blades in aero-engine and power-generation applications due to their unique high temperature performance [1]. During service, the turbine blades are subjected to extreme conditions such as high temperature, changeable mechanical stresses and environmental corrosion. Hence, the initial microstructures undergo an inevitable degradation process at high temperature, which contributes much to the decline in component performance and even the premature failure of the gas turbine blades [2,3]. The strength of a given Ni-based SX superalloy mainly refers to its mechanical properties as well as microstructural stability [4]. As the direct approach to estimate microstructural stability, knowledge of thermal exposure on microstructural evolution and the related mechanical properties is extremely essential to further optimize the alloying design and achieve superior performance during service of Ni-based SX superalloys.

The outstanding properties of Ni-based SX superalloys can be attributed to the microstructures combining the ordered ($L1_2$) intermetallic γ'-Ni_3Al precipitates, coherently embedded in disordered (fcc) γ-Al matrix [5,6]. The γ' phases with a high volume fraction provide high rigidity and low dislocation tolerance, limiting the dislocation movements in the γ channels, which contribute to the high temperature property by the precipitate strengthening effect [7]. Thus, the volume fraction, size, morphology and distribution of the γ' precipitates become the primary concerns in the microstructural evolution when serving under harsh conditions [8–10].

To meet the requirements in high-temperature capabilities, modern Ni-based SX superalloys are always alloyed with amounts of refractory elements, such as W, Mo and, most importantly, Re [5,11,12]. The introduction of these elements, however, can also promote the rapid formation of refractory-rich topologically-close-packed (TCP) precipitates belonging to brittle inclusions at elevated temperatures, which may significantly damage the endurance life of Ni-based SX superalloys [13–16]. Thus, another great concern in evaluating microstructural degradation is the precipitate of TCP phases [17–19].

Obviously, the microstructure degradation induced by thermal exposure, including the changes in the volume fraction, size, morphology and distribution of the γ' precipitates as well as the formation of TCP phases, is critical to the mechanical properties [20,21]. Since different alloys present microstructure degradation at different extents when subjected to different conditions, or even the same conditions, it is important to summarize the microstructural degradation in different aspects for a better understanding of the microstructural stability of modern Ni-based SX superalloys. Therefore, the alloying design can be further optimized when comprehensively considering the microstructural stability of the characterized Ni-based SX superalloys. The purpose of this paper is to review the high temperature characteristics and evolution of γ/γ' phases and the formation of TCP phases as well as the influencing factors and their effect on related mechanical properties based on published experimental results of several modern Ni-based SX superalloys.

2. Microstructural Stability during Thermal Exposure

2.1. γ/γ' Microstructure Evolution

The most remarkable microstructural evolution in Ni-based SX superalloys exposed to high temperature is the growth of the γ' phases, or so-called coarsening [22,23]. In the two-phase mixed system, a large amount of γ/γ' interfacial area is the direct consequence of the polydisperse nature. During thermal exposure, the total energy of the system should be decreased to reach the equilibrium state. Thus, by decreasing the amount of interfacial area, the system tends to have a thermodynamic preference, resulting in the growth of the precipitate size [24]. Figure 1 shows the typical γ/γ' microstructure of a commercial Ni-based SX superalloy CMSX-4 after heat treatments (referring to initial state) and after related thermal exposure at 950 °C for different durations [25]. In the initial state, γ' precipitates exhibit square morphology on each {001} crystallographic plane, illustrating the cuboidal morphology before thermal exposure. During thermal exposure, the γ' precipitates increase their average sizes accompanied by some elongated precipitates, although most of the precipitates still maintain their straight edges and sharp corners. This represents the most common microstructural evolution of γ' precipitates when subjected to high-temperature thermal exposure, indicating the shrink of small particles and the growth of large particles, followed by the well-known Ostwald ripening theory [22,26].

More serious γ' evolution may occur from an initial cuboidal shape into a plate-like morphology aligned along the <100> direction during a stress-free thermal exposure process, or so-called spontaneous rafting. Figure 2a shows the morphology of the spontaneous rafting in a DD11 alloy when subjected to 1070 °C and 300 h [27]. It is confirmed that this phenomenon is closely associated with a higher γ' volume fraction, which leads to the easier interconnection of the growing γ' phases in the coarsening process [28]. Furthermore, the addition of a large amount of refractory elements into Ni-based SX superalloys causes considerable negative lattice misfit, which acts as the driving force for the directional diffusion flow and the formation of γ' rafts aligned along the <100>, despite the absence of applied stress [29]. Meanwhile, the elevate temperature also contributes to the elemental diffusion process and further promotes the faster developed γ' rafts [30,31]. For the modern Ni-based SX superalloys, designed with a considerable addition of refractory elements, the spontaneous rafting is also a representative feature in microstructural instability in many published works [32–34].

It is well-known that in superalloys with extremely high γ' volume fraction, the γ' phases tend to be seriously interconnected and can even become the topological matrix

phase instead of the γ matrix during creep, wherein this process can be called topological phase inversion [35]. Recent research also displayed a similar phenomenon in the interdendritic regions of specimens after thermal exposure, as shown in Figure 2b [36]. This strongly confirmed the effect of the higher γ′ volume fraction as responsible for the serious microstructural evolution, since the γ′ volume fraction in the interdendritic regions is over 65%, which is much higher than that in the dendrite core.

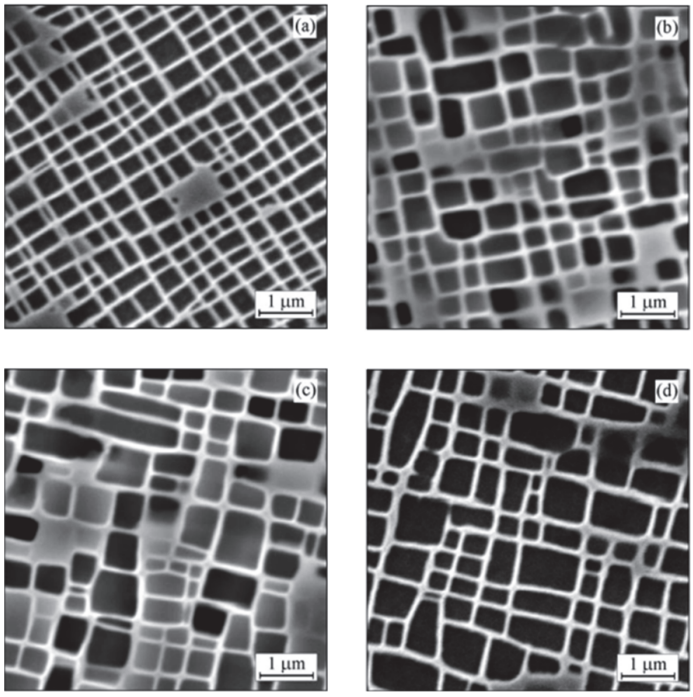

Figure 1. γ/γ′ microstructure evolution of CMSX-4 superalloy at (**a**) initial state; (**b**) 950 °C/500 h; (**c**) 950 °C/1000 h; (**d**) 950 °C/2000 h [25].

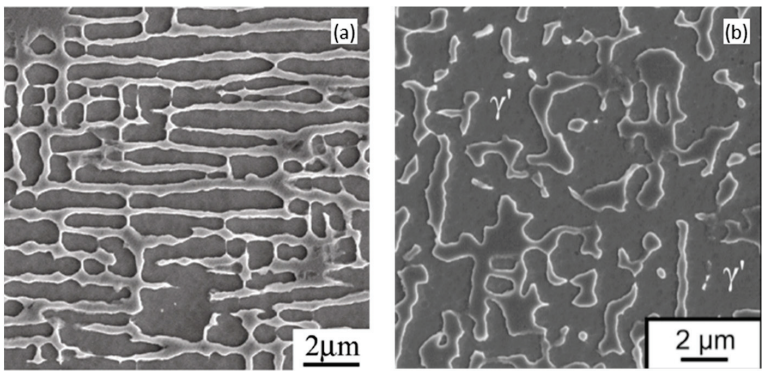

Figure 2. The formation of (**a**) spontaneous rafts in DD11 alloy after thermal exposure of 1070 °C/300 h [27] and (**b**) topological phase inversion in interdendritic areas in ERBO/1 alloy after thermal exposure of 1100 °C/250 h [36].

Figure 3 shows the quantitative microstructural parameters (including the γ′ volume fraction and γ′ and γ phases′ dimensions) of the DD11 alloy after thermal exposure at 1070 °C for different durations. It is suggested that all the microstructural parameters changed gradually until 500 h, after which they tend to approach a constant value under the specific temperature. Here, the dissolution of γ′ is a diffusion-controlled process, following a model from Johnson–Mehl–Avrami–Kolmogorov (JMAK), which predicts the real-time γ′ volume fraction as a function of the time [37,38]. Above all, the decreasing

γ' volume fraction and increasing γ and γ' sizes constituted the important features of γ/γ' microstructural degradation during the thermal exposure process.

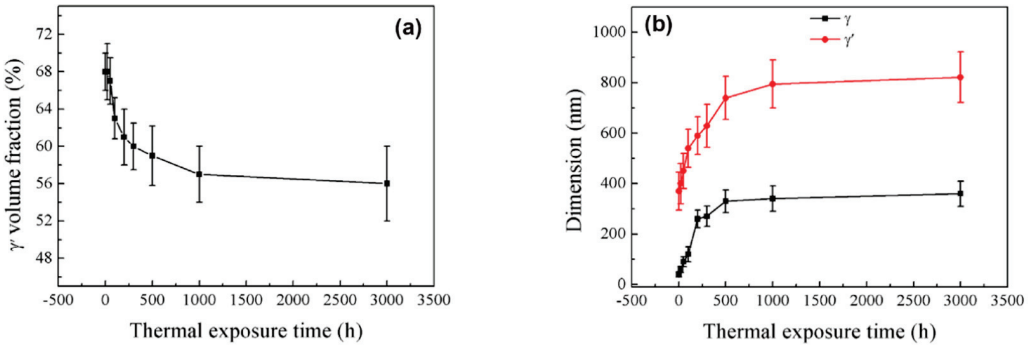

Figure 3. The quantitative microstructural parameters of DD11 alloy after thermal exposure at 1070 °C for different durations. (**a**) γ' volume fraction; (**b**) γ' size and γ channel width [27].

2.2. γ′ Coarsening Mechanisms

To quantitatively describe the precipitate coarsening kinetics, a theory was first proposed by Lifshitz and Slyozof [23] and then by Wagner [26], which is widely known as the LSW theory. The remarkable feature of the developed theory is characterized by the time exponents in the kinetics of precipitate coarsening, which is essential to diffusion-controlled coarsening. Based on the Gibbs–Thomson equation, the LSW theory provided an analytical equation: $\langle r^n \rangle = Kt$, with the exponent of $n = 3$, where $\langle r \rangle$ is the average precipitates radius, K is the coarsening constant and t is the related time. Figure 4b gives the plot of $\langle r^3 \rangle$ versus t of a Ni-Al binary alloy at different temperatures, indicating the accepted goodness-of-fit in the presumed linear behaviors. However, the LSW theory was developed based on binary systems and assumed a dilute system with small volume fraction of precipitates. Thus, some followed models were developed with the consideration of high precipitate volume fraction, such as Modified LSW (MLSW) [9], Davies–Nash–Stevens (LSEM) [39], Brailsford–Wynblatt (BW) [40], etc. More recently, a new model was proposed by Philippe and Voorhees (P-V), taking into account the multi-component effect as well as the precipitate volume fraction [41]. Nevertheless, the LSW theory is still the most well-accepted theory to describe the coarsening behavior, and a large number of studies have successfully expanded the LSW theory to multi-component superalloys.

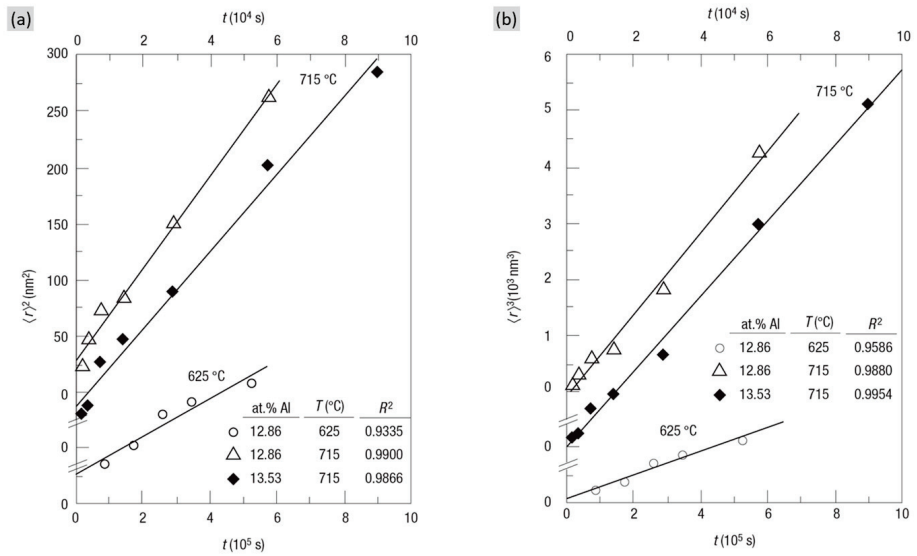

Figure 4. The plots showing the average γ' precipitate size raised in (**a**) square rate law and (**b**) cubic rate law versus thermal exposure time in a Ni-Al binary alloy [42].

Another coarsening model was established which considered that the diffusion through the interface controlled the coarsening process, called the trans-interface diffusion-controlled (TIDC) model. This model excludes the effect of volume fraction while taking the interfacial width into account and the exponent of $n = 2$ in the mentioned power-law function. Figure 4a outlines the relationship between $\langle r^2 \rangle$ versus t, also suggesting good linear behavior, which adapted to the TIDC theory. Recently, the TIDC theory has also been successfully applied for multi-component superalloys [43–45].

The two coarsening controlled mechanisms, referring to matrix-diffusion controlled and interfacial-diffusion controlled, usually emerge simultaneously and compete in a single coarsening process [46]. By the analysis of the particle size distributions (PSDs) within different coarsening stages, the underlying coarsening-controlled mechanism can be determined. Figure 5 shows the experimentally measured PSDs as well as the predictions of PSDs for LSW and TIDC theory in a Ni-Al-Cr-Re alloy, firstly with lower temperature, which is similar to the stage before heat treatment of the experimental alloy, followed by a Re-containing alloy with higher temperature and longer aging time [44]. It is indicated that, in the heat treatment process, the coarsening is mainly controlled by matrix diffusion, since the PSDs are much closer to the prediction in LSW theory while, at a longer thermal exposure time, the coarsening gradually tends to be controlled by interfacial-diffusion. More recent research also confirmed the transition of the coarsening-controlled mechanism from matrix-diffusion to interfacial-diffusion in the long-term coarsening process of a single alloying system, where the decreasing interfacial width acts as the driving force for that transition [45].

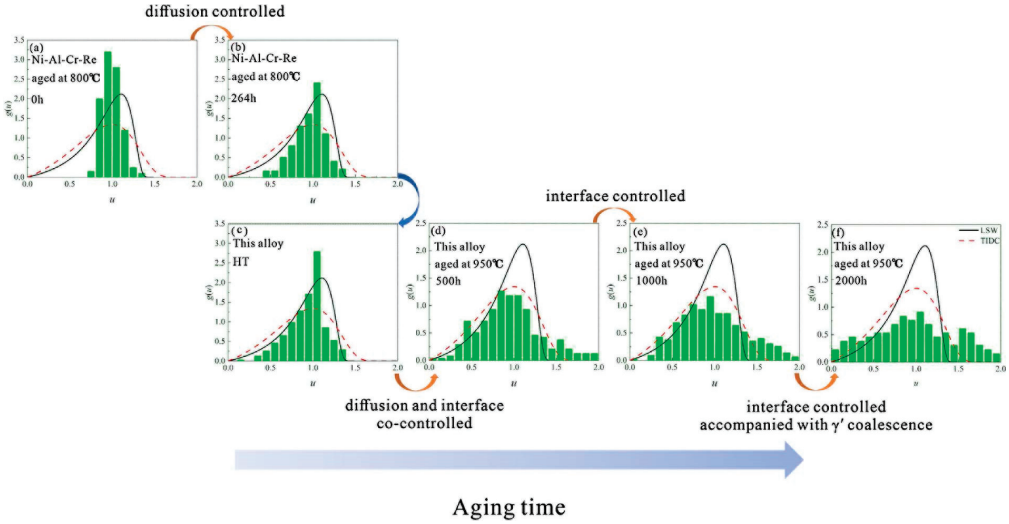

Figure 5. PSDs for Ni-Al-Cr-Re aged for (**a**) 0 h and (**b**) 264 h at 800 °C and PSDs for investigated alloy for (**c**) HT state and aged for (**d**) 500 h, (**e**) 1000 h and (**f**) 2000 h at 950 °C [44]. (u represent the normalized γ′ size).

2.3. Precipitation Behavior of TCP Phases

Excessive addition of refractory elements promotes the precipitate of the topologically close-packed (TCP) phases, such as σ-, μ-, P- or R-phase, during high-temperature thermal exposure in Ni-based SX superalloys [19]. These TCP phases can display a wide variety of different morphologies, as shown in Figure 6 [47,48]. In 2D characterization, σ phases and P phases mainly exist in sheet-like and needle-like morphology (Figure 6a), while in 3D characterization, the P phases present a basket-weave-like morphology, showing the possibility of growing from σ phase after thermal exposure (Figure 6c). The different morphology of TCP phase depends on the different crystallography structures. Furthermore, both of the σ and P phases show a consistent orientation relationship with the matrix, with different thermal exposure conditions.

The needle-like μ phases and Lath-like R phases are shown in Figure 6b,d. In 3D characterization, the basket-weave-like R phases consist of the intersected needle-like μ phase.

The R phases serve as the thermodynamic equilibrium phase, which can precipitate from the matrix as well as μ phases, while it has no direct orientation relationship with the matrix.

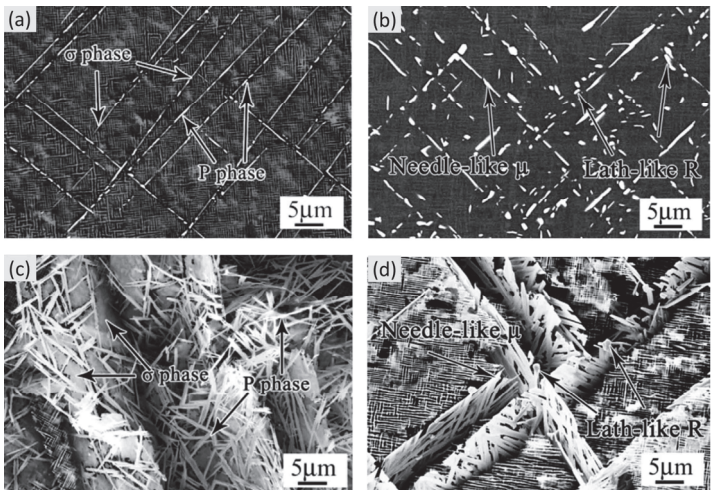

Figure 6. PSDs for Ni-A Typical TCP phases in Ni-based SX superalloys. (**a**) σ phase and P phase (2D-characterization); (**b**) μ phase and R phase (2D-characterization); (**c**) σ phase and P phase (3D-characterization); (**d**) μ phase and R phase (3D-characterization) [47,48].

The TCP phases basically contain a large number of γ-stabilizers, such as Re, W, Mo, Cr and Co, as shown in the APT characterization in Figure 7. Thus, the TCP phases are always surrounded by γ′ phases. While there are still some differences in chemistry among the TCP phases, usually, P and σ phases are very similar in high Re content, μ phases are high in Mo and/or W and low in Re content, and Co content in μ phases is much higher than that in σ phases [49]. Since the precipitates of TCP phases depend on a thermodynamic process, they can be qualitatively determined in CALPHAD calculations.

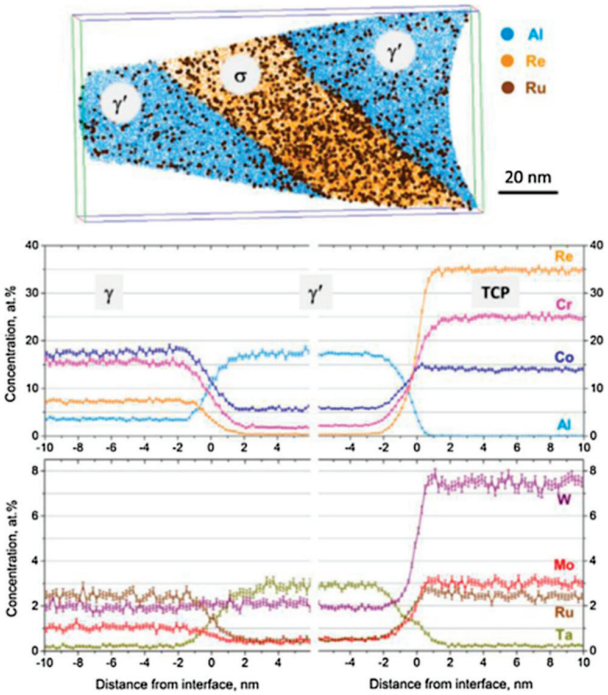

Figure 7. An APT elemental map of a plate-like σ precipitate surrounded by a γ′ envelope (only Al, Re and Ru atoms are shown) and corresponding concentration profiles across γ/γ′ and γ′/γ interfaces for the annealed Astra1-21 alloy. Accumulation of Cr, Mo, W and Re in the σ phase is visible. Ru concentrations in the σ phase and γ matrix are nearly identical. No elemental segregation at phase boundaries can be observed [50].

Figure 8a shows the differentiation within TCP phases' formation between the dendritic and interdendritic region after thermal exposure of ERBO/1C alloy [51]. It indicated the pronounced formation of TCP phases in dendrite cores rather than the interdendrite region, which can be explained by the strong segregation of the refractory elements to dendrite cores after heat treatment of the alloy, especially Re. A threshold Re concentration is necessary for the formation of the TCP phase. The evolution of the TCP phase in Figure 8b also shows the sharp increase in the TCP area fraction in dendrite cores during thermal exposure. Thus, a compatible homogenous process is beneficial for decreasing the driving force for the TCP formation. However, the density of the TCP phases still decreases from the dendrite cores to the interdendritic regions due to the micro-segregation of refractory elements to the dendrite cores retained even after heat treatment [49,52].

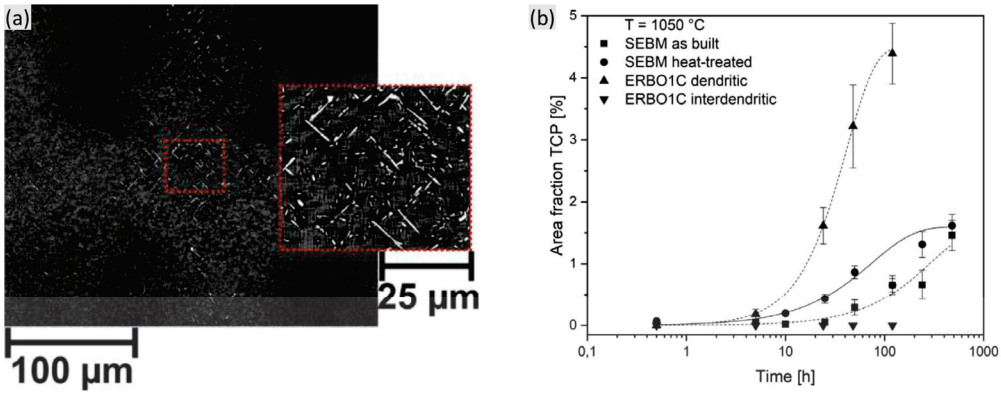

Figure 8. (**a**) Microstructure of the ERBO/1C alloy after thermal exposure at 1050 °C for 120 h and (**b**) area fraction of formed TCPs in dendritic core and interdendritic region [51].

2.4. Influencing Factors on Microstructural Stability

2.4.1. Temperature and Time

Figure 9a shows the dependence of average size of the γ′ precipitates on the thermal exposure time of the CMSX-4 alloy. The average precipitate size increases with the thermal exposure time as well as temperature. Detailed analysis on the growing cuboidal γ′ precipitates showed that the coarsening kinetics follow a cube rate law, and higher temperature promotes the spontaneous rafts, as shown in Figure 9b. Figure 9c shows the temperature dependence of the experimental and calculated coarsening rate of CMSX-4 alloy, indicating the significantly increasing coarsening rate as a function of temperature. The active promotion of the coarsening rate by temperature can be attributed to the increasing diffusion rate at higher temperature [25].

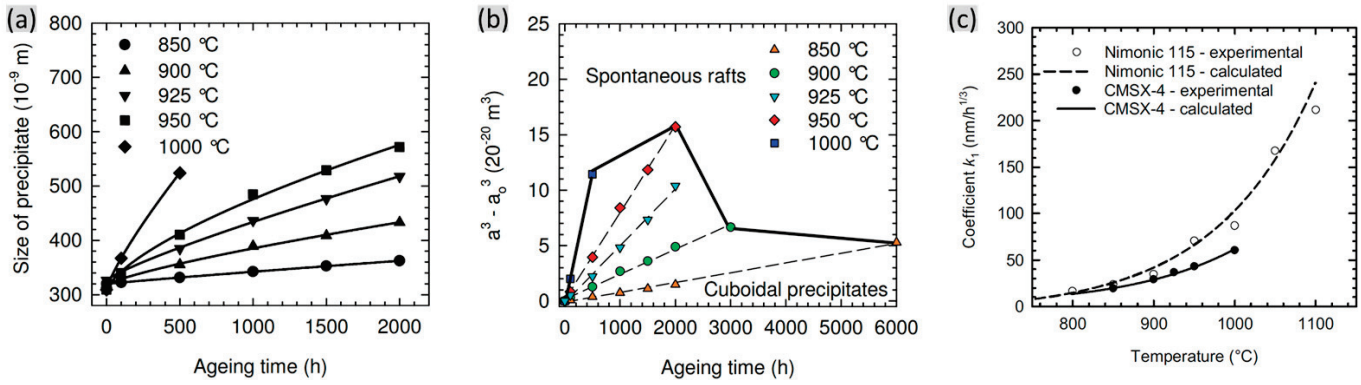

Figure 9. Dependence of the (**a**) average γ′ size and (**b**) normalized γ′ size as a function of thermal exposure time of CMSX-4 alloy after different durations at different temperature [53]. (**c**) Dependence of the coarsening rate as a function of temperature of two alloys [25].

The formation of TCP phases is also closely associated with the temperature and time. In the thermal exposure process of a Re-free alloy, the area fraction of the TCP phase increases with time, together with the decreasing incubation time and the increasing formation rate with the increasing temperature, as shown in Figure 10 [14]. This is mainly due to the higher diffusion rate of TCP formation elements suggested by higher temperature. However, the opposite conclusion has been obtained, indicating the restrained formation of TCP phases induced by increasing temperature, as shown in Figure 11a [54]. Here, although the TCP phases form much earlier with a shorter incubation time in higher temperature (1050 °C), the equilibrium content of TCP phases is obviously lower. Matuszewski et al. [52] presented CALPHAD calculations to predict the driving force for TCP precipitation at different temperatures, also indicating the decreasing driving force for promoting any type of TCP phase formation with the increasing temperature. This can be attributed to the following reasons: one is that the entropy term increases along with the increased temperature, which stabilizes the solid solution strength of the γ matrix, and another is that the γ volume fraction increases with the increased temperature, which restrains the supersaturation of refractory elements.

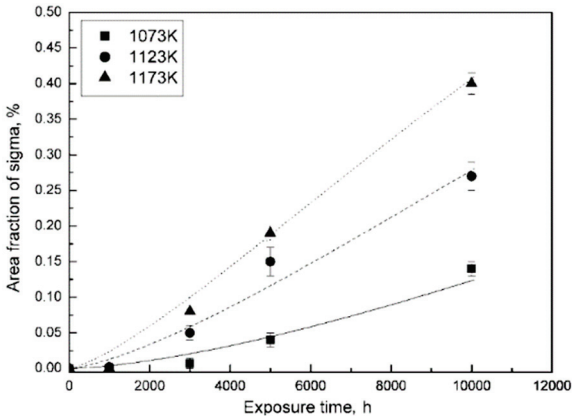

Figure 10. Variations in TCP phase fraction as a function of thermal exposure time in a Re-free Ni-based superalloy [14].

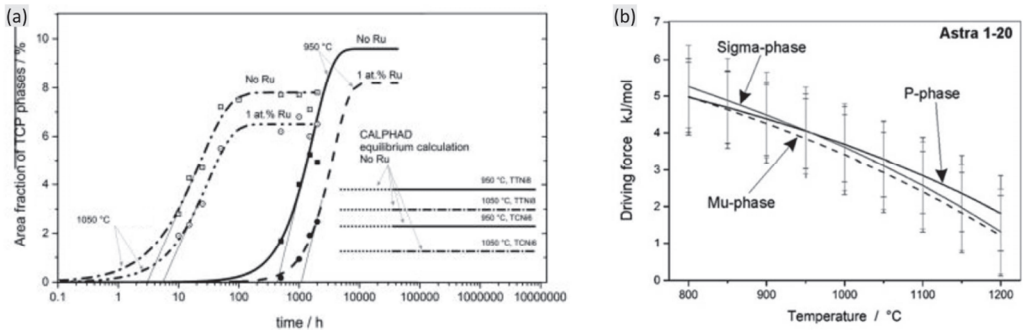

Figure 11. (**a**) Area fraction of TCP phases as a function of time for the alloys Astra 1–20 and Astra 1–21 at 950 °C and 1050 °C [54] and (**b**) the driving force for the precipitation of distinct phases within the alloy Astra 1–20 containing 2 at% Re with varying temperatures [52].

2.4.2. Lattice Misfit and Interfacial Energy

It is widely known that the γ′ phases undergo the coarsening process when subjected to elevated temperature, with the reduction in total interfacial energy as the driving force. Previously, many researchers have been devoted to quantitatively estimating the interfacial energy of the alloys. The most accepted approach is to calculate it from the coarsening rate, with the function provided by LSW theory or the more recent P-V model [41,55]. Another available approach is to calculate it by the interfacial width and interfacial gradient with advanced characterization in Ardell's method [56]. As the significant element in Ni-based

SX superalloy, Re has received much attention in the calculation of the interfacial energy. Zhang et al. [57] summarized the interfacial energy of the alloys with Re addition and without Re, showing the obvious decrease in the interfacial energy induced by Re, as shown in Figure 12. This becomes the primary factor in the stabilized microstructural evolution by the addition of Re.

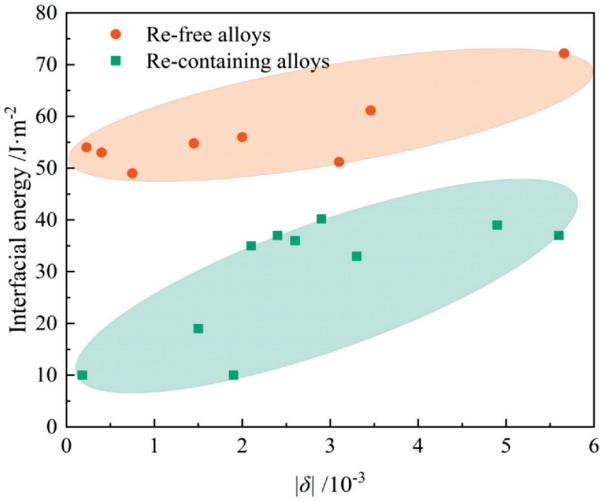

Figure 12. Lattice misfit dependence of interfacial energy in different alloys [57].

Another great concern is the lattice misfit. The alloy should be designed to a compatible composition leading to a reliable lattice misfit for suppressing γ′ coarsening. Although there is still no quantitative relationship between the lattice misfit and the interfacial energy, it can be concluded that interfacial energy may decrease with the decreasing lattice misfit (approach to zero), which has been clarified by a different alloying system [45,58]. Additionally, in Figure 12, there is a supportive tendency of the increasing interfacial energy along with the increasing value of the lattice misfit.

Liang et al. [59] conducted predictions of the interfacial energy induced by temperature using the CALPHAD method. In Figure 13a, the interfacial energy decreases by the increasing driving force, which restrains the driving force for γ′ coarsening, as shown in Figure 13b. Despite the decreasing interfacial energy by the increasing temperature, the elemental diffusion can be simultaneously promoted at higher temperature, which can, on the other hand, boost the coarsening behavior. Thus, the actual real-time coarsening behavior should consider both the interfacial energy and the elemental diffusion.

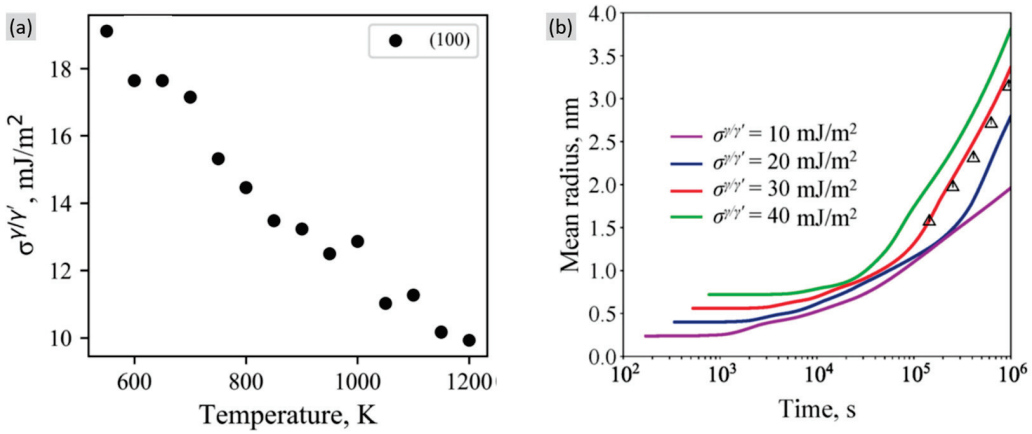

Figure 13. (**a**) Calculated interfacial energy varying with temperature and (**b**) calculated mean radius versus time at 773 K by using different interfacial energy of a Ni-Al binary alloy [59]. (The triangles show the experimental data in this reference.)

2.4.3. Role of the Alloying Elements

The coarsening behavior as well as the TCP formation are all seriously affected by the alloying elements. Zhang et al. [57] summarized the coarsening rate as a function of Re content at various temperatures, as shown in Figure 14. The addition of Re can effectively reduce the γ′ coarsening rate at high temperatures, especially when the Re content increases from 0 to 4 wt.%.

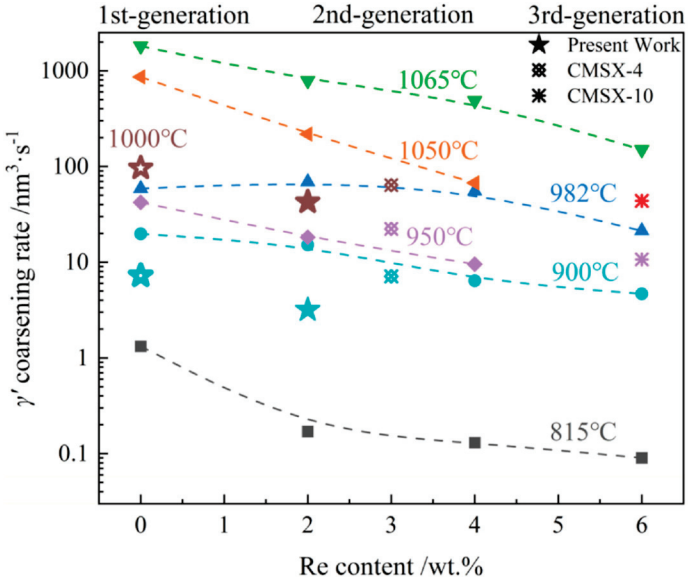

Figure 14. γ′ coarsening rate as a function of Re content at various temperatures [57]. (Different types of symbols indicated the data is extracted from different works.)

The volume fraction of the TCP phase after thermal exposure of different alloys at 1000 °C for 1000 h has been summarized in Figure 15, which presents the effect of alloying elements on the TCP phase formation [60]. The addition of Mo and Re can sharply promote TCP precipitation, and Cr also plays a significant promoted effect. The TCP phase increases slightly by the increased W content. However, the addition of Co can effectively restrain the TCP formation. Interestingly, the commercial Ni-based SX superalloy CMSX-4 is always stable with respect to the TCP precipitate at elevated temperatures, although it has a considerable content of Re, W and Cr. This can be attributed to the lower content of Mo addition [12].

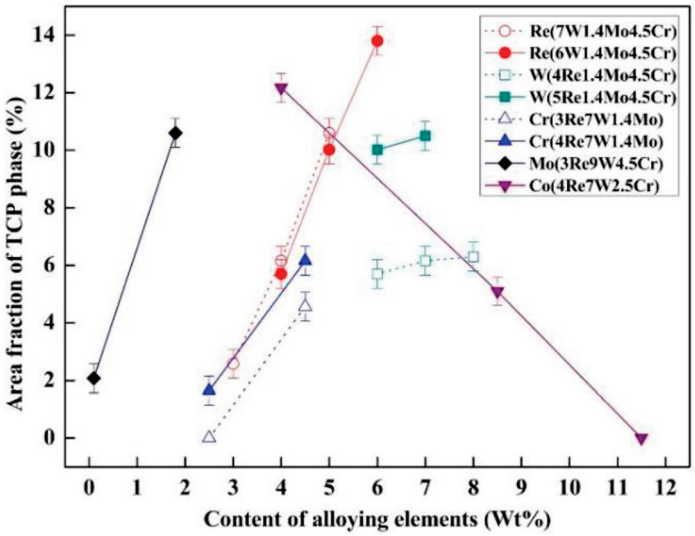

Figure 15. Area fraction of TCP phases of alloys with different alloying elements contents after thermal exposure at 1000 °C for 1000 h [60].

3. Effect of Thermal Exposure on Mechanical Properties

3.1. High-Temperature Tensile Strength and Room-Temperature Hardness

An examination of the related mechanical properties of the unexposed and exposed samples can be a valuable approach to determine the extent of the microstructural degradation. Figure 16a provides the typical strain–stress curves of CMSX-4 alloy after thermal exposure for different times [61]. The yield strength decreases along with the increased time. However, both UTS and the total elongation first increase firstly and then continuously decrease with the increasing time, as shown in Figure 16b. Another concern is the Vickers hardness. It can be seen that a continuous decrease in the Vickers hardness occurs along with the increased thermal exposure time in CMSX-4 alloy, indicating that all studied samples were overaged with respect to expected mechanical property, as shown in Figure 17 [61].

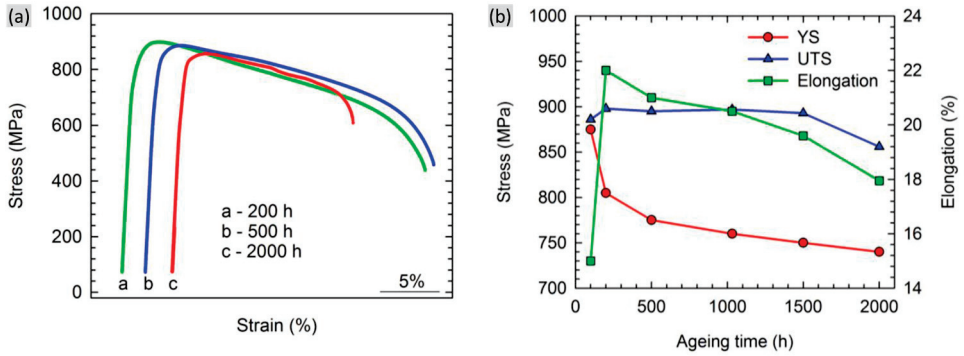

Figure 16. (**a**) Typical strain–stress curves at 950 °C of exposed samples for different time at 950 °C and (**b**) effect of thermal exposure time on 0.2% offset yield strength (YS), ultimate tensile strength (UTS) and plastic elongation to fracture of CMSX-4 alloy [61].

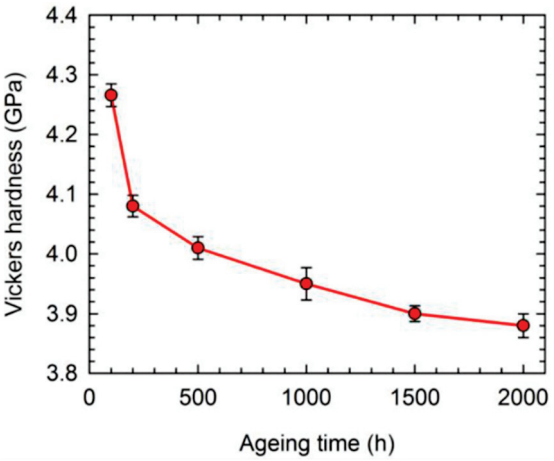

Figure 17. Variation in Vickers hardness with the thermal exposure time [61].

3.2. Creep Property

Since the evolution in volume fraction, size, morphology and distribution of γ' phases as well as the TCP formation induced by thermal exposure mainly contribute to the degradation of creep resistance, another great estimation of the microstructural degradation is the related creep property. Figure 18 shows the creep lifetime of DD6 alloy at 1070 °C/140 MPa after thermal exposure at 980 °C or 1070 °C for different durations [34]. Note that no TCP phases formed in each specimen in this research. The microstructures with the longest thermal exposure time of 1000 h at different temperatures are shown in the corresponding figure, indicating the obvious rafting structure at 1070 °C/1000 h instead of the nearly cuboidal morphology at 980 °C/1000 h. In Figure 18a, obvious decreasing creep life occurs with the extended thermal exposure time until 400 h, which is then followed by the slight

increase in creep life with the prolonged thermal exposure time. This is mainly due to the thermal exposure time (over 400 h) acting as the appropriate heat treatment process for the more proper growth of the γ' phase to obtain the over-estimated property. However, after thermal exposure at 1070 °C for different durations, the related creep life exhibits a continuous decrease due to the serious degradation of γ/γ' phases.

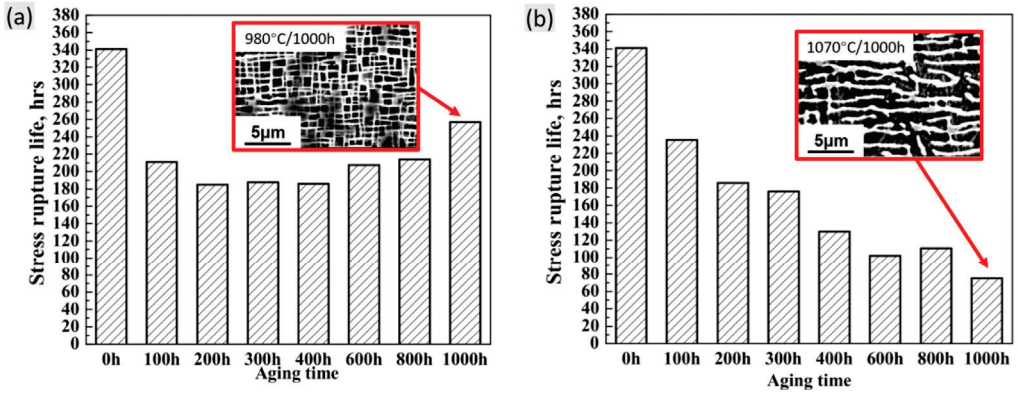

Figure 18. Effects of exposure time on the stress rupture life of DD6 alloy at 1070 °C/140 MPa after long-term exposure at (**a**) 980 °C and (**b**) 1070 °C. The associated microstructures after thermal exposure are also presented [34].

Cheng et al. [62] conducted a series of creep tests on the exposed specimens with TCP phases of CMSX-4 alloy, as shown in Figure 19. Here, more TCP phases formed at 1050 °C/2000 h than that at 950 °C/2000 h. This indicates the decreasing creep properties with increasing thermal exposure temperature or time. Obviously, when conducting thermal exposure at higher temperatures, the creep life exhibits wider separation between the thermal exposure time at 1000 h and 2000 h, which is mainly attributed to the significant increase in the TCP formation at 1050 °C/2000 h.

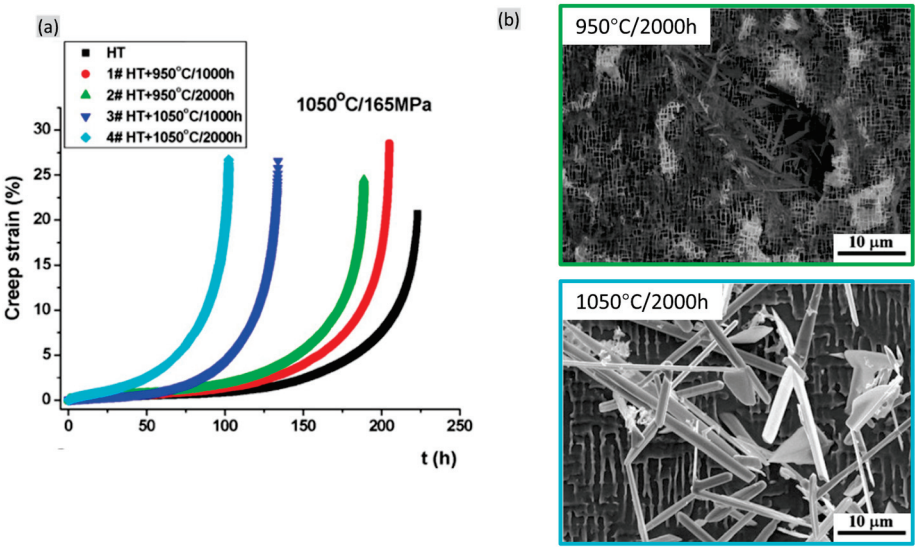

Figure 19. (**a**) Creep properties of specimens at HT state and after thermal exposure at different temperature and time of CMSX-4 alloy and (**b**) the associated microstructures after thermal exposure of 950 °C/1000 h and 1050 °C/1000 h [62].

3.3. Influencing Factors on the Degradation of Mechanical Properties

Since the γ' and γ phases play the leading role in the strengthening effect, which refers to the precipitate strengthening effect and solid solution effect, the γ/γ' degradation should take the primary responsibility for the degradation of mechanical properties. From the

microstructural aspect, the decreasing γ' volume fraction and coarsening γ' average size contribute to the decrease in Vickers hardness and tensile property [61]. Another deleterious factor is the increasing γ channel width during thermal exposure, which provides a decrease in Orowan resistance and leads to the increased dislocation slipping rate in the matrix [27].

The TCP phases are brittle inclusions which are composed of various refractory elements and have higher hardness than γ and γ' phases. Hence, TCP phases are always seen to be greatly harmful for mechanical property. This is mainly due to two aspects: (1) TCP phases deplete the solid solution strengtheners (Re, W, Mo, Cr and Co) from the γ matrix, leading to the impaired solid solution strengthening effect of the alloy. (2) The loss of coherency at the TCP/γ' phases becomes the initiating site of the micro-pores or even cracks. However, some controversies still remain concerning the second point. In Figure 20a, after creep within the exposed samples, the TCP phase showed good coherency with the surrounding γ' phase, remaining free of crack but with only slight twist. In Figure 20b, although some micro-pores or crack initiation were found near the γ' phase, they still did not propagate into macro-cracks [62].

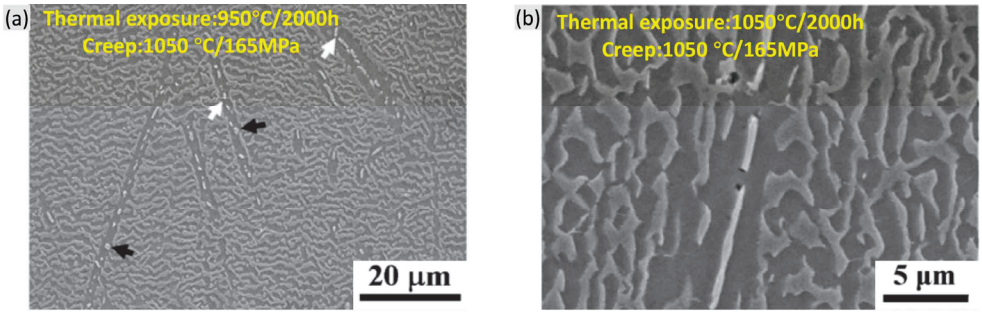

Figure 20. Microstructures in the crept specimens of CMSX-4 alloy after thermal exposure showing (**a**) rotated (white arrow) and coarsened (black arrow) μ particles free of crack and (**b**) crack initiation from the needle-like μ particle but without propagation [62].

Here, when the TCP phases remain in a low volume fraction, they may have no obvious effect on the failure in the creep tests except for depleting the solid solution elements. Sun et al. [63] also found that the deformation pores (D-pores) with small sizes have almost no clear relationship with the TCP phases. Even near the creep fracture, most fatal cracks are produced by initial pores in the interdendritic regions, rather than the TCP phases, as shown in Figure 21.

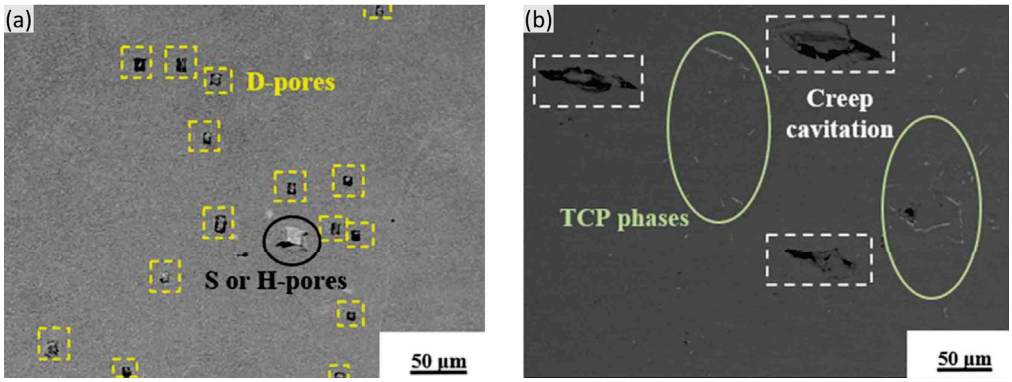

Figure 21. Microstructures in the crept specimen (at 1120 °C/137 MPa) of a Re-containing single crystal superalloy after thermal exposure of 1100 °C/500 h showing (**a**) the distribution of D-pores, and all of them marked by a yellow square dotted line, and (**b**) the crack distribution near the fracture surface, illustrating that the TCP phase does not cause crack directly [63].

However, Zhang et al. [64] demonstrated the microcracks generating and propagating near the TCP phases with a direct angle of approximately 70° between the growth direction of the TCP phase and the microcrack, as shown in Figure 22a. This angle refers to the angle of the slip plane between (111) and (−1–11) as well as the angle of the slip direction between (−1–12) and (112). It is suggested that TCP phases promote the crack initiation at elevated creep temperature. Moreover, in the real tenon of a SX turbine blade, presented in Figure 22b, the macrocrack was propagated with a zigzag morphology, as predicted. The TCP phases, as the obstacles of the dislocation movements leading to the local pile-up of dislocations, also contribute to the crack initiation and propagation near the TCP phases. Although it is widely accepted that the effect of TCP phases on the deteriorated creep property mainly depends on the depleted solid solution elements, the promotion of crack initiation and propagation still cannot be excluded.

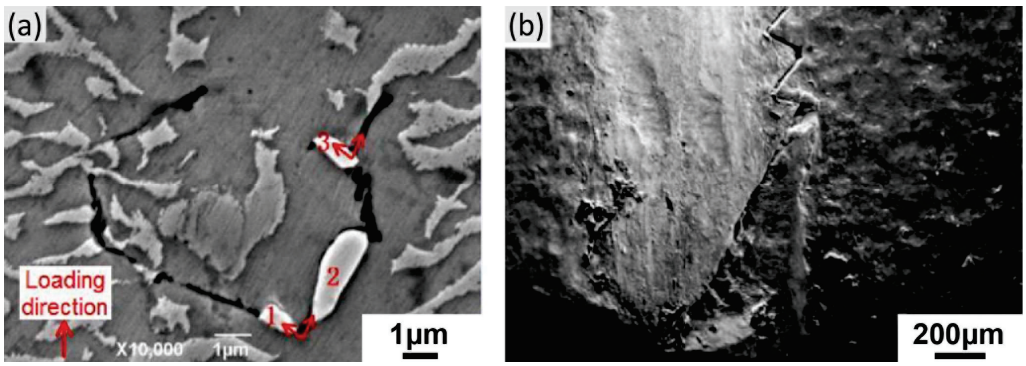

Figure 22. (**a**) The microcrack initiation and propagation near the TCP phase of DD6 alloy after creep at 1100 °C/140 MPa (Numbers 1,2 and 3 mark the TCP phases.) and (**b**) the fracture crack in the tenon of an aero-engine single crystal turbine blade [64].

Ni-based SX superalloys are designed to exclude the effect of a weak grain boundary, and recent research has mainly focused on the microstructural evolution on γ/γ' phases and TCP formation. However, it has been increasingly acknowledged that the γ/γ' phases exhibit a different evolution tendency when suffering thermal exposure; thus, the microstructural evolution in the interdendrite region cannot be ignored [30,65]. Furthermore, the inevitable carbides in the interdendrite region may change and affect the mechanical properties. Huang et al. [32] found that the carbides can affect TCP formation where TCP phases precipitate preferentially within the vicinity of MC carbides. An et al. [66] also found changes in the type of the carbides during creep. The last concern is that the micro-pores formed after heat treatment exhibit growth during the following creep tests [67]. These factors can pose an even more serious effect on the creep property, to which significant attention should be paid in the study of the thermal exposure or creep of the superalloys.

Additionally, the formation of a rafting structure may also play an enhanced role in the mechanical properties. It has been recognized that the plate-like rafting structure can provide a longer distance for dislocations to climb, so as to impede the dislocation movements and enhanced creep property. During creep at high temperatures, the formation of a N-type rafting structure has always appeared at the minimum creep rate after the decreasing creep rate stage [68]. Although M.V. Nathal et al. [69] found that the pre-rafted structure would cause damage to the creep property, U. Tetzlaff et al. [70] conversely found that when achieving the P-type pre-rafted structure in compression, the iso-thermal fatigue strength and tensile creep property would be further enhanced. The enhanced ability depended on the applied stress, which determines the time available for the formation of the rafting structure introduced by the prior compressive creep strain.

Ni-based SX superalloys are still the materials of choice for the components serving at elevated temperatures and under load, where several modern Ni-based SX superalloys are usually considered, such as CMSX-4, René N5, DD6, et al. These alloys always contain a

certain content of Re to improve the mechanical properties at high temperature. Thus far, the manufacturing technology of the SX superalloys has gradually matured and advanced, and many researchers have worked on these types of alloys and achieved lots of data, ensuring the safety of these alloys in real service. It can be deduced that the Ni-based SX superalloys will still be the primary choice in aero-engine blades, although the alloying design should be further optimized.

In summation, the γ/γ' microstructural degradation and the formation of TCP phases are the primary aspects in influencing the microstructural stability of the Ni-based superalloys. Since the γ/γ' microstructural degradation is driven by the interfacial energy, lower interfacial energy should be considered in optimizing the alloying design or, more directly, the lower lattice misfit approaching to zero. Another concern is the alloying additions, where a lower content of refractory elements induces lower driving force for the formation of TCP phases. Additionally, a lower content of refractory elements can also promote lower lattice misfit of the alloy. Generally, limiting the content of refractory elements is necessary to balance the microstructural stability and the mechanical properties of Ni-based SX superalloys.

4. Conclusions

In order to estimate the deterioration of microstructure in service, stress-free thermal exposure tests have become the most widely used approach in Ni-based single crystal (SX) superalloys. During high-temperature thermal exposure, γ/γ' phases exhibit obvious degradation, displaying, as the γ' volume fraction decreases, increasing γ' sizes and a broadening γ matrix. A higher γ' volume fraction can promote serious microstructural evolution, such as directional rafting and topological inversion. The growth in γ' sizes driven by interfacial energy follows the traditional LSW theory as well as the newly developed TIDC theory, where the coarsening process is controlled by matrix-diffusion, at first followed by interfacial-diffusion at longer times. Due to the addition of refractory elements, the TCP phases may precipitate basically from dendrite cores in a variety of types, such as σ-, μ-, P- or R-phase. They usually contain a large number of γ-stabilizers such as Re, W, Mo, Cr and Co, and they can be distinguished by different morphologies and structures. The temperature, time, interfacial energy (and the associated lattice misfit) and alloying elements can pose different effects on the microstructural degradation during thermal exposure.

Microstructural degradation can lead to damage of the related mechanical properties, including tensile property, Vickers hardness and creep property. This is mainly due to the deteriorated precipitate strengthening and solid solution strengthening effect induced by the decreasing γ' volume fraction, coarsening γ' average size as well as the broadening γ channel. The formation of TCP phases can also result in a decrease in mechanical property along with the depleted solid solution elements, while the promotion of crack initiation and propagation still cannot be ignored. Further, the γ/γ' microstructural evolution in the interdendrite region, the evolution of carbides and the formation and growth of micropores should also be carefully considered in the investigations of thermal exposure.

On this basis, in order to achieve better microstructural stability and the related mechanical properties of Ni-based SX superalloys, lower interfacial energy (as well as the lattice misfit approaching to zero) and a lower content of refractory elements should be considered for optimizing the alloying design.

Author Contributions: Conceptualization, review and editing, J.Z.; review and investigation, L.L. and F.L. All authors have read and agreed to the published version of the manuscript.

Funding: This review was funded by the National Science and Technology Major Project (Grant No.: J2019-VI-0010-0124) and National Natural Science Foundation of China (Grant No.: 91860201).

Institutional Review Board Statement: Not applicable.

Informed Consent Statement: Not applicable.

Data Availability Statement: Not applicable.

Conflicts of Interest: The authors declare no conflict of interest.

References

1. Reed, R.C. *The Superalloys: Fundamentals and Applications*; Cambridge University Press: Cambridge, UK, 2006.
2. Sharghi-Moshtaghin, R.; Asgari, S. The Influence of Thermal Exposure on the Γ′ Precipitates Characteristics and Tensile Behavior of Superalloy IN-738LC. *J. Mater. Process. Technol.* **2004**, *147*, 343–350. [CrossRef]
3. Liu, J.L.; Jin, T.; Yu, J.J.; Sun, X.F.; Guan, H.R.; Hu, Z.Q. Effect of Thermal Exposure on Stress Rupture Properties of a Re Bearing Ni Base Single Crystal Superalloy. *Mater. Sci. Eng. A* **2010**, *527*, 890–897. [CrossRef]
4. Antonov, S. Synchrotron In-Situ Aging Study and Correlations to the Γ′ Phase Instabilities in a High-Refractory Content γ-Γ′ Ni-Base Superalloy. *Metall. Mater. Trans. A* **2018**, *49*, 3885–3895. [CrossRef]
5. Pollock, T.M.; Tin, S. Nickel-Based Superalloys for Advanced Turbine Engines: Chemistry, Microstructure and Properties. *J. Propuls. Power* **2006**, *22*, 361–374. [CrossRef]
6. Horst, O.M.; Adler, D.; Git, P.; Wang, H.; Streitberger, J.; Holtkamp, M.; Jöns, N.; Singer, R.F.; Körner, C.; Eggeler, G. Exploring the Fundamentals of Ni-Based Superalloy Single Crystal (SX) Alloy Design: Chemical Composition vs. Microstructure. *Mater. Des.* **2020**, *195*, 108976. [CrossRef]
7. Murakumo, T.; Kobayashi, T.; Koizumi, Y.; Harada, H. Creep Behaviour of Ni-Base Single-Crystal Superalloys with Various Γ′ Volume Fraction. *Acta Mater.* **2004**, *52*, 3737–3744. [CrossRef]
8. Nathal, M.V. Effect of Initial Gamma Prime Size on the Elevated Temperature Creep Properties of Single Crystal Nickel Base Superalloys. *Metall. Trans. A* **1987**, *18*, 1961–1970. [CrossRef]
9. Ardell, A.J. Effect of Volume Fraction on Particle Coarsening—Theoretical Considerations. *Acta Metall.* **1972**, *20*, 61–71. [CrossRef]
10. Davies, C.K.L.; Nash, P.; Stevens, R.N. The Effect of Volume Fraction of Precipitate on Ostwald Ripening. *Acta Metall.* **1980**, *28*, 179–189. [CrossRef]
11. Long, H.; Mao, S.; Liu, Y.; Zhang, Z.; Han, X. Microstructural and Compositional Design of Ni-Based Single Crystalline Superalloys—A Review. *J. Alloys Compd.* **2018**, *743*, 203–220. [CrossRef]
12. Yu, H.; Xu, W.; van der Zwaag, S. The Compositional Dependence of the Microstructure and Properties of CMSX-4 Superalloys. *Metall. Mater. Trans. A* **2018**, *49*, 406–416. [CrossRef]
13. Reed, R.C.; Tao, T.; Warnken, N. Alloys-By-Design: Application to Nickel-Based Single Crystal Superalloys. *Acta Mater.* **2009**, *57*, 5898–5913. [CrossRef]
14. Hou, J.S.; Guo, J.T. Influence of Thermal Exposure on the Microstructures and Mechanical Properties of a Superalloy. *J. Mater. Eng. Perform.* **2006**, *15*, 67–75. [CrossRef]
15. Kang, M.; Sridar, S.; Xiong, W.; Wang, J.; Yu, J.; Sun, B. Influence of Long-Term Aging on Microstructural Stability and Performance of DD6 Superalloy. *Mater. Sci. Technol.* **2021**, *37*, 607–615. [CrossRef]
16. Tan, Z.; Yang, L.; Wang, X.; Du, Y.; Ye, L.; Hou, G.; Yang, Y.; Liu, J.; Liu, J.; Li, J.; et al. Evolution of TCP Phase During Long Term Thermal Exposure in Several Re-Containing Single Crystal Superalloys. *Acta Metall. Sin. Engl. Lett.* **2020**, *33*, 731–740. [CrossRef]
17. Cheng, K.; Jo, C.; Kim, D.; Jin, T.; Hu, Z. Unexpected Precipitation of a Re-Rich Phase in Single Crystal Superalloy CMSX-4 during Thermal Exposure. *J. Metall.* **2012**, *2012*, 308568. [CrossRef]
18. Lopez-Galilea, I.; Koßmann, J.; Kostka, A.; Drautz, R.; Mujica Roncery, L.; Hammerschmidt, T.; Huth, S.; Theisen, W. The Thermal Stability of Topologically Close-Packed Phases in the Single-Crystal Ni-Base Superalloy ERBO/1. *J. Mater. Sci.* **2016**, *51*, 2653–2664. [CrossRef]
19. Wilson, A.S. Formation and Effect of Topologically Close-Packed Phases in Nickel-Base Superalloys. *Mater. Sci. Technol.* **2017**, *33*, 1108–1118. [CrossRef]
20. Shi, Z.; Li, J.; Liu, S. Effect of Long Term Aging on Microstructure and Stress Rupture Properties of a Nickel Based Single Crystal Superalloy. *Prog. Nat. Sci. Mater. Int.* **2012**, *22*, 426–432. [CrossRef]
21. Zrnik, J.; Strunz, P.; Vrchovinsky, V.; Muransky, O.; Novy, Z.; Wiedenmann, A. Degradation of Creep Properties in a Long-Term Thermally Exposed Nickel Base Superalloy. *Mater. Sci. Eng. A* **2004**, *387–389*, 728–733. [CrossRef]
22. Kuehmann, C.J.; Voorhees, P.W. Ostwald Ripening in Ternary Alloys. *Metall. Mater. Trans. A* **1996**, *27*, 937–943. [CrossRef]
23. Lifshitz, I.M.; Slyozov, V.V. The Kinetics of Precipitation from Supersaturated Solid Solutions. *J. Phys. Chem. Solids* **1961**, *19*, 35–50. [CrossRef]
24. Baldan, A. Review Progress in Ostwald Ripening Theories and Their Applications to Nickel-Base Superalloys. *J. Mater. Sci.* **2002**, *37*, 2171–2202. [CrossRef]
25. Lapin, J.; Gebura, M.; Pelachová, T.; Nazmy, M. Coarsening Kinetics of Cuboidal γ′ Precipitates in Single Crystal Nickel Base Superalloy CMSX-4. *Kov. Mater* **2008**, *46*, 313–322.
26. Wagner, C. Theorie der Alterung von Niederschlägen durch Umlösen (Ostwald-Reifung). *Z. Für Elektrochem. Berichte Bunsenges. Für Phys. Chem.* **1961**, *65*, 581–591. [CrossRef]
27. Liu, C.; Zhao, Y.; Zhang, J.; Tang, D.; Li, C.; Zhao, Z. Influence of Thermal Exposure on Microstructure and Stress Rupture Properties of a New Re-Containing Single Crystal Ni-Based Superalloy. *China Foundry* **2018**, *15*, 51–57. [CrossRef]
28. Chellman, D.J.; Ardell, A.J. The Coarsening of γ′ Precipitates at Large Volume Fractions. *Acta Metall.* **1974**, *22*, 577–588. [CrossRef]

29. Cheng, K.Y.; Jo, C.Y.; Kim, D.H.; Jin, T.; Hu, Z.Q. Influence of Local Chemical Segregation on the Γ′ Directional Coarsening Behavior in Single Crystal Superalloy CMSX-4. *Mater. Charact.* **2009**, *60*, 210–218. [CrossRef]
30. Milhet, X.; Arnoux, M.; Cormier, J.; Mendez, J.; Tromas, C. On the Influence of the Dendritic Structure on the Creep Behavior of a Re-Containing Superalloy at High Temperature/Low Stress. *Mater. Sci. Eng. A* **2012**, *546*, 139–145. [CrossRef]
31. Matan, N.; Cox, D.C.; Rae, C.M.F.; Reed, R.C. On the Kinetics of Rafting in CMSX-4 Superalloy Single Crystals. *Acta Mater.* **1999**, *47*, 2031–2045. [CrossRef]
32. Huang, M.; Yang, X.; Liu, W.; Li, J.; Yang, S.; Qin, Y. Precipitation Characteristics of a Nickel-Based Single-Crystal Superalloy after Long-Term Thermal Exposure. *Int. J. Mater. Res.* **2018**, *109*, 811–818. [CrossRef]
33. Liu, L.R.; Jin, T.; Zhao, N.R.; Wang, Z.H.; Sun, X.F.; Guan, H.R.; Hu, Z.Q. Microstructural Evolution of a Single Crystal Nickel-Base Superalloy during Thermal Exposure. *Mater. Lett.* **2003**, *57*, 4540–4546. [CrossRef]
34. Jin, H.P.; Li, J.R.; Liu, S.Z. Stress Rupture Properties of the Second Generation Single Crystal Superalloy DD6 after High Temperature Exposure. *Mater. Sci. Forum* **2007**, *546–549*, 1249–1252. [CrossRef]
35. Epishin, A.; Link, T.; Ckner, U.B.; Portella, P.D. Kinetics of the Topological Inversion of the γ/Γ′-Microstructure during Creep of a Nickel-Based Superalloy. *Acta Mater.* **2001**, *49*, 4017–4023. [CrossRef]
36. Goerler, J.V.; Lopez-Galilea, I.; Mujica Roncery, L.; Shchyglo, O.; Theisen, W.; Steinbach, I. Topological Phase Inversion after Long-Term Thermal Exposure of Nickel-Base Superalloys: Experiment and Phase-Field Simulation. *Acta Mater.* **2017**, *124*, 151–158. [CrossRef]
37. Fuchs, G.E. Solution Heat Treatment Response of a Third Generation Single Crystal Ni-Base Superalloy. *Mater. Sci. Eng. A* **2001**, *300*, 52–60. [CrossRef]
38. Masoumi, F.; Jahazi, M.; Shahriari, D.; Cormier, J. Coarsening and Dissolution of Γ′ Precipitates during Solution Treatment of AD730^{TM} Ni-Based Superalloy: Mechanisms and Kinetics Models. *J. Alloys Compd.* **2016**, *658*, 981–995. [CrossRef]
39. Davies, C.K.L.; Nash, P.; Stevens, N. Precipitation in Ni-Co-Al Alloys. *J. Mater. Sci.* **1980**, *15*, 1521–1532. [CrossRef]
40. Brailsford, A.D.; Wynblatt, P. The Dependence of Ostwald Ripening Kinetics on Particle Volume Fraction. *Acta Metall.* **1979**, *27*, 489–497. [CrossRef]
41. Philippe, T.; Voorhees, P.W. Ostwald Ripening in Multicomponent Alloys. *Acta Mater.* **2013**, *61*, 4237–4244. [CrossRef]
42. Ardell, A.J.; Ozolins, V. Trans-Interface Diffusion-Controlled Coarsening. *Nat. Mater.* **2005**, *4*, 309–316. [CrossRef]
43. Tiley, J.; Viswanathan, G.B.; Srinivasan, R.; Banerjee, R.; Dimiduk, D.M.; Fraser, H.L. Coarsening Kinetics of Γ′ Precipitates in the Commercial Nickel Base Superalloy René 88 DT. *Acta Mater.* **2009**, *57*, 2538–2549. [CrossRef]
44. Zhang, J.; Liu, L.; Huang, T.; Chen, J.; Cao, K.; Liu, X.; Zhang, J.; Fu, H. Coarsening Kinetics of Γ′ Precipitates in a Re-Containing Ni-Based Single Crystal Superalloy during Long-Term Aging. *J. Mater. Sci. Technol.* **2021**, *62*, 1–10. [CrossRef]
45. Lu, F.; Antonov, S.; Lu, S.; Zhang, J.; Li, L.; Wang, D.; Zhang, J.; Feng, Q. Unveiling the Re Effect on Long-Term Coarsening Behaviors of Γ′ Precipitates in Ni-Based Single Crystal Superalloys. *Acta Mater.* **2022**, *233*, 117979. [CrossRef]
46. Sun, W. Kinetics for Coarsening Co-Controlled by Diffusion and a Reversible Interface Reaction. *Acta Mater.* **2007**, *55*, 313–320. [CrossRef]
47. Huo, J.; Shi, Q.; Zheng, Y.; Feng, Q. Microstructural Characteristics of σ Phase and P Phase in Ru-Containing Single Crystal Superalloys. *Mater. Charact.* **2017**, *124*, 73–82. [CrossRef]
48. Huo, J.J.; Shi, Q.Y.; Zheng, Y.R.; Feng, Q. Microstructural Nature and Stability of Co-Rich TCP Phases in Ru-Containing Single Crystal Superalloys. *J. Alloys Compd.* **2017**, *715*, 460–470. [CrossRef]
49. Rae, C.M.F.; Reed, R.C. The Precipitation of Topologically Close-Packed Phases in Rhenium-Containing Superalloys. *Acta Mater.* **2001**, *49*, 4113–4125. [CrossRef]
50. Peng, Z.; Povstugar, I.; Matuszewski, K.; Rettig, R.; Singer, R.; Kostka, A.; Choi, P.-P.; Raabe, D. Effects of Ru on Elemental Partitioning and Precipitation of Topologically Close-Packed Phases in Ni-Based Superalloys. *Scr. Mater.* **2015**, *101*, 44–47. [CrossRef]
51. Pistor, J.; Körner, C. Formation of Topologically Closed Packed Phases within CMSX-4 Single Crystals Produced by Additive Manufacturing. *Mater. Lett. X* **2019**, *1*, 100003. [CrossRef]
52. Matuszewski, K.; Müller, A.; Ritter, N.; Rettig, R.; Kurzydłowski, K.J.; Singer, R.F. On the Thermodynamics and Kinetics of TCP Phase Precipitation in Re- and Ru- Containing Ni-Base Superalloys: On the Thermodynamics and Kinetics of TCP Phase. *Adv. Eng. Mater.* **2015**, *17*, 1127–1133. [CrossRef]
53. Lapin, J.; Gebura, M.; Pelachová, T.; Bajana, O. *Microstructure Degradation of Nickel Base Single Crystal Superalloy CMSX-4*; TANGER Ltd.: Hradec nad Moravicí, Czech Republic, 2009; pp. 304–310.
54. Matuszewski, K.; Rettig, R.; Matysiak, H.; Peng, Z.; Povstugar, I.; Choi, P.; Müller, J.; Raabe, D.; Spiecker, E.; Kurzydłowski, K.J.; et al. Effect of Ruthenium on the Precipitation of Topologically Close Packed Phases in Ni-Based Superalloys of 3rd and 4th Generation. *Acta Mater.* **2015**, *95*, 274–283. [CrossRef]
55. Calderon, H.A.; Voorhees, P.W.; Murray, J.L.; Kostorz, G. Ostwald Ripening in Concentrated Alloys. *Acta Metall. Mater.* **1994**, *42*, 991–1000. [CrossRef]
56. Ardell, A.J. Gradient Energy, Interfacial Energy and Interface Width. *Scr. Mater.* **2012**, *66*, 423–426. [CrossRef]
57. Zhang, J.; Huang, T.; Lu, F.; Cao, K.; Wang, D.; Zhang, J.; Zhang, J.; Su, H.; Liu, L. The Effect of Rhenium on the Microstructure Stability and γ/Γ′ Interfacial Characteristics of Ni-Based Single Crystal Superalloys during Long-Term Aging. *J. Alloys Compd.* **2021**, *876*, 160114. [CrossRef]

58. Zhuang, X.; Antonov, S.; Li, L.; Feng, Q. Effect of Alloying Elements on the Coarsening Rate of Γ′ Precipitates in Multi-Component CoNi-Based Superalloys with High Cr Content. *Scr. Mater.* **2021**, *202*, 114004. [CrossRef]
59. Liang, S.X.; Liu, K.Y.; Zhou, Y.X.; Yin, L.X.; Shi, Y.D.; Zheng, L.Y.; Xing, Z.G. Interfacial Energy between γ/γ' Phases of Ni–Al Alloys Extracted by Using a New Method. *Mater. Chem. Phys.* **2022**, *277*, 125538. [CrossRef]
60. Wang, B.; Zhang, J.; Huang, T.; Su, H.; Li, Z.; Liu, L.; Fu, H. Influence of W, Re, Cr, and Mo on Microstructural Stability of the Third Generation Ni-Based Single Crystal Superalloys. *J. Mater. Res.* **2016**, *31*, 3381–3389. [CrossRef]
61. Lapin, J.; Pelachová, T.; Bajana, O. *The Effect of Microstructure on Mechanical Properties of Single Crystal CMSX-4 Superalloy*; TANGER Ltd.: Brno, Czech Republic, 2013; pp. 922–926.
62. Cheng, K.; Jo, C.; Jin, T.; Hu, Z. Precipitation Behavior of μ Phase and Creep Rupture in Single Crystal Superalloy CMSX-4. *J. Alloys Compd.* **2011**, *509*, 7078–7086. [CrossRef]
63. Sun, J.; Liu, J.; Li, J.; Wang, X.; Liu, J.; Yang, Y.; Zhou, Y.; Sun, X. Microstructural Degradation after Thermal Exposure of a Re-Containing Single Crystal Superalloy. *Mater. Charact.* **2021**, *178*, 111279. [CrossRef]
64. Zhang, Z.; Yue, Z. TCP Phases Growth and Crack Initiation and Propagation in Nickel-Based Single Crystal Superalloys Containing Re. *J. Alloys Compd.* **2018**, *746*, 84–92. [CrossRef]
65. Xia, W.; Zhao, X.; Yue, L.; Yue, Q.; Wang, J.; Ding, Q.; Bei, H.; Zhang, Z. Inconsistent Creep between Dendrite Core and Interdendritic Region under Different Degrees of Elemental Inhomogeneity in Nickel-Based Single Crystal Superalloys. *J. Mater. Sci. Technol.* **2021**, *92*, 88–97. [CrossRef]
66. An, W.; Utada, S.; Guo, X.; Antonov, S.; Zheng, W.; Cormier, J.; Feng, Q. Thermal Cycling Creep Properties of a Directionally Solidified Superalloy DZ125. *J. Mater. Sci. Technol.* **2022**, *104*, 269–284. [CrossRef]
67. He, S.; Zhao, Y.; Lu, F.; Zhang, J.; Li, L.; Feng, Q. Effects of Hot Isostatic Pressure on Microdefects and Stress Rupture Life of Second-Generation Nickel-Based Single Crystal Superalloy in As-Cast and As-Solid-Solution States. *Acta Metall. Sin.* **2020**, *56*, 1195–1205.
68. Tan, X.P.; Liu, J.L.; Jin, T.; Hu, Z.Q.; Hong, H.U.; Choi, B.G.; Kim, I.S.; Jo, C.Y. Effect of Ruthenium on High-Temperature Creep Rupture Life of a Single Crystal Nickel-Based Superalloy. *Mater. Sci. Eng. A* **2011**, *528*, 8381–8388. [CrossRef]
69. Nathal, M.V.; MacKAY, R.A.; Miner, R.V. Influence of Precipitate Morphology on Intermediate Temperature Creep Properties of a Nickel-Base Superalloy Single Crystal. *Metall. Trans. A* **1989**, *20*, 133–141. [CrossRef]
70. Tetzlaff, U.; Mughrabi, H. Enhancement of the high-temperature tensile creep strength of monocrystalline nickel-base superalloys by pre-rafting in compression. In Proceedings of the Superalloys 2000, 9th International Symposium, TMS, Seven Springs, PA, USA, 17–21 September 2000; pp. 273–282.

materials

MDPI

Review

Research Progress on Multi-Component Alloying and Heat Treatment of High Strength and Toughness Al–Si–Cu–Mg Cast Aluminum Alloys

Mingshan Zhang [1], Yaqiang Tian [1], Xiaoping Zheng [1], Yuan Zhang [1], Liansheng Chen [1] and Junsheng Wang [2,3,*]

[1] Key Laboratory of the Ministry of Education for Modern Metallurgy Technology, North China University of Science and Technology, Tangshan 063210, China
[2] School of Materials Science and Engineering, Beijing Institute of Technology, Beijing 100081, China
[3] Advanced Research Institute of Multidisciplinary Science, Beijing Institute of Technology, Beijing 100081, China
* Correspondence: junsheng.wang@bit.edu.cn

Abstract: Al–Si–Cu–Mg cast aluminum alloys have important applications in automobile lightweight due to their advantages such as high strength-to-weight ratio, good heat resistance and excellent casting performance. With the increasing demand for strength and toughness of automotive parts, the development of high strength and toughness Al–Si–Cu–Mg cast aluminum alloys is one of the effective measures to promote the application of cast aluminum alloys in the automotive industry. In this paper, the research progress of improving the strength and toughness of Al–Si–Cu–Mg cast aluminum alloys was described from the aspects of multi-component alloying and heat treatment based on the strengthening mechanism of Al–Si–Cu–Mg cast aluminum alloys. Finally, the development prospects of automotive lightweight Al–Si–Cu–Mg cast aluminum alloys is presented.

Keywords: Al–Si–Cu–Mg cast aluminum alloys; multi-component alloying; heat treatment; microstructural regulation; mechanical property

Citation: Zhang, M.; Tian, Y.; Zheng, X.; Zhang, Y.; Chen, L.; Wang, J. Research Progress on Multi-Component Alloying and Heat Treatment of High Strength and Toughness Al–Si–Cu–Mg Cast Aluminum Alloys. *Materials* **2023**, *16*, 1065. https://doi.org/10.3390/ma16031065

Academic Editor: Joan-Josep Suñol

Received: 9 December 2022
Revised: 19 January 2023
Accepted: 22 January 2023
Published: 25 January 2023

1. Introduction

With the increasingly serious problems of environmental pollution and energy crisis, the automotive industry is developing in an environmentally friendly direction. Relevant data shows that for every 10% weight reduction of automobiles, fuel consumption is reduced by 8%, and exhaust emissions are reduced by 4% [1]. Therefore, automobile lightweighting is the most economical way to reduce energy consumption and mitigate environmental damage [2,3]. In recent years, automotive lightweight materials have been fiercely competitive, and aluminum alloys have been the first choice for automotive lightweight materials due to a series of advantages such as low cost, high specific strength, and good corrosion resistance [4,5].

Among automotive aluminum alloys, cast aluminum alloys are widely used in automotive parts due to their good casting moldability and economy [6]. Cast aluminum alloys usually include Al–Si, Al–Mg, Al–Cu, and Al–Zn alloys. Al–Si cast aluminum alloys have the advantages of good fluidity, wear resistance, high mechanical strength, and high yield, therefore, they are widely used in automobile components. Moreover, Al–Si–Cu–Mg cast aluminum alloys are widely used in cylinder heads and engine blocks due to their high strength-to-weight ratio, good thermal stability and castability [7,8]. At the same time, with the increase of the demand for product performance in the automotive industry, the performance of Al–Si–Cu–Mg cast aluminum alloys have been put forward higher requirements for automotive parts. The development of high-strength Al–Si–Cu–Mg cast aluminum alloy to meet the room temperature and high temperature performance requirements of automotive parts can further promote the application of cast aluminum alloys in automobiles.

In order to realize the development of high-strength Al–Si–Cu–Mg cast aluminum alloy, researchers have been committed to the research of alloy composition, microstructure and mechanical properties. Studies show that the mechanical properties and fracture behavior of cast aluminum alloy mainly depend on the microstructure characteristics of different scales, and alloy elements and heat treatment play an important role in the microstructure evolution and mechanical properties regulation [9,10]. Cao et al. [11] found that the addition of the microalloying element Cd not only promoted the precipitation of θ′-Al_2Cu phase, but also refined the size of θ′-Al_2Cu phase. Zhang et al. [12] found that the Sc element can refine grain and change the morphology of eutectic Si, and form a new nano-precipitated phase to provide an additional fine grain strengthening and precipitation strengthening effect. Wang et al. [13] obtained a mixture of β″-Mg_5Si_6, θ′-Al_2Cu and Q′-$Al_5Cu_2Mg_8Si_6$ nanoprecipitated phases by adjusting artificial aging parameters, resulting in excellent mechanical properties of Al–Si–Cu–Mg alloy. Fang et al. [14] optimized the two-stage solution treatments of Al–Si–Cu–Mg alloy to obtain a high and uniform solute concentration without overburning of the Cu-containing phase, thus improving the solution strengthening. However, although the research on multi-component alloying and heat treatment of Al–Si–Cu–Mg cast alloy has been extensively studied, there is still little comprehensive and exhaustive research on it based on the strengthening mechanism of casting alloy, which is not conducive to the development and application of high strength and toughness Al–Si–Cu–Mg cast aluminum alloys.

Therefore, this article mainly introduces the microstructure regulation of Al–Si–Cu–Mg cast aluminum alloys by the optimization of multi-component alloying and heat treatment, and describes the research progress in improving its strength and toughness based on the strengthening mechanism of Al–Si–Cu–Mg cast aluminum alloys. It provides theoretical guidance for high strength and toughness Al–Si–Cu–Mg cast aluminum alloys for automobile.

2. Strengthening Mechanism

The strength of the alloy materials is related to the ability to resist the deformation of the material. However, the deformation of the alloy materials is mainly related to the movement of the dislocation. Therefore, the methods that can improve the resistance to the movement of the dislocation can increase the strength of the material. At present, the main strengthening mechanisms for cast aluminum alloys include solid solution strengthening, fine grain strengthening, and second phase strengthening.

2.1. Solid Solution Strengthening

Solid solution strengthening refers to the alloy elements dissolve in the aluminum matrix, causing the alloy element to elastically and electrochemically interact with the dislocation, forming lattice distortions, thereby hindering the movement of the dislocation and improving the strength of the alloy material. The strength of the alloy is mainly related to the concentration of solute atoms in the matrix and the radius difference with the matrix atoms. The yield strength and solute atom concentration of the alloy can be expressed by the theoretical Equation (1): the greater the number of solute atoms, the more obvious the strengthening effect of the alloy. In addition, the larger the radius difference between the solute atoms and the matrix atoms, the greater the degree of lattice distortion caused, and the better the solid solution strengthening effect.

$$\sigma = \sigma_0 + k\mathrm{C}^m \quad (1)$$

where: σ—Yield strength;
σ_0—Yield strength of pure metal;
C—Solute atomic concentration;
k, m—Constants related to solute atom type.

2.2. Fine Grain Strengthening

Fine grain strengthening is one of the important strengthening mechanisms of cast aluminum alloys. The smaller the grain size of the alloy material, the more the grain boundaries, which effectively hinder the movement of dislocations and improve the strength of the alloy. The relationship between the fine grain strengthening and the yield strength of the alloy material conforms to the Hall–Petch theoretical formula, As shown in Equation (2) [15]. It can be known from the formula that the yield strength of alloy materials increases with decreasing grain size at room temperature. The refinement of the cast aluminum alloy structure is mainly the refinement of α-Al dendrites. By refining the dendrites, the dendrite arm spacing is reduced and the alloy strength is improved.

$$\sigma_s = \sigma_i + k \cdot d^{-1/2} \tag{2}$$

where: σ_s—Yield strength;
σ_i—material constant for the starting stress for dislocation movement;
k—Constant;
d—Average grain diameter.

2.3. Second Phase Strengthening

The strengthening effect of the second phase is derived from the ability of the second phase to hinder the motion of dislocations. The strength is determined by the size and distribution of the precipitates and the coherence of the precipitates with the matrix [16]. The interaction between dislocations and the second phase can be described by shear and bypass mechanisms. Figure 1 is the relationship between dislocations and precipitated phases [17–19]. The small and not too hard precipitated phases are sheared when they encounter dislocation movement (the shear mechanism is also called the Friedel mechanism), as shown in Figure 1a. When the size of the precipitate is larger and harder, the dislocation bypasses the precipitate by bending (bypasses mechanism), as shown in Figure 1b. As long as the precipitates are sheared by dislocations, the strength of the alloy will increase. With the further growth of the precipitated phase, the shearing process becomes quite difficult. Dislocations are more conducive to bypassing the precipitates, resulting in the reduction of alloy strength. As shown in Figure 1c, the highest strength is obtained when the dislocations pass through the precipitate with shear and bypassing with equal probability. Generally, the bypass mechanism includes two mechanisms, one is Orowan shear loops, and the other is Hirsch prismatic loops [20]. Dislocation with any character angle will form dislocation shear loops around the precipitate after bypassing the precipitate, resulting in Orowan strain hardening. If all dislocations are edge-oriented, when bypassing the precipitate, a prismatic loop will form on either side of the precipitate when bypassed, which is called Hirsch looping. In addition, it has been shown that two dislocations can form a dislocation dipole, which plays an important role in the plastic deformation of materials, especially fatigue and creep [21].

The strengthening effect of different strengthening mechanisms depends on different factors, solid solution strengthening mainly depends on the supersaturation of solid solution atoms in aluminum matrix, fine grain strengthening mainly depends on the degree of grain and phase refinement, and the second phase strengthening mainly depends on the type, size and distribution of the second phase [22]. According to the strengthening mechanism principle and influencing factors of cast aluminum alloy, the methods of multi-component alloying and heat treatment process optimization are usually adopted to improve the microstructure and distribution of cast aluminum alloy and improve the strength of cast aluminum alloy.

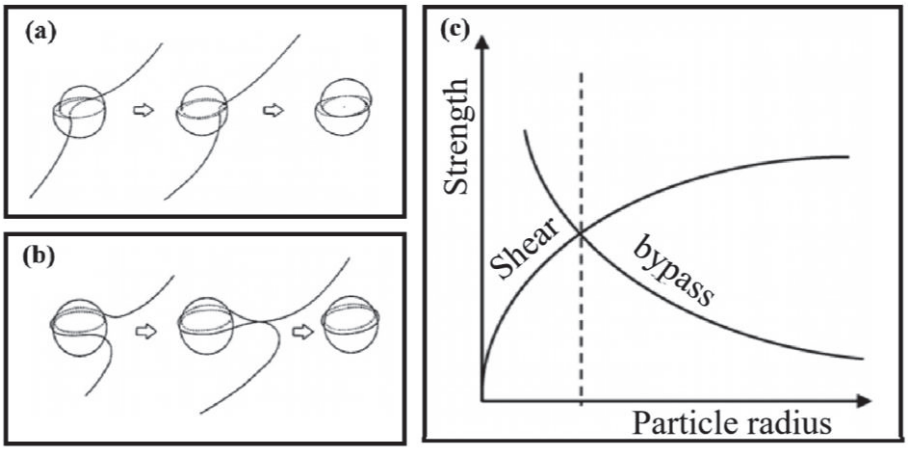

Figure 1. Relationship between dislocation motion and precipitation phase [17]: (**a**) Friedel mechanism. (**b**) Orowan mechanism. (**c**) Relationship between precipitation phase size, alloy strength, and dislocation motion.

3. Multi-Component Alloying Optimization

The alloy composition of cast aluminum alloy determines the microstructure of the alloy, and multicomponent alloying is one of the main methods to improve the properties of cast aluminum alloy. Multi-element alloying usually involves the optimization of main alloying elements and trace elements.

3.1. Main Alloying Elements

The solid solubility of Si in aluminum is 1.65 wt.% (577 °C), but decreased to 0.05 wt.% at room temperature [23]. The addition of Si to aluminum alloy can reduce the volume shrinkage and improve the fluidity, thus improving the casting performance of aluminum alloy [24]. For Al–Si cast aluminum alloy, the Si content is usually selected between 5% and 23%, and the Al–Si eutectic reaction occurs at 12.6 wt.% Si [25]. As shown in Figure 2, different Si contents lead to different microstructure of Al-Si alloys. The influence of Si elements on the mechanical properties of the alloy is related to the Si content and the morphology of eutectic silicon particles: when the Si content is between 4 and 20%, the yield strength first increases and then decreases with the increase of Si content [26]. In addition, the addition of Si to the alloy often results in the formation of large plate-strip eutectic structure, and the morphology of eutectic Si is usually changed from large plate-strip to small fibrous morphology through modification to improve the toughness of the alloy [27].

Mg is one of the important solid solution strengthening elements in cast aluminum alloy. Studies have shown that Mg has a large solid solubility in aluminum, which can reach up to 17.4 wt.% at 450 °C, while only 0.3~0.7 wt.% in Al–Si cast aluminum alloys at room temperature. Therefore, Mg_2Si can be formed when Mg and Si elements are added together [28]. In addition, after the aging heat treatment, the dispersion strengthening phase of the alloy β″-Mg_5Si_6 can be precipitated to improve the alloy strength [29,30].

Cu is also one of the important solid solution strengthening elements of cast aluminum alloy. Since the maximum solid solubility of Cu in aluminum is 5.65 wt.% (546 °C), but it is very small at room temperature, the alloy will precipitate intermetallic compounds during the solidification process, such as θ-Al_2Cu, Q-$Al_5Cu_2Mg_8Si_6$ and so on. The dispersion-strengthened phases θ′-Al_2Cu and Q′-$Al_5Cu_2Mg_8Si_6$ are also precipitated after aging heat treatment, which improve the age hardening strength of the alloy [31,32]. In addition, because the θ ‘and Q’ metastable phases have strong resistance to roughening at high temperatures, the addition of Cu will improve the high-temperature thermal stability of Al–Si cast aluminum alloys [33].

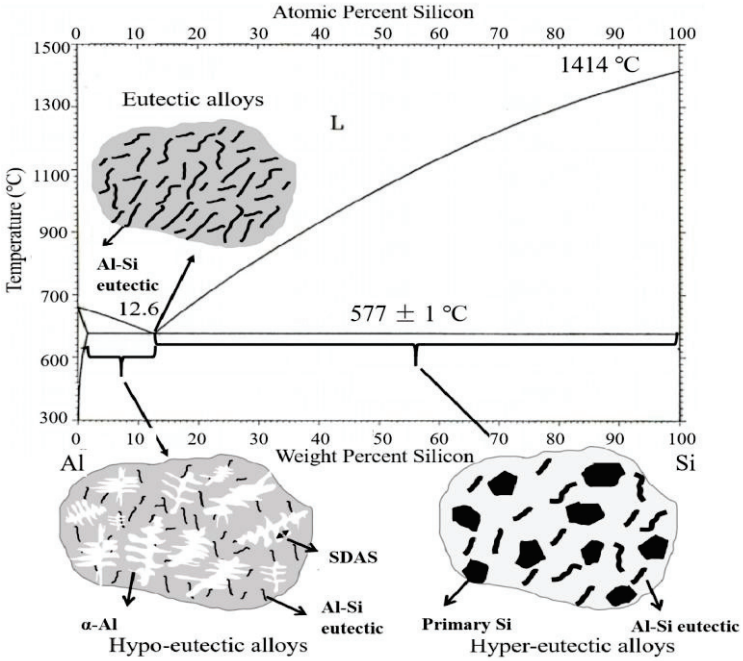

Figure 2. Binary phase diagram and as-cast microstructure diagram of Al–Si cast aluminum alloy.

3.2. Microalloying

At present, the research on the main alloying elements and their proportions of cast aluminum alloys is very mature. Microalloying is an ideal choice to further improve the strength and comprehensive performance of the alloy. The study of microalloying elements in Al–Si–Cu–Mg cast aluminum alloys usually involves the following aspects [34]: (1) modification; (2) grain refinement; (3) formation of new precipitation strengthening phase.

3.2.1. Modification

The eutectic Si of Al–Si–Cu–Mg cast aluminum alloys usually grows in the form of coarse flakes or needles under natural conditions. The primary Si is often polygonal and needle-like. These silicon particles are the source of stress concentration, and the size and morphology of silicon particles have an important impact on the mechanical properties of the alloy, especially the toughness of the alloy [22]. Therefore, silicon particle usually is modified during the solidification process to transform coarse flaky or needle-like eutectic Si into a fine fiber-like morphology and refine the size of the primary Si, thereby improving the strength and toughness of the alloy [35].

The modification methods of eutectic Si include chemical modification and quenching modification. The chemical modification method is widely used in production due to its simple operation, obvious modification effect and high economic benefit. Generally, modifiers such as Sr, Na, Sb, Ba, Ca, Y, Ce, and Eu are selected to modify the eutectic Si. Sr is widely used in hypoeutectic and eutectic Al–Si cast aluminum alloys due to its advantages of good reproducibility, long-term effective modification time, no corrosion to equipment, insensitivity to cooling rate and low environmental pollution [36]. The method of adding P to the melt is usually used for the modification of the primary Si particles. P and Al react with each other to form an AlP compound [37]. In addition, the composite modification can achieve multiple modification effects, which can simultaneously modify eutectic Si and primary Si particles, but there are also some modification elements that inhibit or poison each other, such as Sr-Na, P-Ca and P Eu, etc., which need to be avoided when preparing Al–Si cast aluminum alloys.

Rare earth elements have modification effect on eutectic Si, among which Sc has a greater modification effect. Xu et al. [38] studied the modification effect of Sc element on eutectic Si. As shown in Figure 3, with the increasing content of Sc element, the morphology

of coarse flake eutectic Si transforms into finer fibrous morphology. The addition of 0.8 wt.% Sc resulted in a decrease in the aspect ratio of eutectic Si from 27 to 2. In addition, studies have shown that Mg also has modification effect on eutectic Si morphology by inhibiting the growth of eutectic Si [39]. Samuel et al. [40] found that when the Mg content was lower than 0.35 wt.%, the modification effect of Mg element on eutectic Si was not obvious, but when the Mg content was increased to 0.6 wt.%, it had a modification effect on eutectic Si.

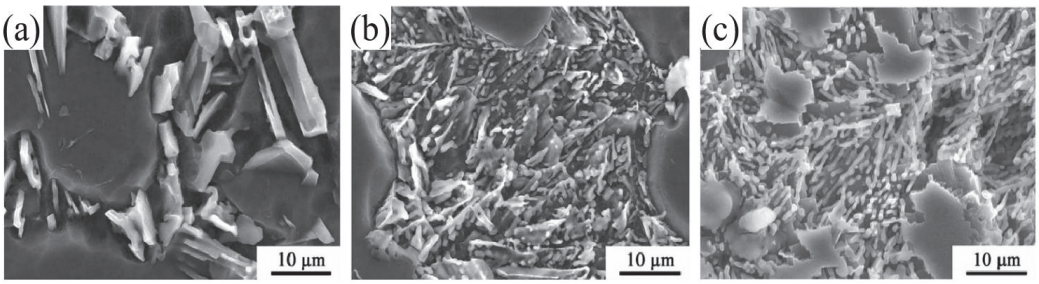

Figure 3. Typical morphology of eutectic Si in Al-Si-Mg cast aluminum alloy with different Sc contents: (**a**) 0 wt.% Sc; (**b**) 0.2 wt.% Sc; (**c**) 0.8 wt.% Sc [38].

Many assumptions about the research on the modification mechanism of eutectic Si are based on the theoretical exploration that the modified atoms inhibit the nucleation and growth of eutectic Si. In recent years, the widely accepted modification mechanisms of eutectic Si are mainly the poisoning of twin plane re-entrant edge (TPRE) proposed by Hamilton and Seidensticker in the 1960s and the impurity-induced twinning (IIT) mechanism proposed by Lu and Hellawell [41,42]. Timpel et al. [43] explored the effect of Sr containing particles with different morphologies on the modification of eutectic Si, and found that the Sr containing particles with different morphologies and sizes have different mechanisms for the modification of eutectic Si. As shown in Figure 4a, nanocrystalline rod-like Sr particles lead to the formation of multiple twins in Si, which grow in different crystal growth directions (IIT); Figure 4b shows the growth of eutectic Si is restricted by the Sr-containing nanocrystalline strips (TPRE).

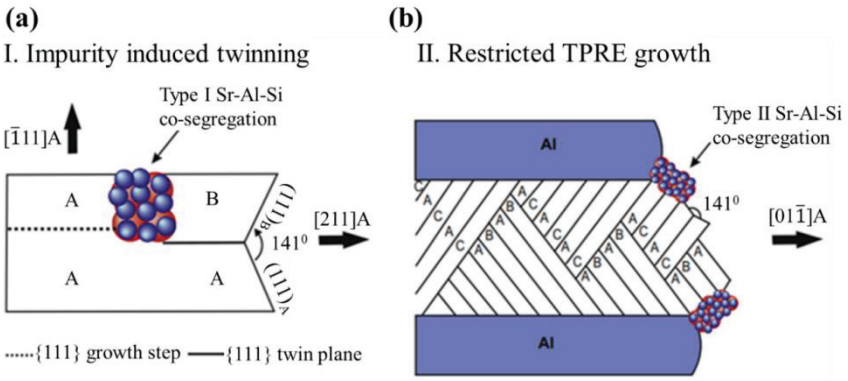

Figure 4. Schematic representation of (011) plane projection of eutectic Si [43]: (**a**) Type I rod-like Sr-Al-Si co-segregation which promotes twinning by changing the stacking sequence; (**b**) Locations of type II extended rod-like Sr–Al–Si co-segregations within the eutectic Si at the re-entrant edges or growing surfaces, which inhibits the growth of eutectic Si.

Most studies on the modification mechanism of eutectic Si is based on the nucleation and growth of eutectic Si [44–46]. Figure 5a shows the mechanism of eutectic Si nucleation and growth of hypo-eutectic Al–Si alloy [47]. Figure 5a shows that when the eutectic temperature is reached, the eutectic Si nucleates on the second phase β-(Al, Si, Fe), and then grows into the liquid in a thin morphology. Most studies on the mechanism of eutectic Si nucleation and growth usually investigate by means of cooling curve analysis, discon-

tinuous solidification experiment and the cellular automata (CA) model [48,49]. However, these methods cannot capture the solidification morphology accurately in real time, and the simulation results are different from the experimental results. The synchronous X-ray method can realize the in-situ observation of the solidification process, which provides a good way for the real-time observation of eutectic Si. Mao et al. [50] studied the nucleation and growth process of eutectic Si in Al–Si alloy using synchronous X-ray technology. Due to the similar atomic number and density of Al and Si, it is difficult to distinguish the two morphologies by contrast. In order to improve the contrast at the solid–liquid interface and further distinguish the morphology of eutectic Si more easily, the researchers added Zn element to the Al–Si alloy. As shown in Figure 5b, the nucleation and growth process of eutectic Si can be clearly observed by in-situ X-ray observation.

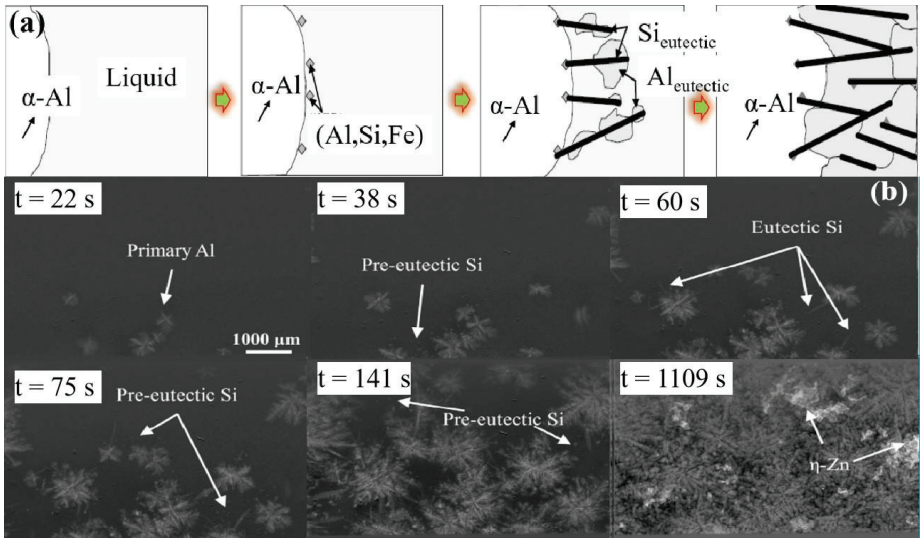

Figure 5. Nucleation and growth of eutectic Si: (**a**) Mechanism diagram of nucleation and growth of eutectic Si [47]; (**b**) in situ observation of eutectic Si nucleation and growth process in Al-40Zn-5Si alloy [50].

3.2.2. Grain Refinement

The refinement structure of Al–Si cast aluminum alloys is mainly to promote the formation of primary α-Al dendrites into fine equiaxed grains. The formation of equiaxed grains can also prevent the occurrence of porosity and shrinkage, and also reduce the tendency of hot cracking and improve the overall mechanical properties of the alloy [51]. Among many methods of grain refinement, the most effective and economical method of adding grain refiner is usually selected in industrial production. The selection of refiners has undergone a series of developments: from the early salt refiners (K2TiF6, KBF4, etc.) to the intermediate alloys (Al–Ti, Al–B, Al–Ti–B, Al–BC and Al–Ti–C, etc.). The addition of intermediate alloys has also evolved from the early bulk or ingot to rod-shaped intermediate alloys [52].

As the solid solubility of trace elements Zr, Ti, V, Er and Sc in Al solid solution gradually decreases with the decrease of temperature, Al_3M (M is Zr, Ti V, Er or Sc etc.) phase is formed during the solidification of the alloy. Due to the small mismatch between Al_3M particles and α-Al solid solution, and causing composition undercooling, it can be used as an effective heterogeneous nucleation point for α-Al during solidification, thereby refining the structure [53,54]. Liu et al. [55] found that the addition of 0.14 wt.% Zr to the Al–Si–Cu–Mg cast aluminum alloy has a significant refinement effect on the grain size of the alloy. The grain size of the base alloy is 335 μm. while the grain size was reduced to 253 μm after the addition of 0.14 wt.% Zr. Studies have shown that the addition of trace elements Zr, Ti, V, Er, and Sc to the melt will cause the composition undercooling [56]. The mechanism of solute elements on the grain refinement can be explained by the growth

restriction factor (GRF) relationship, as shown in Equation (3). GRF refers to the degree of constraint of solute atoms on the solid–liquid interface growth when new grains grow into the melt. Therefore, the above formula indicates that GRF increases with the increase of trace element concentration, and the degree of constraint on grain growth increases, resulting in more obvious refinement effect.

$$GRF = \sum mc_0\ (k-1) \tag{3}$$

where: m—Liquidus slope;
c_0—Solute atomic concentration;
k—Solute distribution coefficient during solidification.

3.2.3. New Precipitated Strengthened Phase

In addition to forming Al_3M phase during solidification, trace elements such as Zr, Ti, V, Er and Sc can also precipitate Al_3M phase during aging heat treatment. Al_3M phase is dispersed and fine distributed in the aluminum alloy matrix, which plays a role of pinning on dislocation, impeding dislocation movement and effectively improving alloy strength [57]. It is found that the tensile and low-cycle fatigue properties of the alloy under peak aging conditions are significantly improved due to the generation of dispersing fine Al_3M phase, and the yield strength was increased by 60–87% when Ti, Zr and V were added to Al–Si–Cu–Mg cast aluminum alloys [58]. In addition, the thermal stability of Al_3M phases are good due to the low solubility and weak diffusion capacity of these elements in aluminum matrix, which can improve the high-temperature mechanical properties of the alloy [59]. Shaha et al. [60] studied the influence of Zr, Ti and V elements on the high-temperature mechanical properties of Al–Si–Cu–Mg cast aluminum alloys, and found that under the peak aging condition, the yield strength and ultimate tensile strength of the alloy with trace elements increased by 30% and 5% compared with that of the alloy without addition due to the effect of the dispersion and precipitation phase.

Xu et al. [38] studied the influence of different Sc content on the microstructure and mechanical properties of the F357 cast aluminum alloy, and found that with the increase of Sc content, when Sc increased to 0.8 wt.%, the eutectic silicon morphology and secondary dendrite arm spacing of the F357 alloy were significantly refined. In addition, the yield strength and ultimate tensile strength of the alloy increased from 258 MPa and 327 MPa to 289 MPa and 356 MPa, respectively, and the elongation increased from 6.9% to 12.8% due to the formation of fine Al_3Sc strengthening phase under T6 peak aging heat treatment. Rahimian et al. [61] studied the effect of Zr on the microstructure and properties of Al–Si–Cu–Mg alloy, and found that after T6 peak aging treatment, Al–Si–Zr–Ti precipitates with a fine dispersion and a size of 80~200 nm were formed, which together with θ' and Q' phases formed the precipitation strengthening phase of the alloy. The yield strength and ultimate tensile strength of the alloy increased from 261 MPa and 282 MPa to 291 MPa and 335 MPa, respectively. Researchers have conducted a lot of research on the influence of trace elements Zr, Ti, V and Sc on the mechanical properties of Al–Si cast aluminum alloy, and it has been shown that the addition of microalloying elements is very beneficial to improve the mechanical properties of Al–Si cast aluminum alloy [38,55,61–64]. Figure 6 shows the strength of microalloyed Al–Si cast aluminum alloy under peak aging in recent years. The results show that the yield strength and ultimate tensile strength of Al–Si cast aluminum alloy are approximately 250~330 MPa and 270~380 MPa, and the yield ratio is between 0.79–0.93 after microalloying regulation. The yield ratio of some alloys is still very high, resulting in low formability and use safety at room temperature.

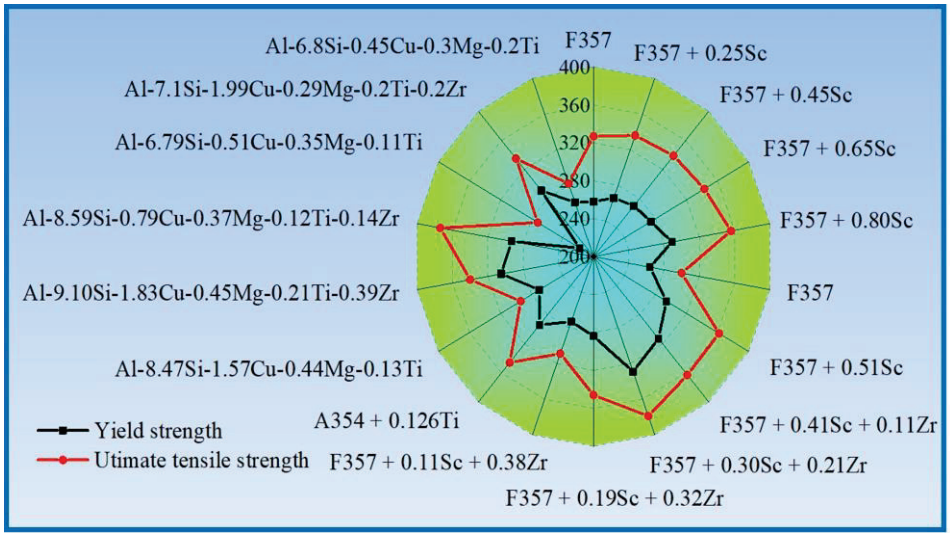

Figure 6. Investigation of the strength of Al–Si alloy. This figure is reproduced based on [38,55,61–64].

4. Heat Treatment Process Optimization

The heat treatment of Al–Si cast aluminum alloys usually includes solution treatment and aging treatment (natural aging at room temperature or artificial aging at high temperature). Heat treatment to improve the strength of cast aluminum alloy is mainly due to the solid solution strengthening, as well as aging precipitation strengthening effect. However, the heat treatment process has a great impact on the solid solution effect and precipitation phase of the alloy. Therefore, the optimization of heat treatment process is very important for improving the alloy structure and improving the strength and toughness of casting parts [65–67].

4.1. Solution Treatment

Solution treatment refers to holding the alloy for a certain time after heating to a specific temperature, and then quenching to room temperature to obtain super-saturated solid solution, which provides a greater driving force for late aging precipitation [68–70]. Generally, the solution temperature should be 5–10 °C lower than the eutectic temperature of eutectic phase with low melting point to prevent over-burning [49]. Solution treatment can dissolve intermetallic compounds (such as Mg_2Si phase, Al_2Cu phase and $Al_5Cu_2Mg_8Si_6$ phase) produced during solidification, and can also change the morphology of Si particles. The dissolution of Si particles in the solid solution process roughly undergoes three processes: crushing, spheroidizing and coarsening [71]. However, the dissolution and homogenization of intermetallic compounds of Al–Si–Cu–Mg cast aluminum alloys are relatively complicated due to the variety of primary phases. The solid solution process of intermetallic compounds is also the process of uniform diffusion of alloying elements. The short solution time does not dissolve all intermetallic compounds, and the longer solution time leads to the coarsening of the microstructure and the generation of secondary holes, as well as unnecessary energy consumption [72,73].

4.1.1. Dissolution Characteristics of Intermetallic Compounds

The Al–Si–Cu–Mg cast aluminum alloys usually dissolve the Mg_2Si phase, Al_2Cu phase and $Al_5Cu_2Mg_8Si_6$ phase during the solid solution process. The time required for solid solution depends on the dendrite arm spacing, the primary phase and solution treatment temperature, etc. [74,75]. The dissolution process of Mg_2Si phase is very rapid due to the large diffusion rate of Mg element in Al. Rometsch [76] studied the solution process of A356 and A357 alloys at 540 °C and found that the A356 alloy could complete the solution and homogenization process of Mg_2Si phase within 15 min due to the low Mg content (0.40 wt.%) and the small secondary dendrite arm spacing (SDAS) (40 m). Even

for A357 (0.62 wt.% Mg) with a large SDAS (55 m), the solution and homogenization time of Mg_2Si phase only needed 50 min. The dissolution of Al_2Cu phase is more difficult than that of Mg_2Si phase due to the low diffusion rate of Cu in Al. Moreover, the Al_2Cu phase in the as-cast structure has a variety of morphologies: for example, the blocky Al_2Cu phase, eutectic Al_2Cu phase or two kinds of mixture, and the solubility of Al_2Cu phase with different morphologies is also different [77–79]. The dissolution process of Al_2Cu phase with different morphologies in the solid solution process is shown in Figure 7 [17]: the eutectic Al_2Cu phase dissolves into smaller particles through fragmentation, and then spheroidizes and finally dissolves through the diffusion of Cu to the surrounding matrix. However, the blocky Al_2Cu phase was gradually dissolved by spherification and diffusion which takes a longer time. Samuel [80] studied the dissolution characteristics of the eutectic and bulk Al_2Cu phases. The study found that even if the solution treatment is performed in the range of over-burning temperature (540 °C), the bulk Al_2Cu phase still exists after solid solution for 24 h, and the eutectic Al_2Cu phase has completely dissolved. In addition to the formation of Mg_2Si phase and Al_2Cu phase, Q-$Al_5Cu_2Mg_8Si_6$ phase is also formed during the solidification. The Q phase is distributed independently of script morphology, or coexists with Al_2Cu and eutectic Si in the final solidification stage to form eutectic morphology [81]. The Q phase may dissolve or not dissolve or even precipitate during the solid solution process, and its dissolution characteristics are related to alloy composition [82]. Lasa et al. [83] investigated the Q phase solution process in Al–Si–Cu–Mg cast aluminum alloys with different Cu contents: for high Cu (4.4 wt.% Cu), different Mg contents (0.58–1.30 wt.% Mg) alloy, the content of Q phase in the solution process is almost unchanged; However, for alloys with low Cu (1.37 wt.% Cu) and high Mg (1.30 wt.% Mg), the quantity of Q phases increased after the solution at 500 °C for 5 h. This is mainly due to the higher Mg content causing more Q phases to be formed in the equilibrium state, but the number of actual Q phases is lower than the equilibrium state due to the faster solidification rate in the actual solidification process. However, the solid solution process is slower than the solidification process, and close to the equilibrium state condition, which leads to the re-precipitation of the unprecipitated Q phase during the solidification process. In addition, the dissolution characteristics of phase Q are also related to the solution temperature. Colley et al. [84] studied the dissolution characteristics of Q phase of Al—8.3 wt.% Si-2.8 wt.% Cu—0.5 wt.% Mg alloy at different solution temperatures and found that Q phase did not dissolve after 24 h at 480 °C, while almost all dissolved after 24 h at 505 °C.

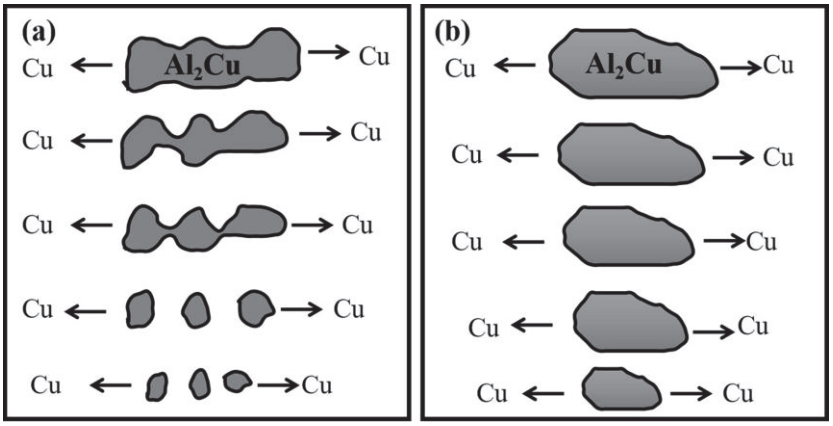

Figure 7. Dissolution process of Al_2Cu particles with different morphologies [17]: (**a**) eutectic Al_2Cu; (**b**) blocky Al_2Cu.

4.1.2. Application of Two-Step Solution and Thermodynamic Calculation in Solution Heat Treatment

In order to avoid over-burning of Cu-containing phase, the solution temperature of Al–Si–Cu–Mg cast aluminum alloys should not exceed the eutectic temperature at the low melting point, usually around 490–505 °C. However, there will still exist the

undissolved flake $Al_5Cu_2Mg_8Si_6$ phase and the blocky Al_2Cu phase after the solid solution treatment. In order to overcome this problem, Al–Si–Cu–Mg cast aluminum alloys is usually treated by two-step solution treatment. Through two-step solution treatment, Cu-containing intermetallic compounds can be completely or mostly dissolved, and the degree of homogenization of alloying elements is also improved, thus improving the strength and toughness of the alloy. Sokolowsk's [85] research found that the Cu-containing phase is significantly refined and the number significantly reduced by the two-step solution treatment (8 h/495 °C + 2 h/520 °C) compared to the traditional single-step (8 h/495 °C) solution treatment, and the tensile strength of the aged alloy increased from 200 MPa to 240 MPa, and the elongation increased from 0.6% to 1.6% compared with the single-step solution treatment after aging at 250 °C for 5 h.

The aluminum alloy industry has made some progress in equipment and processing, but there are still some deficiencies in basic theoretical research such as heat treatment process design. Most of the research on heat treatment process design still focuses on trial and error. With the introduction of integrated computational materials engineering (ICME) in 2008, the traditional research model of "experience optimization", characterized by a large amount of experience accumulation and simple cyclic trial and error, is broken through, and multi-scale simulation and experimental tools have been gradually combined with databases to integrate design and manufacturing. With the continuous development of thermodynamics and phase diagram calculation, the phase diagram calculation method (CALPHAD) is based on the laws of thermodynamics to calculate the phase diagram, diffusion and other related information of multi-component alloys by means of energy minimization [86]. The CALPHAD can effectively predict the phase types and temperatures under alloy equilibrium conditions by combining computer software and thermodynamic database, thus providing theoretical guidance for the design of heat treatment process [87]. In addition, Scheil–Gulliver model is used to predict the solidification path of the alloy to predict the phase formation during solidification [88].

CALPHAD is one of the important methods in integrated computational simulation. Many researchers use this method to solve the problems in phase transition and heat treatment process optimization. Li et al. [89] used Pandat software to study the equilibrium phase diagram of Al–Zn–Mg–Si alloy, and found that α-Al, Si, Mg_2Si and $MgZn_2$ phases existed at 573 K, which was well verified by scanning electron microscopy (SEM) and differential scanning calorimetry (DSC), providing theoretical guidance for phase prediction. Zhang et al. [90] investigated the effects of Zn addition and related heat treatment parameters on the mechanical properties of Al–Si–Mg alloys by using a combination of experimental and thermodynamic methods. In addition, the CALPHAD method was used to optimize the heat treatment process parameters. As shown in Figure 8, the non-equilibrium solidification path was predicted by thermodynamic calculation, and the temperature of low melting point eutectic phase was measured by DSC experiment. In order to prevent the eutectic phase from over-burning, the solution temperature should be lower than the low melting point eutectic phase temperature. On the other hand, the homogenization and diffusion of elements is also the purpose of solution heat treatment. As shown in Figure 8, thermodynamic software was used to predict the time for elements to reach diffusion homogenization at a specific solution temperature, and the best solution time was obtained by combining the evolution of microstructure and hardness at different solution times.

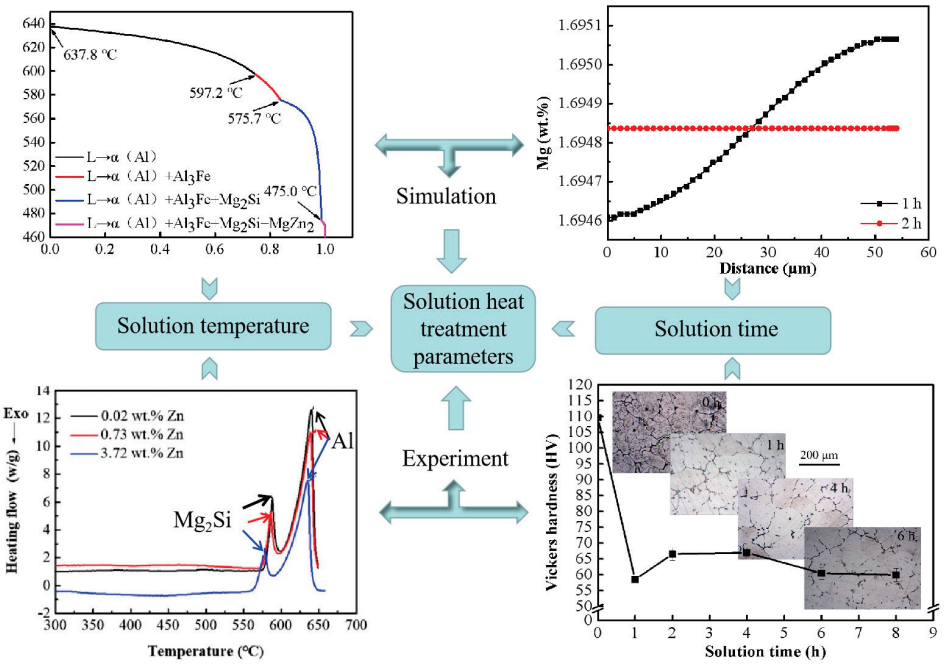

Figure 8. Optimization of solution heat treatment parameters by combining thermodynamic calculation and experiment [90].

4.2. Aging Treatment

Aging treatment is one of the important means to improve the performance of Al–Si–Cu–Mg cast aluminum alloys. Aging means that supersaturated solid solution precipitates finely dispersed solute clusters or precipitated phases from the matrix at room temperature (natural aging) or at high temperature (artificial aging). These solute clusters/precipitated phases can effectively hinder the movement of dislocations, thereby achieving the precipitation strengthening [91,92].

Al–Si–Cu–Mg cast aluminum alloys precipitate strengthening phase (β″-Mg_5Si_6, θ′-Al_2Cu and Q′-$Al_5Cu_2Mg_8Si_6$, etc.) to improve the aging hardening effect after aging heat treatment [29–32]. In addition, the trace elements Zr, Ti, V, Er and Sc added to the Al–Si–Cu–Mg cast aluminum alloys can not only refine grains, but also precipitate dispersed fine Al_3M (M is Zr, Ti, V, Er or Sc) phase during aging heat treatment, and these precipitated phases have good precipitation strengthening effect [57].

Researchers have conducted a lot of research on the aging hardening of Al–Si–Cu–Mg cast aluminum alloys under different aging temperature and time. The regulation of aging hardening effect of Al–Si–Cu–Mg cast aluminum alloys is related to the type, density, size and distribution of precipitated phase in aging sequence [93–96]. For Al–Si–Mg cast aluminum alloys, the aging precipitation sequence is SSSS → atomic cluster → GP Zones → β″ → β′, U1, U2, B′ → β/Si [97]. Zhang et al. [98] found that β″ has a major strengthening effect on the alloy. For Al–Si–Cu cast aluminum alloys, the ageing precipitation sequence is SSSS → atomic cluster → GPI → GPII (θ″) → θ′ → θ, including θ″ and θ′ are the main precipitation strengthening phase [99]. For Al–Si–Cu–Mg cast aluminum alloys, the aging precipitation sequence becomes very complex due to the increase of the types of aging precipitation phases. In addition to the above two precipitated sequences, the following aging sequences may occur: SSSS → atomic cluster → GP Zones → β″, L, QP, QC → β′,Q′ → Q. The types and volume fraction of the aged precipitated strengthening phase in Al–Si–Cu–Mg cast aluminum alloys are not only related to the heat treatment process, but also depend on the Cu content and Cu/Mg content ratio. Mørtsell et al. [100] studied the precipitation behavior of cast aluminum alloy A356 with different Cu contents and found that the precipitation strengthening phase of the A356 cast aluminum alloy has only the needle-shaped β″ phase under peak aging conditions; when 0.5 wt.% Cu is added to the

alloy, L and Q′ appear in addition to the β″ phase; however, when 1 wt.% Cu is added to the alloy, there is only a small amount of β″ phase in the alloy, and the main precipitation strengthening phases are the L and Q′ phases. Zheng et al. [101] studied the precipitation strengthening phase of Al–Si–Cu–Mg cast aluminum alloys (Figure 9) and found that the alloy tends to form the precursor of the β″ phase when the low Cu (1.04 wt.% Cu) and Cu/Mg ratio is 2; when the Cu content is 1.06 wt.% Cu and the Cu/Mg ratio is 1, the alloy tends to form β′ phase; when the high Cu (2.08 wt.% Cu) and Cu/Mg ratio is 4, the alloy tends to form the Q′ phase; however, when the Cu content in the alloy reaches 3.98 wt.% Cu and the Cu/Mg ratio is still 4, in addition to a small amount of Q′, the θ′ phase exists in the alloy.

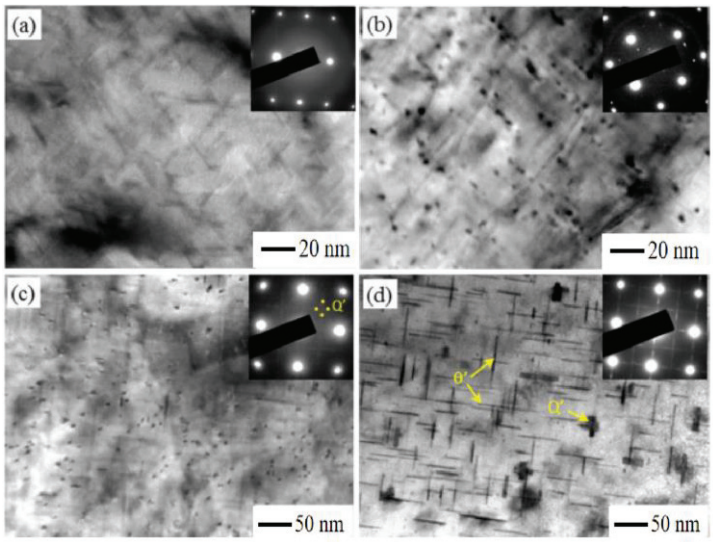

Figure 9. Bright-filed TEM image with corresponding SAED pattern of aged alloy [93]: (**a**) the precursor of the β″ phase; (**b**) β′ phase; (**c**) Q′ phase; (**d**) Q′ and θ′ phase. TEM—Transmission Electron Microscopy; SAED—Selected Area Electron Diffraction.

5. Conclusions

Cast aluminum alloy is one of the candidates for lightweight materials for automobiles. In recent years, the application of lightweight Al–Si–Cu–Mg cast aluminum alloys in automobiles has gradually increased, but it is limited by problems such as strength, toughness, cost, and application environment. The strengthening mechanism of cast aluminum alloy mainly includes solid solution strengthening, fine grain strengthening, and second phase strengthening. Generally, these strengthening mechanisms are related to solid atoms, grain size, and the second phase, respectively. However, microalloying and heat treatment play an important role in the regulation of microstructure and mechanical properties. Therefore, in order to make the development of Al–Si–Cu–Mg cast aluminum alloys for automotive lightweight towards the direction of low-cost, high strength and toughness, researchers systematically comprehend the method of optimizing microalloying and heat treatment based on the strengthening mechanism of cast aluminum alloy, and should pay attention to the following main aspects:

The optimization of multi-component alloying elements includes main alloying elements and microalloying, among which the optimization of main alloying elements (such as Si, Cu and Mg) are mainly related to solution strengthening and precipitation strengthening, and its research has been relatively complete. Optimizing the content of alloy elements, especially exploring the relationship between microalloying and strengthening mechanism is an important research direction to improve the mechanical properties at room temperature and high temperature. The regulation of microalloying on the microstructure of Al–Si–Cu–Mg cast aluminum alloys is mainly achieved by modifying eutectic Si, refining grain and forming new precipitation strengthening phase. Although microalloying has

made some progress in the regulation of microstructure and mechanical properties, some high-efficient microelements are limited in their application due to high cost. For example, the rare earth element Sc has a good refining effect on eutectic Si and grain size, but the high cost of Sc impedes its wide use. Therefore, it is a future research trend to seek for low-cost and efficient trace elements to replace Sc or combine with Sc.

In the process of solution treatment of Al–Si–Cu–Mg cast aluminum alloys, the Si particles undergo crushing, spheroidizing and coarsening. However, the dissolution and homogenization of primary phase (such as Mg_2Si phase, Al_2Cu phase and $Al_5Cu_2Mg_8Si_6$ phase) are relatively complex. The dissolution of Mg_2Si phase is very rapid, roughly between 15–50 min. The dissolution of Al_2Cu phase is more difficult than that of Mg_2Si phase, and the dissolution characteristic of Al_2Cu phase is related to the morphology, in which the blocky Al_2Cu phase is more difficult to dissolve than that of eutectic morphology Al_2Cu phase. However, the dissolution characteristic of $Al_5Cu_2Mg_8Si_6$ phase is related to alloy composition and solution treatment parameters. The high Mg content causes the $Al_5Cu_2Mg_8Si_6$ phase to precipitate again during the solution treatment. In addition, the higher solution temperature is more beneficial to the dissolution of $Al_5Cu_2Mg_8Si_6$ phase than the lower temperature, but the higher solution temperature may lead to the overburning of Al_2Cu phase. Therefore, the study on the dissolution kinetics mechanism of Mg_2Si phase, Al_2Cu phase and $Al_5Cu_2Mg_8Si_6$ phase in the solution treatment has theoretical guidance for the formulation of Al–Si–Cu–Mg alloy solution treatment, especially the two-step solution treatment.

The types and volume fraction of the aged precipitated strengthening phase (β″, Q′ and θ′ phase) in Al–Si–Cu–Mg cast aluminum alloys are not only related to the heat treatment process, but also depend on the Cu content and Cu/Mg content ratio. With the increase of Cu content, the strengthening phase gradually evolves from β″ phase to Q′ and θ′ phase. Exploring the mechanism of solid solution and dispersion strengthening in the heat treatment process of Al–Si–Cu–Mg cast aluminum alloys, especially the adjustment of aging precipitation sequence through alloy element design and heat treatment process optimization is an important means to improve the strength and toughness of the alloy.

Author Contributions: Conceptualization, M.Z. and J.W.; writing—original draft preparation, M.Z., Y.T. and X.Z.; writing—review and editing, J.W. and L.C.; supervision, J.W. and Y.Z. Funding acquisition, M.Z. and Y.Z. All authors have read and agreed to the published version of the manuscript.

Funding: This research was funded by the Natural Science Foundation of Hebei Province (E2022209059, E2020209153). Science and Technology Project of Tangshan (22130217G).

Institutional Review Board Statement: Not applicable.

Informed Consent Statement: Not applicable.

Data Availability Statement: Not applicable.

Conflicts of Interest: The authors declare no conflict of interest.

References

1. Li, H.; Li, X. The present situation and the development trend of new materials used in automobile lightweight. *Appl. Mech. Mater.* **2012**, *189*, 58–62. [CrossRef]
2. Schönemann, M.; Schmidt, C.; Herrmann, C.; Thiede, S. Multi-level Modeling and Simulation of Manufacturing Systems for Lightweight Automotive Components. *Procedia CIRP* **2016**, *41*, 1049–1054. [CrossRef]
3. Witik, R.A.; Payet, J.; Michaud, V.; Ludwig, C.; Månson, J. Assessing the life cycle costs and environmental performance of lightweight materials in automobile applications. *Compos. Part A Appl. Sci. Manuf.* **2011**, *42*, 1694–1709. [CrossRef]
4. Sengupta, B.; Shekhar, S.; Kulkarni, K.N. A novel ultra-high strength and low-cost as-cast titanium alloy. *Mater. Sci. Eng. A* **2017**, *696*, 478–481. [CrossRef]
5. Liu, Z.; Lu, J.; Zhu, P. Lightweight design of automotive composite bumper system using modified particle swarm optimizer. *Compos. Struct.* **2016**, *140*, 630–664. [CrossRef]
6. Shaji, M.C.; Ravikumar, K.K.; Ravi, M.; Sukumaran, K. Development of a High Strength Cast Aluminium Alloy for Possible Automotive Applications. *Mater. Sci. Forum* **2013**, *765*, 54–58. [CrossRef]

7. Nowak, M.; Bolzoni, L.; Babu, N.H. Grain refinement of Al-Si alloys by Nb-B inoculation. Part I: Concept development and effect on binary alloys. *Mater. Des.* **2015**, *66*, 366–375. [CrossRef]
8. Ibrahim, M.F.; Samuel, E.; Samuel, A.M.; Abdulrahman, A.A. Metallurgical parameters controlling the microstructure and hardness of Al-Si-Cu-Mg base alloys. *Mater. Des.* **2011**, *32*, 2130–2142. [CrossRef]
9. Wang, Q.G. Microstructural effects on the tensile and fracture behavior of aluminum casting alloys A356/357. *Metall. Mater. Trans. A.* **2003**, *34*, 2887–2899. [CrossRef]
10. Zheng, Q.J.; Zhang, L.L.; Jiang, H.X.; Zhao, J.Z.; He, J. Effect mechanisms of micro-alloying element La on microstructure and mechanical properties of hypoeutectic Al-Si alloys. *J. Mater. Sci. Technol.* **2020**, *47*, 142–151. [CrossRef]
11. Cao, Y.D.; Chen, X.H.; Wang, Z.D.; Chen, K.X.; Tang, W.Z.; Pan, S.W.; Yang, X.H.; Qin, J.W.; Li, S.H.; Wang, Y.L. Effect of Cd micro-addition on microstructure and mechanical properties in ternary Al-Si-Cu alloy. *J. Alloys Compd.* **2021**, *851*, 156739. [CrossRef]
12. Zhang, M.S.; Wang, J.S.; Wang, B.; Xue, C.P.; Liu, X.G. Improving mechanical properties of Al-Si-Cu-Mg alloys by microallying Sc using thermodynamic calculations. *Calphad* **2022**, *76*, 102394. [CrossRef]
13. Wang, D.T.; Liu, S.C.; Zhang, X.Z.; Li, X.Z.; Zhang, H.T.; Nagaumi, H. Fast aging strengthening by hybrid precipitates in high pressure die-cast Al-Si-Cu-Mg-Zn alloy. *Mater. Charact.* **2021**, *179*, 111312. [CrossRef]
14. Yang, X.F.; Xu, C.; Lu, G.X.; Guan, S.K. Towards strength-ductility synergy through an optimized two-stage solution treatment in Al-7Si-3Cu-0.5Mg alloys. *Mater. Sci. Eng. A* **2022**, *849*, 143504. [CrossRef]
15. Hansen, N. Hall-Petch relation and boundary strengthening. *Scr. Mater.* **2004**, *51*, 801–806. [CrossRef]
16. Eivani, A.R.; Taheri, A.K. Modeling age hardening kinetics of an Al-Mg-Si-Cu aluminum alloy. *J. Mater. Process. Technol.* **2008**, *205*, 388–393. [CrossRef]
17. Sjölander, E.; Seifeddine, S. The heat treatment of Al-Si-Cu-Mg casting alloy. *J. Mater. Process. Technol.* **2010**, *210*, 1249–1259. [CrossRef]
18. Bhat, T.B.; Arunachalam, V.S. Strengthening mechanisms in alloys. *Proc. Indian Acad. Sci. Sect. C Eng. Sci.* **1980**, *3*, 275–296.
19. Zhang, M.S.; Wang, J.S.; Wang, B.; Xue, C.P.; Liu, X.G. Quantifying the effects of Sc and Ag on the microstructure and mechanical properties of Al-Cu alloys. *Mater. Sci. Eng. A* **2022**, *831*, 142355. [CrossRef]
20. Xu, S.Z.; McDowell, D.L.; Beyerlein, I.J. Sequential obstacle interactions with dislocations in a planar array. *Acta Mater.* **2019**, *174*, 160–172. [CrossRef]
21. Zhen, Z.; Wang, H.; Teng, C.Y.; Bai, C.G.; Xu, D.S.; Yang, R. Dislocation self-interaction in TiAl: Evolution of super-dislocation dipoles revealed by atomistic simulations. *J. Mater. Sci. Technol.* **2021**, *69*, 138–147. [CrossRef]
22. Joseph, S.; Kumar, S.A. systematic investigation of fracture mechanisms in Al-Si based eutectic alloy-Effect of Si modification. *Mater. Sci. Eng. A* **2013**, *588*, 111–124. [CrossRef]
23. Haghshenas, M.; Jamali, J. Assessment of circumferential cracks in hypereutectic Al-Si clutch housings. *Case Stud. Eng. Fail. Anal.* **2017**, *8*, 11–20. [CrossRef]
24. Hajkowski, M.; Bernat, Ł.; Hajkowski, J. Mechanical Properties of Al-Si-Mg Alloy Castings as a Function of Structure Refinement and Porosity Fraction. *Arch. Foundry Eng.* **2012**, *12*, 57–64. [CrossRef]
25. Voort, G.V.; Asensio-Lozano, J. The Al-Si Phase Diagram. *Microsc. Microanal.* **2009**, *5*, 60–61. [CrossRef]
26. Dwivedi, D.K.; Sharma, R.; Kumar, A. Influence of silicon content and heat treatment parameters on mechanical properties of cast Al-Si-Mg alloys. *Int. J. Cast Met. Res.* **2006**, *19*, 275–282. [CrossRef]
27. Dybowski, B.; Szymszal, J.; Poloczek, Ł.; Kielbusl, A. Influence of the Chemical Composition on Electrical Conductivity and Mechanical Properties of the Hypoeutectic Al-Si-Mg Alloys. *Arch. Metall. Mater.* **2016**, *61*, 353–360. [CrossRef]
28. Cáceres, C.H.; Svensson, I.L.; Taylor, J.A. Strength-Ductility Behaviour of Al-Si-Cu-Mg Casting Alloys in T6 Temper. *Int. J. Cast Met. Res.* **2003**, *15*, 531–543. [CrossRef]
29. Lv, G.Q.; Yu, B.; Zhang, Y.F.; He, Y.F.; Ma, W.H.; Lei, Y. Effects of electromagnetic directional solidification conditions on the separation of primary silicon from Al-Si alloy with high Si content. *Mat. Sci. Semicon. Proc.* **2018**, *81*, 139–148. [CrossRef]
30. Lin, Y.C.; Luo, S.C.; Huang, J.; Yin, L.X.; Jiang, X.Y. Effects of solution treatment on microstructures and micro-hardness of a Sr-modified Al-Si-Mg alloy. *Mater. Sci. Eng. A* **2018**, *725*, 530–540. [CrossRef]
31. Di Giovanni, M.T.; Cerri, E.; Saito, T.; Akhtar, S.; Åsholt, P.; Li, Y.; Di Sabatino, M. Effect of copper additions and heat treatment optimization of Al-7% Si aluminum alloy. *Metall. Ital.* **2016**, *11*, 43–47.
32. Yang, Y.; Yu, K.L.; Li, Y.G.; Zhao, D.G.; Liu, X.F. Evolution of nickel-rich phases in Al-Si-Cu-Ni-Mg piston alloys with different Cu additions. *Mater. Des.* **2012**, *33*, 220–225. [CrossRef]
33. Alyaldin, L.; Elgallad, E.M.; Samuel, A.; Mdoty, H.W.; Valtierra, S.; Samuel, F.H. Effect of additives and heat treatment on the tensile properties of 354 alloy at 25 °C and 250 °C. *Mater. Sci. Eng. A* **2017**, *708*, 77–90. [CrossRef]
34. Yang, C.; Cao, L.; Gao, Y.; Cheng, P.M.; Zhang, P.; Kuang, J.; Zhang, J.Y.; Liu, G.; Sun, J. Nanostructural Sc-based hierarchy to improve the creep resistance of Al-Cu alloys. *Mater. Des.* **2020**, *186*, 108309. [CrossRef]
35. Li, J.H.; Wang, X.D.; Ludwig, T.H.; Tsunekawa, Y.; Arnberg, L.; Jiang, J.Z.; Schumacher, P. Modification of eutectic Si in Al-Si alloys with Eu addition. *Acta Mater.* **2015**, *84*, 153–163. [CrossRef]
36. Sheng, B.; Yun, X.B.; Pei, J.Y.; Zhao, Y.; Yan, Z.Y.; Zhang, X. Microstructure evolution of Al-Sr master alloy during continuous extrusion. *Trans. Nonferrous Met. Soc. China* **2017**, *27*, 305–311.
37. Weiss, J.C.; Loper, C.R. Primary silicon in hypereutectic aluminum-silicon casting alloys. *AFS Trans.* **1987**, *32*, 51.

38. Xu, C.; Xiao, W.L.; Hanada, S.; Yamagata, H.; Ma, C. The effect of scandium addition on microstructure and mechanical properties of Al-Si-Mg alloy: A multi-refinement modifier. *Mater. Charact.* **2015**, *110*, 160–169. [CrossRef]
39. Aguilera-Luna, I.; Castro-Román, M.J.; Escobedo-Bocardo, J.C.; García-Pastor, F.A.; Herrera-Trejo, M. Effect of cooling rate and Mg content on the Al-Si eutectic for Al-Si-Cu-Mg alloys. *Mater. Charact.* **2014**, *95*, 211–218. [CrossRef]
40. Samuel, A.M.; Ouellet, P.; Samuel, F.H.; Doty, H.W. Microstructural interpretation of the thermal analysis of commercial 319 Al alloy with Mg and Sr additions. *AFS Trans.* **1997**, *156*, 951–962.
41. Hamilton, D.R.; Seidensticker, R.G. Propagation mechanism of germanium dendrites. *J. Appl. Phys.* **1960**, *31*, 1165–1168. [CrossRef]
42. Lu, S.Z.; Hellawell, A. The mechanism of silicon modification in aluminum-silicon alloys: Impurity induced twinning. *Met. Mater. Trans. A* **1987**, *18*, 1721–1733. [CrossRef]
43. Timpel, M.; Wanderka, N.; Schlesiger, R.; Yamamoto, T.; Lazarev, N.; Isheim, D.; Schmitz, G.; Matsumura, S.; Banhart, J. The role of strontium in modifying aluminium-silicon alloys. *Acta Mater.* **2012**, *60*, 3920–3928. [CrossRef]
44. Shamsuzzoha, M.; Hogan, L.M. Twinning in fibrous eutectic silicon in modified Al-Si alloys. *J. Cryst. Growth* **1985**, *72*, 735–737. [CrossRef]
45. Li, B.; Wang, H.; Jie, J.; Wei, Z.J. Microstructure evolution and modification mechanism of the ytterbium modified Al-7.5%Si-0.45%Mg alloys. *J. Alloys Compd.* **2011**, *509*, 3387–3392. [CrossRef]
46. Srirangam, P.; Kramer, M.J.; Shankar, S. Effect of strontium on liquid structure of Al-Si hypoeutectic alloys using high-energy X-ray diffraction. *Acta Mater.* **2011**, *59*, 503–513. [CrossRef]
47. Shankar, S.; Riddle, Y.W.; Makhlouf, M.M. Nucleation mechanism of the eutectic phases in aluminum-silicon hypoeutectic alloys. *Acta Mater.* **2004**, *52*, 4447–4460. [CrossRef]
48. Mao, F.; Yan, G.Y.; Li, J.Q.; Wang, T.M.; Cao, Z.Q. The interaction between Eu and P in high purity Al-7Si alloys. *Mater. Charact.* **2016**, *120*, 129–142. [CrossRef]
49. Lu, Z.; Zhang, L. Thermodynamic description of the quaternary Al-Si-Mg-Sc system and its application to the design of novel Sc-additional A356 alloys. *Mater. Des.* **2017**, *116*, 427–437. [CrossRef]
50. Mao, F.; Li, J.Q.; Yan, G.Y.; Zou, L.J.; Cao, Z.Q.; Wang, T.M. Effect of Eu on the silicon phase in Al-40Zn-5Si alloys. *J. Alloys Compd.* **2017**, *722*, 116–130. [CrossRef]
51. Mohanty, P.S.; Gruzleski, J.E. Grain refinement mechanisms of hypoeutectic Al-Si alloys. *Acta Mater.* **1996**, *44*, 3749–3760. [CrossRef]
52. Doheim, M.A.; Omran, A.M.; Abdel-Gwad, A.; Sayed, G.A. Evaluation of Al-Ti-C master alloys as grain refiner for aluminum and its alloys. *Met. Mater. Trans. A* **2011**, *42*, 2862–2867. [CrossRef]
53. Colombo, M.; Gariboldi, E.; Morri, A. Influences of different Zr additions on the microstructure, room and high temperature mechanical properties of an Al-7Si-0.4Mg alloy modified with 0.25%Er. *Mater. Sci. Eng. A* **2018**, *713*, 151–160. [CrossRef]
54. Vlach, M.; Čížek, J.; Smola, B.; Melikhova, O.; Vlček, M.; Kodetová, V.; Kudrnová, H.; Hruška, P. Heat treatment and age hardening of Al-Si-Mg-Mn commercial alloy with addition of Sc and Zr. *Mater. Charact.* **2017**, *129*, 1–8. [CrossRef]
55. Liu, G.; Blake, P.; Ji, S. Effect of Zr on the high cycle fatigue and mechanical properties of Al-Si-Cu-Mg alloys at elevated temperatures. *J. Alloys Compd.* **2019**, *809*, 151795. [CrossRef]
56. Liu, W.; Xiao, W.; Xu, C.; Liu, M.W.; Ma, C.L. Synergistic effects of Gd and Zr on grain refinement and eutectic Si modification of Al-Si cast alloy. *Mater. Sci. Eng. A* **2017**, *693*, 93–100. [CrossRef]
57. Shen, Y.F.; Guan, R.G.; Zhao, Z.Y.; Misra, R.D.K. Ultrafine-grained Al-0.2Sc-0.1Zr alloy: The mechanistic contribution of nano-sized precipitates on grain refinement during the novel process of accumulative continuous extrusion. *Acta Mater.* **2015**, *100*, 247–255. [CrossRef]
58. Elhadari, H.A.; Patel, H.A.; Chen, D.L.; Kasprzak, W. Tensile and fatigue properties of a cast aluminum alloy with Ti, Zr and V additions. *Mater. Sci. Eng. A* **2011**, *528*, 8128–8138. [CrossRef]
59. Knipling, K.E.; Dunand, D.C.; Seidman, D.N. Criteria for developing castable, creep-resistant aluminum-based alloys—A review. *Z. Metallkd.* **2006**, *97*, 246–265. [CrossRef]
60. Shaha, S.K.; Czerwinski, F.; Kasprzak, W.; Friedman, J.; Chen, D.L. Ageing characteristics and high-temperature tensile properties of Al-Si-Cu-Mg alloys with micro-additions of Cr, Ti, V and Zr. *Mater. Sci. Eng. A* **2016**, *652*, 353–364. [CrossRef]
61. Rahimian, M.; Amirkhanlou, S.; Blake, P.; Ji, S.X. Nanoscale Zr-containing precipitates; a solution for significant improvement of high-temperature strength in Al-Si-Cu-Mg alloys. *Mater. Sci. Eng. A* **2018**, *721*, 328–338. [CrossRef]
62. Xu, C.; Xiao, W.; Zheng, R.; Hanada, S.J.; Yamagata, H.; Ma, C.L. The synergic effects of Sc and Zr on the microstructure and mechanical properties of Al-Si-Mg alloy. *Mater. Des.* **2015**, *88*, 485–492. [CrossRef]
63. Ceschini, L.; Morri, A.; Toschi, S.; Johansson, S.; Seifeddine, S. Microstructural and mechanical properties characterization of heat treated and overaged cast A354 alloy with various SDAS at room and elevated temperature. *Mater. Sci. Eng. A* **2015**, *648*, 340–349. [CrossRef]
64. Mohamed, A.; Samuel, F.H.; Kahtani, S.A. Microstructure, tensile properties and fracture behavior of high temperature Al-Si-Mg-Cu cast alloys. *Mater. Sci. Eng. A* **2013**, *577*, 64–72. [CrossRef]
65. Cui, S.; Jung, I.H. Thermodynamic modeling of the quaternary Al-Cu-Mg-Si system. *Calphad* **2017**, *57*, 1–27. [CrossRef]
66. He, Y.; Jia, Z.; Sanders, R.E.; Liu, Y.Y.; Ding, L.P.; Xing, Y.; Liu, Q. Quantitative study of dissolution of Mg2Si during solution treatment in AA6014 alloy. *J. Alloys Compd.* **2017**, *703*, 272–279. [CrossRef]

67. Chen, G.; Chen, L.; Zhao, G.; Zhang, C.S. Microstructure evolution during solution treatment of extruded Al-Zn-Mg profile containing a longitudinal weld seam. *J. Alloys Compd.* **2017**, *729*, 210–221. [CrossRef]
68. Tang, K.; Du, Q.; Li, Y. Modelling microstructure evolution during casting, homogenization and ageing heat treatment of Al-Mg-Si-Cu-Fe-Mn alloys. *Calphad* **2018**, *63*, 164–184. [CrossRef]
69. Qi, Z.; Cong, B.; Qi, B.; Zhao, G.; Ding, J. Properties of wire+ arc additively manufactured 2024 aluminum alloy with different solution treatment temperature. *Mater. Lett.* **2018**, *230*, 275–278. [CrossRef]
70. Li, B.; Pan, Q.; Chen, C.; Wu, H.H.; Yin, Z.M. Effects of solution treatment on microstructural and mechanical properties of Al-Zn-Mg alloy by microalloying with Sc and Zr. *J. Alloys Compd.* **2016**, *664*, 553–564. [CrossRef]
71. Lados, D.A.; Apelian, D.; Wang, L. Solution treatment effects on microstructure and mechanical properties of Al-(1 to 13 pct) Si-Mg cast alloys. *Met. Mater. Trans. B* **2011**, *42*, 171–180. [CrossRef]
72. Lasa, L.; Rodriguez-Ibabe, J.M. Characterization of the dissolution of the Al_2Cu phase in two Al-Si-Cu-Mg casting alloys using calorimetry. *Mater. Charact.* **2002**, *48*, 371–378. [CrossRef]
73. Kang, H.J.; Jang, H.S.; Oh, S.H.; Yoon, P.H.; Lee, G.H.; Park, J.Y.; Kim, E.S.; Choi, Y.S. Effects of solution treatment temperature and time on the porosities and mechanical properties of vacuum die-casted and T6 heat-treated Al-Si-Mg alloy. *Vacuum* **2012**, *193*, 110536. [CrossRef]
74. Yang, C.L.; Li, Y.B.; Dang, B.; LÜ, H.B.; Liu, F. Effects of cooling rate on solution heat treatment of as-cast A356 alloy. *Trans. Nonferrous Met. Soc. China* **2015**, *25*, 3189–3196. [CrossRef]
75. Liu, M.; Zheng, R.; Xiao, W.; Peng, Q.M.; Yamagata, H.; Ma, C.L. Remarkable enhancement in precipitation hardening of Al7Si1.7Cu alloy by high pressure solution treatment. *Mater. Sci. Eng. A* **2018**, *735*, 378–381. [CrossRef]
76. Rometsch, P.A.; Arnberg, L.; Zhang, D.L. Modelling dissolution of Mg2Si and homogenisation in Al-Si-Mg casting alloys. *Int. J. Cast Met. Res.* **1999**, *12*, 1–8. [CrossRef]
77. Djurdjevic, M.; Stockwell, T.; Sokolowski, J. The effect of strontium on the microstructure of the aluminium-silicon and aluminium-copper eutectics in the 319 aluminium alloy. *Int. J. Cast Met. Res.* **1999**, *12*, 67–73. [CrossRef]
78. Han, Y.M.; Samuel, A.M.; Samuel, F.H.; Doty, H.W. Dissolution of Al2Cu phase in non-modified and Sr modified 319 type alloys. *Int. J. Cast Met. Res.* **2008**, *21*, 387–393. [CrossRef]
79. Han, Y.M.; Samuel, A.M.; Samuel, F.H.; Valtierra, S. Effect of solution heat treatment type on the dissolution of copper phases in Al-Si-Cu-Mg type alloys. *Trans. Am. Fish. Soc.* **2008**, *116*, 79–90.
80. Samuel, F.H. Incipient melting of Al5Mg8Si6Cu2 and Al2Cu intermetallics in unmodified and strontium-modified Al-Si-Cu-Mg (319) alloys during solution heat treatment. *J. Mater. Sci.* **1998**, *33*, 2283–2297. [CrossRef]
81. Zhang, M.S.; Liu, K.L.; Han, J.Q.; Qian, F.; Wang, J.S.; Guan, S.K. Investigating the role of Cu, Zr and V on the evolution of microstructure and properties of Al-Si-Mg cast alloys. *Mater. Today Commun.* **2021**, *26*, 102055. [CrossRef]
82. Toschi, S. Optimization of A354 Al-Si-Cu-Mg alloy heat treatment: Effect on microstructure, hardness, and tensile properties of peak aged and overaged alloy. *Metals* **2018**, *8*, 961. [CrossRef]
83. Lasa, L.; Rodriguez-Ibabe, J.M. Evolution of the main intermetallic phases in Al-Si-Cu-Mg casting alloys during solution treatment. *J. Mater. Sci.* **2004**, *39*, 1343–1355. [CrossRef]
84. Colley, L.J.; Wells, M.; Mackay, R.I.; Kasprzak, W. Dissolution of second phase particles in 319-type aluminium alloy. In *Heat Treating 2011: Proceedings of the 26th Conference, Cincinnati, OH, USA, 31 October–2 November 2011*; ASM International: Materials Park, OH, USA, 2011; pp. 189–198.
85. Sokolowski, J.H.; Sun, X.C.; Byczynski, G.; Northwood, D.O.; Thomas, R.; Esseltine, A. The removal of copper-phase segregation and the subsequent improvement in mechanical properties of cast 319 aluminium alloys by a two-stage solution heat treatment. *J. Mater. Process. Technol.* **1995**, *53*, 385–392. [CrossRef]
86. Ågren, J. Calculation of phase diagrams: Calphad. *Curr. Opin. Solid State Mater. Sci.* **1996**, *1*, 355–360. [CrossRef]
87. Sha, G.; O'Reilly, K.A.O.; Cantor, B.; Titchmarsh, J.M.; Hamerton, R.G. Quasi-peritectic solidification reactions in 6xxx series wrought Al alloys. *Acta Mater.* **2003**, *51*, 1883–1897. [CrossRef]
88. Jung, J.G.; Cho, Y.H.; Lee, J.M.; Kim, H.W.; Euh, K. Designing the composition and processing route of aluminum alloys using CALPHAD: Case studies. *Calphad* **2019**, *64*, 236–247. [CrossRef]
89. Li, Q.; Zhao, Y.Z.; Luo, Q.; Chen, S.L.; Zhang, J.Y.; Chou, K.C. Experimental study and phase diagram calculation in Al-Zn-Mg-Si quaternary system. *J. Alloys Compd.* **2010**, *501*, 282–290. [CrossRef]
90. Zhang, M.S.; Wang, J.S.; Han, J.Q.; Sui, H.M.; Huang, H.B.; Jin, K.; Qian, F. Optimization of heat treatment process of Al-Mg-Si cast alloys with Zn additions by simulation and experimental investigations. *Calphad* **2019**, *67*, 101684. [CrossRef]
91. Liu, Y.; Jiang, D.M.; Li, W.J. The effect of multistage ageing on microstructure and mechanical properties of 7050 alloy. *J. Alloys Compd.* **2016**, *671*, 408–418. [CrossRef]
92. Yang, R.; Liu, Z.; Ying, P.; Li, J.L.; Lin, L.H.; Zeng, S.M. Multistage-aging process effect on formation of GP zones and mechanical properties in Al-Zn-Mg-Cu alloy. *Trans. Nonferrous Met. Soc. China* **2016**, *26*, 1183–1190. [CrossRef]
93. Kasprzak, W.; Amirkhiz, B.S.; Niewczas, M. Structure and properties of cast Al-Si based alloy with Zr-V-Ti additions and its evaluation of high temperature performance. *J. Alloys Compd.* **2014**, *595*, 67–79. [CrossRef]
94. Sjölander, E.; Seifeddine, S. Artificial ageing of Al-Si-Cu-Mg casting alloys. *Mater. Sci. Eng. A* **2011**, *528*, 7402–7409. [CrossRef]
95. Li, R.X.; Li, R.D.; Zhao, Y.H.; He, L.Z.; Li, C.X.; Guan, H.R.; Hu, Z.Q. Age-hardening behavior of cast Al-Si base alloy. *Mater. Lett.* **2004**, *58*, 2096–2101. [CrossRef]

96. Wang, F.; Wen, M.; Zhang, H.; Han, Z.Q. Effects of under-aging treatment on microstructure and mechanical properties of squeeze-cast Al-Zn-Mg-Cu alloy. *Trans. Nonferrous Met. Soc. China* **2018**, *28*, 1920–1927. [CrossRef]
97. Marioara, C.D.; Andersen, S.J.; Stene, T.N.; Hasting, H.; Walmsley, J.; Van Helvoort, A.T.J.; Holmestad, R. The effect of Cu on precipitation in Al-Mg-Si alloys. *Philos. Mag.* **2007**, *87*, 3385–3413. [CrossRef]
98. Zhang, D.L.; Zheng, L.H.; Stjohn, D.H. Effect of a short solution treatment time on microstructure and mechanical properties of modified Al-7wt.%Si-0.3wt.%Mg alloy. *J. Light Met.* **2002**, *2*, 27–36. [CrossRef]
99. Mohamed, A.M.A.; Samuel, F. A Review on the Heat Treatment of Al-Si-Cu/Mg Casting Alloys. In *Heat Treatment: Conventional and Novel Applications*; InTech: Rijeka, Croatia, 2012; pp. 55–72.
100. Mørtsell, E.A.; Qian, F.; Marioara, C.D.; Li, Y.J. Precipitation in an A356 foundry alloy with Cu additions-A transmission electron microscopy study. *J. Alloys Compd.* **2019**, *785*, 1106–1114. [CrossRef]
101. Zheng, Y.; Xiao, W.L.; Ge, S.J.; Zhao, W.T.; Hanada, S.J.; Ma, C.L. Effects of Cu content and Cu/Mg ratio on the microstructure and mechanical properties of Al-Si-Cu-Mg alloys. *J. Alloys Compd.* **2015**, *649*, 291–296. [CrossRef]

materials

MDPI

Article

A Machine Learning Method for Predicting Corrosion Weight Gain of Uranium and Uranium Alloys

Xiaoyuan Wang, Wanying Zhang, Weidong Zhang * and Yibo Ai *

National Center for Materials and Service Safety, University of Science and Technology Beijing, Beijing 100083, China

* Correspondence: zwdpaper@163.com (W.Z.); ybai@ustb.edu.cn (Y.A.)

Abstract: As an irreplaceable structural and functional material in strategic equipment, uranium and uranium alloys are generally susceptible to corrosion reactions during service, and predicting corrosion behavior has important research significance. There have been substantial studies conducted on metal corrosion research. Accelerated experiments can shorten the test time, but there are still differences in real corrosion processes. Numerical simulation methods can avoid radioactive experiments, but it is difficult to fully simulate a real corrosion environment. The modeling of real corrosion data using machine learning methods allows for effective corrosion prediction. This research used machine learning methods to study the corrosion of uranium and uranium alloys in air and established a corrosion weight gain prediction model. Eleven classic machine learning algorithms for regression were compared and a ten-fold cross validation method was used to choose the highest accuracy algorithm, which was the extra trees algorithm. Feature selection methods, including the extra trees and Pearson correlation analysis methods, were used to select the most important four factors in corrosion weight gain. As a result, the prediction accuracy of the corrosion weight gain prediction model was 96.8%, which could determine a good prediction of corrosion for uranium and uranium alloys.

Keywords: uranium; uranium alloy; corrosion; machine learning; extra trees; feature selection

Citation: Wang, X.; Zhang, W.; Zhang, W.; Ai, Y. A Machine Learning Method for Predicting Corrosion Weight Gain of Uranium and Uranium Alloys. *Materials* **2023**, *16*, 631. https://doi.org/10.3390/ma16020631

Academic Editor: Hendra Hermawan

Received: 12 December 2022
Revised: 1 January 2023
Accepted: 4 January 2023
Published: 9 January 2023

1. Introduction

Uranium and uranium alloys are irreplaceable structural and functional materials in strategic equipment. However, uranium's unique $5f^3 6d^1 7s^2$ electron arrangement makes it highly chemically reactive and environmentally sensitive, which makes uranium and uranium alloy key structural components highly susceptible to corrosion during long-term service, which, in severe cases, can affect the function of the components, reduce their life, and even cause the failure of the entire device. The accurate and timely assessment of atmospheric corrosion provides important guidance for the material selection and engineering design for corrosion mitigation [1]. Numerous studies on corrosion have been conducted by various researchers. Kelly et al. [2] investigated the relative oxidation and corrosion rates of U–Nb alloys in different temperatures using X-ray photoelectron spectroscopy and neutral mass spectrometry sputtering depth profiling. Zubelewicz et al. [3] presented a constitutive model of a U–6Nb alloy, including the effects of elasticity, crystal reorientation, phase transformations, and plasticity. Wang et al. [4] investigated the oxidative performance of U–2.5Nb alloys at different temperatures in air using the thick weight and weight gain methods. Wang et al. [5] researched the oxidation kinetics of uranium at different times by using a combination of oxygen depletion and reflectance spectroscopy methods. The above studies were instructive for the data collection and study of corrosion mechanisms of uranium and uranium alloys in this paper.

Accelerated corrosion tests have traditionally been conducted to simulate corrosion behavior in a variety of environments, with various electrochemical techniques widely used

to predict the corrosion behavior of metals [6]. Li et al. [7] established a prediction model of uranium oxidation and verified it via a 4-year experiment with kinetics parameters obtained through simulated storage and accelerated experiments. Tom et al. [8] presented a description of the implementation of corrosion products into a predictive corrosion model that can be used for the numerical simulation or empirical prediction of uniform corrosion progression. Wang et al. [9] built a model to predict the corrosion behavior of a low-alloy steel in an acidic NaCl solution by using the gray system theory. Accelerated corrosion tests were conducted to calculate the corrosion rate; the feasibility of the model was proved with the simulation results. Although the traditional accelerated simulation test can effectively reduce the test time, there still tend to be some deviations between the simulation test and the actual experimental results. Therefore, the modeling method based on experimental data has also been widely studied by many researchers [10]. Corrosion data are often incomplete, noisy, nonuniform, and bulky (sparse data density). In addition, the service corrosion scene is complex and variable, presenting a highly nonlinear system that is difficult to achieve with traditional statistical methods [6]. Machine learning is a subfield of artificial intelligence (AI), which allows a computer to learn from data to solve a specific task. It includes a flexible method of fitting functions that provides an inexpensive and accurate simulation process compared to traditional computational methods [11–13]. Diao et al. [10] collected corrosion data for steels immersed in seawater and built a corrosion rate prediction model of low-alloy steels by using a random forest algorithm. Additionally, they used the gradient boost decision tree (GBDT) algorithm to conduct a feature reduction. However, the GBDT algorithm is sensitive to outliers, and to prevent abnormal data from affecting the feature selection results, extra trees to perform feature selection can be used. Yuan et al. [14] proposed a machine learning model with characteristic parameter embedding to predict and design γ-U alloys in U–Mo–Nb–Ti–Zr systems by using XGBoost regression and genetic algorithm. Using a random forest algorithm, Pei et al. [1] studied the effect of different factors and gas content on atmospheric corrosion. Mythreyi et al. [15] used the extreme gradient boosting algorithm to predict the corrosion performance of the postprocessing and laser-powder-bed-fused (LPBF) Inconel 718. Researchers use a variety of machine learning algorithms when studying corrosion; therefore, in this paper, we first compare 11 classical machine learning regression algorithms in order to select the most applicable one for our data.

As mentioned above, by using machine learning, the data concerning corrosion could be used to achieve more accurate corrosion evaluations. This research applied machine learning methods to the data obtained from previous studies and evaluated the corrosion weight gain of different uranium and uranium alloys in air. Ten-fold cross validation was used to choose the best algorithms, and a combination of extra trees and Pearson correlation coefficient methods was used to perform the feature selection. Finally, a corrosion weight gain prediction model was built.

2. Methods

2.1. Corrosion Data and Data Preprocessing

The corrosion data we utilized in this research were obtained from previous experimental studies [4,16,17]. We collected 442 rows of laboratory oxidation corrosion data for 8 uranium and uranium alloys in dry air and wet air. The 4 material properties (i.e., type, impurity, phase number, and phase type) of uranium and uranium alloys, 3 typical environmental features (i.e., medium, temperature, and pressure), and corrosion time were also recorded. The corrosion of uranium in air is mainly an oxidation reaction:

$$U + \left(\frac{2+x}{2}\right)O_2 = UO_{2+x} \quad (1)$$

$$U + (2+x)H_2O = UO_{2+x} + (2+x)H_2 \quad (2)$$

From the above equation, it can be seen that the overall mass of the sample would increase after being corroded, so the weight gain was used as an output to measure the corrosion process. As shown in Table 1, each corrosion data contained 8 input features and 1 output feature. Furthermore, we employed data preprocessing, removed duplicates and anomalies, and interpolated the data with missing values. We numerated the features whose values were textual, thus, converting categorical features into quantitative variables. For the feature "Type", we denoted it with "m.n", where the values of m were 1 and 2 for uranium and uranium alloys, respectively, n for swelling when m = 1, and n for the alloy composition when m = 2. For the feature "Phase_type", we denoted it with "p.q", where the values of p are the number of phases and q represents the specific phase. For the feature "Medium", 1 was for dry air and 2 for humid air. As shown in Figure 1, we plotted the scatter plot of weight gain with respect to time. It can be seen that the oxidation kinetic curves of uranium and the uranium alloys were different due to different factors, such as alloy composition and temperature.

Table 1. Description of features in corrosion data.

Features		Unit	Data Range
Material	Type	Data	1–3
	Impurity	%	0.0005–0.002
	Phase_number	Number	1,2
	Phase_type	\	1–3
Environmental	Medium	\	1–2
	Temperature	K	323–573
	Pressure	$\times 10^5$ Pa	1.01325
Reaction time	Time	h	0–200,463
Corrosion weight gain	Weight_gain	mg/cm^2	0–25

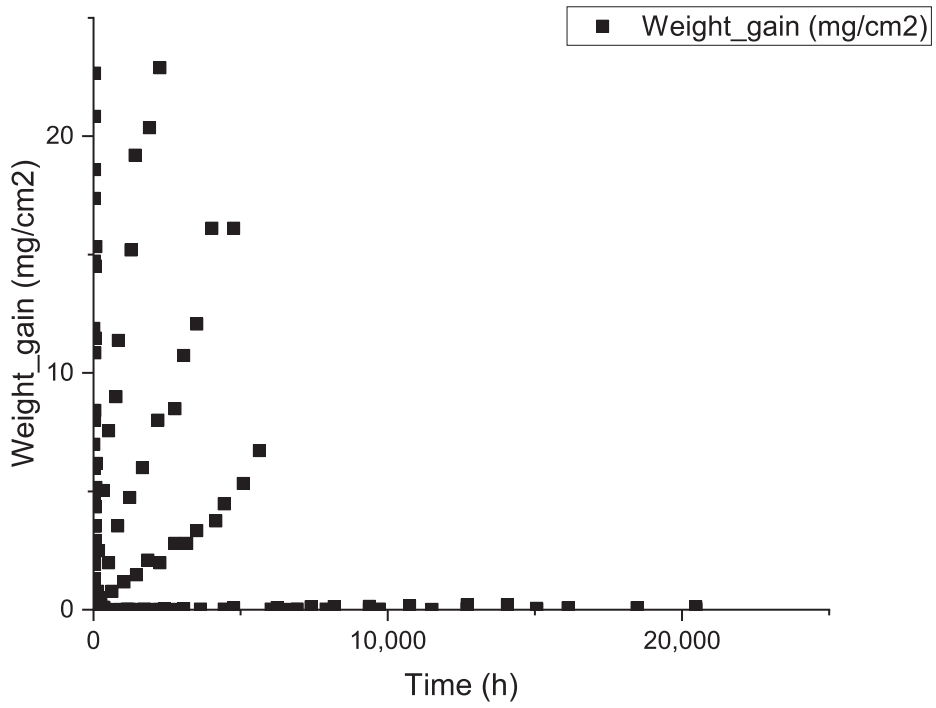

Figure 1. Scatter plot of corrosion weight gain over time for initial data.

2.2. Feature Selection

Feature selection refers to the selection of the most critical features from original features to reduce the dimensionality of a dataset. This can eliminate redundant and less relevant features, mitigating dimensional issues and improving the performance of machine learning models. Feature selection methods are mainly divided into filtered selection, wrapped selection, and embedded selection [18]. In this research, a combination of the extra trees algorithm and Pearson correlation analysis were used to perform the feature selection. The extra trees algorithm is an ensemble learning method in which each decision tree is constructed from the raw training dataset. Each tree randomly selects k features, each feature randomly selects a split node, and then a score for each split node is calculated based on some mathematical metrics (e.g., the Gini index); the node with the highest score is selected as the final split node [19]. This random feature selection makes the randomness of each sub model greater, which suppresses the overfitting of the whole model. In constructing the forest, the normalized total reduction was calculated for each feature using the Gini coefficient, which is the relative importance of that feature. The Pearson correlation method was used to measure the correlation between any two features, and had a value between -1 and 1. A higher Pearson correlation coefficient value indicated a higher correlation between the two variables. Only one of the highest correlation features was selected as an input feature to reduce unnecessary information [20]. Based on the results generated with the two methods mentioned above, several key features could be selected from the original feature set.

2.3. Modeling Process

In this research, the processed dataset was divided into a training set and a validation set with various division ratios (i.e., the percentages of the training set were 40%, 50%, 60%, 70%, 80%, and 90%), where the training set was used in the model training phase to estimate the parameters in the model and the validation set was used in the model evaluation phase to verify the predictive accuracy of the model. Then, the predictive performance of 11 classic machine learning algorithms (linear regression, decision tree, extra trees, random forest regression (RFR), kernel ridge regression (KRR), K nearest neighbors (KNN), AdaBoost, gradient boost, bagging, support vector regression (SVR), and light gradient boosting (LGB)) in corrosion weight gain prediction was first compared. After that, several of the relatively well-performing models were then compared after a ten-fold cross-validation [21], and the algorithm with the highest prediction accuracy was selected for subsequent modeling studies. Secondly, feature methods were used to reduce redundant features. Finally, corrosion weight gain prediction models with and without feature selection were established and compared.

The machine learning algorithms used in this research were implemented in Python V3.9 with the Scikit-learn V1.1.2 library. The parameters used to measure the accuracy of the model were as follows:

The coefficient of determination (R^2) is a standard measurement of how well a model fits the data, and it measures the closeness between the observed values and the fitted regression line. The root mean square error (RMSE) is a standard way to quantify the overall error of a regression model, evaluating the deviation between the predicted values and true values. Their specific equations were as follows:

$$R^2 = 1 - \frac{\sum_{i=1}^{n}(y_i - \hat{y}_i)^2}{\sum_{i=1}^{n}(\hat{y}_i - \overline{y}_i)^2 + \sum_{i=1}^{n}(y_i - \hat{y}_i)^2} \tag{3}$$

$$RMSE = \sqrt{\frac{1}{n}\sum_{i=1}^{n}(y_i - \hat{y}_i)^2} \tag{4}$$

where y_i denotes the actual value, $\hat{y}_i$ represents the predicted value, and $\overline{y}_i$ is the mean value of the output.

3. Results and Discussion

3.1. Comparison of Different Algorithms

The percentages of the training sets to the total datasets were set to 40%, 50%, 60%, 70%, 80%, and 90%, respectively. As shown in Figure 2, the RFR model, extra trees model, gradient boost model, decision tree model, and bagging model had better prediction performance on the validation set than others with different training set division ratios. At the same time, the more data in the training set, the higher the prediction accuracy of most models. In general, the amount of data determines, to some extent, the amount of information it contains. Therefore, in the absence of overfitting, more training data were usually useful for the model to exploit potential relationships that exist in the input features and target attributes. Consequently, a training set ratio of 90% was employed in this research.

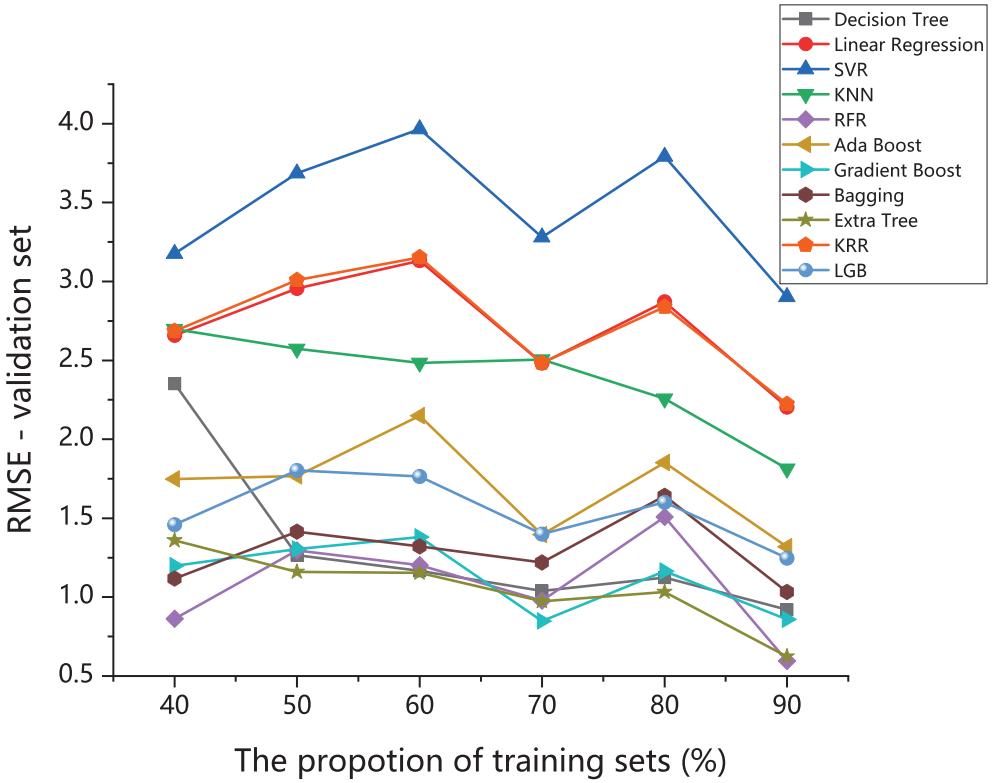

Figure 2. Predictive performance of the decision tree, linear regression, SVR, KNN, KRR, RFR, AdaBoost, gradient boost, bagging, extra trees, and LGB algorithms in different training set division ratios.

In addition, a ten-fold cross-validation was used for the five models mentioned above to reduce the effect of overfitting in the nonlinear regression. As depicted in Figure 3, the extra trees algorithm had the best predictive performance in the ten-fold cross-validation. Thus, the extra trees algorithm was employed in this research. Additionally, for the extra trees algorithm, the maximum RMSE in the ten-fold cross-validation was 1.858, which was more than twice the final average RMSE. Therefore, it can be seen that the ten-fold cross-validation greatly reduced the uncertainty in the selection of the validation set.

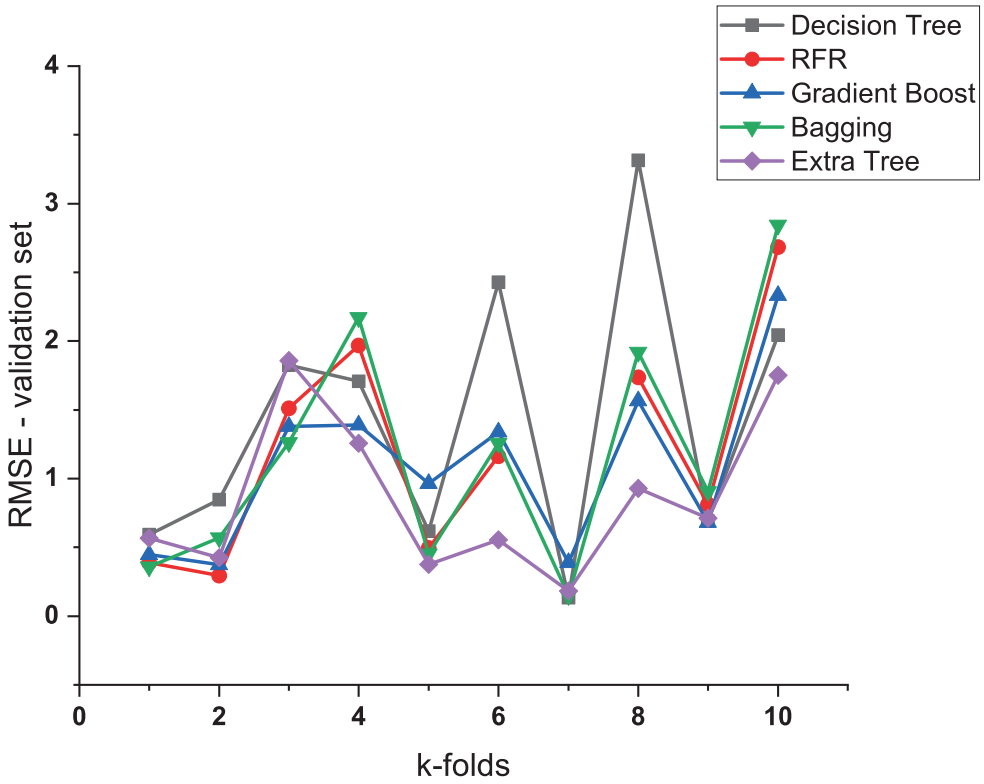

Figure 3. Ten-fold cross-validation comparison of RFR, extra trees, gradient boost, decision tree, and bagging algorithms.

3.2. Results of Feature Selection

The extra trees method was first used to estimate the correlation between the input features and corrosion weight gain, with the relative importance of each feature shown in Figure 4. To ensure that important features were not lost, we selected features with a relative importance value higher than 0.03 (i.e., the type, impurity, phase_number, and phase_type of material factors and the temperature of environmental factors) as inputs to the model. Additionally, it can be seen that the temperature, type, and impurity were the three most important factors affecting the corrosion of uranium and uranium alloys. Different material types have different corrosion mechanisms, and, in general, alloys have better corrosion resistance than original metals. The corrosion resistance of uranium alloys is closely related to the type of alloying elements, especially to the content of solute elements in uranium alloys. The temperature is also an important factor that affects the corrosion behavior of metals. At low temperatures, the oxidation rate of uranium or uranium alloys is slow, and the initial duration of the reaction is long, while at high temperatures, the oxidation rate is very fast and the initial duration of the reaction is usually short. The number of phases and the type of phase in the microstructure of the uranium alloy are also important factors influencing corrosion performance. The reaction medium and ambient pressure also affect the corrosion behavior, but the data used in this research were all corrosion data in air, so the importance of the characteristics of the medium and pressure was low.

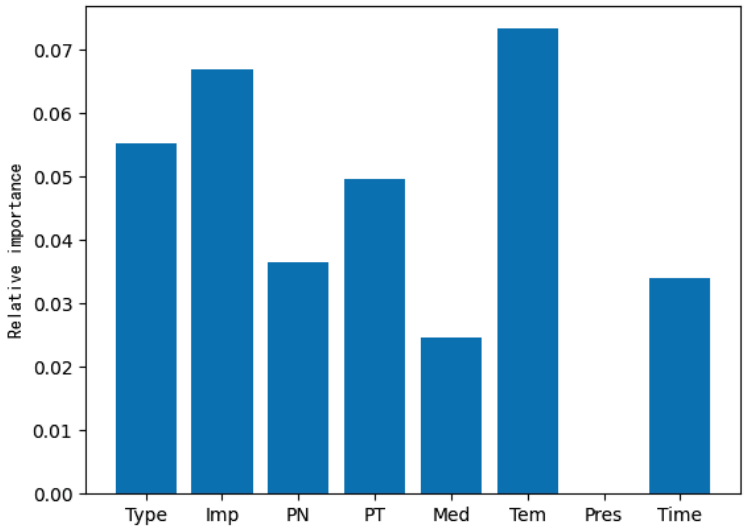

Figure 4. The relative importance of input features with respect to corrosion weight gain evaluated with the extra trees method.

As can be seen in Figure 5, several pairs of input features with strong correlations (i.e., the value of the Pearson correlation coefficient was greater than 0.90) were indicated in red. Among the above selected input features, three pairs of features (i.e., the type and phase_number the type and phase_type, and the phase_number and phase_type) were marked. Simply selecting one feature from each pair of the relevant features mentioned above would give enough information [22]. Typically, features with larger values of relative importance (Figure 3) correlate more with the target attribute (i.e., corrosion weight gain). Therefore, the Type was selected among the three pairs of material features mentioned above. Finally, features, including the Type, Impurity, Temperature, and Time, were selected as the input features of the corrosion weight gain prediction model for uranium and uranium alloys.

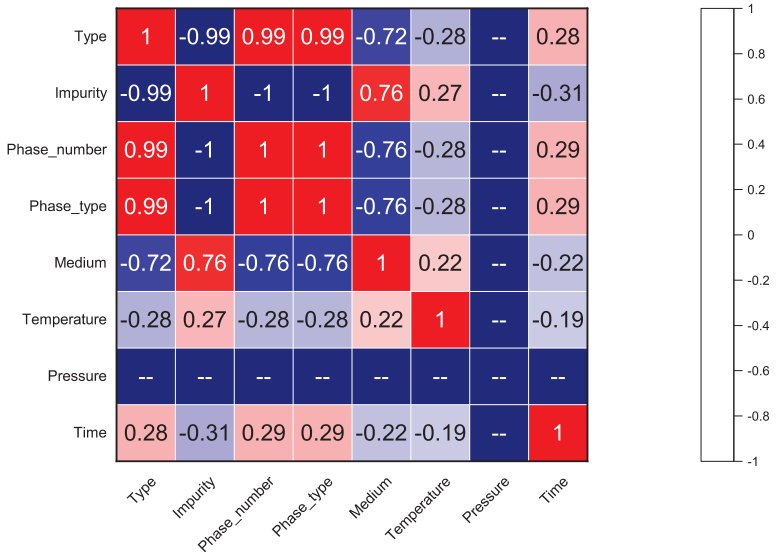

Figure 5. The Pearson correlation map of input features.

3.3. Evaluation Results

The performance of the corrosion weight gain prediction models for uranium and uranium alloys with and without feature selection is shown in Figure 6. The green and red lines represent the true and predicted values of the corrosion weight gain for the validation set data, respectively. The *x*-axis represents the samples in the validation set, where each

sample contains seven input features and the *y*-axis represents the weight gain, which is the output corresponding to each sample. The values of RMSE and R^2 of the two models are given in Table 2. Obviously, the R^2 of both models exceeded 90%, and the RMSE was below 0.7. In addition, by using the out-of-tree and Pearson correlation coefficient methods, R^2 improved by 0.037% and RMSE decreased by 0.118 compared to the model without the feature selection method. Therefore, the prediction accuracy of the model could be improved by performing feature selection. However, the feature selection also removed the phase organization type, which had an important effect on corrosion behavior, probably because the data in this study were not complex enough and the phase organization type was relatively single. Both models, with and without feature selection, had a satisfactory prediction performance. The good prediction accuracy of the model showed that the corrosion weight gain prediction model should have mastered the influence law of each input feature and the effect of their interaction on the corrosion weight gain. Additionally, the hyperparameters of the model were listed in Table 3.

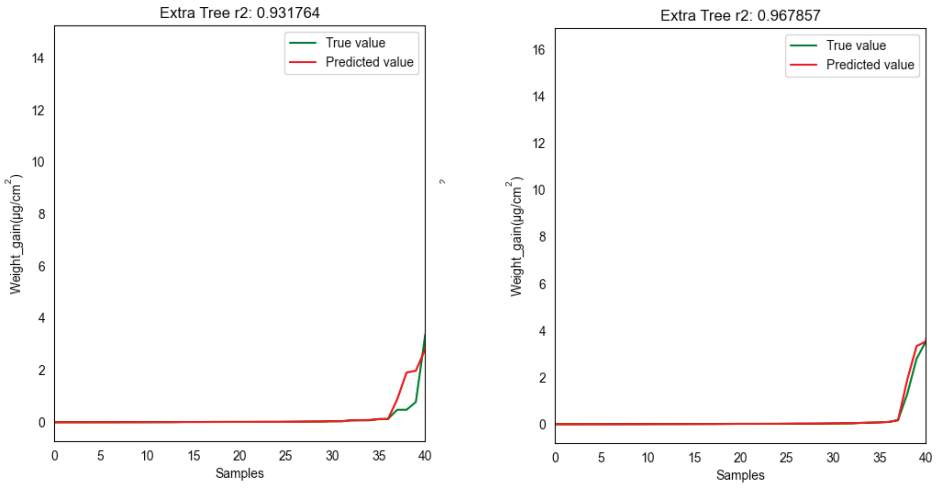

(**a**) (**b**)

Figure 6. Predictive performance of the models (**a**) with and (**b**) without feature selection.

Table 2. RMSE and R^2 values for corrosion weight gain prediction models with and without feature selection.

Methods	RMSE	R^2
Without feature selection	0.634	0.931
With feature selection	0.516	0.968

Table 3. Hyperparameters of the corrosion weight gain prediction model with feature selection.

Hyperparameter	Value
criterion	"squared_error"
splitter	"random"
max_depth	None
min_samples_split	2
min_samples_leaf	1
min_weight_fraction_leaf	0.0
Max_features	1.0
Max_leaf_nodes	None
min_impurity_decrease	0.0
random_state	None
ccp_alpha	0.0

4. Conclusions

In this research, we compared 11 classic machine learning models for the corrosion weight gain prediction of uranium and uranium alloys. The extra trees model, which had the highest prediction accuracy, was selected for predicting corrosion. The model was trained using the following features: type, impurity, phase_number, phase_type, medium, temperature, pressure, and time. Then, a feature selection was performed using the extra trees and Pearson methods, with which redundant features were eliminated. It was found that the prediction accuracy of the model after performing the feature selection was 96.8%, which was a 3% improvement over the previous one, and was able to predict the corrosion data well. Based on the above results, machine learning methods can make sufficient use of corrosion data to determine predictions about corrosion behavior, providing an effective way for performing corrosion research. However, a limitation of this study was that this corrosion weight gain prediction model was only applicable to corrosion data similar to the data in this paper. In our future research, we aim to gather new data that are "unknown" to the model during the training, optimization and validation phases, to create an unbiased evaluation of models, and, if possible, to obtain richer data to further optimize the model for the better prediction of corrosion behavior.

Supplementary Materials: The following supporting information can be downloaded at: https://www.mdpi.com/article/10.3390/ma16020631/s1, Data: manuscript-supplementary.xlsx.

Author Contributions: Conceptualization, X.W. and Y.A.; methodology, X.W.; software, X.W.; validation, X.W. and W.Z. (Wanying Zhang); formal analysis, X.W.; investigation, X.W. and W.Z. (Wanying Zhang); data curation, X.W. and W.Z. (Wanying Zhang); writing—original draft preparation, X.W.; writing—review and editing, X.W. and Y.A.; visualization, X.W.; supervision, Y.A.; project administration, W.Z. (Weidong Zhang); funding acquisition, W.Z. (Weidong Zhang). All authors have read and agreed to the published version of the manuscript.

Funding: This research was funded by the National Key R&D Program of China for Ministry of Science and Technology of the People's Republic of China, grant number 2021YFA1601100.

Institutional Review Board Statement: Not applicable.

Informed Consent Statement: Not applicable.

Data Availability Statement: The data that supported the findings of this research are in the Supplementary Materials. The code for this work is available on GitHub: "https://github.com/Ca11meMaybe/corrosion-prediction", accessed on 2 January 2023.

Conflicts of Interest: The authors declare no conflict of interest.

References

1. Pei, Z.; Zhang, D.; Zhi, Y.; Yang, T.; Jin, L.; Fu, D.; Cheng, X.; Terryn, H.A.; Mol, J.M.C.; Li, X. Towards understanding and prediction of atmospheric corrosion of an Fe/Cu corrosion sensor via machine learning. *Corros. Sci.* **2020**, *170*, 108697. [CrossRef]
2. Kelly, D.; Lillard, J.A. Surface characterization of oxidative corrosion of uranium-niobium alloys. In Proceedings of the American Vacuum Society 2000 Meeting, Boston, MA, USA, 2–6 October 2000.
3. Zubelewicz, A.; Aleksander, F.L. A constitutive model for a uranium-niobium alloy. *J. Appl. Phys.* **2006**, *100*, 013523. [CrossRef]
4. Yang, J.; Wang, X.L.; Zhou, P.; Lang, D.M.; Xiao, H. Oxidation of U-2.5%Nb Alloy in Air. *J. Nucl. Radiochem.* **2009**, *31*, 129–133.
5. Wang, S.P.; Li, H.B.; Li, G.; Tang, T.; Gu, Y.J.; Hu, Y.; Chen, X.L.; Wang, Y.; Lv, J.B.; Luo, W.H. The oxidative kinetics of uranium at different stages. *Corros. Sci.* **2022**, *206*, 110487. [CrossRef]
6. Coelho, L.B.; Zhang, D.W.; Ingelgem, Y.V. Reviewing machine learning of corrosion prediction in a data-oriented perspective. *NPJ Mater. Degrad.* **2022**, *6*, 8. [CrossRef]
7. Li, H.; Ding, Q.; Gu, Y. The initial oxidation behavior of uranium and uranium-titanium alloys in standing storage. *Corros. Sci.* **2020**, *176*, 108879. [CrossRef]
8. Tom, G.; Andreas, M.; Daniel, H.; Mikhail, Z.; Kainer, K.U. Enhanced predictive corrosion modeling with implicit corrosion products. *Mater. Corros.* **2020**, *70*, 2247–2255.
9. Wang, H.W.; Yu, C.; Wang, S.X.; Gao, J. Electrochemical Corrosion Behavior and Prediction of Corrosion Rate for Low Alloy Steel after Tempering Treatment. *Int. J. Electrochem. Sci.* **2015**, *10*, 1169–1185.
10. Diao, Y.P.; Yan, L.C.; Gao, K.W. Improvement of the machine learning-based corrosion rate prediction model through the optimization of input features. *Mater. Des.* **2021**, *198*, 109326. [CrossRef]

11. Liu, Y.; Guo, B.; Zou, X.; Li, Y.; Shi, S. Machine learning assisted materials design and discovery for rechargeable batteries. *Energy Storage Mater.* **2020**, *31*, 434–450. [CrossRef]
12. Chen, A.; Zhang, X.; Zhou, Z. Machine learning: Accelerating materials development for energy storage and conversion. *InfoMat* **2020**, *2*, 553–576. [CrossRef]
13. Deringer, V.L. Modelling and understanding battery materials with machine-learning-driven atomistic simulations. *J. Phys. Energy.* **2020**, *2*, 041003. [CrossRef]
14. Yuan, J.H.; Wang, Q.; Li, Z.; Dong, C.; Zhang, P.C.; Ding, X.L. Domain-knowledge-oriented data pre-processing and machine learning of corrosion-resistant γ-U alloys with a small database. *Comput. Mater. Sci.* **2021**, *194*, 110472. [CrossRef]
15. Mythreyi, O.V.; Srinivaas, M.R.; Kumar, T.A.; Jayaganthan, R. Machine-Learning-Based Prediction of Corrosion Behavior in Additively Manufactured Inconel 718. *Data* **2021**, *6*, 80. [CrossRef]
16. Bennett, M.J.; Myatt, B.L.; Silvester, D.R.V.; Antill, J.E. The oxidation behaviour of uranium in air at 50–300 °C. *J. Nucl. Mater.* **1975**, *57*, 221–236. [CrossRef]
17. Yang, J.; Wang, X.L.; Luo, L.Z.; Zhou, P. Investigation of oxidation of a U-2.5 wt% Nb alloy in air at low temperatures: Kinetic study and oxide characterization. *Surf. Interface Anal.* **2008**, *40*, 299–302.
18. Guyon, I.; Gunn, S.R.; Nikravesh, M.; Zadeh, L.A. *Feature Extraction Foundations and Applications*; Springer: Berlin, Germany, 2006.
19. Alfian, G.; Syafrudin, M.; Fahrurrozi, I.; Fitriyani, N.L.; Atmaji, F.T.D.; Widodo, T.; Bahiyah, N.; Benes, F.; Rhee, J. Predicting Breast Cancer from Risk Factors Using SVM and Extra-Trees-Based FeatureSelection Method. *Computers* **2022**, *11*, 136. [CrossRef]
20. Wen, C.; Zhang, Y.; Wang, C.; Xue, D.; Bai, Y.; Antonov, S.; Dai, L.; Lookman, T.; Su, Y. Machine learning assisted design of high entropy alloys with desired property. *Acta Mater.* **2019**, *170*, 109–117. [CrossRef]
21. Stone, M. Cross-validatory choice and assessment of statistical predictions. *J. R. Stat. Soc. Ser. B* **1974**, *36*, 111–133. [CrossRef]
22. Wang, Y.; Tian, Y.; Kirk, T.; Laris, O.; Ross, J.H.; Noebe, R.D.; Keylin, V.; Arroyave, R. Accelerated design of Fe-based soft magnetic materials using machine learning and stochastic optimization. *Acta Mater.* **2020**, *194*, 144–155. [CrossRef]

MDPI
St. Alban-Anlage 66
4052 Basel
Switzerland
www.mdpi.com

Materials Editorial Office
E-mail: materials@mdpi.com
www.mdpi.com/journal/materials

MDPI

Academic Open
Access Publishing

mdpi.com

ISBN 978-3-7258-1203-5